

Lecture Notes in Nuclear Structure Physics ¹

B. Alex Brown

National Superconducting Cyclotron Laboratory
and Department of Physics and Astronomy
Michigan State University, E. Lansing, MI 48824

¹©Copyright 2021 Michigan State University

Contents

1	Introduction	4
2	Nuclear masses	19
2.1	Masses and binding energies	20
2.2	Q values and separation energies	27
3	Excitation energies of even-even nuclei	45

4 Rms radii	55
4.1 Charge and proton radii	56
4.2 Neutron rms radii and the neutron skin	66
5 Charge densities and form factors	71
6 The liquid-drop model	88
7 Overview of nuclear decays	105
7.1 Decay widths and lifetimes	110
7.2 Alpha and cluster decay	113
7.3 Beta decay	129
7.3.1 Beta decay Q values	135
7.3.2 Allowed beta decay	140
7.3.3 Phase-space for allowed beta decay	144
7.3.4 Weak-interaction coupling constants	148
7.3.5 Double beta decay	150
7.4 Electromagnetic decay	153

7.4.1	Reduced transition probabilities for gamma decay	158
7.4.2	Weisskopf units for gamma decay	167
7.4.3	Measured B(E2) from the ground states of even-even nuclei	168
8	Electromagnetic Moments	177
8.1	Magnetic moments	180
8.2	Electric quadrupole moments	184
9	Conserved quantum numbers	193
9.1	Angular momentum	194
9.2	Parity	195
9.3	Isospin	197
10	Angular momentum and tensor algebra	201
10.1	Angular Momentum Operators	202
10.2	Spherical Harmonics	204
10.3	Angular momentum coupling	209
10.3.1	Coupling of Two Angular Momenta	210

10.3.2	Coupling of Three Angular Momenta	215
10.3.3	Coupling of Four Angular Momenta	221
10.4	Tensors and reduced matrix elements	224
10.4.1	Special reduced matrix elements	229
10.4.2	Products of tensor operators	230
10.5	Single-particle wavefunctions in a spherical basis	235
11	The Isobaric-Mass-Multiplet Equation	244
12	The Fermi gas model	258
13	The general many-body problem for fermions	266
13.1	General forms of the many-body wavefunctions and methods of solution . . .	267
13.2	Closed-shell, particle, and hole configurations	275
13.3	Derivation of the Hartree-Fock equations	278
13.4	The total energy	283
14	Overview of the nuclear shell model	287

15 Single particle (hole) energies	301
16 The harmonic oscillator potential	309
16.1 General properties	310
16.2 The harmonic oscillator in Cartesian coordinates	316
16.3 The deformed harmonic oscillator	319
16.4 Transformation from relative to center-of-mass coordinates for two nucleons .	323
16.5 Separation of intrinsic and center-of-mass motion for many nucleons	326
16.5.1 The kinetic energy part	326
16.5.2 The harmonic-oscillator part	330
17 The Woods-Saxon potential	337
17.1 General form	338
17.2 Computer program for the Woods-Saxon potential	346
17.2.1 Example for bound states	348
17.2.2 Changing the potential parameters	351
17.2.3 Width of an unbound state resonance	354

17.2.4 Width of an unbound state resonance at a fixed energy	357
18 One-body operators in simple configurations	361
18.1 Density for a closed-shell configuration	362
18.2 Angular momenta for closed-shell, and single-particle, and single-hole config- urations	364
18.3 Electromagnetic moments	365
18.4 Moments for single-particle and single-hole configurations	367
18.5 Magnetic moments	371
18.6 Electric quadrupole moments	376
19 Energy density functionals	379
19.1 The Skyrme energy-density functional	380
19.2 Nuclear matter with the Skyrme energy-density functional	393
19.3 Results with the skx functional	403
19.3.1 Binding energies	404
19.3.2 Single-particle energies	408

19.3.3 Rms charge radii and charge densities	418
19.3.4 Displacement energies	421
20 Overview of nuclear collective motion	443
20.1 The Wigner rotation matrix	445
20.2 The Bohr Hamiltonian	447
20.3 Rotations for a rigid rotor	457
20.4 Quadrupole moments and B(E2)	464
20.5 Vibrations	472
20.6 Other collective multiples	478
21 Single-particle energies in a deformed potential	484
22 The Creation operator method	497
22.1 Introduction	498
22.2 Creation Operators and Wavefunctions	498
22.3 One and Two Body Operators	504
22.4 Examples of a^+ and a Matrix Elements	507

22.5 Wick's Theorem	509
22.6 Operators Relative to a Closed-Shell Configuration	515
22.7 The Hartree-Fock Equations	518
23 Two-particle wavefunctions	525
23.1 Relative coordinates	526
23.1.1 Two neutrons or two protons	526
23.1.2 Proton-neutron	529
23.1.3 Two nucleons	530
23.2 Single-particle coordinates	533
24 Many-body wavefunctions	537
24.1 Wavefunctions in the m -scheme	538
24.2 Angular momentum projection	547
24.2.1 Examples for $[5/2]^n$ configurations	556
24.3 Wavefunctions in the J -scheme	561
24.4 Matrix elements in the J scheme	563

25 Two-body hamiltonian matrix elements	569
25.1 Introduction	570
25.2 Form of the two-body matrix elements	570
25.3 Conversion from isospin to proton-neutron form	574
25.4 General types of interactions	577
25.5 Simple potentials	582
25.6 One boson exchange potentials	584
25.7 Realistic potentials	586
25.8 Density-dependent interactions	591
25.9 The M3Y potential	594
25.10 Numerical examples	600
25.11 The N ³ LO potential	601
25.12 Three-body interactions	603
25.13 Multipole and spin-tensor decompositions	606
26 Model spaces	617
26.1 Commonly used model spaces for light and heavy nuclei	618

26.2 Intruder states and islands of inversion	620
27 Particle-hole States	631
27.1 Wavefunctions and energies	632
27.2 One-body matrix elements	636
27.3 The giant dipole excitation	642
27.4 Energy Weighted Sum Rules	645
28 Corrections to Operators in a Model Space	654
28.1 One-body operators and effective charge	656
28.2 Corrections to two-body Hamiltonian matrix elements	664
29 Effective Hamiltonians	676
29.1 Types of Hamiltonians	680
29.2 Hamiltonians for specific model spaces	683
29.3 Hamiltonians in the $jj44$ model space	683
29.4 The singular-value decomposition fit	687
29.4.1 The SVD method	687

29.4.2 Results for the <i>sd</i> shell	693
30 Energies for simple configurations (monopole energies)	707
30.1 Interaction energies for closed shell, one-particle and one-hole configurations	708
30.2 Interaction energies for diagonal two-particle configurations	717
30.3 Interaction energies for diagonal two-hole configurations	720
31 Configuration mixing	724
31.1 General two-state mixing	724
31.2 Two-state mixing for ^{18}O	728
31.3 Three-state mixing for ^{18}O	732
31.4 Many-particle configurations	735
32 Configuration-Interaction Codes	741
32.1 Types of basis states	742
32.2 The Lanczos method	744
32.3 The NuShellX code	748

33 The pairing part of the Hamiltonian	763
33.1 Experimental evidence for pairing	764
33.2 Many-body approximations for pairing	770
33.3 Pairing contributions to the nuclear binding energy	773
33.4 The surface-delta interaction model	779
33.5 The modified surface-delta interaction model	786
33.6 The surface-delta interaction plus Coulomb model	793
33.7 The surface-delta interaction model with a shell gap	793
33.8 Features for the calcium and chromium isotopes	798
33.9 Light nuclei toward the neutron drip line	807
33.10 Global results for neutrons and protons	813
34 Spectroscopic factors	823
34.1 Occupation numbers	826
34.2 Spectroscopic factors in proton-neutron formalism	828
34.3 Isospin dependence	834
34.4 Center-of-mass corrections	841

34.5 Overlap functions	844
34.5.1 Definition and properties	844
34.5.2 Asymptotic properties	845
34.5.3 The well-depth prescription	847
34.5.4 Beyond the well-depth prescription	849
34.6 Fractional parentage coefficients	852
34.7 Experimental results for specific nuclei	859
34.7.1 $^{51}\text{V} \rightarrow ^{50}\text{Ti}$	860
34.7.2 ($^3\text{He},\text{d}$) in the sd shell	861
34.7.3 ($e,e'p$)	868
34.7.4 Proton decay	874
34.7.5 Radioactive beams	875
34.8 Structure models for specific nuclei	877
34.8.1 ^7Li	880
34.8.2 ^{12}C	880
34.8.3 ^{16}O	881
34.8.4 The sd-shell	882

34.8.5 ^{40}Ca and ^{48}Ca	884
34.8.6 ^{51}V	885
34.8.7 ^{208}Pb	885
34.9 Short-range correlations	886
34.10 Conclusions	890
35 One-body transition operators and the OBTD	908
35.1 Isospin and proton-neutron formalism	912
35.2 OBTD for a single-orbital configuration	914
35.3 Scalar one-body matrix elements	915
36 Electromagnetic transitions	918
36.1 Electromagnetic Operators and Matrix Elements	919
36.2 Moments in terms of electromagnetic operators	925
36.3 Single-particle matrix elements	926
36.4 Applications to simple situations	930
36.4.1 Closed shell plus one particle	930

36.4.2	Single-orbit configurations	931
36.5	Results for the <i>sd</i> shell nuclei	934
36.5.1	Magnetic moments and M1 transitions	936
36.5.2	Electric quadrupole moments and transitions	938
37	Allowed beta decay	949
37.1	Fermi decay	951
37.1.1	Operators and matrix elements for Fermi transitions	951
37.1.2	Results for Fermi transitions when isospin is conserved	953
37.1.3	Sum rule for Fermi	955
37.1.4	Data on pure Fermi decays and the KCM matrix	957
37.2	Gamow-Teller	962
37.2.1	Operators and matrix elements for Gamow-Teller transitions	962
37.2.2	Sum rule for Gamow Teller	966
37.2.3	Effective operators for Gamow-Teller matrix elements	968
37.2.4	Gamow-Teller transitions in the <i>sd</i> shell	973
37.2.5	Charge-exchange reactions	973

38 Two-nucleon spectroscopic factors	984
38.1 Connection to CFP for one orbital	988
39 Two-body transition operators and the TBTD	992
39.1 Scalar two-body operators	997
39.2 Scalar TBTD for a single-orbital configuration	998
39.3 Scalar TBTD for a two-orbital configuration	999
39.4 Sample calculations for interaction energies	1003
40 Electron Scattering	1008
40.1 Form Factors and Transition Densities	1017
40.2 Single-Particle Form Factors and Transition Densities	1020
40.3 Relationship With Other Notations	1026
40.4 Derivation of the Transverse Magnetic Matrix Elements	1027
40.5 Relationships Provided by the Continuity Equation	1032
40.6 Gamma-decay Transition Probabilities and Electron Scattering	1037
40.7 Model-Space Truncation Effects for the Longitudinal Transition Densities . .	1042

40.8 Center-of-Mass Correction for the Electric Dipole Transition Density	1046
40.9 Differences between PWBA and DWBA	1048
40.10 Conversion of form factors to q-dependent matrix elements $M(q)$	1050

Chapter 1

Introduction

These lecture notes in nuclear structure physics cover material for graduate level study of nuclear theory. They also contain review of the background material from quantum mechanics that are used.

These notes are hyper-linked to literature on the web. Some links to journals and nuclear data are given below.

[Physical Review C](#)

[Physical Review Letters](#)

[Nuclear Physics A](#)

[Physical Letters B](#)

[European Journal of Physics A](#)

[Nuclear Data Set Retrieval](#)

[Web based nuclear chart with nuclear data links](#)

The study of nuclear physics is part of much broader intellectual endeavor to under-

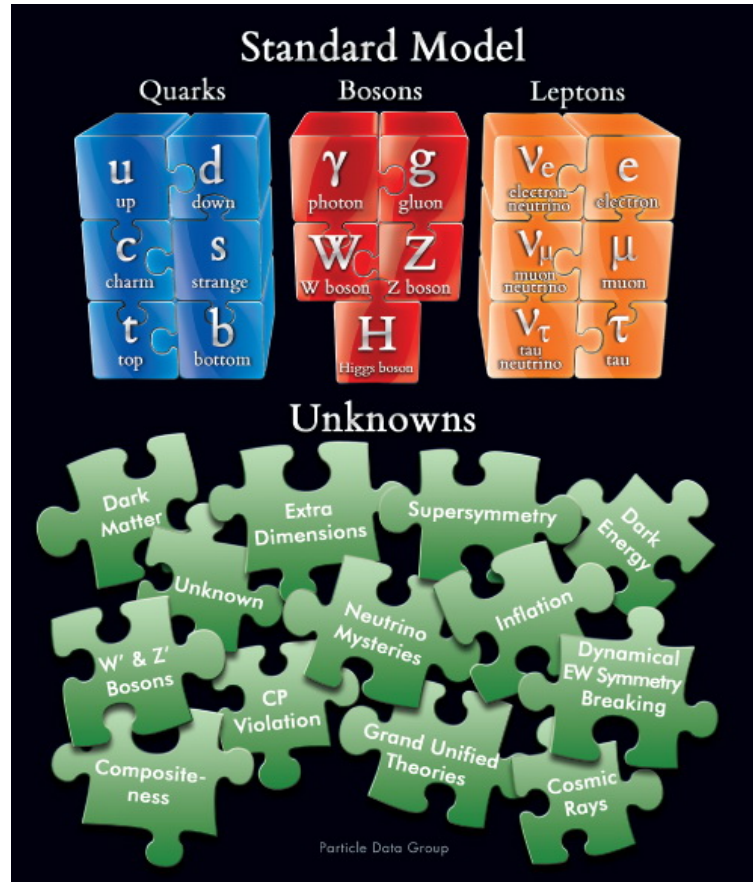


Figure 1.1: The known elementary particles in the standard model. The bottom shows examples of the unknowns. From the cover of the 2014 Review of Particle Physics [Chinese Physics C **38**, 1 (2014)].

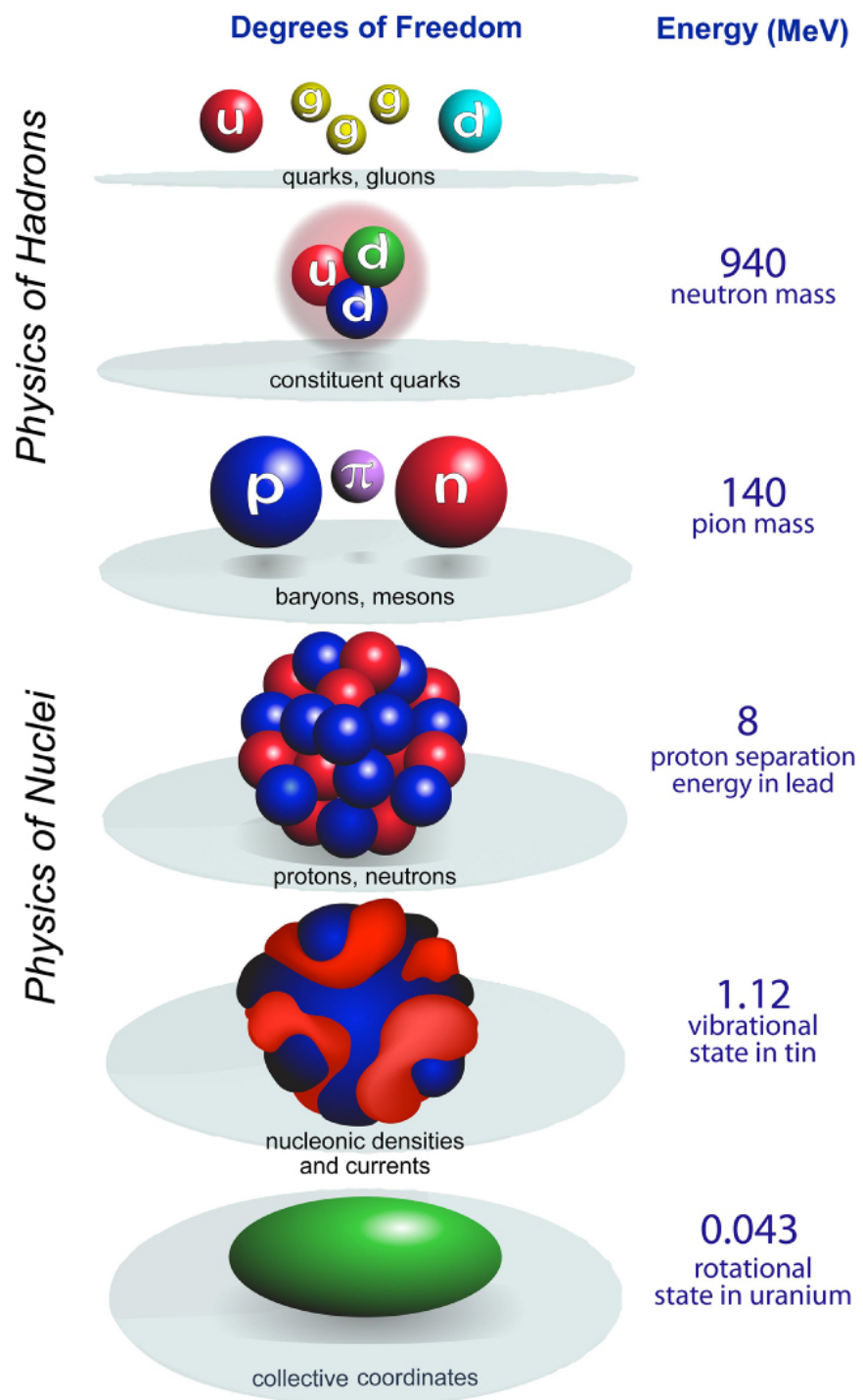


Figure 1.2: Degrees of freedom in nuclear physics.

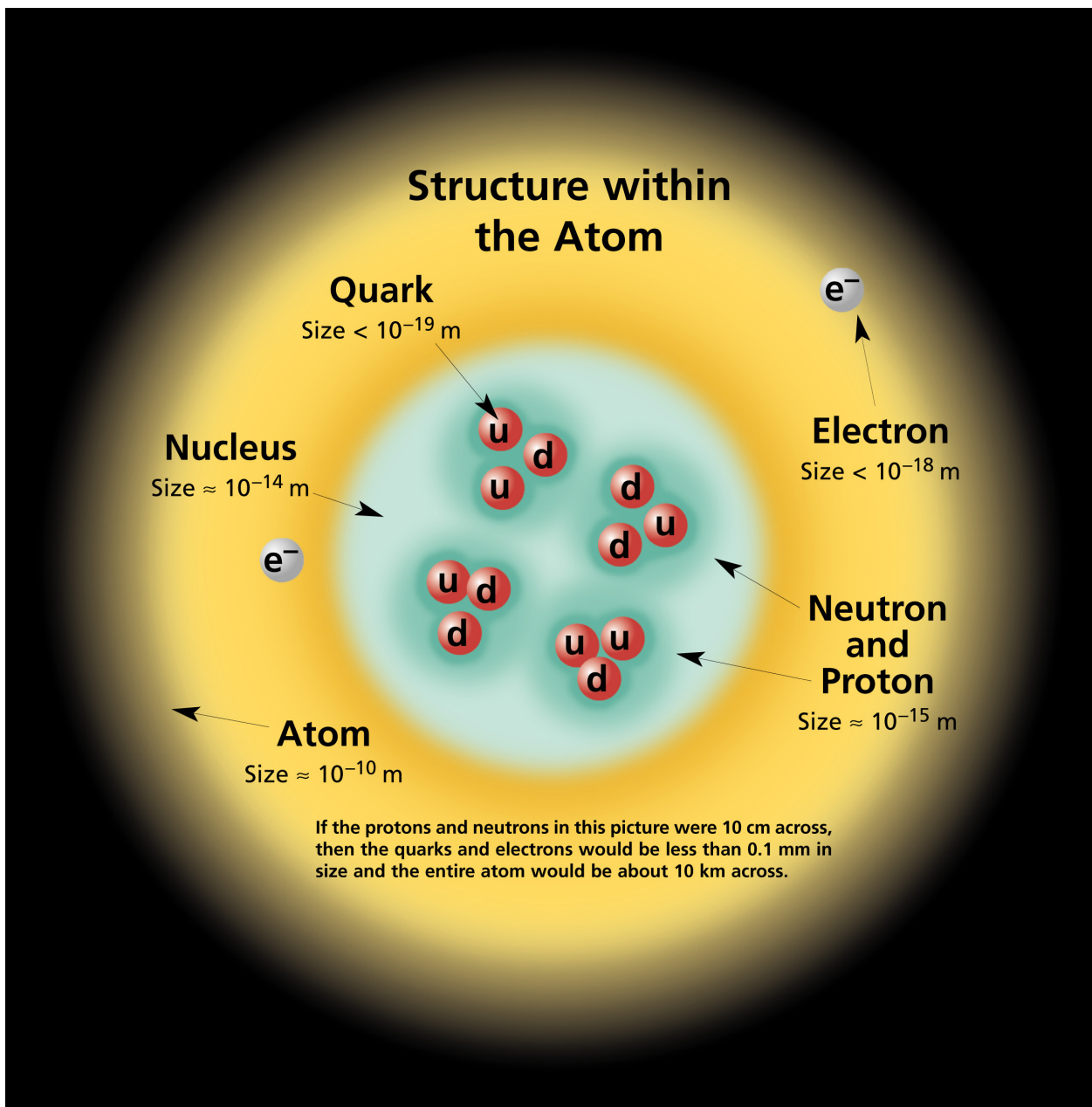


Figure 1.3: The atom.

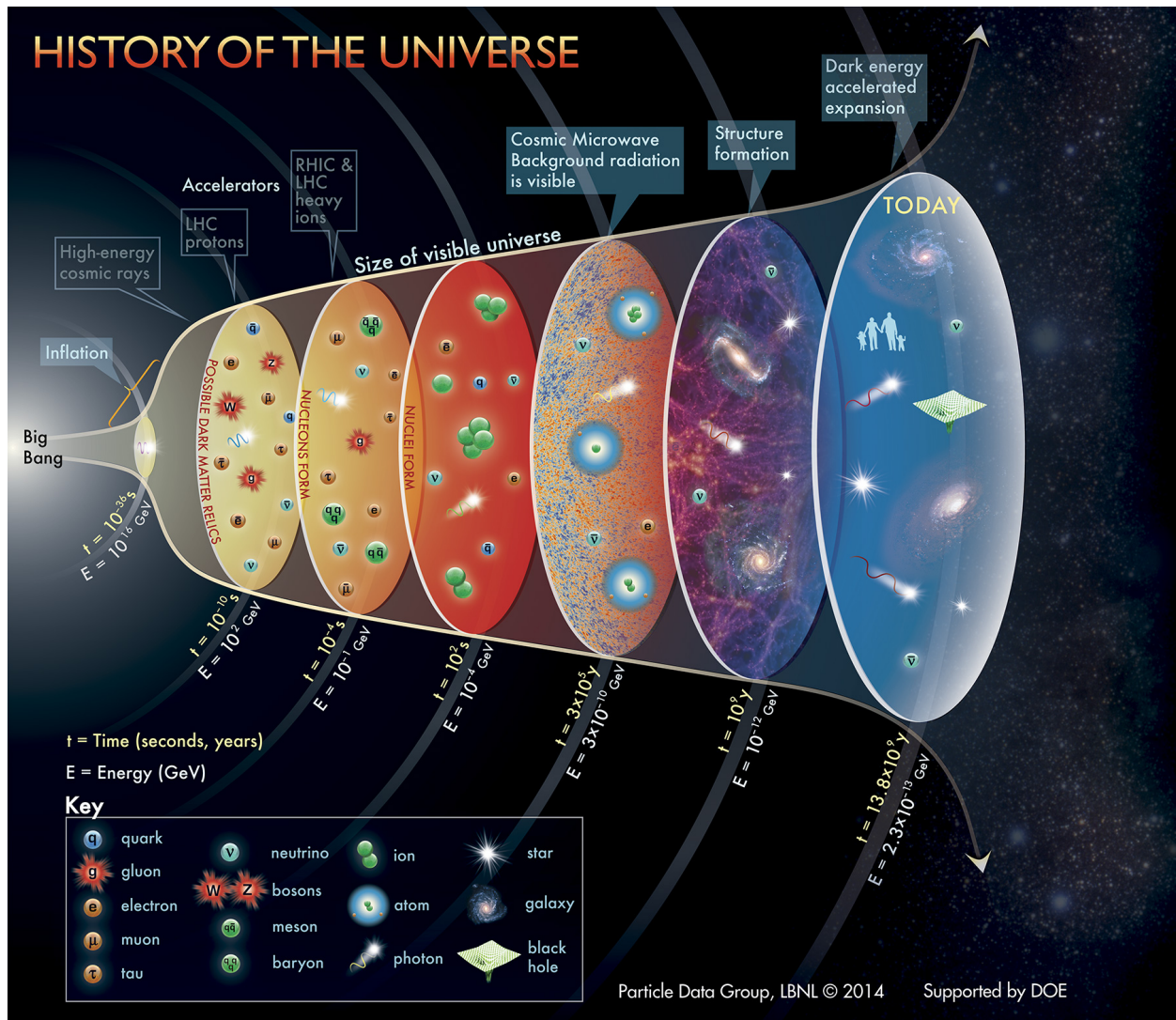


Figure 1.4: Evolution of the universe.

stand the fundamental building blocks of matter and how they combine, interact and evolve to form the universe. This is illustrated in the first few figures. The known fundamental particles are shown in Fig. (1.1). All of the quarks and leptons have anti-particles. They are all part of the Standard Model of electro-weak and strong interactions (link to wiki). But there are many things these models do not explain, and there are other models that predict particles that are not observed, as illustrated by the puzzle pieces at the bottom of Fig. (1.1).

These fundamental particles are the building blocks of nuclei as shown at the top of Fig. (1.2). Quarks and gluons interact to form the proton and neutron. The proton has never been observed to decay (link to wiki), and the neutron beta decays into the proton emitting an electron and a anti-neutrino. Nucleons interact via the exchanges of mesons to form nuclei. The extra binding energy of this interaction means that many nuclei are stable. The heaviest nuclei are unstable due to the repulsive Coulomb interaction between protons. The complex interplay of motion between these nucleons in nuclei leads to a wide variety of mesoscopic structures. At one level this structure gives rise to collective motion involving all of the nucleons such as in the rotations and vibrations at the bottom of Fig. (1.2). At

another level this structure is dominated by the motion of one nucleon relative to the others - the foundation of the nuclear shell model. All nuclei involve an interplay between these extremes which is the subject of nuclear theory.

The nuclei are at the center of atoms as shown in Fig. (1.3). The interaction between the electrons in the atom and nucleus provides an essential experimental tool for studying nuclear properties. Nuclei and atoms constitute matter. Particles, nuclei and matter interact and evolve during the evolution of the universe as shown in Fig. (1.4). How this process proceeds depends upon the properties of nuclei and their extrapolation to the extremes of nucleon number (neutron stars) and temperature.

Fig. (1.5) shows the aspects that need to be considered for a complete theoretical understanding of nuclear properties. Most theoretical models concentrate on just a few of these at a time. The most common models fall into the three broad categories shown in Fig. (1.6). This division is determined by the limitations of each model.

A model based on the quark degrees of freedom is the most fundamental in that all other degrees of freedom, together with the justification for all other models should emerge from

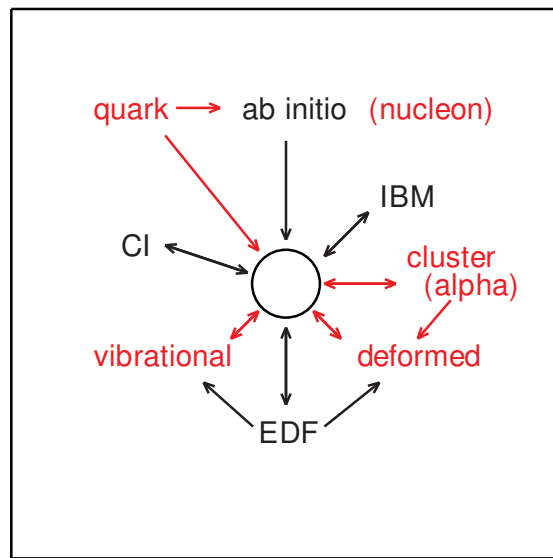


Figure 1.5: Degrees of freedom for nuclei (red) together with types of models that are used to describe them.

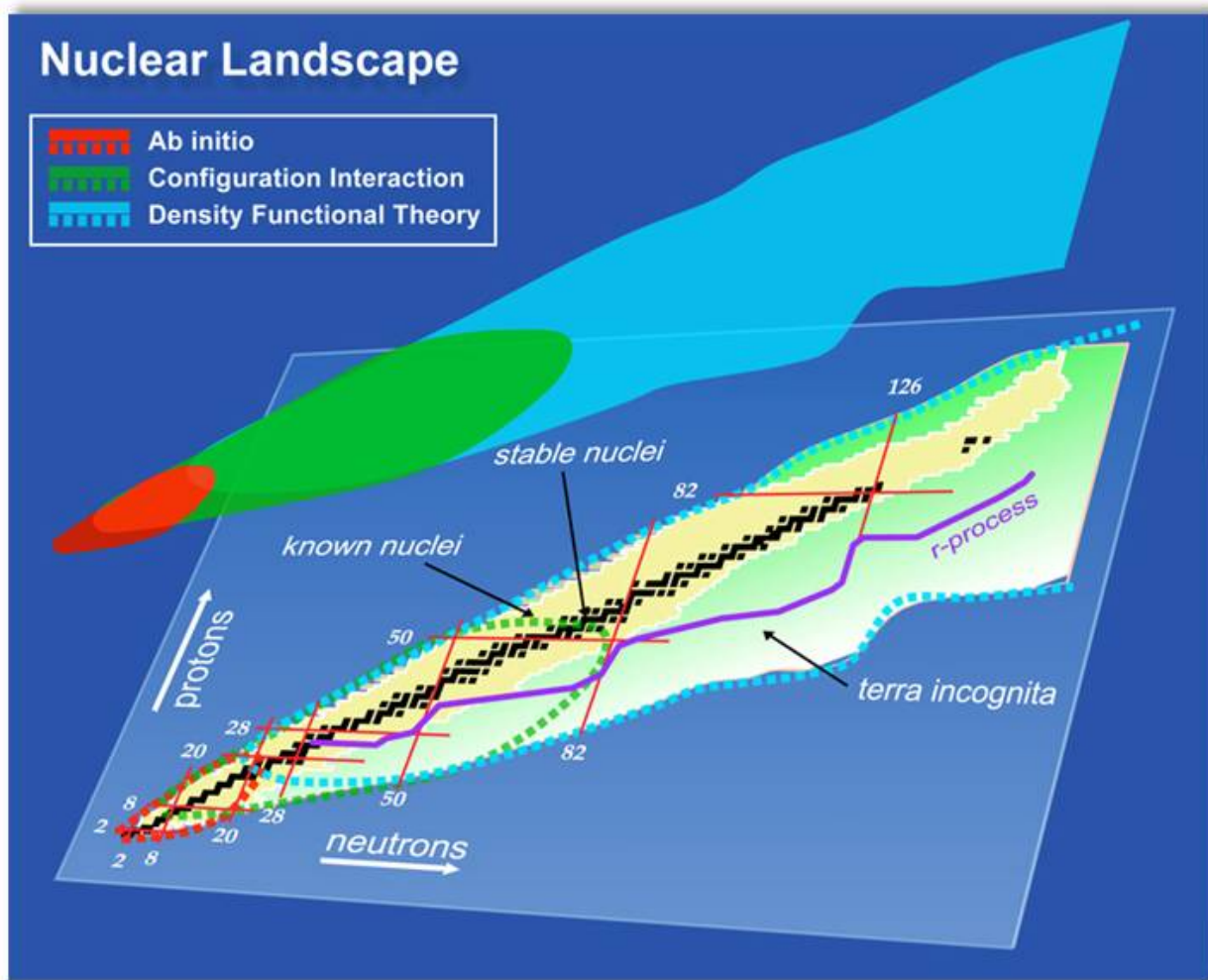


Figure 1.6: The theoretical nuclear landscape.

this. The quantum chromodynamics (QCD) Lagrangian for the quark degrees of freedom is complex and its solution is carried out on a lattice of points in space and time (LQCD). Results have been obtained for the properties the mesons and baryons. The next step will be to obtain realistic interactions between two nucleons with LQCD.

Ab initio models concentrate on the nucleon degrees of freedom and are limited to light nuclei. The observables calculated with the ab-initio methods may show aspects of those expected from the deformed, vibrational and cluster degrees of freedom. Also this may be used to make a more microscopic foundation for other models.

Energy Density Functional (EDF) models start with the single-particle degrees of freedom based upon single Slater determinants as an approximation for the ground state and low-lying excited states. For nuclei near magic numbers, one uses a spherical basis where the angular momentum is automatically conserved. For deformed nuclei, one can use an intrinsic deformed basis followed by an angular momentum projection into the laboratory frame for the observables. Beyond the single Slater determinants one can consider particle-hole configurations that lead to excited states that have properties associated with the vibrational

degrees of freedom.

Configuration Interaction (CI) models include many Slater determinants (up to the order of about one billion). Historically this method was called the nuclear Shell Model. But generally “shell model” refers to the broader class of models that start with a single-particle basis that describes the observed magic numbers. The observables calculated with the CI methods may show aspects of those expected by the deformed, vibrational and cluster degrees of freedom. The limit on the number of Slater determinants limits the applications CI to a subset of low-lying states in nuclei with up to about 100 nucleons, and to nuclei near the closed shells (up to ^{132}Sn and ^{208}Pb). The heavy deformed nuclei cannot be considered in spherical CI due to the extremely large number of Slater determinants that are required. The Interacting Boson model (IBM) is a truncation where the degrees of freedom are those associated with pairs of nucleons coupled to low L values with a phenomenological Hamiltonian for the vibrational and deformed degrees of freedom.

Some of these models are mostly descriptive, while others are more predictive. For example, the basic Bohr collective model and the IBM tell us how different types of nuclear

spectra can be understood in terms of shapes and symmetries. They cannot predict what the shape of a given nucleus will be. The more predictive models are based on nucleonic degrees of freedom as used for example in CI. The Hamiltonian for these nucleonic degrees of freedom are based as much as possible on the fundamental two- and three-body interactions. EDF models (so far) have parameters that are mostly not directly connected to the fundamental interactions. But the EDF parameters are global for all nuclei, and thus they are predictive. The EDF predictions have uncertainties that come from the different EDF forms and parameter sets. For light nuclei ($A < 16$) the nucleonic degrees of freedom can be treated exactly with ab-initio methods. The uncertainty then comes from the uncertainty in the two- and three-body interactions as well as possible four- and higher-body interactions. CI calculations for heavier nuclei usually start with an ab-initio based Hamiltonian. But there are uncertainties coming from the truncation to small set of valence orbitals (the model space). Within a given model space CI can be improved by using some data to constrain the values for some of the renormalized two-body matrix elements. This can lead to improved predictions for nuclei within that model space.

These Lecture Notes touch upon all of these aspects. But they concentrate on the

techniques used for CI models together with some aspects of EDF and the associated single-particle potential models.

The material is divided into groups of Chapters. The first group concentrates on experimental observables. Historically these observables have determined the type of structure models that have been constructed and applied, as well as the parameters used within them. The next group gives some of the basic theoretical tools that are used in the subsequent chapters.

The next group outlines the single-particle shell model. Several types of single-particle potentials are discussed including those from the Energy-Density Functionals based on the Skyrme interaction. This section includes the derivation of single-particle angular momenta and electromagnetic moments for nuclei.

The next group covers methods used for CI calculations. This includes the shell-model Hamiltonian and the codes used to obtain the wavefunctions and energies.

The final group uses CI results to compare with experimental observables including

spectroscopic factors, electromagnetic decay, beta decay, electron scattering, and two-nucleon transfer.

Chapter 2

Nuclear masses

2.1 Masses and binding energies

A basic quantity that can be measured for the ground states of nuclei is the atomic mass $M(N, Z)$ of the neutral atom with atomic mass number A and charge Z . Atomic masses are usually tabulated in terms of the mass excess defined by

$$\Delta(N, Z) \equiv M(N, Z) - uA, \quad (2.1)$$

where u is the Atomic Mass Unit defined by (link to table of constants).

$$u = M(^{12}\text{C})/12 = 931.49386 \text{ MeV}/c^2. \quad (2.2)$$

These masses include the electronic binding energies. For heavy nuclei one observes several chains of nuclei with a constant $N - Z$ value whose masses are obtained from the energy released in alpha decay. The nucleon masses are [1]

$$m_p = 938.27203(8) \text{ MeV}/c^2 = 1.00727646688(13)u \quad (2.3)$$

and

$$m_n = 939.56536(8) \text{MeV}/c^2 = 1.0086649156(6)u. \quad (2.4)$$

We use the data from the 2016 compilation of [2]. Fig. (2.1) shows the position on the nuclear chart for these measured masses together with the experimental error. Fig. (2.2) shows an expanded region for light nuclei.

Nuclear binding energy is defined as the energy required to break up a given nucleus into its constituent parts of N neutrons and Z protons. In terms of the atomic masses $M(N, Z)$ the binding energy is defined by:

$$\text{BE}(N, Z) = ZM_Hc^2 + NM_nc^2 - M(N, Z)c^2, \quad (2.5)$$

where M_H is the mass of the hydrogen atom and M_n is the mass of the neutron.¹ In terms

¹This binding energy also includes contribution from the Coulomb interaction between electrons which is approximately given by $-1.43 \times 10^{-5} Z^{2.39}$ MeV. On the scale of nuclear binding this can usually be ignored. It is most important for heavy nuclei where, for example, for $Z = 120$ the electronic contribution is -1.34 MeV.

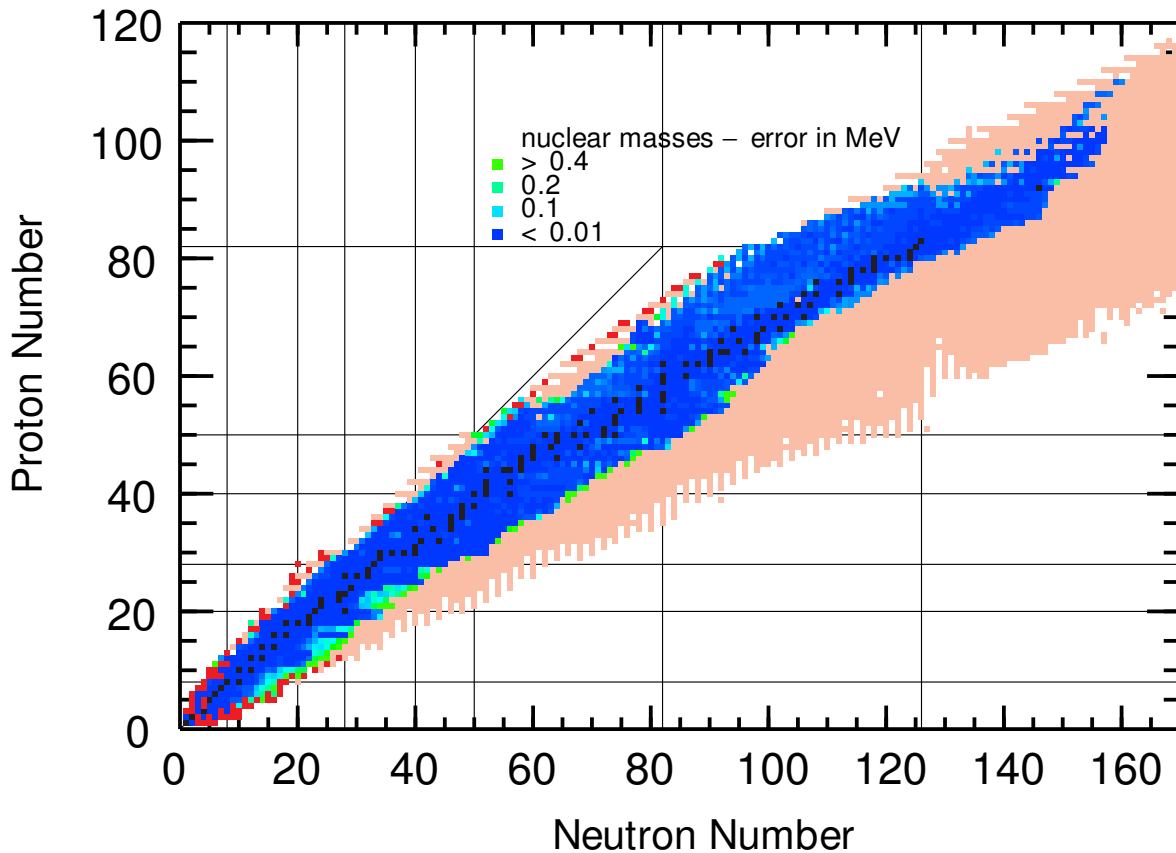


Figure 2.1: The nuclear chart. Stable nuclei are shown in black. Nuclei with measured masses are shown with blue-green colors indicated the error in the experimental mass. The nuclei in dark red are those that have been observed to be outside the drip lines. Nuclei that are predicted to be outside the drip lines by the HFB27 model [3] are shown in light red. The thin lines show $N = Z$ and the magic numbers 8, 20, 28, 40, 50, 82 and 126

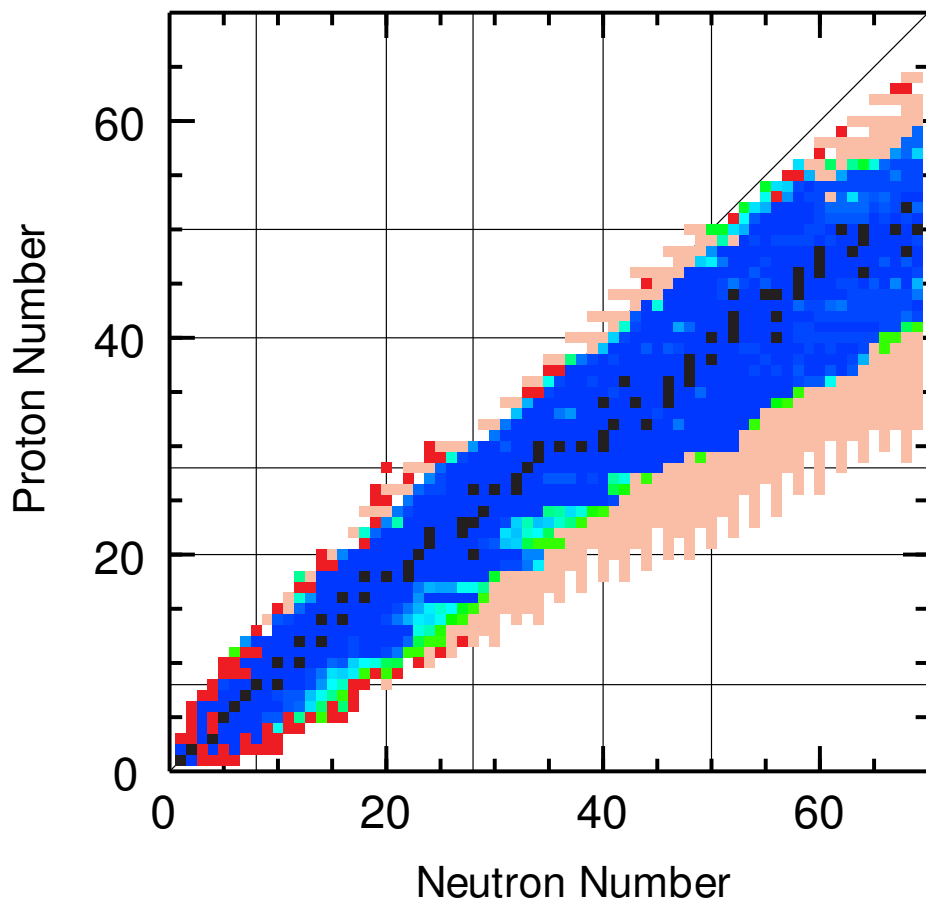


Figure 2.2: An expanded version of Fig. (2.1) for light nuclei.

of the mass excess the binding energy is given by:

$$\text{BE}(N, Z) = Z\Delta_H c^2 + N\Delta_n c^2 - \Delta(N, Z)c^2, \quad (2.6)$$

where $\Delta_H c^2 = 7.2890$ MeV and $\Delta_n c^2 = 8.0713$ MeV.

How do we know that nuclei are made up of protons and neutrons? In the 1920's when it was observed that nuclei decay by the emission of alpha particles, protons and electrons one tried to make nuclear models out of constituent protons and electrons. However, after the discovery of the neutron in 1932, it was observed that the atomic masses can be qualitatively understood by the contribution of the masses of the individual protons and neutrons that make up the nucleus. The largest change in the nuclear masses relative to $ZM_H + NM_n$ is found near $A = 60$ where the total mass is only about one percent smaller than expected from the sum of nucleon masses. Thus, the intrinsic properties of neutrons and protons inside the nucleus similar to those of the free nucleons. Nuclear binding comes from the overall attractive interaction between the nucleons due to exchange of mesons. We can also consider the the energy change due to the modification of the nucleonic properties for nucleons in a nuclear medium, as well as admixtures of other baryons into the nucleonic wavefunctions.

We are interested in understanding the binding energy as a function of N and Z . The binding energies as a function of A are shown in the bottom of Fig. (2.3). One observes an overall linear increase with A reaching a maximum value of about 2 GeV for the heaviest nuclei. One can bring out more detail by plotting BE/A as in the top of Figs. (2.3). The nuclei with the largest BE/A are those in the “valley-of-stability”. For a fixed A value nuclei away from the valley of stability beta decay until they reach the bottom of the valley. Nuclear structure models are used to understand the overall features of these data as well as the deviations from the average.

The maximum in the binding energy per nucleon occurs for ^{58}Fe . ^{58}Fe represents the most bound (lowest energy) state for nucleons. Thus fusion of two light nuclei with a combined mass of $A < 58$ can result in energy release. The fusion of deuterium and tritium is the main reaction being investigated for controlled fusion reactors. Other fusion processes are important for solar energy and for the creation of elements up to $A = 58$ in stellar environments. The falloff in binding energy per nucleon above $A = 58$ implies that most of these nuclei can spontaneously decay into lighter products. The most common of these decay processes are alpha decay, where a ^4He is emitted, and fission, where the nucleus breaks up

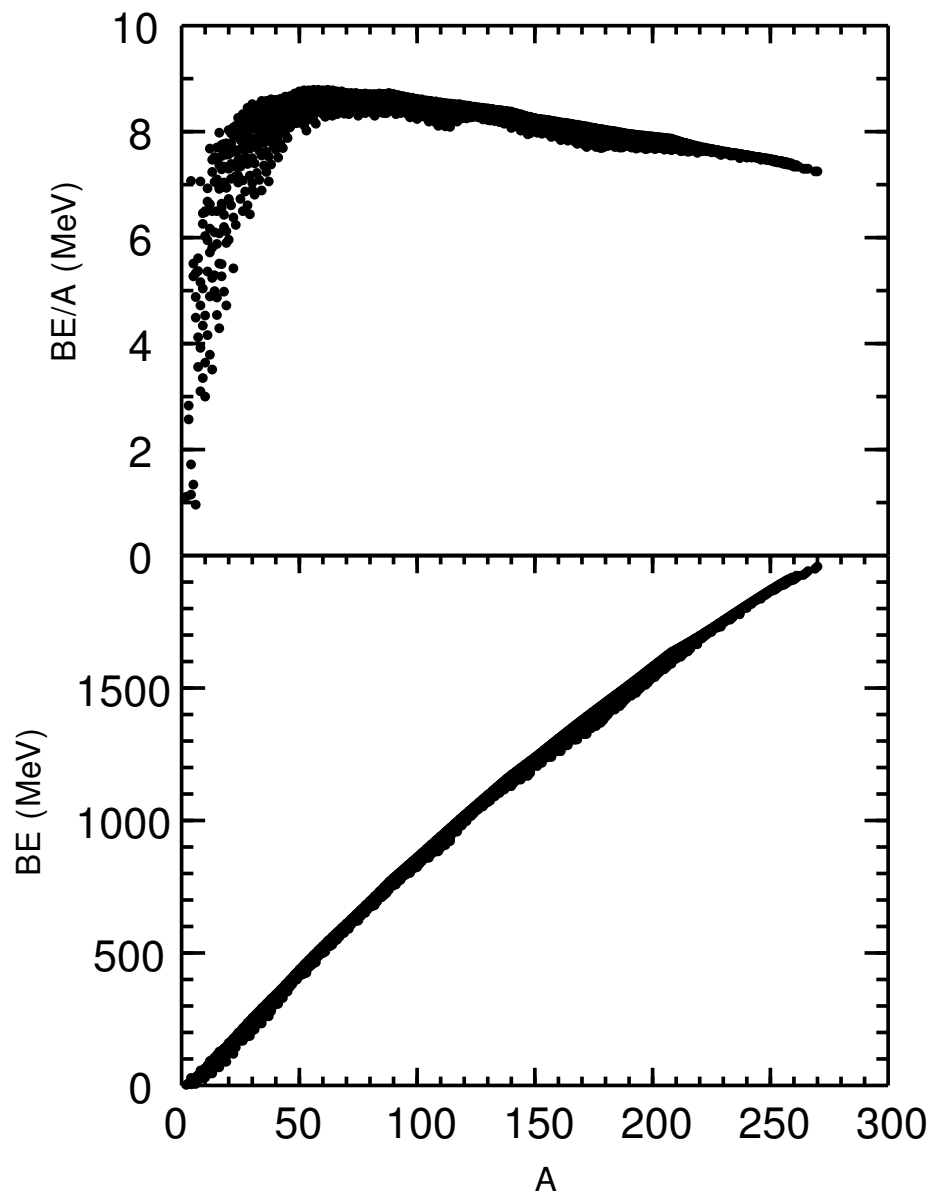


Figure 2.3: BE and BE/A as a function of A .

into two roughly equal mass fragments. The fission products are usually accompanied by neutrons. Intermediate decay modes, where light fragments such as ^{14}C are emitted, are also possible and have also been observed, but their decay rate relative to alpha decay is extremely small. Although most heavy nuclei have a positive Q value for spontaneous decay, many of them have lifetimes on the order of the age of the universe or more, due to the hindrance of tunneling through the Coulomb barrier.

2.2 Q values and separation energies

In this section we consider energy conservation for nuclear transformations that include, for example, the fusion of two nuclei a and b into the combined system c



or the decay of nucleus c into two other nuclei a and b



In general we consider the combinations

$$\sum_i [N, Z]_i \rightarrow \sum_f [N, Z]_f \quad (2.9)$$

where N and Z are conserved

$$\sum_i N_i = \sum_f N_f \text{ and } \sum_i Z_i = \sum_f Z_f. \quad (2.10)$$

This process is characterized by an energy difference called the Q value:

$$Q = \sum_i M(N_i, Z_i)c^2 - \sum_f M(N_f, Z_f)c^2 = \sum_f BE(N_f, Z_f) - \sum_i BE(N_i, Z_i). \quad (2.11)$$

Spontaneous decay involves a single initial nuclear state and is allowed if $Q > 0$. In the decay, energy is released in the form of the kinetic energy of the final products. Reactions involving two initial nuclei and are endothermic (a net loss of energy) if $Q < 0$; the reactions are exothermic (a net release of energy) if $Q > 0$.

We can consider the Q values associated with the removal of one or two nucleons from a nucleus. These are conventionally defined in terms of the one-nucleon and two-nucleon separation energies, S :

$$S_n = -Q_n = \text{BE}(N, Z) - \text{BE}(N - 1, Z), \quad (2.12)$$

$$S_p = -Q_p = \text{BE}(N, Z) - \text{BE}(N, Z - 1), \quad (2.13)$$

$$S_{2n} = -Q_{2n} = \text{BE}(N, Z) - \text{BE}(N - 2, Z), \quad (2.14)$$

and

$$S_{2p} = -Q_{2p} = \text{BE}(N, Z) - \text{BE}(N, Z - 2). \quad (2.15)$$

A negative value for one of these quantities means that the nucleus can spontaneously decay by the emission of neutrons or protons. The boundary between positive and negative values of S is called the drip line. Nuclei inside the drip lines are stable to the spontaneous emission of nucleons, whereas those outside the drip line can spontaneously decay by emission of one and/or two nucleons. The neutron drip line represents a sharp boundary between those nuclei just inside drip line that beta decay with a lifetime on the order of ms, and

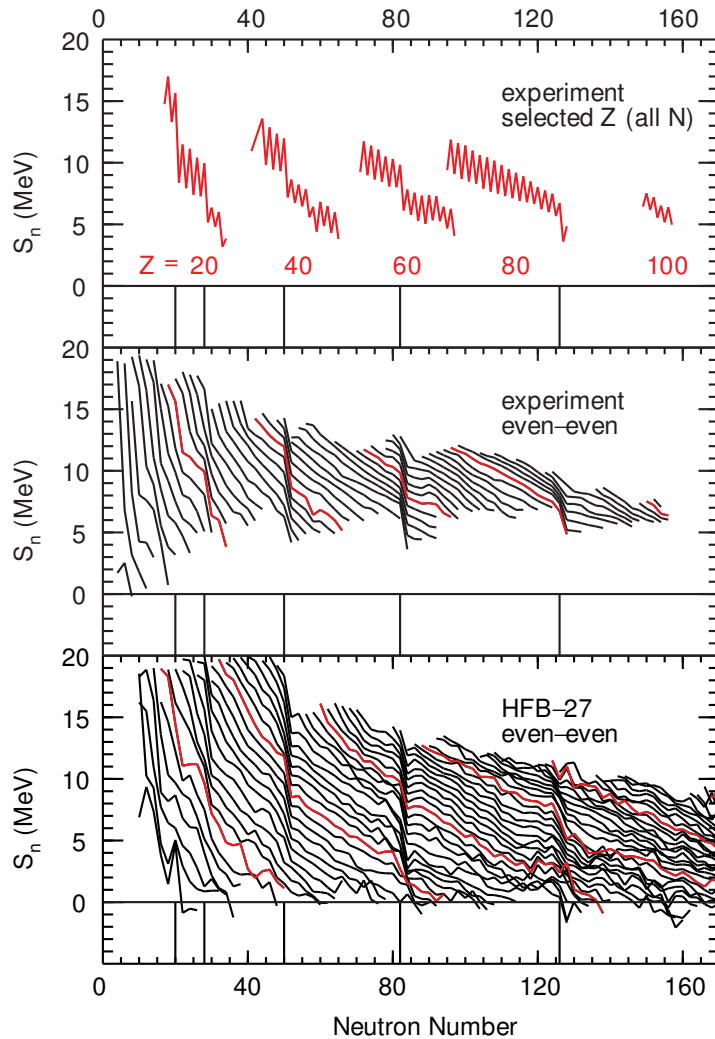


Figure 2.4: One neutron separation energies. The results are plotted vs neutron number with the lines connecting the points for a given Z value. The top panel show the experimental results for a selected set of Z values for all N values. The middle panel shows the experimental results for even Z values and for even N values. The red lines are the even N results from the top panel. The bottom panel shows the results from the HFB27 model. The red lines are the same Z values shown in the top and middle panels. The short vertical lines are located at the magic numbers 20, 28, 50, 82 and 126.

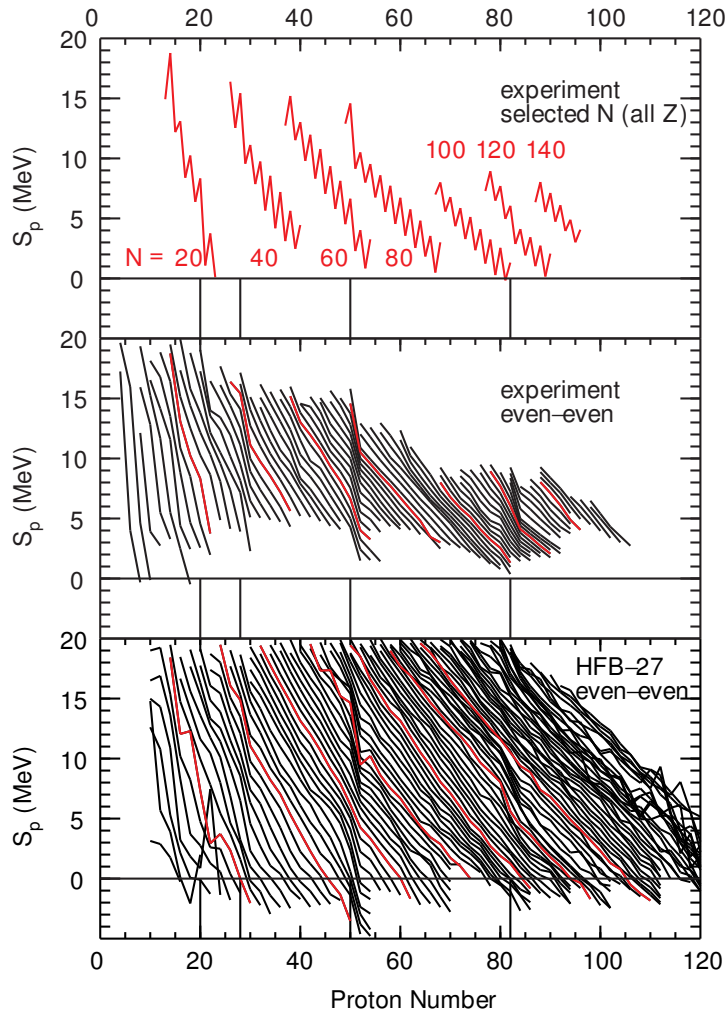


Figure 2.5: One proton separation energies. The results are plotted vs proton number with the lines connecting the points for a given N value. The top panel show the experimental results for a selected set of N values for all Z values. The middle panel shows the experimental results for even N values and for even Z values. The red lines are the even Z results from the top panel. The bottom panel shows the results from the HFB27 model. The red lines are the same N values shown in the top and middle panels. The short vertical lines are located at the magic numbers 20, 28, 50, 82 and 126.

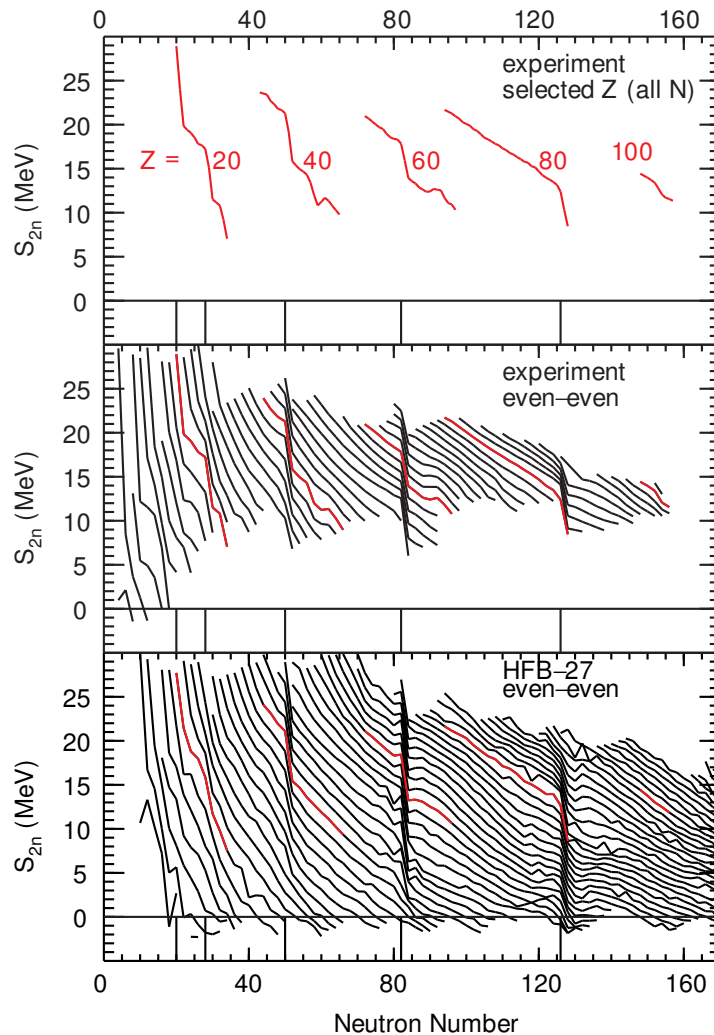


Figure 2.6: Two neutron separation energies. The results are plotted vs neutron number with the lines connecting the points for a given Z value. The top panel shows the experimental results for a selected set of Z values for all N values. The middle panel shows the experimental results for even Z values and for even N values. The red lines are the even N results from the top panel. The bottom panel shows the results from the HFB27 model. The red lines are the same Z values shown in the top and middle panels. The short vertical lines are located at the magic numbers 20, 28, 50, 82 and 126.

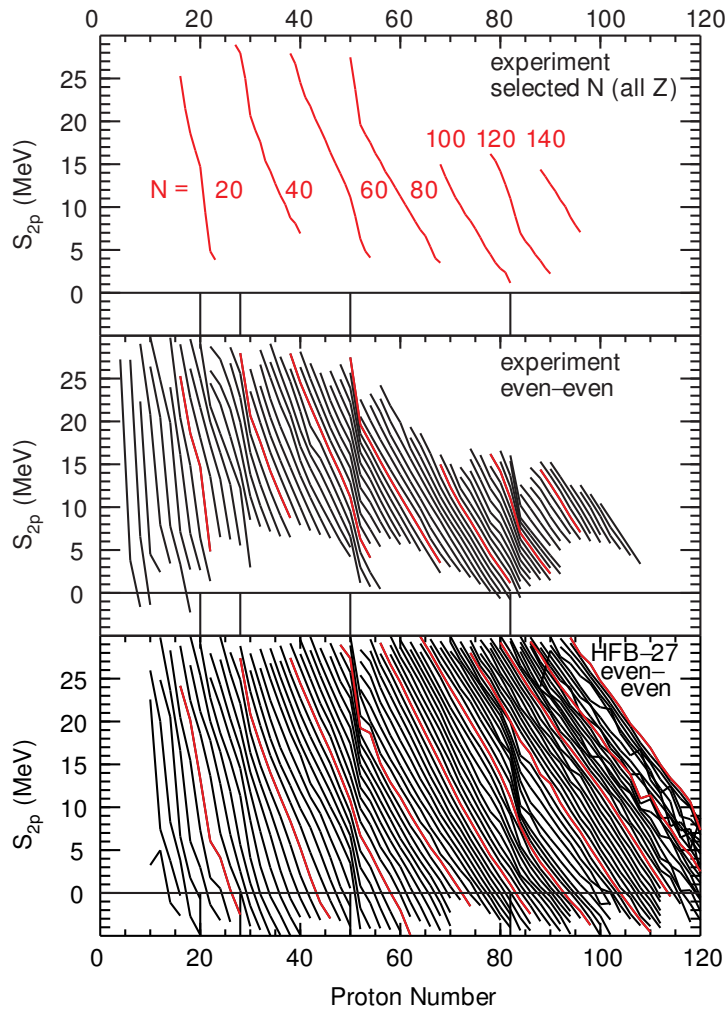


Figure 2.7: Two proton separation energies. The results are plotted vs proton number with the lines connecting the points for a given N value. The top panel shows the experimental results for a selected set of N values for all Z values. The middle panel shows the experimental results for even N values and for even Z values. The red lines are the even Z results from the top panel. The bottom panel shows the results from the HFB27 model. The red lines are the same N values shown in the top and middle panels. The short vertical lines are located at the magic numbers 20, 28, 50, 82 and 126.

those outside the drip line that have lifetimes on the order of 10^{-20} s associated with the strong interaction decay widths of MeV. For heavy nuclei, the Coulomb barrier can greatly hinder the proton decay, and the the lifetimes for the one or two proton decay of nuclei just outside the proton-drip line can be comparable to or even longer than the lifetimes for beta decay.

Fig. (2.1) shows the nuclear chart for nuclei whose masses have been measured together with those that are predicted to lie within the neutron and proton drip lines from a microscopic nuclear model called HFB27 [3]. An expanded version of this figure for light nuclei is shown in Fig. (2.2). These figures also show nuclei with measured masses that lie outside the drip lines. For light nuclei, the masses given in the compilation for nuclei beyond the drip lines are usually obtained from the observation of resonances in nucleon decays. As such, it would be better to call these quantities resonance energies rather than masses or binding energies.

For light nuclei the proton and neutron drip lines are experimentally established only up to about $A = 24$. For heavier nuclei the proton-drip line is observed in a few regions from

the observation of proton decays with relatively long lifetimes. The HFB27 model gives a prediction for the neutron and proton drip lines. Between $A = 40$ and $A = 200$ nearly half of the nuclei expected to be inside the drip lines have not yet been observed in experiments. The properties for many of these unobserved nuclei are critical for the understanding of nuclear models as well as the astrophysical processes in element production.

The systematics of the one-nucleon separation energies are shown in Fig. (2.4) for neutrons and in Fig. (2.5) for protons. As one moves from the proton to the neutron drip lines, the one-neutron separation energies decrease. This decrease is not smooth but shows odd-even oscillations associated with the two-body pairing nature of the strong interaction between neutrons. The systematics of the two-nucleon separation energies are shown in Fig. (2.6) for neutrons and in Fig. (2.7) for protons. The pairing oscillations are averaged out for two-nucleon separation energies. Just after the magic numbers 28, 50, 82 and 126 there is sudden decrease in the separation energy due to the fact that neutrons go into valence orbitals that are loosely bound compared to those that have just been filled at the magic numbers.

This change at the magic numbers can be emphasized by taking the second derivative of the BE:

$$D_n = 2 \text{BE}(N, Z) - \text{BE}(N - 1, Z) - \text{BE}(N + 1, Z). \quad (2.16)$$

$$D_p = 2 \text{BE}(N, Z) - \text{BE}(N, Z - 1) - \text{BE}(N, Z + 1). \quad (2.17)$$

$$D_{2n} = 2 \text{BE}(N, Z) - \text{BE}(N - 2, Z) - \text{BE}(N + 2, Z). \quad (2.18)$$

and

$$D_{2p} = 2 \text{BE}(N, Z) - \text{BE}(N, Z - 2) - \text{BE}(N, Z + 2). \quad (2.19)$$

The results are shown in Figs. (2.8), (2.9), (2.10) and (2.11). All of figures show sharp peaks at the magic numbers. The D_n and D_p values in the top of Figs. (2.8) and (2.9) have a large oscillation around zero due to the pairing effect. In the middle and bottom panels of these figures we only take the positive (even-nucleon) part. One could also plot

$$D'_n = (-1)^N [2 \text{BE}(N, Z) - \text{BE}(N - 1, Z) - \text{BE}(N + 1, Z)]. \quad (2.20)$$

for all N values and

$$D'_p = (-1)^Z [2 \text{BE}(N, Z) - \text{BE}(N, Z - 1) - \text{BE}(N, Z + 1)]. \quad (2.21)$$

for all Z values to give all positive numbers. This quantity is related to the pairing gap Δ used in [4] by $\Delta = D'/2$. Nuclear structure aspects of D' are discussed in Ref. [5]. In particular the height of the peaks in the middle and bottom panels provides a measure of the shell gaps and the average value between the peaks is a measure of the pairing energy.

The results for D_2 removes the pairing part and emphasizes the shell gaps. The height of the peaks in D_2 is related to the attractive pairing interaction between two neutrons or two protons. Careful inspection of the middle panel of Fig. (2.10) shows that $N = 20$ has a peak at $Z = 14$, but that peak goes away for one of the other black lines ($Z = 12$). This sudden change of magic number properties has been called an “island of inversion” [6], [7]. The combined results for D_{2n} and D_{2p} for the HFB27 model are shown in Fig. (2.12). This figure shows that a sudden change of magic numbers may occur for all nuclei near the neutron drip line. FRIB will provide experimental confirmation of these changes.

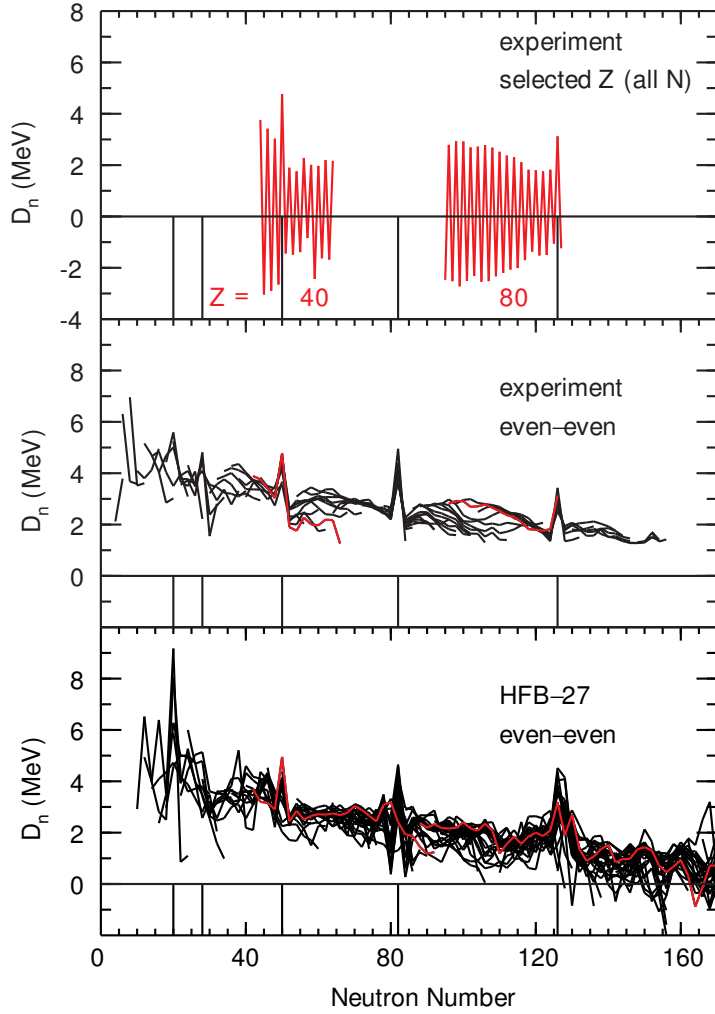


Figure 2.8: D_n values. The results are plotted vs neutron number with the lines connecting the points for a given Z value. The top panel show the experimental results for a selected set of Z values for all N values. The middle panel shows the experimental results for even Z values and for even N values. The red lines are the even N results from the top panel. The bottom panel shows the results from the HFB27 model. The red lines are the same Z values shown in the top and middle panels. The short vertical lines are located at the magic numbers 20, 28, 50, 82 and 126.

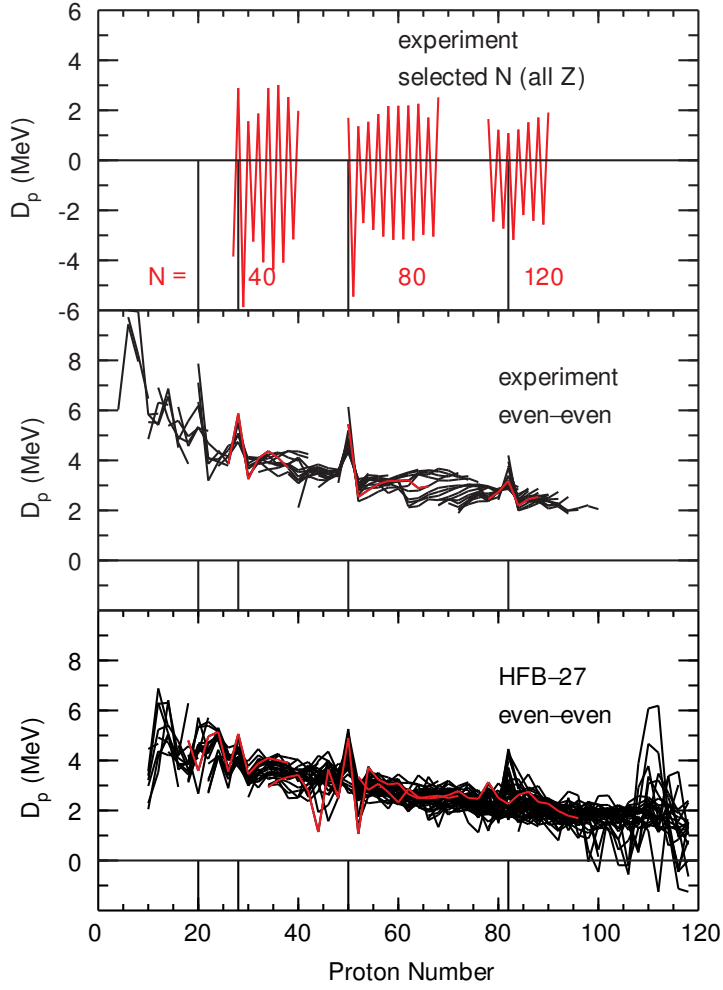


Figure 2.9: D_p values. The results are plotted vs proton number with the lines connecting the points for a given N value. The top panel show the experimental results for a selected set of N values for all Z values. The middle panel shows the experimental results for even N values and for even Z values. The red lines are the even Z results from the top panel. The bottom panel shows the results from the HFB27 model. The red lines are the same N values shown in the top and middle panels. The short vertical lines are located at the magic numbers 20, 28, 50, 82 and 126.

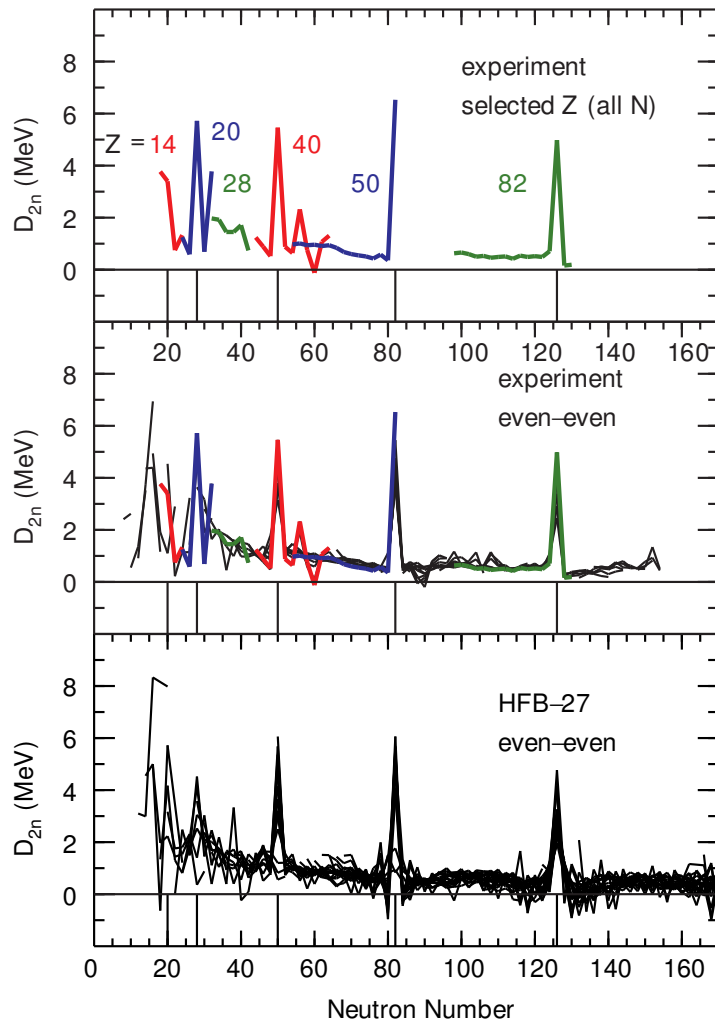


Figure 2.10: D_{2n} values. The results are plotted vs neutron number with the lines connecting the points for a given Z value. The top panel show the experimental results for a selected set of Z values for all N values. The middle panel shows the experimental results for even Z values and for even N values. The red lines are the even N results from the top panel. The bottom panel shows the results from the HFB27 model. The red lines are the same Z values shown in the top and middle panels. The short vertical lines are located at the magic numbers 20, 28, 50, 82 and 126.

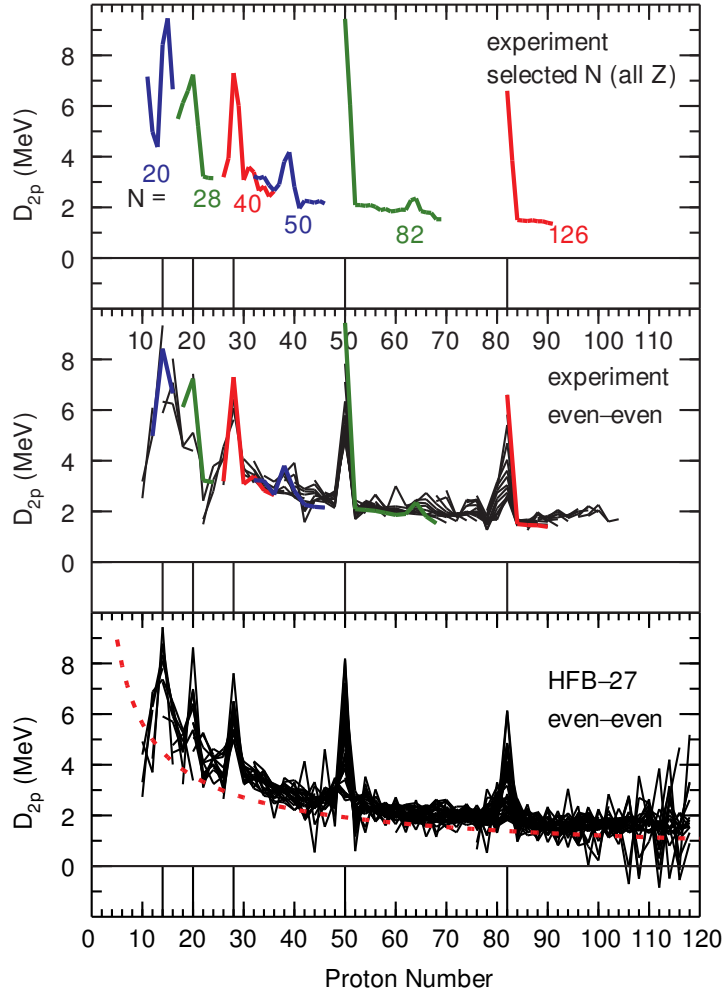


Figure 2.11: D_{2p} values. The results are plotted vs proton number with the lines connecting the points for a given N value. The top panel show the experimental results for a selected set of N values for all Z values. The middle panel shows the experimental results for even N values and for even Z values. The red lines are the even Z results from the top panel. The bottom panel shows the results from the HFB27 model. The red lines are the same N values shown in the top and middle panels. The short vertical lines are located at the magic numbers 20, 28, 50, 82 and 126.

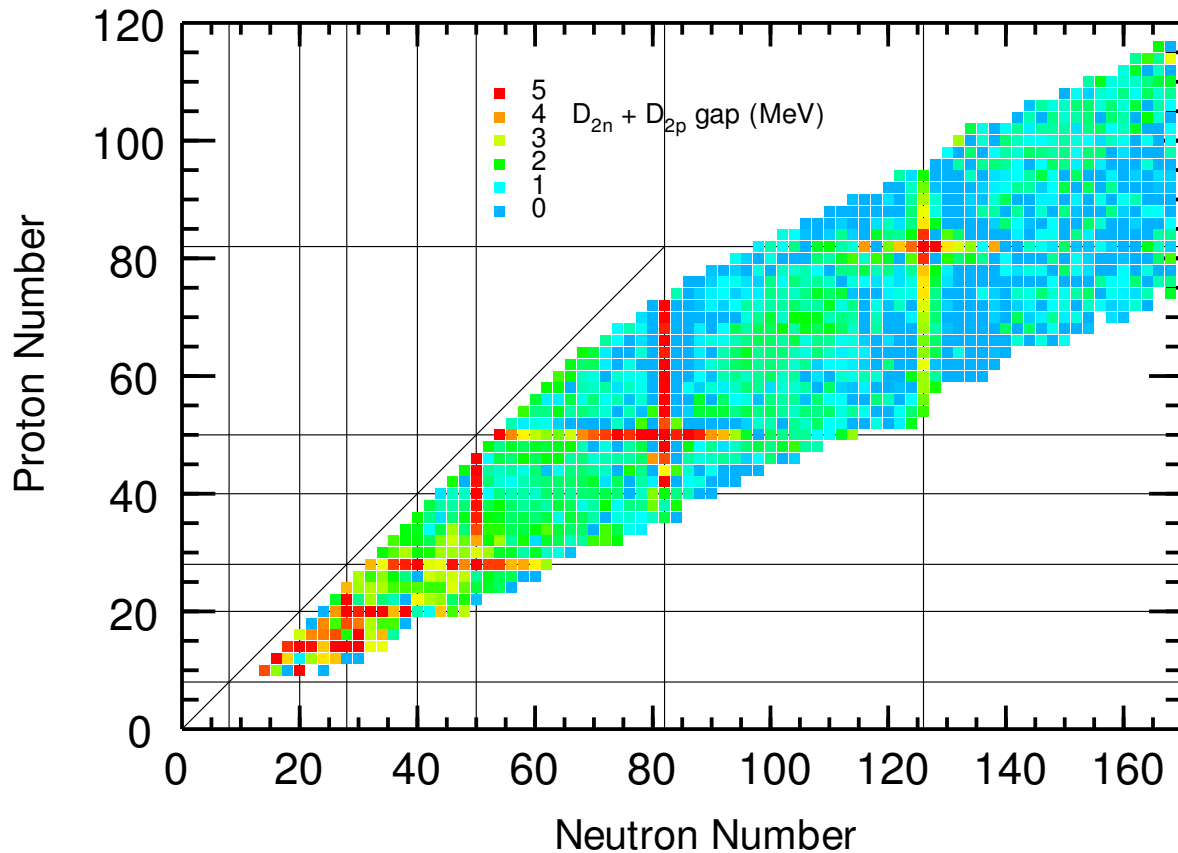


Figure 2.12: $D_2 = D_{2n} + D_{2p} - B$ values plotted vs N and Z for the HFB27 model. B is the dashed line shown in the bottom panel of Fig. (2.11). The thin lines are located at the magic numbers 20, 28, 50, 82 and 126.

Bibliography

- [1] W. M. Yao et al., J. Phys. G **23**, 1 (2006).
- [2] M. Wang, G. Audi, K. G. Kondev, W. J. Huang, S. Naimi, and X. Xu, Chinese Physics C **41**, 030003 (2017).
- [3] S. Goriely, N. Chamel, J.M. Pearson, Phys. Rev. C **88**, 061302(R) (2013). link

- [4] A. Bohr and B. R. Mottelson, *Nuclear Structure* (World Scientific, Singapore, 1988), Vol. I.
- [5] B. A. Brown, Phys. Rev. Lett. **111**, 162502 (2013). link
- [6] E. K. Warburton, J. A. Becker and B. A. Brown, Phys. Rev. C **41**, 1147 (1990). link
- [7] B. A. Brown, Physics **3**, 104 (2010).

Chapter 3

Excitation energies of even-even nuclei

The figures in this section show the systematics for the excitation energies of first-excited 0^+ , 2^+ , 3^- and 4^+ states in even-even nuclei. These spin-parities are those associated with the most collective aspects of nuclear structure.

The energy of the 2^+ states in Fig. (3.3) is compared to that expected from the rotation of a classical rigid sphere. “Spherical” nuclei that are described by closed-shell configurations for the magic numbers can only have $J^\pi = 0^+$. The energies of the excited states in nuclei near the closed shells are related to particle-hole excitations across the shells with energies characterized by the energy gaps between the single-particle states. In the extreme case of ^{208}Pb this particle-hole energy is 60 times that obtained from the classical rigid-body rotation.

The ratio $R(4^+/2^+)$ of the 4^+ to 2^+ energy is shown in Fig. (3.6). The experimental data is obtained from gamma decay energies, except for a ^{244}Pu where only they are based on the alpha decay energies from the decay of ^{248}Cm [1]. The $R(4^+/2^+)$ ratio shows some simple trends relative to the location of the magic numbers. In particular, the highest value becomes close to $R(4^+/2^+) = 10/3$ for many nuclei that are near $N=90-110$ and $N > 130$.

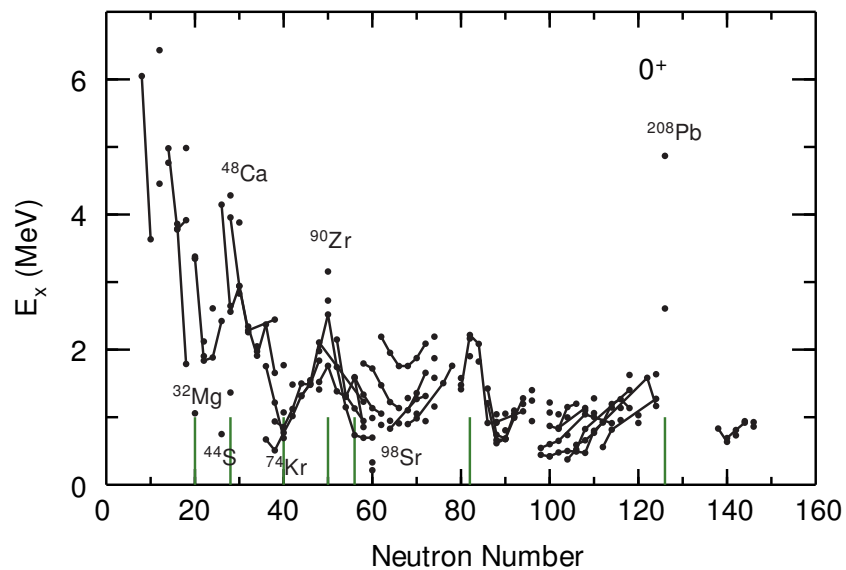


Figure 3.1: Excitation energy of the first excited 0^+ state in even-even nuclei. Isotopic chains are connected by lines. The lower vertical bars show the magic Numbers 20, 28, 40, 56, 82 and 126. Some of the highest points are labeled by their nuclei.

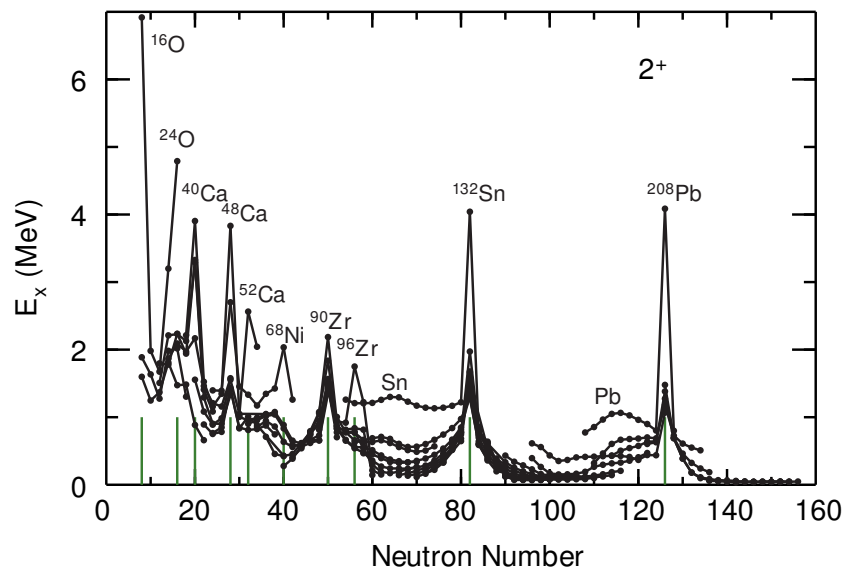


Figure 3.2: Excitation energy of the first 2^+ state in even-even nuclei. Isotopic chains are connected by lines. The lower vertical bars show the magic numbers 8, 16, 20, 28, 40, 50, 56, 82 and 126. Some of the highest points are labeled by their nuclei.

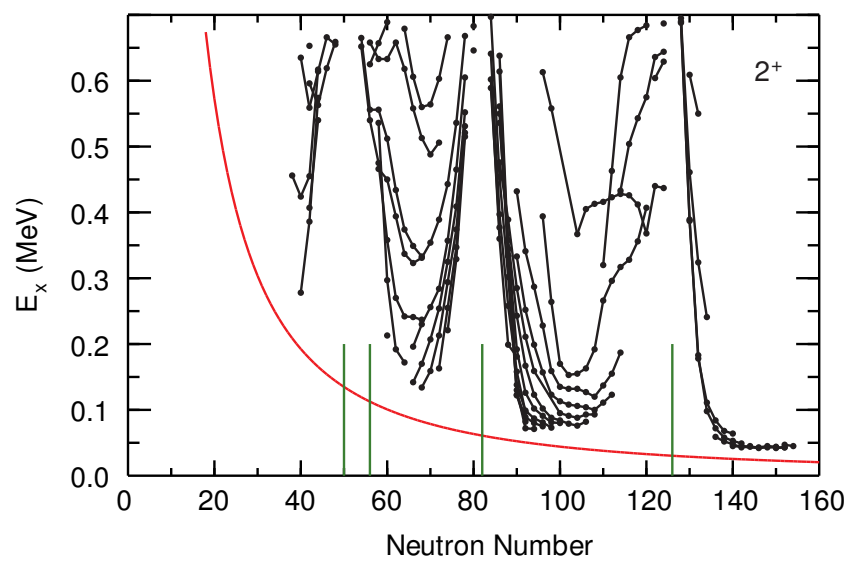


Figure 3.3: Same as Fig. 1 but expanded a factor of ten. The red line is based on the rotation of a solid sphere of radius $R = 1.41N^{1/3}$.

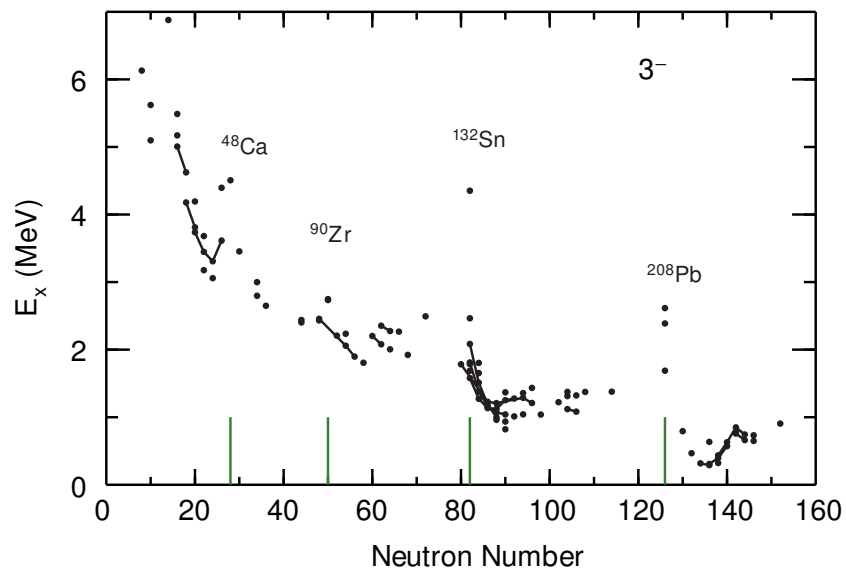


Figure 3.4: Excitation energy of the first 3^- state in even-even nuclei. Isotopic chains are connected by lines. The lower vertical bars show the magic Numbers 28, 50, 82 and 126. Some of the lowest and highest points are labeled by their nuclei.

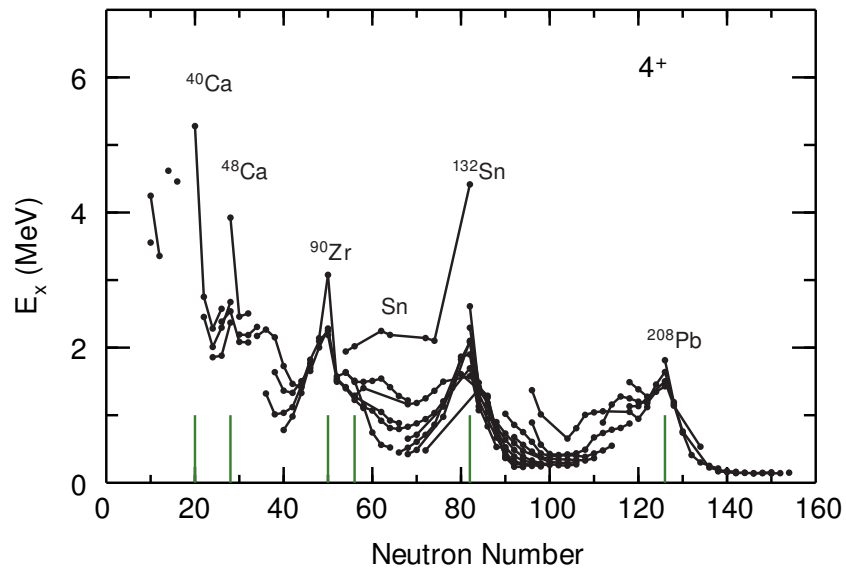


Figure 3.5: Excitation energy of the first 4^+ state in even-even nuclei. Isotopic chains are connected by lines. The lower vertical bars show the magic Numbers 20, 28, 50, 56, 82 and 126. Some of the highest points are labeled by their nuclei.

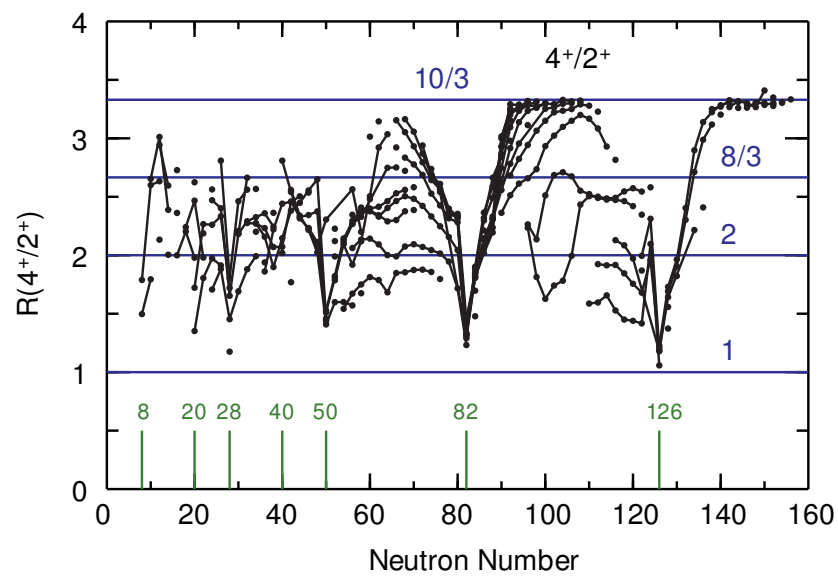


Figure 3.6: Ratio of the 4^+ to 2^+ energies in even-even nuclei. Isotopic chains are connected by lines. The horizontal lines correspond to the ratio expected in various models.

(The anomalously high point for ^{244}Pu may be due to an experimental error in the alpha decay energies obtained in [1].)

The $10/3$ ratio has a simple rotational collective model interpretation that will be discussed in a latter chapter. The states with the lowest energy for a given J value are referred to as the yrast states ("yr" is the Swedish adjective for whirl, and yrast is the superlative whilingest [2]). For these rotational nuclei the yrast energies for even J starts out as $J(J + 1)$. The ratio for a triaxial rigid rotation of $8/3$ is also shown in Fig. (3.6).

Near the magic numbers, $R(4^+/2^+)$ and $R(3^-/2^+)$ (figure not shown) are close to one as expected if the energies for both of these states are related to energy gaps between the single-particle states. The ratio $R(4/2) = 2$ is that expected from a vibrational model.

The excitation energy of the first-excited 0^+ states shown in Fig. (3.1) have a more complicated interpretation. Some of them are related to the energies of two-particle two-hole type configurations that depend on the energy gaps between the single-particle states as well as the two-particle "pairing" interactions in these configurations. In some other cases the energies are determined by the coexistence of different collective shapes.

Bibliography

- [1] S. A. Baranov, V. M. Shatinskii, Sov. J. Nucl. Phys. **26**, 244 (1977).
- [2] J. R. Groyer, Phys. Rev. **157**, 832 (1967). link

Chapter 4

Rms radii

4.1 Charge and proton radii

The root-mean-square (rms) charge radius has been measured for the ground states of many nuclei. For a spherical charge density, $\rho(r)$, the mean-square radius of the density $\rho(r)_x$ is defined by:

$$R_x^2 = \langle r^2 \rangle_x = \frac{\int \rho(r)_x r^2 d\tau}{\int \rho(r)_x d\tau}, \quad (4.1)$$

where x can stand for protons (p), neutrons (n), matter (the sum of the proton and neutron) (m) or charge (ch). The rms radius is denoted by R_x . Experimental values for the charge rms radii have been compiled in [1], [2]. The rms charge radii plotted vs A are shown in Fig. (4.1).

Charge radii can be measured in a variety of ways. The radii for stable nuclei have been deduced from electron scattering form factors and/or from the x-ray transition energies of muonic atoms. The relative radii for a series of isotopes can be extracted from the isotope

shifts of atomic x-ray transitions.

The rms radius for the nuclear point-proton density, R_p is obtained from the rms charge radius by:

$$R_p = \sqrt{R_{ch}^2 - R_{corr}^2}, \quad (4.2)$$

where

$$R_{corr}^2 = R_{op}^2 + (N/Z)R_{on}^2 + R_{rel}^2. \quad (4.3)$$

The rms charge radius of the proton is denoted by R_{op} . Before 2010 one often used the value of $R_{op} = 0.879(11)$ fm obtained from electron-proton scattering [3], [4], [5]. The rms radius of the proton obtained in 2010 from the Lamb shift measurement of muonic hydrogen was $0.8409(4)$ fm [6]. This difference beyond the error limits was known as the “proton-radius puzzle” [7]. A 2020 experiment with atomic hydrogen gives $0.8482(38)$ fm [8]. This result, together with newer data and analysis for electronic data, brings the electronic and muonic data much closer together [7]

$R_{on}^2 = -0.116(2)$ fm² is the mean-square radius obtained from low-energy neutron scattering data [9]. R_{rel}^2 are from the relativistic corrections [10], [11], [12], [13]. These

corrections are proportional to the anomalous magnetic moments of the protons ($2.792 - 1 = 1.792$) and neutrons (-1.913) in the nucleus. The anomalous magnetic moments are the differences of the measured magnetic moments with that expected from the Dirac model for a point particle with spin 1/2. The main part of R_{rel}^2 has the opposite sign for the spin-orbit pairs of states, and is called the relativistic spin-orbit correction [11]. The spin-orbit correction has the opposite sign for protons and neutrons (due to the proportionality to the anomalous magnetic moment), For example, it contributes about -0.019 fm to the rms charge difference between ^{48}Ca and ^{40}Ca where, in the simplest approximation, the eight neutrons fill the $0f_{7/2}$ orbital (see Table I in [13]).

The rms radii for protons in the nucleus from Eq. (4.2) are shown in Fig. (4.2). In the spherical liquid-drop model the density is given by a constant density out to radius c

$$\begin{aligned}\rho(r) &= \rho_o, \text{ for } r < c = r_o A^{1/3}, \text{ and} \\ \rho(r) &= 0, \text{ for } r > c.\end{aligned}\tag{4.4}$$

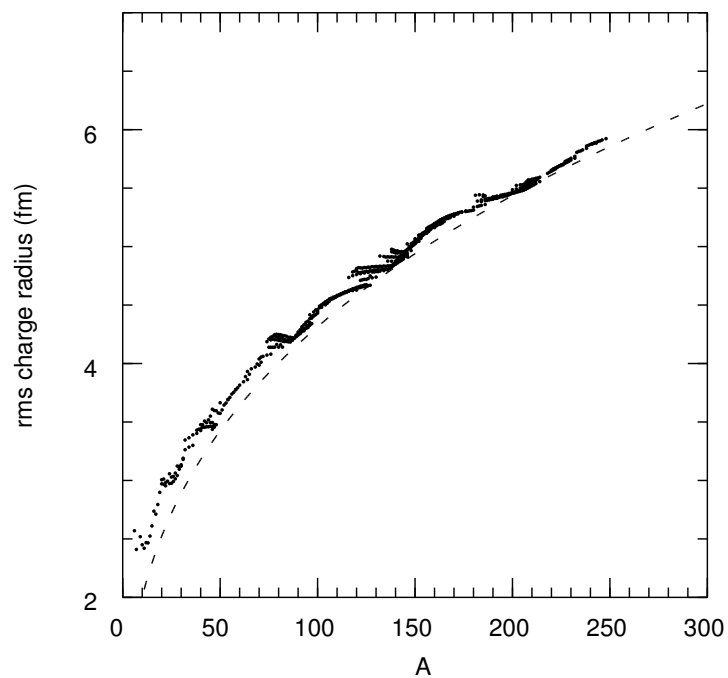


Figure 4.1: The rms charge radii plotted as a function of the atomic number A . The dashed line is the liquid-drop model with a sharp surface $c = r_o A^{1/3}$ with $r_o = 1.20$ fm.

The rms radius for this sharp-surface distribution is given by

$$R_d = \sqrt{\frac{3}{5}}c = \sqrt{\frac{3}{5}}(r_o A^{1/3}). \quad (4.5)$$

The liquid-drop model with $r_o = 1.185$ fm is shown by the dashed line in Fig. (4.2). The value of $r_o = 1.185$ fm is chosen so that the line passes through the lower values of the rms radii for heavy nuclei. (For the charge radii in Fig. (4.1) one needs $r_o = 1.20$ fm.) It is observed that the data follow the liquid-drop line rather closely except for light nuclei and some regions of heavy nuclei where the data is higher than the model. The distribution of neutrons is not known so well but we will start out by assuming that the rms radius for neutrons is the same as that for protons. In the liquid-drop model the density for nucleons in the interior of the nucleus saturates to a value ρ_o .

We can improve the sharp-surface model if we allow the surface to be diffuse. We can do this with the Fermi distribution shape:

$$\rho(r) = \frac{\rho_o}{1 + \exp[(r - c)/a]}. \quad (4.6)$$

The rms radius is given by:

$$R_f = \sqrt{\frac{3}{5}} \sqrt{c^2 + \frac{7}{3} \pi^2 a^2} \quad (4.7)$$

The integrals involving Eq. (4.6) can be carried out with the Sommerfeld expansion (link to wiki). The fit to the point-proton rms radii obtained with $c = r_f A^{1/3}$, $r_f = 1.15$ fm, and $a = 0.35$ fm is shown by the solid line in Fig. (4.2). This is a better overall fit to light and heavy nuclei. But the data still fluctuate around the curve. If we fold in the rms radius of the protons from Eq. (4.3) the charge rms radius is given by

$$R_{ch} = \sqrt{\frac{3}{5}} \sqrt{c^2 + \frac{7}{3} \pi^2 a^2 + \frac{5}{3} R_{op}^2} = \sqrt{0.793 A^{2/3} + 2.46} \text{ fm.} \quad (4.8)$$

In the Fermi distribution model the interior density is given by

$$\rho_o = \frac{A}{\frac{4\pi}{3} c^3 \left(1 + \frac{\pi^2 a^2}{c^2}\right)}. \quad (4.9)$$

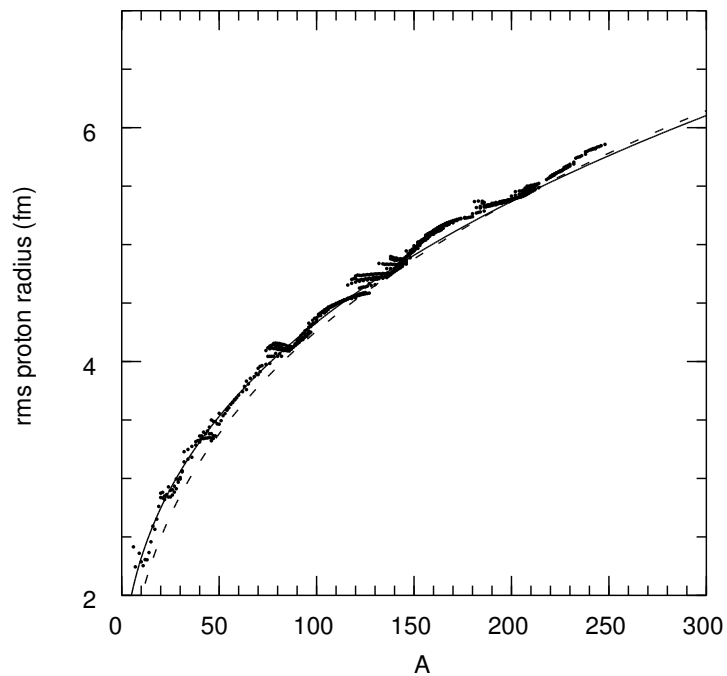


Figure 4.2: The rms proton radii plotted as a function of the atomic number A . The dashed line is the liquid-drop model with a sharp surface $c = r_o A^{1/3}$ with $r_o = 1.185$ fm. The solid line uses the form of Eq. (4.7) that takes into account the diffuseness.

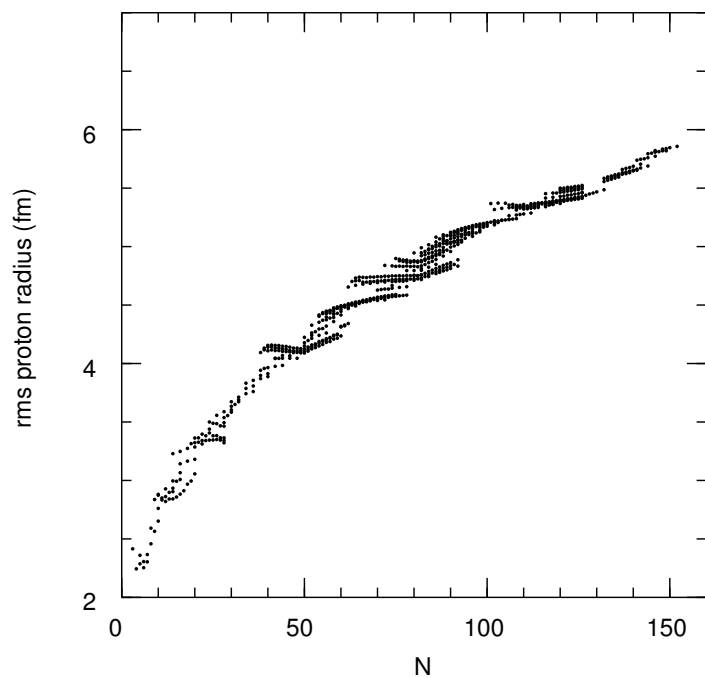


Figure 4.3: The rms proton radii plotted as a function of the neutron number N .

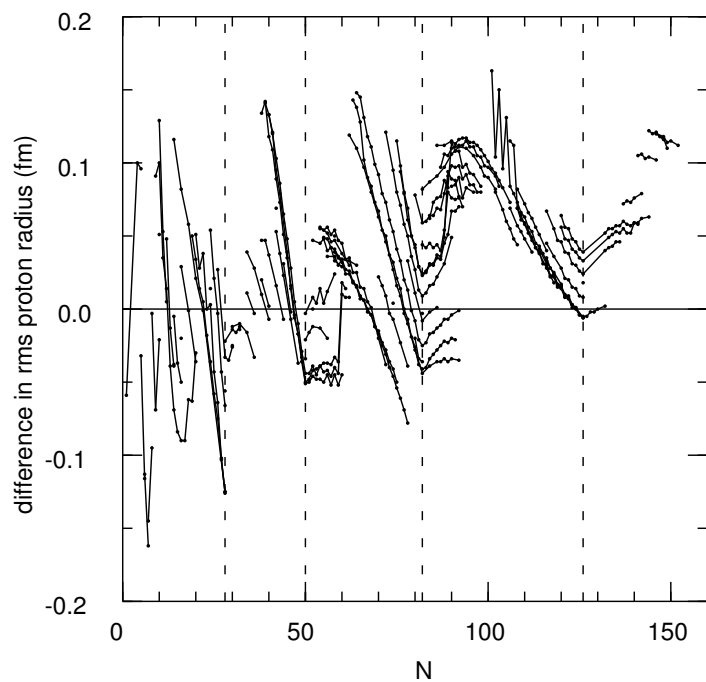


Figure 4.4: The rms proton radii with the diffuse liquid-drop model values of Eq. (4.7) subtracted. The magic numbers 28, 50, 82 and 126 are indicated by the dashed lines.

For large A we can neglect the $\frac{\pi^2 a^2}{c^2}$ term, and if we assume that the rms radius for neutrons is the same as that for the protons then $c^3 = r_f^3 A$ and

$$\rho_o = \frac{3}{4\pi r_f^3} = 0.16 \text{ nucleons/fm}^3, \quad (4.10)$$

with $r_f = 1.15 \text{ fm}$. This is approximately the saturation density of symmetric nuclear matter. The assumption of equal rms radii for protons and neutrons means that the interior density will be divided between protons and neutrons in the ratio Z/N . So, for example, in ^{208}Pb , the interior nucleon density of $0.16 \text{ nucleons/fm}^3$ will be divided into $(82/208)0.16 = 0.06 \text{ protons/fm}^3$ and $(126/208)0.16 = 0.10 \text{ neutrons/fm}^3$.

In order to bring out the differences in the rms radii I show the experimental values plotted vs neutron number in Fig. (4.3) and the difference $R_{exp} - R_f$ in Fig. (4.4). One observes that the experimental rms radii are relatively small at the magic numbers. This means that the nuclei associated with the magic numbers are more compact than those away from the magic numbers. This increase in rms radii away from the magic numbers is qualitatively related to nuclear deformation.

4.2 Neutron rms radii and the neutron skin

Compared to the charge radii that can be measured by model-independent electromagnetic probes, the neutron density and rms radius is much more poorly known. The most model independent method is by parity violating electron scattering [14] where the density is probed by the exchange of a Z boson between the electrons and the neutrons. The difference between the point proton and point neutron rms radii is called the neutron skin

$$R_{np} = R_n - R_p. \quad (4.11)$$

The size of this skin for a heavy nucleus such as ^{208}Pb is strongly correlated with the properties of the neutron matter equation of state and the symmetry energy [15]. These that are required for understanding the properties of neutron stars [16]. Also neutron rms radii are needed for the calculations of atomic parity violation [17].

The error in the parity violating electron scattering experiment on ^{208}Pb is still large, $S = 0.33^{+0.16}_{-0.18}$ fm [14]. There are many experiments measure the neutron skin by hadronic

scattering [18], [19], [20], [21]. But the analysis of these experiments have ingredients that depend upon the models for the strong interaction.

Bibliography

- [1] H. de Vries, C. W. de Jager and C. de Vries, At. Data and Nucl. Data Tables **36**, 495 (1987)
- [2] G. Fricke, C. Bernhardt, K. Heilig, L. A. Schaller, L. Shellenberg, E. B. Shera and C. W. de Jager, At. Data and Nucl. Data Sheets **60**, 177 (1995).
- [3] P. J. Mohr, D. B. Newell and B. N. Taylor, Rev. Mod Phys. **188**, 035009 (2016).

- [4] J. Arrington and I. Sick, *J. Phys. Chem. Ref. Data* **44**, 031204 (2015).
- [5] I. Sick and D. Trautmann, *Phys. Rev. C* **95**, 012501(R), (2017).
- [6] R. Pohl et al., *Nature (London)* **466**, 213 (2010).
- [7] W. Ubachs, *Science* **370**, 1033 (2020).
- [8] A. Grinin et al., *Science* **370**, 1061 (2020).
- [9] C. Amsler et al., *Phys. Lett. B* **667**, 1 (2008); <http://pdg.lbl.gov>.
- [10] T. De Forest and J. D. Wakecka, *Adv. Phys.* **15**, 1 (1966).
- [11] W. Bertozzi, J. Friar, J. Heisenberg and J. W. Negele, *Phys. Lett.* **41B**, 408 (1972).
- [12] A. Ong, J. C. Berengut and V. V. Flambaum, *Phys. Rev. C* **82**, 014320 (2010). link
- [13] C. J. Horowitz adn J. Piekarewicz, *Phys. Rev. C* **86**, 045503 (2012). link
- [14] S. Abrahamyan et al., *Phys. Rev. Lett.* **108**, 112502 (2012). link

- [15] B. A. Brown, Phys. Rev. Lett. **85**, 5296 (2000). link
- [16] A. W. Steiner, J. M. Lattimer, and E. F. Brown, Astrophys. J. **765**, L5 (2013).
- [17] B. A. Brown, A. Derevianko, and V. V. Flambaum, Phys. Rev. C **79**, 035501 (2009). link
- [18] J. Zenihiro et al., Phys. Rev. C **82**, 044611 (2010) link
- [19]] E. Friedman, Nucl. Phys. A **896**, 46 (2012)
- [20] B. A. Brown, G. Shen, G. C. Hillhouse, J. Meng, and A. Trzcinska, Phys. Rev. C **76**, 034305 (2007). link
- [21] C. M. Talbert et al., Phys. Rev. Lett. **112**, 242502 (2014). link

Chapter 5

Charge densities and form factors

Elastic electron scattering from nuclei gives information on the distribution of charge in the ground state. Information extracted from data has evolved from the early determinations of rms charge radii, to much more precise measurements in the 70's and 80's which have provided nearly model-independent determinations of the charge-density distributions of many nuclei. In these density distributions one can observe oscillations in the interior density which represent the quantum "waves" in the nucleus.

The charge-density normalization is given by:

$$\int_0^\infty \rho_{ch}(r) d\tau = 4\pi \int_0^\infty \rho_{ch}(r) r^2 dr = Z, \quad (5.1)$$

where Z is the number of protons in the nucleus. The charge probability density,

$$P_{ch}(r) = \frac{4\pi}{Z} r^2 \rho_{ch}(r), \quad (5.2)$$

represents the probability to find a proton at a given radius r from the center of the nucleus.

The charge density is given by a sum of three terms involving the protons and neutrons

together with the relativistic spin-orbit correction $\rho_{ch}^{ls}(r)$

$$\rho_{ch}(r) = \rho_{ch}^p(r) + \rho_{ch}^n(r) + \rho_{ch}^{ls}(r). \quad (5.3)$$

The spin-orbit correction has its origin in the tensor component of the electromagnetic current [1], [2]. The size of the spin-orbit correction depends upon the orbitals that are occupied [3], [2]. It is maximized when one of the spin-orbit partners is filled and other is empty. For example, for ^{48}Ca assuming that the neutron $0f_{7/2}$ orbital is fully occupied, the correction to the mean-square radius is -0.13 fm^2 [2] (compared to the total mean-squared radius of 12.1 fm). When both spin-orbit partners are filled the relativistic correction is small [2]. There is an additional small relativistic correction that does not depend on the spin-orbit orbitals occupied called the Darwin-Folder term that is included in [1]. The proton and neutron contributions are obtained from the point proton and neutron densities, $\rho^q(r)$ convoluted with the finite-charge size for each G_q

$$\rho_{ch}^q(r) = \int_0^\infty \rho^q(r') G_q(|\vec{r} - \vec{r}'|) d\tau. \quad (5.4)$$

This can be calculated by a product of Fourier transforms, $F^{-1} \{F[\rho(r)] F[G(r)]\}$. Examples of finite-charge distributions expressed as a sum of Gaussian distributions are given in [4].

The integrals of G_q are one for the proton and zero for the neutron. The r^2 integrals of G_q are the mean-square radii of the proton and neutron given in the last chapter.

As an example, the charge density measured for ^{208}Pb is shown in Fig. (5.1). The charge density is shown in the top panel and the probability density in the lower panel. If one were to put the 208 nucleons of ^{208}Pb into a simple cubic lattice, a density of 0.16 nucleons/fm² corresponds to a lattice spacing of 1.85 fm. I have represented this situation in the upper panel of Fig. (5.1) by drawing Gaussian distributions for several nucleons each of which has an rms radius of 0.88 fm and which are spaced a distance of 1.85 fm. One observes in this situation that the overlap between nucleons is small. (In nuclear models the nucleons are not confined to lattice sites but are described by wavefunctions spread over the whole nuclear volume. Nucleons confined to lattice sites would have kinetic energies that are an order of magnitude larger than those allowed to spread over the nuclear volume.)

In the plane-wave approximation for the electron, the ratio of the electron scattering cross section to the Rutherford cross section (scattering from a point) as a function of

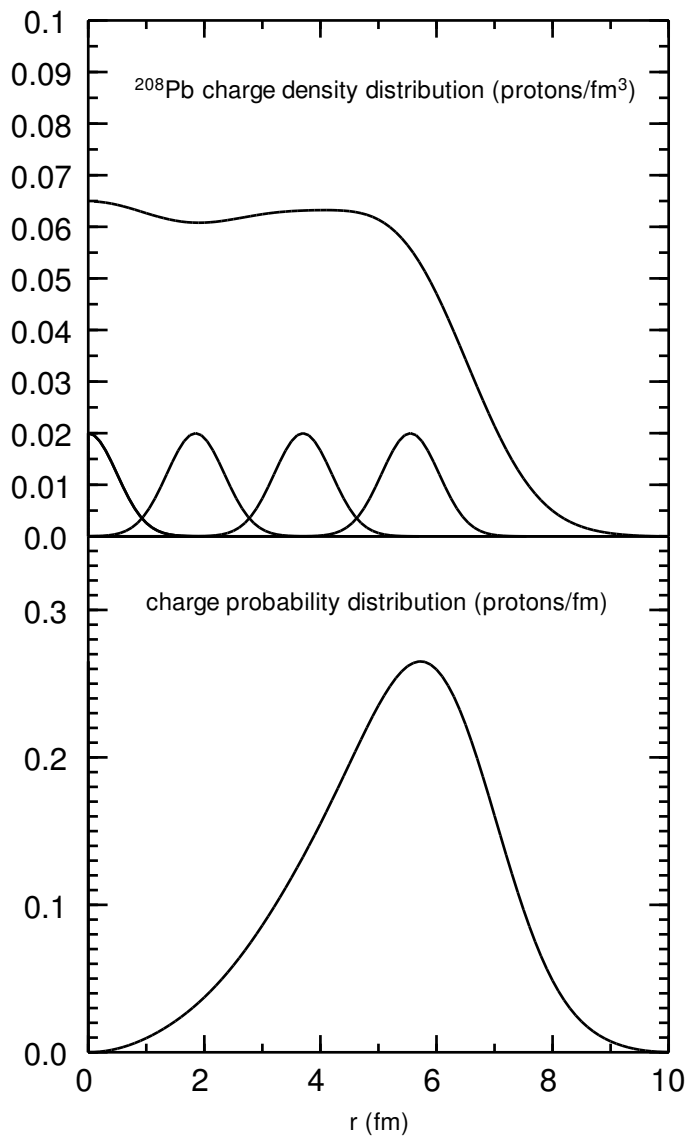


Figure 5.1: Experimental charge-density profile (upper panel) and probability profile (lower panel) for ^{208}Pb . The upper panel also shows the density profiles for some individual nucleons with an rms radius of 0.88 fm and spaced a distance of 1.85 fm.

momentum transfer, q , is related to the charge density in the plane-wave approximation:

$$F(q) = \frac{1}{Z} \int_0^\infty \rho_{ch}(r) e^{i\vec{q}\cdot\vec{r}} d\tau = \frac{4\pi}{Z} \int_0^\infty \rho_{ch}(r) j_o(qr) r^2 dr, \quad (5.5)$$

where

$$j_o(qr) = \frac{\sin(qr)}{qr}. \quad (5.6)$$

The normalization in Eq. (5.5) is chosen to give $F(q=0) = 1$. The function F_q oscillates around zero and $|F_q|^2$ has minima that go to zero. The rms charge radius can be obtained from the curvature of the low- q expansion of $F(q)$

$$F(q) \rightarrow 1 - \frac{R_{ch}^2}{6} q^2. \quad (5.7)$$

From the measured form factors one can obtain the charge-density with the inverse of Eq. (5.5):

$$\rho_{ch}(r) = \frac{Z}{2\pi^2} \int_0^\phi F(q) j_o(qr) q^2 dq. \quad (5.8)$$

One must take into account the distortion of the electron wavefunction coming from the Coulomb attraction of the electron with the protons in the nucleus. This is done with the distorted wave Born approximation (DWBA) as used, for example, in the DUELS code [5]. The distortion results in cross-sections minima that are washed out and do not go to zero. Some of the effects of the distortion can be approximated in the plane wave approximation by replacing the momentum transfer q with an effective value $q_{eff} > q$ that takes into account the increase of the electron energy when the electron interacts in the nucleus (see the chapter on electron scattering). The distortion is large for heavy nuclei (see, for example, Fig. 1 in [6]). A typical procedure is to extract $F(q)$ from a DWBA analysis and then use this in equation (5.8) to obtain the charge density. Since the form factor data are only determined up to some q_{max} , the resulting charge-density has some “error band” which depends upon the assumptions made about $F(q)$ for $q > q_{max}$.

A common method for extracting the charge density from the electron scattering form factors is to make a Fourier-Bessel expansion fit [7] to the data. The Fourier-Bessel expansion

is given by:

$$\rho_{ch}(r) = \sum_{\nu=1}^{n_{max}} a_{\nu} j_o(\nu\pi r/R), \quad (5.9)$$

for $r \leq R$ and $\rho_{ch}(r) = 0$ for $r > R$, with the associated plane-wave transform:

$$F(q) = \frac{4\pi}{Z} \frac{(qR)^2}{\nu q^3} \sum_{\nu=1}^{n_{max}} \alpha_{\nu} [j_o(\nu\pi - qR) - j_o(\nu\pi + qR)]. \quad (5.10)$$

The parameters a_{ν} , n_{max} and R for a wide range of nuclei are given in Refs. [8] and [9].

In order to obtain a qualitative understanding of how the form factors depend upon the properties of the charge density, I show in Figs. (5.2) and (5.3) some results for ^{208}Pb ($Z = 82$) based upon the Fermi distribution:

$$\rho_{ch}(r) = \frac{\rho_o}{1 + \exp[(r - c)/a]} \quad (5.11)$$

The densities are shown in the upper panels and the associated form factors $|F(q)|^2$ are shown in the lower panels.

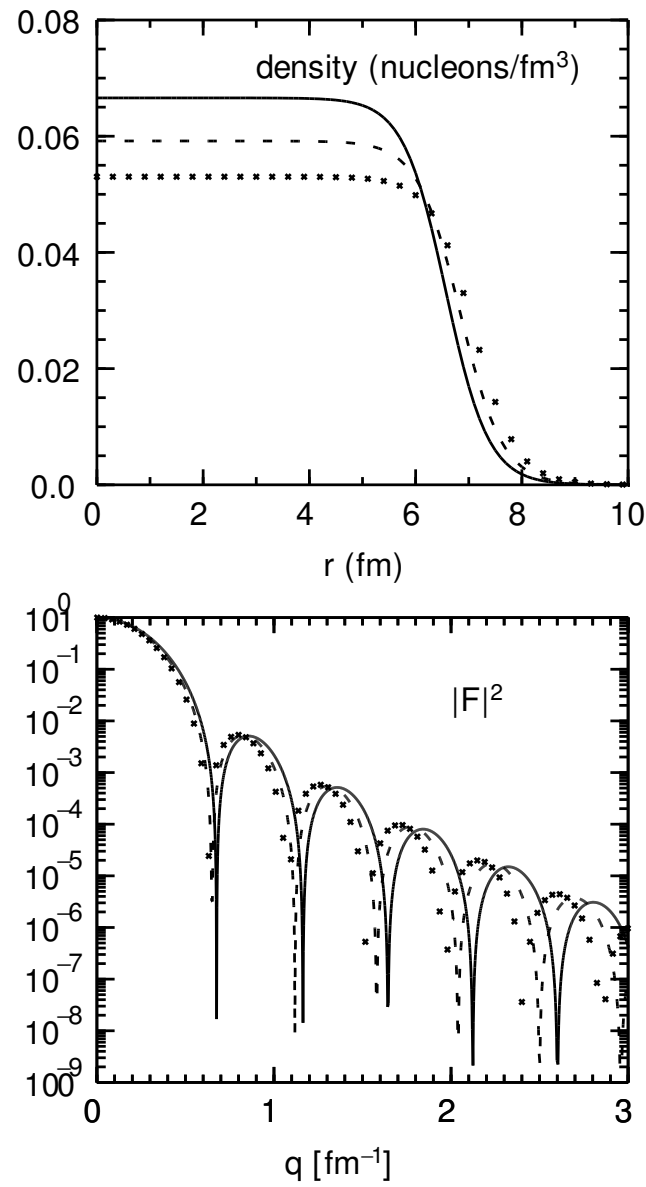


Figure 5.2: Features of the fermi-function densities and the associated form factors when the diffuseness is constrained to $a = 0.4$ fm and the c is used to vary the rms radius to be 5.30 fm (solid line), 5.50 (dashed line) fm and 5.70 fm (crosses).

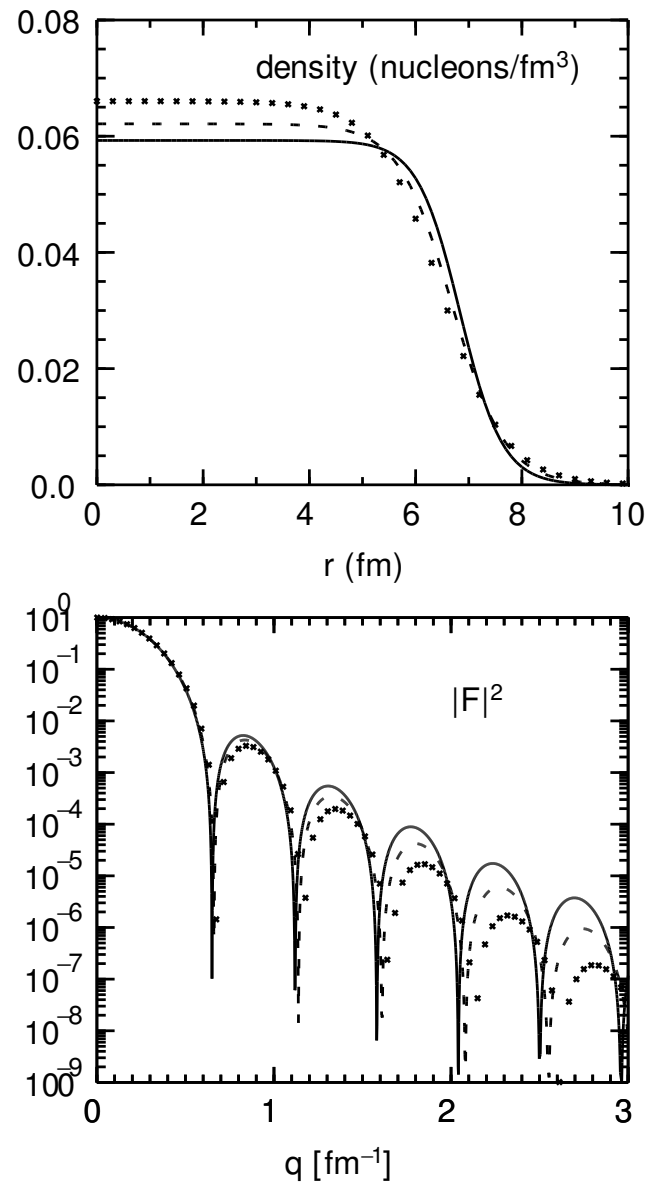


Figure 5.3: Features of the fermi-function densities and the associated form factors when the rms radius is constrained to be 5.5 fm. The results are given for diffuseness values $a = 0.4$ fm (solid line), 0.5 fm (dashed line) and 0.6 fm (crosses).

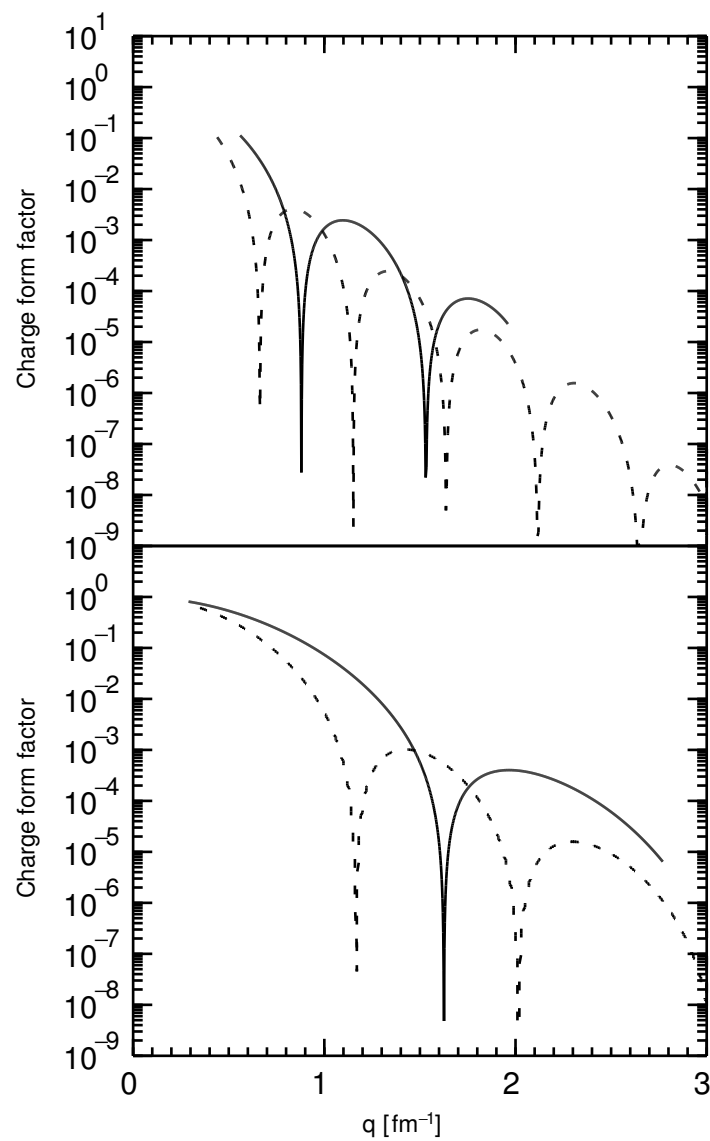


Figure 5.4: Experimental form factors $|F|^2$ for ^{16}O (solid line in the lower panel), ^{40}Ca (dashed line in the lower panel), ^{92}Mo (solid line in the upper panel) and ^{208}Pb (dashed line in the upper panel). The lines are plotted over the range of q values measured.

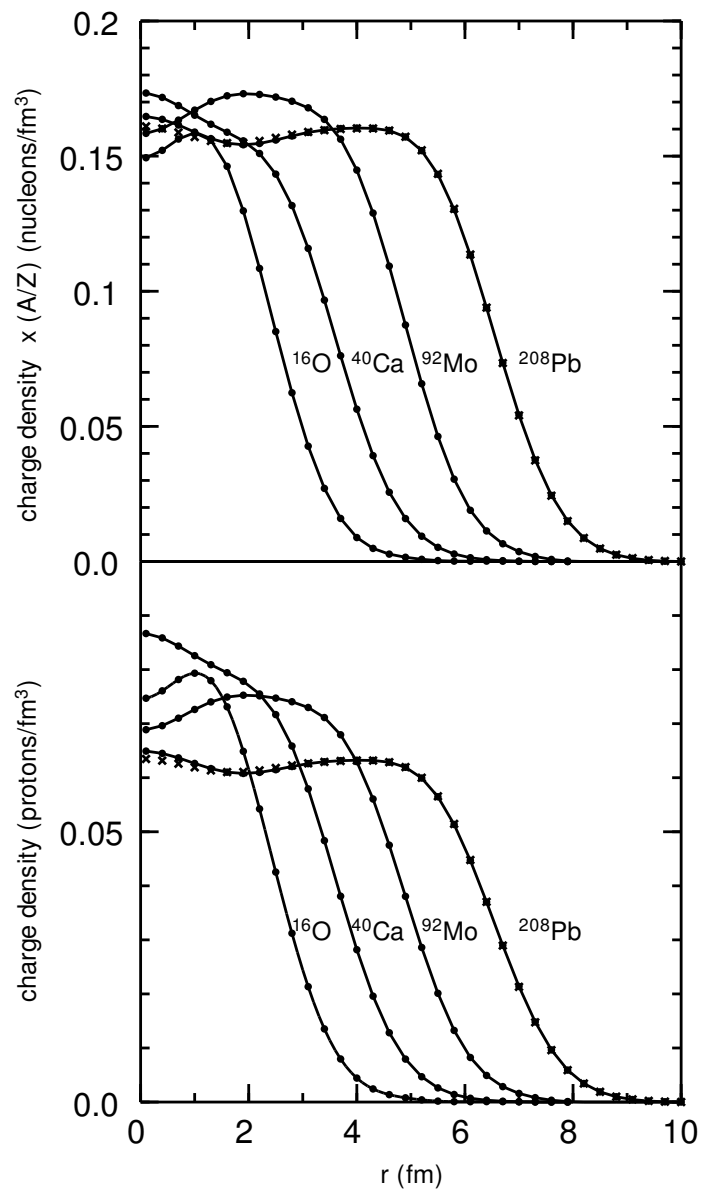


Figure 5.5: Bottom: experimental charge-density distributions for ^{16}O , ^{40}Ca , ^{92}Mo and ^{208}Pb . The results for the analysis of two different data sets for ^{208}Pb are shown by the circles and crosses. Top: charge-density distributions multiplied by (A/Z) .

In Fig. (5.2) I have fixed the diffuseness to be $a = 0.4$ fm and then varied c to make the rms charge radius 5.30 fm (solid line), 5.50 fm (dashed line) and 5.70 fm (crosses). In Fig. (5.3) I have varied the diffuseness from $a=0.4$ (solid line), 0.5 (dashed line) and 0.6 (crosses) but with R chosen to give a fixed rms of 5.50 fm.

Note that an increase in the diffuseness is associated with an increase in the interior density and a large decrease in the form factor maxima at large q values. The qualitative effects of oscillations in the densities on the form factors are discussed in Ref. [10].

The form factors which have been measured for ^{16}O , ^{40}Ca , ^{92}Mo and ^{208}Pb are shown in (5.4). The charge densities which have been extracted from these data are shown in the bottom panel of (5.5). One observes various oscillations in the charge density which is related to the shell structure of nuclei. The surface gradually extends out for heavier nuclei but the diffuseness is rather constant as assumed in the Fermi distribution model. When the charge densities are multiplied by (A/Z) (top panel) one observes that the interior densities for all nuclei tends to saturate at a value of about 0.16 nucleons/fm³.

For ^{208}Pb in Fig. (5.5) the density extracted from two difference sets of set are used to

give an indication of the error. General aspects of the statistical and model-dependent errors in these Fourier-Bessel fits are discussed by Dreher et al., [7] and those related to specific experiments are discussed in the original experimental papers. Generally the width of the error band increases toward the center of the distribution (where the number of protons is small). For example for ^{92}Mo [11] the statistical and model-dependent error is 1.5% at $r = 2$ fm and goes down to 0.6% (about the size of the circles used to represent the experimental data in the figures to be discussed below) for $r = 4$ fm.

One can unfold the measured charge density with that of the finite charge size of the proton [12]. For ^{208}Pb this gives a point-proton density with an rms radius of 5.444 fm and with a shape that is well represented on the surface by the two-parameter Fermi function

$$\rho_p(r) = \frac{\rho_o}{1 + \exp(r - c_p)/a_p}, \quad (5.12)$$

with $c_p = 6.613(40)$ fm and $a_p = 0.497(20)$ fm [12]. It can be improved by fitting to a three-parameter Fermi function

$$\rho_p(r) = \frac{\rho_o(1 + wr^2/c_p^2)}{1 + \exp(r - c_p)/a_p}, \quad (5.13)$$

with $c_p = 6.583(40)$ fm, $a_p = 0.499(20)$ fm and $w_p = 0.0393$ fm. As observed in Fig. (5.5), the interior of the ^{208}Pb charge density has a small oscillation that goes beyond the smooth form of these Fermi distributions.

Bibliography

- [1] J. L. Friar, J. Martorell and D. W. L. Sprung, Phys. Rev. A **56**, 4579 (1997).
- [2] C. J. Horowitz and J. Piekarewicz, Phys. Rev. C **86**, 045503 (2012). link
- [3] A. Ong, J. C. Berengut, and V. V. Flambaum, Phys. Rev. C **82**, 014320 (2010). link
- [4] B. A. Brown, S. E. Massen and P. E. Hodgson, J. Phys. **G5**, 1655 (1979).

- [5] S. T. Tuan, L. E. Wright and D. S. Onley, Nucl. Instr. and Methods **60**, 70 (1968).
- [6] B. Fois et al., Phys. Rev. Lett. **38**, 152 (1977). link
- [7] B. Dreher, J. Friedrich, K. Merle, H. Rothhaas and G. Luhrs, Nucl. Phys. **A235**, 219 (1974).
- [8] H. de Vries, C. W. de Jager and C. de Vries, At. Data and Nucl. Data Tables **36**, 495 (1987).
- [9] G. Fricke, C. Bernhardt, K. Heilig, L. A. Schaller, L. Shellenberg, E. B. Shera and C. W. de Jager, At. Data and Nucl. Data Sheets **60**, 177 (1995).
- [10] P. G. Reinhard, J. Friedrich and N. Voegler, Z. Phys. A **316**, 207 (1984).
- [11] B. Dreher, Phys. Rev. Lett **35**, 716 (1975) link
- [12] A. B. Jones and B. A. Brown, Phys. Rev. C **90**, 067304 (2014). link

Chapter 6

The liquid-drop model

Nuclei are bound due to the overall attractive strong interactions between nucleons. The strong interaction arises from the exchange of mesons. The interactions are short ranged and occur mainly between neighboring nucleons. In addition, the nuclear interaction saturates, resulting in a nearly constant interior nucleon density.

The classical Coulomb interaction for a uniform density out to a spherical radius of c_s is

$$E_C = \frac{3}{5} \frac{e^2 Z(Z-1)}{c_s}. \quad (6.1)$$

For charge density given by the Fermi function

$$\rho(r) = \frac{\rho_0}{1 + \exp(r - c)/a}, \quad (6.2)$$

the Coulomb interaction is given to order $(a/c)^4$ by [1]

$$E_C = \frac{3}{5} \frac{e^2 Z(Z-1)}{c_e} [1 + b_1(a/c_e)^3 + b_2(a/c_e)^4], \quad (6.3)$$

where

$$c_e = \sqrt{5/3} \sqrt{\langle r^2 \rangle} = \sqrt{[c^2 + (7/3)\pi^2 a^2]}, \quad (6.4)$$

and $b_1 = 18.03$ and $b_2 = -85$.

For the Fermionic system of nucleons there is also an exchange correction which can be estimated from the Fermi-gas model. Up to order a/c this estimate for the exchange energy gives [1]

$$E_{\text{exch}} = -3(3/16\pi)^{2/3}(e^2 Z^{4/3}/c_e)[1 + b_7(a/c_e)], \quad (6.5)$$

with $b_7 = -1.34$. The exchange term correction ranges from about a 2% reduction for ^{208}Pb to a about 10% reduction for ^{40}Ca .

For the level of accuracy of the liquid drop model, we will use Eq. (6.1) with $c_s = 1.24 A^{1/3}$. Also at this level of accuracy we replace $Z(Z-1)$ with Z^2 and ignore the exchange term. With these approximations the Coulomb energy of ^{208}Pb is 820 MeV.

The liquid drop model is based on the observation that the interior matter density for nuclei is approximately constant ($\rho_o = 0.16$ nucleons/fm³), and that the interaction between

nucleons has a short range. This is analogous to a drop of liquid. The droplet energy increases linearly with the volume that is proportional to the number of nucleons A . At the surface there is a reduction in energy due to the missing interactions that depends on the surface area proportional to $A^{2/3}$. Isospin symmetry of the $T = 1$ part of the strong interaction means that the strong interaction contribution to the binding energy is the same when protons and neutrons are interchanged, $\text{BE}_s(N, Z) = \text{BE}_s(Z, N)$. In addition the extra attractive interaction between the proton and neutron in the $T = 0$ state mean BE_s is maximized when $N = Z$. These ideas motivate the liquid drop form for the nuclear binding energy given by

$$\text{BE}(N, Z) = \alpha_1 A - \alpha_2 A^{2/3} - \alpha_3 \frac{Z^2}{A^{1/3}} - \alpha_4 \frac{(N - Z)^2}{A}. \quad (6.6)$$

The signs are chosen so that all or the α are positive. The four terms on the right-hand side are referred to as the volume, surface, Coulomb and symmetry energy terms, respectively. The Fermi gas kinetic energy also has the terms with A and $(N - Z)/A$, in particular the kinetic energy is minimized when $N = Z$. The constant $\alpha_3=0.697$ MeV is fixed by the Coulomb interaction discussed above. Typical values of the liquid-drop constants that reproduce the average trends in the experimental data are given by $\alpha_1 = 15.49$ MeV, α_2

$\alpha_3 = 17.23$ MeV and $\alpha_4 = 22.6$ MeV. In addition one can include terms that describe the systematic odd-even oscillations in the binding energy due to the pairing interaction.

The comparison of the liquid-drop model for the most stable nuclei is shown in Fig. (6.1). The total is shown with by the line (D). Combinations of individual terms are also shown: the volume term (A), the volume plus surface terms (B), the volume plus surface plus Coulomb terms (C). [The jagged form of curve (C) is due to the jumps from the Z -dependence of the Coulomb term along the jagged path of the most stable nuclei as a function of Z and A . It turns out the jumps in the symmetry-energy term nearly cancel those in the Coulomb term to make the total binding-energy curve (D) rather smooth.]

The term “symmetric nuclear matter” refers to extrapolation of properties of nuclei with $N = Z$ and with no Coulomb interaction to infinite sized nuclei where the surface can be ignored. Thus the symmetric nuclear matter extrapolation of the liquid-drop model used for this example gives $BE/A = -15.5$ MeV.

The size of the symmetry energy term determines how the binding energy decreases as we move away from stability. To isolate this term we can examine the chain of nuclei

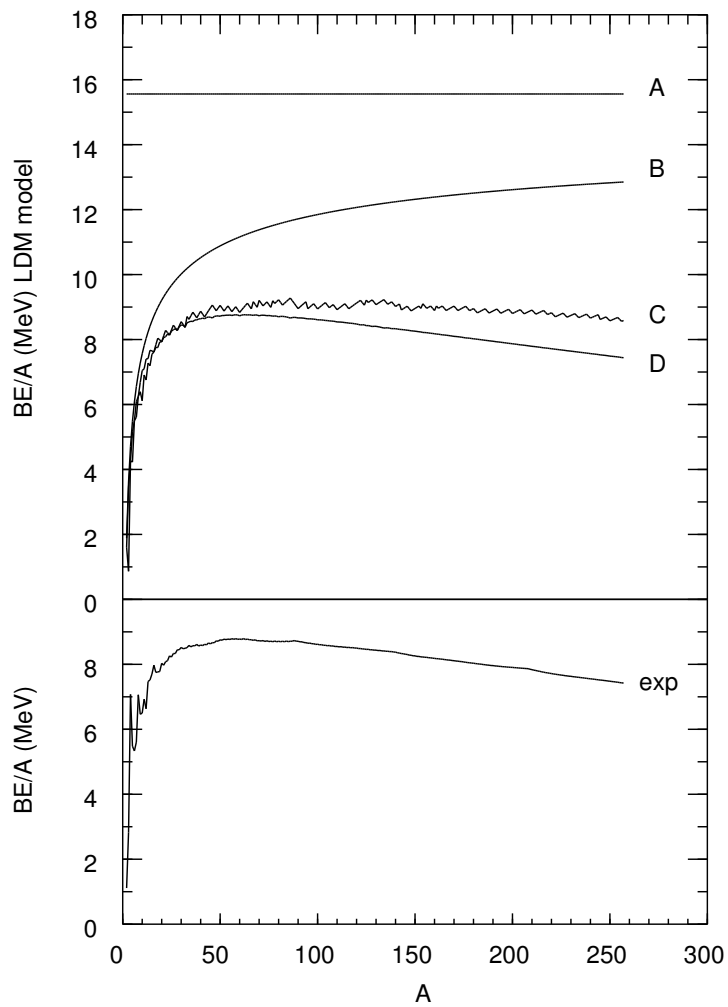


Figure 6.1: Bottom panel: Experimental values for the BE/A as a function of A for the most stable nuclei. Top panel: Liquid-drop model for BE/A (curve D) and shown in terms its components the volume term (A), the volume plus surface terms (B), the volume plus surface plus Coulomb terms (C).

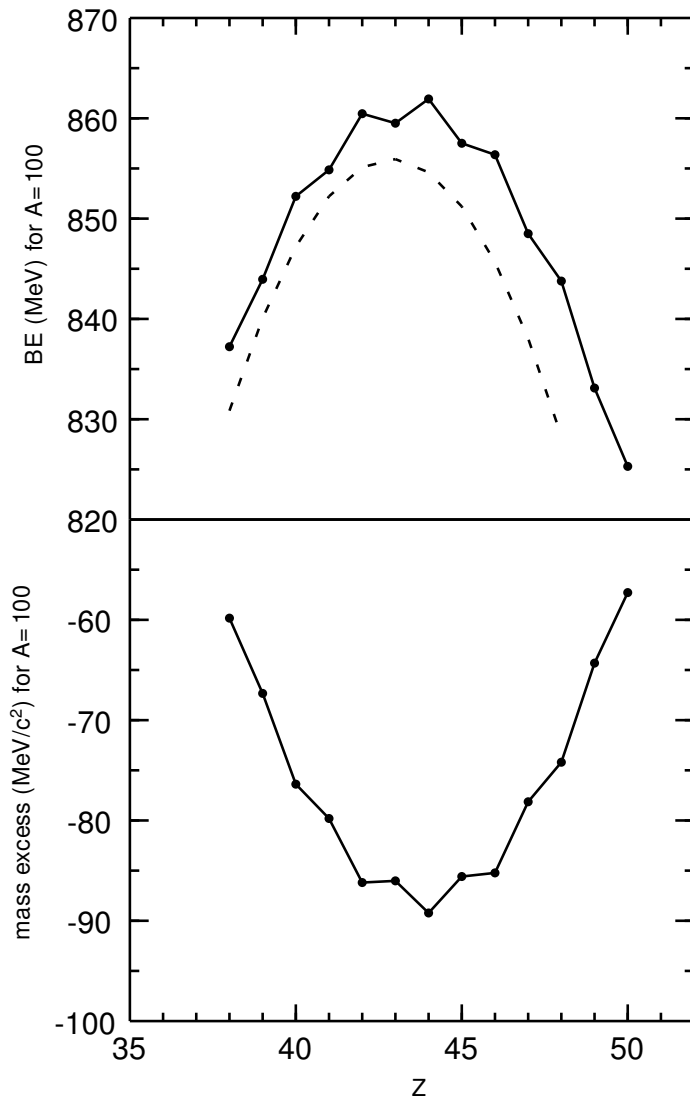


Figure 6.2: Binding energy per nucleon, BE/A , and the mass excess, Δ , for $A = 100$ as a function of Z . The points connected by a line are the experimental values and the liquid-drop model for the binding energy is shown by the dashed line. The bottom plot of the experiment mass excess shows a situation where there are two nuclei that are stable to single-beta decay. $Z = 42$ (^{100}Mo) can decay into $Z = 44$ (^{100}Ru) only by process of double-beta decay.

for a fixed A value as a function of Z . Experimental values $\text{BE}(N, Z)/A$ vs Z are shown in Fig. (6.2) for $A = 100$. The form of this curve for $A = 100$ is similar to those for other A values. The binding energy has a maximum at $Z_{\max} = 44$. Without the Coulomb interaction between protons, the maximum would occur at $N = Z$ due to the symmetry energy (the α_4 term). When the Coulomb interaction between protons (the α_3 term) is added, the peak is shifted to more neutron-rich nuclei. The oscillation in the binding energy curve in Fig. (6.2) is due to nuclear pairing interaction, which gives rise to the fact that nuclei with even numbers of protons or neutrons are more bound than their neighboring (odd) nuclei. The droplet model would predict that $Z = 43$ has the highest binding, but the pairing changes this to $Z = 44$.

The stability of nuclei to beta decay is determined by the differences in the mass excess shown in this example for $A = 100$ in the bottom panel of Fig. (6.2). The differences in the mass excesses are related to differences in the binding energies by $[\Delta(N, Z) - \Delta(N, Z \pm 1)]c^2 = -[\text{BE}(N, Z) - \text{BE}(N, Z \pm 1)] \pm [\Delta_n - \Delta_H]c^2$ where $[\Delta(n) - \Delta(H)]c^2 = 0.782$ MeV. Thus, for example, for $A = 100$ we find two stable isotopes in nature, ^{100}Mo and ^{100}Ru . If we consider the very weak double-beta decay process, ^{100}Mo will eventually decay into ^{100}Ru .

This occurs with a lifetime which is greater than the age of the universe, but such rare decay modes have been detected in experiments.

To go further, we are interested in the deviations between the experimental and liquid-drop models for the binding energies, and in understanding these deviations in terms of microscopic models. The difference between the experimental and liquid-drop model binding energies are Fig. (6.3). In light nuclei the deviations are largest near the neutron drip line. This deviation for light nuclei can be improved by adding another term to Eq. (6.6) related to the “surface symmetry” energy [2]. In Fig. (6.3) there are two strong peaks at $A = 132$ and $A = 208$ which are the “doubly-closed shell” nuclei ^{132}Sn and ^{208}Pb . There is also a peak forming near ^{100}Sn .

The values for the difference between experiment and the liquid-drop model plotted vs N and Z are shown in Figs. (6.4) and (6.5), respectively. One observes several types of deviations. When the differences are plotted vs proton number Z one observes that the nuclei with $Z=28, 50$ and 82 are more bound than average. These are the shell-model magic numbers for the closed-shell configurations at these Z values. For neutrons the same magic

numbers are observed with the addition of $N = 126$. The small oscillations observed in these figures is due to nuclear pairing. This can be removed by plotting the results for only the even-even nuclei as shown in Figs. (6.6) and (6.7).

The Droplet Model was introduced as a refinement of the liquid-drop model [3], [4], [5]. It is a much more elaborate model that takes into account the neutron skin. Also deformed shapes can be taken into account [3].

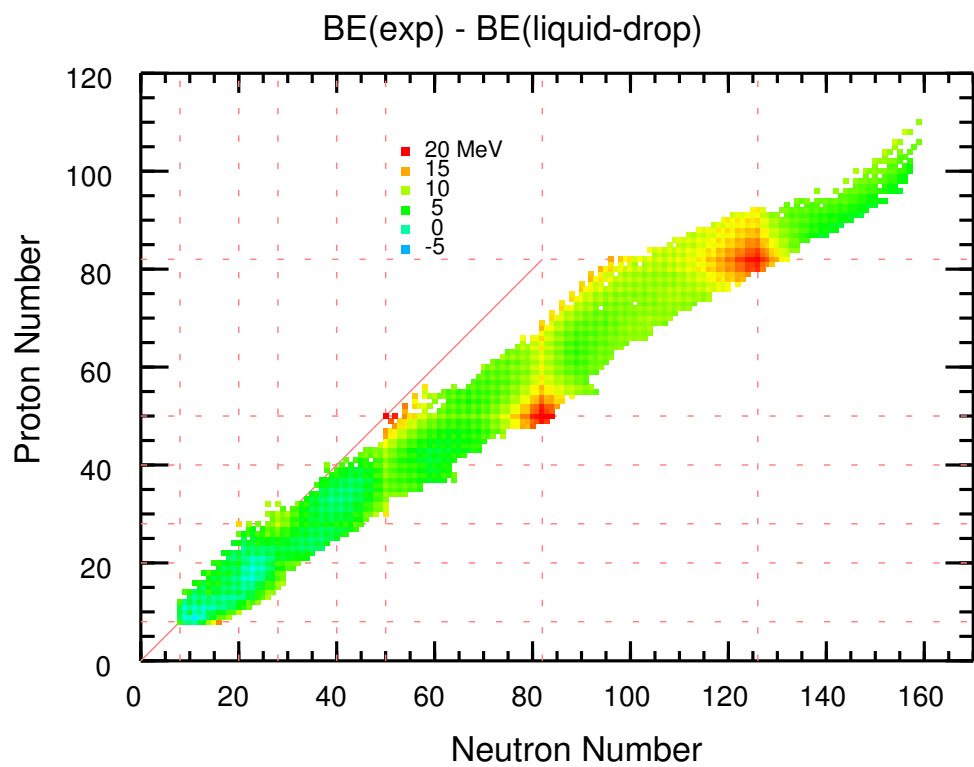


Figure 6.3: The difference between the experimental and liquid-drop binding energies as a function of N and Z .

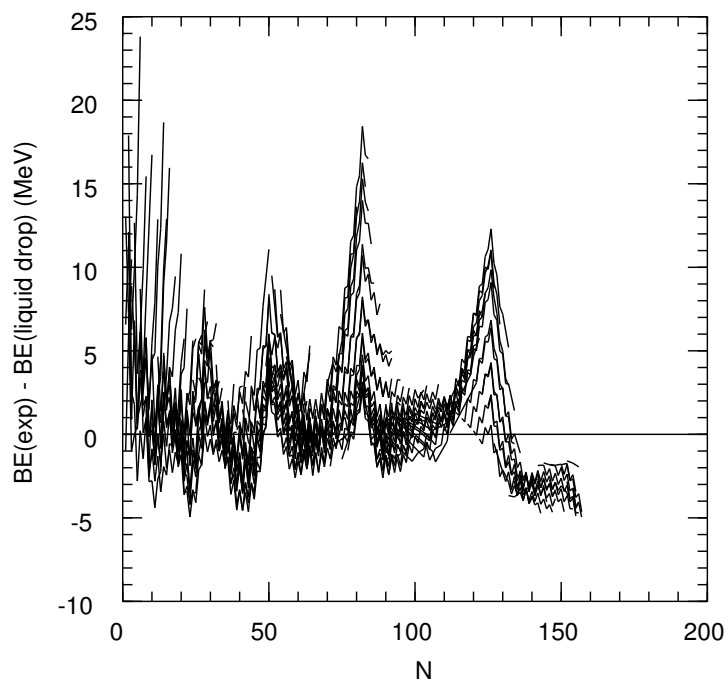


Figure 6.4: The difference between the experimental and liquid-drop binding energies as a function of N . The dashed lines show the magic numbers 28, 50, 82 and 126.

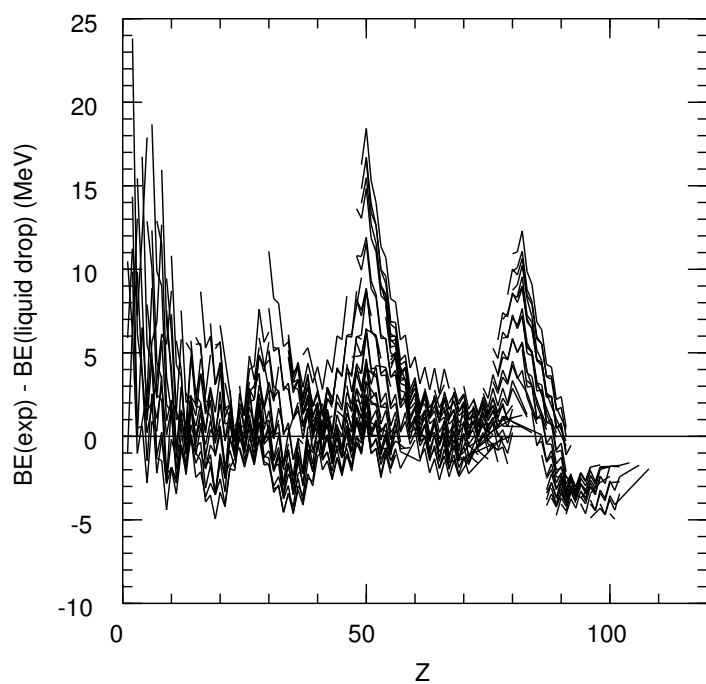


Figure 6.5: The difference between the experimental and liquid-drop binding energies as a function of Z . The dashed lines show the magic numbers 28, 50 and 82.

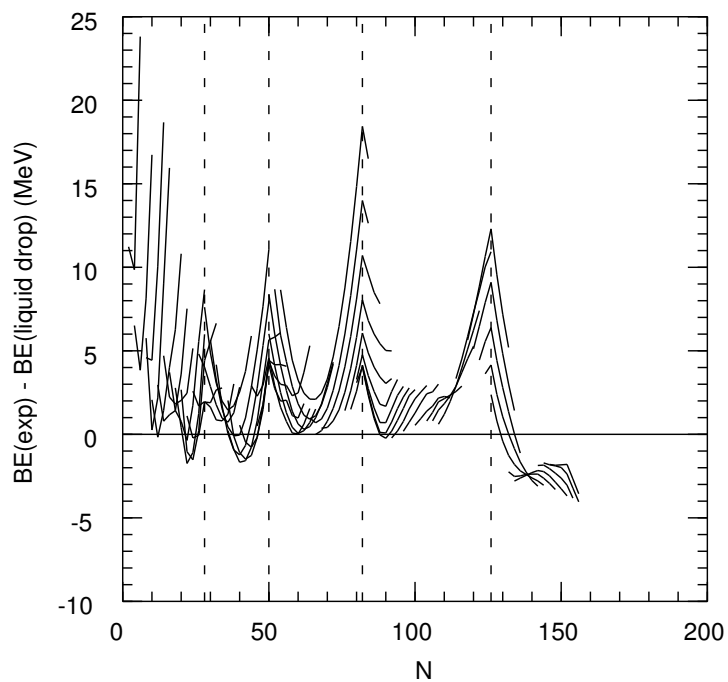


Figure 6.6: The difference between the experimental and liquid-drop binding energies as a function of N for even-even nuclei. The peaks occur at the magic numbers 28, 50, 82 and 126.

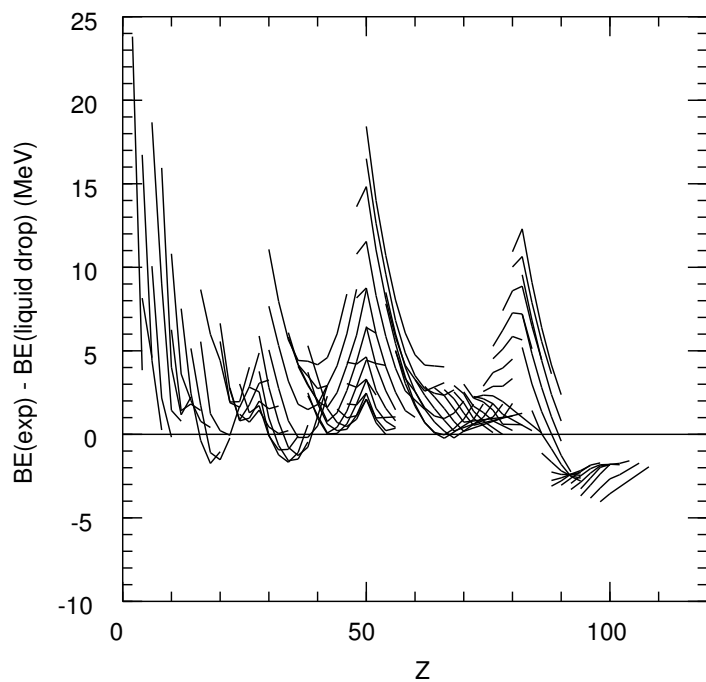


Figure 6.7: The difference between the experimental and liquid-drop binding energies as a function of Z for even-even nuclei. The peaks occur at the magic numbers 28, 50, 82 and 126.

Bibliography

- [1] J. Janecke, Nucl. Phys. **A181**, 49 (1972).
- [2] P. Danielewicz, Nucl. Phys. A **727**, 233 (2003).
- [3] W. D. Meyers and W. J. Swiatekci, Ann. of Phys. **84**, 186 (1974).
- [4] W. D. Myers and W. J. Swiatecki, Nucl. Phys. A **336**, 267 (1980).

- [5] W. D. Meyers and K. H. Schmidt, Nucl. Phys. A **410**, 61 (1983).

Chapter 7

Overview of nuclear decays

In 1896 Antoine Henri Becquerel found radiations that were spontaneously emitted from uranium salts. In 1898 Maria and Pierre Curie found new elements latter called Polonium and Radium that also spontaneously emitted radiations. These radiations were observed to be bent by magnetic field, and were named alpha (α) and beta (β) by Ernest Rutherford in 1899 after the observations that one was easily absorbed (alpha) and one was more penetrating (beta). In 1900, Villard identified a third form of penetrating radiation that could not be bent by a magnetic field, and these were called gamma (γ) radiations.

In 1909, Ernest Rutherford and Thomas Royds established that alpha particles were the nuclei of helium atoms and have atomic mass number $A = 4$ and nuclear charge number $Z = 2$. Antoine Henri Becquerel (1899) and Walter Kaufmann (1902) identified the beta radiation with the electron by its deflection in electric and magnetic fields. The basic theory for beta decay was constructed by Enrico Fermi in 1934 after Wolfgang Pauli's suggestion in the same year about the existence of the neutrino.

Gamma radiation was soon realized to be a high-energy form of the electromagnetic radiation described by Maxwell's equations. Today "gamma" radiation generally refers to

the high-energy region of the electromagnetic-radiation spectrum associated with the decay of particles and nuclei. Gamma-ray energies range from a few keV (where their energy range overlaps with those of X rays that are emitted in the decay of atoms and molecules) up to 10^2 TeV (10^{14} eV) for those found in cosmic rays. The gamma ray, like the X ray, consists of photons that have no mass and no charge. The process of double-gamma decay was first unambiguously observed in 1984 [1].

A group led by Lise Meitner and including Otto Hahn and Fritz Strassmann began studying the products formed when uranium is bombarded by neutrons in the 1930's that led to the discovery of fission in 1938-39. Fission is the induced or spontaneous breakup of a heavy nucleus into two nuclei each of which has about one half of the mass of the parent. The breakup is usually accompanied by the emission of one or more neutrons.

Other forms of ground-state radioactivity we may consider are proton decay discovered in 1981 [2], light cluster emission, $^{223}\text{Ra} \rightarrow ^{209}\text{Bi} + ^{14}\text{C}$ discovered in 1984 [3], two-neutrino double-beta decay discovered in 1987 [4], and two-proton decay discovered in 2002 [5].

Since 1981 a many more cases of one-proton emission have been observed [6]. Also

several other cases of light cluster emission have been observed including the emission of ^{20}O , ^{24}Ne , ^{26}Ne , ^{28}Mg , ^{30}Mg , ^{32}Si and ^{34}Si [7].

Nuclear decays are characterized by their Q value and half-life. The lifetimes we consider vary over an extremely wide range of magnitudes. In terms of $x = \text{Log}_{10}[T_{1/2}(\text{sec})]$ it is useful to keep in mind the values of $x \approx 37$ for the proton lifetime limit, $x \approx 17$ for the age of the universe (10 billion years), $x \approx 5$ for one day, $x \approx -7$ (100 nsec) for the time it takes a nucleus traveling at one third the speed of light to travel 10 meters, and $x \approx -21$ for the lifetime corresponding to a resonance width of 1 MeV.

The physical units in terms of seconds (s), meter (m) and electron volts (eV), and constants involved in decay calculations in units useful for nuclear physics are given in the Table 1.

Table 7.1: Commonly used units and constants

$\text{keV} = 10^3 \text{ eV}$	kilo-electron volts
$\text{MeV} = 10^6 \text{ eV}$	mega-electron volts
$\text{fm} = 10^{-15} \text{ m}$	fermi
$\text{ms} = 10^{-3} \text{ s}$	milli-second
$\mu\text{s} = 10^{-6} \text{ s}$	micro-second
$\text{ns} = 10^{-9} \text{ s}$	nano-second
$\text{ps} = 10^{-12} \text{ s}$	atto-second
$\text{fs} = 10^{-15} \text{ s}$	femto-second
$e^2 = 1.44 \text{ MeV fm}$	electric charge squared
$c = 3.00 \text{ m ns}$	speed of light in meters per nano-second
$\hbar = 6.582 \times 10^{-22} \text{ MeV s}$	Plank's constant divided by 2π
$\hbar c = 197 \text{ MeV fm}$	
$m_p = 938 \text{ MeV c}^2$	proton mass
$\mu_N = (e\hbar)(2m_p c) = 0.105 e \text{ fm}$	nuclear magneton

7.1 Decay widths and lifetimes

The decay of an ensemble of quantum states is described by the rate equation for the number of nuclei present at time t .

$$\frac{dN}{dt} = -WN(t), \quad (7.1)$$

where W is the transition rate or decay constant. The solution of this equation is the exponential decay law

$$N(t) = N_0 e^{-Wt}. \quad (7.2)$$

The time at which the number is reduced by half is the half-life

$$T_{1/2} = \frac{\ln 2}{W} = \frac{0.693}{W}. \quad (7.3)$$

The mean-lifetime τ is the average amount of time it takes to decay

$$\tau = \frac{\int te^{-Wt} dt}{\int e^{-Wt} dt} = \frac{1}{W} = \frac{T_{1/2}}{\ln 2} = \frac{T_{1/2}}{0.693}. \quad (7.4)$$

The time dependence of a decaying wavefunction with a narrow width involves both real and imaginary parts

$$\psi(t) = e^{-i\omega t - Wt/2}, \quad (7.5)$$

where the average energy is $E_o = \hbar\omega$. The Fourier transform of Eq. (7.5) gives

$$A(E) = \frac{1}{2\pi} \frac{1}{-i(E - E_o) + (\hbar W/2)}. \quad (7.6)$$

The probability to find the state in energy E is

$$P(E) = A^*(E) A(E) = \frac{1}{4\pi^2} \frac{1}{(E - E_o)^2 + (\hbar W/2)^2}. \quad (7.7)$$

The value of $E - E_o$ at which $P(E)$ falls by a factor of two is $E - E_o = \hbar W/2$. Thus the full-width at half maximum denoted by Γ is

$$\Gamma = \hbar W = \hbar/\tau. \quad (7.8)$$

For “non-narrow” states the exponential approximaton must be replaced by a more complicated non-exponential with oscillations [8].

The relation between the width and the half-life is

$$\Gamma T_{1/2} = \hbar \ln(2) = 0.456 \text{ eV fs.} \quad (7.9)$$

The recent Nuclear Data Sheets give the half-life for the both the ground states and excited states of nuclei. Older data compilations as well as many of the original papers give the mean-life for excited states (so one has to be sure which one is being used).

A given initial state may decay to several final states. The total transition rate is:

$$W = \sum_f W_{i,f}, \quad (7.10)$$

where $W_{i,f}$ is the partial decay rate to the particular final state f . The branching fraction to this state is:¹

$$b(i \rightarrow f) = \frac{W_{i,f}}{W}. \quad (7.11)$$

¹The branching fraction is often given in terms of the branching ratio (BR) in percent.

When the total lifetime and the branching fraction for a given type of decay are known, we can find the partial half-life T_p related to that specific decay channel by:

$$T_p = T/b. \quad (7.12)$$

7.2 Alpha and cluster decay

Alpha decay occurs when a parent nucleus (A, Z) with atomic mass number A and nuclear charge number Z spontaneously emits an alpha particle leaving a residual (daughter) nucleus ($A - 4, Z - 2$):



Alpha decay usually occurs from the nuclear ground state, but decay from excited states may also occur. The alpha decay of a given parent nucleus often leads to daughter nuclei that are themselves alpha or beta radioactive, thus giving rise to a disintegration series. By 1935 the detailed decay schemes for three naturally occurring series that started with ${}^{238}\text{U}$

(Z=92), ^{235}U , and ^{232}Th (Z=90) had been discovered. The alpha particles observed for these naturally occurring decays have energies in the range of 5 to 10 MeV, and were used as a source of projectiles for nuclear reaction experiments until the use of particle accelerators took over in the 1940's.

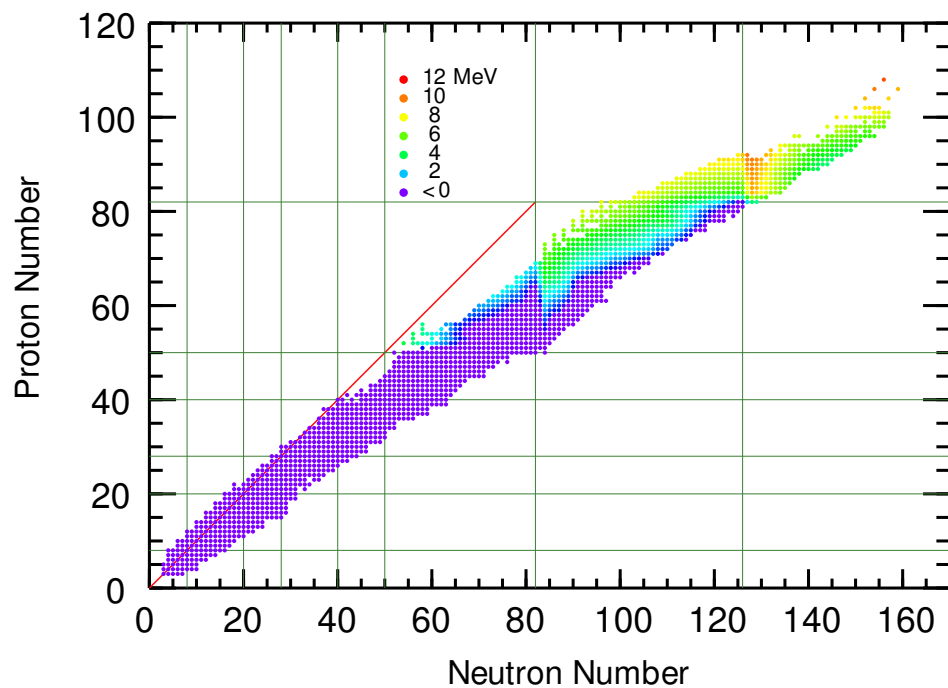
Spontaneous alpha decay is allowed when the Q_α value for the decay is positive. The energy of the emitted alpha particle is given by

$$E_\alpha = Q_\alpha M_d / (M_d + M_\alpha), \quad (7.14)$$

where M_d and M_α are the masses of the daughter nucleus and alpha particle, respectively, and the Q_α is given in terms of binding energies B by:

$$Q_\alpha = \text{BE}(N - 2, Z - 2) + \text{BE}(2, 2) - \text{BE}(N, Z), \quad (7.15)$$

where $\text{BE}(2, 2) = 28.296$ MeV. The values obtained with the experimental binding energies are shown in Figs. (7.1) and (7.2). The alpha-decay Q_α value becomes positive above $Z \approx 50$ and, generally, for nuclei that are proton-rich compared to the most stable. (An exceptional case is that of ^8Be for which the Q_α value is positive for the decay into two alpha particles.)

Figure 7.1: Experimental alpha decay Q values.

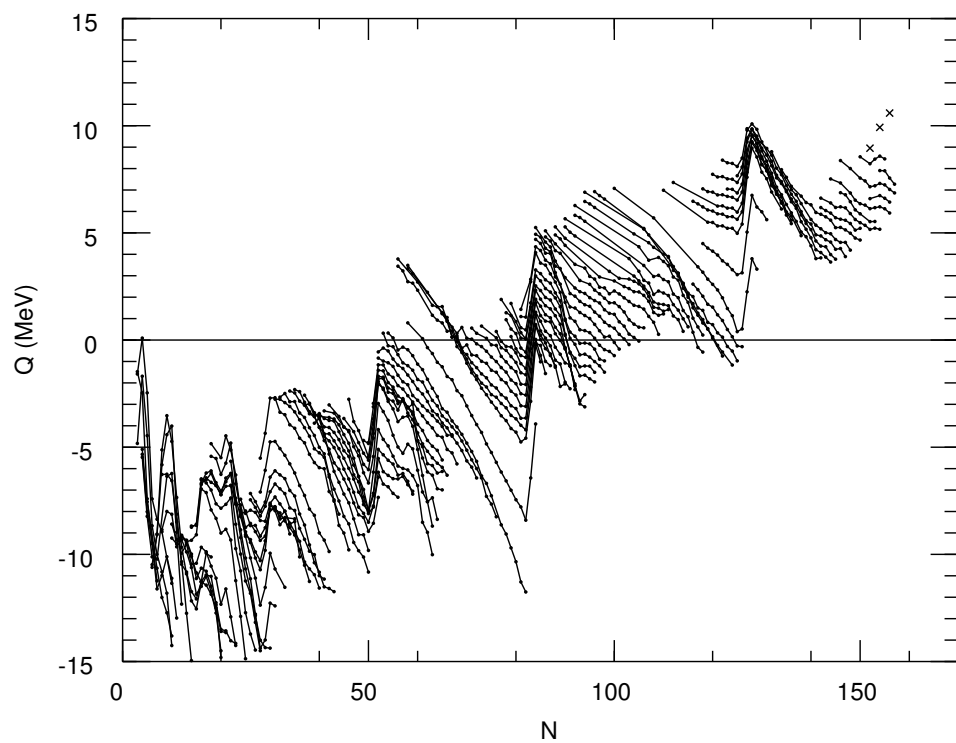


Figure 7.2: Experimental values for the alpha decay Q values.

Alpha decay is more important than other light element emissions because of the relatively large binding energy of the alpha particle together with its small Z value. The alpha decay of nuclear ground states competes with beta decay and fission decay. The alpha decay of nuclear excited states competes, in addition, with gamma decay. Man-made heavy elements are often most easily identified by their characteristic alpha decay series. For example, the element with $Z = 110$ discovered in 1994 at GSI was identified from the detection of an alpha particles with an energy of 11.13 MeV and a half-life of about $400 \mu\text{s}$ in coincidence with the alpha particle from the decay of the $Z = 108$ daughter, whose properties had been studied in previous experiments.

The basic theory for alpha decay was developed by George Gamow and others in 1930 [9]. One postulates an alpha particle moving in the potential well of an attractive strong interaction. The potential energy diagram for the ^{238}U decay is shown in Fig. (7.3) The radius of the strong interaction potential, R_t , is determined by the distance between the centers when the surfaces of the alpha particle and the daughter nucleus touch. This is given approximately by $R_t = R_d + R_\alpha$, where $R_d = 1.2A^{1/3}$ fm is the radius the daughter nucleus and $R_\alpha = 2.15$ fm for the alpha particle. For illustrative purposes the magnitude of the

potential inside R_t has been set to zero. The dashed line shows the Q_α value energy of 4.27 MeV. Beyond the distance R_t the interaction between the alpha particle and the daughter nucleus is determined by the repulsive Coulomb potential

$$V(r) = 2Z_d e^2 / r, \quad (7.16)$$

where Z_d is the nuclear charge number of the daughter nucleus.

The semi-classical picture developed by Gamow envisions an alpha particle moving back and forth classically inside the radius R_t and hitting the potential barrier at R_t with a decay rate

$$W_c = v/(2R_t) = \sqrt{Q_\alpha/(2\mu R_t^2)}, \quad (7.17)$$

where μ is the reduced mass $M_d M_\alpha / (M_d + M_\alpha)$, and we estimate the velocity v by $Q_\alpha = \frac{1}{2}\mu v^2$. When the alpha particle hits the potential barrier it has a probability, P , in the theory of quantum mechanics to tunnel through the barrier given by:

$$P = \exp\left\{-2 \int_{R_t}^{R_c} \sqrt{2\mu[V(r) - Q_\alpha]/\hbar^2} dr\right\}. \quad (7.18)$$

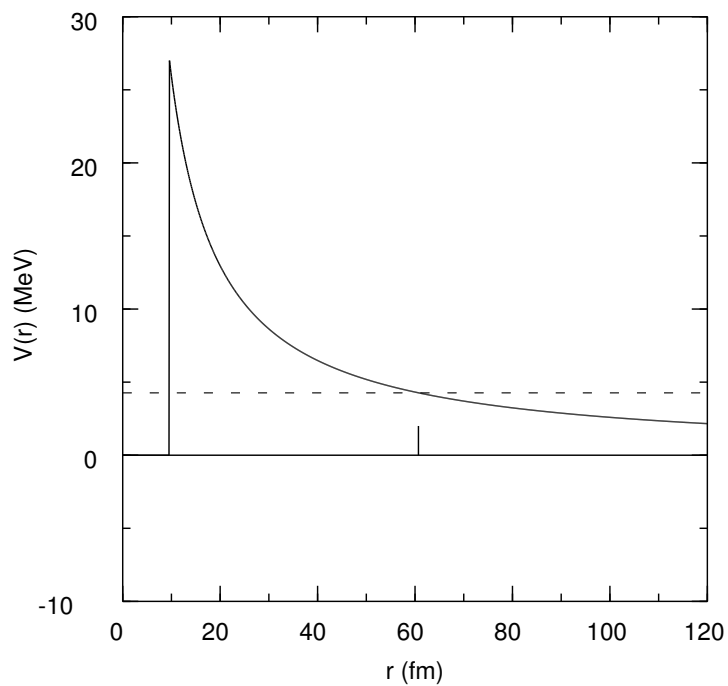


Figure 7.3: The potential energy diagram for the alpha decay of ^{238}U . The solid line is the Coulomb barrier to the radius R_t . the dashed line is the Q_α value.

The radius, $R_c = 2Z_d e^2 / Q_\alpha$, at which $V(r) = Q_\alpha$ is referred to as the classical turning radius, since classically an alpha particle approaching the daughter nucleus from a large radius cannot go beyond this point. Integration gives

$$P = \exp\{-4Z_d e^2 \sqrt{2\mu/(Q_\alpha \hbar^2)} [\cos^{-1}(x) - x\sqrt{1-x^2}]\}, \quad (7.19)$$

where $x = \sqrt{R_t/R_c}$. The total alpha decay rate is $W = W_c P$ and the alpha-decay half-life is given by

$$T_{1/2} = \frac{\ln 2}{(W_c P)}. \quad (7.20)$$

The experimental half-lives for the alpha decays of 119 (even-even) nuclei with ground state angular momenta of $J = 0$ are compared to the Gamow estimate in Fig. (7.4). One observes qualitative agreement with the Gamow estimate over 25 orders of magnitude in the half-life with a systematic trend for the experimental half-lives to be about 10-100 times longer than predicted. This reduction in the decay width can be interpreted as the square of the overlap of the initial nuclear state with the simplified assumption of a the final nucleus plus an alpha. The structure dependence in this hindrance factor can be seen in Fig. (7.5), where the ratio

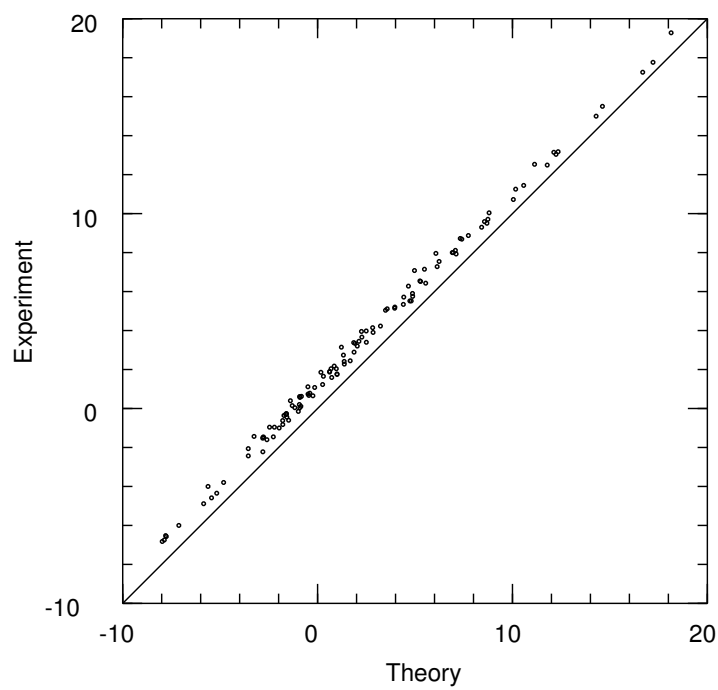


Figure 7.4: Comparison of experimental and theoretical values for $\log_{10}[T_{1/2}(\text{sec})]$.

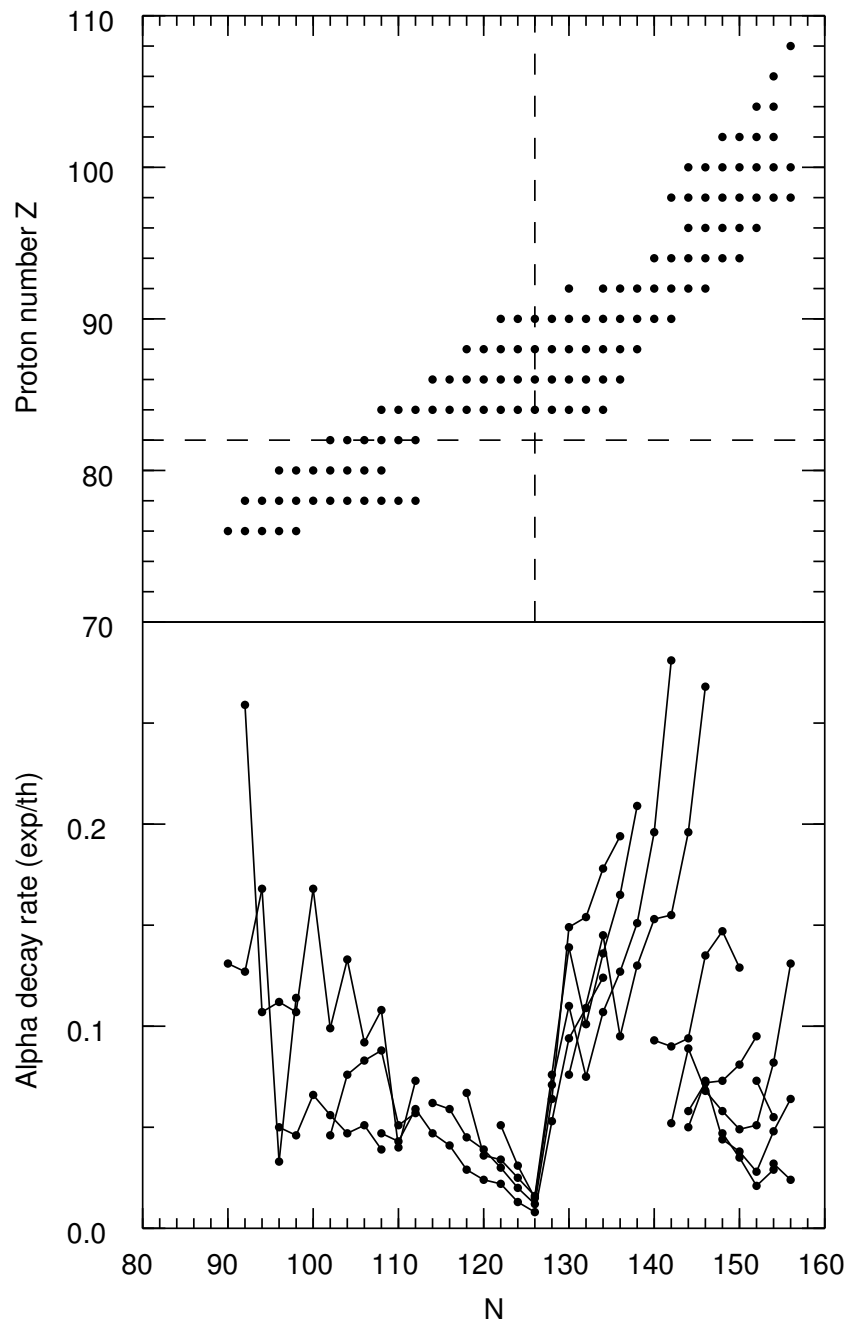


Figure 7.5: Ratio of the experimental to theoretical alpha decay rates (W) plotted as a function of neutron number. The top part of the figure shows the nuclei that are considered in the bottom part with the magic numbers $Z = 82$ and $N = 126$ shown by the dashed lines.

of the experimental to theoretical decay rates are shown. One observes a reduction in the experimental rate as one approaches the magic number 126 and then a sudden jump up.

From the form of Eq. (7.19) one obtains with some approximations the Gieger-Nuttall relation for alpha decay, $\log_{10}[T_{1/2}] \sim Z_d/\sqrt{Q_\alpha}$. However a more accurate empirical relation [10] that is able to reproduce the alpha decay half-lives to within about a factor of three is

$$\log_{10}[T_{1/2}(\text{sec})] = -51.37 + 9.54Z_d^{0.6}/\sqrt{Q_\alpha}. \quad (7.21)$$

where Z_d is the charge of the daughter nucleus and Q_α is in units of MeV. Generally equation (7.21) has the same accuracy as Eq. (7.20), and neither equation contains the structure dependence observed in Fig. (7.5).

Eq. (7.21) has been used to calculate the alpha-decay half-life for those nuclei in Fig. (7.1). The results for all nuclei are shown in Fig. (7.6). Results based on the HFB27 model are shown (7.7). One observes that alpha decay is responsible for the instability of nuclei above ^{208}Pb except for a small region of nuclei around ^{232}Th and $^{234-238}\text{U}$.

The Gamow model can be extended to the decay of non-zero spin nuclei by adding a

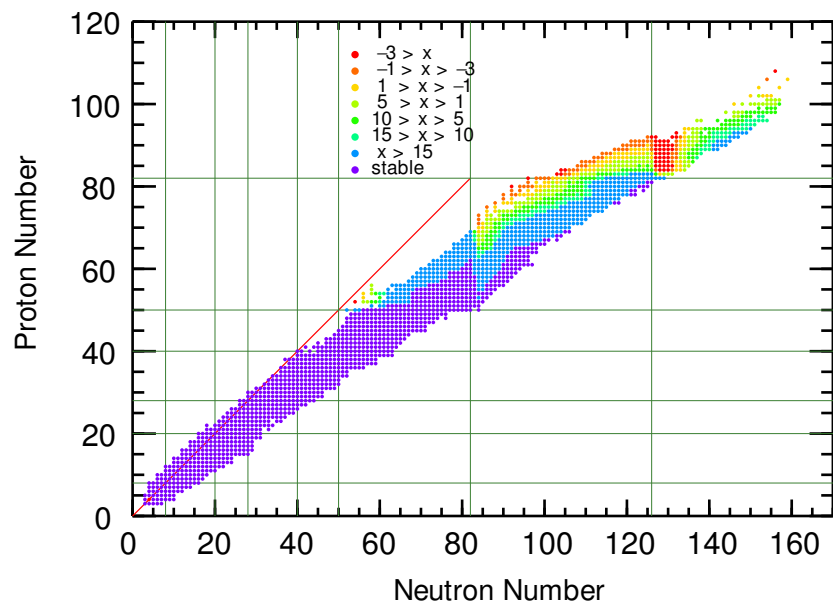


Figure 7.6: Alpha decay half-lives. The symbols represent different ranges of $x = \log_{10}[T_{1/2}(\text{sec})]$ as calculated with equation (7.21) with the experimental Q_α values.

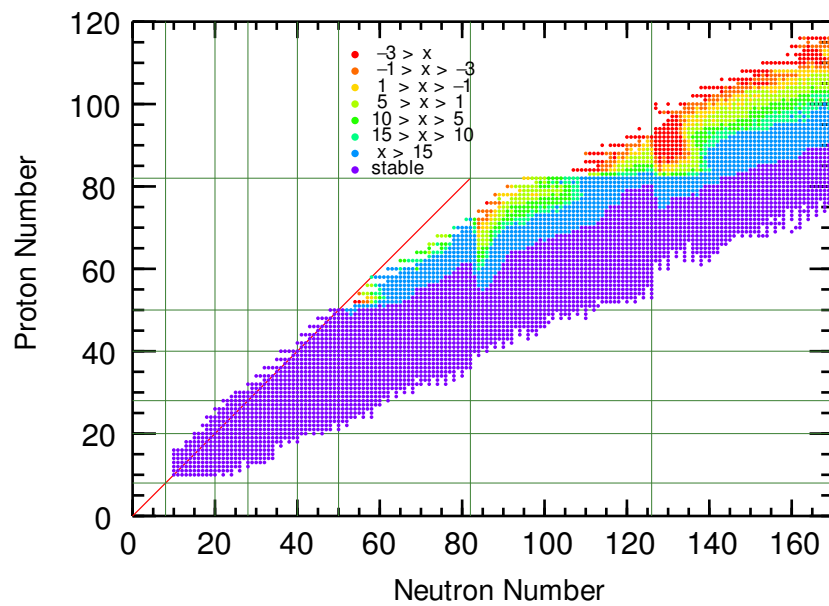


Figure 7.7: Alpha decay half-lives. The symbols represent different ranges of $x = \log_{10}[T_{1/2}(\text{sec})]$ as calculated with equation (7.21) with the HFB27 Q_α values.

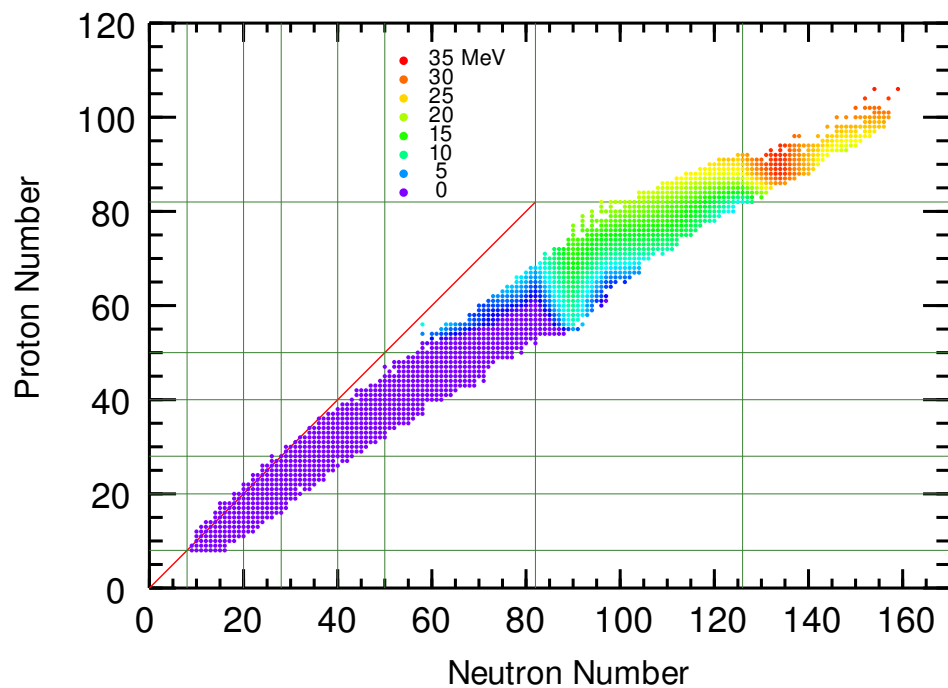


Figure 7.8: Experimental values for ^{14}C decay Q values.

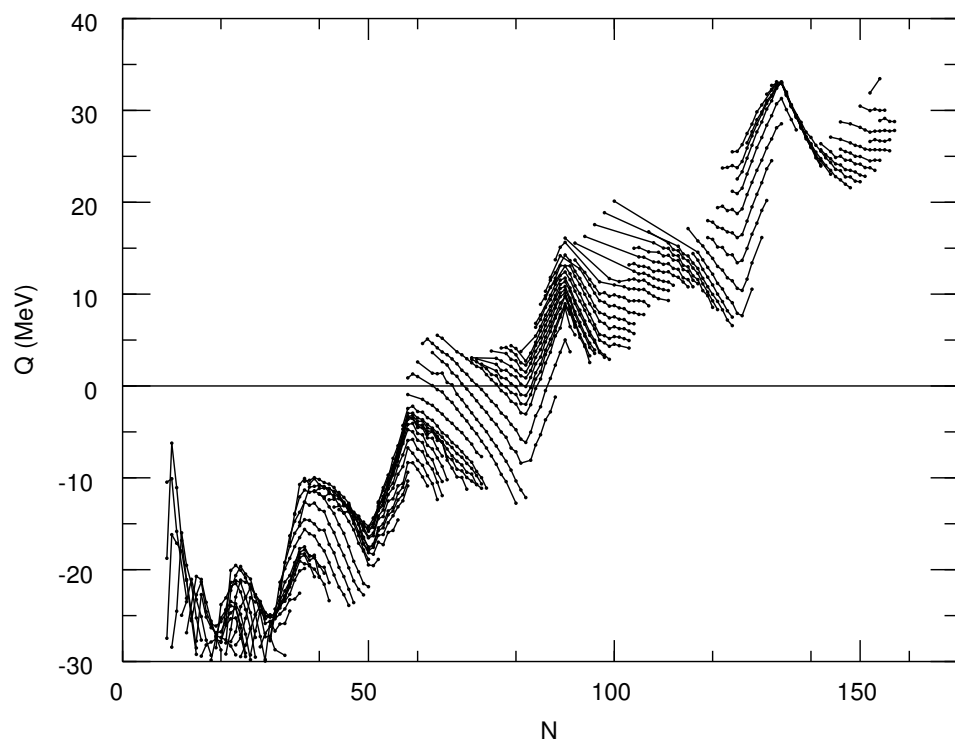


Figure 7.9: Experimental values for ^{14}C decay Q values.

centrifugal barrier to the potential $V(r)$ corresponding to the relative angular momentum L between the daughter nucleus and the emitted nucleus:

$$V_L = \frac{L(L+1)\hbar^2}{2\mu r^2}$$

The model can be refined by considering a more realistic shape for the interior and surface region of the potential. A more quantitative understanding of alpha decay relies on using many-body wave functions for all three particles involved in the decay that incorporate the individual proton and neutron degrees of freedom. The experimental data as well as the microscopic calculations indicate deviations from the Gamow model that are related to change in shape and change in shell-structure between nuclei. The basic idea behind the Gamow model can also be used to calculate lifetimes for proton and cluster decay [11]. [12]. The Q value systematics is the essential ingredient that determined the existence and half-lives of these charged particle decay. For example I show in Figs. (7.8) and (7.9) the Q values for ^{14}C decay. The large peak in the Q values just above ^{208}Pb is what determines the the region of nuclei that have been observed to have a ^{14}C decay branch, although even in the most likely case cluster emission is extremely small ($\approx 10^{-12}$ or less) compared to alpha decay.

7.3 Beta decay

The most elementary form of nuclear beta decay is that of the neutron into a proton, an electron, and an electron antineutrino:

$$n \rightarrow p + e^- + \bar{\nu}_e. \quad (7.22)$$

Nuclei are composed of protons and neutrons bound together by the strong interaction. In the beta decay of nuclei, a given initial nuclear state ${}^{A_i}Z_i$ is converted into the ground state or an excited state of the final nucleus ${}^{A_f}Z_f$, where $Z_f = Z_i \pm 1$. The transition rate for nuclear beta decay is determined by the Q_β value or energy release and the structure of the initial and final nuclear states.

The dependence of the decay rate upon the energy release can usually be calculated to a precision of about 0.1 percent, and beta decay thus provides a precise test of the strength of the weak interaction, as well as of the internal structure of particles and nuclei. In the limit when Z is small and Q_β is large, the transition rate for “allowed” beta transitions is

proportional to Q_β^5 .

In 1956 Tsung Dao Lee and Chen Ning Yang suggested that beta decay should violate the principle of parity non-conservation, and they proposed an experiment to test this idea. In 1957 parity non-conservation was confirmed by experiments carried out by Wu, Ambler, Hayward, Hoppes and Hudson on the beta decay of ^{60}Co .

The modern theory of beta decay is based upon the Standard Model that unifies the weak and electromagnetic interactions. The Standard Model of beta decay involves the W^\pm bosons at an intermediate stage of the decay process. The most elementary of these processes involved in nuclear beta decays are:

$$d \rightarrow u + W^- \rightarrow u + e^- + \bar{\nu}_e, \quad (7.23)$$

and

$$u \rightarrow d + W^+ \rightarrow d + e^+ + \nu_e, \quad (7.24)$$

where u and d are the “up” and “down” quarks, respectively. These transformations are examples of a larger class of transformations that involve all quarks and leptons. Each step

in the elementary decay process is proportional to the weak-interaction coupling constant g . The Standard Model relates the value of g to the mass of the W boson and value of the electric charge e . Also in the standard model, beta decay is unified with a larger class of weak interaction processes that involve the Z boson as an intermediate particle.

One starts by making a multipole expansion in terms of the angular momentum \vec{L} carried away by the two leptons. The beta-decay rates are classified in terms of their n -th forbiddennes, where $n = L = |\vec{L}|$. The general form for the decay rate is

$$W_\beta = \frac{M_n^2 f}{C_n (\bar{\lambda}_{ce})^{2n}},$$

were C_n is a constant, M_n^2 contains one or more nuclear nuclear matrix elements, and $\bar{\lambda}_{ce} = 386$ fm is the Compton wavelength of the electron. The decay rate is strongly dependent on n due to the $(\bar{\lambda}_{ce})^{2n}$ factor. $f = f(Z_i, Z_f, A, Q)$ is a dimensionless phase-space factor that depends on the initial and final nucleus and the beta-decay Q value. The phase space is defined as the basic (allowed) three-body phase space corrected by the electron distortion factor. For example, one can use the quantity $f = f_{WM} f_{Z=0}$ from [13] discussed in a following

section. It is conventional to define an “ft” value

$$f T_{1/2} = \frac{C_n \ln(2)(\bar{\lambda}_{ce})^{2n}}{M_n^2},$$

where $T_{1/2}$ is the partial half life. Mainly due to the factor $(\bar{\lambda}_{ce})^{2n}$, the “ft” can vary over orders of magnitude, and one usually gives the “logft” defined by $\log_{10}[f T_{1/2}]$, were $T_{1/2}$ is given in seconds.

The two leptons each have spin 1/2 that couple to total spin S . S and L couple to a total angular momentum tensor of rank R . In terms of the initial and final nuclear spins we have $\Delta J = |J_f - J_i| \leq R$ and the parity change is $(-1)^L$.

The fastest decay rate (shortest $T_{1/2}$) is obtained for $n = L = 0$, and these are traditionally called “allowed” decays, in contrast to the more hindered (“forbidden”) rates associated with $L > 0$. The traditional names given to different S, L, R combinations are given in Table 2. For $L = 0$, the nuclear matrix elements just involve the unit operator (Fermi) and spin operator \vec{s} (Gamow-Teller). All beta decay matrix elements involves the isospin operator raising and lower operators \vec{t}_\pm . For $L > 0$ there are many combinations of

operators that involve $\vec{\sigma}$ and \vec{L} . For the stretched case $R = L + S$ only one nuclear matrix element is involved. These transitions must have $\Delta J = R$, and are called “unique”. Unique first- and third-forbidden beta decay in light nuclei was considered in [14], [15], [16]. Unique second-forbidden beta decay in light nuclei was considered in [17], [15]. The first-forbidden transitions with $L = 1$, $S = 1$ and $R = 0$ are also relatively simple and have been extensively studied for their enhancement due to mesonic-exchange currents [18], [19], [20], [21].

Experimental logft values have been tabulated in [22]. This compilation lists only three third-forbidden and four fourth-forbidden transitions (such as ^{50}V 6^+ to ^{50}Ti 2^+). Sometimes this experimental range of logft values can be used to “assign” an L value to a new transition. For example, for $\log ft < 5$, it is probably allowed $L = 0$. But one must be careful of the pandemonium effect [23], where the apparent branching to low-lying states may be influenced by the feeding of many unobserved weak gamma transitions from higher-lying states.

The complete theory of nuclear beta decay is complex [16], [25], [26]. For light nuclei most of the observed transitions are “allowed” Fermi and Gamow-Teller. We will limit the detailed discussion to allowed type. For heavy nuclei (A greater than about 70) the first-

Table 7.2: Types of beta decay. The min and max values of the logft are from [22]. References to some related paper are given.

name	<i>S</i>	<i>L</i>	<i>R</i>	$\Delta\pi$	logft _{min}	logft _{max}	refs
Superallowed	0	0	0	0	3	13	
Allowed (Gamow-Teller)	1	0	1	0	3	10	
First forbidden	0,1	1	0,1,2	1	5	15	
Unique first forbidden	1	1	2	1	7.5	13	
Second forbidden	0,1	2	1,2,3	0	10.6	14	[24]
Unique second forbidden	1	2	3	0	13.9	18	
Third forbidden	0,1	3	2,3,4	1	17.5	17.5	
Unique third forbidden	1	3	4	1	20.7	21.4	
Four forbidden	0,1	4	2,3,4	0	22.5	24.3	

forbidden type transitions become more common and more important for the total decay rate. There are a few exceptional beta decays that involve low Q values and high R values [22].

7.3.1 Beta decay Q values

Beta minus, β^- , decay involves the emission of an electron and electron antineutrino:

$${}^A Z \rightarrow {}^A(Z+1)_{-e} + e^- + \bar{\nu}_e, \quad (7.25)$$

where the subscript $-e$ indicates that this nucleus has Z rather than $(Z+1)$ electrons. The Q value for β^- decay is given in terms of atomic masses M and nuclear binding energies B by

$$\begin{aligned} Q(\beta^-) &= [M(A, Z) - M_{-e}(A, Z+1) - m_e]c^2 = [M(A, Z) - M(A, Z+1)]c^2 \\ &= BE(A, Z+1) - BE(N, Z) + \delta_{nH}, \end{aligned} \quad (7.26)$$

where $m_e c^2 = 0.511 \text{ MeV}$ is the mass of the electron,

$$M_{-e}(A, Z + 1) = M(A, Z + 1) - m_e \quad (7.27)$$

is the mass of the final nucleus with one electron missing (we ignore the electron ionization energy which is on the order of 10 eV), and

$$\delta_{nH} = \Delta_n c^2 - \Delta_H c^2 = 0.782 \text{ MeV} \quad (7.28)$$

comes from the mass difference between the neutron and the Hydrogen atom. In these expressions we assume that the mass of the neutrino is zero and we ignore the electronic binding energy.

Beta plus, β^+ , decay involves emission of a positron and electron neutrino:

$${}^A Z \rightarrow {}^A(Z-1)_{+e} + e^+ + \nu_e, \quad (7.29)$$

where the subscript $+e$ indicates that this nucleus has Z rather than $(Z-1)$ electrons. The Q value for β^+ decay is given by

$$Q(\beta^+) = [M(A, Z) - M_{+e}(A, Z-1) - m_e]c^2 = [M(A, Z) - M(A, Z-1) - 2m_e]c^2$$

$$= \text{BE}(A, Z - 1) - \text{BE}(A, Z) - 2m_e c^2 - \delta_{nH}. \quad (7.30)$$

where

$$M_{+e}(A, Z - 1) = M(A, Z - 1) + m_e \quad (7.31)$$

is the mass of the final nucleus with one extra electron.

Another form of beta decay that competes with β^+ decay is electron capture (EC) in which one of the atomic electrons is captured by the nucleus and an electron-neutrino is emitted:



The Q value for electron capture decay is given by

$$Q(EC) = [M(A, Z) - M(A, Z - 1)]c^2 = \text{BE}(A, Z - 1) - \text{BE}(A, Z) - \delta_{nH}. \quad (7.33)$$

The experimental beta decay Q values are shown in Fig. (7.10) and those for the HFB27 predictions are shown in (7.11). The energy released in β^- or β^+ decay is shared between the recoiling nucleus, the electron and the neutrino. Since the nucleus is heavy compared to the

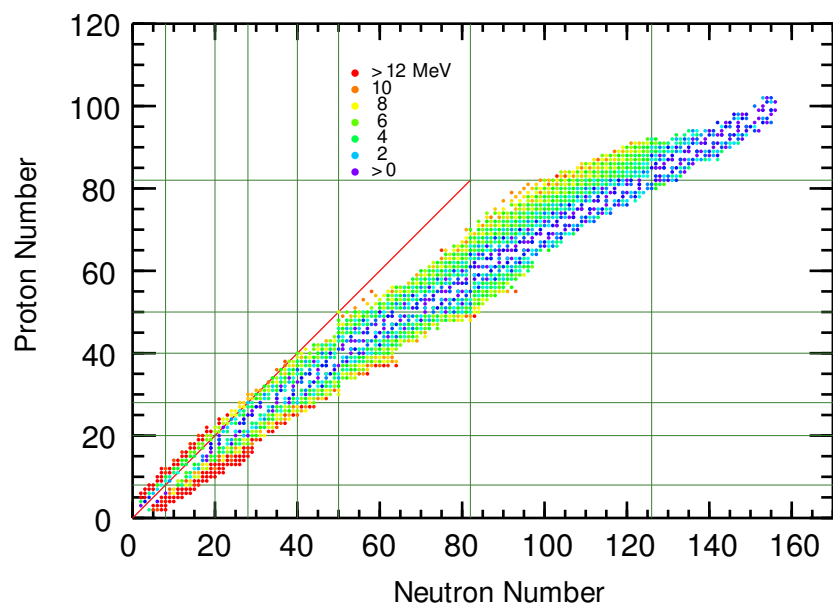


Figure 7.10: Experimental beta decay Q values.

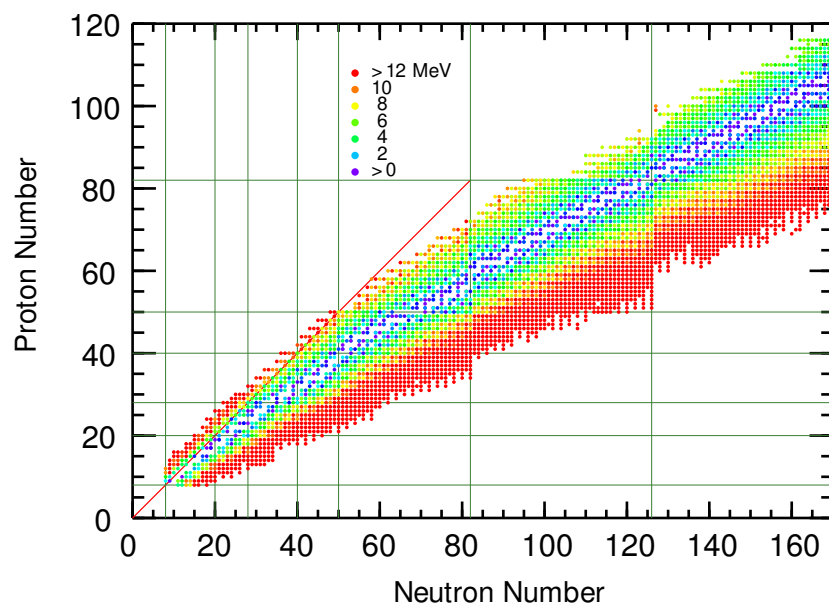


Figure 7.11: HFB27 beta decay Q values.

electron and neutrino, most of the energy is shared between the electron and the neutrino with a probability distribution for each that can be accurately calculated. Usually only the electron or positron is detected, and it has a range of kinetic energies ranging from zero up to Q_β (the end-point energy), assuming that the mass of the neutrino is zero. If the neutrino has a mass, the end-point energy of the electron would be reduced. The end-point energy of the tritium beta decay has been used to set a limit of about $m_\nu < 9 \text{ eV}/c^2$ for the mass of the electron antineutrino. In the electron-capture process all of the energy goes into that of the neutrino. An experimental signature of electron capture is the X ray emitted when the vacancy left by the inner electron that was absorbed by the nucleus is filled by one of outer electrons.

7.3.2 Allowed beta decay

The allowed beta decay rate W between a specific set of initial and final states is given by:

$$W_{i,f} = (f/K_o) [g_V^2 B_{i,f}(F_\pm) + g_A^2 B_{i,f}(GT_\pm)], \quad (7.34)$$

where f is dimensionless three-body phase-space factor that depends upon the beta-decay Q value, and K_o is a specific combination of fundamental constants:

$$K_o = \frac{2\pi^3 \hbar^7}{m_e^5 c^4} = 1.8844 \times 10^{-94} \text{ erg}^2 \text{ cm}^6 \text{ s.} \quad (7.35)$$

The \pm refer to β_{\pm} decay of nucleus (A_i, Z_i) into nucleus $(A_i, Z_i \mp 1)$. The weak-interaction vector (V) and axial-vector (A) coupling constants for the decay of neutron into a proton are denoted by g_V and g_A , respectively.

The operators for Fermi and Gamow-Teller beta decay in terms of sums over nucleons are:

$$\mathcal{O}(F_{\pm}) = \sum_k t_{k\pm}, \quad (7.36)$$

and

$$\mathcal{O}(GT_{\pm}) = \sum_k \sigma_k t_{k\pm}. \quad (7.37)$$

In terms of these operators the reduced matrix elements [27] in Eq. (7.34) are:

$$B_{i,f}(F_{\pm}) = \frac{|\langle f || \mathcal{O}(F_{\pm}) || i \rangle|^2}{(2J_i + 1)}, \quad (7.38)$$

and

$$B_{i,f}(GT_{\pm}) = \frac{|\langle f || \mathcal{O}(GT_{\pm}) || i \rangle|^2}{(2J_i + 1)} = \frac{[M_{i,f}(GT_{\pm})]^2}{(2J_i + 1)}, \quad (7.39)$$

where

$$M_{i,f}(GT_{\pm}) = \langle f || \mathcal{O}(GT_{\pm}) || i \rangle \quad (7.40)$$

The matrix elements are reduced in orbital space and the $(2J_i + 1)$ factor comes from the average over initial M_i states. The magnitude of reduced matrix element $M(GT)$ does not depend on the direction of the transition, i.e.,

$$| M(GT, a \rightarrow b) | = | M(GT, b \rightarrow a) | \quad (7.41)$$

whereas

$$B(GT, a \rightarrow b) = \frac{(2J_b + 1)}{(2J_a + 1)} B(GT, b \rightarrow a). \quad (7.42)$$

The matrix elements obey the triangle conditions $J_f = J_i$ ($\Delta J = 0$) for Fermi and $\Delta(J_i, j_i, 1)$ ($\Delta J = 1$) for Gamow-Teller.

Historically one combines the partial half-life for a particular decay with the calculated phase-space factor f to obtain from Eq. (7.34) an “ft” value given by:

$$ft_{1/2} = \frac{C}{[B(F) + (g_A/g_V)^2 B(GT)]} \quad (7.43)$$

where

$$C = \frac{\ln(2) K_o}{(g_V)^2} \quad (7.44)$$

One often compiles the allowed beta decay rates in terms of a “logft” which stands for $\log_{10}(ft_{1/2})$, where $t_{1/2}$ is the partial half-life.

7.3.3 Phase-space for allowed beta decay

The phase-space factors f are given by Wilkinson and collaborators [28], [13], [29]. The starting point is the analytic result for a nucleus of $Z = 0$ given by

$$f_{Z=0} = \frac{1}{60}(2W_o^4 - 9W_o^2 - 8)p_o + \frac{1}{4}W_o \ln(W_o + p_o) \quad (7.45)$$

In this expression W_o is the total electron (positron) endpoint energy in units of $m_e c^2$

$$W_o = \frac{E_o}{m_e c^2} + 1, \quad (7.46)$$

and

$$p_o = \sqrt{(W_o^2 - 1)}. \quad (7.47)$$

The end point energy of the electron in units of MeV is

$$E_o = (Q + E_i) - E_f \text{ for } \beta_-, \quad (7.48)$$

and

$$E_o = (Q + E_i) - E_f - 2m_e c^2 \text{ for } \beta_+, \quad (7.49)$$

where Q is the beta decay Q value, and E_i and E_f are the excitation energies of the initial and final states.

In the limit when $E_o \gg m_e c^2$:

$$f_{Z=0} \rightarrow \frac{1}{30} W_o^5, \quad (7.50)$$

can be used as a qualitative estimate of the phase space factor and its dependence on the decay energy.

To a higher level of accuracy one must take into account the distortion of the electron energy due to the nuclear Coulomb field and the effects of nuclear finite size as well as other smaller corrections [13]. The finite size corrections are slightly different for the Fermi and Gamow-Teller decays [13] and thus at this more precise level one introduced two factors $f = f_A$ for the axial vector matrix element and f_V for the vector matrix element. Eq. (7.43)

written in terms of the “ft” value is:

$$ft_{1/2} = \frac{C}{\left[\left(\frac{f_V}{f} \right) B(F) + \left(\frac{g_A}{g_V} \right)^2 B(GT) \right]} \quad (7.51)$$

Several correction factors are applied to Eq. (7.45) to obtain f . A 2018 review and formulation of these corrections including the recoil-order corrections is given in [30]. The 2020 analysis of pure Fermi decays to obtain C is given [31]. In the following I will outline an older formulation used by Wilkinson and Macefield [13]. The corrected phase space is given as a product of several factors

$$f = \delta_D \delta_R \delta_{WM} f_{Z=0}. \quad (7.52)$$

This is the form used in the Oxbash and NuShellX codes to calculate the allowed beta decay half-lives.

The most important of these correction factors is δ_{WM} that takes into account the electron distortion factors. The values are tabulated in [13] in the form

$$\delta_{WM} = \exp \left[\sum_{n=0,3} a_n (\ln E_o)^n \right], \quad (7.53)$$

The calculation of δ_{WM} uses electron wave functions for an atom generated from a uniform spherical nuclear charge distribution whose radius is adjusted to fit the appropriate electron scattering and muonic x-ray data and which is corrected for the screening of the atomic electrons. Also included in the values of δ_{WM} are the effects of the energy-dependent “outer” radiative correction to order α and of the finite mass of the nucleus. The parametrization of the values of δ_{WM} by Eq. (7.53) is accurate to better than 0.1% throughout [13].

The factor δ_R incorporates the effects of the “outer” radiative correction to orders $Z\alpha^2$ and $Z^2\alpha^3$ and is given [28], [13] by

$$\delta_R = 1 + 3.67 \times 10^{-4} |Z| + 3.60 \times 10^{-6} Z^2. \quad (7.54)$$

where Z is the proton number of the daughter nucleus. The factor δ_D incorporates the effects of the diffuseness of the actual nuclear charge distribution [29]

$$\delta_D = 1 + 1.8 \times 10^{-5} |Z|^{1.36} - 1.2 \times 10^{-6} |Z| W_o. \quad (7.55)$$

The Fermi phase-space factor f_V is related [13] to the factor f by

$$f_V = \delta_V f, \quad (7.56)$$

where

$$\delta_V = 1 \pm (2/15)W_oR\alpha Z - (4/105)(W_oR)^2 \quad (7.57)$$

for beta \pm decay, where $\alpha = 1/137$ and where we have used

$$R = 1.35A^{1/3}\text{fm} \quad (7.58)$$

The process of electron capture is combined with that of β_+ decay in terms of a total phase space factor:

$$f_+ = f(\beta_+) + f(ec). \quad (7.59)$$

Electron-capture phase-space factors are given in the tables of Behrens and Janecke [32].

7.3.4 Weak-interaction coupling constants

The values of the coupling constants for Fermi decay, g_V , and Gamow-Teller decay, g_A , in the combinations in which they appear in Eq. (7.51) are obtained as follows.

For a $0^+ \rightarrow 0^+$ nuclear transition $B(GT) = 0$, and for a transition between $T = 1$ analogue states with $B(F) = 2$ Eq. (7.51) reduces to

$$C = 2t_{1/2}f_V. \quad (7.60)$$

The partial half-lives and Q values for several $0^+ \rightarrow 0^+$ analogue transitions have been measured to an accuracy of about one part in 10000. One obtains [29]:

$$C = 6170(4) \quad (7.61)$$

This result, together with the value of K_o in Eq. (7.35), can be used with Eq. (7.44) to obtain g_V .

At the quark level $g_V = -g_A$. For nuclear structure we use the value obtained from the neutron to proton beta decay [33] of

$$g_A/g_V = -1.2764(6). \quad (7.62)$$

To the precision of about one percent, Eq. (7.51) becomes

$$ft_{1/2} = \frac{6170}{[B(F) + (1.629)B(GT)]} \quad (7.63)$$

7.3.5 Double beta decay

Nuclear double-beta decay takes place in situations where a nucleus is energetically stable to single-beta decay but unstable to the simultaneous emission of two electrons (or two positrons) [34]. For example, for the nuclei with atomic mass number A=100, $^{100}\text{Mo} \rightarrow ^{100}\text{Ru}$ double-beta decay may occur. The Q values for double-beta decay for those nuclei with single-beta decay Q values of 0.3 MeV or less is shown in Fig. (7.12).

The $2\beta^-$ decay has the form

$$^A Z \rightarrow ^A(Z + 2) + 2e^- + (2\bar{\nu}_e). \quad (7.64)$$

In the case of the standard (2ν) decay mode the two neutrinos are present. In neutrinoless double beta decay (0ν) there are no neutrinos in the final state. The Q value is

$$Q(2\beta^-) = \text{BE}(A, Z + 2) - \text{BE}(N, Z) + 2\delta_{nH}, \quad (7.65)$$

where δ_{nH} is given by Eq. (7.28). For (0ν) all of the decay energy is contained in the kinetic energy of the two electrons (and the nuclear recoil) and this shows up in the summed electron

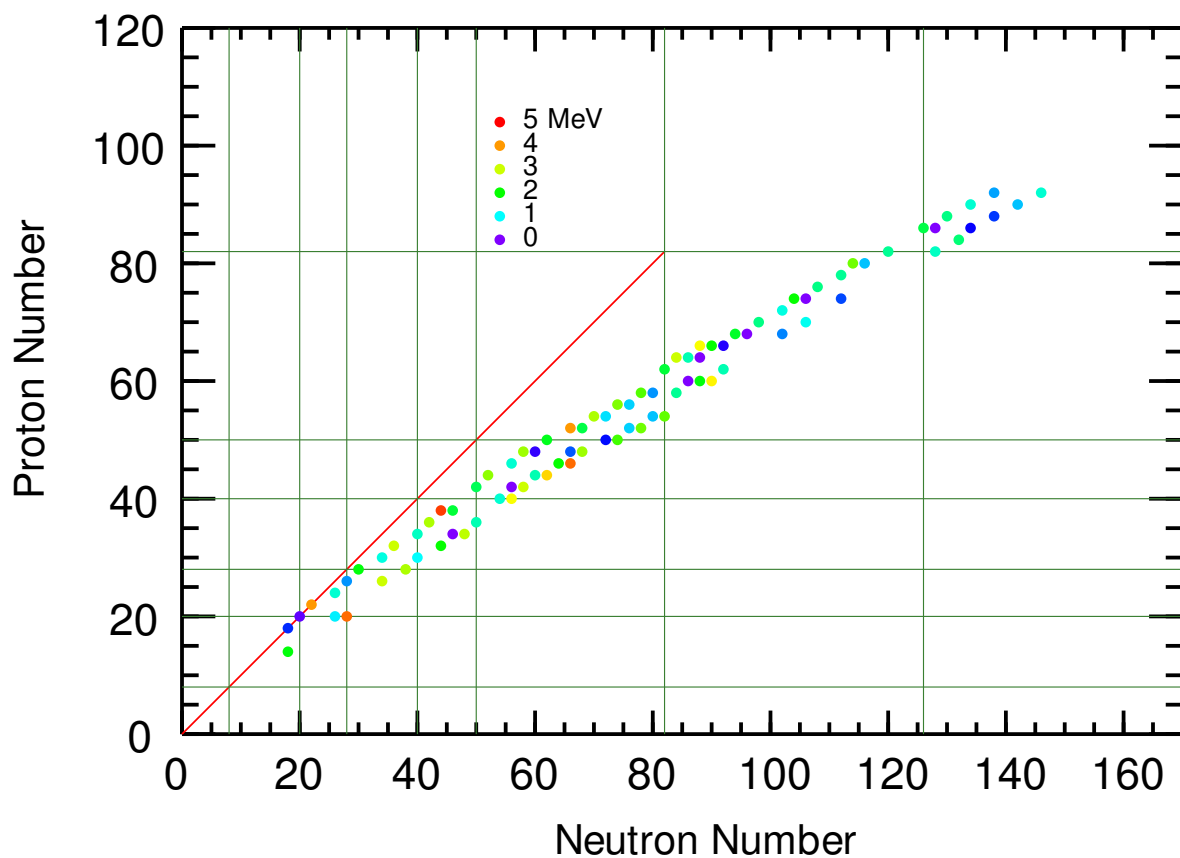
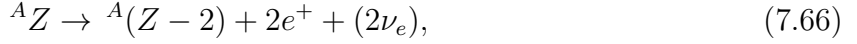


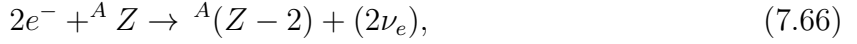
Figure 7.12: Experimental double-beta decay Q values.

energy as peak. For (2ν) all of the decay energy is shared between the two electrons and the two neutrinos. This shows up as a spread in the summed energy of the two electrons. The (2ν) decays have been observed for about 14 nuclei. (link to wiki).

One can also have $2\beta^+$



and double-electron capture



with

$$Q(2\beta^+) = \text{BE}(A, Z - 2) - \text{BE}(A, Z) - 2\delta_{nH}. \quad (7.67)$$

Double electron capture has been observed in a few cases ${}^{78}\text{Kr}$ and ${}^{124}\text{Xe}$ and ${}^{130}\text{Ba}$ (see the wiki link).

The (0ν) decay mode is being searched for experimentally, but has not yet been observed [35]. The (0ν) decay mode is possible only if the neutrinos are Majorana particles

(the neutrino and anti-neutrino are the same particle). Neutrino-oscillation experiments can be interpreted in terms of a mass splittings (on the order of meV) of three-types of neutrinos. (link to wiki). The observation of (0ν) decay is one way to determine the absolute neutrino mass (it depends on a linear combination of the neutrino masses) [35].

7.4 Electromagnetic decay

There are three types of electromagnetic decay; gamma decay, internal conversion and pair production. Transitions between states within a nucleus can always occur by process of electron capture, where the energy of the nuclear transition is transferred to one of the electrons in the atom [36]. Pair production can occur when the nuclear transition energy is larger than $2m_e c^2$ and the energy of the nuclear transition is used to make electron-positron pair. In gamma decay the energy of nuclear decay is converted into the energy of the gamma ray.

One can also have double-gamma decay, whose rate is determined by the product of two electromagnetic interactions, and its decay rate is very small compared to these other type of decay. The process of double-gamma decay was first unambiguously observed in 0^+ to 0^+ decays in 1984 [1]. In 2015, double gamma decay was observed to compete with single gamma decay in ^{137}Ba [37].

For an electromagnetic transition from an initial nuclear state i (where the nucleus is at rest) to nuclear state f , the momentum of the nucleus in state f (after the transition) and the emitted gamma ray are equal and opposite. The nucleus recoils with a kinetic energy $T_f = (\Delta E)^2/(2m_f c^2)$ and the gamma ray has an energy $E_\gamma = \Delta E - T_f$, where $\Delta E = E_i - E_f$ (the transition energy) is the rest-mass energy difference between initial and final nuclear states. T_f is much smaller than ΔE and thus to a good approximation $E_\gamma = \Delta E$. The energy and angular frequency ω of the photon are related by $E_\gamma = \hbar\omega$. The wavelength is $\lambda = hc/E_\gamma = 1237 \text{ MeV-fm}/E_\gamma$.

The electromagnetic transition between them can take place only if the emitted gamma ray carries away an amount of angular momentum \vec{l} such that $\vec{J}_f = \vec{J}_i + \vec{l}$. This means that

$| J_i - J_f | \leq \ell \leq J_i + J_f$ where $J = |\vec{J}|$. The photon has spin one, $S = 1$, and since it is massless it is always polarized perpendicular to the direction of motion with $M_S = \pm 1$ (or some combinations of these). Thus, there is no tensor operator of rank zero for gamma decay. $J_i = 0 \rightarrow J_f = 0$ gamma decays are strictly forbidden.

In nuclei there are some cases of 0^+ first excited states. The $0^+ \rightarrow 0^+$ ($\ell=0$) gamma decay of these states is forbidden and they must decay by internal conversion and pair production. The $\ell=0$ transitions that take place via internal conversion are called electric monopole ($E0$) transitions. The total $E0$ transition probability, $W(E0) = \Omega(E0)\rho^2(E0)$, for a transition between the initial and final states, $|i\rangle$ and $|f\rangle$, can be separated into electronic, $\Omega(E0)$, and nuclear, $\rho(E0)$, factors. The quantity $\rho(E0)$ is the dimensionless monopole transition strength, carrying all the information about the nuclear structure, and is related to the monopole matrix element, $M(E0)$, by

$$\rho(E0) = \langle f | M(E0) | i \rangle / (eR^2), \quad (7.68)$$

where R is the nuclear radius in fm defined by $R = 1.2A^{1/3}$. The operator is $M(E0) = e\Sigma_i r_i^2$, where the sum is over all protons in the nucleus. Experimental data for ρ are compiled in

[38], and some nuclear structure aspects are discussed in [39]. E0 transitions have also been observed and measured for some $J^\pi \rightarrow J^\pi$ transitions [38].

The $\ell(> 0)$ value for gamma decay determines the multipolarity of the gamma radiation; $\ell=1$ is called dipole, $\ell=2$ is called quadrupole, etc. In addition, when states can be labeled with a definite parity $\pi_i=\pm 1$ and $\pi_f=\pm 1$, the transitions between them are restricted to the “electric” type of radiation when $\pi_i\pi_f(-1)^\ell$ is even and the “magnetic” type of radiation when $\pi_i\pi_f(-1)^\ell$ is odd.

The gamma transition rate is determined by the transition energy ΔE , the multipolarity, and a factor that depends upon the details of the internal nuclear structure. For example, the power for electric-dipole radiation (E1) from classical electromagnetism is given by $P = \omega^4 e^2 d^2 / (3c^3)$ where d is the average distance between the positive and negative charge, $\omega = 2\pi f$, f is the frequency of the vibration in the distance between the positive and negative charge, and c is the speed of light. The E1 transition rate $W(E1)$ (the number of gamma rays per second) is the power divided by the energy per gamma ray ($E_\gamma = \hbar\omega$): $W = P/E_\gamma = \omega^3 e^2 d^2 / (3\hbar c^3) = 2.9 \times 10^{15} E_\gamma^3 d^2 \text{ MeV}^{-3} \text{ fm}^{-2}$. The quantity d^2 depends upon

the internal structure of the nuclear states. An estimate for the lifetime associated with electric dipole radiation can be obtained by taking a typical nuclear transition energy of $E_\gamma = 1 \text{ MeV}$ and a typical nuclear size scale of $d^2 = 1 \text{ fm}^2$ that gives a mean lifetime of $\tau = 1/W \approx 0.3 \times 10^{-15} \text{ s}$.

The lowest allowed multipolarity in the decay rate dominates over the next higher one (when more than one is allowed) by several orders of magnitude. The most common types of transitions are electric dipole (E1), magnetic dipole (M1), and electric quadrupole (E2). Electromagnetic transition rates provide one of the most unambiguous tests for models of nuclear structure. The strong interaction conserves parity, and to the extent that the protons and neutrons are held together in the nucleus by the strong interaction, their states can be labeled by a definite parity. Since the weak interaction does not conserve parity, the weak interaction between protons and neutrons leads to nuclear states that have a slightly mixed parity. The electromagnetic decay between nuclear states that have a mixed parity gives rise to “mixed” transitions (such as E1 plus M1), that produce circularly polarized gamma rays (gamma rays in which the electric field vector rotates around the axis of propagation). Recent observations of circular polarized gamma rays have provided a test of the weak interaction

between protons and neutrons in the nucleus.

7.4.1 Reduced transition probabilities for gamma decay

This section summarizes results that have been derived in [40], [41], [42]. The interaction of the electromagnetic field with the nucleons can be expressed in terms of a sum of tensor operators of rank λ called electric $\mathcal{O}(E\lambda)_\mu$ and magnetic $\mathcal{O}(M\lambda)_\mu$. The decay rate between an initial state $| J_i, M_i \rangle$ and final state $| J_f, M_f \rangle$ is given by

$$W_{M_i, M_f, \mu} = \sum_{\pi, \lambda} \left(\frac{8\pi(\lambda + 1)}{\lambda[(2\lambda + 1)!!]^2} \right) \left(\frac{k^{2\lambda+1}}{\hbar} \right) | \langle J_f M_f | \mathcal{O}(\pi\lambda)_\mu | J_i M_i \rangle |^2, \quad (7.69)$$

where $\pi = E$ (electric) or $\pi = M$ (magnetic). In this expression k is the wave-number for the electromagnetic transition of energy E_γ given by:

$$k = \frac{E_\gamma}{\hbar c}. \quad (7.70)$$

W is explicitly labeled by the M values but depends implicitly on the wavefunctions and operator.

Since M_f and μ are not observed we sum over them to obtain the decay rate in terms of reduced matrix elements

$$W = \sum_{M_f, \mu} W_{M_i, M_f, \mu} = \sum_{\pi, \lambda} \left(\frac{8\pi(\lambda + 1)}{\lambda[(2\lambda + 1)!!]^2} \right) \left(\frac{k^{2\lambda+1}}{\hbar} \right) \frac{|< J_f || \mathcal{O}(\pi\lambda) || J_i >|^2}{(2J_i + 1)}, \quad (7.71)$$

The decay rate is independent of M_i .

For the electroweak integrations in the nucleus one starts with the “impulse” approximation [43] where the operators $\mathcal{O}(\pi\lambda)$ are given by a sum over operators for the individual nucleons

$$\mathcal{O}(\pi\lambda) = \sum_k O(\pi\lambda, k). \quad (7.72)$$

To go beyond the impulse approximation we would need to introduce two-body operators associated with electroweak field operating on the exchanged mesons, the “mesonic-exchange”

corrections. The mesonic-exchange corrections are typically on the order of 10% or less of the one-body contribution. But they can be much larger, as in the case of some first-forbidden beta decay [18], [19], [20], [21].

The one-body electric transition operator is given by:

$$O(E\lambda, k) = r_k^\lambda Y_\mu^\lambda(\hat{r}_k) e_k e, \quad (7.73)$$

where Y_μ^λ are the spherical harmonics. For a proton $e_p = 1$ and for a neutron $e_n = 0$. Gamma transitions with $\lambda=0$ are forbidden because the photon must carry off at least one unit of angular momentum.

The one-body magnetic transition operator is given by:

$$\begin{aligned} O(M\lambda, k) &= \left[\vec{\ell}_k \frac{2g_k^\ell}{(\lambda+1)} + \vec{s}_k g_k^s \right] \vec{\nabla}[r_k^\lambda Y_\mu^\lambda(\hat{r}_k)] \mu_N \\ &= \sqrt{\lambda(2\lambda+1)} \left[[Y^{\lambda-1}(\hat{r}_k) \otimes \vec{\ell}_k]_\mu^\lambda \frac{2g_k^\ell}{(\lambda+1)} + [Y^{\lambda-1}(\hat{r}_k) \otimes \vec{s}]_\mu^\lambda g_k^s \right] r_k^{\lambda-1} \mu_N, \quad (7.999). \end{aligned}$$

The g-factors g_k^ℓ and g_k^s are the orbital and spin g-factors for the proton and neutron, respectively. The free-nucleon values for the g-factors are $g_p^\ell = 1$, $g_n^\ell = 0$, $g_p^s = 5.586$ and $g_n^s = -3.826$.

The last factor in Eq. (7.71) is referred to as a “reduced transition probability” B defined by:

$$B(i \rightarrow f) = \frac{|\langle J_f || \mathcal{O}(\pi\lambda) || J_i \rangle|^2}{(2J_i + 1)}. \quad (7.74)$$

B depends upon the direction of the transition. For electromagnetic transitions J_i is the higher-energy initial state. But in Coulomb excitation the initial state is the lower state, and one often uses the notation $B(\uparrow)$ for this situation. If J_a is the lower state, J_b is the higher state, and $B(\uparrow) = B(a \rightarrow b)$ is given, then the value used for the electromagnetic decay $J_b \rightarrow J_a$ is:

$$B(b \rightarrow a) = \frac{(2J_a + 1)}{(2J_b + 1)} B(a \rightarrow b). \quad (7.75)$$

In particular for the $E2$ transition from the 0^+ ground state, $B(2^+ \rightarrow 0^+) = B(0^+ \rightarrow 2^+)/5$.

A state may gamma decay by several multipoles to a given final state:

$$W = \sum_{\lambda} [W(E\lambda) + W(M\lambda)]. \quad (7.76)$$

One observes from the factors in Eq. (7.71) (with $E_{\gamma} \approx 1$ MeV) that the rate for electric (magnetic) transitions with $\lambda+2$ about seven orders of magnitude smaller than those electric (magnetic) transitions for λ . Thus in most cases only the lowest multipole for a given type of transition is important. Comparing rates for electric and magnetic transitions we observe that the lowest allowed multipole may be equally important. Thus (if allowed by the triangle condition) we need to consider mixed transitions of the form ($E1$ and $M2$); ($M1$ and $E2$); etc. For these mixed transition we define a mixing ratio δ by:

$$\delta^2(M2/E1) = \frac{W(M2)}{W(E1)}, \quad (7.77)$$

and

$$\delta^2(E2/M1) = \frac{W(E2)}{W(M1)}. \quad (7.78)$$

The convention is that the rate for the higher λ value is on top. With the phase convention of Krane and Steffan [44] the sign of the mixing ratio is

$$\text{sign}[\delta(M2/E1)] = \text{sign} \frac{\langle J_f || O(M2) || J_i \rangle}{\langle J_f || O(E1) || J_i \rangle}, \quad (7.79)$$

and

$$\text{sign}[\delta(E2/M1)] = -\text{sign} \frac{\langle J_f || O(E2) || J_i \rangle}{\langle J_f || O(M1) || J_i \rangle}, \quad (7.80)$$

where “sign” is the sign of the ratio of the reduced matrix elements. Our wavefunctions are defined such that the reduced matrix elements are all real numbers. These mixing ratios can be measured from the angular distribution of the gamma rays when the initial state is aligned (e.g. the M_i state population is not uniform) [44]. For a mixed transition the branching fraction, b , for a given type of transition is related to δ . For example for a mixed $M1$ and $E2$ transition, the $E2$ branching fraction is:

$$b(E2) = \frac{W(E2)}{W(M1) + W(E2)} = \frac{\delta^2}{1 + \delta^2}, \quad (7.81)$$

and the $M1$ branching fraction is:

$$b(M1) = \frac{W(M1)}{W(M1) + W(E2)} = \frac{1}{1 + \delta^2}. \quad (7.82)$$

In addition we need to take into account the rates for internal conversion and pair production defined by the internal conversion coefficient α defined for a pure multipole transition by

$$\alpha = W_{\text{ic+pair}}/W, \quad (7.83)$$

where W is the rate for gamma emission. If there is a mixing ratio we need to calculate

$$\alpha = \frac{\alpha(\pi L) + \delta^2 \alpha(\pi' L')}{1 + \delta^2}. \quad (7.84)$$

A review of the theory and a web based program for internal conversion and pair production is given by [45]. α can be often be ignored, in particular for $M1$ and $E2$ transitions in light nuclei. It becomes important for low-energy gamma transitions energies, higher multipoles

and the large Z values in heavy nuclei. When in doubt it should always be checked with [45].

The partial half-life for a given multipolarity (πL) to a specific final state f is given by

$$T_p(\pi L) = \frac{T(1 + \alpha)}{b_f b(\pi L)}, \quad (7.85)$$

where T is the half-life, and b_f is the branching fraction to state f .

It is convenient to make an explicit list of the factors that relate the partial half-life T_p and reduced transition probability B . The results for electric transitions are:

$$B(E1 \downarrow) = \frac{0.435}{E_\gamma^3 T_p(E1)} e^2 \text{ fm}^2 \text{ MeV}^3 \text{ fs} \quad (7.86)$$

$$B(E2 \downarrow) = \frac{564}{E_\gamma^5 T_p(E2)} e^2 \text{ fm}^4 \text{ MeV}^5 \text{ ps} \quad (7.87)$$

$$B(E3 \downarrow) = \frac{1212}{E_\gamma^7 T_p(E3)} e^2 \text{ fm}^6 \text{ MeV}^7 \text{ } \mu\text{s} \quad (7.88)$$

$$B(E4 \downarrow) = \frac{4076}{E_\gamma^9 T_p(E4)} e^2 \text{ fm}^8 \text{ MeV}^9 \text{ s} \quad (7.89)$$

$$B(E5 \downarrow) = \frac{2.00 \times 10^{10}}{E_\gamma^{11} T_p(E5)} e^2 \text{ fm}^{10} \text{ MeV}^{11} \text{ s} \quad (7.90)$$

$$B(E6 \downarrow) = \frac{1.35 \times 10^{17}}{E_\gamma^{13} T_p(E6)} e^2 \text{ fm}^{12} \text{ MeV}^{13} \text{ s} \quad (7.91)$$

The results for magnetic transitions are:

$$B(M1 \downarrow) = \frac{39.5}{E_\gamma^3 T_p(M1)} \mu_N^2 \text{ MeV}^3 \text{ fs} \quad (7.92)$$

$$B(M2 \downarrow) = \frac{51.2}{E_\gamma^5 T_p(M2)} \mu_N^2 \text{ fm}^2 \text{ MeV}^5 \text{ ns} \quad (7.93)$$

$$B(M3 \downarrow) = \frac{0.110}{E_\gamma^7 T_p(M3)} \mu_N^2 \text{ fm}^4 \text{ MeV}^7 \text{ s} \quad (7.94)$$

$$B(M4 \downarrow) = \frac{0.370 \times 10^6}{E_\gamma^9 T_p(M4)} \mu_N^2 \text{ fm}^6 \text{ MeV}^9 \text{ s} \quad (7.95)$$

7.4.2 Weisskopf units for gamma decay

In order to judge whether a transition is relatively weak or strong, one often gives the B value in “single-particle” or Weisskopf units. This Weisskopf unit is an estimate of the B value for a single-particle (proton or neutron) and how it depends upon mass. By convention it is defined by:

$$B_W(E\lambda) = \left(\frac{1}{4\pi}\right) \left[\frac{3}{(3+\lambda)}\right]^2 (1.2A^{1/3})^{2\lambda} e^2 \text{ fm}^{2\lambda}, \quad (7.96)$$

and

$$B_W(M\lambda) = \left(\frac{10}{\pi}\right) \left[\frac{3}{(3+\lambda)}\right]^2 (1.2A^{1/3})^{2\lambda-2} \mu_N^2 \text{ fm}^{2\lambda-2}. \quad (7.97)$$

The most commonly used are:

$$B_W(E1) = 0.0645 A^{2/3} e^2 \text{ fm}^2, \quad (7.98)$$

$$B_W(E2) = 0.0594 A^{4/3} e^2 \text{ fm}^4, \quad (7.99)$$

and

$$B_W(M1) = 1.790 \mu_N^2. \quad (7.100)$$

Weisskopf units for the decay widths are:

$$\Gamma_W(E2)(\text{eV}) = 4.9 \times 10^{-8} A^{4/3} [E_\gamma(\text{MeV})]^5 \quad (7.101)$$

$$\Gamma_W(M1)(\text{eV}) = 2.1 \times 10^{-2} [E_\gamma(\text{MeV})]^3 \quad (7.102)$$

7.4.3 Measured $B(E2)$ from the ground states of even-even nuclei

Experimental information on the $B(E2)$ for 0_1^+ to 2_1^+ for even-even nuclei has been compiled in [46]. The results are shown in Fig. (7.13). The $B(E2)$ have minima at the magic numbers 20, 28, 50, 82 and 126.

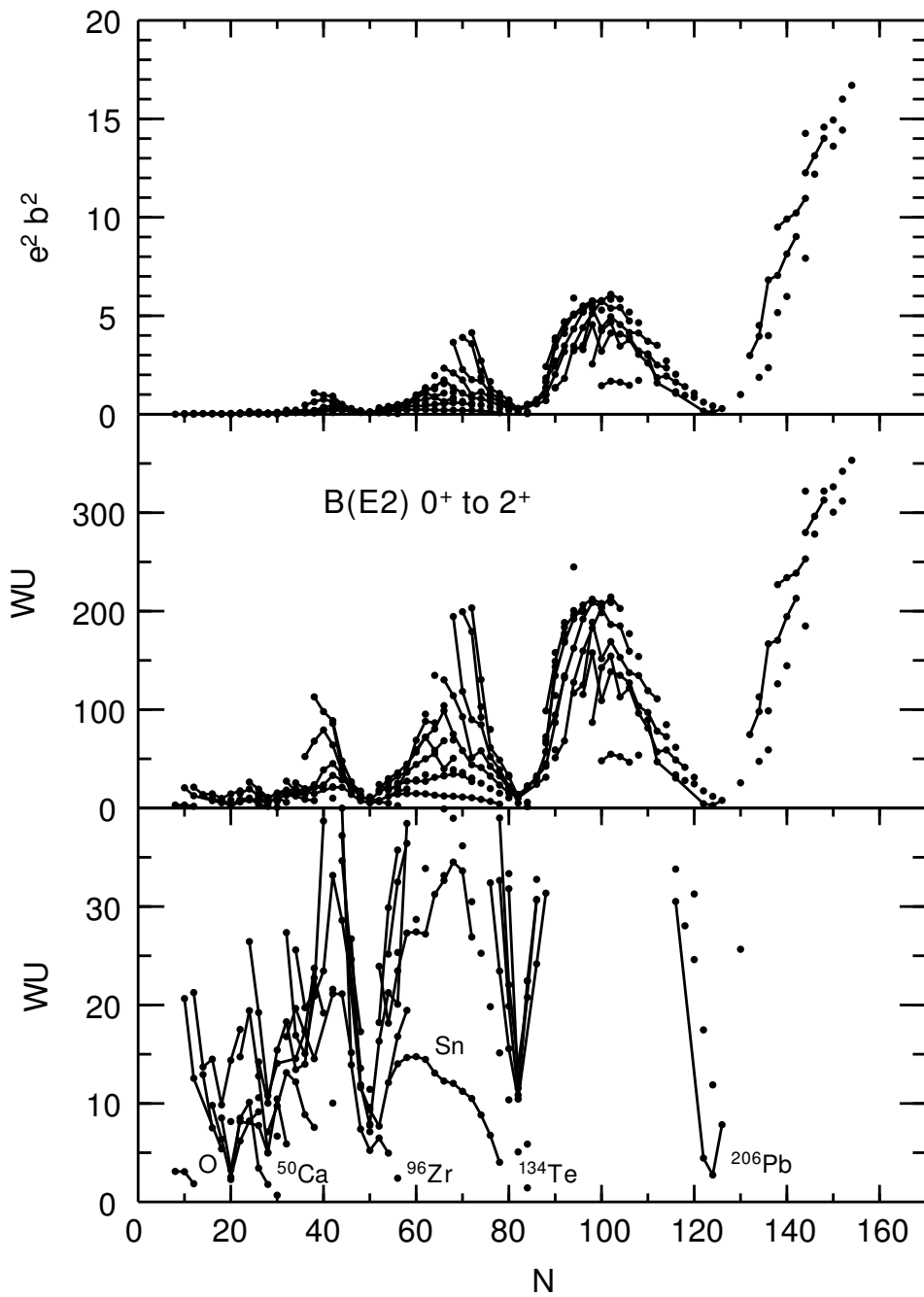


Figure 7.13: Experimental results for the $0_1^+ \rightarrow 2_1^+$ $B(E2)$ values from [46]. The top panel is in units of $e^2 b^2$ where $b = 100 \text{ fm}^2$. The bottom two panels are in Weisskopf units.

Bibliography

- [1] J. Schirmer D. Habs, R. Kroth, N. Kwong, D. Schwalm, M. Zirnbauer, and C. Broude, Phys. Rev. Lett. **53**, 1897 (1984). link
- [2] S. Hofmann et al., Z. Phys. A **305**, 111 (1982); O. Klepper et al., Z. Phys. A **305**, 125 (1982).
- [3] H. J. Rose and G. A. Jones, Nature **307**, 345 (1984); D. V. Aleksandov et al., JEPT

- Lett. **40**, 909 (1984).
- [4] S. R. Elliott, A. A. Hahn and M. K. Moe, Phys. Rev. Lett. **59**, 2020 (1987). link
 - [5] M. Pfutzner et al., Eur. Phys. J. **A14**, 279 (2002); J. Giovinazzo et al., Phys. Rev. Lett. **89**, 102501 (2002). link
 - [6] P. Woods and C. Davids, Annu. Rev. Nucl. Part. Sci. **47**, 541 (1997).
 - [7] G. Ardisson and M. Hussonnois, Radiochim. Acta. **70/71**, 123 (1995); A. A. Oglobin et al., Phys. Rev. C **61**, 034301 (2000). link
 - [8] M. Peshkin, A. Volya and V. Zelevinsky, Europhysics Letters **107**, 40001 (2014).
 - [9] G. Gamow, Z. Physik **51**, 204 (1928).
 - [10] B. A. Brown, Phys. Rev. C **46**, 811 (1992). link
 - [11] S. B. Duarte et al., Atomic Data Nucl. Data Tables **80**, 235 (2002).

- [12] D. Ni, Z. Ren, T. Dong and C. Xu, Phys. Rev. C **78**, 044310 (2008). link
- [13] D. H. Wilkinson and B. E. F. Macefield, Nucl. Phys. A232, 58 (1974)
- [14] I. S. Towner, E. K. Warburton, and G. T. Garvey, Annals of Physics **66**, 674 (1971).
- [15] E. K. Warburton, G. T. Garvey and I. S. Towner, Annals of Physics **57**, 174 (1970).
The half-life for ^{10}Be given in Table I of this paper should be replaced by 4.8×10^{13} . The results in Table II are changes to $f_o t = 7.6 \times 10^{14}$ and $|G_n|^2 = 53.0(7)$.
- [16] E. K. Warburton, J. A. Becker, D. J. Millener and B. A. Brown, Ann. Phys. 187, 471 (1988).
- [17] E. K. Warburton, Phys. Rev. C **45**, 463 (1992). link
- [18] E. K. Warburton, Phys. Rev. C **44**, 233 (1991). link
- [19] E. K. Warburton, Phys. Lett. Lett. **66**, 1823 (1991).
- [20] E. K. Warburton and I. S. Towner, Physics Reports **243**, 103 (1994).

- [21] J. Kostensalo and J. Suhonen, Phys. Lett. B **781**, 480 (2018).
- [22] B. Singh, J. L. Rodriguez, S. S. M. Wong and J. K. Tuli, Nuclear Data Sheets, **84**, 487 (1998).
- [23] J. C. Hardy, L. C. Carraz, B. Jonson and P. G. Hansen, Phys. Lett. B **71**, 307 (1977).
- [24] A. Kumar, P. C. Srivastava, J. Kostensalo, and J. Suhonen, Phys. Rev. C **101**, 064304 (2020). link
- [25] H. Behrens and W. Burhring, Nucl Phys. **A162**, 111 (1971).
- [26] I. S. Towner and J. C. Hardy, Nucl. Phys. **A179**, 489 (1972), and references therein.
- [27] Material covered in latter chapters.
- [28] D. H. Wilkinson, Nucl Phys. A209, 470 (1973)
- [29] D. H. Wilkinson, A. Gallman and D. E. Alburger, Phys. Rev. C18, 401 (1978) link

- [30] L. Hayden, N. Severijns, K. Bodek, D. Rozpedzik and X. Mougeot, Rev. Mod. Phys. **90**, 015008 (2018).
- [31] J. C. Hardy and I. S. Towner, Phys. Rev. C **102**, 045501 (2020). link
- [32] H. Behrens and J. Janecke, in Landolt-Bornstein, Numerical Data dn Functional Relationships in Science and Technology, New Series, editor in cheif K. -H. Hellwege, Group I: Nuclear Physics and Technology, Vol 4, ed. by H. Schopper (Springer-Verlag) 1969.
- [33] B. Markisch, et al., Phys. Rev. Lett. **122**, 242501 (2019). link
- [34] S. E. Elliott and P. Vogel, Annu. Rev. Nucl. and Part. Sci. **52**, 115 (2002).
- [35] M. J. Dolinski, A. W. Poon and W. Rodejohann Annu. Rev. Nucl. and Part. Sci. **69**, 219 (2002).
- [36] W. Bambynek, H. Behrens, M. H. Chen, B. Crasemann, M. L. Fitzpatrick, K. W. D. Ledingham, H. Genz, M. Mutterer, and R. L. Intemann Rev. Mod. Phys. **49**, 77 (1977).

- [37] C. Walz, H. Schiet, N. Pietralla, T. Aumann, R. Lefol, and V. Yu. Ponomarev, *Nature* **406**, 526 (2015).
- [38] T. Kibedi and R. H. Spear, *At. Data Nucl. Data Tables* **89**, 77 (2005).
- [39] B. A. Brown, A. B. Garnsworthy, T. Kibedi and A. E. Stuchbery, *Phys. Rev. C* **95**, 011301(R) (2017). link
- [40] K. Alder and R. M. Steffen, “Emission and Absorption of Electromagnetic Radiation”, in “The Electromagnetic Interaction in Nuclear Spectroscopy” edited by W. D. Hamilton, North-Holland Publishing Company, 1975.
- [41] J. D. Jackson, *Classical Electrodynamics*, Wiley, 1998.
- [42] J. M. Blatt and V. F. Weisskopf, *Theoretical Nuclear Physics*, Wiley, 1952.
- [43] G. F. Chew and G. C. Wick, *Phys. Rev.* **85**, 636 (1952). link
- [44] K. S. Krane and R. M. Steffen, *Phys. Rev. C* **2**, 724 (1970). link

- [45] T. Kibedi, T. W. Burrows, M. B. Trzhaskovskaya, P. M. Davidson, and C. W. Nestor, Nuclear Instruments and Methods in Physics Research Section A **589**, 202 (2008); <http://bricc.anu.edu.au/>
- [46] B. Pritychenko, M. Birch, B. Singh and M. Horoi, Atomic Data and Nuclear Data Tables **107**, 1 (2016).

Chapter 8

Electromagnetic Moments

Electromagnetic moments are found the diagonal matrix element of the one-body electromagnetic operator in the state with $M = J$:

$$\begin{aligned}\mathcal{M}(\pi\lambda) &\equiv \sqrt{\frac{4\pi}{(2\lambda+1)}} \langle \Psi, J, M = J | \mathcal{O}(\pi\lambda) | \Psi, J, M = J \rangle, \\ &= \sqrt{\frac{4\pi}{(2\lambda+1)}} \left(\begin{array}{ccc} J & \lambda & J \\ -J & 0 & J \end{array} \right) \langle \Psi, J | \mathcal{O}(\pi\lambda) | \Psi, J \rangle\end{aligned}\quad (8.1)$$

where () is the three-j symbol and $\langle \Psi, J | \mathcal{O}(\pi\lambda) | \Psi, J \rangle$ is the reduced matrix element [1]. These electric ($\pi=E$) and magnetic ($\pi=M$) operators are the same as those defined in the previous chapter for electromagnetic transitions. For a given J value, the allowed values of the λ are determined by the triangle condition, $\Delta(J, \lambda, J)$.

There are two type of electromagnetic moments: the electric moments associated with the static distribution of charge and the magnetic moments associated with the magnetic currents. Parity conservation requires $\lambda=\text{even}$ for the static moments and $\lambda=\text{odd}$ for the magnetic moments. The names relate to the Greek word for the 2^λ poles. By convention we define the moments as

$\mu = M(M1)$ (magnetic dipole)

$Q = 2 M(E2)$ (electric quadrupole)

$\Omega = -M(M3)$ (magnetic octupole)

$Q'_4 = 8 M(E4)$ (electric hexadecapole)

$\Gamma = M(M5)$ (magnetic triakontadupole)

The definition for Ω comes from [2] and Q'_4 comes from [3].

The existence of electric dipole moments (EDM) also violates time-reversal invariance [4]. (link to wiki). The experimental limit on EDM of the neutron is $|d_n| < 1.3 \times 10^{-26} e \text{ cm}$ [5]. These limits are important for understanding physics beyond the standard model. Experimental work for EDM in nuclei is also being carried out. The most sensitive nuclear EDM search so far is for ^{199}Hg [6]. It has been realized that nuclear structure can enhance EDM in nuclei when there are closely spaced parity doublets [4]. Examples are ^{233}Ra , ^{235}Ra and ^{220}Pa . One can also use heavy diatomic molecules, such as RaF for EDM searches [7].

Results for magnetic dipole and electric quadrupole moments will be discussed in the following subsections. A compilation of all types of moments from 1976 is given by Fuller

[3]. A compilation magnetic and quadrupole moments updated to 2005 is given by Stone [8]. Relatively few moments for $\lambda \geq 3$ have been measured. Ref. [9] gives some calculations for $\lambda=3-5$. Also these higher moments can be inferred from form factors obtained in elastic electron scattering [9]. For example, electron scattering data for ^{51}V gives information on the M3, M5 and M7 moments [10].

8.1 Magnetic moments

The magnetic moment operator simplifies to

$$\hat{\mu} = [\hat{\ell}_z g_q^\ell + \hat{s}_z g_q^s] \mu_N, \quad (8.2)$$

where g_q^ℓ and g_q^s are the orbital and spin g-factors for the proton ($q = p$) and neutron ($q = n$). The free-nucleon values for the g-factors are $g_p^\ell = 1$, $g_n^\ell = 0$, $g_p^s = 5.586$ and $g_n^s = -3.826$. The values of the magnetic moments are conventionally taken to be in units of the nuclear

magneton,

$$\mu_N = \frac{e\hbar}{2m_p c} = 0.105 \text{ e fm} \quad (8.3)$$

where m_p is the mass of the proton.

For a single-particle orbital in the nucleus specified by $(k) = (n, \ell, j)$, the magnetic moment is given by [1]

$$\frac{\mu}{\mu_N} = j \left[g_q^\ell \pm \frac{g_q^s - g_q^\ell}{2\ell + 1} \right], \quad (8.4)$$

where the + sign goes with $j - \frac{1}{2}$ and the - sign goes with $j + \frac{1}{2}$. The g-factor is defined as

$$g = \frac{\mu}{(\mu_N J)} = \left[g_q^\ell \pm \frac{g_q^s - g_q^\ell}{2\ell + 1} \right]. \quad (8.5)$$

These single-particle magnetic moments are also called the Schmidt values. In the case where the nuclear state can be described by a single hole in orbital k , the results is the same [1].

The result for neutrons in the state $j = \ell + \frac{1}{2}$ with $g_n^\ell = 0$ reduces to

$$\mu(j = \ell + \frac{1}{2}, \text{neutron}) = \frac{g_n^s \mu_N}{2} = \mu_n = -1.913 \mu_N$$

where μ_n is the magnetic moment of the neutron.

The magnetic moments data from the compilation of Stone [8] are shown in Fig. (8.1) in comparison with the single-particle values. The data are shown for the odd-neutron and odd-proton nuclei. For a given J^π value one can associate the unique ℓ and the data can be divided into two groups with $j = \ell + \frac{1}{2}$ and $j = \ell - \frac{1}{2}$. There is a pronounced difference between the odd-neutron and odd-proton plots that is related to the influence of the orbital contribution for protons. With few exceptions all of the data for a given kind of nucleon lies in between the limits given by the $j = \ell \pm \frac{1}{2}$ single-particle values. The reason for this can be understood as a result of configuration mixing beyond the single-particle model.

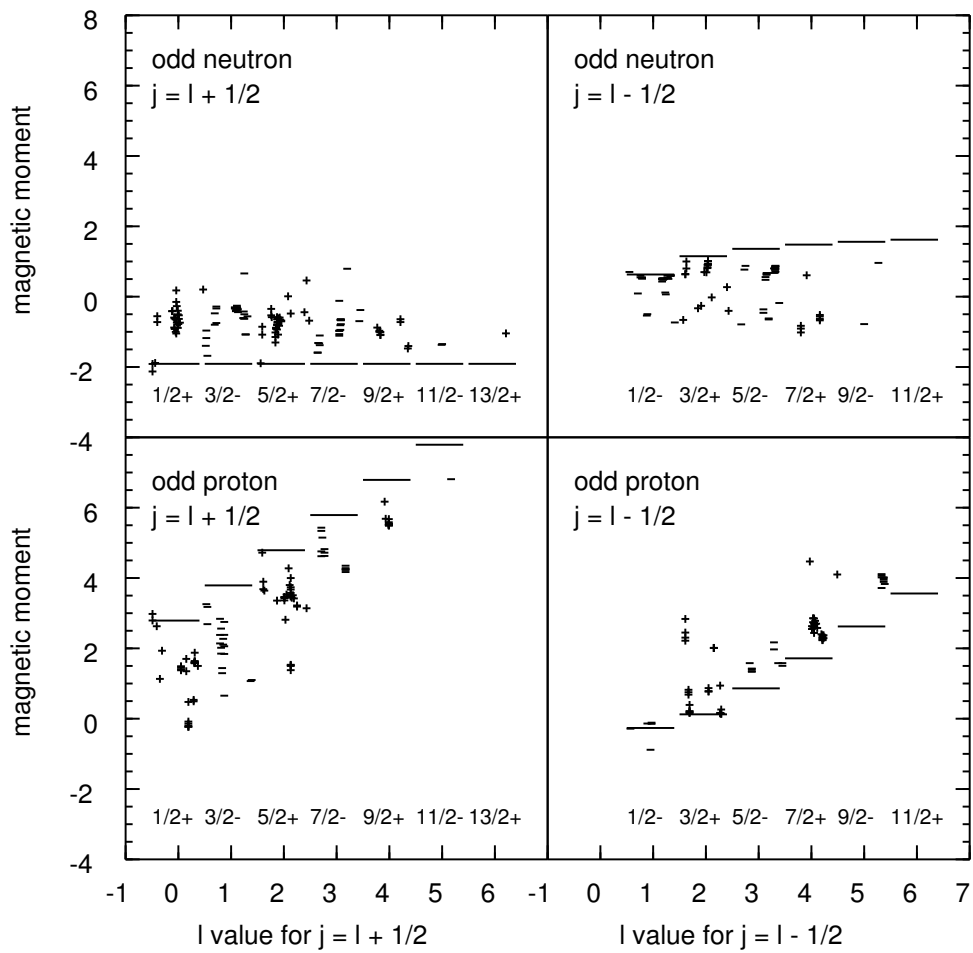


Figure 8.1: Experimental magnetic moments compared to the single-particle (Schmidt) values. For a given J^π value the data are plotted vs increasing neutron or proton number with plus signs for positive parity and minus signs for negative parity.

8.2 Electric quadrupole moments

The electric quadrupole moment operator simplifies to

$$\hat{Q} = (3\hat{z}^2 - \hat{r}^2)e_q, \quad (8.6)$$

where e_q are the electric charges for the proton, $e_p = e$, and neutron $e_n = 0$. Quadrupole moments are usually quoted in units of $e \text{ fm}^2$ or eb where b is the “barn”, $b = 100 \text{ fm}^2$.

For a single-particle orbital specified by $(k) = (n, \ell, j)$, the quadrupole moment is given by [1]

$$Q(k) = - \left(\frac{2j-1}{2j+2} \right) \langle n\ell j | r^2 | n\ell j \rangle e_q, \quad (8.7)$$

where $\langle n\ell j | r^2 | n\ell j \rangle$ is the integral of the radial wavefunction over r^2 . This gives $Q = 0$ for $j = 1/2$ as expected from the triangle condition $\Delta(j, 2, j)$.

In the case where the nucleus can be described by a single hole in orbital k , the results

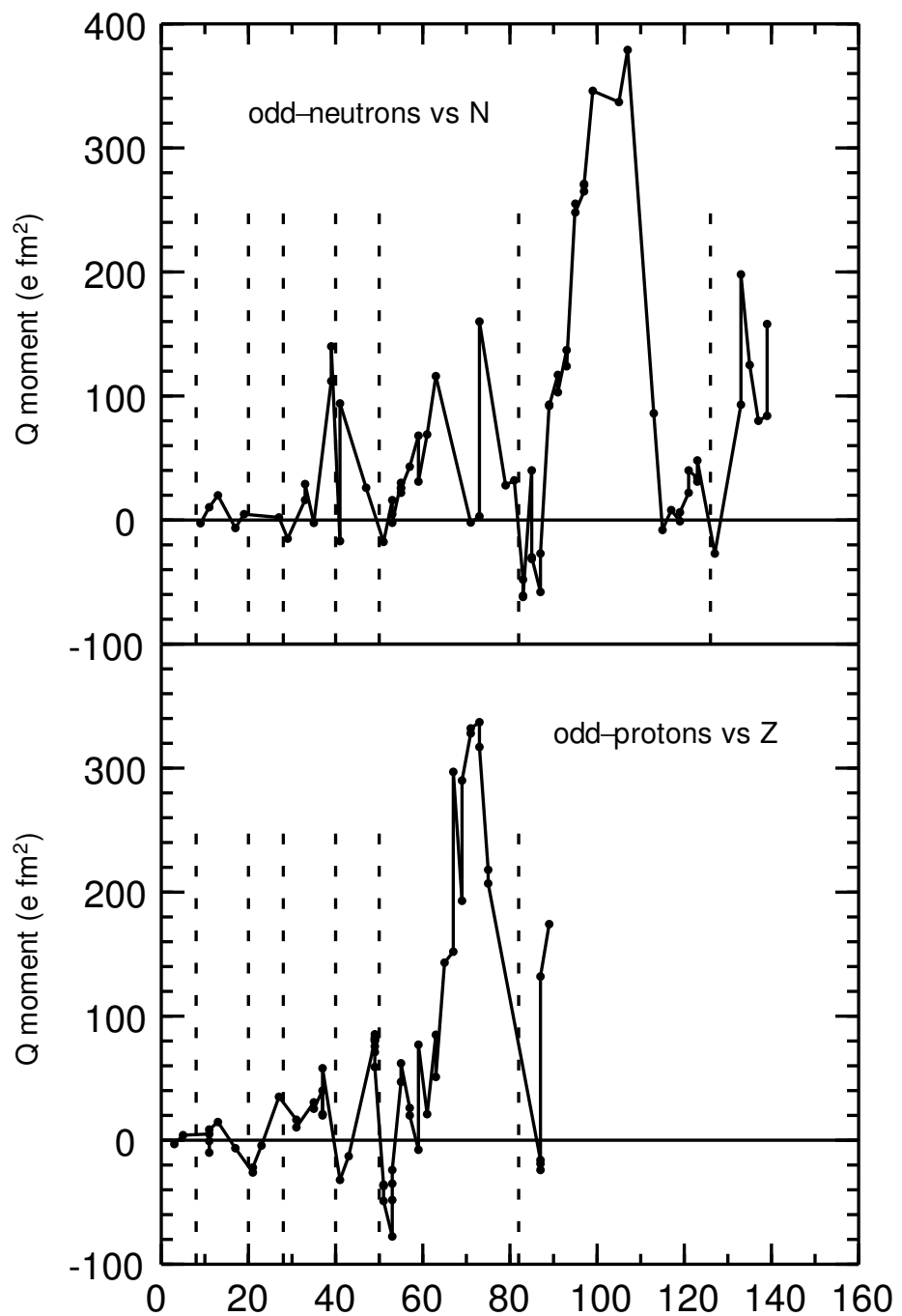
changes sign [1]

$$Q(k^{-1}) = \left(\frac{2j-1}{2j+2} \right) \langle n\ell j | r^2 | n\ell j \rangle e_q. \quad (8.8)$$

The sign of the quadrupole moment has a simple interpretation in terms of the Cartesian co-ordinates for the operator $(3z^2 - r^2) = (2z^2 - x^2 - y^2)$. If the density is spherical $Q = 0$. If the density extends more along the z axis it has a prolate shape with $Q > 0$, and if the density is concentrated in the $x - y$ plane it has a oblate shape with $Q < 0$.

For the single-particle orbital in the state $m = \pm j$ the density lies in the $x - y$ plane [1] and has an oblate shape with $Q < 0$. For a hole state with the absence of a nucleon in the state with $m = \pm j$. the remaining density has a prolate shape with $Q > 0$.

The experimental data for the quadrupole moments of the ground states of odd-even nuclei are shown in Fig. (8.2). In order to qualitatively divide out the mass dependence implied by the $\langle r^2 \rangle$ matrix elements in Eqs. (8.7) and (8.8), the experimental moments can be divided by R^2 where $R = 1.2A^{1/3}$. These scaled quadrupole moments are shown in



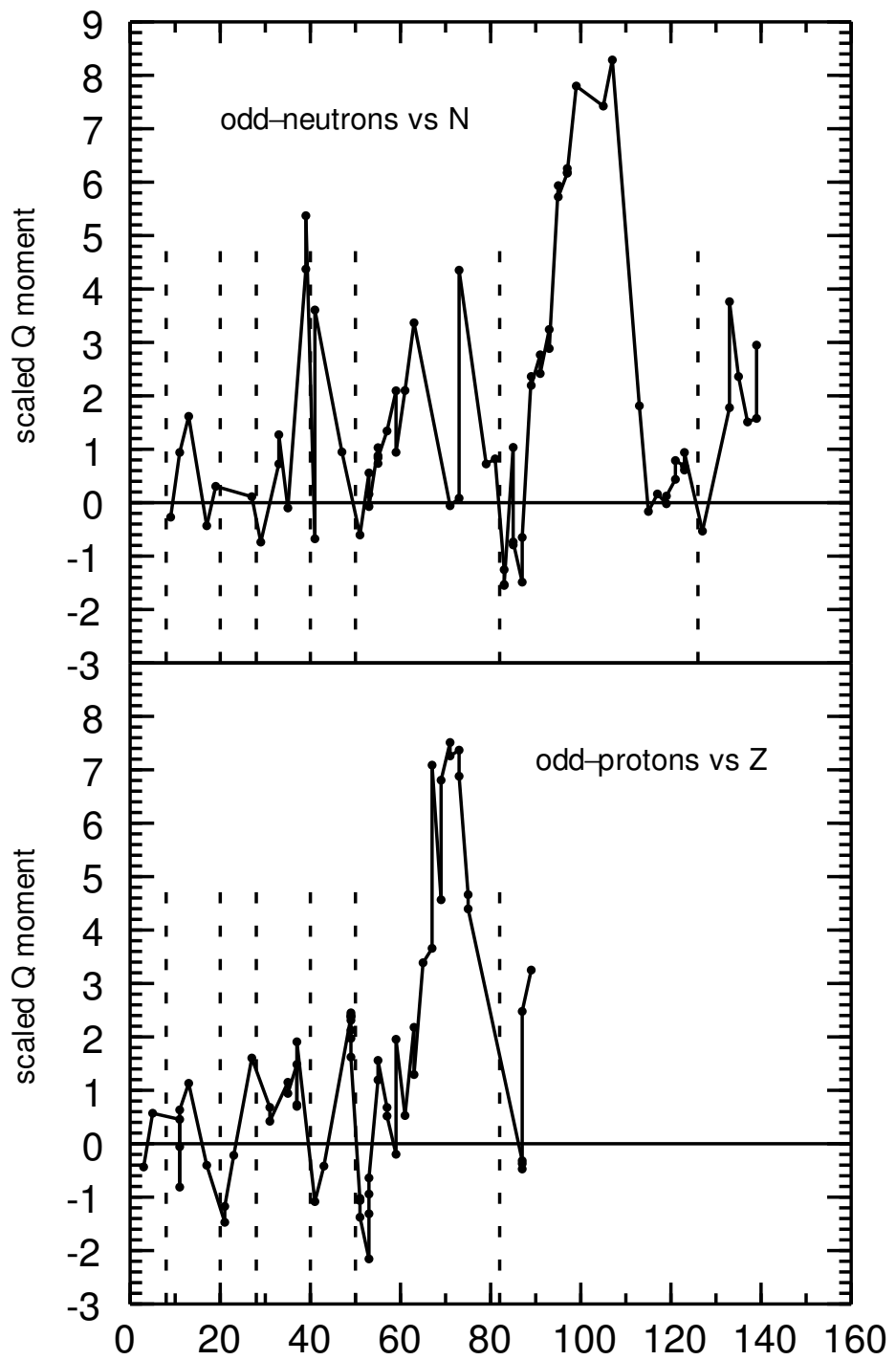


Figure 8.3: Scaled experimental quadrupole moments for the ground states of odd-even nuclei. The dashed lines show the magic numbers 8, 20, 28, 40, 50, 82 and 126.

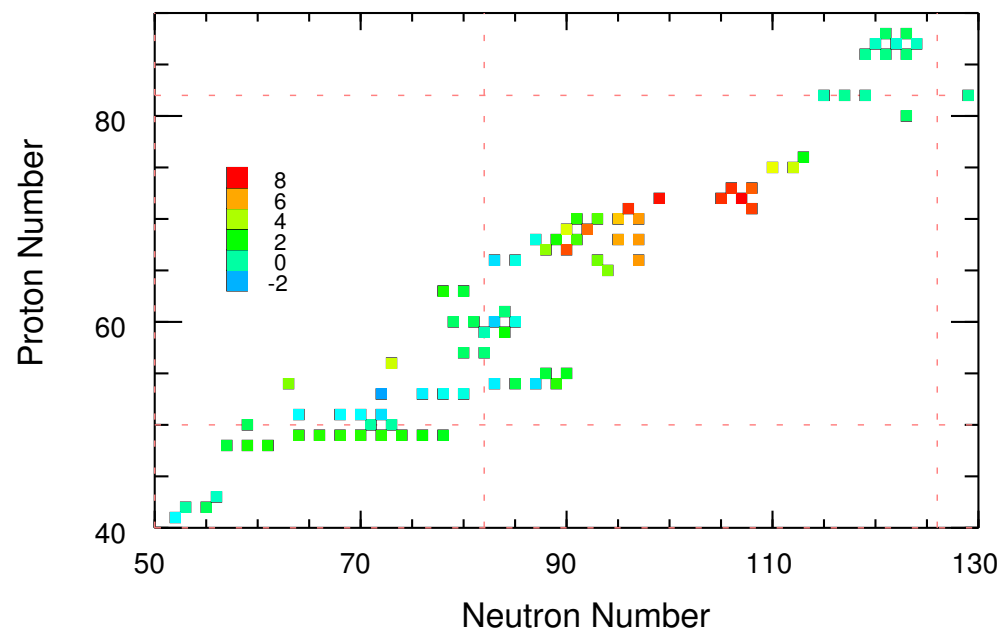


Figure 8.4: Scaled experimental quadrupole moments for the ground states of odd-even nuclei for a region of nuclei. The dashed lines show the magic numbers 50 and 82 for protons and 82 and 126 for neutrons.

Fig. (8.3). The scaled data are shown for a region of the nuclear chart in Fig. (8.4).

There are several places where the sign change between particle (oblate) and hole (prolate) states can be observed, for example, for odd-protons in Fig. (8.2) just above and below $Z = 50$. There are regions where the Q moments are much larger than expected from one proton in a single-orbital. In those cases the density comes from the coherent distribution of many protons. These can be described by a deformed intrinsic state. Although one might expect to have both oblate and prolate deformed shapes, experiment is dominated by the prolate shapes. This result also comes out of calculations for these deformed nuclei, but there appears to be no simple reason why prolate shapes dominate.

In the single-particle model we would expect the Q moments for the neutrons orbitals to be zero. But one observes in Fig. (8.2) that the Q moments for odd-proton and odd-neutron nuclei are about the same. This shows that the nuclear wavefunctions are always more complicated than single-particle configurations. However, it is often useful to start with single-particle states that become “dressed” via their interactions with all other nucleons. The “core” becomes polarized in the presence of single-particle states. This idea leads to use

of core-polarization or effective charges e_q . Empirical values that are used with cores that are associated with the nuclear magic numbers are on the order of $e_p = 1.5e$ and $e_n = 0.5e$.

Bibliography

- [1] Material covered in latter chapters.
- [2] C. Schwartz, Phys. Rev. **97**, 380 (1955). link
- [3] H. Fuller, J. Phys. Chem. Ref. Data **5**, 835 (1976).
- [4] J. Engel, M. J. Ramsey-Musolf, and U. van Kolck, Prog. Part. Nucl. Phys. **71**, 21 (2013).

- [5] C. Abel et al., Phys. Rev. Lett. **124**, 081803 (2020). link
- [6] W. C. Griffith et al., Phys. Rev. Lett. **102**, 101601 (2009). link
- [7] A. Sunaga, M. Abe, H. Hada and B. P. Das, Phys. Rev. A **99**, 062506 (2018).
- [8] N. J. Stone, Atomic Data and Nuclear Data Tables **90**, 75 (2005).
- [9] B. A. Brown, W. Chung and B. H. Wildenthal, Phys. Rev. C **22**, 774 (1980). link
- [10] K. Arita, et al., Phys. Rev. C **23**, 1482 (1981). link

Chapter 9

Conserved quantum numbers

9.1 Angular momentum

The Hamiltonian is a scalar in the spatial coordinates - the expectation value does not depend on the orientation of the system. Thus the Hamiltonian commutes with total angular momentum operators:

$$[H, \hat{J}^2] = 0, \quad (9.1)$$

$$[H, \hat{J}_z] = 0. \quad (9.2)$$

The many-body wave functions are eigenstates of \hat{J}^2 and \hat{J}_z with:

$$\hat{J}^2 |\Psi\rangle = J(J+1) |\Psi\rangle, \quad (9.3)$$

$$\hat{J}_z |\Psi\rangle = M |\Psi\rangle, \quad (9.4)$$

where there are $(2J + 1)$ values of M going from $M = -J$ up to $M = +J$ in integer steps. Thus one of our goals is to construct wave functions which have good J and J_z . One can construct basis states which have good J and J_z - this is called the J-scheme. Sometimes one constructs a basis which has only good J_z but not good J - this is called the M-scheme. If

this M-scheme basis is complete with regard to rotations in the J -space, then the eigenstates will have good J and J_z . For a nucleus composed of nucleons the total angular momentum is sum of the orbital and spin angular momenta of all nucleons.

9.2 Parity

The strong and electromagnetic Hamiltonians conserve parity. Thus the eigenstates can be broken down into two classes of states labeled by their parity $\pi = +1$ or $\pi = -1$, and the Hamiltonian does not mix these two classes. For nuclear structure the total parity originates from the intrinsic parity of the nucleon which is $\pi_{int}=+1$ and the parities associated with the orbital angular momenta $\pi_\ell = (-1)^\ell$. The total parity is the product over all nucleons

$$\pi = \prod_i \pi_{int}(i) \pi_\ell(i) = \prod_i (-1)^{\ell_i} \quad (9.5)$$

One usually constructs basis states and eigenstates which have a definite parity.

The weak Hamiltonian does not conserve parity. When considered as a perturbation the matrix elements of the weak Hamiltonian are typically on the order of a few eV or less. Thus, parity mixing can always be calculated in first-order perturbation theory.

The effects of parity nonconservation can be observed in several types of experiment in which the observable must be zero in the absence of parity nonconservation [1], [2]. For example, when parity is conserved a $\Delta L = 1$ electromagnetic transition must either be M1 if the two states do not change parity ($\pi_i\pi_f = +1$), or E1 if the two states change parity ($\pi_i\pi_f = -1$). The angular distribution of both E1 and M1 gamma rays is symmetric around the spin axis of the nucleus. When parity is not conserved then there can be interference between E1 and M1 which leads to an left-right asymmetry in the angular distribution.

9.3 Isospin

Since the spin of the proton and neutron are both 1/2 and the masses are nearly the same, it is useful to think of them as members of an isospin doublet of the nucleon. Thus they have isospin $t = 1/2$ and projection $t_z = -1/2$ and $t_z = +1/2$ for the proton and neutron, respectively. The isospin operator \vec{t} for the isospin degrees of freedom is analogous to the spin operator \vec{s} for the spin degrees of freedom. For many nucleons the total isospin and its z projection are given by

$$\vec{T} = \sum_i \vec{t}(i). \quad (9.6)$$

$$\hat{T}_z = \sum_i \hat{t}_z(i). \quad (9.7)$$

The strong interaction conserves isospin, that is, the expectation value of H_s does not depend on the orientation in isospin space. Thus H_s commutes with the total isospin operators:

$$[H_s, \hat{T}^2] = 0 \quad (9.8)$$

$$[H_s, \hat{T}_z] = 0 \quad (9.9)$$

The many-body wave functions are eigenstates of \hat{T}^2 and \hat{T}_z with:

$$\hat{T}^2 |\Psi\rangle = T(T+1) |\Psi\rangle, \quad (9.10)$$

$$\hat{T}_z |\Psi\rangle = T_z |\Psi\rangle, \quad (9.11)$$

where there are $2T+1$ values of T_z going from $T_z = -T$ up to $T_z = +T$ in integer steps. For a nucleus with Z protons and N neutrons, $T_z = (N-Z)/2$. The sign convention here is chosen so that the more common neutron-rich nuclei will have positive T_z (but other books may use a difference convention). For a given T_z value the minimum value of T is $T_{min} = |T_z|$ and the maximum value is $T_{max} = A/2$. The lowest level in a nucleus usually has $T = T_z$ (there are a few exceptions for odd-odd nuclei with $N = Z$). This is related to the fact that the nuclear interaction in the $T = 0$ two-nucleon system is a stronger than in the $T = 1$ system (only the deuteron has a bound state).

The experimental evidence for isospin conservation comes from a comparison of the proton-proton, proton-neutron and neutron-neutron scattering lengths in their $T = 1$ state,

and the observation that the energy levels of nuclei can be organized into T multiplets of $(2T + 1)$ nuclei with $T_z = -T$ up to $T_z = T$.

One of the special consequences of isospin conservation is mirror symmetry. The energy spectrum of a nucleus should be identical to that of another nucleus in which the protons and neutrons numbers are interchanged. These are called mirror nuclei. There are many examples of mirror nuclei whose spectra can be compared in this way. The deviation from mirror symmetry is attributed to the Coulomb interaction.

The Coulomb Hamiltonian does not conserve isospin since it only enters into the interaction between protons. If the Coulomb interaction is treated as a perturbation, then its off-diagonal matrix elements are typically on the order of 100 keV or less. For many nuclear structure problems this is small (at least compared to the uncertainty in the strong interaction matrix elements) and we can start with basis states and eigenfunctions which are constructed to have good isospin. Isospin non-conservation is often treated in first-order perturbation theory.

Bibliography

- [1] E. G. Adelberger and W. C. Haxton, *Annu. Rev. Nucl. Part. Sci.* **35** 501 (1985).
- [2] M. J. Ramsey-Musolf and S. A. Page, *Annu. Rev. Nucl. Part. Sci.* **56**, 1 (2006).

Chapter 10

Angular momentum and tensor algebra

10.1 Angular Momentum Operators

The material in this chapter is a review of results derived in textbooks on quantum mechanics, for example [1].

The angular momentum operator L (in units with $\hbar=1$) is defined by

$$\vec{L} = \vec{r} \times \vec{p} = -i(\vec{r} \times \vec{\nabla}). \quad (10.1)$$

The coordinate form of this operator is

$$\begin{aligned} L_z &= -i \frac{\partial}{\partial \phi}, \\ L_{\pm} &= L_x \pm i L_y = e^{\pm i \phi} \left[i \cot \theta \frac{\partial}{\partial \phi} \pm \frac{\partial}{\partial \theta} \right], \\ L^2 &= - \left[\frac{1}{\sin \theta} \frac{\partial}{\partial \theta} \left(\sin \theta \frac{\partial}{\partial \theta} \right) + \frac{1}{\sin^2 \theta} \frac{\partial^2}{\partial \phi^2} \right]. \end{aligned} \quad (10.2)$$

The commutation relations ($[a, b] = ab - ba$) are

$$[L_x, L_y] = iL_z,$$

$$[L_z, L_x] = iL_y,$$

$$[L_y, L_z] = iL_x,$$

and

$$[\vec{L}, L^2] = 0. \quad (10.3)$$

The eigenstates of the L^2 and L_z operators are

$$L^2 |\ell, m\rangle = \ell(\ell + 1) |\ell, m\rangle \quad (10.4)$$

$$L_z |\ell, m\rangle = m |\ell, m\rangle. \quad (10.5)$$

The spatial representation of these wavefunctions are given by the spherical harmonics

$$\langle \theta, \phi | \ell, m \rangle = Y_m^\ell(\theta, \phi).$$

10.2 Spherical Harmonics

The spherical harmonics Y_m^ℓ are defined by

$$Y_m^\ell(\theta, \phi) = e^{im\phi} \sqrt{\frac{(2\ell+1)(\ell-m)!}{4\pi(\ell+m)!}} P_m^\ell(\cos \theta), \quad (10.6)$$

where P_m^ℓ are the associated Legendre polynomials. These functions are orthonormal

$$\int [Y_m^\ell(\theta, \phi)]^* Y_{m'}^{\ell'}(\theta, \phi) d\Omega = \delta_{\ell,\ell'} \delta_{m,m'}, \quad (10.7)$$

and can be used to expand any angular function of θ and ϕ .

$$f(\theta, \phi) = \sum_{\ell,m} a_{\ell,m} Y_m^\ell(\theta, \phi). \quad (10.8)$$

Hermitian conjugation gives

$$[Y_m^\ell(\theta, \phi)]^+ = [Y_m^\ell(\theta, \phi)]^* = (-1)^m Y_{-m}^\ell(\theta, \phi). \quad (10.9)$$

This is obtained from Eq. (10.6) together with the property of the associated Legendre polynomials

$$P_{-m}^\ell(\cos \theta) = (-1)^m \frac{(\ell - m)!}{(\ell + m)!} P_m^\ell(\cos \theta). \quad (10.10)$$

The properties under coordinate inversion $\hat{P}(\vec{r}) = -\vec{r}$ are

$$\hat{P}Y_m^\ell(\theta, \phi) = (-1)^\ell Y_m^\ell(\theta, \phi). \quad (10.11)$$

The addition theorem for spherical harmonics is

$$P_\ell(\cos \omega_{12}) = \frac{4\pi}{(2l+1)} \sum_m [Y_m^\ell(\Omega_1)]^* Y_m^\ell(\Omega_2), \quad (10.12)$$

where ω_{12} is the angle between the two directions determined by Ω_1 and Ω_2 , and P_ℓ is the Legendre polynomial

$$P_\ell(\cos \theta) = \sqrt{\frac{4\pi}{(2\ell+1)}} Y_{m=0}^\ell(\theta, \phi). \quad (10.13)$$

When $\Omega=\Omega_1=\Omega_2$ Eq. (10.12) gives

$$\sum_m |Y_m^\ell(\Omega)|^2 = \frac{2\ell+1}{4\pi} P_\ell(1) = \frac{2\ell+1}{4\pi}. \quad (10.14)$$

The functions for some low ℓ values are:

$$Y_0^0(\theta, \phi) = \sqrt{\frac{1}{4\pi}} \quad (10.15)$$

$$Y_0^1(\theta, \phi) = \sqrt{\frac{3}{4\pi}} \cos \theta = \sqrt{\frac{3}{4\pi}} \frac{z}{r} \quad (10.16)$$

$$Y_{\pm 1}^1(\theta, \phi) = \mp \sqrt{\frac{3}{8\pi}} \sin \theta e^{\pm i\phi} = \mp \sqrt{\frac{3}{8\pi}} \frac{(x \pm iy)}{r} \quad (10.17)$$

$$Y_0^2(\theta, \phi) = \sqrt{\frac{5}{16\pi}} (3 \cos^2 \theta - 1) = \sqrt{\frac{5}{16\pi}} \frac{(-x^2 - y^2 + 2z^2)}{r^2} \quad (10.18)$$

$$Y_{\pm 1}^2(\theta, \phi) = \mp \sqrt{\frac{15}{8\pi}} \cos \theta \sin \theta e^{\pm i\phi} = \mp \sqrt{\frac{15}{8\pi}} \frac{(x \pm iy)z}{r^2} \quad (10.19)$$

$$Y_{\pm 2}^2(\theta, \phi) = \sqrt{\frac{15}{32\pi}} \sin^2 \theta e^{\pm 2i\phi} = \sqrt{\frac{15}{32\pi}} \frac{(x \pm iy)^2}{r^2} \quad (10.20)$$

The commutation relations between the angular momentum operators and the spherical harmonics are

$$[L_z, Y_m^\ell] = m Y_m^\ell \quad (10.21)$$

and

$$[L_\pm, Y_m^\ell] = [L_x \pm iL_y, Y_m^\ell] = \sqrt{\ell(\ell+1) - m(m \pm 1)} Y_{m \pm 1}^\ell. \quad (10.22)$$

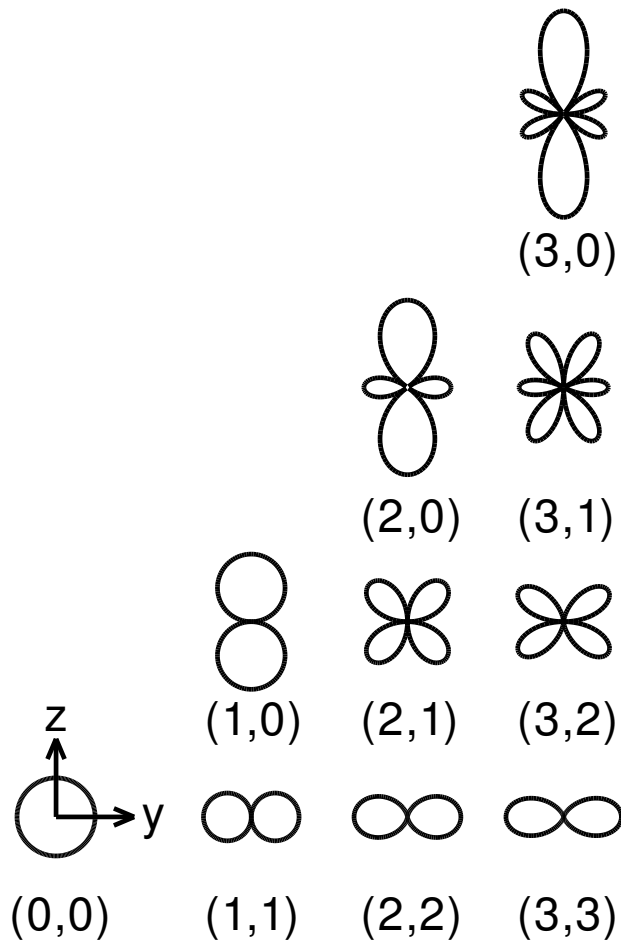


Figure 10.1: Plots of $|Y_m^l(\theta, \phi)|$ in the (y, z) plane labeled by (ℓ, m) . The three-dimensional surface is obtained by a rotation of these curves around the z axis.

10.3 Angular momentum coupling

The total angular momentum of a system is conserved. The total angular momentum may be composed of the sum of orbital and intrinsic spins, or it may be composed of the sum of the angular momenta \vec{j} for two or more nucleons. In this section \vec{J} will denote a generalized angular momentum, it could be orbital, intrinsic-spin or some combinations of both. Results for the coupling of up to four angular momenta and the notation relating these to the $3j$, $6j$ and $9j$ coefficients will be summarized. Computer programs for these can be found in the books by Thompson [2] and [3] as well as in the OXBASH shell-model computer package [4]. The $3j$ and $6j$ coefficients are tabulated in many references for small and intermediate values of angular momentum. Some of the more useful special relations and values for these coefficients will be given below. Many others are available in the literature [5] [6] [2] [7] [8] [9].

10.3.1 Coupling of Two Angular Momenta

The coupling of two angular momenta will be considered first. The total angular momentum, $\vec{J} = \vec{J}_1 + \vec{J}_2$, is conserved, and the quantum numbers J associated with the vector \vec{J} take on the integer values from $J_{min} = |J_1 - J_2|$ to $J_{max} = J_1 + J_2$. This condition on the J values will be referred to as the triangle condition, $\Delta(J_1 J_2 J)$. The sum of the J values in the triangle condition, $J_t = J_1 + J_2 + J$ in this case, is always an integer, and the factor $(-1)^{2J_t} = 1$ can be multiplied in order to simplify a phase factor.

The wave functions associated with the states $|J_1 J_2 JM\rangle$ are linear combinations of the states $|J_1 M_1 J_2 M_2\rangle$

$$|J_1 J_2 JM\rangle = \sum_{M_1 M_2} |J_1 M_1 J_2 M_2\rangle \langle J_1 M_1 J_2 M_2 | J_1 J_2 JM\rangle, \quad (10.23)$$

where $M_1 + M_2 = M$. The Clebsch-Gordan coefficients [5] are a specific normalization and phase convention for the overlaps

$$\langle J_1 M_1 J_2 M_2 | JM \rangle \equiv \langle J_1 M_1 J_2 M_2 | J_1 J_2 JM \rangle. \quad (10.24)$$

In particular, they are all real and

$$\langle J_1 M_1 J_2 M_2 | J_{max}, M = J_{max} \rangle = 1. \quad (10.25)$$

Since they are real,

$$\langle J_1 M_1 J_2 M_2 | JM \rangle = \langle JM | J_1 M_1 J_2 M_2 \rangle. \quad (10.26)$$

The Clebsch-Gordan coefficients can be used, for example, to couple the two wave functions ϕ^{J_1} and χ^{J_2} to the product wave function $\psi(J_1, J_2)^J$

$$\psi(J_1, J_2)_M^J = \sum_{M_1 M_2} \langle J_1 M_1 J_2 M_2 | J_1 J_2 JM \rangle \phi_{M_1}^{J_1} \chi_{M_2}^{J_2} \equiv [\phi^{J_1} \otimes \chi^{J_2}]_M^J. \quad (10.27)$$

An explicit expression for Clebsch-Gordan coefficient is given in [10]. The Clebsch-Gordan coefficients obey the orthonormality conditions

$$\sum_{J, M} \langle J_1 M_1 J_2 M_2 | JM \rangle \langle J_1 M'_1 J_2 M'_2 | JM \rangle = \delta_{M_1 M'_1} \delta_{M_2 M'_2}, \quad (10.28)$$

and

$$\sum_{M_1 M_2} \langle J_1 M_1 J_2 M_2 | JM \rangle \langle J_1 M_1 J_2 M_2 | J' M' \rangle = \delta_{JJ'} \delta_{MM'}. \quad (10.29)$$

The symmetry properties of the Clebsch-Gordan coefficients are

$$\langle J_1 M_1 J_2 M_2 | JM \rangle = (-1)^{J_1 + J_2 - J} \langle J_2 M_2 J_1 M_1 | JM \rangle, \quad (10.30)$$

$$\langle J_1 M_1 J_2 M_2 | JM \rangle = (-1)^{J_1 + J_2 - J} \langle J_1, -M_1 J_2, -M_2 | J, -M \rangle, \quad (10.31)$$

and

$$\langle J_1 M_1 J_2 M_2 | JM \rangle = (-1)^{J_2 + M_2} \sqrt{\frac{2J+1}{2J_1+1}} \langle J_2, -M_2 | JM | J_1 M_1 \rangle. \quad (10.32)$$

When we couple orbital angular momenta $\ell > 0$ with spin $J_2 = s = 1/2$ there are only two terms in the sum in Eq. (10.27) for $M_2 = m_s = \pm s$. With of $J_1 = \ell$, for $J = j = \ell + s$

$$\psi(\ell, s)_m^{j=\ell+s} = \sqrt{\frac{\ell+s+m}{2\ell+1}} \phi_{m-s}^\ell \chi_s + \sqrt{\frac{\ell+s-m}{2\ell+1}} \phi_{m+s}^\ell \chi_{-s}, \quad (10.33)$$

and for $J = j = \ell - s$

$$\psi_c(\ell, s)_m^{j=\ell-s} = \sqrt{\frac{\ell+s-m}{2\ell+1}} \phi_{m-s}^\ell \chi_s - \sqrt{\frac{\ell+s+m}{2\ell+1}} \phi_{m+s}^\ell \chi_{-s}. \quad (10.34)$$

The $3j$ coefficient $\begin{pmatrix} J_1 & J_2 & J \\ M_1 & M_2 & M \end{pmatrix}$ is related to the Clebsch-Gordan coefficient by

$$\langle J_1 M_1 J_2 M_2 | JM \rangle \equiv (-1)^{J_1-J_2+M} \sqrt{2J+1} \begin{pmatrix} J_1 & J_2 & J \\ M_1 & M_2 & -M \end{pmatrix}, \quad (10.35)$$

where the sum of the M values in the bottom row must be zero: $M_1 + M_2 - M = 0$. The symmetry properties of the Clebsch-Gordan coefficients are given compactly in terms of those for the $3j$ coefficients and can be summarized by

$$\begin{pmatrix} J_1 & J_2 & J_3 \\ M_1 & M_2 & M_3 \end{pmatrix} = (-1)^p \begin{pmatrix} J_a & J_b & J_c \\ M_a & M_b & M_c \end{pmatrix}, \quad (10.36)$$

where $p = J_a + J_b + J_c$. The $3j$ on the right is obtained by the interchange of any two neighboring columns (a permutation of the columns) of the $3j$ on the left. Since p always an integer, two such interchanges gives $(-1)^{2p} = 1$. In addition, $p = J_a + J_b + J_c$ if the top row is unchanged but the bottom row is changed in sign. ($M_1 = -M_a$, $M_2 = -M_b$ and $M_3 = -M_c$). The orthogonality relations for the $3j$ coefficients that are equivalent to Eqs. (10.28) and (10.29) take the form

$$\sum_{J,M} (2J+1) \begin{pmatrix} J_1 & J_2 & J \\ M_1 & M_2 & M \end{pmatrix} \begin{pmatrix} J_1 & J_2 & J \\ M'_1 & M'_2 & M \end{pmatrix} = \delta_{M_1 M'_1} \delta_{M_2 M'_2}, \quad (10.37)$$

and

$$\sum_{M_1, M_2} (2J+1) \begin{pmatrix} J_1 & J_2 & J \\ M_1 & M_2 & M \end{pmatrix} \begin{pmatrix} J_1 & J_2 & J' \\ M_1 & M_2 & M' \end{pmatrix} = \delta_{JJ'} \delta_{MM'}. \quad (10.38)$$

Useful expressions for some special cases are

$$\begin{pmatrix} J & 0 & J \\ -M & 0 & M' \end{pmatrix} = \frac{(-1)^{J-M} \delta_{MM'}}{\sqrt{2J+1}}, \quad (10.39)$$

$$\begin{pmatrix} J & 1 & J \\ -M & 0 & M' \end{pmatrix} = \frac{(-1)^{J-M} M \delta_{MM'}}{\sqrt{J(2J+1)(J+1)}}, \quad (10.40)$$

and

$$\begin{pmatrix} J & 2 & J \\ -M & 0 & M' \end{pmatrix} = \frac{(-1)^{J-M} [3M^2 - J(J+1)] \delta_{MM'}}{\sqrt{(2J-1)J(2J+1)(J+1)(2J+3)}}. \quad (10.41)$$

10.3.2 Coupling of Three Angular Momenta

In this section we use the notation $| (J_1 J_2 J_{12}) J_3 JM \rangle$ for the three particle wave functions formed from the Clebsch-Gordan coupling of J_1 and J_2 to make J_{12} and then the Clebsch-Gordan coupling of J_{12} to J_3 to make the total angular momentum J and projection M . The wave functions may require other quantum numbers for their complete specification, but only the explicit representation for J is required in this section. The three angular momenta can be coupled in various ways. For example,

$$| (J_1 J_2 J_{12}) J_3 JM \rangle$$

$$\begin{aligned}
&= \sum_{M_{12}M_3} \langle J_{12}M_{12}J_3M_3 | JM \rangle | (J_1J_2J_{12}M_{12})J_3M_3 \rangle \\
&= \sum_{M_1M_2M_3} \langle J_{12}M_{12}J_3M_3 | JM \rangle \langle J_1M_1J_2M_2 | J_{12}M_{12} \rangle \\
&\quad \times | J_1M_1J_2M_2J_3M_3 \rangle,
\end{aligned} \tag{10.42}$$

and

$$\begin{aligned}
&| J_1(J_2J_3J_{23})J'M' \rangle \\
&= \sum_{M_{23}M'_1} \langle J_1M'_1J_{23}M_{23} | J'M' \rangle | J_1M'_1(J_2J_3J_{23}M_{23}) \rangle \\
&= \sum_{M'_1M'_2M'_3} \langle J_1M'_1J_{23}M_{23} | J'M' \rangle \langle J_2M'_2J_3M'_3 | J_{23}M_{23} \rangle \\
&\quad \times | J_1M'_1J_2M'_2J_3M'_3 \rangle.
\end{aligned} \tag{10.43}$$

The overlaps between these two ways of coupling are defined in terms of the $6j$ coefficients

$$\langle (J_1J_2J_{12})J_3JM | J_1(J_2J_3J_{23})J'M' \rangle =$$

$$\begin{aligned}
&= \delta_{JJ'} \delta_{MM'} \sum_{M_1 M_2 M_3} < J_{12} M_{12} J_3 M_3 | JM > < J_1 M_1 J_2 M_2 | J_{12} M_{12} > \\
&\quad \times < J_1 M_1 J_{23} M_{23} | JM > < J_2 M_2 J_3 M_3 | J_{23} M_{23} > \\
&\equiv (-1)^{J_1+J_2+J_3+J} \sqrt{(2J_{12}+1)(2J_{23}+1)} \left\{ \begin{array}{ccc} J_1 & J_2 & J_{12} \\ J_3 & J & J_{23} \end{array} \right\}, \tag{10.44}
\end{aligned}$$

and thus

$$\begin{aligned}
| J_1 (J_2 J_3 J_{23}) JM > &= \sum_{J_{12}} (-1)^{J_1+J_2+J_3+J} \sqrt{(2J_{12}+1)(2J_{23}+1)} \\
&\quad \times \left\{ \begin{array}{ccc} J_1 & J_2 & J_{12} \\ J_3 & J & J_{23} \end{array} \right\} | (J_1 J_2 J_{12}) J_3 JM >. \tag{10.45}
\end{aligned}$$

The allowed values of J are restricted by the triangle conditions $\Delta(J_1 J_2 J_{12})$, $\Delta(J_3 J J_{12})$, $\Delta(J_3 J_2 J_{23})$ and $\Delta(J_1 J J_{23})$, as represented by the circles in

$$\left\{ \begin{array}{ccc} o & o & o \end{array} \right\}, \left\{ \begin{array}{ccc} o & o & o \end{array} \right\}, \left\{ \begin{array}{ccc} o & o & o \end{array} \right\} \text{ and } \left\{ \begin{array}{ccc} o & o & o \end{array} \right\}.$$

A relationship that is used for deriving the Pandya transformation is

$$\begin{aligned} & \sum_M \langle j_b m_b j_a - m_a | JM \rangle \langle j_d m_d j_c - m_c | JM \rangle (-1)^{j_a - m_a + j_c - m_c} \\ &= (2J+1) \sum_{J'M'} \left\{ \begin{array}{ccc} j_b & j_c & J' \\ j_d & j_a & J \end{array} \right\} \langle j_b m_b j_c m_c | J'M' \rangle \langle j_d m_d j_a m_a | J'M' \rangle. \end{aligned} \quad (10.46)$$

The symmetry properties of the $6j$ coefficient can be summarized by

$$\left\{ \begin{array}{ccc} J_1 & J_2 & J_3 \\ J'_1 & J'_2 & J'_3 \end{array} \right\} = \left\{ \begin{array}{ccc} J_a & J_b & J_c \\ J'_a & J'_b & J'_c \end{array} \right\}, \quad (10.47)$$

when the columns (a, b, c) are any permutation of the columns $(1, 2, 3)$. In addition,

$$\left\{ \begin{array}{ccc} J_1 & J_2 & J_3 \\ J'_1 & J'_2 & J'_3 \end{array} \right\} = \left\{ \begin{array}{ccc} J'_1 & J'_2 & J'_3 \\ J_1 & J_2 & J'_3 \end{array} \right\}. \quad (10.48)$$

An orthogonality condition for the $6j$ coefficients is

$$\sum_{J_3} (2J_3 + 1) (2J_6 + 1) \left\{ \begin{array}{ccc} J_1 & J_2 & J_3 \\ J_4 & J_5 & J_6 \end{array} \right\} \left\{ \begin{array}{ccc} J_1 & J_2 & J_3 \\ J_4 & J_5 & J'_6 \end{array} \right\} = \delta_{J_6 J'_6}. \quad (10.49)$$

A sum-rule for the $6j$ coefficients is

$$\sum_J (-1)^{j_1+j_2+J} (2J+1) \left\{ \begin{array}{ccc} j_1 & j_2 & J \\ j_2 & j_1 & k \end{array} \right\} = \sqrt{(2j_1+1)(2j_2+1)} \delta_{k,0}. \quad (10.50)$$

Another useful relation for the $6j$ coefficients is

$$\begin{aligned} & \sum_k (-1)^{k+k_1+k_2} (2k+1) \left\{ \begin{array}{ccc} k_1 & J'_1 & k \\ J'_2 & J_2 & J \end{array} \right\} \\ & \times \left\{ \begin{array}{ccc} k_1 & k_2 & k \\ J'_1 & J_1 & J''_2 \end{array} \right\} \left\{ \begin{array}{ccc} k_1 & k_2 & k \\ J'_2 & J_2 & J''_1 \end{array} \right\} \\ & = (-1)^{J_1+J_2+J'_1+J'_2+J''_1+J''_2+J} \left\{ \begin{array}{ccc} J_1 & J_2 & J \\ J''_1 & J''_2 & k_1 \end{array} \right\} \left\{ \begin{array}{ccc} J'_1 & J'_2 & J \\ J''_1 & J''_2 & k_2 \end{array} \right\}. \end{aligned} \quad (10.50)$$

When one of the arguments is zero, the $6j$ reduces to

$$\left\{ \begin{array}{ccc} J_1 & J_2 & J_3 \\ J_4 & J_5 & 0 \end{array} \right\} = \frac{(-1)^{J_1+J_2+J_3} \delta_{J_5 J_1} \delta_{J_4 J_2}}{\sqrt{(2J_1+1)(2J_2+1)}}. \quad (10.51)$$

A special cases is

$$\begin{aligned} & \left\{ \begin{array}{ccc} J_1 & J_1 & 1 \\ J_2 & J_2 & J_3 \end{array} \right\} \\ & = (-1)^{J_1+J_2+J_3+1} \frac{J_1(J_1+1) + J_2(J_2+1) - J_3(J_3+1)}{2\sqrt{J_1(J_1+1)(2J_1+1)J_2(J_2+1)(2J_2+1)}}. \end{aligned} \quad (10.52)$$

Historically, the related Racah W -coefficient was used [10] that is related to the $6j$ symbol by

$$\left\{ \begin{array}{ccc} J_1 & J_2 & J_3 \\ J_4 & J_5 & J_6 \end{array} \right\} = (-1)^{J_1+J_2+J_4+J_5} W(J_1, J_2, J_4, J_5; J_3, J_6)$$

An explicit expression for the Racah coefficient is given in [10].

10.3.3 Coupling of Four Angular Momenta

The $9j$ coefficient is defined by the overlap between two ways of coupling four angular momenta

$$\begin{aligned}
 & <(J_1 J_3 J_{13})(J_2 J_4 J_{24})J \mid (J_1 J_2 J_{12})(J_3 J_4 J_{34})J> \\
 & \equiv \sqrt{(2J_{13}+1)(2J_{24}+1)(2J_{12}+1)(2J_{34}+1)} \left\{ \begin{array}{ccc} J_1 & J_2 & J_{12} \\ J_3 & J_4 & J_{34} \\ J_{13} & J_{24} & J \end{array} \right\} \\
 & \equiv \left[\begin{array}{ccc} J_1 & J_2 & J_{12} \\ J_3 & J_4 & J_{34} \\ J_{13} & J_{24} & J \end{array} \right]. \tag{10.53}
 \end{aligned}$$

The $\{ \}$ symbol with nine arguments is the $9j$ coefficient, and the $[]$ symbol with nine arguments will be referred to as the normalized $9j$ coefficient. The allowed values of J are restricted by the triangle condition associated with any row or column. The value of the $9j$ coefficient is unchanged for any even permutation of the rows or columns and changes only

by a phase factor $(-1)^{J_1+J_2+J_{12}+J_3+J_4+J_{34}+J_{13}+J_{24}+J}$ for any odd permutation of the rows or columns. An orthogonality condition for the normalized $9j$ coefficients is

$$\sum_{J_{13}J_{24}} \begin{bmatrix} J_1 & J_2 & J_{12} \\ J_3 & J_4 & J_{34} \\ J_{13} & J_{24} & J \end{bmatrix} \begin{bmatrix} J_1 & J_2 & J'_{12} \\ J_3 & J_4 & J'_{34} \\ J_{13} & j_{24} & J \end{bmatrix} = \delta_{J_{12}J'_{12}} \delta_{J_{34}J'_{34}}. \quad (10.54)$$

The $9j$ symbol can be expressed as sum over three $6j$ symbols

$$\begin{aligned} & \left\{ \begin{array}{ccc} J_1 & J_2 & J_{12} \\ J_3 & J_4 & J_{34} \\ J_{13} & J_{24} & J \end{array} \right\} = \\ & = \sum_{J'} (-1)^{2J'} (2J' + 1) \left\{ \begin{array}{ccc} J_1 & J_3 & J_{13} \\ J_{24} & J & J' \end{array} \right\} \left\{ \begin{array}{ccc} J_2 & J_4 & J_{24} \\ J_3 & J' & J_{34} \end{array} \right\} \\ & \times \left\{ \begin{array}{ccc} J_{12} & J_{34} & J \\ J' & J_1 & J_2 \end{array} \right\}. \end{aligned} \quad (10.55)$$

When one of the arguments is zero, the $9j$ coefficient reduces to

$$\left\{ \begin{array}{ccc} J_1 & J_2 & J_{12} \\ J_3 & J_4 & J_{34} \\ J_{13} & J_{24} & 0 \end{array} \right\} = \frac{(-1)^{J_2+J_3+J_{12}+J_{13}} \delta_{J_{12}J_{34}} \delta_{J_{13}J_{24}}}{\sqrt{(2J_{12}+1)(2J_{13}+1)}} \left\{ \begin{array}{ccc} J_1 & J_3 & J_{13} \\ J_4 & J_2 & J_{12} \end{array} \right\}. \quad (10.56)$$

10.4 Tensors and reduced matrix elements

The expectation value of a one-body operator with single-particle wavefunctions

$$\langle \psi(\ell_1, m_1) | Y_{m_2}^{\ell_2}(\Omega) | \psi(\ell_3, m_3) \rangle \quad (10.57)$$

involves the angular integral

$$\begin{aligned} & \int [Y_{m_1}^{\ell_1}(\Omega)]^* Y_{m_2}^{\ell_2}(\Omega) Y_{m_3}^{\ell_3}(\Omega) d\Omega \\ &= \sqrt{\frac{(2\ell_1 + 1)(2\ell_2 + 1)(2\ell_3 + 1)}{4\pi}} \begin{pmatrix} \ell_1 & \ell_2 & \ell_3 \\ 0 & 0 & 0 \end{pmatrix} \\ & \quad \times (-1)^{-m_1} \begin{pmatrix} \ell_1 & \ell_2 & \ell_3 \\ -m_1 & m_2 & m_3 \end{pmatrix}, \end{aligned} \quad (10.58)$$

where we have used $[Y_{m_1}^{\ell_1}(\Omega)]^* = (-1)^{-m_1} Y_{-m_1}^{\ell_1}(\Omega)$. Note that all of the dependence on m_i are in the last two terms. This motivates us to write this integral as a product of two terms

one of which does not depend on m_i . The convention we use gives

$$\begin{aligned} \int [Y_{m_1}^{\ell_1}(\Omega)]^* Y_{m_2}^{\ell_2}(\Omega) Y_{m_3}^{\ell_3}(\Omega) d\Omega = & \langle \ell_1 || Y^{\ell_2} || \ell_3 \rangle \\ & \times (-1)^{\ell_1-m_1} \begin{pmatrix} \ell_1 & \ell_2 & \ell_3 \\ -m_1 & m_2 & m_3 \end{pmatrix}, \end{aligned} \quad (10.59)$$

where the first term on the right-hand side is

$$\langle l_1 || Y^{\ell_2} || l_3 \rangle = (-1)^{\ell_1} \sqrt{\frac{(2\ell_1+1)(2\ell_2+1)(2\ell_3+1)}{4\pi}} \begin{pmatrix} \ell_1 & \ell_2 & \ell_3 \\ 0 & 0 & 0 \end{pmatrix}. \quad (10.60)$$

This is called a “reduced” matrix element because it does not contain any dependence on m_i .

A tensor T_μ^λ of rank λ is a set of $2\lambda + 1$ operators, $\mu = -\lambda, -\lambda + 1, \dots, \lambda$, that obey the commutation of Eqs. (10.21) and (10.22), but for the generalized angular momentum operators J_\pm and J_z

$$[J_z, T_\mu^\lambda] = \mu T_\mu^\lambda, \quad (10.61)$$

and

$$[J_{\pm}, T_{\mu}^{\lambda}] = [J_x \pm i J_y, T_{\mu}^{\lambda}] = \sqrt{\lambda(\lambda+1) - \mu(\mu \pm 1)} T_{\mu \pm 1}^{\lambda}. \quad (10.62)$$

The spherical harmonics, Y_{μ}^{λ} , are the most obvious example of a tensor of rank λ . Based on the components of Y_{μ}^1 in cartesian coordinates, the components of a vector \vec{r} can be arranged into a tensor of rank $\lambda = 1$ as: $r_0^1 = z$, and $r_{\pm}^1 = \mp(x \pm iy)/\sqrt{2}$. The use of tensor operators reduces the M -state dependence of matrix elements to a simple dependence on the Clebsch-Gordan or $3j$ coefficient via the Wigner-Eckhart theorem

$$\begin{aligned} < JM | T_{\mu}^{\lambda} | J'M' > &= (-1)^{J-M} \begin{pmatrix} J & \lambda & J' \\ -M & \mu & M' \end{pmatrix} < J || T^{\lambda} || J' > \\ &= (-1)^{2\lambda} \frac{< J'M'\lambda\mu | JM >}{\sqrt{(2J+1)}} < J || T^{\lambda} || J' >, \end{aligned} \quad (10.63)$$

where $< J || T^{\lambda} || J' >$ is the reduced matrix element. The reduced matrix element convention followed in this book is common [5] [11] [7] [8] [12] [13] but not universal. The Wigner-Eckhart theory is a generalization of the result obtained in Eq. (10.59) for the spherical

harmonics. A more general derivation and discussion of the Wigner-Eckhart theorem can be found in quantum physics textbooks such as [1].

If T_μ^λ is a tensor of rank λ , then its Hermitian conjugate, $(T_\mu^\lambda)^+$, is not a tensor of rank λ . However, the quantity

$$\tilde{T}_\mu^\lambda \equiv (-1)^{p+\mu} (T_{-\mu}^\lambda)^+ \quad (10.64)$$

is a tensor of rank λ . This can be proven by taking the Hermitian conjugate of both sides of Eqs. (10.62) and (10.61) and then making the substitution

$$(T_\mu^\lambda)^+ = (-1)^{\mu-p} \tilde{T}_{-\mu}^\lambda. \quad (10.65)$$

The arbitrary phase factor p is chosen for convenience. In order to ensure that the phase factors are real, one can choose $p = 0$ for integer values of λ , and $p = \lambda$ for half-integer values of λ . The phase factor is real and, $(-1)^{\mu-p} = (-1)^{p-\mu}$.

The relationship between $\langle J | T_\mu^\lambda | J' \rangle$ and $\langle J' | \tilde{T}_\mu^\lambda | J \rangle$ can be obtained by considering

$$\langle JM | T_\mu^\lambda | J'M' \rangle = \langle J'M' | (T_\mu^\lambda)^+ | JM \rangle^+$$

$$\begin{aligned}
&= \langle J' M' | (T_\mu^\lambda)^+ | JM \rangle^* = (-1)^{p-\mu} \langle J' M' | \tilde{T}_{-\mu}^\lambda | JM \rangle^* \\
&= (-1)^{p-\mu+J'-M'} \begin{pmatrix} J' & \lambda & J \\ -M' & -\mu & M \end{pmatrix} \langle J' || \tilde{T}^\lambda || J \rangle^* \\
&= (-1)^{p+J'-M} \begin{pmatrix} J & \lambda & J' \\ -M & \mu & M' \end{pmatrix} \langle J' || \tilde{T}^\lambda || J \rangle^*, \tag{10.66}
\end{aligned}$$

where Eq. (10.36) has been used in the last line together with $M = M' + \mu$. Thus by comparison with Eq. (10.63)

$$\langle J || T^\lambda || J' \rangle = (-1)^{p+J'-J} \langle J' || \tilde{T}^\lambda || J \rangle^*. \tag{10.67}$$

Taking the * of both sides and interchanging J and J'

$$\langle J || \tilde{T}^\lambda || J' \rangle = (-1)^{J-J'+p} \langle J' || T^\lambda || J \rangle^*, \tag{10.68}$$

where * indicates complex conjugation. For spherical harmonics we use $p = 0$ and they have the property that $(Y_\mu^\lambda)^+ = (-1)^\mu Y_{-\mu}^\lambda$ and $\tilde{Y}_\mu^\lambda = Y_\mu^\lambda$, and hence

$$\langle J || Y^\lambda || J' \rangle = (-1)^{J-J'} \langle J' || Y^\lambda || J \rangle^*. \tag{10.69}$$

If wave functions are chosen to be real (as will be the case in this book), this expression simplifies further to

$$\langle J || Y^\lambda || J' \rangle = (-1)^{J-J'} \langle J' || Y^\lambda || J \rangle. \quad (10.70)$$

10.4.1 Special reduced matrix elements

Reduced matrix element by evaluating the left-hand side of Eq. (10.63) for a particular choice of M , μ and M' for which the $3j$ coefficient does not vanish. Reduced matrix elements for many types of operators can be found in the literature [7] [5] [6]. Some commonly used reduced matrix elements are

$$\langle J || 1 || J' \rangle = \delta_{JJ'} \sqrt{2J+1}, \quad (10.71)$$

$$\langle J || J^{\lambda=1} || J' \rangle = \delta_{JJ'} \sqrt{J(J+1)(2J+1)}, \quad (10.72)$$

and

$$\langle \ell || Y^\lambda || \ell' \rangle = (-1)^\ell \sqrt{\frac{(2\ell+1)(2\lambda+1)(2\ell'+1)}{4\pi}} \begin{pmatrix} \ell & \lambda & \ell' \\ 0 & 0 & 0 \end{pmatrix} \quad (10.73)$$

It is clear from Eqs. (10.39) and (10.63) (and from rotational invariance) that the matrix element of a scalar is independent of M and can be written as

$$\begin{aligned} \langle JM | T^{\lambda=0} | J'M' \rangle &= \delta_{JJ'} \delta_{MM'} \langle J | T^{\lambda=0} | J \rangle \\ &= \delta_{JJ'} \delta_{MM'} \frac{\langle J | T^{\lambda=0} | J \rangle}{\sqrt{2J+1}}. \end{aligned} \quad (10.74)$$

10.4.2 Products of tensor operators

The components of two tensors T^{λ_1} and U^{λ_2} can be combined to form a third tensor S^λ by

$$S_\mu^\lambda = [T^{\lambda_1} \otimes U^{\lambda_2}]_\mu^\lambda = \sum_{\mu_1 \mu_2} \langle \lambda_1 \mu_1 \lambda_2 \mu_2 | \lambda \mu \rangle T_{\mu_1}^{\lambda_1} U_{\mu_2}^{\lambda_2} \quad (10.75)$$

It is straightforward to show that the components of S^λ satisfy Eqs. (10.62) and (10.61). Useful results for the reduced matrix elements involving products of tensor operators will be discussed in this section. The dot product (e.g. $\vec{\ell} \cdot \vec{s}$) is related to this tensor cross product by

$$T^{\lambda_1} \cdot U^{\lambda_1} = (-1)^{\lambda_1} \sqrt{(2\lambda_1 + 1)} [T^{\lambda_1} \otimes U^{\lambda_1}]^0. \quad (10.76)$$

When T and U operate in the same space (e.g. $[Y^{\lambda_1}(\hat{r}) \otimes Y^{\lambda_2}(\hat{r})]^\lambda$), the reduced matrix element can be evaluated by summing over a complete set of intermediate states J_c

$$\begin{aligned} & \langle J_a | |[T^{\lambda_1} \otimes U^{\lambda_2}]^\lambda| | J_b \rangle = (-1)^{J_a + \lambda + J_b} \sqrt{(2\lambda + 1)} \\ & \times \sum_{J_c} \left\{ \begin{array}{ccc} J_b & J_a & \lambda \\ \lambda_1 & \lambda_2 & J_c \end{array} \right\} \langle J_a | |T^{\lambda_1}| | J_c \rangle \langle J_c | |U^{\lambda_2}| | J_b \rangle. \end{aligned} \quad (10.77)$$

When T and U operate in different spaces (e.g. $\vec{\ell} \cdot \vec{s}$), one obtains

$$\langle J_a J_b J | |[T^{\lambda_1} \otimes U^{\lambda_2}]^\lambda| | J_c J_d J' \rangle = \sqrt{(2J+1)(2\lambda+1)(2J'+1)}$$

$$\times \left\{ \begin{array}{ccc} J_a & J_b & J \\ J_c & J_d & J' \\ \lambda_1 & \lambda_2 & \lambda \end{array} \right\} \langle J_a | |T^{\lambda_1}| |J_c \rangle \langle J_b | |U^{\lambda_2}| |J_d \rangle, \quad (10.78)$$

where T^{λ_1} operates in the space of $| J_a \rangle$ and $| J_c \rangle$, and U^{λ_2} operates in the space of $| J_b \rangle$ and $| J_d \rangle$.

Special cases of Eq. (10.78) can be obtained from the reduction of the $9j$ coefficient given in Eq. (10.56). For $\lambda = 0$ Eq. (10.78) reduces to

$$\begin{aligned} \langle J_a J_b J | |[T^{\lambda_1} \otimes U^{\lambda_1}]^0| |J_c J_d J' \rangle &= \delta_{JJ'} (-1)^{J_b + J_c + J + \lambda_1} \sqrt{\frac{2J+1}{2\lambda_1+1}} \\ &\times \left\{ \begin{array}{ccc} J_a & J_b & J \\ J_d & J_c & \lambda_1 \end{array} \right\} \langle J_a | |T^{\lambda_1}| |J_c \rangle \langle J_b | |U^{\lambda_1}| |J_d \rangle. \end{aligned} \quad (10.79)$$

For $\lambda_1 = 0$ and $T^{\lambda_1} = 1$, Eq. (10.78) reduces to

$$\langle J_a J_b J | |U^{\lambda_2}| |J_c J_d J' \rangle = (-1)^{J_c + J_d + J + \lambda_2} \sqrt{(2J+1)(2J'+1)}$$

$$\times \delta_{J_a J_c} \left\{ \begin{array}{ccc} J_b & J_d & \lambda_2 \\ J' & J & J_a \end{array} \right\} < J_b || U^{\lambda_2} || J_d >, \quad (10.80)$$

and for $\lambda_2 = 0$ and $U^{\lambda_2} = 1$, Eq. (10.78) reduces to

$$\begin{aligned} < J_a J_b J || T^{\lambda_1} || J_c J_d J' > &= (-1)^{J_a + J_b + J' + \lambda_1} \sqrt{(2J+1)(2J'+1)} \\ &\times \delta_{J_b J_d} \left\{ \begin{array}{ccc} J_a & J_c & \lambda_1 \\ J' & J & J_b \end{array} \right\} < J_a || T^{\lambda_1} || J_c >. \end{aligned} \quad (10.81)$$

Eq. (10.81) can be used, for example, to obtain the single-particle j -coupled matrix element of Y^λ

$$\begin{aligned} < \ell s j || Y^\lambda || \ell' s j' > &= (-1)^{\ell+1/2+j'+\lambda} \sqrt{(2j+1)(2j'+1)} \\ &\times \left\{ \begin{array}{ccc} \ell & \ell' & \lambda \\ j' & j & 1/2 \end{array} \right\} < \ell || Y^\lambda || \ell' >, \end{aligned} \quad (10.82)$$

that can be combined with Eq. (10.73) and simplified [5] to obtain

$$< \ell s j || Y^\lambda || \ell' s j' > = \frac{1}{2} [1 + (-1)^{\ell+\lambda+\ell'}] (-1)^{j+1/2}$$

$$\times \sqrt{\frac{(2j+1)(2\lambda+1)(2j'+1)}{4\pi}} \begin{pmatrix} j & \lambda & j' \\ 1/2 & 0 & -1/2 \end{pmatrix}. \quad (10.83)$$

Other conventions for reduced matrix elements analogous to Eq. (10.63) often used. Lawson [14] uses

$$\langle JM | T_\mu^\lambda | J'M' \rangle = \langle J'M'\lambda\mu | JM \rangle \langle J | |T^\lambda| |J' \rangle_L. \quad (10.84)$$

Brink and Satchler [9], Towner [15] and Thompson [2] use

$$\langle JM | T_\mu^\lambda | J'M' \rangle = (-1)^{2\lambda} \langle J'M'\lambda\mu | JM \rangle \langle J | |T^\lambda| |J' \rangle_B. \quad (10.85)$$

An advantage of using Eq. (10.63) instead of one of the above alternatives is that Eq. (10.70) only involves a phase factor, and a disadvantage is the extra $\sqrt{2J+1}$ factor that appears in Eqs. (10.71) and (10.74). When expressions involving reduced matrix elements are taken from the literature, it is obviously important to be consistent and to know which convention is being used.

10.5 Single-particle wavefunctions in a spherical basis

The Schrödinger equation for a particle of mass m in a spin-independent central potential, U_o , is

$$H_o |\alpha\rangle = (T + U_o) |\alpha\rangle = \epsilon_\alpha |\alpha\rangle, \quad (10.86)$$

where T is the kinetic energy operator given in coordinate space by

$$T = -\frac{\hbar^2}{2m} \nabla^2 = -\frac{\hbar^2}{2m} \left\{ \frac{1}{r} \frac{d^2}{dr^2} r - \frac{L^2}{r^2} \right\}, \quad (10.87)$$

L is the angular momentum operator (unit units of \hbar), the ket $|\alpha\rangle$ is the single-particle wave function, and ϵ_α is the eigenvalue. The coordinate space solution of this equation has the form

$$\phi_\alpha(\vec{r}) = \frac{R_\alpha(r)}{r} Y_{m_\ell}^\ell(\hat{r}), \quad (10.88)$$

where $Y_{m_\ell}^\ell$ are the spherical harmonics. The subscript α stands for the set of quantum numbers (n, ℓ, m_ℓ) , with n being the radial quantum number. We will use the quantum

numbers $n = 0, 1, 2, \dots$ that indicate the number of times the radial wave functions crosses the r axis. (Some references use a convention that starts at one, $n = 1, 2, 3, \dots$, and one must be careful to know which convention is being used.) The spherical harmonics are eigenfunctions of the ℓ^2 and ℓ_z operators

$$L^2 Y_{m_\ell}^\ell(\hat{r}) = \ell(\ell + 1) Y_{m_\ell}^\ell(\hat{r}), \quad (10.89)$$

and

$$L_z Y_{m_\ell}^\ell(\hat{r}) = m_\ell Y_{m_\ell}^\ell(\hat{r}), \quad (10.90)$$

and are orthonormal functions

$$\int [Y_{m_\ell}^\ell(\hat{r})]^* Y_{m'_\ell}^{\ell'}(\hat{r}) d\Omega = \delta_{\ell\ell'} \delta_{m_\ell m'_\ell}. \quad (10.91)$$

The angular momentum quantum ℓ are often represented by the letters given in Table 1. The radial wave function $R_\alpha(r)$ is a solution of the one-dimensional radial equation

$$-\frac{\hbar^2}{2m} R_\alpha''(r) + \frac{\hbar^2}{2m} \frac{\ell(\ell + 1)}{r^2} R_\alpha(r) + U_o(r) R_\alpha(r) = \epsilon_\alpha R_\alpha(r), \quad (10.92)$$

Table 10.1: Names of the first ten angular momentum quantum numbers

ℓ	0	1	2	3	4	5	6	7	8	9	...
name	s	p	d	f	g	h	i	j	k	ℓ	...

where $R''(r)$ indicates the second derivative of $R(r)$ with respect to r . The solution to Eq. (10.92) is independent of m_ℓ .

For a particle with an intrinsic spin, \vec{s} , the central potential may also contain a spin-orbit term of the form

$$U_{so}(r) = f_{so}(r) \vec{\ell} \cdot \vec{\sigma}, \quad (10.93)$$

where $\vec{\sigma} = 2\vec{s}$. The total angular momentum, $\vec{j} = \vec{\ell} + \vec{s}$, is conserved and the wave function takes the form

$$\phi_{k,m}(\vec{r}) = \frac{R_k(r)}{r} [Y^\ell \otimes \chi^s]_m^j, \quad (10.94)$$

where χ^s is the intrinsic-spin wave function, k stands for the set of quantum numbers

(n, ℓ, s, j) (since s is always $1/2$ it is usually not written explicitly), and the cross symbol \otimes denotes the Clebsch-Gordan product

$$[Y^\ell \otimes \chi^s]_m^j = \sum_{m_\ell, m_s} \langle \ell, m_\ell, s, m_s | j, m \rangle Y_{m_\ell}^\ell(\hat{r}) \chi_{m_s}^s. \quad (10.95)$$

This equation defines the ordering and phase convention associated with spin-orbit coupling used in this book. The intrinsic-spin wave functions are also assumed to be orthonormal

$$\langle \chi_{m_s}^s | \chi_{m'_s}^{s'} \rangle = \delta_{ss'} \delta_{m_s m'_s}. \quad (10.96)$$

The operation of $\vec{\ell} \cdot \vec{\sigma}$ on $\phi_{k,m}(\vec{r})$ gives

$$(\vec{\ell} \cdot \vec{\sigma}) \phi_{k,m}(\vec{r}) = [j(j+1) - \ell(\ell+1) - s(s+1)] \phi_{k,m}(\vec{r}) = a_{so} \phi_{k,m}(\vec{r}). \quad (10.97)$$

Taking $s = \frac{1}{2}$ and $j = \ell \pm \frac{1}{2}$,

$$a_{so} = -(\ell+1) \text{ for } j = \ell - \frac{1}{2} \text{ and } \ell > 0$$

and

$$a_{so} = \ell \text{ for } j = \ell + \frac{1}{2}.$$

Thus $R_k(r)$ satisfies the equation

$$-\frac{\hbar^2}{2m}R_k''(r) + \frac{\hbar^2}{2m}\frac{\ell(\ell+1)}{r^2}R_k(r) + [U_o(r) + a_{so}f_{so}(r)]R_k(r) = \epsilon_k R_k(r). \quad (10.98)$$

Eq. (10.98) has discrete solutions for bound states with $\epsilon < 0$ as well as continuum solutions for $\epsilon > 0$. The normalization convention for bound states is

$$\begin{aligned} \int |\phi_{k,m}(\vec{r})|^2 d\tau &= \sum_{\substack{m_\ell, m_s \\ m'_\ell, m'_s}} \langle \ell, m_\ell, s, m_s | j, m \rangle \langle \ell, m'_\ell, s, m'_s | j, m \rangle \\ &\times \int |R_k(r)|^2 dr \int [Y_{m_\ell}^\ell(\hat{r})]^* Y_{m'_\ell}^\ell(\hat{r}) d\Omega \langle \chi_{m_s}^s | \chi_{m'_s}^s \rangle. \end{aligned} \quad (10.99)$$

The spherical harmonics and intrinsic-spin wave functions are orthonormal and thus

$$\int |\phi_{k,m}(\vec{r})|^2 d\tau = \int |R_k(r)|^2 dr = 1. \quad (10.100)$$

Eq. (10.100) defines the normalization of the radial wave functions. In addition, the radial wave functions will be chosen to be real and positive at the origin. Observables are, of course, independent of this phase convention, however, it is important to keep the phase convention consistent throughout intermediate steps of a calculations that involve $R(r)$ or matrix elements of $R(r)$. The quantity $|R_k(r)/r|^2$ is the radial profile function – the density observed for a thin slice at $z = 0$ in the xy plane. The quantity $P(r) = |R_k(r)|^2$ is the radial probability distribution – the probability of finding the particle at a distance r from the origin. The $\ell = 0$ states are the only ones with a nonvanishing radial-profile at the origin.

There are a variety of numerical methods for solving the radial differential equation for the eigenvalues and the eigenfunctions. As a function of increasing n for a fixed ℓ -value, the excitation energy relative to the ground state (gs) $\epsilon_\alpha - \epsilon_{\text{gs}}$ and the root-mean-square radius of the radial probability distribution increases. Other properties will depend upon the details of the potential. For example, the Coulomb potential with $U_o(r) = 1/r$ has energies proportional to $-1/n_p^2$, where $n_p = n + \ell + 1$ is the “principal” quantum number. In the following chapters, results for the harmonic-oscillator and Woods-Saxon forms for the central potential, which are commonly used in nuclear physics, are presented.

Bibliography

- [1] “Quantum Physics, Volume 1”, by Vladimir Zelevinsky, WILEY-VCH, Verlag GmbH and Co. KGaA, Weinheim, ISBN:978-3-527-40979-2.
- [2] W. J. Thompson, *Angular Momentum*, (John Wiley and Sons, Inc., 1994)
- [3] K. L. G. Heyde, *The Nuclear Shell Model*, (Springer-Verlag, 1994)
- [4] B. A. Brown, et al., the computer code OXBASH.

- [5] A. R. Edmonds, *Angular Momentum in Quantum Mechanics*, (Princeton University Press, 1957).
- [6] D. A. Varshalovich, A. N. Moskalev and V. K. Khersonskii, *Quantum Theory of Angular Momentum*, (World Scientific, 1988).
- [7] A. de Shalit and I. Talmi, *Nuclear Shell Theory*, (Academic Press, 1963).
- [8] I. Talmi, *Simple Models of Complex Nuclei*, (Harwood Academic Publishers, 1993).
- [9] D. M. Brink and G. R. Satchler, *Angular Momentum*, (Clarendon Press, Oxford, 1968).
- [10] G. Racah, Phys. Rev. **62**, 438 (1953). link
- [11] A. Messiah, *Quantum Mechanics*, Vol. 1, (North Holland, Amsterdam, 1975).
- [12] A. Bohr and B. R. Mottelson, *Nuclear Structure*, Vol. I, (W. A. Benjamin, 1969), *Nuclear Structure* Vol. II, (W. A. Benjamin, 1975).

- [13] A. de Shalit and H. Feshbach, *Theoretical Nuclear Physics Vol. I: Nuclear Structure*, (John Wiley and Sons, 1974).
- [14] R. D. Lawson, *Theory of the Nuclear Shell Model*, (Clarendon Press, 1980).
- [15] I. S. Towner, *A Shell Model Description of Light Nuclei*, (Clarendon Press, 1977).

Chapter 11

The Isobaric-Mass-Mulitplet Equation

An isobaric mass multiplet for a state with isospin T are those $(2T + 1)$ states in different nuclei which have $T_z = -T$ up to $T_z = T$. The isobaric mass multiplet equation (IMME) is an expression for the masses of these levels in terms of an expansion in T_z . We can also write the IMME in terms of binding energies:

$$\text{BE}(T, T_z) = a + bT_z - cT_z^2. \quad (11.1)$$

where the signs are chosen so that a , b and c will be positive. The strong interaction does not depend on T_z , and only contributes to the first term in Eqs. (11.1). When the Coulomb interaction is treated in first order-perturbation theory one can show that its contribution to the binding energy does not have terms higher than T_z^2 . This comes from the fact that the Coulomb interaction can be written in terms of isospin tensors of rank 0, 1 and 2. One then uses the Wigner-Eckart theorem to show T_z^2 is the highest power of T_z which is allowed. The b coefficient of the IMME can be determined from the binding energy differences between mirror nuclei:

$$b = \frac{\text{BE}(T, T_z = T) - \text{BE}(T, T_z = -T)}{2T}. \quad (11.2)$$

For $T = 1$ we also have

$$c = \frac{2 \text{BE}(T, T_z = 0) - \text{BE}(T, T_z = 1) - \text{BE}(T, T_z = -1)}{2}. \quad (11.3)$$

The experimental masses (binding energies) have been used to obtain the coefficients a , b and c in Eq. (11.1) with results given in Ref. [1]. States with $T = 1/2$ are called isobaric doublets, and only the first two terms in Eq. (11.1) are needed to fit the two binding energies. States with $T = 1$ are called isobaric triplets, and all three terms are needed. States with $T = 3/2$ are called isobaric quartets. For quartets, the most general expansion in terms of T_z would require a term of the form dT_z^3 . For $T = 2$ and higher we also could have eT_z^4 term. One finds that the d and e terms are zero within experimental error, with the exceptions if $A=8, 9$ and 35 [1]. A possible reason for the d term in $A = 9$ was discussed in [2]. The possible need for d or e terms for $A = 20$ $T = 2$ states [3] was resolved in [4].

In the liquid drop model the form of the IMME comes from the Coulomb term. Using a uniformly charged sphere of radius c_s , and $Z = (A/2) - T_z$

$$\text{BE}_c(ld) = -\frac{3e^2 Z^2}{5c_s} = -\frac{3e^2}{5c_s} \left[\frac{A^2}{4} - AT_z + T_z^2 \right]. \quad (11.4)$$

Thus the liquid-drop model for the IMME terminates at T_z^2 and

$$b(ld) = \frac{3e^2 A}{5c_s} \quad \text{and} \quad c(ld) = \frac{3e^2}{5c_s}. \quad (11.5)$$

The b coefficients obtained from the experimental binding energy are shown in Fig. (11.1). They are compared with the prediction of the liquid drop model. The liquid drop model is always higher than experiment. The reason is that the observed displacement energy is related to a change in proton-neutron occupancy of the orbits near the Fermi surface (the valence orbits that are the most loosely bound) which have an rms radius which is larger than the average rms radius implicit in the liquid drop model (R in the denominator is effectively larger). One can observe in Fig. (11.1) some small downward glitches in the data at $A = 16$ and $A = 40$ corresponding to the magic numbers 8 and 20, respectively. This is due to the increase in rms radius of the orbit at the Fermi surface going from the p to sd ($A = 16$) and sd to pf ($A = 40$) valence shells.

The idea of isospin conservation can be illustrated by looking the experimental energies of states in the nuclei with $A = 16$ as shown in the bottom panel of Fig. (11.2). The results

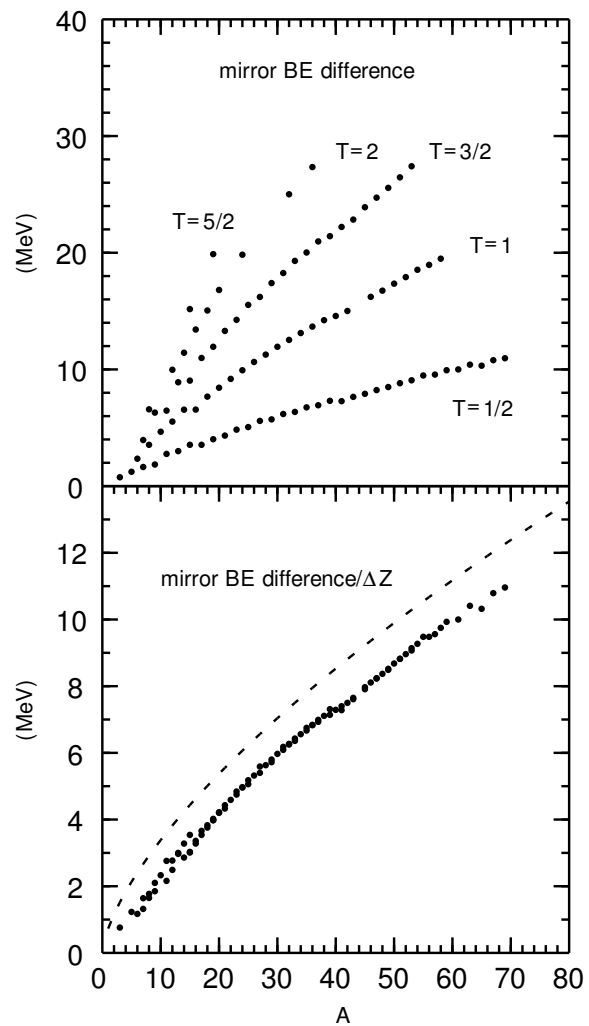


Figure 11.1: The top panel shows the binding energy differences between the ground states of mirror nuclei labedled by the isospin T . The bottom panel show the b-coefficients for the IMME obtained by dividing the results of the top panel by $2T = \Delta Z$. The dashed line is the result from the liquid drop model.

can be interpreted in terms of a strong interaction which has energies independent of T_z plus a Coulomb energy. With the approximation $E_c = aZ^2$ we find $a = 0.2097$ MeV from the experimental difference between the $T = 2$ ground states of ^{16}Ne and ^{16}C . Then we can subtract this Coulomb energy to obtain the strong interaction contribution to the energy shown in the top panel. There one observes that the states with $T = 1$ and $T = 2$ have the same energy within a few hundred keV independent of T_z . These are the lowest energy states for each of these T values. With the Coulomb correction, every known $T = 1$ state in ^{16}N and ^{16}F should have an isobaric analogue state in ^{16}O with the same energy, and every known $T = 2$ state in ^{16}C and ^{16}Ne should have isobaric analogue states in ^{16}N , ^{16}O and ^{16}F . The $T = 2$ state in ^{16}F has not yet been found experimentally.

In the liquid drop model without the Coulomb term for a given isospin T we have $2T + 1$ degenerate energies associated with the isobaric multiplets, as seen in the bottom panel of Fig. (11.2). When the Coulomb term is added the members of the multiplets are shifted up with increasing Z according to Eqs. (11.1) and (11.4). Even though there is a large energy shift, isospin is still mostly conserved since this diagonal energy shift is the same within about 100 keV for every level for a given T_z . Isospin violation comes from matrix

elements of the Hamiltonian that are off diagonal in T .

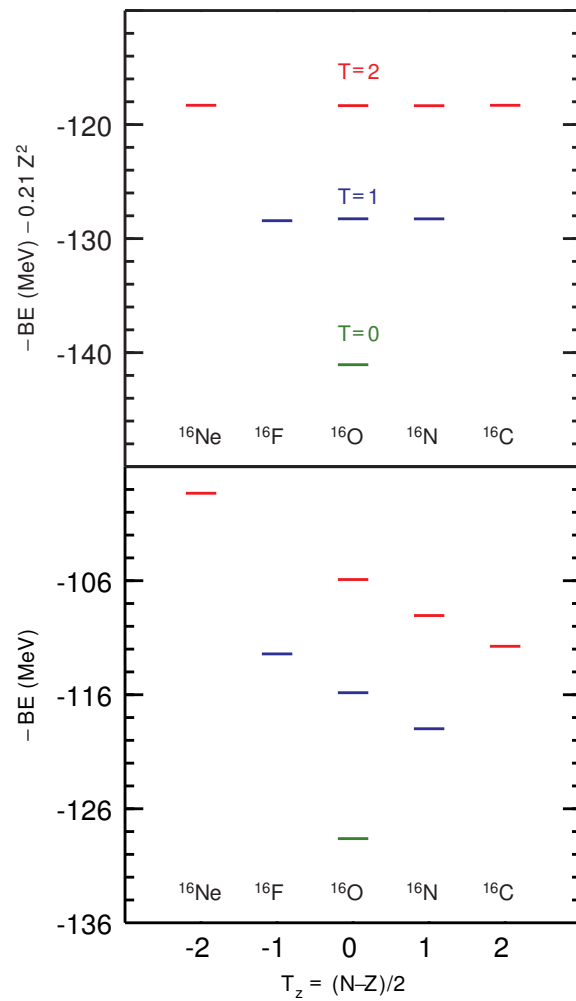
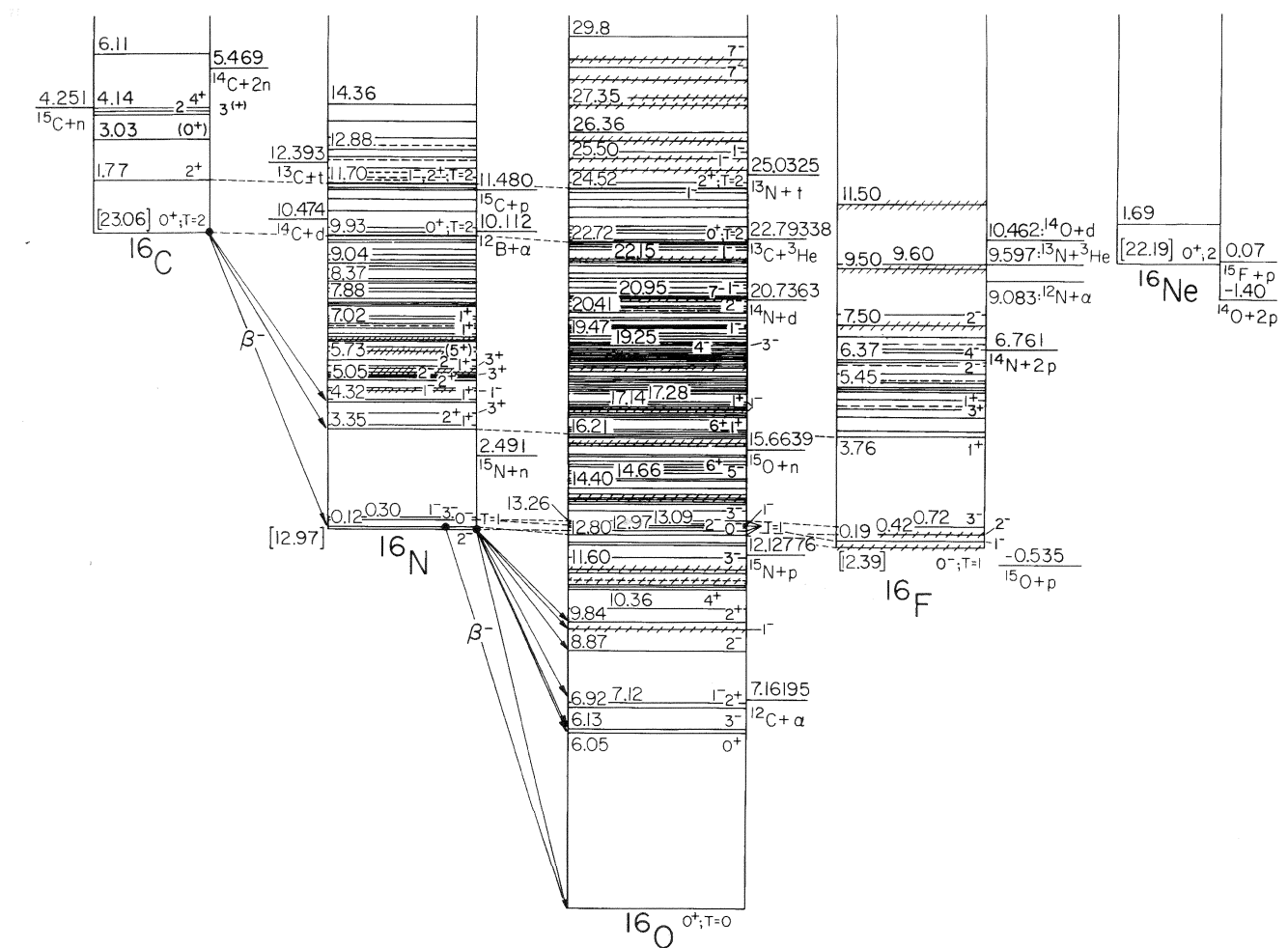
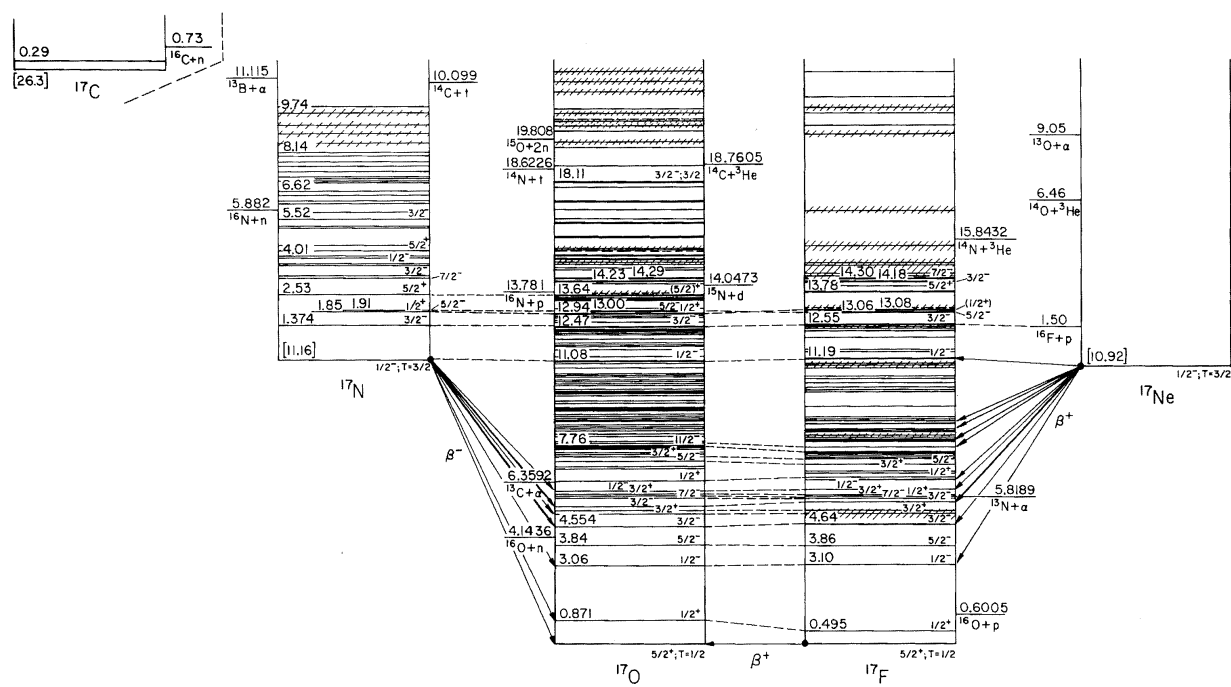
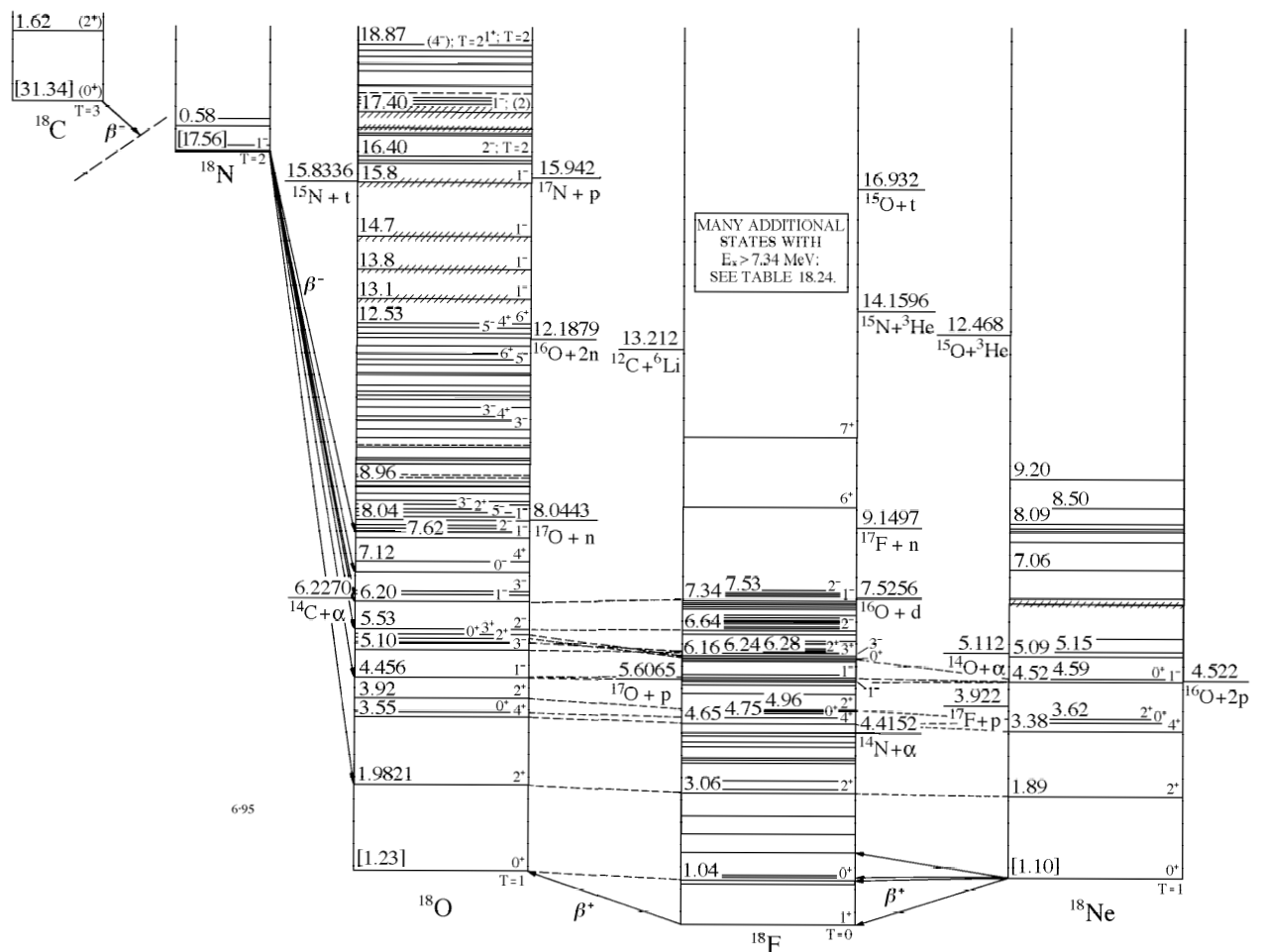


Figure 11.2: The bottom panel shows the experimental energies of nuclei with $A=16$ for the lowest states known for $T=0$ (green), $T=1$ (blue) and $T=2$ (red). The upper panel shows the same data corrected by an empirical Coulomb correction of the form $0.21 Z^2 \text{ MeV}$.

Figure 11.3: Isobaric levels for $A = 16$.

Figure 11.4: Isobaric levels for $A = 17$.

Figure 11.5: Isobaric levels for $A = 18$.

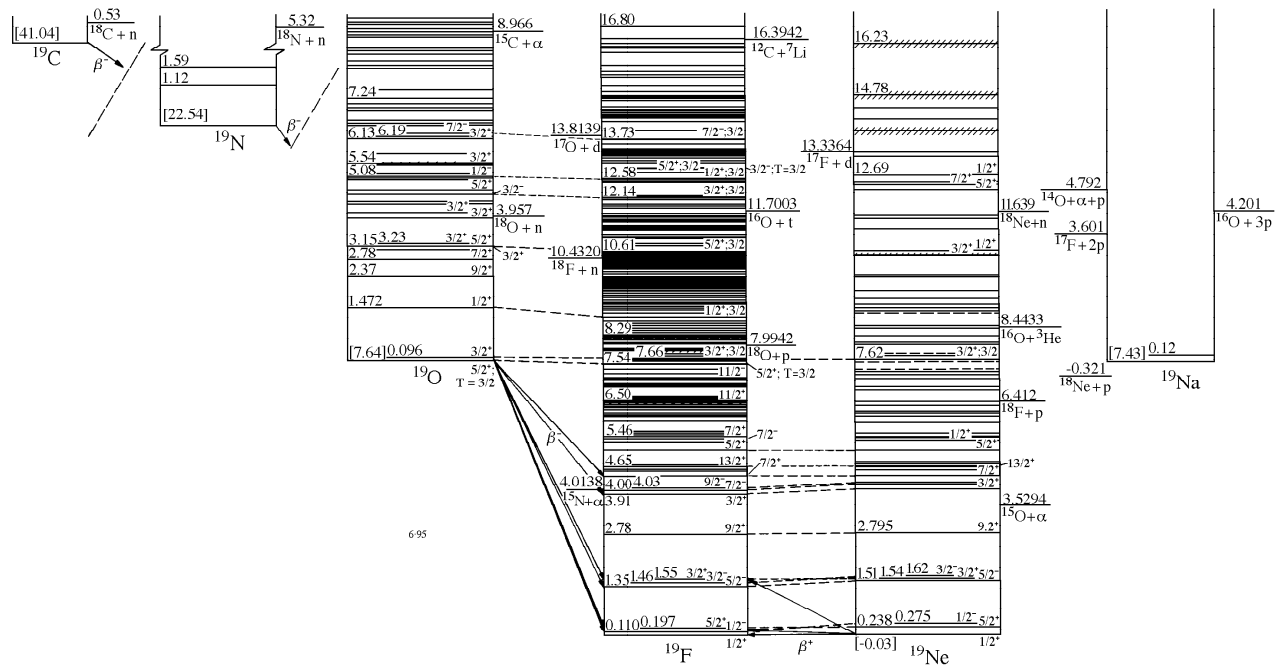
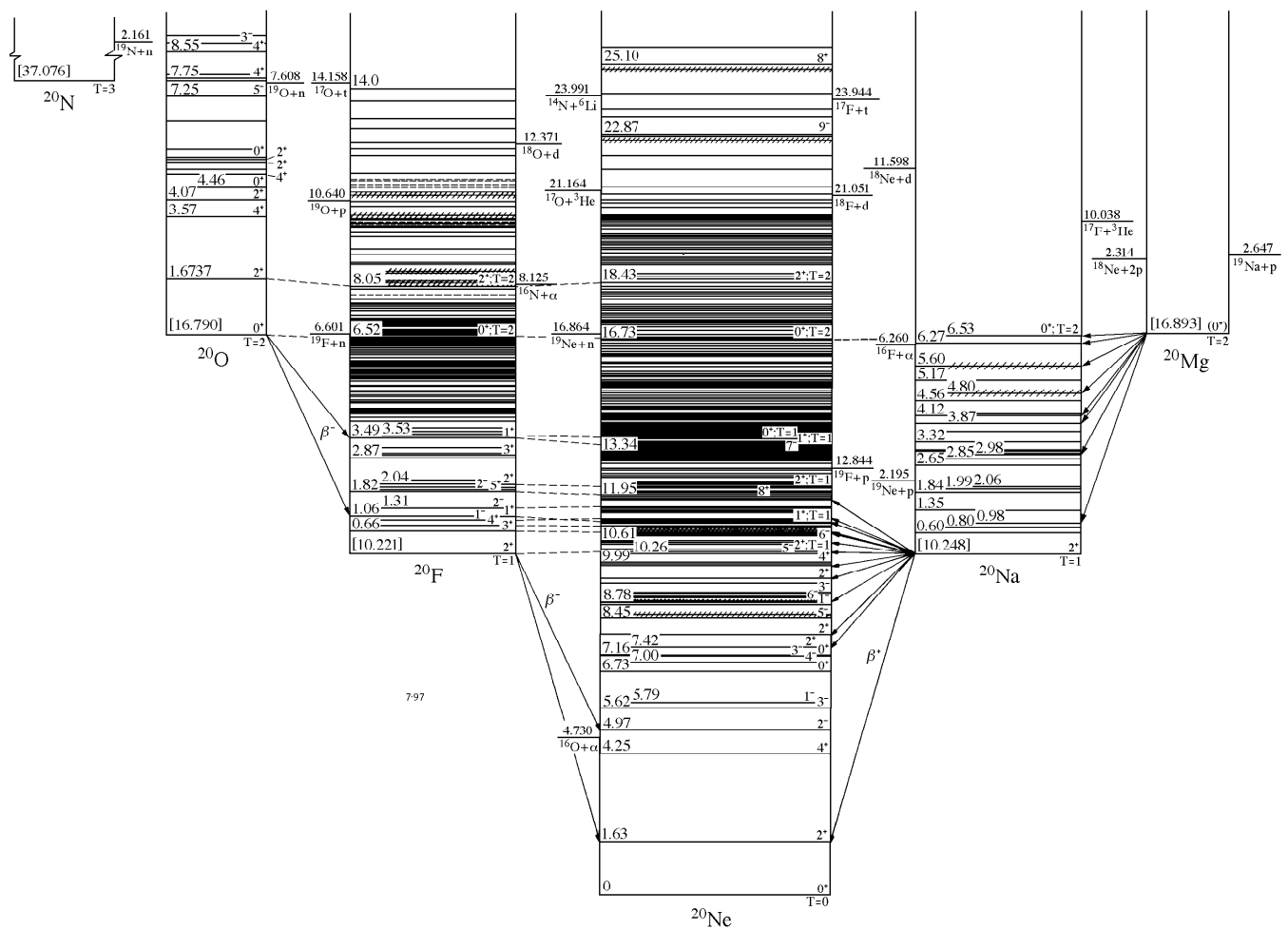


Figure 11.6: Isobaric levels for $A = 19$.

Figure 11.7: Isobaric levels for $A = 20$.

Bibliography

- [1] M. MacCormick and G. Audi, Nucl. Phys. A **925**, 61 (2014).
- [2] M. Brodeur, et al., Phys. Rev. Lett. **108**, 212501 (2012). link
- [3] A. T. Gallant, et al., Phys. Rev. Lett. **113**, 082501 (2014). link
- [4] B. E. Glassman, et al., Phys. Rev. C **92**, 042501(R) (2015). link

Chapter 12

The Fermi gas model

The fermi-gas model is used to obtain an approximate distribution for the kinetic energy of nucleons confined to a volume V with density $\rho = A/V$. It is evaluated for the conditions present in nuclear matter and will give an approximate result for the kinetic energy distribution in heavy nuclei. One assumes the lowest energy state allowed by the Pauli exclusion principle. We will start with symmetric nuclear matter ($N = Z$) with A nucleons confined to a box of length L on each side. The interaction between nucleons enters indirectly in determining the saturation density and the size of the box. The normalized wave function for a nucleon is given by:

$$\phi(\vec{r}) = \left(\frac{2}{L}\right)^{3/2} \sin(k_x x) \sin(k_y y) \sin(k_z z). \quad (12.1)$$

The condition that the wave functions vanish on the boundary L means that:

$$k_x = \frac{\pi n_x}{L} \quad (12.2)$$

with $n_x = 1, 2, 3, \dots$ with similar conditions for k_y and k_z . Each state is represented by a

set of quantum numbers $i = (n_x, n_y, n_z)$ with energy:

$$\epsilon_i = \frac{\hbar^2 k^2}{2m} = \frac{\hbar^2}{2m} \left(\frac{\pi}{L}\right)^2 (n_x^2 + n_y^2 + n_z^2), \quad (12.3)$$

and wave number

$$k_i = \frac{\pi}{L} \sqrt{(n_x^2 + n_y^2 + n_z^2)}. \quad (12.4)$$

From the Pauli principle each state can be occupied by at most one identical fermion. For nucleons we have protons and neutrons each of which can have spin up or down, so the state degeneracy is $g = 4$. To get the lowest energy state we would consider all states filled up to some radius:

$$n = \sqrt{(n_x^2 + n_y^2 + n_z^2)} = \frac{Lk}{\pi}. \quad (12.5)$$

The total number of states inside the radius n is equal to $1/8$ of the volume of the sphere:

$$N = \left(\frac{g}{8}\right) \left(\frac{4}{3}\pi n^3\right) = \frac{gL^3 k^3}{6\pi^2}, \quad (12.6)$$

and the number of states inside the ring dk is:

$$dN = \frac{gL^3 k^2 dk}{2\pi^2}. \quad (12.7)$$

The maximum value for the wave number is called k_f with the associated Fermi energy:

$$\epsilon_f = \frac{\hbar^2 k_f^2}{2m}. \quad (12.8)$$

The total number of states up to k_f is the number of nucleons A :

$$A = \int_0^{k_f} dN = \int_0^{k_f} \frac{gL^3 k^2 dk}{2\pi^2} = \frac{gL^3 k_f^3}{6\pi^2}. \quad (12.9)$$

The total kinetic energy up to k_f :

$$\langle T \rangle = \int_0^{k_f} \frac{\hbar^2 k^2}{2m} dN = \int_0^{k_f} \frac{\hbar^2 k^2}{2m} \frac{gL^3 k^2 dk}{2\pi^2} = \left(\frac{1}{5}\right) \left(\frac{\hbar^2}{2m}\right) \frac{gL^3 k_f^5}{2\pi^2}. \quad (12.10)$$

With Eq. (12.9) for A and Eq. (12.8) for ϵ_f we have for the total kinetic energy:

$$\langle T \rangle = \frac{3}{5} A \epsilon_f, \quad (12.11)$$

and for the average kinetic energy:

$$\frac{\langle T \rangle}{A} = \frac{3}{5} \epsilon_f. \quad (12.12)$$

These results can be evaluated in terms of the density for symmetric nuclear matter with Eq. (12.6):

$$\rho = \frac{A}{L^3} = \frac{g}{6\pi^2} k_f^3, \quad (12.13)$$

with $\rho = \rho_o = 0.16$ nucleons/fm³ to obtain:

$$k_f = \left(\frac{6\pi^2 \rho_o}{g} \right)^{1/3} = 1.33 \text{ fm}^{-1}, \quad (12.14)$$

$$\epsilon_f = \frac{\hbar^2 k_f^2}{2m} = 36.7 \text{ MeV}, \quad (12.15)$$

and for the average kinetic energy:

$$\frac{\langle T \rangle}{A} = \frac{3}{5} \epsilon_f = 22.0 \text{ MeV}. \quad (12.16)$$

For unequal numbers of protons and neutrons we take two overlapping Fermi gases in the same size box with densities for protons and neutrons given by

$$\rho_p = \frac{Z}{A} \rho, \quad (12.17)$$

and

$$\rho_n = \frac{N}{A} \rho, \quad (12.18)$$

With the spin degeneracy for one kind of nucleon of $g' = 2$ we obtain for protons

$$k_{fp} = \left(\frac{6\pi^2}{g'} \rho_p \right)^{1/3} = \left(\frac{6\pi^2 Z}{g' A} \rho \right)^{1/3} = \left(\frac{g Z}{g' A} \right)^{1/3} k_f = \left(\frac{2Z}{A} \right)^{1/3} k_f, \quad (12.19)$$

$$\epsilon_{fp} = \frac{\hbar^2 k_{fp}^2}{2m} = \left(\frac{2Z}{A}\right)^{2/3} \epsilon_f, \quad (12.20)$$

and for the average kinetic energy:

$$\frac{\langle T \rangle_p}{Z} = \frac{3}{5} \epsilon_{fp}. \quad (12.21)$$

Likewise for the neutrons:

$$k_{fn} = \left(\frac{2N}{A}\right)^{1/3} k_f, \quad (12.22)$$

$$\epsilon_{fn} = \left(\frac{2N}{A}\right)^{2/3} \epsilon_f, \quad (12.23)$$

and for the average energy:

$$\frac{\langle T \rangle_n}{N} = \frac{3}{5} \epsilon_{fn}. \quad (12.24)$$

The total kinetic energy is thus given by

$$\langle T \rangle = \langle T \rangle_p + \langle T \rangle_n = \frac{3}{5} \left[Z \left(\frac{2Z}{A}\right)^{2/3} + N \left(\frac{2N}{A}\right)^{2/3} \right] \epsilon_f. \quad (12.25)$$

The numerical values for ^{208}Pb with $Z = 82$ and $N = 126$ are $\epsilon_{fp} = 31.6$ MeV, $\epsilon_{fn} = 42.0$ MeV, $\langle T \rangle = 4700$ MeV and $\frac{\langle T \rangle}{A} = 22.8$ MeV. The average kinetic energy is larger than the value of 22.0 MeV obtained for $N = Z$ (Eq. (12.16)).

One can expand Eq. (12.25) to first order in $\frac{(N-Z)}{A}^2$ to obtain:

$$\langle T \rangle = \frac{3}{5} A \epsilon_f + \frac{2}{5} \epsilon_f \frac{(N-Z)^2}{A} = 22 A + 15 \frac{(N-Z)^2}{A} \text{ MeV.} \quad (12.26)$$

Comparing this with the volume total energy obtained empirically with the liquid drop model ($E = -BE$):

$$E = \langle T \rangle + \langle V \rangle = -16 A + 23 \frac{(N-Z)^2}{A} \text{ MeV,} \quad (12.27)$$

we would deduce for the interaction energy:

$$\langle V \rangle = -38 A + 8 \frac{(N-Z)^2}{A} \text{ MeV.} \quad (12.28)$$

Chapter 13

The general many-body problem for fermions

13.1 General forms of the many-body wavefunctions and methods of solution

The Schrödinger equation for a system of n particles each of mass m in a central potential, U_k , which interact via a two-body potential, V_{kl} , is

$$H |\Psi\rangle = E |\Psi\rangle, \quad (13.1)$$

with

$$H = \left\{ \sum_{k=1}^n (T_k + U_k) \right\} + \left\{ \sum_{k < l} V_{kl} \right\} \equiv H^{(0)} + W, \quad (13.2)$$

where T_k is the kinetic energy operator, $-(\hbar^2/2m)\nabla_k^2$, and Ψ is the n -particle wave function represented in coordinate space by $\Psi(\vec{r}_1 \dots \vec{r}_n)$. In applications to atomic physics, U_k is the Coulomb potential between the nucleus and the electrons. In applications to nuclear physics one takes $U_k = 0$. The coordinate space forms of U_k and V_{kl} will be denoted by $U(r_k)$ and $V(\vec{r}_k \vec{r}_l)$, respectively

The standard technique for solving this equation involves first solving the simpler problem

$$H^{(0)} |\Phi_a\rangle = E_a^{(0)} |\Phi_a\rangle, \quad (13.3)$$

which has the solution

$$|\Phi_a\rangle = \prod_{k=1}^n |\alpha_k\rangle = \phi_{\alpha_1}(\vec{r}_1) \phi_{\alpha_2}(\vec{r}_2) \phi_{\alpha_3}(\vec{r}_3) \dots \phi_{\alpha_n}(\vec{r}_n), \quad (13.4)$$

with

$$E_a^{(0)} = \sum_{k=1}^n \epsilon_{\alpha_k}. \quad (13.5)$$

The $|\alpha\rangle$ are solutions of the single-particle equation

$$(T + U) |\alpha\rangle = \epsilon_\alpha |\alpha\rangle, \quad (13.6)$$

and label a represents one particular choice for the set of quantum numbers α_k . There are infinitely many different sets a which can be ordered by their total energy $E_a^{(0)}$.

The states ϕ_α are assumed to form a complete orthonormal single-particle basis:

$$\langle \alpha_k | \alpha_l \rangle = \delta_{kl}$$

The states Φ are assumed to form a complete orthonormal basis for the solution of Eq. (13.1). In a spherical basis α would represent the set of quantum numbers (n_r, ℓ, m_ℓ) . If the spin coupling is included the quantum numbers would be (n_r, ℓ, j, m_j) .

The full exact many-particle problem can then be reformulated in terms of the Φ basis by expanding Ψ over the basis,

$$| \Psi \rangle = \sum_a c_a | \Phi_a \rangle, \quad (13.7)$$

and then solving the matrix equation

$$\sum_a \langle \Phi_b | H | \Phi_a \rangle c_a = E c_b. \quad (13.8)$$

Alternatively, solutions can be obtained with many-body perturbation theory (MBPT).

Nondegenerate Rayleigh-Schroedinger perturbation theory gives

$$E_a = E_a^{(0)} + E_a^{(1)} + E_a^{(2)} \dots \quad (13.9)$$

and

$$|\Psi_a\rangle = |\Psi_a^{(0)}\rangle + |\Psi_a^{(1)}\rangle + \dots, \quad (13.10)$$

where

$$E_a^{(0)} = \langle \Phi_a | H^{(0)} | \Phi_a \rangle, \quad (13.11)$$

$$E_a^{(1)} = \langle \Phi_a | W | \Phi_a \rangle, \quad (13.12)$$

$$E_a^{(2)} = \sum_{b \neq a} \frac{\langle \Phi_a | W | \Phi_b \rangle \langle \Phi_b | W | \Phi_a \rangle}{E_a^{(0)} - E_b^{(0)}}, \quad (13.13)$$

and

$$|\Psi_a^{(0)}\rangle = |\Phi_a\rangle, \quad (13.14)$$

$$|\Psi_a^{(1)}\rangle = \sum_{b \neq a} \frac{\langle \Phi_b | W | \Phi_a \rangle}{E_a^{(0)} - E_b^{(0)}} |\Phi_b\rangle. \quad (13.15)$$

The ingredients of the calculations are the matrix elements of one- and two-body operators between the many-body basis states. There are many modern variations for the implementations of MBPT [1] [2], [3], [4]. They also include three-body interactions. The In-Medium Similarity Renormalization Group (IMSRG) method is widely used [5]. IMSRG relies on a unitary similarity transform of the many-body problem [5]. An older cousin of IMSRG is the non-unitary Coupled-Cluster (CC) method [6].

These methods of solution are limited by the fact that in practice one must deal with finite matrices and/or that the perturbation series must converge. In the extreme, MBPT will not work if Φ_a is only a very small part of the full wavefunction.

Improved solutions by the above methods can often be achieved by adding and subtracting a single-particle potential in Eq. (13.2) to obtain

$$H = \left\{ \sum_{k=1}^n (T_k + U_k + U'_k) \right\} + \left\{ \sum_{k < l} V_{kl} - \sum_{k=1}^n U'_k \right\} \equiv H^{(0)} + W. \quad (13.16)$$

U'_k is chosen in order to minimize the size of off-diagonal matrix elements of W in the Φ

basis, thus providing a means of truncating the matrix and/or improving the convergence of the perturbation expansion. One systematic way of choosing U'_k is the Hartree-Fock method.

When the particles are identical fermions, the wave functions must be totally anti-symmetric with respect to the interchange of the coordinates of any two particles. This is arranged by constructing Slater determinants within the Φ basis. For the two-particle system the Slater determinant is given by

$$\begin{aligned} |\Phi_a\rangle &= |\alpha\beta\rangle = \frac{1}{\sqrt{2}} \begin{vmatrix} \phi_\alpha(1) & \phi_\alpha(2) \\ \phi_\beta(1) & \phi_\beta(2) \end{vmatrix} \\ &= \frac{1}{\sqrt{2}} \{\phi_\alpha(1)\phi_\beta(2) - \phi_\beta(1)\phi_\alpha(2)\}. \end{aligned} \quad (13.17)$$

or, in Dirac notation, as

$$|\Phi_a\rangle = |\alpha\beta\rangle = \frac{1}{\sqrt{2}} \{|\alpha\beta\rangle_p - |\beta\alpha\rangle_p\}, \quad (13.18)$$

where the subscript p denotes the product wave function given in coordinate space by Eq. (13.4). Note that $|\alpha\alpha\rangle = 0$ and $|\alpha\beta\rangle = -|\beta\alpha\rangle$. For the n -particle system there are $n!$

terms and the normalization is $1/\sqrt{n!}$. The Slater determinant enforces the Pauli principle - the fact that no two members of the set of quantum numbers α_k can be identical or the wave function will vanish.

The matrix elements of H between these Slater determinants are straightforward but tedious to evaluate. However, the diagonal matrix elements are particularly simple. The diagonal matrix element for the one-body operator $T_k + U_k$ is

$$\langle \Phi_a | \sum_{k=1}^n (T_k + U_k) | \Phi_a \rangle = \sum_{\alpha} \langle \alpha | T + U | \alpha \rangle, \quad (13.19)$$

where the sum over α runs over the set of n occupied single-particle states in Φ_a , and $\langle \alpha | T + U | \alpha \rangle$ stands for the single-particle matrix element

$$\int \phi_{\alpha}^*(\vec{r}) \left[\frac{-\hbar^2}{2m} \nabla^2 + U(\vec{r}) \right] \phi_{\alpha}(\vec{r}) d\tau. \quad (13.20)$$

The diagonal matrix element for the two-body operator V_{kl} is

$$\langle \Phi_a | \sum_{k < l} V_{kl} | \Phi_a \rangle = \sum_{\alpha < \beta} \langle \alpha \beta | V | \alpha \beta \rangle$$

$$= \frac{1}{2} \sum_{\alpha \neq \beta} < \alpha \beta | V | \alpha \beta > = \frac{1}{2} \sum_{\alpha \beta} < \alpha \beta | V | \alpha \beta >. \quad (13.21)$$

where the sums over α and β run over the set of n occupied single-particle states in Φ_a . The summation over $(\alpha \neq \beta)$ can be replaced by the unrestricted summation $(\alpha \beta)$ because the two-particle wave function automatically vanishes when $\alpha = \beta$.

The two-body matrix element is given by

$$\begin{aligned} < \alpha \beta | V | \alpha \beta > &= < \alpha \beta | V | \alpha \beta >_p - < \alpha \beta | V | \beta \alpha >_p \\ &= \int \int \phi_\alpha^*(\vec{r}_1) \phi_\beta^*(\vec{r}_2) V(\vec{r}_1 \vec{r}_2) \phi_\alpha(\vec{r}_1) \phi_\beta(\vec{r}_2) d\tau_1 d\tau_2 \\ &\quad - \int \int \phi_\alpha^*(\vec{r}_1) \phi_\beta^*(\vec{r}_2) V(\vec{r}_1 \vec{r}_2) \phi_\beta(\vec{r}_1) \phi_\alpha(\vec{r}_2) d\tau_1 d\tau_2 \end{aligned} \quad (13.22)$$

where $V(\vec{r}_1 \vec{r}_2) = V(\vec{r}_2 \vec{r}_1)$ has been used, and the subscript p indicates that the product wave functions of Eq. (13.4) are used. The two terms in Eq. (13.22) are referred to as the direct and exchange terms, respectively. Evaluation of the most general case will be considered in the framework of the creation and destruction operators.

13.2 Closed-shell, particle, and hole configurations

Before deriving the Hartree-Fock equations it is useful to give some special cases of some diagonal matrix elements. The eigenstates of $H^{(0)}$ can be ordered with respect to the total energy $E^{(0)}$, with the lowest energy state being the one in which all of the particles occupy the lowest energy set of single-particle states allowed by the Pauli principle. This lowest-energy state will be denoted by $|C\rangle$. (This notation derives from the fact that it will be associated with the closed-shell configuration.) The n single-particle states occupied in $|C\rangle$ will be labeled by $\alpha, \beta, \gamma, \dots$. The total energy $E(C)$ of the state $|C\rangle$ is

$$E(C) = \langle C | H | C \rangle = \sum_{\alpha} \langle \alpha | T | \alpha \rangle + \frac{1}{2} \sum_{\alpha\beta} \langle \alpha\beta | V | \alpha\beta \rangle. \quad (13.23)$$

I will use i and j to label specific states above or below the fermi surface which will be considered explicitly in the summations. The total energy of a system with the configuration $|C\rangle$ plus one particle in the state i above the fermi surface (a state unoccupied in $|C\rangle$)

is

$$\begin{aligned} E(Ci) &= \langle Ci | H | Ci \rangle \\ &= E(C) + \langle i | T | i \rangle + \sum_{\alpha} \langle i\alpha | V | i\alpha \rangle. \end{aligned} \quad (13.24)$$

The difference between $E(Ci)$ and $E(C)$ will be denoted by, e_i , the single-particle energy:

$$e_i = E(Ci) - E(C) = \langle i | T | i \rangle + \sum_{\alpha} \langle i\alpha | V | i\alpha \rangle. \quad (13.25)$$

The total energy of a system with the configuration $|C\rangle$ plus particles in the states i and j above the fermi surface is

$$\begin{aligned} E(Cij) &= \langle Cij | H | Cij \rangle \\ &= E(C) + \langle i | T | i \rangle + \sum_{\alpha} \langle i\alpha | V | i\alpha \rangle \\ &\quad + \langle j | T | j \rangle + \sum_{\alpha} \langle j\alpha | V | j\alpha \rangle + \langle ij | V | ij \rangle \\ &= E(C) + e_i + e_j + \langle ij | V | ij \rangle \end{aligned} \quad (13.26)$$

The total energy of a system with the configuration $|C\rangle$ with one particle absent in the state h (normally occupied in $|C\rangle$) is

$$\begin{aligned} E(Ch^{-1}) &= \langle Ch^{-1} | H | Ch^{-1} \rangle \\ &= E(C) - \langle h | T | h \rangle - \sum_{\alpha} \langle h\alpha | V | h\alpha \rangle. \end{aligned} \quad (13.27)$$

The difference between $E(Ch^{-1})$ and $E(C)$ is

$$e_h = E(C) - E(Ch^{-1}) = \langle h | T | h \rangle + \sum_{\alpha} \langle h\alpha | V | h\alpha \rangle, \quad (13.28)$$

which has the same form as the single-particle energy in (13.25). Finally, the total energy of a system with the configuration $|C\rangle$ plus particles absent in the states h and h' is

$$\begin{aligned} E(Ch^{-1}h'^{-1}) &= \langle Ch^{-1}h'^{-1} | H | Ch^{-1}h'^{-1} \rangle \\ &= E(C) - e_h - e_{h'} + \langle hh' | V | hh' \rangle \end{aligned} \quad (13.29)$$

13.3 Derivation of the Hartree-Fock equations

In the Hartree-Fock approximation, $E(C)$ is minimized with respect to variation of the single-particle wave functions $\phi_i(\vec{r})$ [or equivalently with respect to $\phi_i^*(\vec{r})$]. With the coordinate space matrix elements of T and V , one obtains

$$\begin{aligned} \frac{\partial}{\partial \phi_i^*(\vec{r})} & \left\{ E(C) - \sum_{\alpha} \lambda_{\alpha} \left[\int |\phi_{\alpha}(\vec{r}_1)|^2 d\tau_1 - 1 \right] \right\} = 0 \\ &= T\phi_i(\vec{r}) - \lambda_i \phi_i(\vec{r}) + \frac{1}{2} \left\{ \sum_{\beta} \int \phi_{\beta}^*(\vec{r}_2) V(\vec{r}, \vec{r}_2) \phi_i(\vec{r}) \phi_{\beta}(\vec{r}_2) d\tau_2 \right. \\ &\quad + \sum_{\alpha} \int \phi_{\alpha}^*(\vec{r}_1) V(\vec{r}_1, \vec{r}) \phi_{\alpha}(\vec{r}_1) \phi_i(\vec{r}) d\tau_1 \\ &\quad - \sum_{\beta} \int \phi_{\beta}^*(\vec{r}_2) V(\vec{r}, \vec{r}_2) \phi_{\beta}(\vec{r}) \phi_i(\vec{r}_2) d\tau_2 \\ &\quad \left. - \sum_{\alpha} \int \phi_{\alpha}^*(\vec{r}_1) V(\vec{r}_1, \vec{r}) \phi_i(\vec{r}_1) \phi_{\alpha}(\vec{r}) d\tau_1 \right\}, \end{aligned} \quad (13.30)$$

where λ are Lagrange multipliers which are introduced to enforce the normalization. Using $V(\vec{r}_1 \vec{r}_2) = V(\vec{r}_2 \vec{r}_1)$, this reduces to

$$\begin{aligned} T\phi_i(\vec{r}) + \left\{ \sum_{\alpha} \int \phi_{\alpha}^*(\vec{r}_1) V(\vec{r}, \vec{r}_1) \phi_{\alpha}(\vec{r}_1) d\tau_1 \right\} \phi_i(\vec{r}) \\ - \int \left\{ \sum_{\alpha} \phi_{\alpha}^*(\vec{r}_1) V(\vec{r}, \vec{r}_1) \phi_{\alpha}(\vec{r}) \right\} \phi_i(\vec{r}_1) d\tau_1 = \lambda_i \phi_i(\vec{r}). \end{aligned} \quad (13.31)$$

A condensed form of this equation is

$$T\phi_i(\vec{r}) + U_a(\vec{r})\phi_i(\vec{r}) - \int U_b(\vec{r}_1, \vec{r}) \phi_i(\vec{r}_1) d\tau_1 = \lambda_i \phi_i(\vec{r}), \quad (13.32)$$

where U_a is a local potential and U_b is a non-local potential.

This nonlocal differential equation can be used to solve for λ_i and $\phi_i(\vec{r})$. It can be solved in an iterative fashion: (i) choose some initial guess for $\phi_i(\vec{r})$ and calculate the integrals as a function of \vec{r} , (ii) solve the differential equation for λ_i and $\phi_i(\vec{r})$, (iii) recalculate the integrals, and (iv) iterate until the λ_i and $\phi_i(\vec{r})$ converge.

Multiplying Eq. (13.31) by $\phi_i^*(\vec{r})$ on both sides and integrating gives

$$\langle i | T | i \rangle + \sum_{\alpha} \langle i\alpha | V | i\alpha \rangle = \lambda_i = e_i, \quad (13.33)$$

where the Lagrange multiplier has been equated to the single-particle energy by comparison to Eqs. (13.25) and (13.28). The term $\sum_{\alpha} \langle i\alpha | V | i\alpha \rangle$ can be identified as the expectation value of the mean-field potential U^{HF} .

$$\langle i | U^{HF} | i \rangle \equiv \sum_{\alpha} \langle i\alpha | V | i\alpha \rangle. \quad (13.34)$$

The full Hartree-Fock hamiltonian is

$$H = H^{(0)} + W, \quad (13.35)$$

with

$$H^{(0)} = \sum_k (T + U^{HF})_k, \quad (13.36)$$

and

$$W = \sum_{k>l} V_{kl} - \sum_k U_k^{\text{HF}}. \quad (13.37)$$

The state $|C\rangle$ with the Hartree-Fock condition of Eq. (13.34) enforced will be denoted by $|\Phi_{\text{HF}}\rangle$. The zeroth-order and first-order matrix elements are

$$E_{\text{HF}}^{(0)} = \langle \Phi_{\text{HF}} | \sum_k (T + U^{\text{HF}})_k | \Phi_{\text{HF}} \rangle = \sum_\alpha e_\alpha, \quad (13.38)$$

and

$$\begin{aligned} E_{\text{HF}}^{(1)} &= \langle \Phi_{\text{HF}} | W | \Phi_{\text{HF}} \rangle = \langle \Phi_{\text{HF}} | \sum_{k>l} V_{kl} - \sum_k (U^{\text{HF}})_k | \Phi_{\text{HF}} \rangle \\ &= \frac{1}{2} \sum_{\alpha\beta} \langle \alpha\beta | V | \alpha\beta \rangle - \sum_\beta \langle \beta | U^{\text{HF}} | \beta \rangle \\ &= -\frac{1}{2} \sum_{\alpha\beta} \langle \alpha\beta | V | \alpha\beta \rangle. \end{aligned} \quad (13.39)$$

The total unperturbed energy can thus be expressed in several ways:

$$\begin{aligned}
 E_{\text{HF}}^{(0)} + E_{\text{HF}}^{(1)} &= \sum_{\alpha} e_{\alpha} - \frac{1}{2} \sum_{\alpha\beta} \langle \alpha\beta | V | \alpha\beta \rangle \\
 &= \sum_{\alpha} \langle \alpha | T | \alpha \rangle + \frac{1}{2} \sum_{\alpha\beta} \langle \alpha\beta | V | \alpha\beta \rangle \\
 &= \frac{1}{2} \left\{ \sum_{\alpha} e_{\alpha} + \sum_{\alpha} \langle \alpha | T | \alpha \rangle \right\}, \tag{13.40}
 \end{aligned}$$

where the last line is the sum of the first two lines divided by two. It is to be noted that the Hartree-Fock condition does not make $E^{(1)}$ vanish. The advantage of the Hartree-Fock procedure is that an important class of matrix elements $\langle \Phi_{\text{HF}} | W | \Phi \rangle$ which enter into the second-order corrections vanish - namely, all of those for which Φ differs from Φ_{HF} by the addition of one particle above the fermi surface and the removal of one particle below the fermi surface. These are called one-particle one-hole (1p-1h) configurations. The addition of 1p-1h configurations has the effect of changing the radial wavefunctions of the occupied

orbitals in the closed-shell configuration. But these are already optimized to give the lowest energy by the HF equations.

The most important corrections are those in which the Φ differs from Φ_{HF} by addition of two-particle above the fermi surface and the removal of two particles below the fermi surface (2p-2h configurations).

13.4 The total energy

As an example, We start with Eq. (13.40) for the total energy of ^{16}O . The sum over α is for the three filled orbitals $0s_{1/2}$, $0p_{3/2}$ and $0p_{1/2}$ with their $(2j + 1)$ m -state degeneracy. The kinetic energy part of this can be estimated using the harmonic-oscillator model; for ^{16}O with $\hbar\omega=14$ MeV this is

$$\sum_{\alpha} \langle \alpha | T | \alpha \rangle = 18 \hbar\omega = 250 \text{ MeV}.$$

The contribution from the $e(\alpha)$ obtained with the single-particle energies in the next chapter is

$$\sum_{\alpha} e(\alpha) \approx -440 \text{ MeV}.$$

The sum from Eq. (13.40) is about -95 MeV to be compared to the experimental energy of -127 MeV for ^{16}O . Thus, the basic Hartree-Fock model is not enough. One must include the change in energy coming from configuration mixing beyond the closed-shell configuration involving n particle - n hole configurations with $n > 1$. Also one must include three-body interactions. The Kohn-Sham theorem ([link to wiki](#)) says that there exists an effective interaction that can be written in terms of a functional of the nuclear HF densities that gives a ground state energy that implicitly takes into account correlations and three-body interactions. This is the justification for using the energy-density functional extension of Hartree-Fock. But the Kohn-Sham theory does not specify the effective interaction, and up to now, the functional form and its associated parameters must be obtained by constraints (fits) to experimental data.

Bibliography

- [1] M. Hjorth-Jensen, T. T. S. Kuo and E. Osnes E. Phys Rept. (1995) **261**, 125 (1995).
- [2] W. Kutzelnigg, International Journal of Quantum Chemistry **109**, 3858 (2009).
- [3] A. Tichai, R. Roth and T. Duguet, Front. Phys. Physics **8**, 164 (2020).
- [4] H. Hergert, Front. Phys. Physics **8**, 379 (2020).

- [5] H. Hergert, S. K. Bogner, T. D. Morris, S. Binder, A. Calci, and J. Langhammer, et al., Phys. Rev. C **90**, 041302) (2014). link
- [6] G. Hagen, T. Papenbrock, M. Hjorth-Jensen and D. J. Dean, Rept. Prog. Phys. **77**, 06302 (2014).

Chapter 14

Overview of the nuclear shell model

Evidence for the validity of the nuclear shell model comes from the observation of “magic numbers” in experimental observables such as binding energy, size, spin, and level density. In particular, the nuclear binding energy is not a smooth function of proton and neutron number, but exhibits small fluctuations. The liquid-drop model binding energy is a smooth function of proton and neutron number. When the liquid-drop values for the binding energies are subtracted from the experimental values (see liquid drop model), the differences show peaks at the magic numbers 28, 50, 82 and 126. The peaks indicate that the nuclei with these magic numbers are more tightly bound than average. Those nuclei that are magic with respect to both neutron and proton numbers are referred to as doubly-magic; an example is the nucleus ^{208}Pb with $N = 126$ and $Z = 82$. Near the line of stability, the first and second derivatives of the binding energies and the excitation energy of 2^+ states show magic numbers at 2, 6, 8, 20, 28, 80 82 and 126.

Electron ionization energies for atoms are shown in Fig. (14.1). One observes peaks corresponding to the electron numbers of the Nobel (inert) gases. These magic numbers for atoms can be qualitatively understood in terms of the sequential filling of eigenstates of a single-particle potential for the electron obtained from the attractive Coulomb interaction

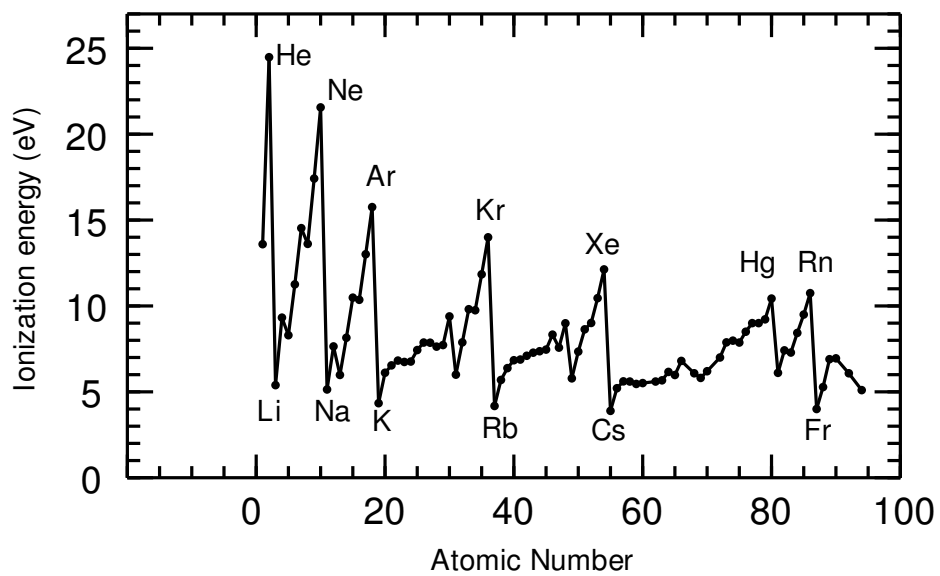


Figure 14.1: Ionization energy for atoms. The lowest minima occur for the alkali metals just after the peaks for atomic numbers of the Noble gases with $Z = 2, 10, 18, 36, 54$ and 86 . Smaller peaks are observed for $Z = 30, 58$ and 80 .

with the protons in the nucleus (given by $[-13.6 Z/(n + \ell + 1)^2]$ eV.) plus an average over the repulsive Coulomb interaction with all other electrons. The resulting energy ordering of the single-particle states for (n, ℓ) is given by Aufbau principle that the ordering is in terms of increasing values of $[n + 2\ell]$ and within each of these groups in order of higher to lower ℓ : $0s, 1s, [0p, 2s], [1p, 3s], [0d, 2p, 4s], [1d, 3p, 5s], [0f, 2d, 4p, 6s], \dots$

(link to wiki).

The Pauli exclusion principle for fermions allows a maximum of $2(2\ell + 1)$ electrons in each state (electron spin up and spin down, together with the $(2\ell + 1)$, m states for a given ℓ). With this maximum occupancy the sum of the filled-shell configurations have atomic numbers

$2, (4), [10, (12)], [18, (20)], [30, 36, (38)], [48, 54, (56)], [70, 80, 86, (88)], \dots$,

where the numbers in brackets correspond to the (n, s) filling. The atomic numbers observed for the Noble gases are reproduced by this ordering, in particular the filled shells followed by (n, s) states.

So it appeared that the nuclear properties might also be qualitatively understood in

terms of energy levels for a potential for a single nucleon obtained by averaging its strong interaction over all other nucleons. Since the strong interaction is short ranged this should give rise to an average potential that is proportional to the density distribution of nucleons in the nucleus. A good starting model for this is the Woods-Saxon potential,

$$V(r) = \frac{V_o}{[1 + \exp(r - c)/a]}. \quad (14.1)$$

The middle panel of Fig. (14.2) shows the neutron single-particle energies for this potential for ^{208}Pb obtained with $c \approx 1.2A^{1/3}$ fm and $a \approx 0.60$ fm, and $V_o \approx -50$ MeV. Magic numbers would be associated with the filling of the various (n, ℓ) shown in the figure. Only a few of these, 2, 8, and 20, correspond to those observed in experiment. The Woods-Saxon results are compared to the levels of an harmonic oscillator potential on the left-hand side of Fig. (14.2). Note that the ℓ degeneracy present in the oscillator is broken in the Woods-Saxon potential with levels of larger ℓ coming lower in energy.

In 1949 the key role of the spin-orbit splitting in the one-body potential was proposed by Maria Goeppert Mayer [1] and Otto Haxel, J. Hans D. Jensen and Hans Suess [2]. This one-body potential model is the starting point for the nuclear shell model [3]. The spin-orbit

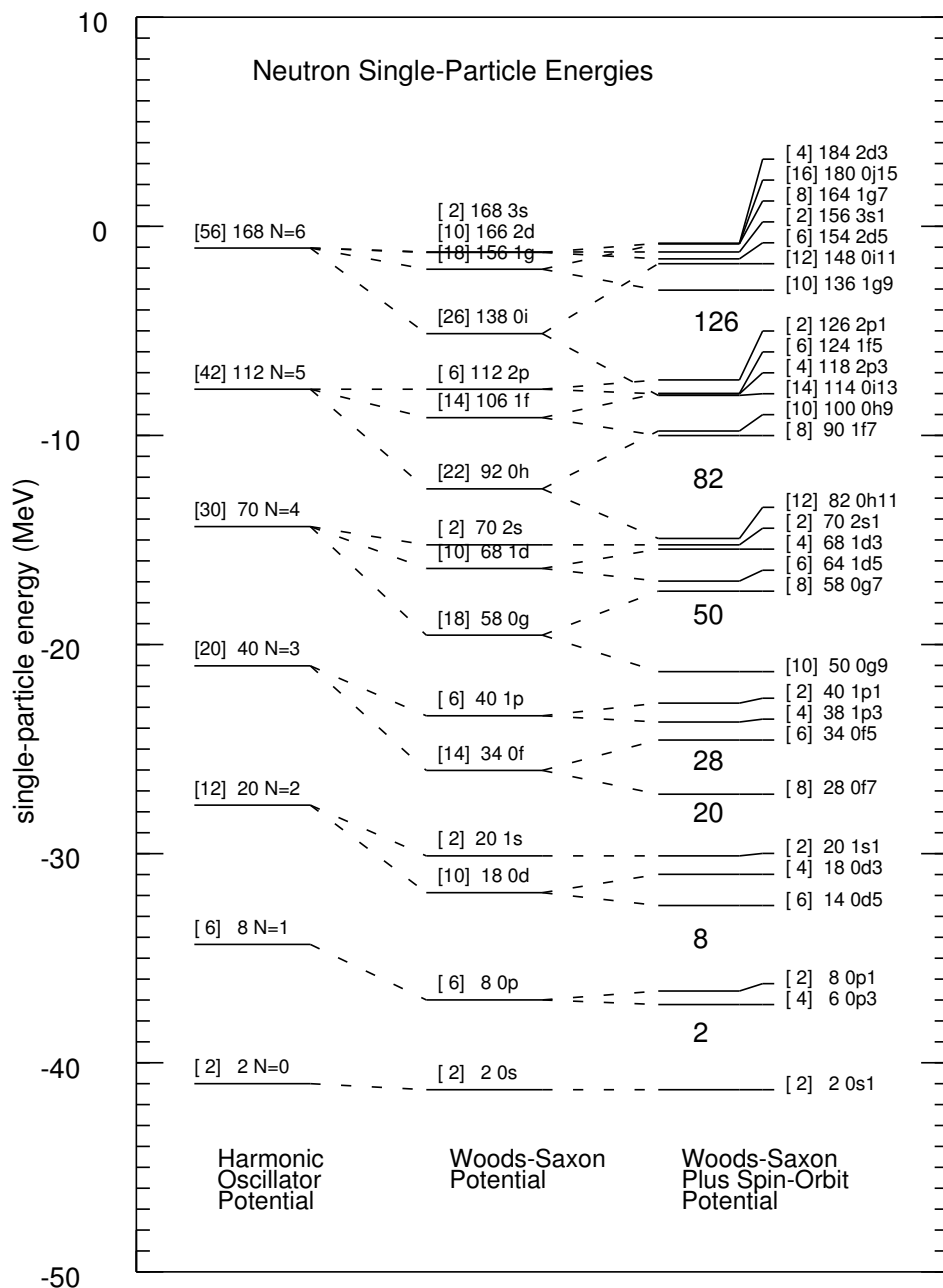


Figure 14.2: Neutron single-particle states in ^{208}Pb with three potential models, harmonic oscillator (left), Woods-Saxon without spin-orbit (middle) and Woods-Saxon with spin orbit (right). The numbers in square brackets are the maximum number of neutrons in that each level can contain, the following number is a running sum of the total. In addition the harmonic oscillator is labeled by the major quantum number $N = 2n + \ell$, the Woods Saxon is labeled by (n, ℓ) and the Woods-Saxon with spin-orbit is labeled by $(n, \ell, 2j)$.

potential has the form, $V_{so}(r)\vec{\ell}\cdot\vec{\sigma}$, where $\vec{\ell}$ is the orbital angular momentum. $\underline{\sigma} = 2\vec{s}$ where \vec{s} is the intrinsic spin angular momentum of the nucleon. The radial shape conventionally takes the form

$$V_{so}(r) = V_{so} \frac{1}{r} \frac{df_{so}(r)}{dr}, \quad (14.2)$$

with

$$f_{so}(r) = \frac{1}{1 + [\exp(r - c_{so})/a_{so}]}. \quad (14.3)$$

$c_{so} = c$ and $a_{so} = a$ are good starting approximations. There is a term of the type in Eq. (14.2) in the atomic potential coming from the relativistic Thomas interaction energy [4]. The nuclear physics the spin-orbit term is much larger and opposite in sign to that in atomic physics.

The energy levels obtained when the spin-orbit potential is added to the Woods-Saxon potential are shown on the right-hand side of Fig. (14.2). The strength of the spin-orbit potential has been determined empirically. The dashed lines that connect to the middle of Fig. (14.2) indicate the effect of the spin-orbit potential in splitting the states of a given ℓ value. With the quantum numbers (n, ℓ, s, j, m) , the maximum number of neutrons in a

given state is $2(2j + 1)$. Each level is labeled by the occupation number (in square brackets), the cumulative occupation number, and the values for $n, \ell, 2j$. The values of the neutron number for which there are large gaps in the cumulative occupation number now reproduce all of the observed magic numbers (as emphasized by the numbers shown in the energy gaps on the right-hand side).

Given the complexity of the strong interactions taking place in such a confined space, the results of the shell model came as a surprise. Wilkinson says “The Mayer-Jensen shell model had burst upon us in 1949, bringing order to a mass of previously uncorrelated data on spins, magnetic moments and beta decay. To those of us brought up on the Bohr-Wheeler liquid drop model it seemed absurd that the shell model would work at all” [5]. The essential physics behind the shell model is that the many-nucleon collisions that might be expected are greatly suppressed in the nuclear ground states and low-lying nuclear levels because the nucleons would have to be scattered into states which are forbidden by the Pauli principle. At higher excitation energy the number of allowed states becomes much greater and the nuclear properties indeed become complex and chaotic.

The shell model in its simplest form is able to successfully predict the properties of nuclei which are one nucleon removed or added to the one of the magic numbers. The shell model can also be extended to include the more complex configurations that arise for the nuclei with nucleon numbers that are in between the magic numbers. For many applications these complex configurations can be taken into account exactly by the diagonalization of a Hamiltonian matrix. In other cases approximations must be used; these include the use of a deformed intrinsic single-particle potential, and the use of group theory to classify the configurations.

We will refer to the closed-shell configurations for the oscillator magic numbers as LS closed shells since they can be described in a basis with good ℓ and s quantum numbers. An equation for the LS sequence of magic numbers, 2, 8, 20, 40, 70, 112, ..., is

$$N = i(i + 1)(i + 2)/3, \quad (14.4)$$

where $i = 1, 2, 3, \dots$. We will refer to the closed-shell configurations for cases where only one of the spin-orbit partners is filled as JJ closed shells since only the total angular momentum j is a good quantum number. An equation for the JJ sequence of magic numbers, 2, 6, 14,

28, 50, 82, 126, . . . , is

$$N = (i^3 + 5i)/3, \quad (14.5)$$

where $i = 1, 2, 3, \dots$

Some magic numbers near stability are localized on the atomic chart: $Z = 14$ (^{34}Si), $Z = 16$ (^{36}S), $Z = 38$ (^{88}Sr) and $Z = 40$ (^{68}Ni , ^{90}Zr and ^{96}Zr). In neutron-rich nuclei, new magic numbers are localized in new regions of the atomic chart: $N = 14$ (^{22}O), $N = 16$ (^{24}O), $N = 32$ (^{52}Ca) and $N = 34$ (^{54}Ca).

Many of these shell gaps are weakened in neutron-rich nuclei to these extent that the energy of particle-hole configurations can come lower in energy than those for the filled shell in the “islands of inversion” [6]. This occurs for $N = 8$ (^{12}Be), $N = 20$ (^{32}Mg), $N = 28$ (^{42}Si), $N = 40$ (^{66}Fe) and is predicted to occur in for $N = 50$ (^{76}Fe) [7].

With the event of Rare Isotope Beam accelerators we are able to explore new regions of nuclei far from stability. From the historical perspective of the nuclear shell model the key question will be to what extent the magic numbers continue to exist for nuclei far from

stability. The key overall question is how we can understand shell structure and its evolution as a function of N and Z with microscopic (ab initio) methods.

Metal clusters are also mesoscopic systems where the ideas associated with average potentials and magic numbers are a good starting point [8]. One uses the jellium model where the ionic core structure is ignored and replaced by a uniform positive background (link to wiki). For example, metal clusters show enhanced stability at the magic numbers 8, 20, 40, 58, 92 and 138 [8], [9]. All of these magic numbers are those expected for the Woods-Saxon potential without the spin-orbit term shown in the middle of Fig. (14.2). Fig. (14.3) shows the labels and commonly groupings used in the nuclear shell model. The k label provide a unique short-hand for (n, ℓ, j) . The k values can be computed from:

$$k = \frac{1}{2}[(2n + \ell)(2n + \ell + 3) - 2j + 3]. \quad (14.6)$$

k	n	l	$2j$	$\Sigma(2j+1)$				
1	0s1		2		12	0g7		0 s
					13	1d5		1 p
					14	1d3	j5	2 d
					15	2s1		3 f
					16	0h11	82	4 g
							-----	5 h
					17	0h9		6 i
					18	1f7		7 j
					19	1f5	j6	8 k
					20	2p3		
					21	2p1		
					22	0i13	126	

					23	0i 11		
					24	1g 9		
					25	1g7		
					26	2d5	j7	
					27	2d3		
					28	2s1		
					29	0j15	184	

Figure 14.3: Labels for the shell model orbitals and commonly used group names. The right-hand side shows the names for the orbital angular momentum.

Bibliography

- [1] M. G. Mayer, Phys. Rev. **75**, 1969 (1949). link
- [2] O. Haxel, J. H. D. Jensen and H. E. Suess, Phys. Rev. **75**, 1766 (1949). link
- [3] K. E. Johnson, “Maria Goeppert Mayer: Atoms, molecules and nuclear shells”, Physics Today **39**, 44 (1986).
- [4] L. H. Thomas, Nature (London) **117**, 514 (1926).

- [5] D. H. Wilkinson, Ann. Rev. Nucl. Part. Sci. **45**, 1 (1995).
- [6] B. A. Brown, Physics **3**, 104 (2010).
- [7] F. Nowacki, A. Poves, E. Caurier, and B. Bounthong, Phys. Rev. Lett. **117**, 272501 (2016). link
- [8] W. A. de Heer, Rev. Mod. Phys. **65**, 611 (1993).
- [9] H. Gohlisch, T. Lange, T Bergmann and T. P Martin, Phys. Rev. Lett. **65**, 748 (1990). link

Chapter 15

Single particle (hole) energies

Single-particle energies are not observables [1]. Rather they are model-dependent quantities that can be used to test the model within the model assumptions. They are the most important ingredient for understanding the details of nuclear structure. Single-particle energies can be calculated with various single-particle potential models that will be discussed later. One can also use the basic ideas of Hartree-Fock theory to extract single-particle energies from experimental data starting with the assumption that the one has a closed-shell configuration. This is best satisfied for doubly-closed shell nuclei. These can provide the single-particle part of the Hamiltonians for configuration-interaction calculations near these doubly-magic nuclei. They can also be used to compare to the single-particle potential model results. Detailed results will be given for ^{16}O and then the results obtained for ^{208}Pb will be shown.

For a closed-shell configuration, the Hartree-Fock potential has single-particle energies for the HF states α given by $e(\alpha) = E(C, \alpha) - E(C)$ for unfilled (particle) states, and $e(\alpha) = E(C) - E(C, \alpha^{-1})$ for filled (hole) states. $E = -\text{BE} + E_x$, where BE is the ground state binding energy, and E_x is the excitation energy for the state α . (This relationship between the single-particle energies of the HF potential and the energy differences between

nuclei differing by one nucleon is known as the Koopmans' theorem from atomic physics (link to wiki).)

Using this idea for particle and hole states in ^{16}O we obtain energies for protons and neutrons (in units of MeV):

$$E(C) = E(^{16}\text{O}) = -127.62$$

$$E[C, 1s_{1/2} \text{ neutron}] = E(^{17}\text{O}) + E_x(1/2^+) = -131.76 + 0.87 = -130.89$$

$$E[C, 1s_{1/2} \text{ proton}] = E(^{17}\text{F}) + E_x(1/2^+) = -128.22 + 0.50 = -127.72$$

$$E[C, 0d_{5/2} \text{ neutron}] = E(^{17}\text{O}) = -131.76$$

$$E[C, 0d_{5/2} \text{ proton}] = E(^{17}\text{F}) = -128.22$$

$$E[C, (0p_{1/2})^{-1} \text{ neutron}] = E(^{15}\text{O}) = -111.96$$

$$E[C, (0p_{1/2})^{-1} \text{ proton}] = E(^{15}\text{N}) = -115.49$$

$$E[C, (0p_{3/2})^{-1} \text{ neutron}] = E(^{15}\text{O}) + E_x(3/2^-) = -111.96 + 6.18 = -105.78$$

$$E[C, (0p_{3/2})^{-1} \text{ proton}] = E(^{15}\text{N}) + E_x(3/2^-) = -115.49 + 6.32 = -109.17$$

$$E[C, (0s_{1/2})^{-1} \text{ neutron}] = E(^{15}\text{O}) + E_x(1/2^+) = -111.96 + 41 = -71$$

$$E[C, (0s_{1/2})^{-1} \text{ proton}] = E(^{15}\text{N}) + E_x(1/2^+) = -115.49 + 41 = -76$$

The ℓ, j values are inferred from the spin-parity of the odd-even states and the radial quantum n is based on the Hartree-Fock model. The E_x values for $A = 17$ are the energies of the lowest $1/2^+$ states in ^{17}F and ^{17}O . The E_x values for $A = 15$ are the energies of the lowest $3/2^-$ states in ^{15}O and ^{15}N . In the $^{16}\text{O}(e, e'p)$ reaction the $s_{1/2}$ state is observed as broad asymmetric structure centered at $E_x = 41$ MeV [2]. The approximate single-particle character for all of these states is reinforced by their large cross sections obtained in one-nucleon transfer experiments from ^{16}O . The single-particle energies for these states obtained under the above assumptions are (in units of MeV):

$$\begin{aligned} e(1s_{1/2} \text{ neutron}) &= E[C, 1s_{1/2} \text{ neutron}] - E(C) = -3.27 \\ e(1s_{1/2} \text{ proton}) &= E[C, 1s_{1/2} \text{ proton}] - E(C) = -0.10 \\ e(0d_{5/2} \text{ neutron}) &= E[C, 0d_{5/2} \text{ neutron}] - E(C) = -4.14 \\ e(0d_{5/2} \text{ proton}) &= E[C, 0d_{5/2} \text{ proton}] - E(C) = -0.60 \\ e(0p_{1/2} \text{ neutron}) &= E(C) - E[C, (0p_{1/2})^{-1} \text{ neutron}] = -15.66 \\ e(0p_{1/2} \text{ proton}) &= E(C) - E[C, (0p_{1/2})^{-1} \text{ proton}] = -12.13 \\ e(0p_{3/2} \text{ neutron}) &= E(C) - E[C, (0p_{3/2})^{-1} \text{ neutron}] = -21.84 \\ e(0p_{3/2} \text{ proton}) &= E(C) - E[C, (0p_{3/2})^{-1} \text{ proton}] = -18.45 \end{aligned}$$

$$\begin{aligned} e(0s_{1/2} \text{ neutron}) &= E(C) - E[C, (0s_{1/2})^{-1} \text{ neutron}] \approx -57 \\ e(0s_{1/2} \text{ proton}) &= E(C) - E[C, (0s_{1/2})^{-1} \text{ proton}] \approx -53 \end{aligned}$$

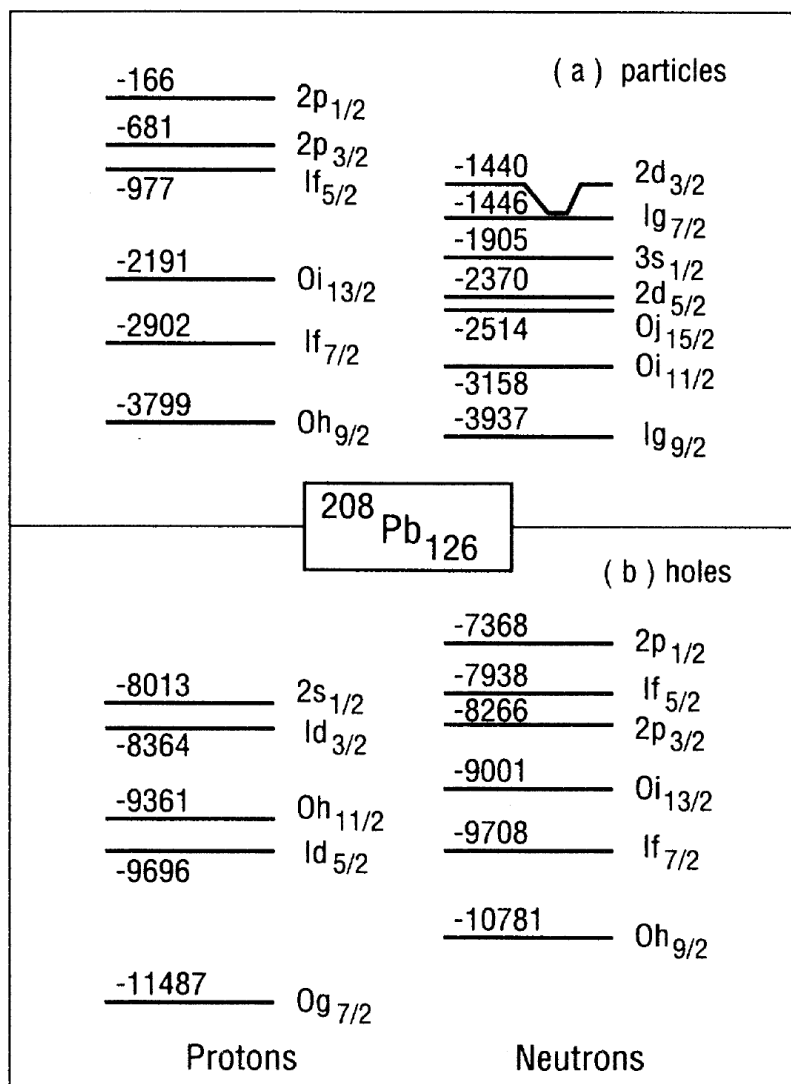
The single-particle energies for other states can be inferred from the energies E associated with excited states in the A=17 nuclei. There are many excited states. The ones that should be associated with the single-particle states in the Hartree-Fock model are those with large spectroscopic factors.

Spectroscopic factors are not observables [1]. They are used together with reaction theory within an assumed model to calculate observables. For example, we may assume that the overlap function between two nuclei involved in a one-nucleon transfer reaction is described by the radial density of the single-particle Hartree-Fock wavefunction for the (ℓ, j) value involved. These can be used in a reaction model to calculate cross sections for one-nucleon transfer. If the cross section agrees with experiment, it indicates that the model is not wrong. How good the model is depends upon its prediction for observables (such as magnetic moments) and their comparison to experiment. Experiment and theory may not agree, and that indicates that the model (nuclear structure plus reaction aspects) is incomplete. It is

common that a model is “good” for some limited set of observables and that other observables lie outside the model’s range of applicability. For example, the Hartree-Fock model does not explicitly take into account the strong short-ranged part of the nucleon-nucleon interaction that gives rise to high-momentum tails observed in $(e, e'p)$ reactions at large momentum transfers.

The closed-shell configuration for ^{16}O is a first approximation. The complete theory must involve a much larger basis. Within this larger basis one can calculate observables to understand how they differ from the closed-shell approximation.

Single-particle energies for region of ^{208}Pb obtained assuming that ^{208}Pb has a closed shell configuration are shown in Fig. (15.1). They are obtained from the binding energies are spectra for $^{207-209}\text{Pb}$, ^{207}Tl and ^{209}Bi in [3].

Figure 15.1: Single-particle energies for region of ^{208}Pb given in units of keV.

Bibliography

- [1] T. Duguet, H. Herger, J. D. Holt and V. Soma, Phys. Rev. C **92**, 034313 (2015). link
- [2] F. Ajzenberg-Selove, Nucl. Phys. **A360**, 1 (1981).
- [3] E. K. Warburton and B. A. Brown, Phys. Rev. C 43, 602 (1991). link

Chapter 16

The harmonic oscillator potential

16.1 General properties

A very useful form for $U_o(r)$ used in nuclear physics is the harmonic-oscillator (HO) potential given by

$$U_o^{\text{HO}}(r) = \frac{1}{2}m\omega^2 r^2, \quad (16.1)$$

where m is the nucleon mass and ω is a parameter. This potential has nice analytical properties, the most important of which is that the many-body HO Hamiltonian can be exactly separated into a sum of intrinsic and center-of-mass terms. This will be discussed below. The single-particle energy levels are given by

$$e_\alpha = (N + 3/2)\hbar\omega, \quad (16.2)$$

where N is the major-shell HO quantum number given by

$$N = 2n_r + \ell. \quad (16.3)$$

The single-particle wavefunction for state α will be denoted by $|\phi_\alpha\rangle$, with the radial wavefunction given by

$$\begin{aligned}
R_\alpha(r) &= \sqrt{\frac{2^{\ell-n_r+2} (2\ell+2n_r+1)!!}{\sqrt{\pi} (n_r)! b^{2\ell+3} [(2\ell+1)!!]^2}} r^{\ell+1} e^{-r^2/2b^2} \\
&\times \sum_{k=0}^{n_r} \frac{(-1)^k 2^k (n_r)! (2\ell+1)!!}{k! (n_r-k)! (2\ell+2k+1)!!} (r/b)^{2k},
\end{aligned} \tag{16.4}$$

where

$$b = \sqrt{\frac{\hbar}{m\omega}}, \tag{16.5}$$

is the HO length parameter. Taking $\hbar c = 197$ MeV-fm and $mc^2 = 938$ MeV

$$b^2 = \frac{(\hbar c)^2}{(mc^2)(\hbar\omega)} = \frac{41.4 \text{ MeV fm}^2}{\hbar\omega}. \tag{16.6}$$

The diagonal matrix single-particle element of r^2 can be obtained by using the virial theorem (link to wiki) (for a potential of the form $V(r) = ar^n$, we have $2 < T > = n < V >$). For

the HO potential

$$\langle \phi_\alpha | U_o^{\text{HO}} | \phi_\alpha \rangle = \frac{1}{2} m \omega^2 \langle \phi_\alpha | r^2 | \phi_\alpha \rangle = \langle \phi_\alpha | T | \phi_\alpha \rangle,$$

together with

$$\langle \phi_\alpha | U_o^{\text{HO}} | \phi_\alpha \rangle + \langle \phi_\alpha | T | \phi_\alpha \rangle = (N + 3/2) \hbar \omega$$

to give

$$\langle \phi_\alpha | r^2 | \phi_\alpha \rangle = \langle N | r^2 | N \rangle = (N + 3/2) b^2, \quad (16.7)$$

and

$$\langle \phi_\alpha | T | \phi_\alpha \rangle = \frac{\hbar \omega}{2} (N + 3/2). \quad (16.8)$$

The notation $\langle N | r^2 | N \rangle$ is to indicate that the r^2 matrix element only depends on the combination $N = 2n_r + \ell$ (but the radial wavefunction depends on both n_r and ℓ .). An analytic expression for the general matrix elements of r^λ . Fortran programs for these matrix elements are contained in the RME Fortran codes that are part of NuShell16.

The maximum number of spin $\frac{1}{2}$ fermions that can occupy a given N value is given by

$$D_N = (N + 1)(N + 2). \quad (16.9)$$

The total number of states that can be occupied up to N_{\max} is given by

$$\sum_{N=0}^{N_{\max}} D_N = \frac{1}{3}(N_{\max} + 1)(N_{\max} + 2)(N_{\max} + 3). \quad (16.10)$$

The harmonic oscillator parameter ω is conventionally chosen to reproduce the observed mean-square charge radius. This is related to the mean-square radius for protons in the nucleus whose harmonic oscillator levels are filled up to N_{\max}

$$R_p^2 = \frac{\sum_{N=0}^{N_{\max}} D_N \langle N | r^2 | N \rangle}{\sum_{N=0}^{N_{\max}} D_N} = \frac{3}{4}(N_{\max} + 2)b^2. \quad (16.11)$$

(Note that this result only applies to cases where all of the states for a given N are filled. The result for partially filled orbitals must be calculated starting from Eq. (16.7).)

A common way of choosing the appropriate value of $\hbar\omega$ is to compare Eq. (16.11) to the observed proton mean-square radius as obtained from measured charge mean-square radius by

$$R_p^2 = R_{ch}^2 - R_o^2, \quad (16.12)$$

where $R_o^2 = 0.77 \text{ fm}^2$ is the mean-square charge radius of the proton. For example, for the nucleus ^{16}O , where the eight protons fill the $N = 0$ and $N = 1$ major shells, $N_{\max} = 1$ and $R^2(^{16}\text{O}) = (9/4)b^2$. The experimental root-mean-square (rms) charge radius for ^{16}O is [1] $R_{ch}^2 = 2.71 \text{ fm}$, and hence $R_p^2 = 6.57 \text{ fm}^2$, $b^2 = 2.92 \text{ fm}^2$ and $\hbar\omega = 14.2 \text{ MeV}$ for the point protons. Since there are equal numbers of neutrons and protons in ^{16}O and since they should have about the same rms radii, it is a good approximation to use the same oscillator parameter for the neutrons as was obtained for protons.

For heavy nuclei, one can use the large N_{\max} approximation for the sum in Eq. (16.10), $Z \approx (N_{\max} + 2)^3/3$, to obtain from (16.11)

$$R_p^2 \approx \frac{3}{4}(3Z)^{1/3}b^2. \quad (16.13)$$

For example, for ^{208}Pb ($Z=82$) the experimental rms charge radius is [1] 5.50 fm, giving

$R_p^2 = 29.4 \text{ fm}^2$, $b^2 = 6.27 \text{ fm}^2$ and $\hbar\omega_p = 6.6 \text{ MeV}$ for the point protons. It is observed experimentally that the proton and neutron rms radii in ^{208}Pb are about equal [2]: $R_n^2 \approx R_p^2$. The oscillator parameter for neutrons in ^{208}Pb , obtained by using an rms radius of 5.5 fm and Eq. (16.13) with N in place of Z , is $\hbar\omega_n = 7.6 \text{ MeV}$.

Along the valley of stability the rms proton radii are approximately given by $1.08A^{1/3}$. Rewriting Eq. (16.13) in terms of $A \approx 2.5Z$, one obtains for heavy nuclei $\hbar\omega_p \approx 39A^{-1/3} \text{ MeV}$. A better smooth approximation for the proton oscillator parameter in both light and heavy nuclei is [3]

$$\hbar\omega_p \approx 45A^{-1/3} - 25A^{-2/3}. \quad (16.14)$$

16.2 The harmonic oscillator in Cartesian coordinates

The harmonic oscillator potential is separable in Cartesian coordinates

$$\begin{aligned}\frac{U}{\hbar\omega} &= \frac{1}{2} \left(-\frac{\partial^2}{\partial x'^2} + x'^2 \right) + \frac{1}{2} \left(-\frac{\partial^2}{\partial y'^2} + y'^2 \right) + \frac{1}{2} \left(-\frac{\partial^2}{\partial z'^2} + z'^2 \right) \\ &= \frac{U_x + U_y + U_z}{\hbar\omega},\end{aligned}\quad (16.15)$$

where $(x', y', z') = (x, y, z)/b$. The solutions are thus product wavefunctions of the form

$$\psi_{n_x, n_y, n_z}(r) = \phi_{n_x} \phi_{n_y} \phi_{n_z}, \quad (16.16)$$

where n_i are the quantum numbers that give the number of nodes in the one-dimensional wavefunctions (not including the node at infinity).

The solutions of the one-dimensional oscillator can be obtained by writing the Hamiltonian as

$$U_x = \hbar\omega[a^+a + \frac{1}{2}], \quad (16.17)$$

with

$$a^+ = \frac{1}{\sqrt{2}} \left(x' - \frac{\partial}{\partial x'} \right), \quad a = \frac{1}{\sqrt{2}} \left(x' + \frac{\partial}{\partial x'} \right). \quad (16.18)$$

The commutation relation is $[a, a^+] = 1$. If ϕ_n is an eigenstate of energy E_n , then $a^+ \phi_n$ is also an eigenstate and has energy $E_n + \hbar\omega$

$$\begin{aligned} H(a^+ \phi_n) &= a^+ H \phi_n + [H, a^+] \phi_n = a^+ E_n \phi_n + \hbar\omega a^+ \phi_n \\ &= (E_n + \hbar\omega)(a^+ \phi_n). \end{aligned} \quad (16.19)$$

The normalized wavefunction is

$$\phi_{n+1} = \frac{1}{\sqrt{n+1}} (a^+ \phi_n).$$

Starting with the lowest state ϕ_0 with energy $\frac{1}{2}\hbar\omega$, excited states with n nodes can be generated by applying $(a^+)^n$ and have energy

$$E_n = \hbar\omega \left(n + \frac{1}{2} \right), \quad (16.20)$$

and for the three dimensional Hamiltonian of Eq. (16.15)

$$E_{n_x, n_y, n_z} = \hbar\omega(n_x + n_y + n_z + \frac{3}{2}) = \hbar\omega(N + \frac{3}{2}), \quad (16.21)$$

with $N = n_x + n_y + n_z$.

The coordinate matrix elements can be obtained by using

$$x' = \frac{1}{\sqrt{2}}(a^+ + a), \quad (16.22)$$

and

$$\langle n | a^+ | m \rangle = \langle m | a | n \rangle = \delta_{n,m+1}\sqrt{n}. \quad (16.23)$$

For example

$$\begin{aligned} 2 \langle n_x | x'^2 | n_x \rangle &= \langle n_x | (a^+ + a)^2 | n_x \rangle \\ &= \langle n_x | a^+ a + a a^+ | n_x \rangle \\ &= [\langle n_x | a^+ | n_x - 1 \rangle \langle n_x - 1 | a | n_x \rangle] \end{aligned}$$

$$\begin{aligned}
& + \langle n_x | a | n_x + 1 \rangle \langle n_x + 1 | a^+ | n_x \rangle \\
& = (2n_x + 1),
\end{aligned} \tag{16.24}$$

and thus

$$\langle N | r^2 | N \rangle = \frac{1}{2}[2(n_x + n_y + n_z) + 3]b^2 = [N + 3/2]b^2. \tag{16.25}$$

If we consider radial matrix elements of the form $\langle N | r^\lambda | M \rangle$, with $r^\lambda = (x^2 + y^2 + z^2)^{\lambda/2}$ the matrix elements are zero if one of the n_i (or N) change by more than λ . Thus

$$\langle N | r^\lambda | M \rangle = 0 \quad \text{if} \quad |N - M| > \lambda. \tag{16.26}$$

16.3 The deformed harmonic oscillator

In the Bohr collective model, solutions for the many-body problem are expressed in terms of an intrinsic state that is deformed. The deformed harmonic oscillator provides a convenient basis for expanding single-particle wavefunctions in a deformed system. We start with the

harmonic oscillator in cartesian coordinates. We will assume axial symmetry along the z axis with two oscillator frequencies, ω_ρ and ω_s

$$U_d = \frac{1}{2}M[\omega_\rho^2(x^2 + y^2) + \omega_z^2 z^2]. \quad (16.27)$$

An equipotential surface for this Hamiltonian is a spheroid with axes $R_x = R_y = R_\rho$ and R_z given related by

$$\omega_\rho^2 R_x^2 = \omega_\rho^2 R_y^2 = \omega_z^2 R_z^2. \quad (16.28)$$

In order that the density be independent of the deformation we have

$$\omega_x \omega_y, \omega_z = \omega_\rho^2 \omega_z = \omega_o^3. \quad (16.29)$$

This can be satisfied by having to order ϵ by having

$$\omega_\rho^2 = \omega_x^2 = \omega_y^2 = \omega_o^2(1 + \epsilon/3), \quad (16.30)$$

and

$$\omega_z^2 = \omega_o^2(1 - 2\epsilon/3). \quad (16.31)$$

The energy is

$$E = \hbar[\omega_x(n_x + 1/2) + \omega_y(n_y + 1/2) + \omega_z(n_z + 1/2)] = \hbar[\omega_\rho(n_\rho + 1) + \omega_z(n_z + 1/2)], \quad (16.32)$$

where $n_\rho = n_x + n_y$, and the quanta are constrained by $(n_\rho + n_z) = N$. Each of the (n_ρ, n_z) are two fold degenerate due to spin up and spin down. For example, for $N = 0$ we have $(n_x, n_y, n_z) = (0, 0, 0)$ with a degeneracy of $D = 2$. For $N = 1$ we have $(1, 0, 0)$ and $(0, 1, 0)$ with a total $D = 4$, and $(0, 0, 1)$ with $D = 2$.

For $N = 2$ we have $(2, 0, 0)$, $(1, 1, 0)$ and $(0, 2, 0)$ with a total $D = 6$, $(1, 0, 1)$ and $(0, 1, 1)$ with a total $D = 4$ and $(0, 0, 2)$ with $D = 2$. The general results is

$$D = 2(n_\rho + 1) = 2(N - n_z + 1). \quad (16.30)$$

The energy levels for the deformed oscillator are shown in Fig. (16.1). The results show that there can be shell gaps at large deformation. The details are not applicable to nuclei, but the more applicable results for deformed potentials results can also have “deformed shell gaps” that would give rise to extra stability for deformed configurations. There is a quantitave difference in the patterns for oblate and prolate deformations.

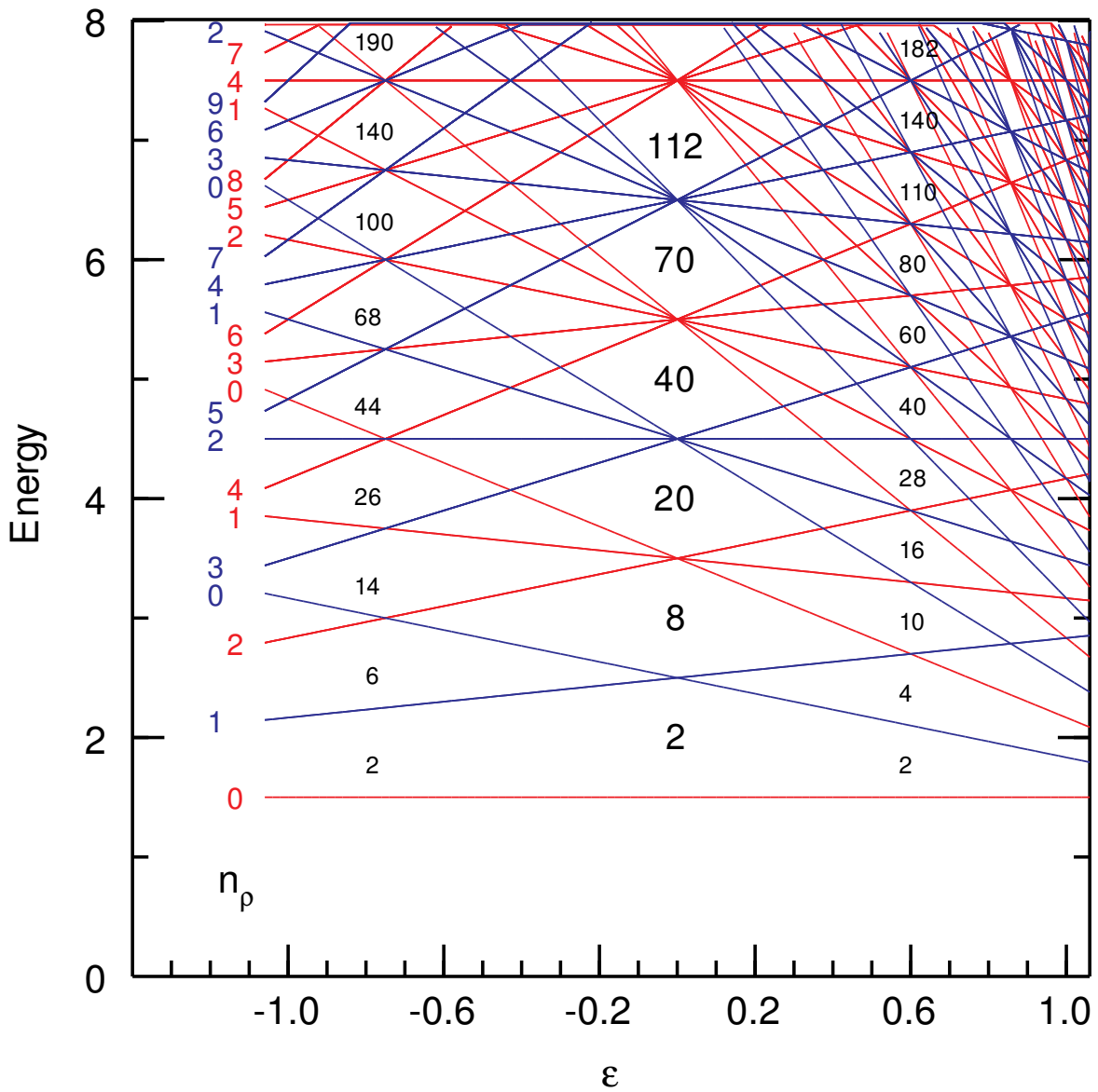


Figure 16.1: Energies for the deformed harmonic oscillator in units of $\hbar\omega_0$. The cumulative number of filled states are shown for three value values of ϵ . The degeneracies for the lowest few states are given on the left-hand side.

The wavefunctions for the deformed harmonic oscillator are express in a cylindrical coordinates (ρ, z, ϕ) with $\rho^2 = x^2 + y^2$, as a product of three functions

$$| n_\rho, n_z, \Lambda \rangle = \psi_{n_\rho}(\rho) \psi_{n_z}(z) \psi_\Lambda(\phi), \quad (16.33)$$

where Λ quantum number for L_z on the z axis. The wavefunctions ψ are given in [4].

16.4 Transformation from relative to center-of-mass coordinates for two nucleons

The shell-model wavefunctions are expressed in terms of the coordinates \vec{r}_1 and \vec{r}_2 with respect to a fixed center, but the NN interaction depends on the relative coordinate \vec{r} . The transformation between center-of-mass and relative coordinates can be carried out in an oscillator basis [5]. The reason is that the oscillator hamiltonian is seperable in both

coordinates:

$$\begin{aligned} H &= \frac{p_1^2}{2m} + \frac{p_2^2}{2m} + \frac{1}{2}m\omega^2r_1^2 + \frac{1}{2}m\omega^2r_2^2 \\ &= \frac{Q^2}{2M} + \frac{1}{2}M\omega^2R^2 + \frac{p^2}{2\mu} + \frac{1}{2}\mu\omega^2r^2, \end{aligned} \quad (16.34)$$

where

$$\begin{aligned} \vec{R} &= (\vec{r}_1 + \vec{r}_2)/2, & \vec{r} &= (\vec{r}_2 - \vec{r}_1), \\ \vec{Q} &= (\vec{p}_1 + \vec{p}_2), & \text{and} & \vec{p} = (\vec{p}_1 - \vec{p}_2)/2. \end{aligned}$$

$M = 2m$ and $\mu = m/2$ (m is the nucleon mass). The quantum numbers of the usual shell-model basis are:

$$|k_1 k_2 L\rangle = |(n_1 \ell_1)(n_2 \ell_2)L\rangle, \quad (16.35)$$

and the quantum numbers associated with the relative coordinates are:

$$|(n\lambda)(N\Lambda)L\rangle, \quad (16.36)$$

where (n, λ) are the radial and angular-momentum quantum numbers associated with the relative coordinate \vec{r} , and (N, Λ) go with the center-of-mass coordinate \vec{R} . The transformation between these two sets of coordinates is given by:

$$\begin{aligned} | k_1 k_2 L \rangle &= | (n_1 \ell_1)(n_2 \ell_2)L \rangle \\ &= \sum_{n\lambda N\Lambda} \langle n\lambda N\Lambda | n_1 \ell_1 n_2 \ell_2 L \rangle | (n\lambda)(N\Lambda)L \rangle. \end{aligned} \quad (16.37)$$

Given $(n_1 \ell_1)(n_2 \ell_2)L$ the quantum numbers $(n\lambda N\Lambda)$ are constrained by energy conservation

$$2n + \lambda + 2N + \Lambda = 2n_1 + \ell_1 + 2n_2 + \ell_2 \quad (16.38)$$

and the triangle condition for the angular momenta $\Delta(\lambda\Lambda L)$.

These transformation coefficients are called Moshinsky or Talmi-Moshinsky brackets after the authors who first calculated their properties. Note that changing the mass from m to $\mu = m/2$ for the relative motion means that the relative radial wavefunctions use an oscillator parameter that is effectively smaller than ω by a factor of two. A analytic formulae for the Talmi-Moshinsky brackets is given in [6]. They are used in the TBME program that is part of NuShell16.

16.5 Separation of intrinsic and center-of-mass motion for many nucleons

16.5.1 The kinetic energy part

The many-body nuclear Hamiltonian for A nucleons with two-body interactions has the form

$$H = \frac{1}{2m} \sum_i^A p_i^2 + \sum_{i < j}^A V(|\vec{r}_i - \vec{r}_j|). \quad (16.39)$$

The coordinates refer to a fixed point in space. For the internal structure of a given nucleus we are not interested in the center-of-mass motion, and we would like to rewrite the Hamiltonian as a sum of an intrinsic part H_{int} and a center-of-mass part H_{cm}

$$H = H_{int} + H_{cm}. \quad (16.40)$$

The center-of-mass Hamiltonian depends only on the center-of-mass position \vec{R}

$$\vec{R} = \frac{1}{A} \sum_i^A \vec{r}_i, \quad (16.41)$$

and momentum \vec{Q}

$$\vec{Q} = \sum_i^A \vec{p}_i. \quad (16.42)$$

The intrinsic Hamiltonian depends upon the coordinates relative to the the center-of-mass:

$$\vec{\rho}_i = \vec{r}_i - \vec{R}, \quad (16.43)$$

and

$$\vec{q}_i = \vec{p}_i - \frac{1}{A} \vec{Q}. \quad (16.44)$$

Note that in the center of mass system

$$\sum_i \vec{\rho}_i = 0. \quad (16.45)$$

The two-body interaction is explicitly a function of the center-of-mass coordinates $\vec{\rho}_i - \vec{\rho}_j = \vec{r}_i - \vec{r}_j$. The kinetic energy part of H can be rewritten as

$$T = T_{int} + T_{cm}, \quad (16.46)$$

where

$$T_{int} = \frac{1}{2m} \sum_i^A q_i^2 = \frac{2}{M} \sum_{i < j}^A (\vec{p}_{ij})^2, \quad (16.47)$$

and

$$T_{cm} = \frac{1}{2M} Q^2, \quad (16.48)$$

where

$$\vec{p}_{ij} = (\vec{p}_i - \vec{p}_j)/2, \quad (16.49)$$

and

$$M = m A. \quad (16.50)$$

Thus H separates into

$$H = H_{int} + H_{cm},$$

with

$$H_{int} = \frac{1}{2m} \sum_i^A q_i^2 + \sum_{i < j}^A V(|\vec{\rho}_i - \vec{\rho}_j|) \quad (16.51)$$

and

$$H_{cm} = T_{cm} = \frac{1}{MA} Q^2. \quad (16.52)$$

The solution to

$$H\Psi = (H_{int} + H_{cm})\Psi = E\Psi \quad (16.53)$$

has the form

$$\Psi = \Psi_{int} \Psi_{cm}, \quad (16.54)$$

with

$$H_{int}\Psi_{int} = E_{int}\Psi_{int}, \quad (16.55)$$

$$H_{cm}\Psi_{cm} = E_{cm}\Psi_{cm}, \quad (16.56)$$

and

$$E = E_{int} + E_{cm}. \quad (16.57)$$

The coordinates \vec{r}_i are not independent and therefore the equation for the intrinsic Hamiltonian Eq. (16.55) is more difficult to solve than that for the full Hamiltonian Eq. (16.53). Thus, one usually solves the full problem constrained in a way that guarantees that the center-of-mass is in a known state, such as a plane wave or the ground state of a harmonic oscillator. The intrinsic energy is obtained by subtracting E_{cm} from E , and other intrinsic properties can be obtained for the expectation value of some operators.

16.5.2 The harmonic-oscillator part

In the nuclear many-body problem one divides the hamiltonian into a mean-field (single-particle) potential U plus a residual interaction W :

$$H = \frac{1}{2m} \sum_i^A p_i^2 + \sum_i^A U(r_i) + \sum_{i < j}^A W(|\vec{r}_i - \vec{r}_j|). \quad (16.58)$$

In general $U(r_i)$ does not easily separate into an intrinsic and center-of-mass part. However, in the special case of the harmonic-oscillator potential the separation can be made

analytically:

$$\sum_i^A U^{HO}(r_i) = \frac{1}{2}m\omega^2 \sum_i^A r_i^2 = \frac{1}{2}m\omega^2 \sum_i^A \rho_i^2 + \frac{1}{2}\omega^2 MR^2. \quad (16.59)$$

Thus H separates into

$$H = H_{int} + H_{cm}, \quad (16.60)$$

with

$$H_{int} = \frac{1}{2m} \sum_i^A q_i^2 + \frac{1}{2}m\omega^2 \sum_i^A \rho_i^2 + \sum_{i < j}^A W(|\vec{\rho}_i - \vec{\rho}_j|) \quad (16.61)$$

and

$$H_{cm} = \frac{1}{MA} Q^2 + \frac{1}{2}M\omega^2 R^2, \quad (16.62)$$

Thus, if one solves Eq. (16.58) such a way that the center-of-mass is guaranteed to be in a $0s$ oscillator state, the intrinsic wavefunction and energy can be obtained.

When the single-particle levels of the oscillator potential are filled in their lowest energy state the center of mass must also be in its lowest energy energy state of $0s$ for the nucleus

with mass $M = Am$ in the potential $\frac{1}{2}M\omega^2R^2$, with a center of mass energy of

$$\langle \Psi | H_{cm} | \Psi \rangle = \frac{3}{2}\hbar\omega, \quad (16.63)$$

Many-body states for which the center-of-mass is in the $0s$ ground state are referred to as nonspurious states.

Excitations of nucleons across major shells or from a filled major shell to partially filled major shells are characterized by a single-particle energy change $\Delta E_{sp} = \Delta N\hbar\omega$, where

$$H_{sp} = \frac{1}{2m} \sum_i^A p_i^2 + \sum_i^A U^{HO}(r_i). \quad (16.64)$$

This energy change may occur all in the intrinsic motion, all in the center-of-mass motion, or partly in each.

Spurious states are formed when the center-of-mass is excited from its $0s$ ground state into its excited states. These states can be explicitly constructed by operating with \vec{R} on

one of the nonspurious states in which the center-of-mass is in the $0s$ ground state. The complete set of spurious states can be obtained from the angular momentum coupling of all such spurious states with all of the nonspurious states. For example, if one starts with the ^{16}O ground state, the $1\hbar\omega$ excitations lead to negative parity states. One of these states with $J^\pi=1^-$ (and $T=0$) is spurious.

For the special situations where the excited configuration cannot be connected to the original nonspurious configuration by the \vec{R} (vector) operator, these states are also nonspurious. The pure $0\text{p}_{1/2}$ to $0\text{d}_{5/2}$ excitation, for example, is completely nonspurious due to the triangle condition $\Delta(1/2, 5/2, 1) = 0$. There are also special SU(3) configurations that are nonspurious [7].

In order to carry out the transformation of Ψ into Ψ_{int} and Ψ_{cm} one must be sure that the basis states Ψ are complete with respect to all center-of-mass modes of a given ΔE_{sp} . The center-of-mass wavefunctions can then be explicitly constructed within the Ψ basis and projected out. Alternatively one can add a fictitious Hamiltonian that acts only on the

center-of-mass:

$$H'_{cm} = \beta \left\{ \frac{Q^2}{2Am} + \frac{1}{2}Am\omega^2R^2 - \frac{3}{2}\hbar\omega \right\}. \quad (16.65)$$

The center-of-mass for the full Hamiltonian $H + H'_{cm}$ will be in the $0s$ ground state if the constant β is made large enough so that the excitation energies of the center-of-mass are larger than all of the intrinsic excitation energies of interest. Subtraction of the constant $\frac{3}{2}\hbar\omega$ means that $E_{cm} = 0$ when the center-of-mass is in the $0s$ ground state.

Thus, the Hamiltonian

$$H + H'_{cm} - (3/2)\hbar\omega \quad (16.66)$$

with H given by Eq. (16.58), H'_{cm} given by Eq. (16.65), and the last term from (16.63), can be used to solve the nuclear many-body problem in terms of the fixed space coordinates \vec{r}_i . If one is starting with the original Hamiltonian of Eq. (16.39) in an harmonic-oscillator basis one can construct a Hamiltonian taht generates nonspurious states and is also corrected for the kinetic energy of the center-of-mass by use of Eq. (16.66).

Bibliography

- [1] B. A. Brown, C. R. Bronk and P. E. Hodgson, J. Phys. G **10**, 1683 (1984) and references therin.
- [2] B. A. Brown, S. E. Massen, J. I. Escudero, P. E. Hodgson, G. Madurga and J. Vinas, J. Phys. G **9**, 423 (1983).
- [3] J. Blomqvist and A. Molinari, Nucl. Phys. **A106**, 545 (1968).

- [4] S. Cwiok, J. Dudek, W. Nazarewicz, J. Skalski and T. Werner, Comput. Phys. Comm. **46**, 379 (1987).
- [5] M. Moshinsky, Nucl. Phys. **13**, 104 (1950).
- [6] L. Trlifaj, Phys. Rev. C **5**, 1534 (1972). link
- [7] J. Millener et al., private communication.

Chapter 17

The Woods-Saxon potential

17.1 General form

The Woods-Saxon potential is a convenient phenomenological choice for the one-body potential. It provides a model for the properties of bound-state and continuum single-particle wavefunctions. The Woods-Saxon potential (or any other one-body potential) cannot be used for the total binding energy since it is not based upon a specific two-body interaction. The parameters of the Woods-Saxon are chosen for a best fit of nuclear single-particle energies and nuclear radii. The Woods-Saxon potential is based upon the sum of a spin-independent central potential, a spin-orbit potential, and the Coulomb potential:

$$V(r) = V_o(r) + V_{so}(r) \vec{\ell} \cdot \vec{\sigma} + V_c(r), \quad (17.1)$$

where $V_o(r)$ is the spin-independent central potential:

$$V_o(r) = V_o f_o(r), \quad (17.2)$$

with a fermi shape

$$f_o(r) = \frac{1}{1 + [\exp(r - R_o)/a_o]}, \quad (17.3)$$

$V_{so}(r)$ is the spin-orbit potential:

$$V_{so}(r) = V_{so} \frac{1}{r} \frac{df_{so}(r)}{dr}, \quad (17.4)$$

with

$$f_{so}(r) = \frac{1}{1 + [\exp(r - R_{so})/a_{so}]}, \quad (17.5)$$

and $V_c(r)$ is the Coulomb potential for protons based upon the Coulomb potential for a sphere of radius R_c :

$$V_c(r) = \frac{Ze^2}{r} \text{ for } r \geq R_c$$

and

$$V_c(r) = \frac{Ze^2}{R_c} \left[\frac{3}{2} - \frac{r^2}{2R_c^2} \right] \text{ for } r \leq R_c. \quad (17.6)$$

The radii R_o , R_{so} and R_c are usually expressed as:

$$R_i = r_i A^{1/3}. \quad (17.7)$$

For nuclei with a neutron excess the protons will feel a stronger potential than the neutrons, since the average proton-neutron potential is stronger than the average neutron-neutron (or proton-proton) potential. Thus we take:

$$V_{op} = V_0 + \frac{(N - Z)}{A} V_1 \text{ for protons} \quad (17.8)$$

and

$$V_{on} = V_0 - \frac{(N - Z)}{A} V_1 \text{ for neutrons} \quad (17.9)$$

In principle, r_o and a_o could also be a little different for proton and neutrons in a nucleus with $N \neq Z$. Thus the spin-independent potential could have six parameters (and even more if any of them are allowed to take some additional mass dependence). The values of these parameters are chosen to give an overall accounting of the observed single-particle energies, the rms charge radii, and the electron scattering form factors.

The form of the spin-orbit interaction was originally taken from the form of the spin-orbit interaction used for electrons in atoms that was derived from the Dirac theory by Thomas and Frenkel [1]. For nuclear physics the spin-orbit interaction ultimately comes

from the nucleon-nucleon interaction, but there is still some debate over whether or not relativistic effects are very important. The spin-orbit interaction for nucleons in the nucleus has the opposite sign and is much larger than for electrons in the atom. In the nuclear interior a nucleon sees an equal number of spin-up and spin-down nucleons on both sides and the spin-orbit interaction must vanish. Thus, the spin-orbit potential is peaked at the nuclear surface as in Eq. (17.4), and the particular form of this equation gives a good overall description of the ℓ and mass dependence observed experimentally. In analogy to the spin-independent potential, one could introduce up to six parameters for the spin-orbit interaction. The strength of the spin-orbit interaction is chosen to reproduce spin-orbit splittings (especially for large ℓ). For $N \neq Z$ the strength V_{so} could be different for protons and neutrons, but in practice they are nearly the same. For the geometry one usually takes $r_{so} = r_o$ and $a_{so} = a_o$. Thus, the introduction of one parameter in the spin-orbit interaction V_{so} gives a good overall accounting of the data.

A typical set of parameters for the Woods-Saxon potential is [2] $V_0 = -51$ MeV, $V_1 = -33$ MeV and $V_{so} = 22$ MeV for the strengths, and $r_o = r_{so} = 1.27$ fm and $a_o = a_{so} = 0.67$ fm for the geometry. For the Coulomb term the radius is a little smaller with $r_c = 1.20$

fm. One can find in the literature many other sets of parameters that are better for specific nuclei or mass regions.

Fig. (17.2) from page 239 of Bohr and Mottelson Vol I [2] shows the neutron single-particle energies for nuclei obtained with a set of Woods-Saxon parameters for nuclei near stability similar to those given above (note that the radial quantum numbers in this figure start with one rather than with our convention of zero). One observed that as A increases more single-particle states become bound so that the energy of the most loosely bound filled orbit is always around -8 MeV.

One of the important features seen in Fig. (17.2) is that the E_n for orbitals with low- ℓ have a different slope compared to those with higher- ℓ . This results in an orbital energy crossing as a function of A that can change the magic numbers. Also as E_n becomes small the energies for the orbitals with low- ℓ tend to flatten out. For low- ℓ (with a small centrifugal barrier), a large part of the wavefunction lies outside of the potential, and thus its energy E_n becomes less sensitive to the strength of the potential. In Fig. (17.2), the orbitals with small E_n relate to excited states in nuclei near stability. As one moves towards the neutron

drip line, the orbital crossing and flattening for low- ℓ can occur for low-lying single-particle states. This effect is important for understanding the location of the neutron drip line, and the properties of nuclei near the drip line. Results for this low- ℓ effect in a deformed Woods-Saxon potential are discussed in [3], [4], [5].

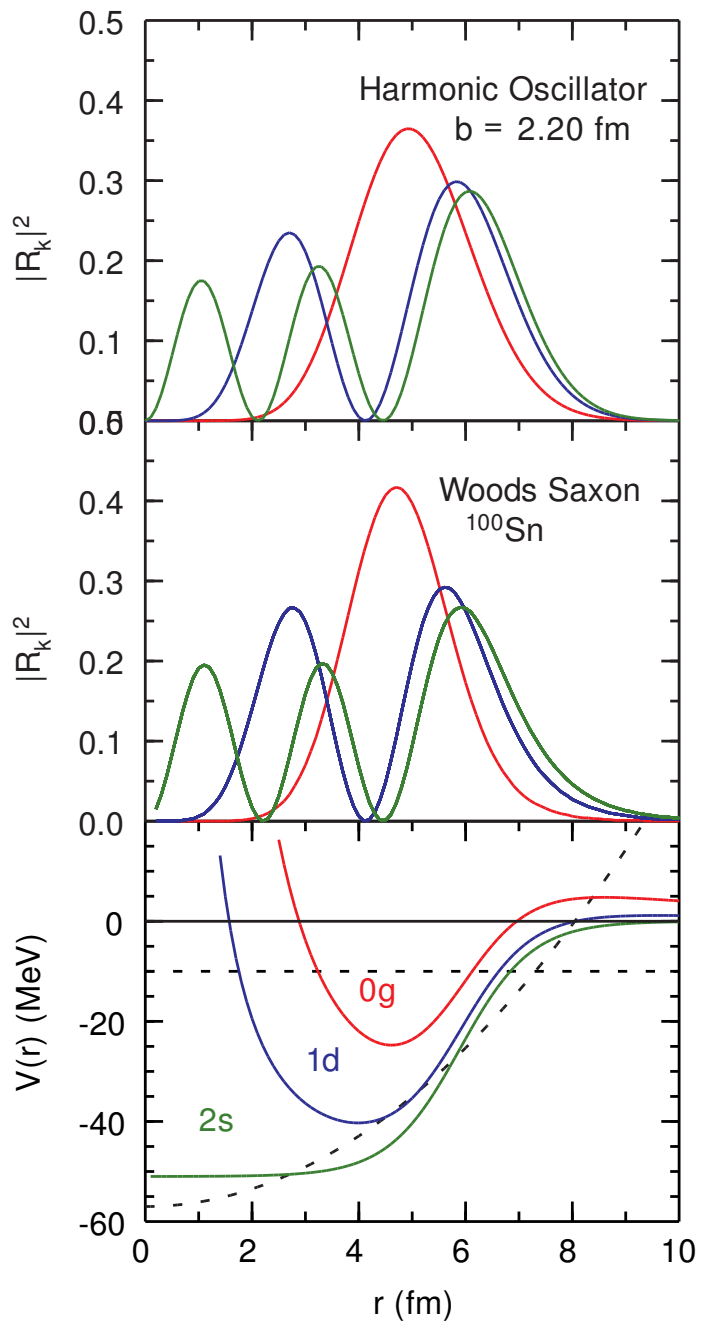


Figure 17.1: Comparison of harmonic oscillator and Woods-Saxon potentials and wavefunctions for the neutrons in ^{100}Sn . The bottom panel shows the harmonic-oscillator potential (dashed line) compared to the Woods-Saxon potential (green line labeled 2s). The lines labeled 1d (blue) and 0g (red) have the centrifugal potential for added to the Woods-Saxon. The harmonic-oscillator energy is shown by the horizontal dashed line. The spin-orbit potential is not included. The top panels show the square of the radial wavefunctions for these two potentials.

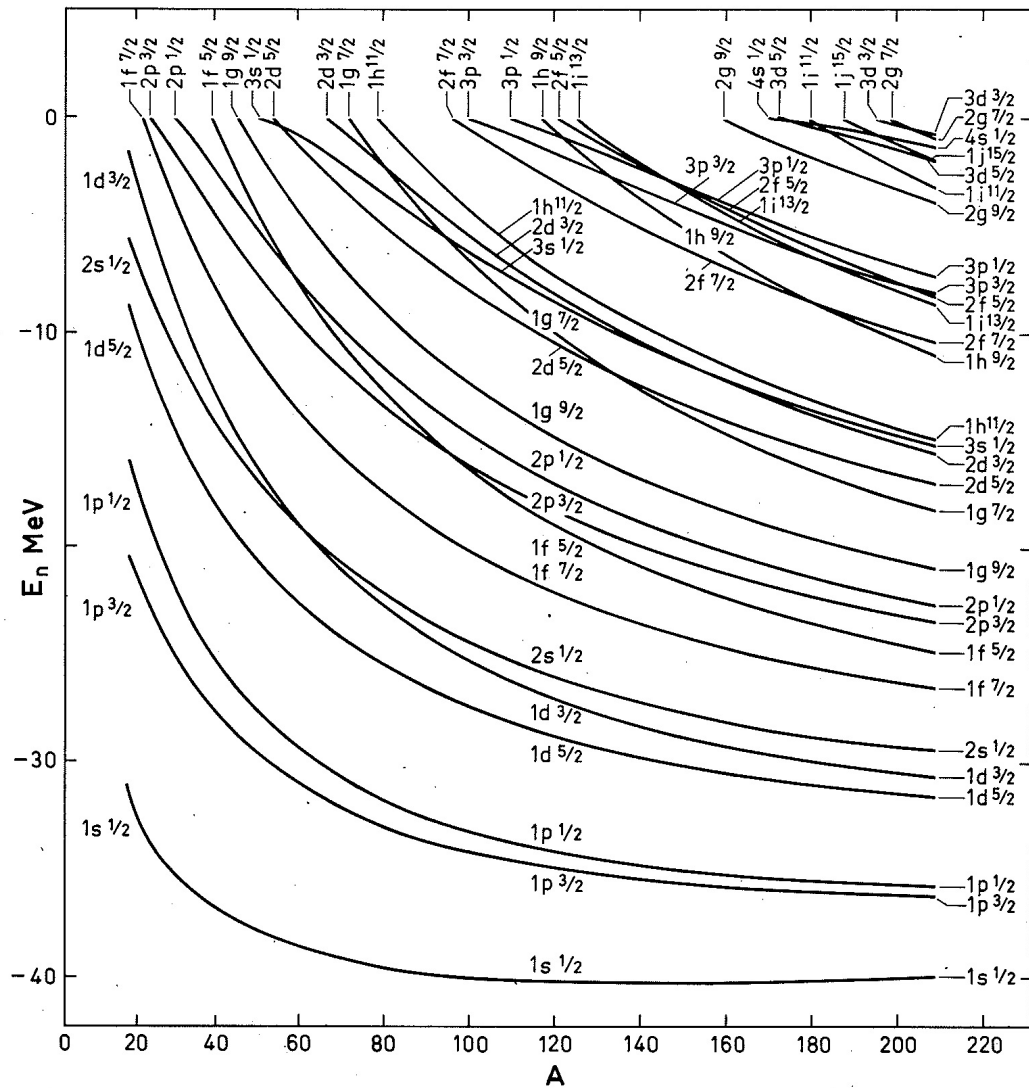


Figure 17.2: Neutron single-particle energies for nuclei near the valley of stability as a function of mass (from page 239 of Bohr and Mottelson Vol I [2]).

17.2 Computer program for the Woods-Saxon potential

The program WSPOT can be used to obtain the single-particle energies and single-particle radial wavefunctions for the bound states of the Woods-Saxon potential with quantum numbers n_r , ℓ and j . (It could also be used for other potentials if the program is modified.) It can also be used to calculate the nucleon scattering cross sections for given ℓ and j values. The program is initialized with the BM set of Woods-Saxon parameters as used in Bohr and Mottelson [2]

$$V_0 = -51 \text{ MeV},$$

$$V_1 = -33 \text{ MeV},$$

$$V_{so} = 22 \text{ MeV},$$

$$r_o = r_{so} = 1.27 \text{ fm},$$

$$a_o = a_{so} = 0.67 \text{ fm} \text{ and}$$

$$r_c = 1.20 \text{ fm}.$$

These parameters can be modified in the input files. For a given mass region, the Woods-Saxon parameters can be modified to better reproduce observables. Some examples: the rms charge radius may require an a change in r_o ; a specific spin-orbit splitting may require a change in V_{so} .

The input file is called x.dai. To run the WSPOT program with this input file type

```
wspot x
```

The output in the file x.dao.

The following provides some sample inputs for various type of calculations.

17.2.1 Example for bound states

To obtain results for protons in ^{16}O the input is, o16.dai,

```
16 8 1 1
```

```
0 0 1
0 1 3
0 1 1
1 0 1
0 2 5
0 2 3
```

The first line is (A, Z) of the nucleus and (a, z) of the nucleon. A proton would be $(a, z) = (1, 1)$ and a neutron is $(a, z) = (1, 0)$. After the blank line the next lines are a list of $n_r, \ell, 2j$ values.

The output will give (n_r , ℓ , $2j$, spe, ke, ket, rms, rmst)

for each orbit, where spe is the single-particle energy, ke is the expectation value of the kinetic energy $\langle T \rangle$, and rms is $\sqrt{\langle r^2 \rangle}$. The program will indicate if the orbit is unbound. Ket means

$$\sum_i (2j_i + 1) \langle T \rangle_i$$

where the sum runs over all orbits up to the current one, with the assumption that there are $(2j_i + 1)$ nucleons in orbit j_i . At the end this will tell you the total kinetic energy for neutrons (if the complete set is included in the input). Rmst is obtained from:

$$x_1 = \sum_i (2j_i + 1) \langle r^2 \rangle_i$$

$$x_2 = \sum_i (2j_i + 1)$$

where $\langle r^2 \rangle_i$ is the mean \sqrt{aure} radius of orbital i . The sum runs over all orbits up to the current one. Rmst = $\sqrt{(x_1/x_2)}$ is the total rms radius for all orbits up to the current one.

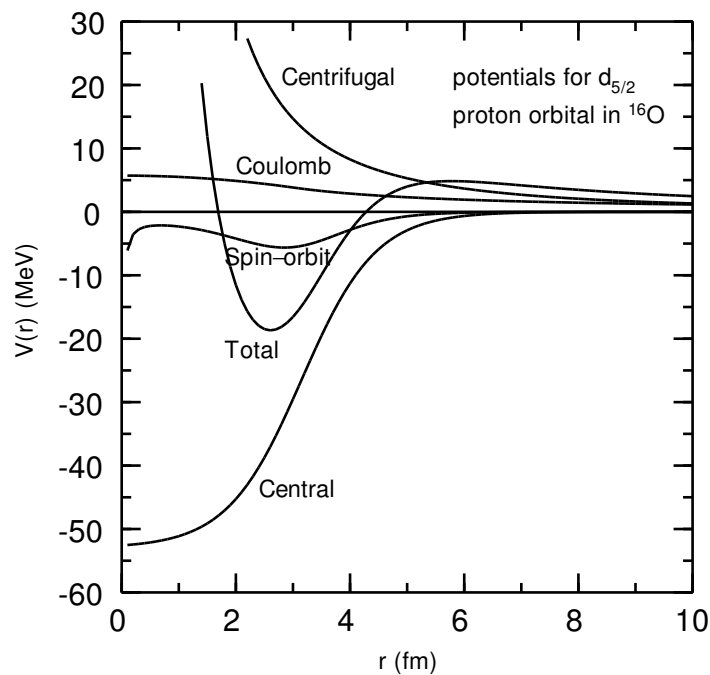


Figure 17.3: Woods-Saxon potential for a $0d_{5/2}$ proton with an ^{16}O core. The total and parts of the potential are shown.

17.2.2 Changing the potential parameters

In order to change the parameters of the central spin-independent potential the input can be modified as shown below for the example of a neutron in ^{40}Ca , ca40.dai,

```
40 20 1 0
```

```
0 0 1 0.9 0.7 1.3
0 1 3
0 1 1
1 0 1
0 2 5
0 2 3
```

where $V_N = 0.9$ modifies the central potential strength to $V'_o = V_N V_o$, and a_o and r_o are changed to $a'_o = 0.7$ and $r'_o = 1.3$. These values are used for this and all following orbits.

Other parameters can be changed by modifying the program.

One can loop over both protons and neutrons in the following way, ca40b.dai,

```
40 20 1 1
```

```
0 0 1 0.9 0.7 1.3
```

```
0 1 3
```

```
0 1 1
```

```
1 0 1
```

```
0 2 5
```

```
0 2 3
```

```
-1
```

```
40 20 1 0
```

```
0 0 1 0.9 0.7 1.3
```

```
0 1 3
```

0 1 1
1 0 1
0 2 5
0 2 3

17.2.3 Width of an unbound state resonance

For a given (ℓ, j) value the program calculates the phase shift $\delta(E)$ and the scattering cross section $\sigma(E)$ as a function of (positive) energy, where

$$\sigma(E) = \frac{4\pi(2\ell + 1)}{k^2} [\sin(\delta)]^2$$

where $E = \hbar^2 k^2 / 2m$ (m is the mass of the nucleon).

As an example, the input for the $0d_{5/2}$ proton resonance in ^{13}N , n13.dai,

```
12 6 1 1
0.1 10.0
0 2 5
```

The first line is (A, Z) of the “core” nucleus and (a, z) of the nucleon. The next line contains

emin , emax for the energy interval over which to look for a resonance. The next line contains $n_r, \ell, 2j$.

If a resonance peak is found in that interval, the program iterates over a series of steps in which this energy interval is narrowed down until the full resonance curve is found. It outputs $\text{ei}=\text{E}_r$ and $\text{G}=\Gamma$ where E_r is the resonance energy peak and Γ is the full width at half maximum of the resonance. This particular input gives $\text{E}_r=1.24$ MeV and $\Gamma=27$ keV. The output for the cross section vs E is given in the output file `x.dao`. Also a `x.top` file is made. Typing “`cps x`” will produce an `x.eps` file that shows a picture of the resonance.

The width is obtained by finding the values of sigma above and below the peak energy where the value is a factor of two smaller than that at the peak. No attempt is made to subtract a possible background due to non-resonant scattering. Making the appropriate modifications for subtracting this background would make a addition to this code.

For the scattering n_r is not a quantum number and the value in the input has no effect on the output. The value given in the `x.dao` file indicates how often the wavefunction crosses zero. Sometimes the resonance is a quasi-bound state corresponding to a particular the n_r .

value of interest. One should check in the output that the correct n_r value is given. If not, the correct value may correspond to a different energy range (or to a different value for V_N discussed in the next section).

A resonance width is useful if the resonance is reasonably sharp. Broad resonances will be asymmetry and the width itself is not a full measure of its nature. Rather one must look at the full function of σ vs E . Narrow resonances (if they exist) are at an energy below the Coulomb plus centrifugal barrier. For these light nuclei this is not more than 10 MeV which is what determines e_{\max} in this input.

17.2.4 Width of an unbound state resonance at a fixed energy

Experimentally one observes a $5/2^+$ resonance at an excitation energy of 3.547 MeV in ^{13}N with a one-proton resonance energy of $E_r = 1.60$ MeV. This is not equal to the single-particle energy obtained with the BM potential parameters. We could ask - if the potential is slightly adjusted so that the resonance is exactly at 1.60 MeV then what is the width? We need to slightly reduce the potential in order to increase the resonance energy. We could do this by hand, for example, n13b.dai,

```
12 6 1 1
0.1 10.
0 2 5 0.96
```

where the potential depth has been multiplied by 0.96 to give the resonance energy at 1.88 MeV (closer but not exactly the required value). We would then change V_N by trial and

error until the resonance is at the correct position. However, the program will automatically search for the correct V_N by the following input, n13c.dai,

```
12 6 1 1
1.60 1.60 0.8 1.2
0 2 5
```

The input 1.60,1.60,0.8,1.2 will search on V_N over the interval 0.8 to 1.2 to put the $0d_{5/2}$ resonance (single-particle energy) at exactly 1.6 MeV. Then WSPOT will scan from $E_r/2$ to $2E_r$ to find the width. The result is 67 keV which is not far from the observed width of 47(7) keV. The ratio of experiment over theory provides a measure of the spectroscopic factor, $S = 0.73(9)$, in this case.

Bibliography

- [1] Thomas, Nature **107**, 514 (1926); Frenkel, Zeits. fur Phys. **37**, 243 (1926).
- [2] A. Bohr and B. R. Mottelson, *Nuclear Structure*, Vol. I, (W. A. Benjamin, 1969), *Nuclear Structure* Vol. II, (W. A. Benjamin, 1975), page 239.
- [3] I. Hamamoto, Jour. of Phys. Conf. Series **267**, 012005 (2011).
- [4] I. Hamamoto, Phys. Rev. C **72**, 024301 (2005). link

- [5] I. Hamamoto, Phys. Rev. C **73**, 064308 (2006). link

Chapter 18

One-body operators in simple configurations

The results in this section are based on diagonal matrix elements for a one-body tensor operator and rank λ , F^λ , in the configuration Φ where all states $\alpha = (k, m) = (n, \ell, j, m)$ are filled as given by

$$\langle \Phi | \sum_i F_i^\lambda | \Phi \rangle = \sum_\alpha \langle \alpha | F^\lambda | \alpha \rangle . \quad (18.1)$$

18.1 Density for a closed-shell configuration

The density operator for $\lambda=0$ is $\delta(r - r_i)$. For the closed-shell configuration $| C \rangle$ there are several $k = (n, \ell, j)$ orbits that are completely filled. For each of these orbits there is an m degeneracy of $(2j + 1)$. The scalar density, $\rho_{qk}(r)$ for particle type ($q=\text{proton/neutron}$) in a single filled shell is given by

$$\rho_{qk}(r) = \sum_m \left[\frac{R_{qk}(r)}{r} [Y^\ell(r) \otimes \chi^s]_m^j \right]^2$$

$$= \frac{(2j+1)}{4\pi} \left[\frac{R_{qk}(r)}{r} \right]^2. \quad (18.2)$$

The total number of particles is

$$N_{qk} = \int \rho_{qk}(r) d\tau = (2j+1). \quad (18.3)$$

For many filled k states the total density is

$$\rho_q(r) = \sum_k \rho_{qk}(r), \quad (18.4)$$

and total number of particles of type q is

$$N_q = \sum_k (2j+1), \quad (18.5)$$

where the sum extends over the orbitals occupied by q .

18.2 Angular momenta for closed-shell, and single-particle, and single-hole configurations

For a filled orbital $k = (n, \ell, j)$ the total M_j value is:

$$M_j = \sum_{m=-j}^{m=j} \langle k, m | \hat{j}_z | k, m \rangle = \sum_{m=-j}^{m=j} m = 0. \quad (18.6)$$

Thus each filled j orbit has $J = 0$. The sum over all M_j gives $M = 0$, and thus we have $J^\pi = 0^+$ for the closed shell. The parity is positive since the number of particles in each j orbit is even. Only the $\lambda = 0$ term in Eq. (18.1) contribute the closed shell configurations.

For the single-particle configuration in orbital k outside of a closed shell, $|Ck\rangle$, the nucleon will go into one of states (n, ℓ, j, m) above the fermi surface. There are $(2j + 1)$ allowed M values from $-j$ to j . Thus the total angular momentum is $J = j$, and the parity is $(-1)^\ell$. For the moments we need the M -state with $M = m = j$.

For the single-hole configuration, $| Ck^{-1} \rangle$, the nucleon will be removed from one of the filled states (n, ℓ, j, m') below the fermi surface. The M value of the state is:

$$M = \sum_{m \neq m'} m = -m' + \sum_{m=-j}^{m=j} m = -m'. \quad (18.7)$$

There are $(2j + 1)$ values for M from $-j$ to j . Thus the total angular momentum is $J = j$, and the parity parity is $(-1)^\ell$. If we want to have a many-body state with $M = J = j$, then the nucleon must be removed from the single-particle state with $m' = -j$.

18.3 Electromagnetic moments

Electromagnetic moments have the general form:

$$\mathcal{M}_{em} \equiv <\Psi, J, M = J | \sum_i T_{\mu=0}^\lambda(i) | \Psi, J, M = J>, \quad (18.8)$$

where T_μ^λ is a one-body tensor operator of rank λ associated with the interaction of the nucleus with the multipole components of the electromagnetic field. This is a diagonal matrix element, and by definition we take M to have its maximum value $M = J$. The matrix elements with other M values are related to \mathcal{M}_{em} by the Wigner-Eckart theorem:

$$\langle \Psi, J, M | \sum_i T_{\mu=0}^\lambda(i) | \Psi, J, M \rangle = \frac{\langle J, M, \lambda, \mu = 0 | J, M \rangle}{\langle J, J, \lambda, \mu = 0 | J, J \rangle} \mathcal{M}_{em}. \quad (18.9)$$

For a given J value, the allowed values of the λ are determined by the triangle condition, $\Delta(J, \lambda, J)$. In particular, $\lambda_{max} = 2J$, and for $J = 0$ only $\lambda = 0$ is allowed.

18.4 Moments for single-particle and single-hole configurations

We consider the moments for $\lambda > 0$. For one-particle in orbital $k = (n, \ell, j)$ outside of a closed-shell configuration, $|\Psi\rangle = |Ck\rangle$, the moment is:

$$\mathcal{M}(Ck)_{em} = \sum_{\alpha} \langle \alpha | T_{\mu=0}^{\lambda} | \alpha \rangle + \langle k | T_{\mu=0}^{\lambda} | k \rangle, \quad (18.10)$$

where the sum over α runs over the states filled in the closed shell. Since the closed shell has $J^\pi = 0^+$ the first term in Eq. (18.10) is zero unless $\lambda=0$. For $\lambda > 0$ we have for the $|Ck\rangle$ configuration:

$$\mathcal{M}(Ck)_{em} = \langle k | T_{\mu=0}^{\lambda} | k \rangle = \langle k, m=j | T_{\mu=0}^{\lambda} | k, m=j \rangle. \quad (18.11)$$

For the one-hole configuration:

$$\mathcal{M}(Ck^{-1})_{em} = \sum_{\alpha} \langle \alpha | T_{\mu=0}^{\lambda} | \alpha \rangle - \langle k | T_{\mu=0}^{\lambda} | k \rangle, \quad (18.12)$$

and for $\lambda > 0$:

$$\begin{aligned}\mathcal{M}(Ck^{-1})_{em} &= - \langle k | T_{\mu=0}^{\lambda} | k \rangle \\ &= - \langle k, m = -j | T_{\mu=0}^{\lambda} | k, m = -j \rangle.\end{aligned}\quad (18.13)$$

Note that the particle is removed from the state $m = -j$ so that $M = J = j$. A special result of the Wigner-Eckart theorem of Eq. (18.9) is:

$$\begin{aligned}&\langle k, m = -j | T_{\mu=0}^{\lambda} | k, m = -j \rangle = \\ &= \frac{\langle j, -j, \lambda, \mu = 0 | j, -j \rangle}{\langle j, j, \lambda, \mu = 0 | j, j \rangle} \langle k, m = j | T_{\mu=0}^{\lambda} | k, m = j \rangle \\ &= (-1)^{\lambda} \langle k, m = j | T_{\mu=0}^{\lambda} | k, m = j \rangle.\end{aligned}\quad (18.14)$$

Thus, for the hole states:

$$\mathcal{M}(Ck^{-1})_{em} = (-1)^{\lambda+1} \langle k, m = j | T_{\mu=0}^{\lambda} | k, m = j \rangle. \quad (18.15)$$

The one-body operator T^λ will have terms that operate separately on the space and spin parts of the wave function. Thus, the general evaluation of the single-particle moments starts with the decomposition of the state k into its space ϕ and spin χ components:

$$|\ell, j, m\rangle = \sum_{m_\ell, m_s} \langle \ell, m_\ell, s, m_s | j, m \rangle |\phi(\ell, m_\ell) \chi(m_s)\rangle.$$

The special cases we need for the moments are:

$$|\ell, j = \ell + \frac{1}{2}, m = j\rangle = |\phi(\ell, \ell) \chi(\frac{1}{2})\rangle, \quad (18.16)$$

and

$$|\ell, j = \ell - \frac{1}{2}, m = j\rangle = \sqrt{\frac{1}{2\ell+1}} |\phi(\ell, \ell-1) \chi(\frac{1}{2})\rangle - \sqrt{\frac{2\ell}{2\ell+1}} |\phi(\ell, \ell) \chi(-\frac{1}{2})\rangle. \quad (18.17)$$

The matrix elements of T_0^λ have the form:

$$\langle n_r, \ell, j = \ell + \frac{1}{2}, m = j | T_0^\lambda | n_r, \ell, j = \ell + \frac{1}{2}, m = j \rangle$$

$$= \langle \phi(\ell, \ell) \chi\left(\frac{1}{2}\right) | T^\lambda | \phi(\ell, \ell) \chi\left(\frac{1}{2}\right) \rangle, \quad (18.18)$$

and:

$$\begin{aligned} & \langle n_r, \ell, j = \ell - \frac{1}{2}, m = j | T_0^\lambda | n_r, \ell, j = \ell - \frac{1}{2}, m = j \rangle \\ &= \left(\frac{1}{2\ell + 1} \right) \langle \phi(\ell, \ell - 1) \chi\left(\frac{1}{2}\right) | T_0^\lambda | \phi(\ell, \ell - 1) \chi\left(\frac{1}{2}\right) \rangle \\ &+ \left(\frac{2\ell}{2\ell + 1} \right) \langle \phi(\ell, \ell) \chi\left(-\frac{1}{2}\right) | T_0^\lambda | \phi(\ell, \ell) \chi\left(-\frac{1}{2}\right) \rangle. \end{aligned} \quad (18.19)$$

For these expressions I have used the fact that the electromagnetic operator T^λ is diagonal in m_s (it does not connect the states with $m_s = \frac{1}{2}$ and $m'_s = -\frac{1}{2}$).

18.5 Magnetic moments

The magnetic moment operator is defined to be

$$T_{\mu=0}^{\lambda=1} = \hat{\mu}_z = [\hat{\ell}_z g_q^\ell + \hat{s}_z g_q^s] \mu_N, \quad (18.20)$$

where g_q^ℓ and g_q^s are the orbital and spin g-factors for the proton ($q = p$) and neutron ($q = n$). Note that the operators $\hat{\ell}_z$ and \hat{s}_z are diagonal in all of the quantum numbers ℓ , m_ℓ , and m_s . The free-nucleon values for the g-factors are $g_p^\ell = 1$, $g_n^\ell = 0$, $g_p^s = 5.586$ and $g_n^s = -3.826$. The values of the magnetic moments are conventionally taken to be in units of the nuclear magneton,

$$\mu_N = \frac{e\hbar}{2m_p c} = 0.105 \text{ e fm} \quad (18.21)$$

where m_p is the mass of the proton.

From Eq. (18.15), the single-particle and single-hole magnetic moments are the same.

From Eq. (18.18) for $m = j$ and $j = \ell + \frac{1}{2}$ we have

$$\frac{\mu(j = \ell + \frac{1}{2})}{\mu_N} = \ell g_q^\ell + \frac{1}{2} g_q^s, \quad (18.22)$$

and from Eq. (18.19) for $m = j$ and $j = \ell - \frac{1}{2}$ we have

$$\begin{aligned} \frac{\mu(j = \ell - \frac{1}{2})}{\mu_N} &= \left[\frac{1}{(2\ell + 1)}(\ell - 1) + \frac{2\ell}{(2\ell + 1)}\ell \right] g_q^\ell + \left[\frac{1}{2\ell + 1} \left(\frac{1}{2} \right) + \frac{2\ell}{2\ell + 1} \left(-\frac{1}{2} \right) \right] g_q^s \\ &= \frac{(2\ell - 1)(\ell + 1)}{(2\ell + 1)} g_q^\ell - \frac{(2\ell - 1)}{(4\ell + 2)} g_q^s. \end{aligned} \quad (18.23)$$

The traditional and most compact way to write these expressions is:

$$\frac{\mu}{\mu_N} = j \left[g_q^\ell \pm \frac{g_q^s - g_q^\ell}{2\ell + 1} \right], \quad (18.24)$$

where the + sign goes with $j - \frac{1}{2}$ and the - sign goes with $j + \frac{1}{2}$. The g-factor is defined as $\mu/(\mu_N J)$ which for the single-particle case gives:

$$g = \left[g_q^\ell \pm \frac{g_q^s - g_q^\ell}{2\ell + 1} \right]. \quad (18.25)$$

These single-particle magnetic moments are called the Schmidt values. The result for neutrons in the state $j = \ell + \frac{1}{2}$ with $g_n^\ell = 0$ reduces to

$$\mu(j = \ell + \frac{1}{2}, \text{neutron}) = \frac{g_n^s \mu_N}{2} = \mu_n = -1.913 \mu_N$$

where μ_n is the magnetic moment of the neutron.

There is a short-cut for deriving these results by using the projection theorem:

$$\langle j, m | \hat{v}_z | j, m \rangle = \frac{\langle j | (\vec{j} \cdot \vec{v}) | j \rangle}{j(j+1)} \langle j, m | \hat{j}_z | j, m \rangle, \quad (18.26)$$

where v_z is any vector operating in the j -space, and the matrix element of $\vec{j} \cdot \vec{v}$ has been written without the m to indicate that the scalar matrix element does not depend upon m .

This can be derived by inserting a complete set of states $| j'm' \rangle \langle j'm' |$ (the matrix element $\langle jm | j_\mu | j'm' \rangle$ restricts $j' = j$) in the dot-product and then using the Wigner-Eckart theorem.

For the single-particle magnetic moment with $m = j$:

$$\langle j, m = j | \hat{\mu}_z | j, m = j \rangle = \frac{\langle j | (\vec{j} \cdot \vec{\mu}) | j \rangle}{(j + 1)}. \quad (18.27)$$

We can save some algebra by writing:

$$\begin{aligned} \frac{\hat{\mu}_z}{\mu_N} &= \hat{\ell}_z g_q^\ell + \hat{s}_z g_q^s = (\hat{\ell}_z + \hat{s}_z) g_q^\ell + \hat{s}_z (g_q^s - g_q^\ell) \\ &= \hat{j}_z g_q^\ell + \hat{s}_z (g_q^s - g_q^\ell) \end{aligned}$$

The matrix elements for the magnetic moment is then:

$$\frac{\langle j, m = j | \hat{\mu}_z | j, m = j \rangle}{\mu_N} = \frac{\langle j | \hat{j}^2 g_q^\ell + (\vec{j} \cdot \vec{s})(g_q^s - g_q^\ell) | j \rangle}{(j + 1)}$$

$$= j g_q^\ell + \frac{\langle j | (\vec{j} \cdot \vec{s}) | j \rangle (g_q^s - g_q^\ell)}{(j+1)}$$

The scalar matrix element of $\vec{j} \cdot \vec{s}$ can be derived using the identity $\vec{j} - \vec{s} = \vec{\ell}$ to obtain

$$\vec{j} \cdot \vec{s} = \frac{\hat{j}^2 + \hat{s}^2 - \hat{\ell}^2}{2}$$

whose expectation value is:

$$\langle j | \vec{j} \cdot \vec{s} | j \rangle = \frac{j(j+1) + s(s+1) - \ell(\ell+1)}{2},$$

and after some simplification one obtains the same result as in Eq. (18.24).

18.6 Electric quadrupole moments

The electric quadrupole operator is defined to be

$$T_{\mu=0}^{\lambda=2} = \hat{Q} = (3\hat{z}^2 - \hat{r}^2)e_q e = \sqrt{\frac{16\pi}{5}} r^2 \hat{Y}_0^2(\theta, \phi) e_q e, \quad (18.28)$$

were Y_μ^λ are the spherical harmonics. The e_q are the charges for the proton and neutron in units of e . For the free-nucleon charge we would take $e_p = 1$ and $e_n = 0$, for the proton and neutron, respectively. Although the initial operator for quadrupole moments only acts upon the protons, we will keep the general expression in terms of e_q because later we will introduce “effective charges” for the proton and neutron. By convention the electric quadrupole moment is taken to be in units of e : Quadrupole moments are usually quoted in units of $e \text{ fm}^2$ or eb where b is the “barn”, $b = 100 \text{ fm}^2$ (sometimes the e is implicit).

From Eq. (18.18) the single-particle quadrupole moment in the state $j = \ell + \frac{1}{2}$ is:

$$\frac{Q}{e} = \sqrt{\frac{16\pi}{5}} \langle Y_\ell^\ell | \hat{Y}_0^2(\theta, \phi) | Y_\ell^\ell \rangle \langle n\ell j | r^2 | n\ell j \rangle e_q. \quad (18.29)$$

where

$$\langle n\ell j | r^2 | n\ell j \rangle = \int R_{n_r, \ell, j}^2 r^2 dr.$$

The angular integral is given by:

$$\begin{aligned} \langle Y_\ell^\ell | Y_0^2 | Y_\ell^\ell \rangle &= (-1)^\ell \begin{pmatrix} \ell & 2 & \ell \\ -\ell & 0 & \ell \end{pmatrix} (2\ell+1) \sqrt{\frac{5}{4\pi}} \begin{pmatrix} \ell & 2 & \ell \\ 0 & 0 & 0 \end{pmatrix} \\ &= -\sqrt{\frac{5}{4\pi}} \left(\frac{\ell}{2\ell+3} \right). \end{aligned} \quad (18.30)$$

Thus, the single-particle quadrupole moment in the state $j = \ell + \frac{1}{2}$ simplifies to:

$$\frac{Q(i)}{e} = - \left(\frac{2\ell}{2\ell+3} \right) \langle n\ell j | r^2 | n\ell j \rangle e_q. \quad (18.31)$$

From (18.15), the single-hole quadrupole moment in the state $j = \ell + \frac{1}{2}$ is:

$$\frac{Q(i^{-1})}{e} = \left(\frac{2\ell}{2\ell+3} \right) \langle n\ell j | r^2 | n\ell j \rangle e_q. \quad (18.32)$$

The radial integrals can be evaluated with the chosen radial wavefunctions such as harmonic-oscillator or Woods-Saxon.

For the general case that includes both $j = \ell + \frac{1}{2}$ and $j = \ell - \frac{1}{2}$ one obtains for particle states:

$$\frac{Q(i)}{e} = - \left(\frac{2j-1}{2j+2} \right) \langle n\ell j | r^2 | n\ell j \rangle e_q. \quad (18.33)$$

and for hole states:

$$\frac{Q(i^{-1})}{e} = \left(\frac{2j-1}{2j+2} \right) \langle n\ell j | r^2 | n\ell j \rangle e_q. \quad (18.34)$$

Chapter 19

Energy density functionals

394

19.1 The Skyrme energy-density functional

The Skyrme approximation [1], [2], [3] is an $s-$ and $p-$ wave expansion of an effective two-body interaction together with an $s-$ wave density dependent interaction. It is given by

$$V_{\text{Skyrme}} = V_s + V_p + V_{so} + V_{coul}, \quad (19.1)$$

where

$$V_s = t_0(1 + x_0 P_\sigma) \delta + \frac{1}{6} t_3(1 + x_3 P_\sigma) \rho^\alpha(\mathbf{R}) \delta, \quad (19.2)$$

$$V_p = \frac{1}{2} t_1(1 + x_1 P_\sigma) (\mathbf{k}'^2 \delta + \delta \mathbf{k}^2) + t_2(1 + x_2 P_\sigma) \mathbf{k}' \cdot \delta \mathbf{k}, \quad (19.3)$$

and

$$V_{so} = i W_0(\sigma_i + \sigma_j) \cdot \mathbf{k} \times \delta \mathbf{k}. \quad (19.4)$$

$\delta = \delta(\mathbf{r}_i - \mathbf{r}_j)$, $\mathbf{k} = (1/2i)(\nabla_i - \nabla_j)$ is the relative momentum operator acting on the wave function to the right, and \mathbf{k}' is the adjoint of \mathbf{k} . P_σ is the spin-exchange operator and $\mathbf{R} = (\mathbf{r}_i + \mathbf{r}_j)/2$.

The spin-exchange operator is given by

$$\frac{1}{2}(1 + \vec{\sigma}_1 \cdot \vec{\sigma}_2), \quad (19.5)$$

and has the property that when acting on the two-nucleon spin wavefunction that

$$P_\sigma | \chi(s_1)\chi(s_2) S, S_z > = | \chi(s_2)\chi(s_1) S, S_z > = (-1)^{S+1} | \chi(s_1)\chi(s_2) S, S_z >. \quad (19.6)$$

We can calculate the closed-shell expectation value of the first term in Eq. (19.1) as

$$\begin{aligned} < C | V | C > &= \frac{1}{2} \sum_{\alpha\beta} < \alpha\beta | t_0(1 + x_0 P_\sigma) \delta | \alpha\beta > \\ &= \frac{1}{2} \sum_{\alpha\beta} < \alpha_1\beta_2 | t_0(1 + x_0 P_\sigma) \delta (1 - P_{12}) | \alpha_1\beta_2 >_p, \end{aligned} \quad (19.7)$$

where P_{12} is the particle exchange operator given by

$$P_{12} = (-1)^\ell P_\sigma P_\tau. \quad (19.8)$$

The wavefunctions the right-hand side of Eq. (19.7) are product wavefunctions. P_τ is the isospin-exchange operator. For the delta function the relative angular momentum must be $\ell=0$. For two neutrons, $P_\tau = 1$ and we have

$$\langle C | V | C \rangle_{nn} = \frac{t_o}{2} \sum_{\alpha\beta} \int [\phi_\alpha^*(\vec{r})\phi_\alpha(\vec{r})] [\phi_\beta^*(\vec{r})\phi_\beta(\vec{r})] (1 - x_o)(1 - P_\sigma) d\tau, \quad (19.9)$$

where $d\tau$ indicates integration over the volume, and we have used $P_\sigma^2 = 1$. One can show that the expectation value the $\sigma_1 \cdot \sigma_2$ part of P_σ is zero [2]. Thus we have for two neutrons

$$\langle C | V | C \rangle_{nn} = \frac{t_o}{4}(1 - x_o) \int \rho_n^2 d\tau = \frac{a_{T1}}{4} \int \rho_n^2 d\tau, \quad (19.10)$$

with an analogous result for two protons. Here I have introduced the parameter $a_{T1} = t_o(1 - x_o)$ that is the strength of the delta function for the $T = 1$ part of the interaction. For the proton-neutron interaction, $P_\tau = 0$, and we have

$$\langle C | V | C \rangle_{pn} = \frac{t_o}{4}(2 + x_o) \int (\rho_p \rho_n + \rho_p \rho_n) d\tau = \frac{t_o}{2}(2 + x_o) \int \rho_p \rho_n d\tau$$

$$= \frac{a_{T1}}{4} \int \rho_p \rho_n d\tau + \frac{3a_{T0}}{4} \int \rho_p \rho_n d\tau. \quad (19.11)$$

Here I have introduced the parameter $a_{T0} = t_o(1 + x_o)$ that is the strength of the delta function for the $T = 0$ part of the interaction. The integrands in these equations together with those of the density-dependence s -wave term of Eq. (19.1) can be combined to obtain the s -wave energy density for a closed-shell configuration defined as

$$\langle C | V_s | C \rangle = \int \mathcal{E}_s d\tau, \quad (19.12)$$

with

$$\mathcal{E}_s = \frac{1}{4} t_0 [(x_0 + 2)\rho^2 - (2x_0 + 1)(\rho_p^2 + \rho_n^2)] + \frac{1}{24} t_3 \rho^\alpha [(x_3 + 2)\rho^2 - (2x_3 + 1)(\rho_p^2 + \rho_n^2)]. \quad (19.13)$$

The more complicated p -wave integrals are derived in [2]. The total energy density is a sum of terms [4]

$$\mathcal{E} = \mathcal{E}_s + \mathcal{E}_{pv} + \mathcal{E}_{ps} + \mathcal{E}_{so} + \mathcal{E}_{sot}, \quad (19.14)$$

with

$$\mathcal{E}_{pv} = \frac{1}{8}[t_1(x_1 + 2) + t_2(x_2 + 2)]\tau\rho + \frac{1}{8}[t_2(2x_2 + 1) - t_1(2x_1 + 1)](\tau_p\rho_p + \tau_n\rho_n), \quad (19.15)$$

$$\begin{aligned} \mathcal{E}_{ps} &= \frac{1}{32}[3t_1(x_1 + 2) - t_2(x_2 + 2)](\nabla\rho)^2 \\ &- \frac{1}{32}[3t_1(2x_1 + 1) + t_2(2x_2 + 1)][(\nabla\rho_p)^2 + (\nabla\rho_n)^2] \end{aligned} \quad (19.16)$$

$$\mathcal{E}_{so} = \frac{W_0}{2}[\mathbf{J} \cdot \nabla\rho_p + \mathbf{J}_p \cdot \nabla_p\rho_p + \mathbf{J}_n \cdot \nabla\rho_n], \quad (19.17)$$

$$\mathcal{E}_{sot} = -\frac{1}{16}(t_1x_1 + t_2x_2)\mathbf{J}^2 + \frac{1}{16}(t_1 - t_2)[\mathbf{J}_p^2 + \mathbf{J}_n^2]. \quad (19.18)$$

The densities in these equations are

$$\rho_q(r) = \sum_{\alpha} |\phi_{q\alpha}(r)|^2, \quad (19.19)$$

$$\tau_q(r) = \sum_{\alpha} |\nabla \phi_{q\alpha}(r)|^2 \quad (19.20)$$

$$\mathbf{J}_q(r) = i \sum_{\alpha} \phi_{q\alpha}^*(r) [\sigma \times \phi_{q\alpha}(\mathbf{r})], \quad (19.21)$$

$$\rho(r) = \rho_p(r) + \rho_n(r), \quad (19.22)$$

$$\tau(r) = \tau_p(r) + \tau_n(r), \quad (19.23)$$

$$\mathbf{J}(r) = \mathbf{J}_p(r) + \mathbf{J}_n(r), \quad (19.24)$$

and

$$(\Delta f) = \frac{1}{r} \left[\frac{d^2}{dr^2} r f(r) \right], \quad (19.25)$$

where the derivative operates only inside the brackets.

The p -wave term has been divided into two terms, a volume term \mathcal{E}_{pv} , and a surface term \mathcal{E}_{ps} . The spin-orbit term is divided into two terms, \mathcal{E}_{so} coming from Eq. (19.4) that depends on W_o , and the other \mathcal{E}_{sot} coming from Eq. (19.3). The second term is often not included. The zero-range form of the two-body tensor interaction also contributes to \mathcal{E}_{sot}

[5] (that is why it is called “sot”). The implications of this tensor contribution have been considered in [6].

The advantage of this formulation is that all of these results are analytic in the densities. Hence the calculations are relatively fast. Starting with the energy density of Eq. (19.14) we can derive Hartree-Fock potential by taking the derivative with respect to the wavefunctions contained in the densities. This results in with the results in a non-local potential for protons ($q = p$) and neutrons ($q = n$) given by

$$U_q(r) = U_{q,0}(r) + U_{q,e}(r), \quad (19.26)$$

where

$$U_{q,0}(r) = U_{q,s}(r) + U_{q,p}(r) + U_{q,so}(r) + U_{q,sot}(r). \quad (19.26)$$

The terms are given by

$$U_{q,s}(r) = \frac{t_0}{2} ([2 + x_0] \rho - [2x_0 + 1] \rho_q) + \frac{t_3}{12} ([2 + x_3] \rho - [2x_3 + 1] \rho_q) \rho^\alpha, \quad (19.27)$$

$$U_{q,p}(r) = \frac{t_1}{16} ([2 + x_1] [2\tau - 3(\Delta\rho)] - [2x_1 + 1] [2\tau_q - 3(\Delta\rho_q)]), \quad (19.28)$$

$$+ \frac{t_2}{4} ([2 + x_2] [2\tau + (\Delta\rho)] + [2x_2 + 1]) [2\tau_q + (\Delta\rho_q)], \quad (19.29)$$

$$U_{q,so}(r) = \frac{1}{r} \left\{ \frac{W_0}{2} \left[\frac{d}{dr} (\rho + \rho_q) \right] \right\} [\ell \cdot \sigma], \quad (19.30)$$

$$U_{q,sot}(r) = \left\{ \frac{1}{8} [(t_1 - t_2) J_q] - \frac{1}{8} [t_1 x_1 + t_2 x_2] J \right\} [\ell \cdot \sigma] \quad (19.31)$$

and

$$U_{q,e}(r) = -\nabla \cdot [G(t_1, t_2, x_1, x_2, \rho, \rho_q)] \nabla, \quad (19.32)$$

where

$$G = \frac{t_1}{8} ([2 + x_1] \rho - [x_1 + 1] \rho_q) + \frac{t_2}{8} [(2 + x_2) \rho + (2x_2 + 1) \rho_q]. \quad (19.33)$$

The $U_{q,e}$ term of Eq. (19.32) can be combined with the kinetic energy operator to write a Schroedinger-like equation with an effective mass:

$$\left\{ -\nabla \cdot \frac{\hbar^2}{2m_q^*(r)} \nabla + U_{q,0}(r) \right\} \phi_{i,q}(\mathbf{r}) = \epsilon_{i,q} \phi_{i,q}(\mathbf{r}). \quad (19.34)$$

where the effective mass is defined by

$$\frac{\hbar^2}{2m_q^*(r)} = \frac{\hbar^2}{2m} + G(t_1, t_2, x_1, x_2, \rho, \rho_q) \quad (19.35)$$

Eq. (19.34) can be rewritten in terms of the Schrödinger equation with an energy-dependent potential [7]:

$$\left\{ -\frac{\hbar^2}{2m_q} \nabla^2 + U_q^*(r, \epsilon) \right\} \phi_{i,q}(\mathbf{r}) = \epsilon_{i,q} \phi_{i,q}(\mathbf{r}), \quad (19.36)$$

where

$$U_q^*(r, \epsilon) = \frac{m_q^*(r)}{m} \left[U_{q,0}(r) + \frac{1}{2} \left(\frac{d^2}{dr^2} \frac{\hbar^2}{2m_q^*(r)} \right) - \frac{m_q^*(r)}{2\hbar^2} \left(\frac{d}{dr} \frac{\hbar^2}{2m_q^*(r)} \right)^2 \right] + \left[1 - \frac{m_q^*(r)}{m} \right] \epsilon_{i,q} \quad (19.37)$$

The procedure for solving these equations for a given nucleus is as follows. (1) Make a reasonable guess for the shape of the potential, for example, by using a Woods-Saxon

potential. (2) Use this potential to calculate the radial wavefunctions for all of the orbitals up to the Fermi surface of a closed-shell configuration. (3) Use the radial wavefunctions to contract the densities. (4) Use these densities with a set of Skyrme parameters to construct the Skyrme potential. (5) Use this Skyrme potential to obtain a new set of radial wavefunctions. (6) Repeat (3-5) until the result converges according to some criteria for the change in binding energy and radius. It can happen that the iterative procedure diverges indicated that the parameters are probably not suitable. The parameters can be determined by doing the calculations for a chosen set of nuclei that might be described by doubly-closed shell configuration. The one can be a least-squares fit of the parameters to the binding energy and charge radius data for these nuclei. In addition one might include information on the single-particle energies as was done in [8].

The Kohn-Sham theorem [9], [10] says that an energy density functional (EDF) exists that will give the exact energy for a complex wavefunction within the context of the Hartree-Fock equations for a closed-shell system. However, the theorem does not tell how to derive this functional. One has to make reasonable physical guesses as to its form and see how well it works. The EDF does not have to be derivable from an interaction. One can regard the

Skyrme formulation as a specific guess for a form for the EDF that is obtained starting with an interaction.

In principle one would like to derive the Skyrme parameters from the experimental nucleon-nucleon interaction. This involves understanding the effect of the truncation of the actual many-body wave function to the closed-shell structure assumed in the derivation. It also requires an understanding of the contributions of real three-body forces. There has not yet been a quantitative derivation of the Skyrme parameters from the first principles.

The simplest EDF calculations are those obtained in a spherical basis without the pairing interaction. Results for these type of calculations with the Skx EDF are discussed in the next section. These calculations can be improved by calculating the energy in a deformed basis and finding the minimum as a function of the quadrupole deformation β . One can also add the pairing interaction, either directly in the EDF calculations by using the Hartree-Fock Bogoliubov (HFB) method, or by using one of BCS-type methods on top of HF.

There are hundreds of parameter sets for the Skyrme EDF [11]. We will discuss some details of the Skx set [8] below. A recent example that uses HFB in a deformed basis is

UNEDF2 [12]. The binding energies obtained with UNEDF2 compared to experiment are shown in Fig. (19.1). The rms deviation for the binding energies is 1.95 MeV [12]. One can improve the rms deviation by adding semi-phenomenological terms. For example, the BSk25 model of [13] obtains 0.54 MeV for the rms. There are large uncertainties in the extrapolation of these models to the location of the neutron drip line [14], [15].

The relativistic mean-field is an alternative to the Skyrme HF. The relativistic description of nuclear systems uses a field theoretical approach (quantum hydrodynamics) where the interaction of nucleons is described by an exchange of mesons. [16] I will use the non-linear parameter set NL3 [17] that gives a good description of binding energies and radii.

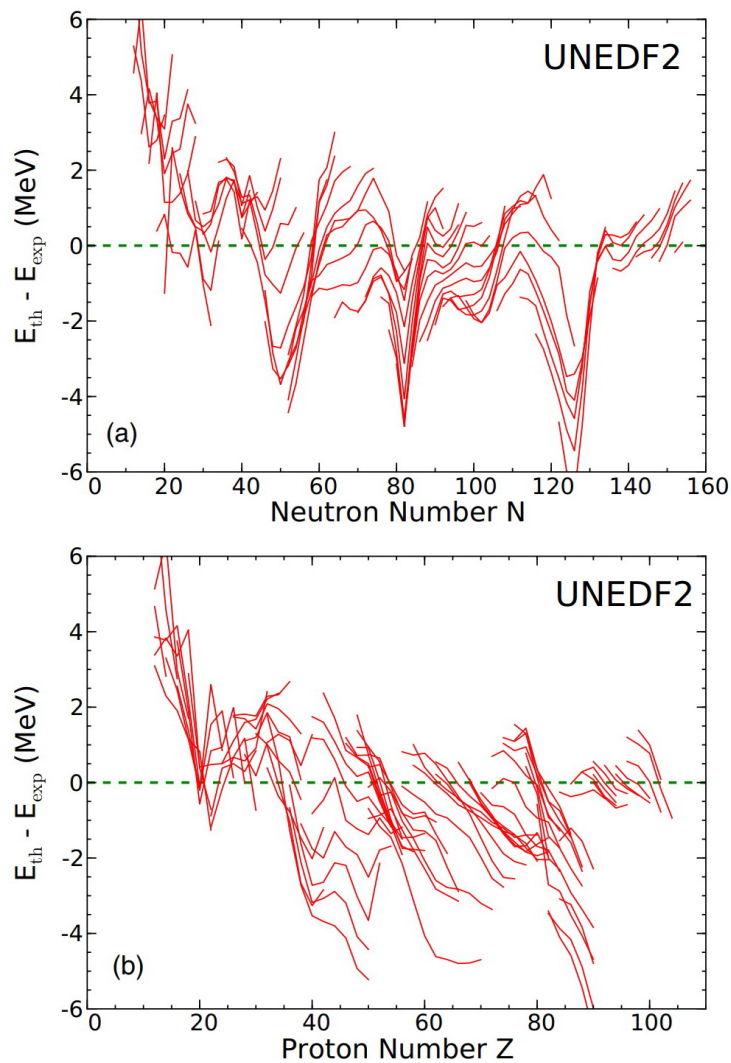


Figure 19.1: The difference between the experimental binding energies and those obtained with the UNEDF2 EDF.

19.2 Nuclear matter with the Skyrme energy-density functional

For A nucleons in volume V , the density is $\rho = A/V$. The energy density is $\mathcal{E} = E/V = (E\rho)/A$. Thus we obtain for nuclear matter

$$[E/A] = \mathcal{E}/\rho. \quad (19.38)$$

The pressure in terms of $[E/A]$ (for fixed A) is given by

$$P = -\frac{\partial E}{\partial V} = \frac{A}{V^2} \frac{\partial E}{\partial \rho} = \rho^2 \frac{\partial}{\partial \rho} [E/A], \quad (19.39)$$

and in terms of the energy density \mathcal{E} the pressure is

$$P = \rho^2 \frac{\partial}{\partial \rho} [\mathcal{E}/\rho] = \rho \frac{\partial \mathcal{E}}{\partial \rho} - \mathcal{E}. \quad (19.39)$$

In the limit of nuclear matter the surface terms \mathcal{E}_{ps} , \mathcal{E}_{so} and \mathcal{E}_{sot} , can be neglected. And the kinetic energy densities, τ , are replaced by the form obtained in the Fermi gas limit. The result is commonly expressed [4] in terms of the asymmetry parameter,

$$I = (N - Z)/A, \quad (19.40)$$

with the result

$$[E/A] = [E/A]_{kin} + [E/A]_s + [E/A]_p, \quad (19.41)$$

with

$$[E/A]_{kin} = \frac{3}{5} \frac{\hbar^2}{2m} \left(\frac{3\pi^2}{2} \right)^{2/3} \rho^{2/3} F_{5/3}, \quad (19.42)$$

$$[E/A]_s = \frac{1}{8} t_0 \rho [2(x_0 + 2) - (2x_0 + 1)F_2] + \frac{1}{48} t_3 \rho^{\alpha+1} [2(x_3 + 2) - (2x_3 + 1)F_2], \quad (19.43)$$

$$[E/A]_p = \frac{3}{40} \left(\frac{3\pi^2}{2} \right)^{2/3} \rho^{5/3} \left\{ [t_1(x_1 + 2) + t_2(x_2 + 2)]F_{3/2} + \frac{1}{2}[t_2(2x_2 + 1) - t_1(2x_1 + 1)]F_{8/3} \right\}, \quad (19.44)$$

where

$$F_m(I) = \frac{1}{2}[(1 + I)^m + (1 - I)^m]. \quad (19.45)$$

These are called equations of state (EOS). These expressions contain four terms that can be summarized as

$$[E/A](\rho) = a\rho + b\rho^\gamma + c\rho^{2/3} + d\rho^{5/3}, \quad (19.46)$$

where $\gamma = \alpha + 1$, and a, b, c and d are constants that depend on the Skyrme parameters. The first term is from the delta-function part that depends on t_0 and x_0 , the second term is from the density dependent part that depends on t_3 and x_3 , the third term is the Fermi-gas kinetic energy, and the fourth term depends on t_1, t_2, x_1 and x_2 . The effective mass is given by

$$\frac{m^*(\rho)}{m} = \frac{c}{c + d\rho}. \quad (19.47)$$

One usually applies these equations to two limits. One the for symmetric nuclear matter EOS where $N = Z$ and $I = 0$, and the other for the neutron matter EOS where $Z = 0$, $A = N$ and $I = 1$. The difference between these two is called the symmetry energy

$$S(\rho) = [E/A]_{(I=1)}(\rho) - [E/A]_{(I=0)}(\rho). \quad (19.48)$$

The expansion of $[E/A]_{(I=0)}$ around $\rho = \rho_o = 0.16$ nucleons/fm³ is expressed as

$$[E/A](\rho) = [E/A]_o + \frac{K_o}{2} \left[\frac{(\rho - \rho_o)}{3\rho_o} \right]^2, \quad (19.49)$$

where $[E/A]_o = -16$ MeV, the first derivative is zero, and K_o is the symmetric nuclear matter incompressibility coefficient. The expansion of the symmetry energy around ρ_o nucleons/fm³ is expressed as

$$S(\rho) = J + L \frac{(\rho - \rho_o)}{3\rho_o} + \frac{K_{sym}}{2} \left[\frac{(\rho - \rho_o)}{3\rho_o} \right]^2. \quad (19.50)$$

Note that one is able to extrapolate properties of nuclei all the way to neutron matter due to the specific analytic form of the assumed Skyrme functional. If one does not start from such an assumed form it is much more difficult to make the extrapolation [19].

One can understand the Skyrme functional by looking at symmetric nuclear matter EOS as shown in Fig. (19.2). The delta-function part (term a) by itself would lead to infinitely bound diverging system. In order to obtain nuclear saturation of $(E/A) = -16$

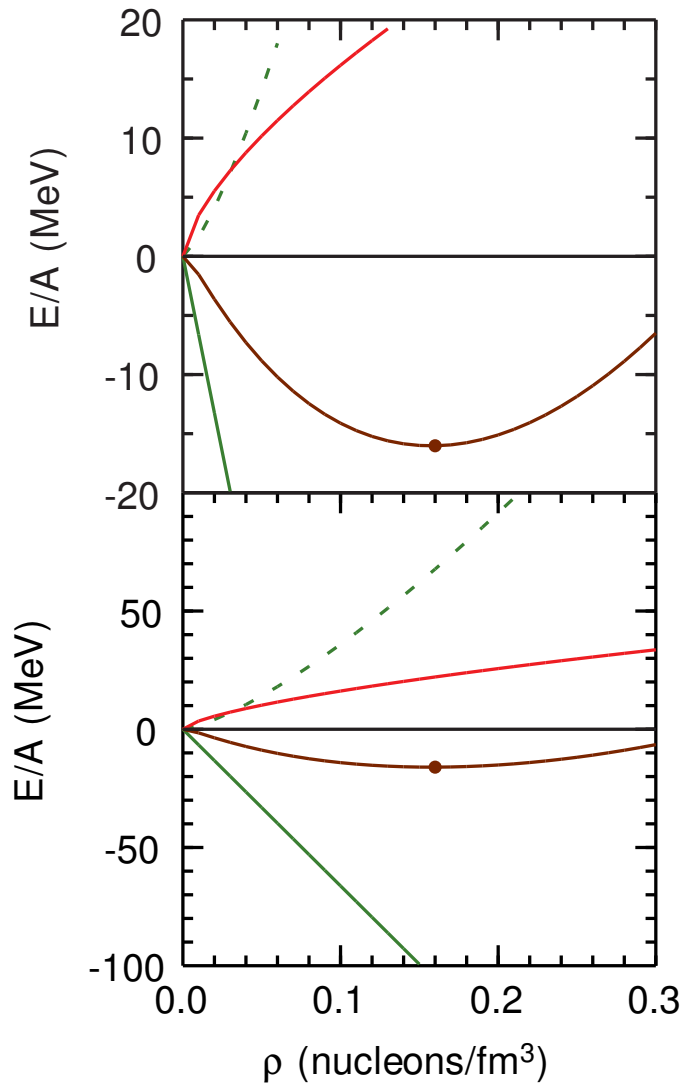


Figure 19.2: The symmetric nuclear matter EOS obtained with the Ska35 functional from [18]. The green line is from the delta-function contribution (term a), the dashed green line from the density-dependent delta function (term b), the red line if the kinetic energy contribution (term c), and the brown line is the total. In this case the effective-mass contribution (term d) is small.

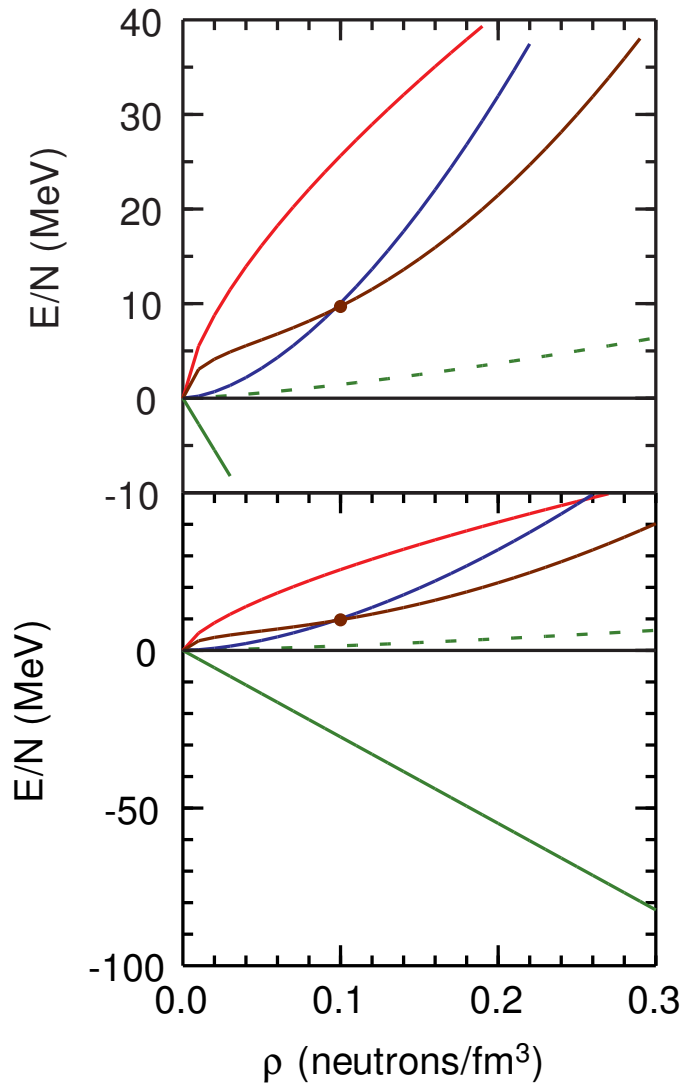


Figure 19.3: The neutron matter EOS obtained with the Ska35 functional from [18]. The color codes are the same as in Fig. (19.2), but the brown line has been added for the contribution from the d term

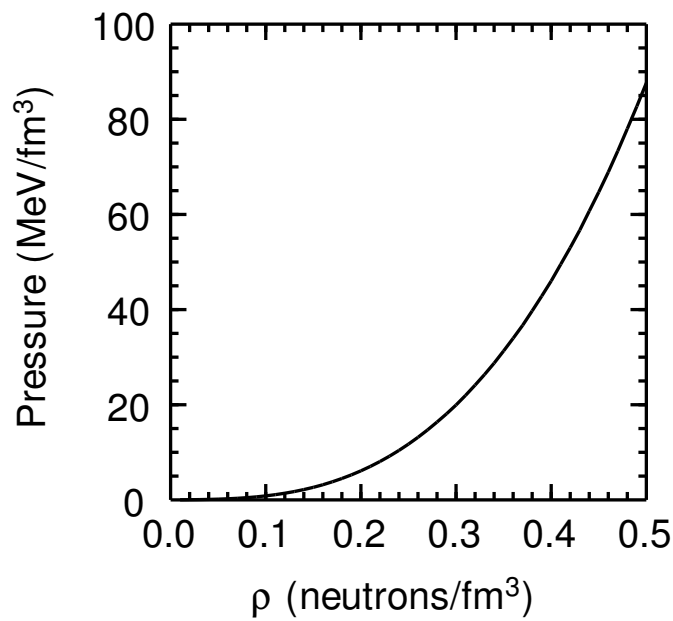


Figure 19.4: The pressure for neutron matter obtained with the Ska35 functional form [18].

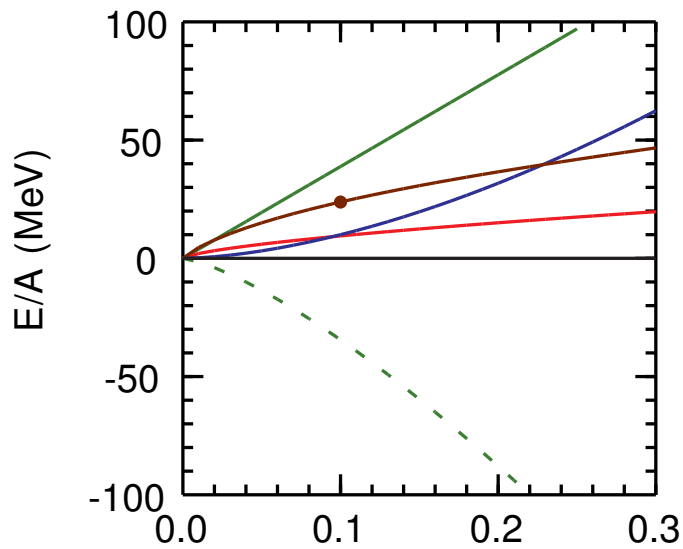


Figure 19.5: The symmetry energy obtained with the Ska35 functional from [18]. The color codes are the same as in Fig. (19.3).

MeV at $\rho_o = 0.16$ nucleons/fm³ (the brown point in Fig. (19.2)), one adds a repulsive density-dependence delta interaction (term b). By fitting the Skyrme parameters to nuclear binding energies and radii, one determines the relative strengths of a and b that are required to achieve saturation. The individual parts may not be physically meaningful, but they give a total EOS that describes nuclear properties. In the relativistic form of the EDF one obtains these two parts from the sum of σ and ω exchange potentials obtained in the Walecka model [20]. In this model there is a large cancellation between an attractive scalar potential (from σ) and a repulsive vector potential (from ω). The strengths of these two terms are obtained from a fit to nuclear properties.

The energy of the giant monopole resonance depends strongly on K_o , and the data is consistent with the range of 217-240 MeV [21]. In the Skyrme functional the value of K_o is highly correlated with the power of the density dependence α . For example, the range of $\alpha=0.14$ to 0.35 used in [18] corresponds to a K_o range of 212-242 MeV.

The results for the neutron matter EOS are shown in Fig. (19.3). In this the density-dependent term is small, and the neutron EOS at low density is a result of a cancellation

between the attractive delta function part and the repulsive kinetic energy. The relatively large d term contribution in Fig. (19.3) is a result of requiring that the maximum mass of a neutron star is about 2.1 solar masses [18]. From Eq. (19.46) this means that the effective mass is smaller than unity. Binding energies and rms charge radii constrain the value of the neutron matter EOS at $\rho_{10} = 0.10$ neutron/fm³ [22], [23] shown by the brown point in Fig. (19.3). In Fig. (19.5) the symmetry energy from Eq. (19.48) is shown.

The slope of the neutron EOS near ρ_o or ρ_{10} is very poorly determined from nuclear binding energies and charge radii [24]. This means that the slope of the symmetry energy L in Eq. (19.50) is poorly determined. However, there is a very high correlation between the size of the neutron skin (the difference in the neutron and proton rms radii) and the slope [24], [25], [22]. This result has lead to investigation of neutron radii from parity-violating electron scattering experiments [26], [27]. One can also determine the neutron rms radius in neutron-rich nuclei from a measurement of the charge radius in its proton-rich mirror nucleus [28]. One can also constrain the slope in the Skyrme neutron EOS by fitting to the results of ab-initio calculations of the EOS for very low-density neutron matter [23].

19.3 Results with the skx functional

The have been many attempts to obtain the Skyrme parameters from various types of experimental data. In this book I will concentrate on two recent results. One is the skx Hamiltonian that is obtained by applying the above equations to the eleven closed-shell nuclei: ^{16}O , ^{34}Si , ^{40}Ca , ^{48}Ca , ^{48}Ni , ^{88}Sr , ^{100}Sn , ^{132}Sn and ^{208}Pb . The data include the binding energies of these nuclei, together with five rms charge radii and 65 single-particle energies. Ten parameters in Eq. (19.1) were varied (although only six linear-combinations are well determined). The skx spin-orbit energy-density leaves out terms involving t_1 , t_2 , x_1 and x_2 , and a generalized two-parameter spin-orbit force based upon the Hartree reduction was used [29]. skx uses the Friedman-Pandharipande neutron matter equation of state [30] as a constraint skx also introduces a new parameter that is needed to reproduce the mirror displacement energies by the addition of a charge symmetry breaking (CSB) interaction (skxcsb [31]). The values of the Skyrme parameters for skx are given in [8].

19.3.1 Binding energies

The binding energies for the region of nuclei up to $A = 60$ vary by hundreds of MeV, yet we consider theoretical calculations that reproduce experiment to the level of several hundred keV to an MeV. The “coast to coast” situation for all nuclei between the drip lines is illustrated in Fig. (19.6) where the BE obtained with the MSk7 HF calculations [32] are shown for all nuclei between the proton and neutron drip lines centered on $Z = 20$ (left-hand side) and $N = 20$ (right-hand side) and compared to experiment where known.

The drip line is reached in each case when the derivative of the BE curve with respect to proton or neutron number goes to zero. One observes in the bottom panels of Fig. (19.6) an apparently featureless and smooth curve with the data in agreement with theory. However, we are interested in a much higher level of detail which is illustrated in the top panel by subtracting a smooth curve given by the liquid drop model (LDM) from theory and experiment. This top curve brings out the detail related the microscopic aspects of the nuclear shell model.

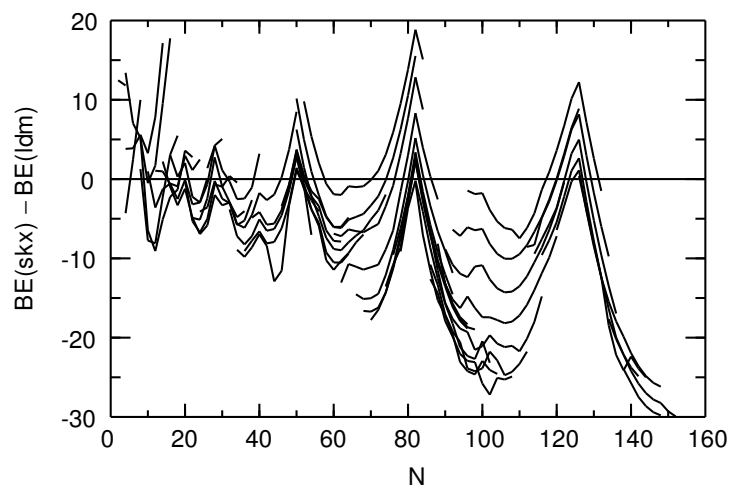


Figure 19.6: The difference between the binding energies obtained from the liquid-drop model and those obtained with Skx in a spherical basis without pairing for even-even nuclei.

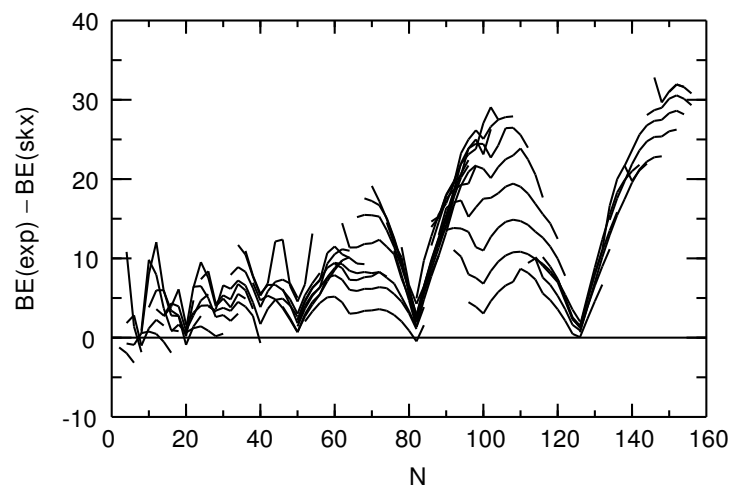


Figure 19.7: The difference between the experimental binding energies and those obtained with Skx in a spherical basis without pairing for even-even nuclei.

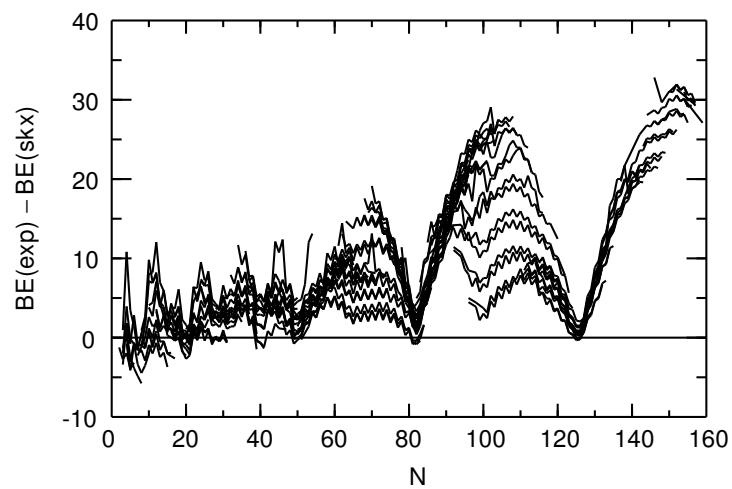


Figure 19.8: The difference between the experimental binding energies and those obtained with Skx in a spherical basis without pairing for all nuclei.

19.3.2 Single-particle energies

The experimental single-particle energies for ^{16}O , ^{40}Ca , ^{48}Ca , ^{132}Sn and ^{208}Pb are compared with the skx Hartree-Fock and NL3 Dirac Hartree calculations in Figs. (19.10), (19.11), (19.12), and (19.13). Both mean-field calculations are in qualitative agreement with experiment. For light nuclei the NL3 results are in better, but for heavy nuclei the skx results are better. The difference between skx and NL3 is mainly related to the effective mass (m^*/m), which is about 1.0 for skx and 0.6 for NL3. The effective mass for the Skyrme interaction can be tuned by the parameters [2] and those for skx are determined primarily from the SPE of heavy nuclei where the spacing around the Fermi surface requires an effective mass of about 1.0 [8]. For NL3 on the other hand, an effective mass of about 0.6 is intrinsic to the model. An effective mass of 0.6 gives SPE in heavy nuclei that are spread out compared to experiment as shown by NL3 in Figs. (19.12) and (19.13). Typical Brueckner G matrix interactions also give an effective mass of about 0.6, and the reason for an empirical value of near unity in heavy nuclei is attributed to configuration mixing due to coupling of the single-particle states to surface vibrations [33], [34]. For a Hamiltonian like skx with an effective mass of unity, these surface vibrations effectively included in terms of a modified

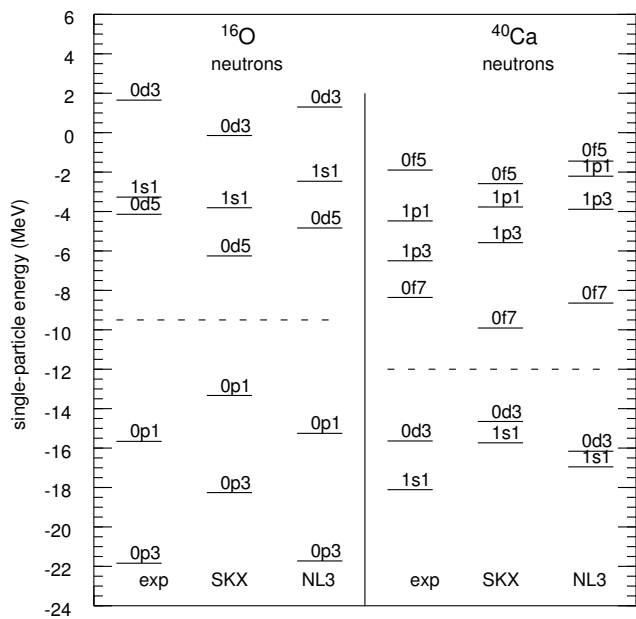


Figure 19.9: Experimental and theoretical neutron single-particle energies for ^{16}O and ^{40}Ca . The orbits are labeled by $(n, \ell, 2j)$, and the dashed line is the Fermi energy.

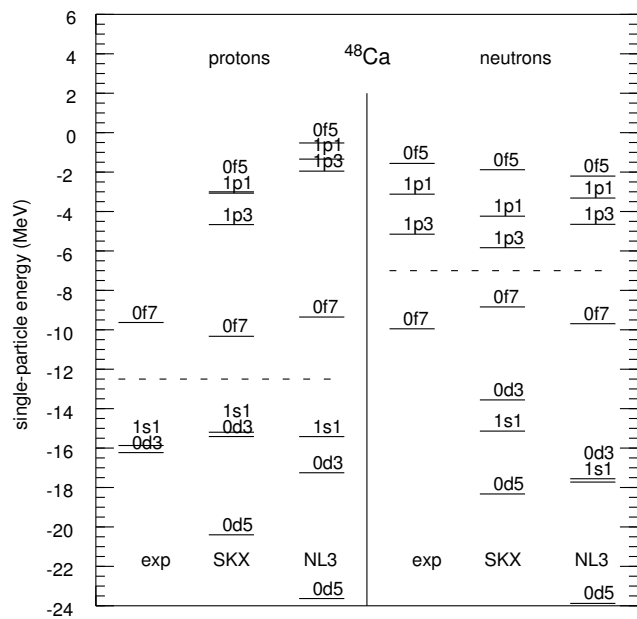


Figure 19.10: Experimental and theoretical proton and neutron single-particle energies for ^{48}Ca . The orbits are labeled by $(n, \ell, 2j)$, and the dashed line is the Fermi energy.

(renormalized) Hamiltonian.

Experimental values of the SPE are usually used as input to shell-model calculations. For nuclei near the drip lines where the experimental SPE are not known, one needs a theoretical model for predicting or extrapolating the SPE. The HF parameter model such as skx and NL3 provide perhaps the most reliable way to extrapolate the SPE from nuclei near stability to the most exotic nuclei near the drip lines. The predictions for the ^{60}Ca and ^{78}Ni SPE are given in Figs. (19.14) and (19.15), respectively. Other recent predictions for ^{60}Ca are given in [35]. It will remain for future experiments to test these extrapolations.

As a guide to the ordering of the single-particle states as a function of N and Z , I show in Fig. (19.16) the single-particle energies for nuclei with $N = Z$ obtained from with skx . Fig. (19.17) shows the skx single-particle energies for the calcium isotopes as a function of neutron number. Beyond ^{60}Ca one observes that the $0g_{9/2}$ orbital becomes bound, and thus ^{70}Ca will be bound with skx . The even-even calcium nuclei between ^{60}Ca and ^{70}Ca will probably be bound due to pairing (which has been neglected in this particular skx HF calculation).

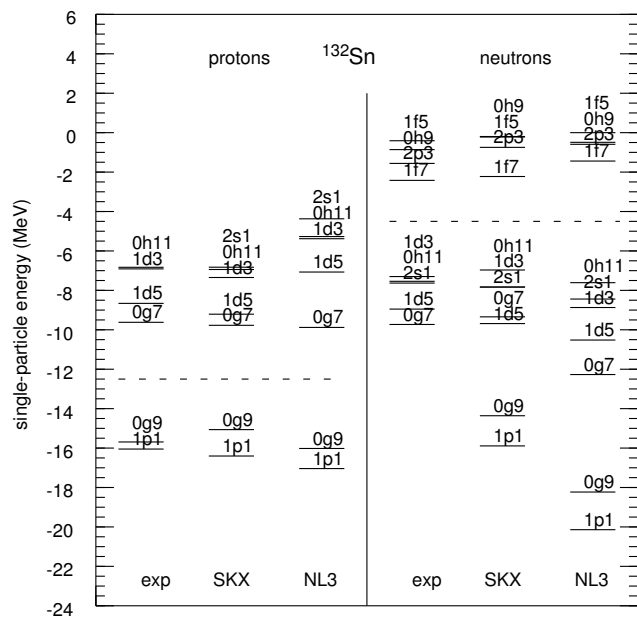


Figure 19.11: Experimental and theoretical proton and neutron single-particle energies for ^{132}Sn . The orbits are labeled by $(n, \ell, 2j)$, and the dashed line is the Fermi energy.

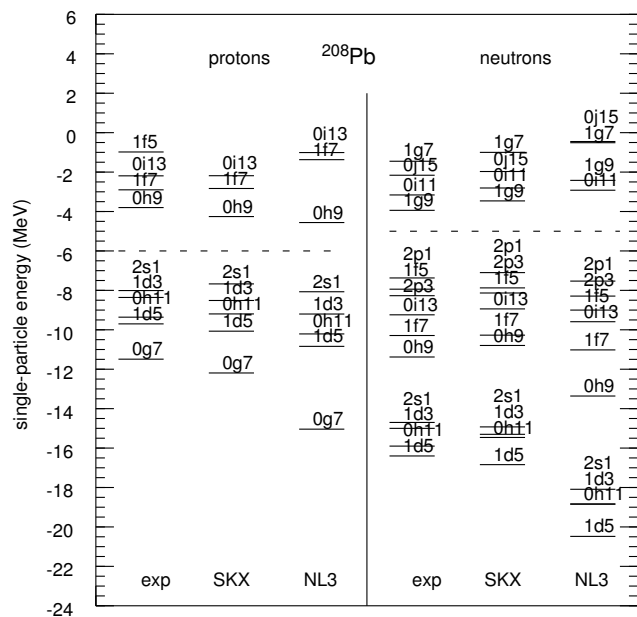


Figure 19.12: Experimental and theoretical proton and neutron single-particle energies for ^{132}Sn . The orbits are labeled by $(n, \ell, 2j)$, and the dashed line is the Fermi energy.

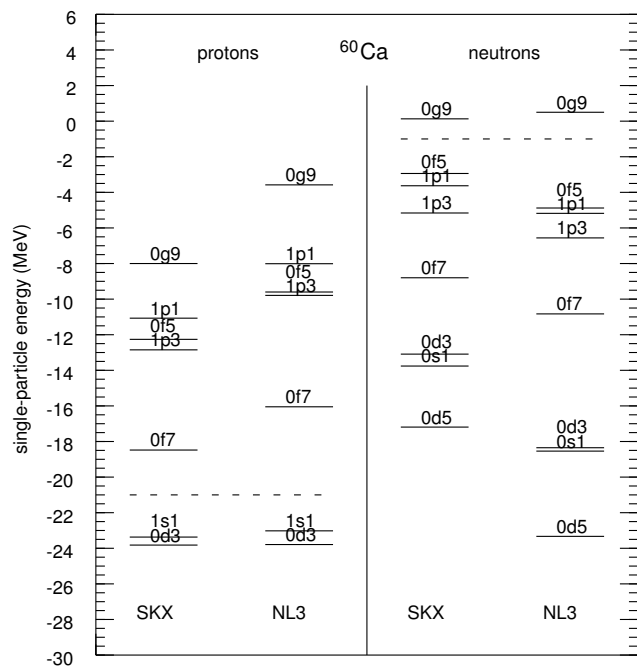


Figure 19.13: Theoretical proton and neutron single-particle energies for ^{60}Ca . The orbits are labeled by $(n, \ell, 2j)$, and the dashed line is the Fermi energy.

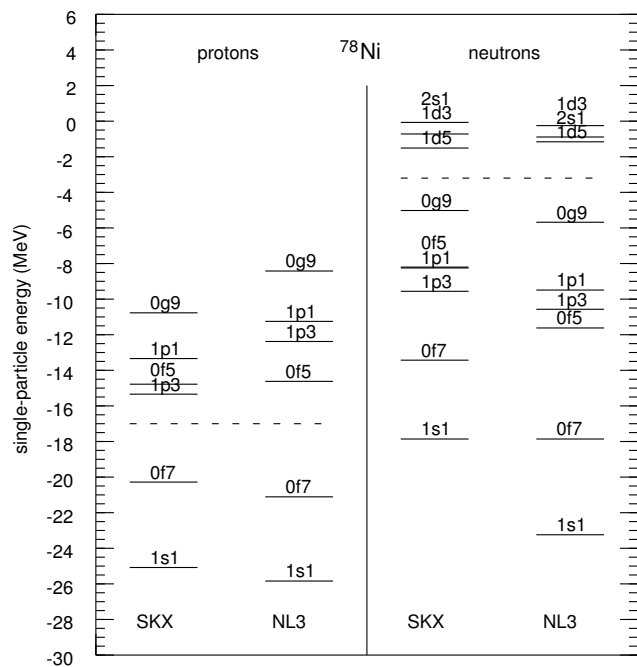


Figure 19.14: Theoretical proton and neutron single-particle energies for ^{78}Ni . The orbits are labeled by $(n, \ell, 2j)$, and the dashed line is the Fermi energy.

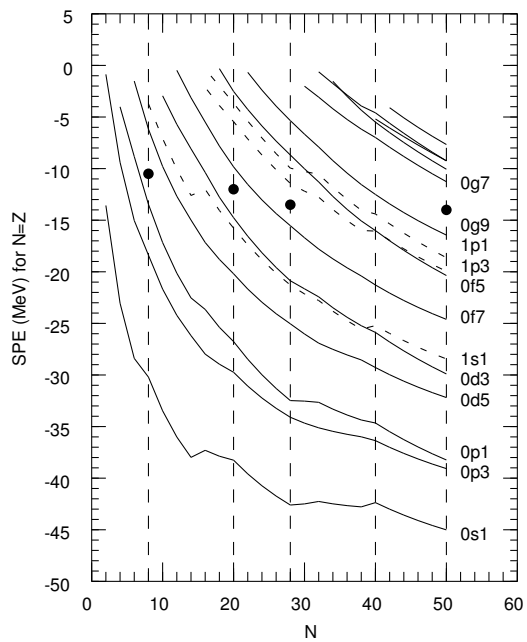


Figure 19.15: Neutron single-particle energies for nuclei with $N = Z$ as a function of neutron number obtained with the skx spherical Hartree-Fock calculation. The vertical dashed lines show some of the magic number discussed in the text. The large circles show the approximate Fermi energies for ^{16}O , ^{40}Ca , ^{56}Ni and ^{100}Sn . The orbits are labeled by $(n, \ell, 2j)$.

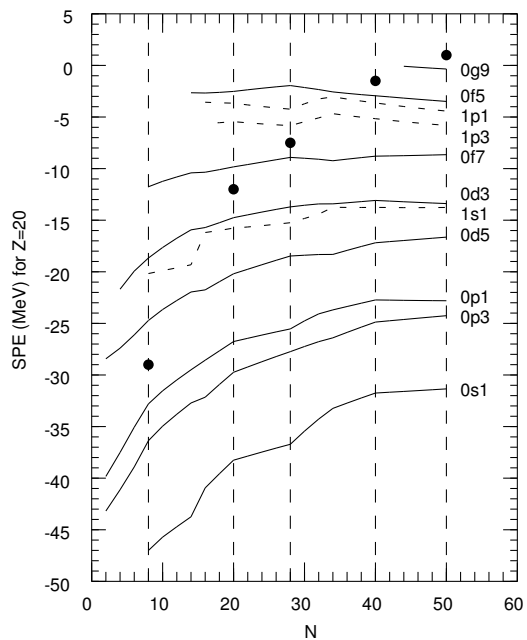


Figure 19.16: Neutron single-particle energies for the calcium isotopes obtained with the skx spherical Hartree-Fock calculation. The vertical dashed lines show some of the magic number discussed in the text. The large circles show the approximate Fermi energies for ^{28}Ca , ^{40}Ca , ^{48}Ca , ^{60}Ca and ^{70}Ca . The orbits are labeled by $(n, \ell, 2j)$.

19.3.3 Rms charge radii and charge densities

In this section I will discuss the results for rms charge and charge densities obtained with the Skyrme parameter sets skx [8] and SKM* [36]

The experimental and theoretical rms charge radii are compared in Fig. (19.18). The experimental radii are from Refs. [37] and [38], with those with the smallest errors selected in the case of more than one data set. The error in the experimental data is typically smaller than the size of the data points. The Hartree-Fock results for the two interactions SKM* (bottom panel) and skx (top panel) are obtained with the CM (fractional) occupations (those obtained with ESP occupations are essentially the same). The excellent overall agreement between experiment and theory is not surprising since these rms charge radii are used to constrain the values of the Skyrme parameters. The deviations increase for light nuclei going up to 5% for ^{12}C . In general one may expect the mean-field approximation to be less valid for light nuclei.

In order to illustrate how the features of the charge density are built out of the specific

shell model orbitals that are filled, we show in Fig. (19.19) the point-proton density of ^{40}Ca (points) obtained with skx with the assumption that the $0s$, $0p$, $1s$ and $0d$ orbits are filled. The individual contributions of the filled orbits to the proton density are shown. The $0s$ and $1s$ are the contributions from two protons in each of these orbits respectively. The $0p$ indicates the sum of the four protons in the $0p_{3/2}$ orbit and two protons in the $0p_{1/2}$ orbit. The $0d$ indicates the sum of the six protons in the $0d_{5/2}$ orbit and four protons in the $0d_{3/2}$ orbit. In the top panel the densities associated with the (unfilled) valence orbits above the Fermi-surface are shown; $0f$ for eight protons in the $0f_{7/2}$ orbit and $1p$ for four protons in the $1p_{3/2}$ orbit.

For comparison between experimental and theoretical charge densities I consider in Fig. (19.20) a set of data for nuclei that cover a wide mass range for which there is the good electron scattering data: ^{28}Si from Ref. [39], ^{32}S from Ref. [40] (circles) and Ref. [41] (squares), ^{40}Ca and ^{48}Ca from Ref. [42], ^{50}Ti and ^{52}Cr from Ref. [43], ^{54}Fe from Ref. [44], ^{58}Ni from Refs. [45] (circles) and [44] (squares), ^{88}Sr from Ref. [46], ^{90}Zr from Ref. [47], ^{92}Mo from Ref. [48], ^{204}Hg from Ref. [49], and ^{208}Pb from Refs. [50] (circles) and [51] (squares). The data are compared to the skx (dashed lines) and SKM* (solid lines) are calculations.

Both skx and SKM* nicely reproduce the nucleus-dependent oscillations. The Hamiltonian parameters are obtained from fits to the rms charge radii, binding energies and excited state energies of these nuclei. Thus the good agreement between experiment and theory for the nucleus-dependent oscillations observed in Fig. (19.20) are not a result of a “fit” to these data but arise naturally from the underlying shell structure.

The main difference between the skx and SKM* results is that the interior density is about 5% higher with SKM* compared to skx, with SKM* in best overall agreement with experiment. Close inspection of the curves in Fig. (19.20) in the region where the density falls off reveals a slightly larger surface diffuseness for SKM* compared to skx (the dashed line for skx is slightly steeper than the line for SKM* in the surface). The correlation between the increased interior height with the increased diffuseness (when the rms radius is the same) is consistent with what is expected from the Fermi model shown in Fig. 3.2. The change between skx and SKM* corresponds to a $\Delta a = 0.036$ fm for ^{208}Pb . The change in the diffuseness is connected to the difference in the density-dependent part of the Hamiltonians, namely $[\rho(r)]^{1/2}$ for skx and $[\rho(r)]^{1/6}$ for SKM*. There is agreement between experiment and theory to an accuracy of about 2% or better for $r > 1$ fm with SKM*. As discussed above,

this is about the level of the accuracy with which these densities can be experimentally determined.

In the overview of Fig. (19.20) one can observe several interesting features associated with how the quantum waves change with shell structure and mass. Between ^{28}Si and ^{32}S in the sd shell there is a large increase in the interior density due to the filling of the $1s_{1/2}$ orbital (see also [41]). Likewise between ^{204}Hg and ^{208}Pb there is a large increase in the interior related to the filling of the $2s_{1/2}$ orbital. Between ^{40}Ca and ^{48}Ca one observes a redistribution of the charge (proton) density due to the interaction with the valence $0f_{7/2}$ neutrons. The theoretical density distributions for the sequence ^{48}Ca , ^{50}Ti , ^{52}Cr and ^{54}Fe show a smoothly varying trend due to dominance of the proton $0f_{7/2}$ subshell filling.

19.3.4 Displacement energies

The displacement energy is the binding energy difference between mirror nuclei (those with the same atomic number A but with the proton number Z and neutron number N inter-

changed). For a given mass A and isospin T the displacement energy is:

$$D(A, T) = \text{BE}(A, T_z^<) - \text{BE}(A, T_z^>), \quad (19.51)$$

where $T = |T_z^<| = |T_z^>|$, $\text{BE}(A, T_z^<)$ is the binding energy of the proton-rich nucleus and $\text{BE}(A, T_z^>)$ is the binding energy of the neutron-rich nucleus. If the nuclear force is charge symmetric, then this binding energy difference can be related to the well-understood Coulomb interaction between the protons. However, it was shown by Nolen and Schiffer [52] that there is a systematic increase in the experimental displacement energies compared to those calculated with a charge symmetric strong interaction (the Nolen-Schiffer anomaly). In the usual HF calculation one has both direct and exchange terms in the Coulomb-energy density functional. For the exchange one uses the Fermi-gas approximation that is a good approximation to the exact calculation [53]. The ground-state displacement energies obtained with the Coulomb plus Coulomb-exchange HF approach (from the skxce interaction of [8]) are shown on the right-hand side of Fig. (19.21). One observes the systematic deviation between experiment and theory associated with the Nolen-Schiffer anomaly. For the heaviest nuclei the ratio shown in Fig. (19.22) goes to a constant value of about 1.06. It is well known [52] that the displacement energies are sensitive to the rms charge radii; the

skx interactions reproduce the experimental charge radii of ^{16}O , ^{40}Ca and ^{48}Ca to better than one percent (see Fig. 10 of [8]). The displacement energies are also sensitive to the rms radius of the valence orbits, and the skx interactions give radii for the $d_{5/2}$ orbit in ^{17}O and the $0f_{7/2}$ orbit in ^{41}Ca that are within 2% of those deduced from the magnetic electron scattering form factors [54].

In the fit to closed-shell nuclei the displacement energy is represented by the pair of nuclei ^{48}Ni - ^{48}Ca . The binding energy of ^{48}Ni is not measured but can be extrapolated to within an uncertainty of a few hundred keV from the $0f_{7/2}$ shell displacement energy systematics [55], [56], [57], [58], [59]. The recent discovery of ^{48}Ni [60] is consistent with the mass obtained from the $0f_{7/2}$ extrapolations.

In order to improve agreement with experiment it was found that the HF theory could be improved in two ways. One of them consists of leaving out the Coulomb exchange term, with the result shown in the middle panel of Figs. (19.21) and (19.22). This may be interpreted as a correction from nuclear correlation (configuration mixing) that happens to cancel the exchange term. This has been discussed in the general HF framework by Bulgac

and Shaginyan [61], [62], [63] in terms of a surface-vibration contribution to the Coulomb correlation energy. I note that the relativistic approach leaves out the Coulomb exchange by default, and that most Woods-Saxon programs [64], [65] leave out the Coulomb exchange.

Another way to improve agreement with experiment is to add a charge-symmetry breaking (CSB) term to the Skyrme interaction that can be expressed as a change to the proton-proton (pp) and neutron-neutron (nn) s -wave interactions:

$$V_{\text{Skyrme}}^{pp} = t_0(1 - x_0)(1 + x_a)\delta$$

and

$$V_{\text{Skyrme}}^{nn} = t_0(1 - x_0)(1 - x_a)\delta, \quad (19.52)$$

where x_a is a parameter to be determined.

The $A = 48$ closed shell nuclei require $x_a = -0.014 \pm 0.002$ for the interaction called skxcsb. The results for the all displacement energies are shown on the right-hand side of Figs. (19.21) and (19.22).

A correct description of the displacement energies within the mean field approximation is obviously important for understanding the position of the proton drip lines. $A = 99$ is the heaviest $T = 1/2$ isobaric doublet for which the proton-rich nucleus is expected to be bound. The calculated displacement energies for $A = 99$ are -13.54 MeV (skxce), -14.03 MeV MeV (skx) and -14.15 MeV (skxcsb). The introduction of the extra terms in the Skyrme Hamiltonian that are needed for the displacement energies, also has an influence on the neutron drip line; for example the binding energy of ^{176}Sn is predicted to be -1158.0 MeV (skxce), -1149.0 MeV (skx) and -1148.4 MeV (skxcsb).

The skxcsb interaction should ultimately be related to the CSB nucleon-nucleon (NN) scattering data. Analysis of the NN scattering data together with a model for the NN interaction gives [66], [67] a value of $\Delta a_{CSB} = a_{pp} - a_{nn} = 1.5 \pm 0.5$ fm for the difference in the pp and nn scattering lengths. Modern NN potentials such as the AV18 [68] and CDbonn99 [69] are designed to reproduce this difference. It is not easy to interpret the CSB contribution to the displacement energies directly in terms of a NN potential due the short-range nuclear correlations and their dependence on the strong NN potential. Probably the most realistic way to do this is to consider the CSB contribution to the displacement energies

obtained with the variational Monte Carlo approach for $A = 7$ [70] and the BHF approach for $A = 15$ and $A = 17$ [69]. For example, the CSB displacement energy for the $A = 17$, $d_{5/2}$ state is 92 keV with AV18 [69] to be compared with 355 keV with skxcsb. From these comparisons one finds that the effect of the empirical CSB interaction obtained for skxcsb is a factor of 3-4 larger than expected from AV18 or CDbonn99. Thus one concludes that either there is a significant NNN or many-body CSB contribution whose origin is unknown, or that a major part of the displacement energy anomaly is due to nuclear correlations. Possible many-body CSB effects at the quark level have recently been examined [71], [72].

The systematics associated with the Coulomb displacement energies can be used to obtain theoretical binding-energies of proton-rich nuclei from the experimental binding energies of neutron-rich nuclei. The displacement energies of Eq. (19.51) can be modeled on smooth systematics [56], [57], [73]; shell-model configuration mixing that contains the Coulomb and CSB interactions [55], [58], [59]; or on the mean-field models. One can combine the experimental binding energy for the neutron-rich nucleus $\text{BE}(A, T_z^>)_{\text{exp}}$ together with the calculated value for $D(A, T)$ to give an extrapolation for the proton-rich binding

energy:

$$\text{BE}(A, T_z^<) = D(A, T)_{\text{theory}} + \text{BE}(A, T_z^>)_{\text{exp}}. \quad (19.53)$$

For most of the nuclei out to the proton drip line the binding energy $\text{BE}(A, T_z^>)_{\text{exp}}$ of the mirror neutron-rich nucleus is known to 100 keV or better. This method has been used to predict the binding energies and the drip line for $Z = 19 - 28$ [55], [59], [56] and $Z = 28 - 38$ [59], [74]. The latter calculations have been used [74] to study the rapid-proton (rp) capture path in the astrophysical explosive hydrogen burning process [75]. The rp-process in light nuclei depends upon theoretical calculations of the displacement energies of ground and excited states and upon the spectroscopic factors that enter into the (p, γ) reaction [76], [77].

EDF models have been extended to include isovector and isotensor isospin breaking parts of the strong interaction [78]. These are able to describe the samll odd-even oscillations in the displacement energies as well as the oscilaltions in the c coefficient of the IMME.

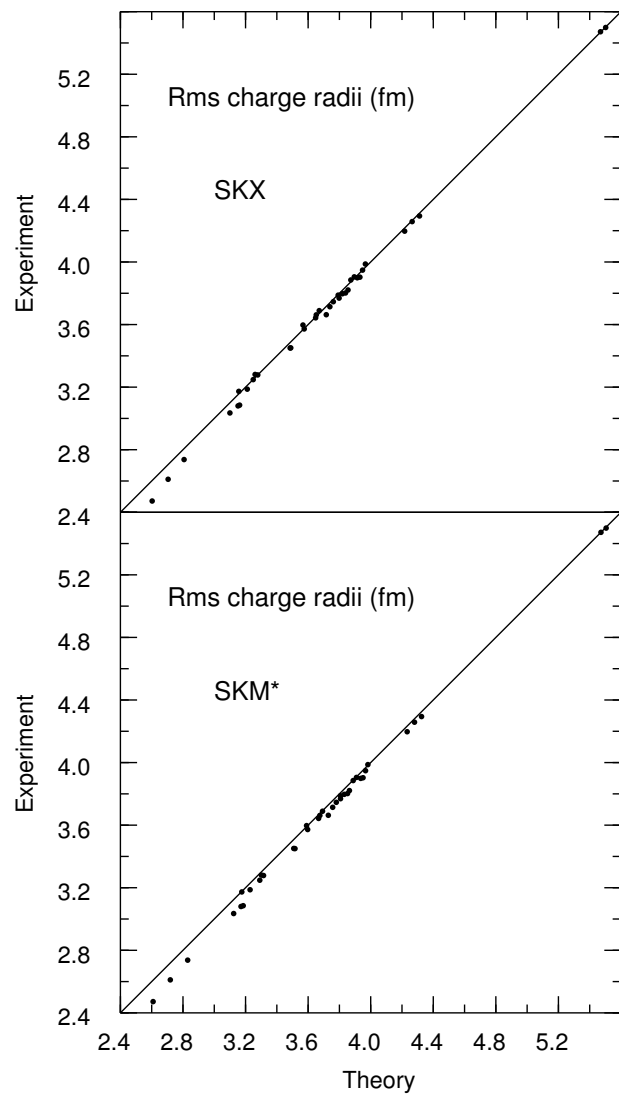


Figure 19.17: Comparison of experimental and theoretical rms charge radii for the Skyrme interactions skx (top panel) and SKM* (bottom panel).

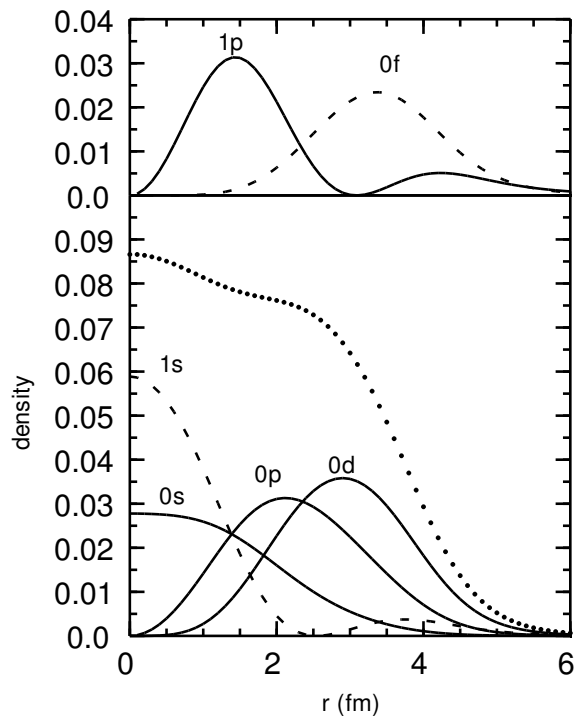


Figure 19.18: The point-proton density (points) of ^{40}Ca in the skx model with a closed shell configuration. The total density is decomposed in terms of the contributions from the individual filled orbitals. In the upper panel the densities for protons in the orbitals just above the Fermi-surface of ^{40}Ca are shown, for eight protons in the $0f_{7/2}$ orbit and for four protons in the $1p_{3/2}$ orbit.

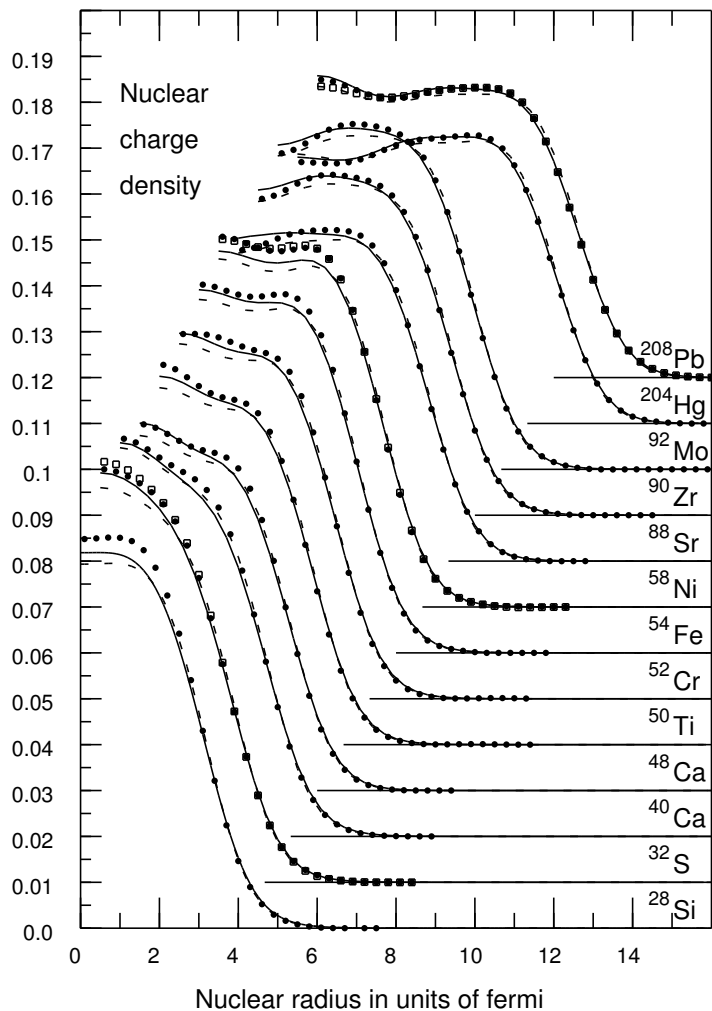


Figure 19.19: Experimental charge-density distributions (filled circles) compared with the skx (dashed lines) and SKM* (solid lines) calculations. The charge density units are $e \text{ fm}^{-3}$. Beyond ^{28}Si the curves and data have been progressively offset by 1 fm and 0.01 in the charge density. The data are discussed in the text.

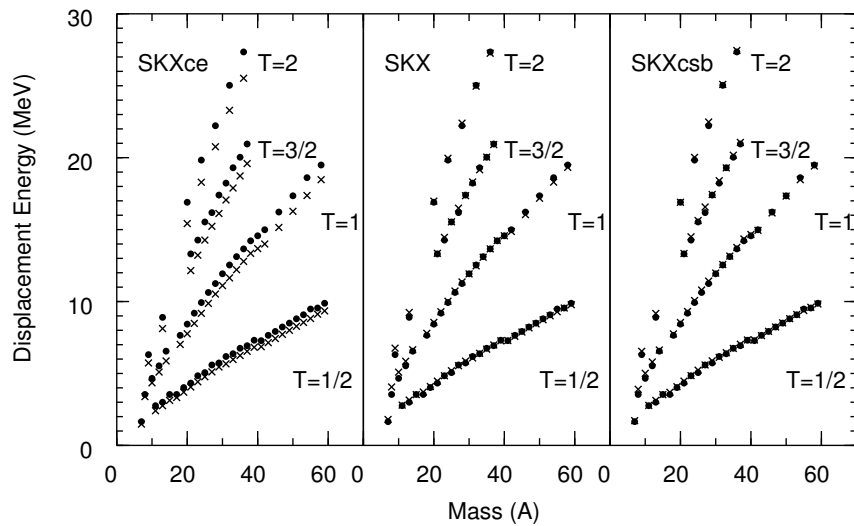


Figure 19.20: Ground-state displacement energies as a function of A for skxce (with the normal Coulomb exchange term), skx (without the exchange term) and skxcsb (with the exchange term and with a CSB interaction). The experimental data are filled circles and the calculations are given as crosses.

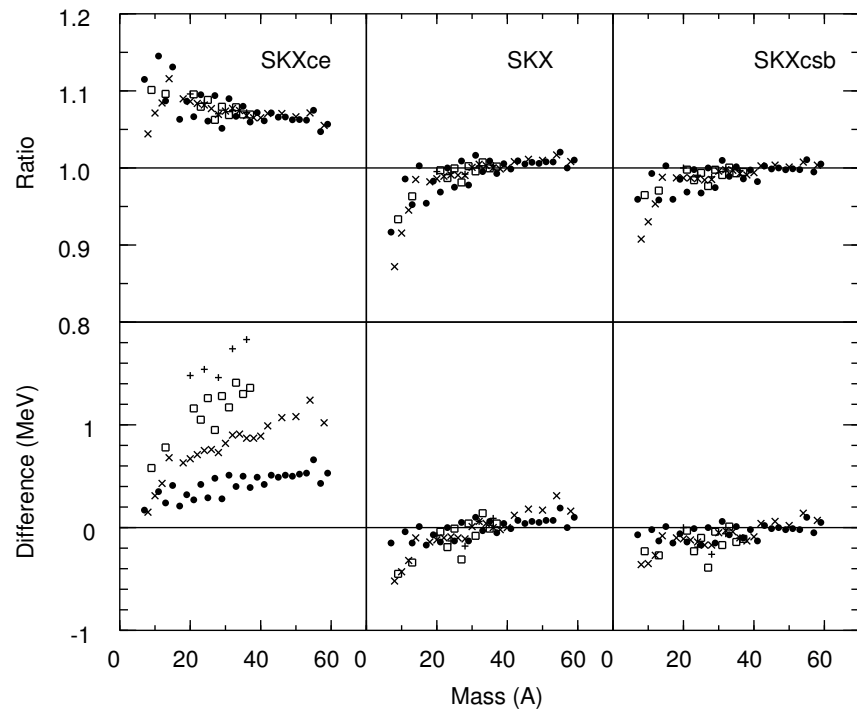


Figure 19.21: Top: the ratio experiment/theory for the data shown in Fig. (19.21); Bottom: the difference experiment-theory. The symbols are filled circles for $T = 1/2$, crosses for $T = 1$, squares for $T = 3/2$ and plus signs for $T = 2$.

Bibliography

- [1] T. R. H. Skyrme. Philos. Mag. **1**, 1043 (1956); Nucl. Phys. **9**, 615 (1959); **9**, 635 (1959).
- [2] D. Vautherin and D. M. Brink, Phys. Rev. C **5**, 626 (1972). link
- [3] D. Vautherin, Phys. Rev. C **7**, 296 (1973). link
- [4] E. Chabanat, P. Bonche, P. Haensel, J. Meyer and R. Schaeffer, Nucl. Phys. A **627**, 710 (1997).

- [5] F. Stancu, B. M. Brink, and H. Flocard, Phys. Lett. **B68**, 108 (1977).
- [6] B. A. Brown, T. Duguet, T. Otsuka, D. Abe and T. Suzuki, Phys. Rev. C **74**, 061303(R) (2006). link
- [7] C. B. Dover and N. Van Giai, Nucl. Phys. **A190**, 373 (1972).
- [8] B. A. Brown, Phys. Rev. C **58**, 220 (1998). link
- [9] W. Kohn and L. J. Sham, Phys. Rev. **140** A1133 (1965). link
- [10] R. M. Dreizler and E. K. U. Gross, “Density Functional Theory: An Approach to the Quantum Many-Body Problem”, (Springer, Berlin, 1990).
- [11] M. Dutra, O. Lourenco, J. S. SaMartins, A. Delfino, J. R. Stone, and P. D. Stevenson, Phys. Rev. C **85**, 035201 (2012). link
- [12] M. Kortelainen, J. McDonnell, W. Nazarewicz, E. Olsen, P.-G. Reinhard, J. Sarich, N. Schunck, S. M. Wild, D. Davesne, J. Erler, and A. Pastore, Phys. Rev. C **89**, 054314 (2014). link

- [13] S. Goriely, N. Chamel and J. M. Pearson, Phys. Rev. C **88**, 024308 (2013). link
- [14] J. Erler, N. Birge, M. Kortelainen, W. Nazarewicz, E. Olsen, A. Perhac, and M. Stoitsov, Nature (London) **486**, 509 (2012).
- [15] L. Neufcourt, Y. Cao, W. Nazarewicz, E. Olsen, and F. Viens, Phys. Rev. Lett. **122**, 062502 (2019). link
- [16] J. D. Walecka, Ann. Phys. (N. Y.) **83**, 491 (1974).
- [17] G. A. Lalazissis, J. König and P. Ring, Phys. Rev. C **55**, 540 (1997). link
- [18] C. Y. Tsang, B. A. Brown, F. J. Fattoyev, W. G. Lynch, and M. B. Tsang, Phys. Rev. C **100**, 062801(R) (2019). link
- [19] A. Bulgac, M. M. Forbes, S. Jin, R. N. Perez, and N. Schunck, Phys. Rev. C **97**, 044313 (2018). link
- [20] B. D. Serot , Rep. Prog. Physics, **55** , 1855 (1992).

- [21] L.-G. Cao, H. Sagawa, and G. Colo, Phys. Rev. C **86**, 054313 (2012). link
- [22] B. A. Brown, Phys. Rev. Lett. **111**, 232502 (2013). link
- [23] B. A. Brown and Achim Schwenk, Phys. Rev. C **89**, 011307(R) (2014). link
- [24] B. A. Brown, Phys. Rev. Lett. **85**, 5296 (2000). link
- [25] S. Typel and B. A. Brown, Phys. Rev. C **64**, 027302 (2001). link
- [26] S. Abrahamyan, Z. Ahmed, H. Albataineh, K. Aniol, D. S. Armstrong et al., Phys. Rev. Lett. **108**, 112502 (2012). link
- [27] C. J. Horowitz, Z. Ahmed, C. M. Jen, A. Rakhman, P. A. Souder et al., Phys. Rev. C **85**, 032501(R) (2012). link
- [28] B. A. Brown, Phys. Rev. Lett. **119**, 122502 (2017). link
- [29] M. M. Sharma, G. Lalazissis, J. Konig and P. Ring, Phys. Rev. Lett. **74**, 3744 (1995). link

- [30] B. Friedman and V. R. Pandharipande, Nucl. Phys. **A361**, 502 (1981).
- [31] B. A. Brown, W. A. Richter and R. Lindsay, Phys. Lett. B **483**, 49 (2000).
- [32] S. Goriely, F. Tondeur and J. M. Pearson, At. Data Nucl. Data Sheets **77**, 311 (2001).
- [33] S. O. Backman, G. E. Brown and J. A. Niskanen, Phys. Rep. **124**, 1 (1985).
- [34] C. Mahaux, P. F. Bortignon, R. A. Broglia and C. G. Dasso, Phys. Rep. **120**, 1 (1985).
- [35] I. Hamamoto, H. Sagawa and X . Z. Zhang, Phys. Rev. C **64**, 024313 (2001). link
- [36] J. Bartel, P. Quentin, M. Brack, C. Guet, and M. B. Hakansson, Nucl. Phys. **A386**, 79 (1982).
- [37] H. de Vries, C. W. de Jager and C. de Vries, At. Data and Nucl. Data Tables **36**, 495 (1987).
- [38] G. Fricke, C. Bernhardt, K. Heilig, L. A. Schaller, L. Shellenberg, E. B. Shera and C. W. de Jager, At. Data and Nucl. Data Sheets **60**, 177 (1995).

- [39] H. Miessen, Ph.D. Thesis, University of Mainz, 1982 (unpublished).
- [40] D. Rychel, Ph.D. Thesis, University of Mainz, 1983 (unpublished)
- [41] J. Wesseling, C. W. de Jager, L. Lapikas, H. de Vries, L. W. Fagg, M. N. Harakeh, N. Kalantar-Nayestanaki, R. A. Lindgren, E. Moya De Guerra, and P. Sarriguren, Phys. Rev. **C55**, 2773 (1997) link
- [42] H. J. Emrich, Ph.D. Thesis, University of Mainz, 1983 (unpublished)
- [43] J. W. Lightbody, Jr., J. B. Bellicard, J. M. Cavedon, B. Frois, D. Goutte, m. Huet, Ph. Leconte, A. Nakada, Phan Xuan Ho, S. K. Platchkov, S. Turck-Chieze, C. W. de Jager, J. J. Lapikas, and P. K. A. de Witt Huberts. Phys. Rev. **C27**, 113 (1983) link
- [44] H. D. Wohlfahrt, Habilitationsschrift, University of Mainz, 1976 (unpublished)
- [45] G. Beuscher, Ph.D. Thesis, University of Mainz, 1983 (unpublished)
- [46] G. Stephan, Ph.D. Thesis, University of Mainz, 1976 (unpublished)

- [47] H. Rothhaas, Ph.D. Thesis, University of Mainz, 1976 (unpublished)
- [48] B. Dreher, Phys. Rev. Lett **35**, 716 (1975) link
- [49] A. J. C. Burghardt, Ph.D. Thesis, University of Amsterdam, 1989 (unpublished)
- [50] H. Euteneuer, J. Friedrich and N. Vögler, Nucl. Phys. **A298**, 452 (1978)
- [51] J. L. Friar, J. Heisenberg and J. W. Negele, Proceedings of the June Workshop in Intermediate Energy Electromagnetic Interactions, edited by A. M. Bernstein, Massachusetts Institute of Technology (1977), p. 325
- [52] J. A. Nolen and J.P. Schiffer, Ann. Rev. Nucl. Sci. **19**, 471 (1969).
- [53] C. Titin-Schnaider and P. Quentin, Phys. Lett. **49B**, 397 (1974).
- [54] T. Suzuki, H. Sagawa and A. Arima, Nucl. Phys. **A536**, 141 (1992)
- [55] B. A. Brown, Phys. Rev. C **43**, R1513 (1991); C **44**, 924 (1991).

- [56] B. J. Cole, Phys. Rev. C **54**, 1240 (1996). link
- [57] Phys. Rev. C **58**, 2831 (1998).
- [58] W. E. Ormand, Phys. Rev. C **53**, 214 (1996); Phys. Rev. C **55**, 2407 (1997). link
- [59] W. E. Ormand, Phys. Rev. C **55**, 2407 (1997). link
- [60] B. Blank et al., Phys. Rev. Lett. **84**, 1116 (2000). link
- [61] A. Bulgac and V. R. Shaginyan, Nucl. Phys. **A601**, 103 (1996).
- [62] A. Bulgac and V. R. Shaginyan, Phys. Lett. B **469**, 1 (1999).
- [63] A. Bulgac and V. R. Shaginyan, Eur. Phys. J. A **5**, 247 (1999).
- [64] R. Sherr and G. Bertsch, Phys. Rev. C **32**, 1809 (1985). link
- [65] B. A. Brown, A. Csoto and R. Sherr, Nucl. Phys. **A597**, 66 (1996).
- [66] G. A. Miller, B. M. K. Nefkens and I. Slaus, Phys. Rep. **194**, 1 (1990).

- [67] G. Q. Li and R. Machleidt, Phys. Rev. C **58**, 3153 (1998). link
- [68] R. B. Wiringa, V. G. J. Stoks and R. Schiavilla, Phys. Rev. C **49**, 2950 (1995). link
- [69] C. Harzer, H. Muther and R. Machleidt, Phys. Lett. B **459**, 1 (1999).
- [70] B. S. Pudliner, V. R. Pandharipande, J. Carlson, S. C. Pieper, and R. B. Wiringa, Phys. Rev. C **56**, 1720 (1997). link
- [71] K. Tsushima, K. Saito and A. W. Thomas, Phys. Lett. B **465**, 36 (1999).
- [72] C. J. Horowitz and J. Piekarewicz, Phys. Rev. C **63**, 01330(R), (2000).
- [73] B. A. Brown and P. G. Hansen, Phys. Lett. B **391** (1996).
- [74] B. A. Brown, R. Clement, H. Schatz, W. A. Richter, A. Volya and W. A. Richter, Phys. Rev. C65, 045802 (2002). link
- [75] H. Schatz et al., Phys. Rep. **294**, 167 (1998).

- [76] H. T. Fortune, R. Sherr and B. A. Brown, Phys. Rev. C **61**, 057303 (2000). link
- [77] H. Herndl, J. Goerres, M. Wiescher, B. A. Brown and L. Van Wormer, Phys. Rev. C **52**, 1078 (1995). link
- [78] P. Baczyk, J. Dobaczewski, M. Konieczka, W. Satula, T. Nakatusukasa and K. Sato, Phys. Lett. B **778**, 178 (2018).

Chapter 20

Overview of nuclear collective motion

The nuclear shell model is most directly applicable to properties of nuclei with protons and/or neutrons near the magic numbers. In between the magic numbers one can use the shell model to construct set of basis states that can be diagonalized with an effective Hamiltonian. The number of basis states increases exponentially as a function of the number of valence particles beyond a closed shell. On the other hand, the spectra of heavy even-even nuclei with proton and neutron numbers about half-way between the magic numbers show a remarkable simplicity in terms the ratio of the 4^+ and 2^+ excitation energies of $R(4^+/2^+) = 10/3$ (see the chapter on excitation energies of even-even nuclei). In the 1950's this lead to Bohr-Mottelson collective models for nuclei. In their review [1] they say, "The establishment of the nuclear shell structure provided a description in terms of single-particle motion that might seem to preclude the occurrence of collective rotation. However, a new situation was created by the recognition that the shell structure may lead to equilibrium shapes that deviate from spherical symmetry. It was evident that such a collective deformation that defines an orientation of the system as a whole would imply rotational degrees of freedom, but one was faced with the need for a generalized treatment of rotations applicable to quantal systems that do not have a rigid or semi rigid structure like that of molecules." The theory that emerged started with the general quantum theory of the motion of a deformed top.

Quoting Bohr [2], “In a general theory of rotation, symmetry plays a central role. Indeed, the very occurrence of collective rotational degrees of freedom may be said to originate in a breaking of rotational invariance, which introduces a “deformation” that makes it possible to specify an orientation of the system. Rotation represents the collective mode associated with such a spontaneous symmetry breaking (Goldstone boson).” There is an analogy with the Jahn-Teller effect in molecular physics [3].

20.1 The Wigner rotation matrix

For the results below we will need the Wigner rotation matrix. We want to transform a spherical tensor wavefunction $|J, M\rangle$ described in the coordinate system (x, y, z) in terms its components $|J, K\rangle$ in new coordinate system $(1, 2, 3)$ that is obtained by a Euler-angle rotation $\theta = (\alpha, \beta, \gamma)$. This means we have a rotation by an angle α about the z -axis, followed by a rotation β about the new y -axis, followed by a rotation γ about the new z -axis

(the 3-axis). The quantum mechanical operator for this rotation is

$$\mathcal{R}(\theta) = e^{-i\alpha \hat{J}_z} e^{-i\beta \hat{J}_z} e^{-i\gamma \hat{J}_z}. \quad (20.1)$$

Thus

$$\mathcal{R}(\theta) | J, M \rangle = \sum_K | J, K \rangle \mathcal{D}_{K,M}^J, \quad (20.2)$$

where \mathcal{D} is the Wigner function given by

$$\mathcal{D}_{K,M}^J = \langle J, K | \mathcal{R}(\theta) | J, M \rangle = e^{-i\alpha K} d_{K,M}^J(\beta) e^{-i\gamma M}, \quad (20.3)$$

and d is Wigner's d -matrix

$$d_{K,M}^J(\beta) = \langle J, K | e^{-i\beta \hat{J}_z} | J, M \rangle. \quad (20.4)$$

More details about the Wigner rotation matrix are given in (link to wiki).

20.2 The Bohr Hamiltonian

We start with the Bohr Hamiltonian that is written as a sum of terms for kinetic energy for vibrations (V) and rotations (R) plus a potential energy term V

$$H_B = T_V + T_R + V. \quad (20.5)$$

Ref. [4] gives a compendium of results this equation.

The Bohr Hamiltonian starts with an expansion of the nuclear surface in terms of its multipole degrees of freedom

$$R(\theta, \phi) = R_o \left[1 + \sum_{\lambda, \mu} \alpha_{\lambda, \mu} Y_{\lambda, \mu}(\theta, \phi) \right], \quad (20.6)$$

where R_o is the radius of the nucleus when it has the spherical equilibrium shape, and Y^λ is the spherical harmonic. The requirement of reality for R implies that

$$(\alpha_{\lambda, \mu})^* = (-1)^\mu \alpha_{\lambda, -\mu}. \quad (20.7)$$

$\lambda=0$ only comes into the volume integral and the value of $\alpha_{0,0}$ can be used to converse the volume. $\lambda=1$ correspond to a displacement of the center of mass.

Since the most accurately measured quantities are for the proton density. The following equations for the multiple moments will be given for the proton density. The nuclear Hamiltonian of course contains both protons and neutrons.

To order α^2 , the volume integral of (20.6) is

$$I_0 = \int_{\Omega} \int_0^{R(\theta,\phi)} r^2 dr d\Omega = \frac{1}{3} \int_{\Omega} [R(\theta, \phi)]^3 d\Omega = \frac{R_o^3}{3} [4\pi + 3\alpha_o \sqrt{4\pi} + 3\Sigma_{\lambda} \beta_{\lambda}^2], \quad (20.8)$$

where

$$\beta_{\lambda}^2 = \Sigma_{\mu} |\alpha_{\lambda,\mu}|^2 \quad (20.9)$$

If we impose the condition of saturation (that the average interior density remains constant), then the volume must be conserved, $I_0 = 4\pi R_o^3 / 3$. This condition can be imposed by having

$$\alpha_o = -\frac{\Sigma_{\lambda} \beta_{\lambda}^2}{\sqrt{4\pi}}. \quad (20.10)$$

To order α^2 , the r^2 integral is

$$I_2 = \int_{\Omega} \int_0^{R(\theta,\phi)} r^4 dr d\Omega = \frac{1}{5} \int_{\Omega} [R(\theta, \phi)]^5 d\Omega = \frac{R_o^5}{5} [4\pi + 5\alpha_o \sqrt{4\pi} + 10\Sigma_{\lambda} \beta_{\lambda}^2]. \quad (20.11)$$

With the condition of volume conservation from Eq. (20.10), the mean-square radius without β_{λ} is

$$\langle r^2 \rangle_o = \frac{I_2(\text{with } \beta_{\lambda} = 0)}{I_0} = \frac{3R_o^2}{5}, \quad (20.12)$$

and to order β_{λ} it is

$$\langle r^2 \rangle = \frac{I_2}{I_0} = \frac{3R_o^2}{5} \left(1 + \frac{5}{4\pi} \beta^2\right) = \langle r^2 \rangle_o \left(1 + \frac{5}{4\pi} \beta^2\right), \quad (20.13)$$

where

$$\beta^2 = \Sigma_{\lambda} \beta_{\lambda}^2, \quad (20.14)$$

Eq. (20.14) implies that the rms charge radii increase for “deformed” nuclei. This can be observed in the figures in the chapter on experimental charge radii.

The multipole matrix elements are given by

$$M_{\lambda,\mu} = \int \rho(\vec{r}) r^\lambda Y_{\lambda,\mu}(\Omega) d\tau. \quad (20.15)$$

Using the density defined Eq. (20.6) we have

$$\begin{aligned} M_{\lambda,\mu} &= \rho_o \int_{\Omega} \int_0^{R(\theta,\phi)} r^\lambda Y_{\lambda,\mu}(\Omega) r^2 dr d\Omega = \frac{\rho_o}{(\lambda+2)} \int_{\Omega} [R(\theta,\phi)]^{\lambda+2} Y_{\lambda,\mu}(\Omega) d\Omega \\ &= \rho_o R_o^{\lambda+2} \int_{\Omega} \sum_{\mu'} \alpha_{\lambda,\mu'} Y_{\lambda,\mu'}(\Omega) Y_{\lambda,\mu}(\Omega) d\Omega = \rho_o R_o^{\lambda+2} \alpha_{\lambda,\mu} = \frac{3}{4\pi} Z R_o^{\lambda} \alpha_{\lambda,\mu}, \end{aligned} \quad (20.16)$$

where $[R(\theta,\phi)]^{\lambda+2}$ has been expanded to leading order in α , and ρ_o has been replaced using the charge density is given by

$$\int \rho(\vec{r}) d\tau = \rho_o \frac{4\pi}{3} R_o^2 = Z. \quad (20.17)$$

From Eqs. (20.999), (20.13), and (20.14), Q can be written as a function of β (to order

β) as

$$Q(\beta) = \sqrt{\frac{9}{5\pi}} Z R_o^2 \beta = \sqrt{\frac{5}{\pi}} Z \langle r^2 \rangle_o \beta. \quad (20.18)$$

For $\lambda=2$ and assuming axial symmetry around the R_3 axis, Eq. (20.6) takes the form

$$R(\theta, \phi) = R_o \left[1 + \beta Y_{2,0}(\theta, \phi) \right] = R_o \left[1 + \sqrt{\frac{5}{16\pi}} \beta (3\cos^2\theta - 1) \right]. \quad (20.19)$$

$\beta > 0$, Eq. (20.19) describes a quadrupole prolate (cigar) shape with respect to the symmetry axis. When $\beta < 0$, Eq. (20.19) describes a quadrupole oblate (disk) shape with respect to the symmetry axis. At this level the Bohr model is descriptive. To make it prescriptive requires an underlying microscopic model that finds the energy as a function of deformation [6]. Results from an deformed EDF model assuming axial symmetry [5] is shown in Fig. (20.2). In all cases the minimum as a function of $Q(\beta)$ comes within 1-2 MeV from experiment (the horizontal black line). For ^{208}PB the minimum is at $\beta=0$ indicative of its spherical shape. For all other nuclei there are two minima with the lowest one being for $\beta > 0$ (prolate shape). The minimum at $\beta < 0$ indicates that there is an excited 0^+ state with an

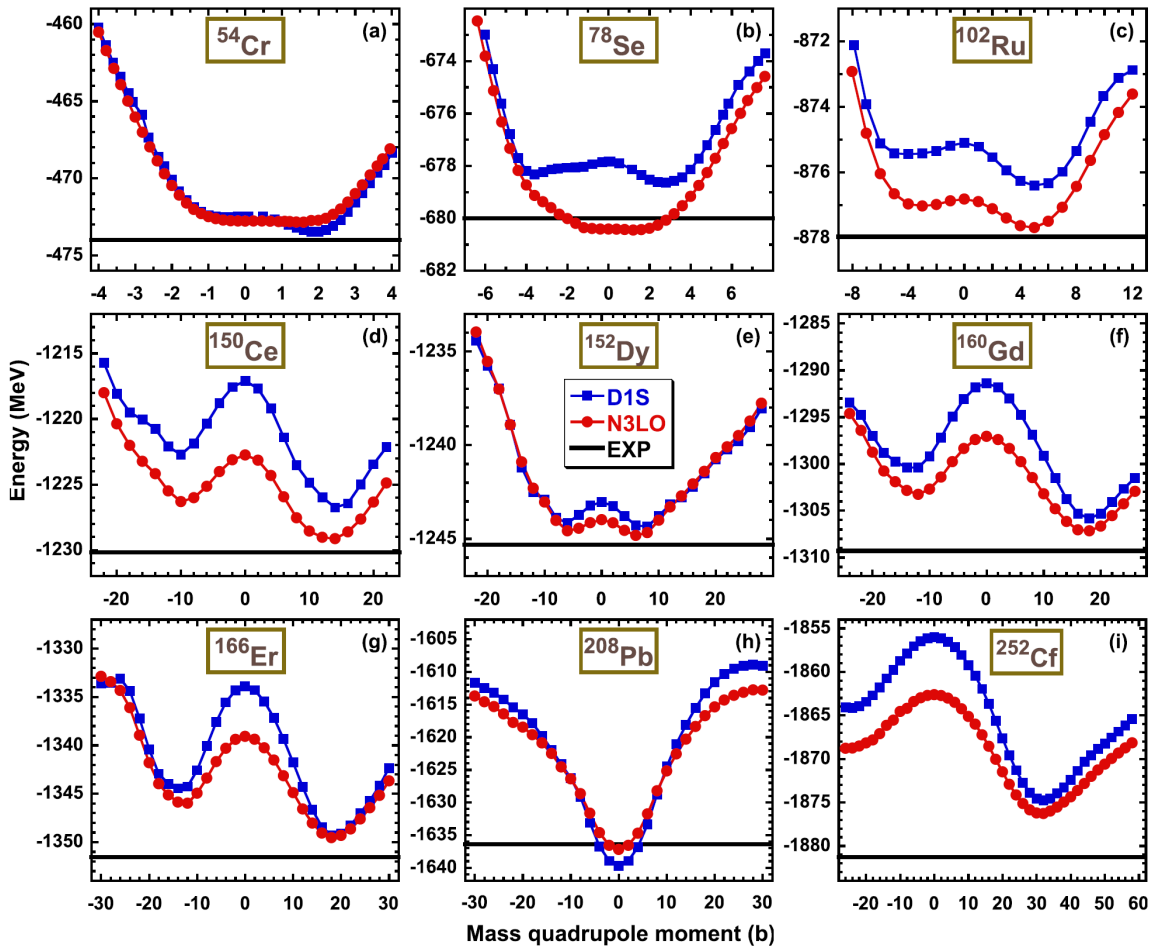


Figure 20.1: Deformation energies of selected nuclei from [5]. These were obtained from EDF calculations in a deformed axially symmetric basis with two different Hamiltonians. The x-axis shows the $Q(\beta)$ as defined by Eq. (20.18).

oblate shape. In some cases there is only a small difference between the energies oblate and prolate shapes. For these the spectra will depend on the solution of the Bhor-Hamiltonian for these rather broad minima. This will involve the γ degree of freedom.

Non-axially symmetry shapes required the introduction of a second parameters γ . First we consider the most important quadrupole ($\lambda=2$) degree of freedom. For this part we will replace $\alpha_{2,v}$ by just α_μ and β_2 by β . Because of reflection symmetry of the ellipsoid $\alpha_{-1} = \alpha_1 = 0$ and $\alpha_{-2} = \alpha_2$. Thus for $\lambda=2$ there are only two independent terms, α_0 and α_2 . It is conventional to rewrite these in terms of a magnitude β and an angle γ ,

$$\alpha_0 = \beta \cos\gamma, \quad (20.20)$$

and

$$\alpha_2 = \beta \sin\gamma / \sqrt{2}. \quad (20.21)$$

The body fixed radii, R_1, R_2, R_3 are

$$R_k = R_o \left[1 + \frac{5}{4\pi} \beta C(\gamma, k) \right], \quad (20.22)$$

Table 20.1: Values of $C(\gamma, k)$ and $S^2(\gamma, k)$ for some γ .

k	$C(0, k)$	$C(\pi/6, k)$	$C(\pi/3, k)$	$S^2(0, k)$	$S^2(\pi/6, k)$	$S^2(\pi/3, k)$
1	-0.5	0.5	0.5	0.75	1	0.75
2	-0.5	-0.866	-1	0.75	0.25	0
3	1.0	0.866	0.5	0	0.25	0.75

with

$$C(\gamma, k) = \cos(\gamma - 2\pi k/3). \quad (20.23)$$

Some values for $C(\gamma, k)$ are given in Table (20.1).

The shapes given by (20.22) are shown in Fig. (20.3) taken from the book by Zelevinsky and Volya [7] For the most general shape we can take just one segment of the polar diagram described by $\beta > 0$ and $0 \geq \gamma \leq 60^\circ$.

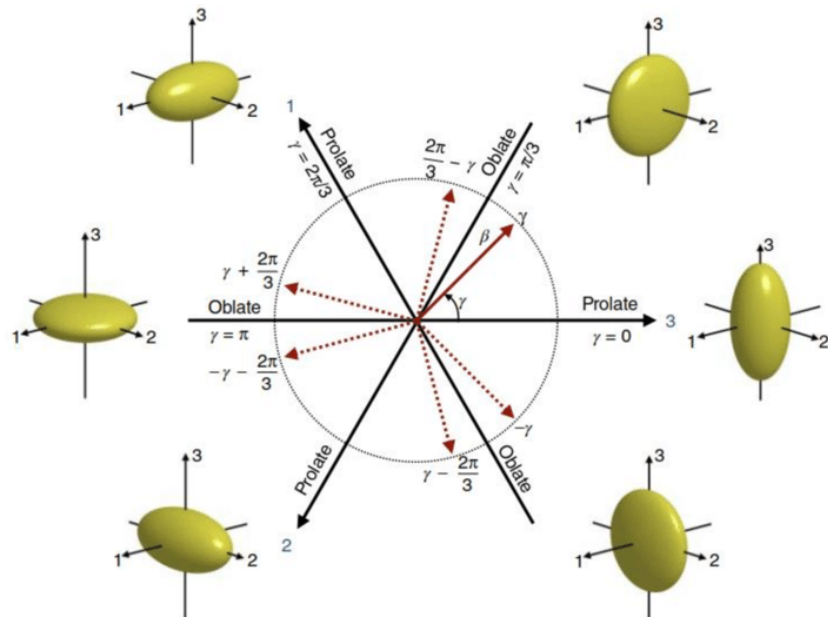


Figure 20.2: Polar diagram of the deformation plane. The shapes along the red arrow at angle γ shown with a solid line are the same as those for the other five dashed arrows.

For $\beta=0$ the shape is spherical. For $\beta > 0$ and For $\gamma=0$, the shape is prolate around the R_3 axis. For $\beta > 0$ and for $\gamma=60^\circ$ the shape is oblate around the R_2 axis.

Using (20.16), the intrinsic quadrupole moments are defined by the tensor operator $(Q2)_{2,\mu}$ of rank ($\lambda=2$)

$$(Q2)_{2,\mu} = \sqrt{\frac{16\pi}{5}} M_{2,\mu} = \sqrt{\frac{9}{5\pi}} Z R_o^2 \alpha_\mu. \quad (20.24)$$

In analogy with Eqs. (20.20) and (20.21), this is expressed in terms of (β, γ) as

$$(Q2)_{2,0} = Q \cos \gamma, \quad (20.25)$$

$$(Q2)_{2,1} = (Q2)_{2,-1} = 0, \quad (20.26)$$

and

$$(Q2)_{2,2} = (Q2)_{2,-2} = Q \sin \gamma / \sqrt{2}, \quad (20.27)$$

where Q is the magnitude of $Q2$

These are descriptive examples where one could use some electromagnetic properties (see below) to determine $(\beta \gamma)$. A prescriptive model would come from microscopic calculation for the energy as a function of $(\beta \gamma)$. There are many such calculations. An example from [8] for ^{160}Yb is shown in Fig. (20.4). In this case there are two minima. The one with the lowest energy is near has $(\beta, \gamma) = (0.24, 0^\circ)$. The higher energy minima is much more deformed. It is proposed that this corresponds to the 0_2^+ state in ^{160}Yb [8].

20.3 Rotations for a rigid rotor

In this case we assume that there are no vibrations, so that $H = T_R$. The rotational kinetic energy operator is given by

$$T_R = \sum_{k=1,2,3} \frac{\hbar^2 \hat{L}_k^2}{2I_k}, \quad (20.28)$$

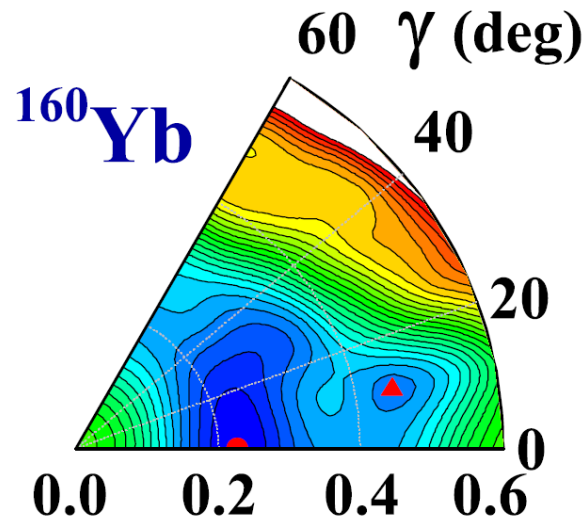


Figure 20.3: The (β, γ) energy surface for ^{162}Yb obtained in [8]. It is based on a five-dimensional collective Bohr Hamiltonian based on covariant density functional thoery [9], [10]. The energy scale starts at 0 (blue) and goes up to 12 MeV (red).

where I_k are the moments of inertia in the intrinsic system

$$I_k = 4B\beta^2 S^2(\gamma, k) \quad \text{with} \quad S^2(\gamma, k) = \sin^2\left(\gamma - \frac{2}{3}\pi k\right). \quad (20.29)$$

B is the Bohr mass parameter. The value of B depends upon the fraction of the total mass that participates in the rotation. Some values for S^2 are given in Table (20.1). Note that for spherical nuclei ($\beta=0$) that all of these moments of inertial are zero. This is a consequence of the fact that for a spherical (closed-shell) wavefunction, any amount of rotation leads to the same wavefunction.

When $\gamma=0$ or $\gamma=\pi/3$, we have axial symmetry where one of the moments of inertia is zero (see the S^2 values in Table 1). For these cases the Hamiltonian is just

$$T_R = \frac{\hbar^2 \hat{L}^2}{2I} \quad (20.30)$$

where

$$\hat{L}^2 = \sum_k \hat{L}_k^2, \quad (20.31)$$

and I is the moment of inertia for rotation perpendicular to the symmetry axis. The energy spectrum is

$$E_R = \frac{\hbar^2 L(L+1)}{2I} \quad (20.32)$$

This gives $R(4^+/2^+) = 10/3$ for the ratio of the 4^+ and 2^+ excitation energies that is observed in many nuclei that lie in between the magic numbers in heavy nuclei.

For the moment of inertia we can start with the result for a rigid sphere of radius R_o

$$I_{\text{sphere}} = \frac{2}{5} A m R_o^2 = 0.0138 A^{5/3} (\hbar/\text{MeV}), \quad (20.33)$$

where we have used $R_o = 1.2A^{1/3}$ and $mc^2 = 938$ MeV for the nucleon mass. As an example for comparison to experiment, the energy of the first 2^+ state in ^{166}Er is 81 keV. From Eq. (20.32) the moment of inertia is

$$I_{\text{exp}} = 37 \hbar^2 / \text{MeV} \quad (20.34)$$

to be compared with Eq. (20.33) we have

$$R_{\text{sphere}} = \frac{I_{\text{exp}}}{I_{\text{sphere}}} = \frac{37}{69} = 0.53. \quad (20.35)$$

If we include the deformation and assume $\gamma=0$, the rigid-body moment of inertia increases to [11]

$$I_{\text{ridged}} = I_{\text{sphere}} \left[1 + \sqrt{\frac{5}{16\pi}} \beta \right], \quad (20.36)$$

and with $\beta = 0.32$ the ratio decreases to 0.48.

The other extreme is to just take the moment of inertia for the “caps” assuming that the spherical core does not contribute (it is irrotational) and the moment of inertia takes the form of Eq. (20.29) with

$$B = \frac{15}{16\pi} I_{\text{sphere}}, \quad (20.37)$$

and

$$I_{\text{irrot}} = \frac{45}{16\pi} I_{\text{sphere}} \beta^2. \quad (20.38)$$

With $\beta = 0.32$, this would give

$$R_{\text{sphere}} = \frac{I_{\text{exp}}}{I_{\text{irrot}}} = \frac{37}{6.7} = 5.5. \quad (20.39)$$

These results are similar to those of other deformed nuclei shown in [11].

One can also use Eq. (20.32) to find the moment of inertial as a function of J . Here we use J to denote the total angular momentum that comes from the simple rotation associated with L plus the additional angular momentum that comes from coupling to vibrations and quasi-particle states. In the simple rotational model I does not depend on $J = L$. But in more detailed models I depends on J . One of the earlier investigations of this developed the variable moment of inertial (VMI) model [12]. There are a limited number of orbitals that can contribute to the rotation, and when the maximum is reached one has a “band termination” [13]. Also there are many bands that come from different quasi-particle states and different intrinsic shapes. Only J is a good quantum number. The mixing results in complex patterns for the moment of inertial as a function of J .

The nucleus is fully triaxial when $\gamma=\pi/6$ with $I = I_1 = 4I_2 = 4I_3 = 8B\beta_2^2$. the Hamiltonian is given by

$$T_R = \frac{\hbar^2(4\hat{L}^2 - 3\hat{L}_1^2)}{I}, \quad (20.40)$$

with an energy spectrum

$$E_T = \frac{\hbar^2[4L(L+1) - 3K^2]}{I} = \frac{\hbar^2[L(L+4) + 3n(2L-n)]}{I}, \quad (20.41)$$

where K is the projection of the angular momentum onto the R_1 axis, and $n = L - K$ (called the wobbling quantum number [14]). The yrast band has $n = 0$ and the γ band has $n = 2$. This gives $R(4^+/2^+) = 8/3$

The wavefunctions for $\gamma=30^\circ$ are given in terms Wigner rotation matrices \mathcal{D}

$$\Psi_{K,M}(\Omega) = \sqrt{\frac{2L+1}{16\pi^2(1+\delta_{K,0})}} [\mathcal{D}_{M,K}^L(\Omega) + (-1)^L \mathcal{D}_{M,-K}^L(\Omega)], \quad (20.42)$$

where $K = 0, 2, 4, \dots$ is the projection of the angular momentum \vec{L} on the R_3 axis. For $K = 0$, $L = 0, 2, 4, \dots$, and for $K > 0$, $L = K, K+1, K+2, \dots$. In general, for γ in-between 0 and $\pi/3$ the three moments of inertia are all different. The wavefunctions for the numerical solutions of Eq. (20.28) can be expanded in terms of Eq. (20.42). The spectra as a function of γ are shown in Fig. 2 of [15].

For γ between 0 and 30° , the spectra show two bands, the ground state band with $L = 0, 2, 4, \dots$ and an excited “ γ band” band with $L = 2, 3, 4, \dots$. The 0^+ ground state has $K = 0$, and there are two 2^+ states that are mixtures of $K = 0$ and $K = 2$. The values of β , γ and the 2^+ mixing parameters can be inferred from an analysis of experimental Coulomb excitation data for well deformed nuclei [16].

20.4 Quadrupole moments and $B(E2)$

One can use the deformed wavefunctions to calculate observable quadrupole moments and the $B(E2)$ for electromagnetic transitions in terms of the intrinsic quadrupole moment [17], [18]. One can connect the intrinsic quadrupole moments to experimental observables in the laboratory frame by considering the scalar combination. Since they are scalars they do not depend on the frame in which they are evaluated. The lowest two are

$$[(Q2) \otimes (Q2)]_{0,0} = \sqrt{\frac{1}{5}} Q^2, \quad (20.43)$$

and

$$\{[(Q2) \otimes (Q2)]_2 \otimes (Q2)\}_{0,0} = -\sqrt{\frac{2}{35}} Q^3 \cos(3\gamma). \quad (20.44)$$

The expectation values in the 0^+ nuclear ground state evaluated with the intermediate 2_1^+ state can be expressed in terms of the observables

$$B(\uparrow) = B(E2, 0_1^+ \rightarrow 2_1^+), \quad (20.45)$$

and the spectroscopic quadrupole moment Q_s of the 2^+ state

$$\langle 0^+ | \{[(Q2) \otimes (Q2)]_2 \otimes (Q2)\}_{0,0} | 0^+ \rangle = \sqrt{\frac{1}{5}} \frac{16\pi}{5} \frac{B(\uparrow)}{e^2}, \quad (20.46)$$

and

$$\langle 0^+ | \{[(Q2) \otimes (Q2)]_2 \otimes (Q2)\}_{0,0} | 0^+ \rangle = \sqrt{\frac{7}{10}} \frac{16\pi}{5} \frac{B(\uparrow)}{e^2} \frac{Q_s}{e}. \quad (20.47)$$

Equating these results in the intrinsic and laboratory frame we can find the intrinsic quadrupole moment from B

$$Q = \frac{16\pi}{5} \frac{B(\uparrow)}{e^2}, \quad (20.48)$$

and then the angle γ from Q_s

$$\cos(3\gamma) = -\frac{7}{2} \frac{Q_s}{Q e}. \quad (20.49)$$

With Eq. (20.18), we can find β

$$\beta = \frac{4\pi}{5} \frac{\sqrt{B(\uparrow)}}{(e Z < r^2 >_o)}. \quad (20.50)$$

We can define a normalized spectroscopic moment q by

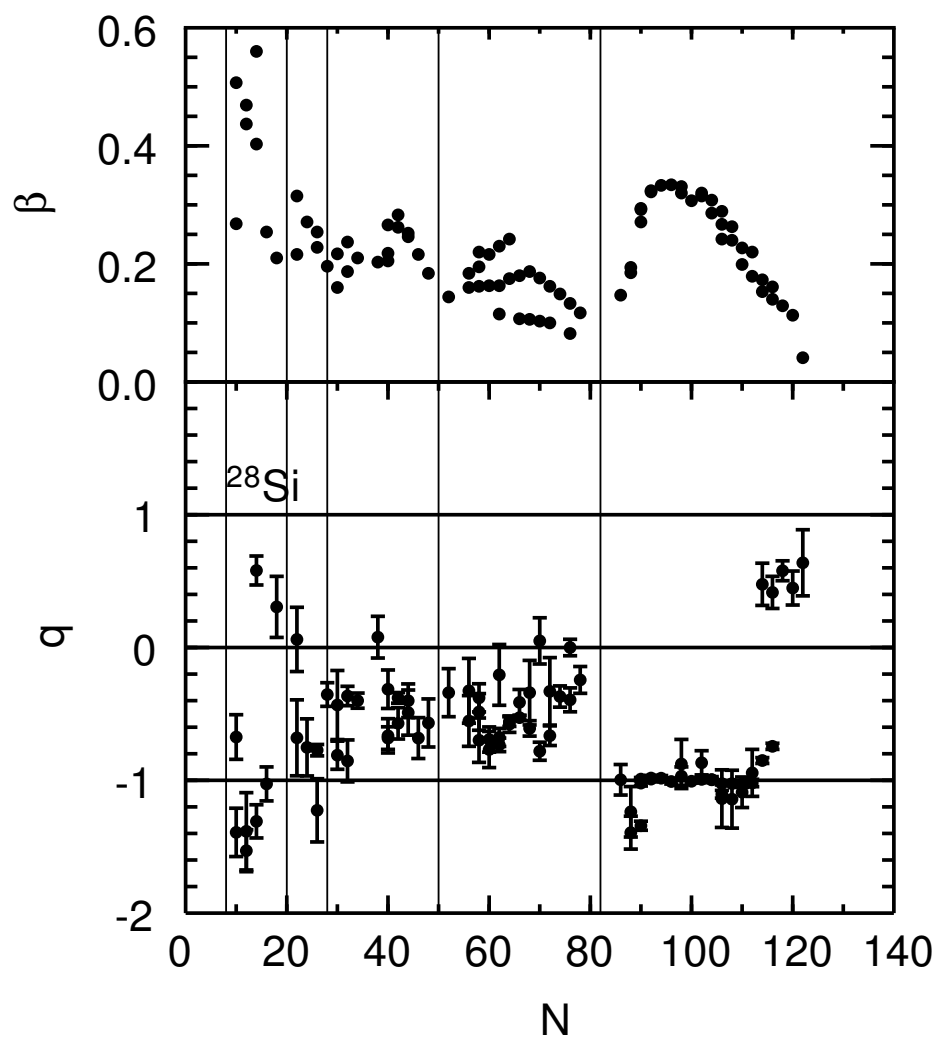
$$q = \frac{Q_s(2_1^+)}{\sqrt{c B(\uparrow)}} = -\cos(3\gamma), \quad (20.51)$$

where the constant c is

$$c = \frac{64\pi}{245} = 0.82. \quad (20.52)$$

As an example of these results for a well deformed nucleus, we can consider ^{172}Yb ($Z = 70$) with $B(\uparrow) = 6.09(15) \text{ e}^2 \text{ b}^2$, (where b “barn” area unit of $b^2 = 100 \text{ fm}^2$), and $\langle r^2 \rangle = (5.30)^2 \text{ fm}^2$. From the results above we find $Q = 782 \text{ fm}^2$, $\beta = 0.315$. The mean-square charge radius increases by $(1 + \frac{5}{4\pi}\beta^2) = 1.039$. The measured spectroscopic quadrupole moment is $-222(4) \text{ e fm}^2$. This gives $q = -0.99(2)$ and $\gamma=0$ which implies a near perfect prolate deformation.

Experimental data for Q_s and $B(\uparrow)$ have been compiled in [20] and [21]. Most of these results are obtained from the Coulomb excitation (Coulomex) of stable nuclei where the data are sensitive to the $E2$ matrix elements connecting many excited states as well as the quadrupole moments [18]. These are used to make the plot for β and q shown in Fig. (20.5). From $N = 90 - 105$ all of the data are close to $q = -1$ and $\gamma=0$ indicating that these nuclei have a prolate shape, even though the β value changes from 0.15 to 0.32. Many other nuclei have $q \approx -0.5$ which would give $\gamma \approx 40$ degrees - a triaxial shape. There are only a few

Figure 20.4: Normalized quadrupole moments and β for 2_1^+ states

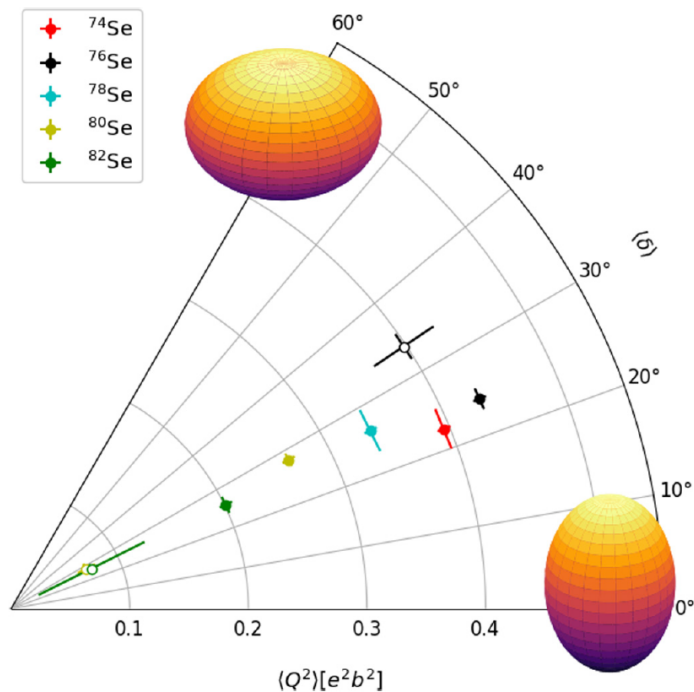


Figure 20.5: Results of the shape analysis of experimental data [19] for $^{74-82}\text{Se}$. The filled circles are for the 0_1^+ (ground states) and the open circles are for the 0_2^+ states. For this figure $\gamma = \delta$.

nuclei with $q > 0$ indicative of an oblate shape. The most precise and largest positive value in light nuclei is for ^{28}Si .

The fact that there are many more prolate shaped nuclei than oblate shaped nuclei is not well understood. In [22] it was argued that it was related to order in which the shell-model orbitals are filled.

For the evaluation of β for non-zero γ one should consider the sum of the $B(E2)$ to both 2^+ states. Fig. 1 of [16] shows the ratio of the $B(E2)$ for the $2_2^+ \rightarrow 0_1^+$ to the $2_1^+ \rightarrow 0_1^+$ transitions for well deformed nuclei and interprets the results in terms of K mixing. The ratio is 0.005 to 0.10. So it is a reasonable approximation to extract β from just the $B(E2)$ to the first 2^+ state. Ref. [16] shows that the (β, γ) extracted with the Kumar-Cline method (see below) does not depend on the mixing angle of the 2^+ states $K = 0$ and $K = 2$.

To take into account vibrations we need to understand the spread in β and γ . This can be done by using higher-order scalar invariants of the $E2$ operator, as well as including other excited states in their evaluations. This was first done by Kumar [17] and Cline [18]. A recent example of its use is the analysis of data and theory for $^{74-82}\text{Se}$ [19], where it was

found that $\gamma \approx 28^\circ$. The results from [19] are shown in Fig. (20.6). This method has been used to analyze microscopic calculations [23], [19], [24]. These analysis only take into account the $E2$ matrix elements that come into the Kumar-Cline invariants. The implications for the energy spectrum and more detailed pattern of $E2$ matrix elements are not considered.

20.5 Vibrations

The vibrational part of the kinetic energy can be written as [25]

$$T_V = -\frac{\hbar^2}{2B} \left[\frac{1}{\beta^4} \frac{\partial}{\partial \beta} \beta^4 \frac{\partial}{\partial \beta} + \frac{1}{\beta^2 \sin 3\gamma} \frac{\partial}{\partial \gamma} \sin(3\gamma) \frac{\partial}{\partial \gamma} \right]. \quad (20.53)$$

When the potential is only a function of β , then the Hamiltonian is separable [26] in (β, γ) . The wavefunctions are eigenfunctions of L^2 , L_z and L_3 with quantum numbers L , M and K . The solution also involves the $SO(5)$ group seniority τ . The first model that used this approximation was Bohr's Harmonic oscillator-potential model Hamiltonian for oscillations around $\beta=0$

$$H = -\frac{\hbar^2}{2B} \nabla^2 + \frac{1}{2} C \beta^2, \quad (20.54)$$

where C is the oscillator strength. The resulting energy is

$$E = (N + 5/2)\hbar\omega, \quad (20.55)$$

with $\omega = \sqrt{C/B}$. In this case the energy ratio is just $R(4^+/2^+) = 2$. Table 2 gives the resulting allowed sets of quantum numbers in order of excitation energy up to $N = 3$. We call these N -phonon excitations. We also have

$$\frac{B(E2)(N = 2 \rightarrow N = 1)}{B(E2)(N = 1 \rightarrow N = 2)} = 2, \quad (20.56)$$

independent of L . There are many nuclei that have energy spectra that look like the Bohr vibrations, when they can be measured, but most of these violate the expectation of Eq. (20.56) for the 0_2^+ to 2_1^+ transition.

The Wilets-Jean model also assume that the potential depends only on β , but the harmonic-oscillator is displaced around a fixed value β_o . In this case we have

$$N = 2n_\beta + \tau, \quad (20.57)$$

and only the $n_\beta = 0$ states from Table 2 are allowed. The energy spectrum is

$$E_v = \frac{\hbar^2}{2B\beta_0^2} v(v+3), \quad (20.58)$$

Table 20.2: Quantum numbers for the β vibrational around $\beta=0$.

N	n_β	τ	L
0	0	0	0
1	0	1	2
2	0	2	2,4
2	1	0	0
3	0	3	0,3,4,6
3	1	1	2

with $R(4^+/2^+) = 14/5$. Other references to the wavefunctions and resulting $B(E2)$ values are given in [14]. The Wilets-Jean model has been compared to the rigid triaxial rotor model in [14]. Figure 1 of [14] shows the relative $B(E2)$ values for these two models.

For more general configurations the energy spectrum given by Eq. (20.32) is extended

to

$$E_R = \frac{\hbar^2 J(J+1) - K^2}{2I_1} + \frac{\hbar^2 K^2}{2I_3}, \quad (20.59)$$

where K is the projection of the total angular momentum J onto the symmetry axis. $K = 0$ gives the rotational spectrum of (20.32) built on the ground state. Vibrations in the β direction give rise to an excited rotational band with $K = 0$ and $L = 0, 2, 4, \dots$, and vibrations in the γ direction give rise to an excited rotational band with $K = 2$ and $L = K, K+1, K+2, \dots$. The experimental spectrum of ^{152}Sm with bands interpreted in terms of β and γ vibrations are shown in Fig. (20.7).

The electromagnetic properties for bands built on K are [27]

$$Q_s(JK) = (\pm) \frac{3K^2 - J(J+1)}{(J+1)(2J+3)} e Q, \quad (20.60)$$

$$B(E2; JK \rightarrow J'K) = \frac{5}{16\pi} \langle J, K, 2, 0 | J', K \rangle^2 e^2 Q^2, \quad (20.61)$$

$$\mu = g_R J + (g_K - g_R)^2 \frac{K^2}{(J+1)}, \quad (20.62)$$

and

$$B(M1; JK \rightarrow J'K) = \frac{3}{4\pi} (g_K - g_R)^2 \langle K, K, 1, 0 | J', K \rangle^2 \mu_N^2, \quad (20.63)$$

$G_R \approx (Z/A)$ is the rotational g-factor, and g_K is the g-factor associated with the band-head state K . These results apply to basic rotational bands in even-even nuclei where $J = L$, as well as to more complicated configuration in all nuclei where J comes from the coupling of \vec{L} to deformed single-particle degrees of freedom.

There is often controversy about the assignment of the structure of excited bands. The reason is that they can also be due to, or mix, with excited states with a different deformation, or to the excitations of nucleons in deformed orbitals. Interpretations must be made on the basis of whether or not their detailed electromagnetic properties are consistent.

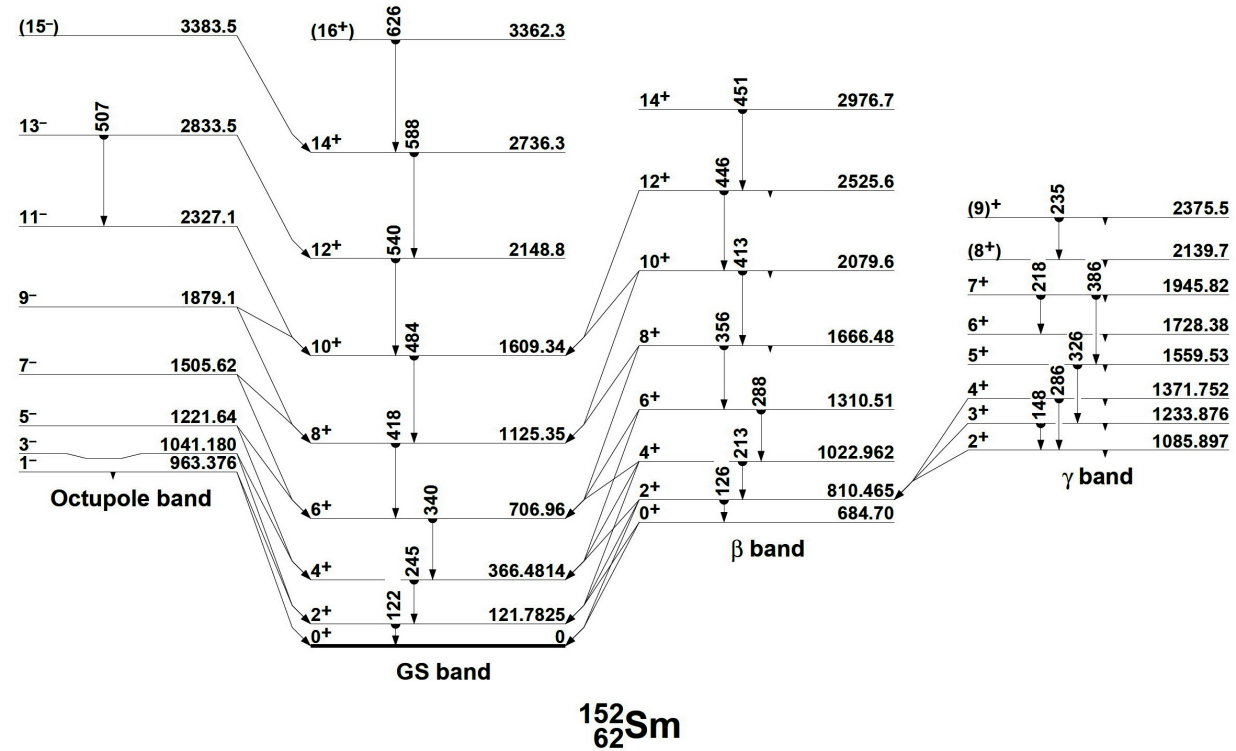


Figure 20.6: Experimental energy levels for ^{152}Sm labeled by their suggested interpretation in terms of β , γ and octupole bands [28].

20.6 Other collective multiples

The discussion above has concentrated on the quadrupole $\lambda=2$ collective degree of freedom. The $\alpha_{\lambda,\mu}$ in the geometric shape can contain higher multipoles. The rms radii given by Eq. (20.13) on a sum over all of these as in Eq. (20.14). In particular, some nuclei exhibit strong octupole deformed shapes that are come from $\lambda = 3$ in Eq. (20.6). The octupole deformed bands contain both positive and negative parity states (see Ref. [29], [30]. The electromagnetic B(E1) and B(E3) in these band are large.

The $\lambda=4$ shapes are associated with strong B(E4) from the 0^+ ground state to the first 4^+ state. Some early references for β_4 are [31], [32] and [33]. The largest experimental β_4 values are around 0.10.

Calculated β_λ up to $\lambda=6$ for many nuclei obtained with a macroscopic-microscopic model are given in [34].

Bibliography

- [1] A. Bohr and B. R. Mottelson, Ann. Rev. Nucl. Phys. **23**, 363 (1973).
- [2] A. Bohr, Rev. Mod. Phys. **48**, 365 (1976).
- [3] P. G. Reinhard and E. W. Otten, Nucl. Phys. **A420**, 173 (1984).
- [4] L. Fortuna, Eur. Phys. Jour. A **26**, s01, 1 (2005).

- [5] K. Bennaceur, J. Dobaczewski, T. Haverinen, and M Kortelainen, *Jour. Phys. G* **47**, 105101 (2020).
- [6] D. Vautherin, *Phys. Rev. C* **7**, 296 (1973). link
- [7] “Physics of Atomic Nuclei”, Vladimir Zelevinsky and Alexander Volya, Wiley-VCH (2017).
- [8] S. N. T. Majola et al., *Phys. Rev. C* **100**, 044324 (2019). link
- [9] T. Niksie, Z. P. Li, D. Vretenar, L. Prochniak, J. Meng, and P. Ring, *Phys. Rev. C* **79**, 034303 (2009). link
- [10] Z. P. Li, T. Niksie, D. Vretenar, J. Meng, G. A. Lalazissis, and P. Ring, *Phys. Rev. C* **79**, 054301 (2009). link
- [11] J. M. Allmond and J. L. Wood, *Phys. Lett. B* **767**, 226 (2017).
- [12] G. Scharff-Goldhaber, C. B. Dover and A. L. Goodman, *Ann. Rev. Nucl. Sci.* **26**, 239 (1976).

- [13] A. V. Afanasjev, D. B. Fossan, G. J. Lane, and I. Ragnarsson, Phys. Rep. **322**, 1 (1999).
- [14] J. Meyer-Ter-Vehn, Phys. Lett. **86B**, 10 (1979).
- [15] J. Meyer-ter-vehn, Nucl. Phys. A **249**, 111 (1975).
- [16] J. L. Wood, A-M. Oros-Peusquens, R. Zaballa, J. M. Allmond, and W. D. Kulp, Phys. Rev. C **70**, 024308 (2004). link
- [17] K. Kumar, Phys. Rev. Lett. **28**, 249 (1972). link
- [18] D. Cline, Ann. Rev. Nucl. Part. Sci. **36**, 683 (1986).
- [19] J. Henderson et al., Phys. Rev. C **99**, 054313 (2019). link
- [20] Y. Y. Sharon, N. Benczer-Koller, G. J. Kumbartzki, L. Zamick and R. F. Casten, Nucl. Phys. A **980**, 131 (2018).
- [21] P. Petkov, D. S. Delion and C. Mueller-Gatermann, Phys. Rev. C **102**, 044317 (2020). link

- [22] M. Horoi and V. Zelevinsky, Phys. Rev. C **81**, 034306 (2010). link
- [23] A. Poves, F. Nowacki and Y. Alhassid, arXiv:1906.07542v1 (2019).
- [24] J. Henderson, Phys. Rev. C **102**, 054306 (2020). link
- [25] M. Jean, Nucl. Phys. **21**, 142 (1960).
- [26] L. Wilets and M. Jean, Phys. Rev. **102**, 788 (1956). link
- [27] K. E. G. Loebner, M. Vetter and V. Hoenig, Nucl. Data Tables **A7**, 495 (970).
- [28] Table of Isotopes, R. B. Firestone, V. S. Shirley S. Y. F, Chu Chu, C. M. Baglin and J. Zipkin, Wiley Interscience (1996).
- [29] I. Ahmad and P. A. Butler, Annu. Rev. Nucl. Part. Sci. **43**, 71 (1993).
- [30] P. A. Butler and W. Nazarewicz, Rev. Mod. Phys. **68**, 349 (1996).
- [31] G. F. Bertsch, Phys. Lett. B **130**, 130 (1968).

- [32] P. Moeller, B. Nilsson, S. G. Nilsson, A. Sobiczewski, Z. Szymanski, and S. Wycech, Phys. Lett. B **26**, 418 (1968).
- [33] D. L. Hendrie et al., Phys. Lett. B **26**, 127 (1968).
- [34] P. Moeller, J. R. Nix, W. D. Myers and W. J. Swiatecki, Atomic Data and Nuclear Data Tables, **59**, 185 (1995).

Chapter 21

Single-particle energies in a deformed potential

In the chapter in collective motion we introduced the idea of an intrinsic deformed state. The wavefunction for this state described rotational spectra in the laboratory frame. The next step is to obtain the single-particle wavefunctions for these deformed states.

We start with the deformed harmonic oscillator

$$U = \frac{1}{2}M[\omega_\rho^2(x^2 + y^2) + \omega_z^2 z^2] \quad (21.1)$$

with

$$\omega_\rho^2 = \omega_x^2 = \omega_y^2 = \omega_o^2(1 + \epsilon_2/3), \quad (21.2)$$

and

$$\omega_z^2 = \omega_o^2(1 - 2\epsilon_2/3). \quad (21.3)$$

Eq. (21.1) can be written in the form

$$U = U_o + U_{\text{def}}, \quad (21.4)$$

where

$$U_{\text{def}} = \frac{\epsilon_2}{3} M \omega_o^2 (x^2 + y^2 - 2z^2) = -\epsilon_2 \frac{4}{3} \sqrt{\frac{\pi}{5}} M \omega_o^2 r^2 Y_{2,0}(\theta). \quad (21.5)$$

For $\epsilon_2 > 0$ the potential is prolate around the z axis, and for $\epsilon_2 < 0$ the potential is oblate. The β_2 parameter of the Bohr model is related to ϵ (to order ϵ_2) by

$$\beta_2 = \sqrt{\frac{16\pi}{45}} \epsilon_2. \quad (21.6)$$

The expansion to higher order is given in [1].

The total Hamiltonian is the rotational kinetic energy plus U .

$$H = \frac{\hbar^2 \hat{L}^2}{2I} + U = \frac{\hbar^2 \hat{J}^2}{2I} + \frac{\hbar^2 \hat{j}^2}{2I} - \frac{\hbar^2 \hat{J} \cdot \hat{j}}{I} + U, \quad (21.7)$$

where \hat{j} is the angular momentum of the odd particle, and the total angular momentum of the nucleus is

$$\hat{J} = \hat{L} + \hat{j}. \quad (21.8)$$

The last two terms in Eq. (21.7) are called the rotation-particle coupling interactions. In a first approximation we will neglect the these; they can later be included in perturbation theory.

The Nilsson Hamiltonian has the form [2], [3]

$$H_{\text{Nilsson}} = H + D \hat{\ell}^2 + \chi \hat{\ell} \cdot \hat{s}, \quad (21.9)$$

where the deformed part is given by

$$U_{\text{def}} = -\frac{4}{3} \sqrt{\frac{\pi}{5}} M \omega_o^2 r^2 Y_{2,0}(\tau) = \frac{1}{3} M \omega_o^2 (x^2 + y^2 - 2z^2). \quad (21.5)$$

Eq. (21.9) also contains the spin-orbit interaction, and an $\hat{\ell}^2$ term that takes into account that in a more realistic Woods-Saxon potential that the single-particle energies within a given N depend on ℓ with the states with higher ℓ coming lower in energy.

There are two limits of the Nilsson Hamiltonian that can be solved exactly. For small

deformation we treat U_{def} as a perturbation

$$\langle n, \ell, j | U_{\text{def}} | n, \ell, j \rangle = \frac{2\epsilon}{3} (N + 3/2) \frac{[3\Omega^2 - j(j+1)]}{4j(j+1)}, \quad (21.10)$$

where Ω is the projection of the single-particle angular momentum along the z axis. These states are two-fold degenerate with those with $\pm\Omega$ having the same energy.

For large deformations $\frac{p^2}{2m} + U$ can be solved exactly in cylindrical coordinates. The $D\hat{\ell}^2 + \chi\hat{\ell}\cdot\hat{s}$ would then be treated as a perturbation. The wavefunctions in this limit are labeled by these asymptotic quantum numbers

$$| \Omega | [N, n_z, \Lambda], \quad (21.11)$$

where n_z are the number of oscillator quanta for the $\omega_z^2 z^2$ part of the Hamiltonian, and Λ is the eigenvalue of $\hat{\ell}_z$. U_{def} connects states with N and $N \pm 2$. The asymptotic wavefunctions are dominated by N , but also contain some smaller $N \pm 2$ configurations. These $N \pm 2$ components give rise to the effective charge that is required if the model space is truncated to single N value. In between these the limits of the exactly solutions, one has to diagonalize

a small matrix to find the results. In general the solution of the full Hamiltonian can be obtained in terms of basis states given by Eq. (21.11).

The spectra of odd-even nuclei are given by rotational bands built upon these deformed single-particle states with $K = |\Omega|$. The states in the rotational band have $J = K, K + 1, K + 2, \dots$. In many cases the bands are regular as a function of $J(J + 1)$. But the term $\hbar^2 \hat{J} \cdot \hat{j}$ in Eq. (21.7) called the coriolis term [4] leads to oscillations in the energies of band with $K = 1/2$ given by [4], [5]

$$E(J, K) = E(K) + AJ(J + 1) + a(-1)^{j+1/2}(J + 1/2)\delta_{K,1/2}, \quad (21.12)$$

where a is called decoupling parameter.

The electromagnetic properties have the same form as those given in the chapter on collective motion. For odd-odd nuclei we can consider deformed single-particle states for both the odd proton with $K_p = |W|_p$ and the odd neutron with $K_n = |W|_n$. The possible total K values are $K_p + K_n$ and $|K_p - K_n|$. For even-even nuclei we can also consider the states made from putting two nucleons into deformed single-particle orbitals, where the possible total K values are $K_1 + K_2$ and $|K_1 - K_2|$. If we include pairing, these are quasi-particle

configurations. In the examples above we would have one and two quasi-particle states. The can be continued up to n-quasi-particles configurations. Many of these configurations have been observed [6] and [7]. One of the most famous case is the four-quasi-particle $K^\pi=16^+$ state in ^{178}Hf at 2.4 MeV with a half-life of 31 years.

The next step is to calculate single-particle states in a deformed Woods-Saxon potential. An example of this is given by the program WSBETA documented in [9]. The wavefunctions are expanded in terms of the deformed axially symmetric harmonic oscillator in cylindrical coordinates. The wavefunctions are obtained for specific values of β_λ . The program DEFWS takes to output from WSBETA and plots the results for $\beta_2 = -0.4$ to 0.4 for a specific nucleus. The highest filled single-particle states are marked. The results depend on the choice of Woods-Saxon potential parameters given in Table I of [9]. An example of the results for ^{42}S is shown in Fig. (21.3). If we add one more neutron for a prolate deformation the lowest Nilsson orbitals have $|\Omega|^\pi = 1/2^-$ and $7/2^-$. Low-lying states of states of ^{43}S observed in a Coulex experiment at the NSCL have been associated with deformed bands built on negative parity states with $K = 1/2$ and $K = 7/2$ [10]. The band with $K = 1/2$ shows a strong staggering in $J(J+1)$ due tp the coriolis term.

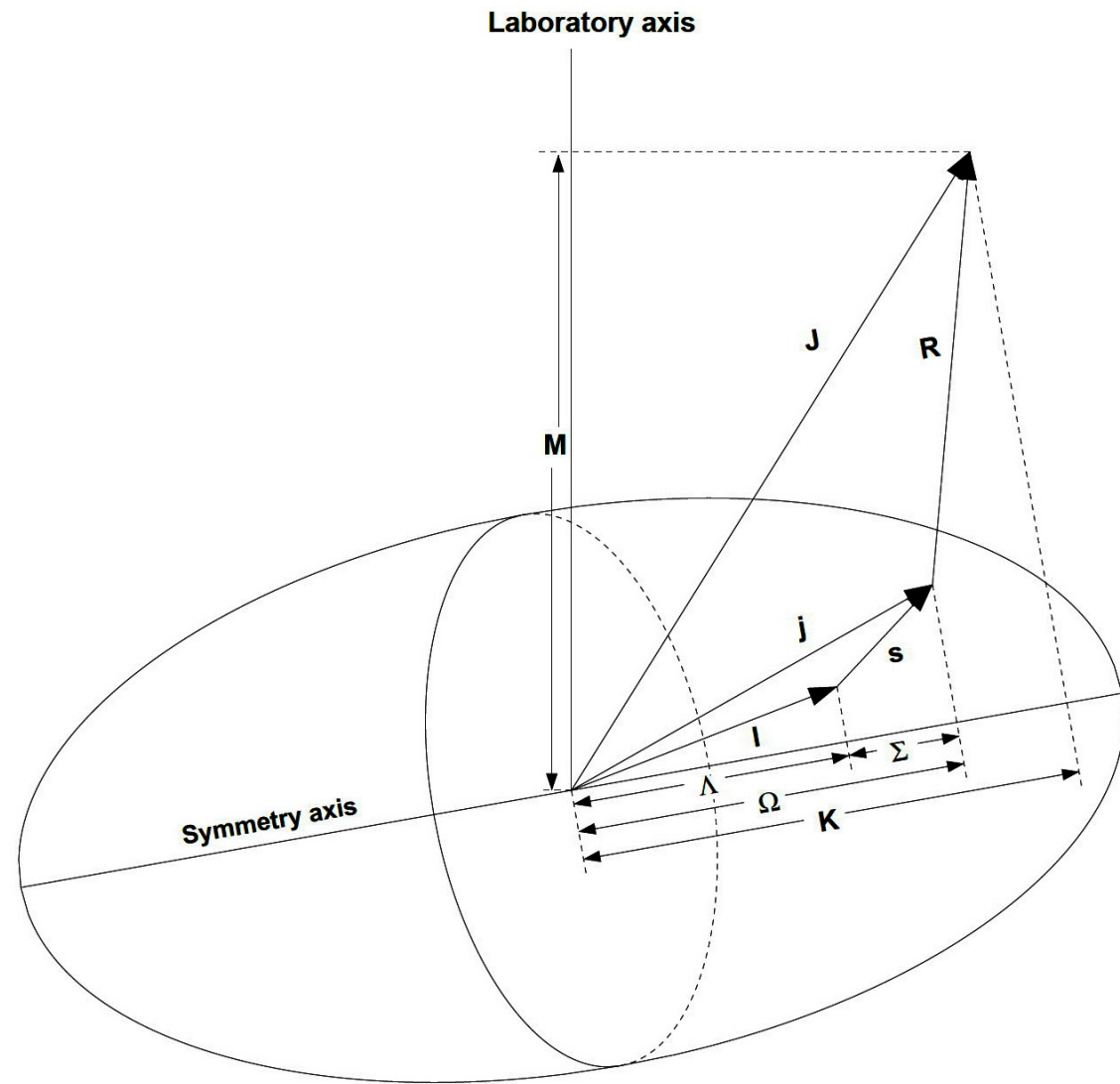


Figure 21.1: Asymptotic quantum numbers for the deformed oscillator [8]. In this figure the rotational angular momentum is labeled by \hat{R} which is the same as \hat{L} used in the text.

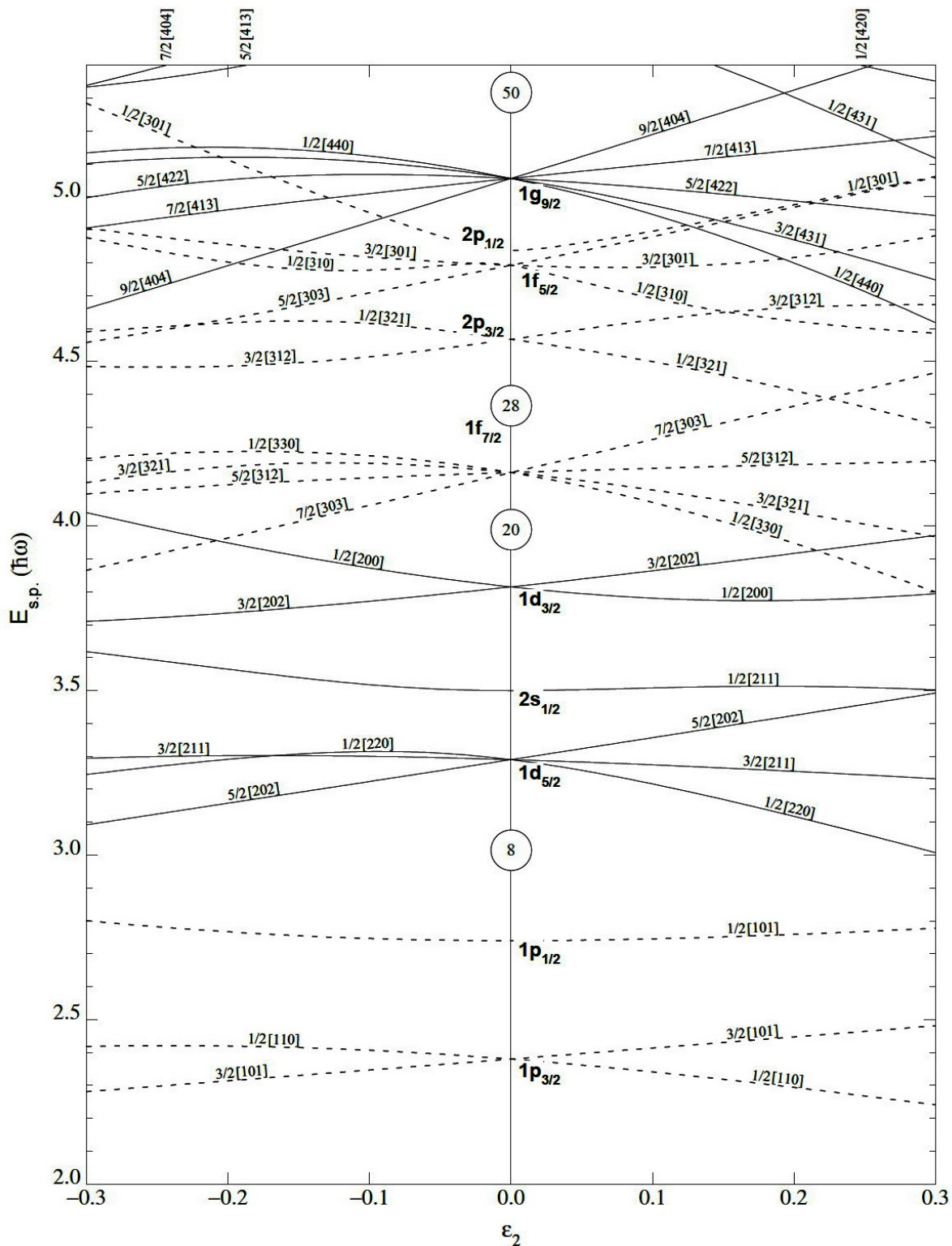


Figure 21.2: Deformed single-particle energies for light nuclei obtained from the Nilsson potential [8]. The lines are labeled by their asymptotic quantum numbers $|\Omega| [N, n_z, \Lambda]$.

The deformed Nilsson or deformed Woods-Saxon calculations can give some descriptive insight into the spectra of odd-even nuclei if the value of β_2 is known from some experimental properties. For predictive applications we need to be able to calculate the total energy as a function of β_2 (or in general as a function of β_λ). This can be done with deformed EDF calculations [11], [12].

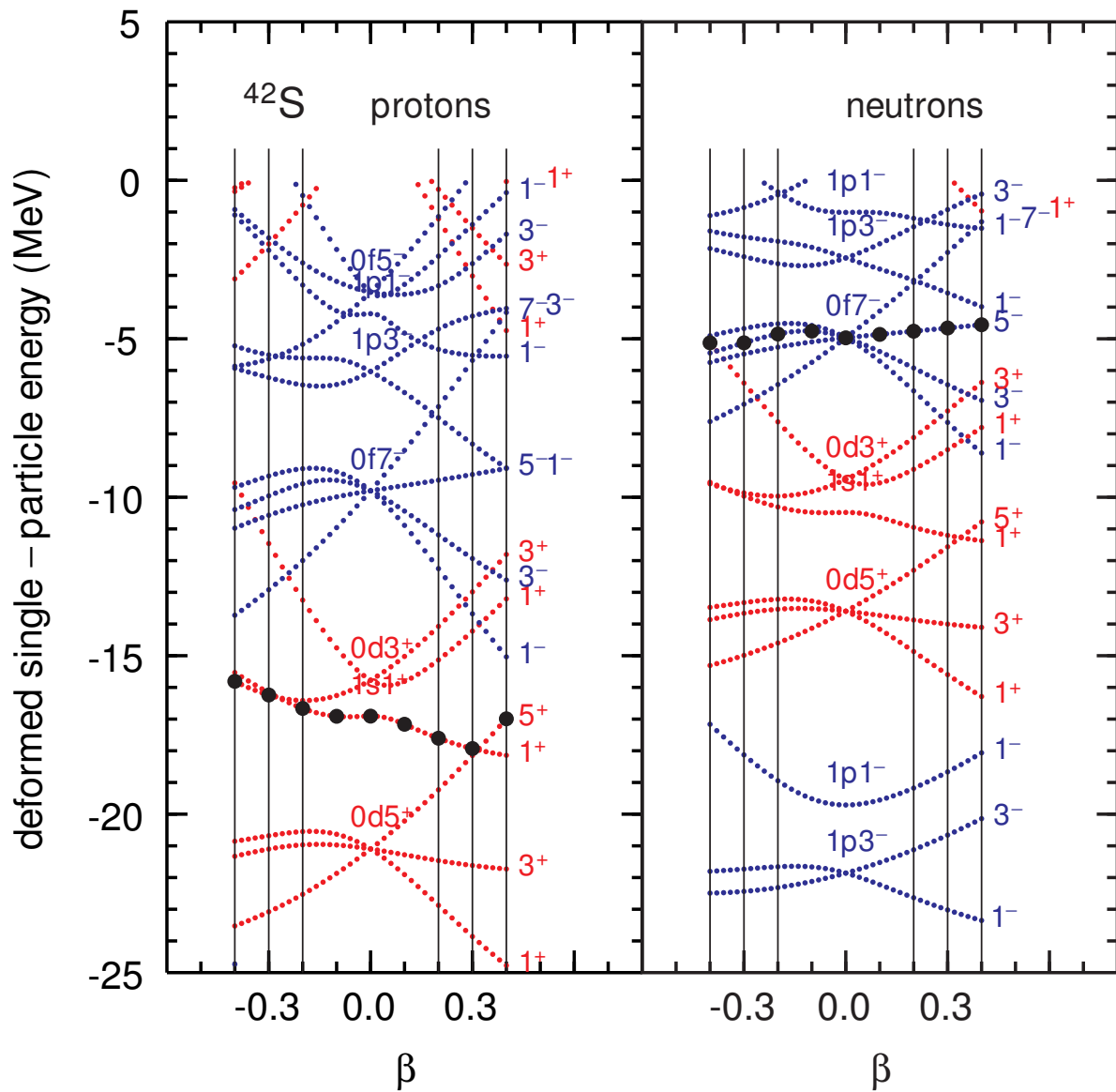


Figure 21.3: Deformed single-particle energies for for ^{42}S from the Woods-Saxon potential with the WSBETA code. The states are labeled by $2|\Omega|^\pi$. The highest state filled as a function of β_2 is shown by the filled circles.

Bibliography

- [1] K. E. G. Loebner, M. Vetter and V. Hoenig, Nucl. Data Tables **A7**, 495 (1970).
- [2] S. G. Nilsson, Dan. Mat-Fys Medd. **29**, 16 (1955).
- [3] B. R. Mottelson and S. G. Nilsson, Phys. Rev. **99**, 1615 (1955). link
- [4] W. Scholz and F. B. Malik, Phys. Rev. **153**, 1071 (1967). link

- [5] S. L. Heller and J. N. Friedman, Phys. Rev. C **10**, 1509 (1974). link
- [6] P. M. Walker and G. D. Dracoulis, Nature **399**, 35 (1999).
- [7] P. M. Walker and G. D. Dracoulis, Hyperfine Interact. **135**, 83 (2001).
- [8] Table of Itotopes, R. B. Firestone, V. S. Shirley S. Y. F, Chu Chu, C. M. Baglin and J. Zipkin, Wiley Interscience (1996).
- [9] S. Cwiok, J. Dudek, W. Nazarewicz, J. Skalski and T. Werner, Comput. Phys. Comm. **46**, 379 (1987).
- [10] B. Longfellow, D. Weisshaar, A. Gade, B. A. Brown, D. Bazin, K. W. Brown, B. Elman, J. Pereira, D. Rhodes, and M. Spieker, Phys. Rev. Lett. 125, 232501 (2020). link
- [11] M. V. Stoitsov, J. Dobaczewski, W. Nazarewicz, and P. Ring, Comput. Phys. Commun. **167**, 43 (2005).
- [12] N. Schunck, et al., Comput. Phys. Commun. **216** 145 (2017).

Chapter 22

The Creation operator method

22.1 Introduction

A convenient method for taking into account the antisymmetry of the many-body wavefunctions is to express them in second-quantized form in terms of creation and destruction operators. The antisymmetry is enforced by the anticommutation relations of the operators. The sections summarize the properties of the creation operator and their use in constructing wavefunctions and operators and many-body matrix elements.

22.2 Creation Operators and Wavefunctions

The operator a_α^+ creates the one-particle state $|\alpha\rangle$

$$a_\alpha^+ | \rangle = |\alpha\rangle, \quad (22.1)$$

where $| \rangle$ represents the vacuum state. The label α represents, for example, the set of quantum numbers $(n_r\ell jm)$ used in the spherical shell-model basis. The n -particle state is

formed from the product of these creation operators. For example, for $n = 3$

$$a_\lambda^+ a_\beta^+ a_\alpha^+ |> = | \alpha \beta \lambda >. \quad (22.2)$$

We use the convention that the order of the labels on the right-hand side is the inverse of that on the left hand side. The Hermitian conjugates of Eqs. (22.1) and (22.2) are

$$<| (a_\alpha^+)^+ = <| \alpha | \equiv <| a_\alpha, \quad (22.3)$$

and

$$<| (a_\lambda^+ a_\beta^+ a_\alpha^+)^+ = <| a_\alpha a_\beta a_\lambda = <| \alpha \beta \lambda | . \quad (22.4)$$

The a^+ and a operators obey the anticommutation relations

$$\{a_\alpha^+, a_\beta^+\} = a_\alpha^+ a_\beta^+ + a_\beta^+ a_\alpha^+ = 0, \quad (22.5)$$

$$\{a_\alpha, a_\beta\} = a_\alpha a_\beta + a_\beta a_\alpha = 0, \quad (22.6)$$

and

$$\{a_\alpha^+, a_\beta\} = a_\alpha^+ a_\beta + a_\beta a_\alpha^+ = \delta_{\alpha\beta}. \quad (22.7)$$

Use of the creation operators a^+ and annihilation operators a together with their anti-commutation relationships are completely equivalent to the results obtained from Slater determinants. In particular, we must show either that the anticommutation relations can be obtained directly from the structure of the antisymmetric wavefunctions, or that the anticommutation relations give the same result when applied to any wavefunction.

Antisymmetry of the Slater determinant means that

$$|\lambda\beta\alpha_1\dots\alpha_n> = - |\beta\lambda\alpha_1\dots\alpha_n>, \quad (22.8)$$

and

$$|\lambda\alpha_1\dots\alpha_n\beta> = (-1)^n |\lambda\beta\alpha_1\dots\alpha_n>, \quad (22.9)$$

Non-vanishing of the wavefunctions in Eqs. (22.8) and (22.9) implies that all of the labels are different. Eq. (22.8) implies that

$$a_\lambda^+ a_\beta^+ |\alpha_1\dots\alpha_n> + a_\beta^+ a_\lambda^+ |\alpha_1\dots\alpha_n> = 0. \quad (22.10)$$

Since the wavefunction itself is assumed not to vanish, one must have

$$a_\lambda^+ a_\beta^+ + a_\beta^+ a_\lambda^+ = 0, \quad (22.11)$$

which is the first the first anticommutation relation, Eq. (22.5). The Hermitian conjugate of this gives the second anticommutation relation, Eq. (22.6). The case when $\lambda=\beta$ in Eqs. (22.5) and (22.6) implies in particular that

$$a_\lambda^+ a_\lambda^+ = a_\lambda a_\lambda = 0. \quad (22.12)$$

Before deriving Eq. (22.7), some intermediate results are useful, first ($\lambda \neq \alpha_n$):

$$a_\lambda^+ | \alpha_1 \dots \alpha_n \lambda \rangle = 0, \quad (22.13)$$

$$a_\lambda | \alpha_1 \dots \alpha_n \lambda \rangle = | \alpha_1 \dots \alpha_n \rangle, \quad (22.14)$$

$$a_\lambda^+ | \alpha_1 \dots \alpha_n \rangle = | \alpha_1 \dots \alpha_n \lambda \rangle, \quad (22.15)$$

and

$$a_\lambda | \alpha_1 \dots \alpha_n \rangle = 0, \quad (22.16)$$

Eq. (22.13) follows from Eq. (22.12), and Eq. (22.15) follows from the basic definition of Eq. (22.2). The results for operating with a to the right in Eqs. (22.14) and (22.16) can be

inferred from the normalization condition

$$\langle \lambda | \beta \rangle = \langle a_\lambda | \beta \rangle = \delta_{\lambda\beta}, \quad (22.17)$$

which can be satisfied by the two relations

$$a_\lambda | \beta \rangle = 0 \quad \text{if} \quad \lambda \neq \beta \quad (22.18)$$

and

$$a_\lambda | \beta \rangle = | \rangle \quad \text{if} \quad \lambda = \beta. \quad (22.19)$$

In particular,

$$a_\lambda | \rangle = 0, \quad (22.20)$$

and

$$a_\lambda | \lambda \rangle = | \rangle. \quad (22.21)$$

Next, from Eqs. (22.13)-(22.16) it is straightforward to show that

$$a_\lambda a_\lambda^\dagger | \alpha_1 \dots \alpha_n \lambda \rangle = 0, \quad (22.22)$$

$$a_\lambda^+ a_\lambda | \alpha_1 \dots \alpha_n \lambda \rangle = | \alpha_1 \dots \alpha_n \lambda \rangle, \quad (22.23)$$

$$a_\lambda a_\lambda^+ | \alpha_1 \dots \alpha_n \rangle = | \alpha_1 \dots \alpha_n \rangle, \quad (22.24)$$

and

$$a_\lambda^+ a_\lambda | \alpha_1 \dots \alpha_n \rangle = 0, \quad (22.25)$$

Note that $a_\lambda a_\lambda^+$ or $a_\lambda^+ a_\lambda$ cannot always be replaced by unity.

The anticommutation relation of Eq. (22.7) can now be proven by showing that it holds for its application on all possible wavefunctions. The results for the case $\lambda = \beta$:

$$(a_\lambda^+ a_\lambda + a_\lambda a_\lambda^+) | \alpha_1 \dots \alpha_n \lambda \rangle = | \alpha_1 \dots \alpha_n \lambda \rangle, \quad (22.26)$$

and

$$(a_\lambda^+ a_\lambda + a_\lambda a_\lambda^+) | \alpha_1 \dots \alpha_n \rangle = | \alpha_1 \dots \alpha_n \rangle, \quad (22.27)$$

are obtained immediately from Eqs. (22.22) - (22.25). For $\lambda \neq \beta$ the results

$$(a_\lambda^+ a_\beta + a_\beta a_\lambda^+) | \alpha_1 \dots \alpha_n \lambda \rangle = 0, \quad (22.28)$$

and

$$(a_\lambda^+ a_\beta + a_\beta a_\lambda^+) | \alpha_1 \dots \alpha_n \rangle = 0, \quad (22.29)$$

follow from Eqs. (22.13) and (22.16), respectively. The final case is

$$\begin{aligned} (a_\lambda^+ a_\beta + a_\beta a_\lambda^+) | \alpha_1 \dots \alpha_n \beta \rangle &= (a_\lambda^+ a_\beta a_\beta^+ + a_\beta a_\lambda^+ a_\beta^+) | \alpha_1 \dots \alpha_n \rangle \\ &= (a_\lambda^+ a_\beta a_\beta^+ - a_\beta a_\beta^+ a_\lambda^+) | \alpha_1 \dots \alpha_n \rangle = (a_\lambda^+ - a_\lambda^+) | \alpha_1 \dots \alpha_n \rangle = 0, \end{aligned} \quad (22.30)$$

where (22.24) has been used to replace the $a_\beta a_\beta^+$ by unity. Eqs. (22.26) - (22.30) are equivalent to Eq. (22.7).

22.3 One and Two Body Operators

One- (F) and two-body (G) operators can be expressed in terms of these creation and destruction operators:

$$\hat{F} = \sum_{\alpha\beta} \langle \alpha | F | \beta \rangle a_\alpha^+ a_\beta, \quad (22.31)$$

and

$$\hat{G} = \frac{1}{4} \sum_{\alpha\beta\gamma\delta} < \alpha\beta | G | \gamma\delta > a_\alpha^+ a_\beta^+ a_\delta a_\gamma, \quad (22.32)$$

where the sums run over the infinite set of single-particle states. In their application the sums become limited due to finite number of states in the wavefunctions that will be acted on. Note the order of γ and δ at the end of this equation for T are different from their order in $| \gamma\delta >$. Angular momentum coupled versions of these operators will be given in a following chapter.

A simple one-body operator is the scalar number operator

$$N = \sum_{i=1}^n 1 = n,$$

which in second-quantized form becomes

$$\hat{N} = \sum_{\alpha\beta} < \alpha | 1 | \beta > a_\alpha^+ a_\beta = \sum_{\alpha} a_\alpha^+ a_\alpha. \quad (22.33)$$

When operating on a state to the right, \hat{N} will give unity if the state α is occupied [Eq. (22.23)] and zero if it is unoccupied [Eq. (22.25)], and the sum will thus give the total number of particles, n .

The creation operator method is well suited for computer codes, since the basis states Φ can be represented by binary bit patterns, with (1) denoting an occupied state and (0) an unoccupied state. The operations amount to binary additions and keeping track of phase factors. Computer codes have been developed which make use of these techniques. These computations are based on some finite set of single-particle quantum numbers $(\alpha_1, \dots, \alpha_n)$. It is convenient to choose some arbitrary but fixed ordering for these. For example, if one considers only the state with $j = 3/2$, there are four m -states which could put in the order $(-3/2, -1/2, 1/2, 3/2)$. The complete set of many-body states for two particles in this basis is then, (0011), (0101), (1001), (0110), (1010) and (1100).

22.4 Examples of a^+ and a Matrix Elements

This section will provide a few explicit examples for evaluating matrix elements of operators in the a^+ - a representation. The basic trick is to commute the operators until one has $a |> = 0$. For the basic overlap we have

$$\langle i | k \rangle = \langle | a_i a_k^+ | \rangle = \langle | \delta_{ik} - a_k^+ a_i | \rangle = \delta_{ik}. \quad (22.34)$$

The simplest one-body matrix element is

$$\begin{aligned} \langle i | \hat{F} | k \rangle &= \sum_{\alpha\beta} \langle \alpha | F | \beta \rangle \langle i | a_\alpha^+ a_\beta | k \rangle \\ &= \sum_{\alpha} \langle \alpha | F | k \rangle \langle i | a_\alpha^+ | \rangle = \langle i | F | k \rangle \langle | \rangle = \langle i | F | k \rangle. \end{aligned} \quad (22.35)$$

A diagonal one-body matrix element involving three particle is states (i, k, l) represented by the vector (111)

$$\begin{aligned}
& \langle (111) | \hat{F} | (111) \rangle = \sum_{\alpha\beta} \langle \alpha | F | \beta \rangle \langle (111) | a_\alpha^+ a_\beta | (111) \rangle \\
& = \langle (111) | \sum_\alpha a_\alpha^+ \left\{ \langle \alpha | F | i \rangle | (011) \rangle - \langle \alpha | F | k \rangle | (101) \rangle + \langle \alpha | F | l \rangle | (110) \rangle \right\} \\
& = \langle i | F | i \rangle \langle (111) | (111) \rangle + \langle k | F | k \rangle \langle (111) | (111) \rangle + \langle l | F | l \rangle \langle (111) | (111) \rangle \\
& = \langle i | F | i \rangle + \langle k | F | k \rangle + \langle l | F | l \rangle, \tag{22.36}
\end{aligned}$$

which is result expected for a diagonal matrix element. An example for an off-diagonal matrix element involving the states (i, k, l, m)

$$\begin{aligned}
& \langle (1110) | \hat{F} | (1101) \rangle = \sum_{\alpha\beta} \langle \alpha | F | \beta \rangle \langle (1110) | a_\alpha^+ a_\beta | (1101) \rangle \\
& = \langle (1110) | \sum_\alpha a_\alpha^+ \left\{ \langle \alpha | F | i \rangle | (0101) \rangle - \langle \alpha | F | k \rangle | (1001) \rangle + \langle \alpha | F | m \rangle | (1100) \rangle \right\} \\
& = \langle l | F | m \rangle \langle (1110) | (1110) \rangle = \langle l | F | m \rangle. \tag{22.37}
\end{aligned}$$

22.5 Wick's Theorem

Wick's theorem applies to the evaluation of a product of operators

$$A_1 A_2 \dots A_n$$

where A_i is a_i^+ or a_i . Wick's theorem [1] provides a way to rearrange this product with an equivalent and more useful expression that contains only *normal* ordered products times terms in which pairs of operators are evaluated in the vacuum (*contracted*).

Normal ordering means that the a_i operators that give zero when acting on the vacuum $|>$ are moved to the right of others. For this rearrangement an overall minus sign is introduced if an odd permutation is required to bring them into normal order (the $\delta_{\alpha,\beta}$ term is not included when normal ordering). For two operators there are four possibilities for A_1 and A_2 ,

$$N(a_\alpha^+, a_\beta) = a_\alpha^+ a_\beta,$$

$$N(a_\alpha, a_\beta^+) = -a_\beta^+ a_\alpha,$$

$$N(a_\alpha^+, a_\beta^+) = a_\alpha^+ a_\beta^+,$$

and

$$N(a_\alpha, a_\beta) = a_\alpha a_\beta. \quad (22.38)$$

For the last two either order is allowed. The vacuum expectation value of a normal ordered product is zero,

$$\langle | N(A_1, A_2, \dots, A_n) | \rangle = 0, \quad (22.39)$$

since there must be the same number of creation operators (a^+) and destruction operators (a) and since $a_\alpha | \rangle = 0$.

Contraction of two operators is defined as their expectation value (a number) in the vacuum state

$$A_\alpha^c A_\beta^c = \langle | A_\alpha A_\beta | \rangle, \quad (22.40)$$

where the superscript c indicates which two operators are contracted. Two operators out of a larger number can be contracted as

$$A_\alpha^c A_\gamma A_\beta^c A_\delta = - \langle | A_\alpha A_\beta | \rangle A_\gamma A_\delta, \quad (22.41)$$

where the minus sign follows from the odd-number of permutations required to bring the contracted product together. More than one contraction can be made, i.e.,

$$A_\alpha^{c_1} A_\beta^{c_2} A_\gamma^{c_1} A_\delta^{c_2} = - \langle | A_\alpha A_\gamma | \rangle \langle | A_\beta A_\delta | \rangle . \quad (22.42)$$

The four possible contractions are

$$\langle | a_\alpha^+ a_\beta^+ | \rangle = 0,$$

$$\langle | a_\alpha a_\beta | \rangle = 0,$$

$$\langle | a_\alpha^+ a_\beta | \rangle = 0,$$

and

$$\langle | a_\alpha a_\beta^+ | \rangle = \delta_{\alpha,\beta}. \quad (22.43)$$

Wick's theorem states that a product of P operators is equivalent to the normal-ordered product plus a sum over all possible contractions of normal-ordered Q pairs times the normal-ordered product of the other $P - 2Q$ operators. The sum includes all possible contractions

from $Q = 1$ up to $Q = P/2$ (P even) or $Q = (P-1)/2$ (P odd). When evaluated, the sum is simplified because many terms will automatically be zero from Eq. (22.39) or from (22.43).

For two operators A , Wick's theorem is

$$A_\alpha A_\beta = N(A_\alpha A_\beta) + A_\alpha^c A_\beta^c = N(A_\alpha A_\beta) + \langle | A_\alpha A_\beta | \rangle . \quad (22.44)$$

If the operators are already in normal order then $A_\alpha^c A_\beta^c = \langle | A_\alpha^c A_\beta^c | \rangle = 0$ and Eq. (22.44) is true by definition. If the operators are not in normal order, i.e. when $A_\alpha = a_\alpha$ and $A_\beta = a_\beta^+$, then $N(a_\alpha a_\beta^+) = -a_\beta^+ a_\alpha$ and Eq. (22.44) reduces to:

$$a_\alpha a_\beta^+ + a_\beta^+ a_\alpha = \langle | a_\alpha a_\beta^+ | \rangle = \delta_{\alpha,\beta}, \quad (22.45)$$

which is the usual commutation relation.

Wick's theorem can be expressed mathematically as

$$\begin{aligned} A_1 A_2 \dots A_n &= N(A_1, A_2, \dots, A_n) \\ &+ \sum_{j < k} (-1)^{j+k-1} \langle | A_j A_k | \rangle N(A_1, \dots, A_{j-1}, A_{j+1}, \dots, A_{k-1}, A_{k+1}, \dots, A_n) \end{aligned}$$

$$\begin{aligned}
& + \sum (-1)^P (2 \text{ contracted terms}) \times (N \text{ products of } n-4 \text{ operators}) \\
& + \sum (-1)^P (3 \text{ contracted terms}) \times (N \text{ products of } n-6 \text{ operators}) + \dots,
\end{aligned} \tag{22.46}$$

where P is the number of pair interchanges required to remove the contracted terms. The proof follows by induction; it holds for two terms and the equation for $n+1$ terms follows from that of n terms. For $n+1$ terms the left-hand side of Eq. (22.46) is

$$A_1 A_2 \dots A_n A_{n+1}$$

and the terms on the right-hand side have the form

$$N(A_1, A_2, \dots, A_k) A_{n+1}. \tag{22.47}$$

If we can show that

$$\begin{aligned}
N(A_1, A_2, \dots, A_k) A_{n+1} &= N(A_1, A_2, \dots, A_k, A_{n+1}) \\
& + \sum_j (-1)^{j+k} \langle | A_j A_{n+1} | \rangle N(A_1, A_2, \dots, A_{j-1}, A_{j+1}, \dots, A_k),
\end{aligned} \tag{22.48}$$

then Eq. (22.46) for $n + 1$ will have the same form as the equation n terms and we prove Wick's theorem. If A_{n+1} is a destruction operator the left-hand side of Eq. (22.48) is already in normal order and $\langle | A_j A_{n+1} | \rangle$ is zero, so (22.48) holds by definition. If A_{n+1} is a creation operator it needs to be commuted through the k operators in Eq. (22.47) using $A_j A_{n+1} = \{A_j, A_{n+1}\} - A_{n+1} A_j$ to give

$$\begin{aligned} N(A_1, A_2, \dots, A_k) A_{n+1} &= (-1)^k A_{n+1} N(A_1, A_2, \dots, A_k) \\ &+ \sum_j (-1)^{j+k} \{A_j, A_{n+1}\} N(A_1, A_2, \dots, A_{j-1}, A_{j+1}, \dots, A_k). \end{aligned} \quad (22.49)$$

Using

$$N(A_1, A_2, \dots, A_k, A_{n+1}) = (-1)^k A_{n+1} N(A_1, A_2, \dots, A_k)$$

and

$$\{A_j, A_{n+1}\} = \langle | A_j, A_{n+1} | \rangle$$

we prove Eq. (22.48) and prove Wick's theorem by induction.

22.6 Operators Relative to a Closed-Shell Configuration

Some calculations are carried out with a basis defined relative to some closed-shell configuration $|C\rangle$, where some subset of orbitals labeled by h are filled (occupied), and the remaining orbitals labeled by p are empty. The absence of a nucleon from one of the h states will be called a “hole”. The operator c_h^+ will be defined to create a hole in the state h

$$c_h^+ |C\rangle = a_h |C\rangle = |C, h^{-1}\rangle \quad (22.50)$$

When the unfilled states are labeled by p we can define a complete set of operators by

$$c_h^+ = a_h,$$

$$c_h = a_h^+,$$

$$c_p^+ = a_p^+,$$

and

$$c_p = a_p. \quad (22.51)$$

For the closed-shell configuration these c operators have the property that

$$c_\alpha | C > = 0 \quad (22.52)$$

for all α since there are no particles or holes to destroy. The c^+ and c operators obey the Fermion anticommutation relations

$$\{c_\alpha^+, c_\beta^+\} = c_\alpha^+ c_\beta^+ + c_\beta^+ c_\alpha^+ = 0,$$

$$\{c_\alpha, c_\beta\} = c_\alpha c_\beta + c_\beta c_\alpha = 0,$$

and

$$\{c_\alpha^+, c_\beta\} = c_\alpha^+ c_\beta + c_\beta c_\alpha^+ = \delta_{\alpha\beta}. \quad (22.53)$$

Wick's theorem applies to the c operators when the vacuum is replaced by the closed-shell configuration $| C >$. Normal ordering is made in terms of the c and c^+ operators.

The one-body operator can be written as a sum of four terms representing the four particle-hole possibilities

$$\begin{aligned} a_\alpha^+ a_\beta &= a_{p_1}^+ a_{p_2} + a_{h_1}^+ a_{p_2} + a_{p_1}^+ a_{h_2} + a_{h_1}^+ a_{h_2} \\ &= c_{p_1}^+ c_{p_2} + c_{h_1} c_{p_2} + c_{p_1}^+ c_{h_2}^+ + c_{h_1} c_{h_2}^+. \end{aligned} \quad (22.54)$$

The normal-ordered product is

$$\begin{aligned} N(a_\alpha^+ a_\beta) &= c_{p_1}^+ c_{p_2} + c_{h_1} c_{p_2} + c_{p_1}^+ c_{h_2}^+ - c_{h_2}^+ c_{h_1} \\ &= a_{p_1}^+ a_{p_2} + a_{h_1}^+ a_{p_2} + a_{p_1}^+ a_{h_2} - a_{h_2} a_{h_1}^+. \end{aligned} \quad (22.55)$$

The only non-zero contraction is

$$\langle C | a_\alpha^+ a_\beta | C \rangle = \langle C | a_h^+ a_{h'} | C \rangle = \delta_{h,h'}. \quad (22.56)$$

For the one-body operator Wick's theorem gives

$$a_\alpha^+ a_\beta = N(a_\alpha^+ a_\beta) + \langle C | a_\alpha^+ a_\beta | C \rangle. \quad (22.57)$$

For the two-body operator Wick's theorem gives

$$\begin{aligned}
 a_\alpha^+ a_\beta^+ a_\delta a_\gamma &= N(a_\alpha^+ a_\beta^+ a_\delta a_\gamma) + N(a_\alpha^+ a_\gamma) < C | a_\beta^+ a_\delta | C > + N(a_\beta^+ a_\delta) < C | a_\alpha^+ a_\gamma | C > \\
 &\quad - N(a_\alpha^+ a_\delta) < C | a_\beta^+ a_\gamma | C > - N(a_\beta^+ a_\gamma) < C | a_\alpha^+ a_\delta | C > \\
 &+ < C | a_\alpha^+ a_\gamma | C > < C | a_\beta^+ a_\delta | C > - < C | a_\alpha^+ a_\delta | C > < C | a_\beta^+ a_\gamma | C > . \quad (22.58)
 \end{aligned}$$

22.7 The Hartree-Fock Equations

In this section we rederive the Hartree-Fock relations for the many-body Hamiltonian $H = T + V$ where T is the one body kinetic energy operator and V is the two-body interaction operator. With the results of Wick's theorem relative to a closed-shell configuration C , Eqs. (22.57) and (22.58)

$$H = \sum_{\alpha\beta} < \alpha | T | \beta > a_\alpha^+ a_\beta + \frac{1}{4} \sum_{\alpha,\beta,\gamma,\delta} < \alpha\beta | V | \gamma\delta > a_\alpha^+ a_\beta^+ a_\delta a_\gamma$$

$$\begin{aligned}
&= \sum_h \langle h | T | h \rangle + \frac{1}{2} \sum_{h,h'} \langle h, h' | V | h, h' \rangle \\
&+ \sum_{\alpha,\gamma} [\langle \alpha | T | \gamma \rangle + \sum_h \langle \alpha h | V | \gamma h \rangle] N(a_\alpha^+ a_\gamma^-) \\
&+ \frac{1}{4} \sum_{\alpha,\beta,\gamma,\delta} \langle \alpha\beta | V | \gamma\delta \rangle N(a_\alpha^+ a_\beta^+ a_\delta a_\gamma^-). \tag{22.59}
\end{aligned}$$

where α is shorthand for $k_\alpha = (n_\alpha, \ell_\alpha, j_\alpha, m_\alpha)$ and h is shorthand for $k_h = (n_h, \ell_h, j_h, m_h)$. The contractions in Eqs. (22.57) and (22.58) vanish unless both indices are h , $\langle C | a_h^+ a_{h'}^- | C \rangle = \langle C | c_h c_{h'}^+ | C \rangle = \delta_{h,h'}$. Terms have been added making use of the antisymmetry properties

$$\langle \alpha\beta | V | \gamma\delta \rangle = - \langle \alpha\beta | V | \delta\gamma \rangle = - \langle \beta\alpha | V | \gamma\delta \rangle. \tag{22.60}$$

For the total energy of the closed-shell configuration $\langle C | H | C \rangle$, the last two terms in Eq. (22.59) give zero (since $\langle C | N(\dots) | C \rangle = 0$), and the first two terms give

$$E_C = \langle C | H | C \rangle = \sum_h \langle h | T | h \rangle + \frac{1}{2} \sum_{h,h'} \langle h, h' | V | h, h' \rangle. \tag{22.61}$$

For the configuration of a closed-shell plus one particle in state p , the total energy is the core energy plus the term from the third line of Eq. (22.59) with

$$\langle C, p | N(a_\alpha^+ a_\gamma^-) | C, p \rangle = \langle C | a_p a_\alpha^+ a_\gamma^- a_{p_2}^+ | C \rangle = \delta_{p,p_1} \delta_{p,p_2}$$

(with $\alpha = p_1$ and $\gamma = p_2$) to give

$$\langle C, p | H | C, p \rangle = \langle C | H | C \rangle + \langle p | T | p \rangle + \sum_h \langle ph | V | ph \rangle. \quad (22.62)$$

The single-particle energy is given by the difference

$$e_p = \langle C, p | H | C, p \rangle - \langle C | H | C \rangle = \langle p | T | p \rangle + \sum_h \langle ph | V | ph \rangle. \quad (22.63)$$

For the configuration of a closed-shell minus one particle in state h , the total energy is the core energy plus the term from the third line of Eq. (22.59) with

$$\langle C, h^{-1} | N(a_\alpha^+ a_\gamma^-) | C, h^{-1} \rangle = - \langle C, h^{-1} | a_{h_2} a_{h_1}^+ | C, h^{-1} \rangle = -\delta_{h,h_2} \delta_{h,h_1}$$

(with $\alpha = h_1$ and $\gamma = h_2$) to give

$$\langle C, h^{-1} | H | C, h^{-1} \rangle = \langle C | H | C \rangle - (\langle h | T | h \rangle + \sum_{h'} \langle h' h | V | h' h \rangle). \quad (22.64)$$

The single-hole energy is given by the difference

$$e_h = \langle C | H | C \rangle - \langle C, h^{-1} | H | C, h^{-1} \rangle = \langle h | T | h \rangle + \sum_{h'} \langle h' h | V | h' h \rangle. \quad (22.65)$$

One can formulate the Hartree-Fock equations in terms of diagonalizing the matrix

$$\langle \alpha | T | \beta \rangle + \sum_h \langle \alpha h | V | \beta h \rangle = e_\alpha \delta_{\alpha,\beta}. \quad (22.66)$$

The Hartree-Fock single-particle potential is defined as

$$\langle \alpha | U | \beta \rangle = \sum_h \langle \alpha h | V | \beta h \rangle$$

The fourth line in Eq. (22.59) is the residual interation, those terms in $\langle \Psi | H | \Psi \rangle$ that are not contained in E_C or e_α where Ψ is a wavefunction with particles and or holes added to C . Thus Eq. (22.59) can be rewritten as,

$$H = E_C + \sum_{\alpha} e_{\alpha} N(a_{\alpha}^+ a_{\alpha}) + \frac{1}{4} \sum_{\alpha, \beta, \gamma, \delta} \langle \alpha \beta | V | \gamma \delta \rangle N(a_{\alpha}^+ a_{\beta}^+ a_{\delta} a_{\gamma}). \quad (22.67)$$

It is convenient to represent these wavefunctions and matrix elements by Goldstone diagrams [2]. The vertical line with an up arrow in Fig. 1A represents the single-particle state and the vertical line with a down arrow in Fig. 1B represents the single-hole state. The terms on the right-hand side of Eq. (22.63) are represented by Fig. 1C with a horizontal line for the kinetic energy operator T and Fig. 1D with a horizontal line for the two-body operator V that connects the single-particle state to a sum over all hole states represented by the circle.

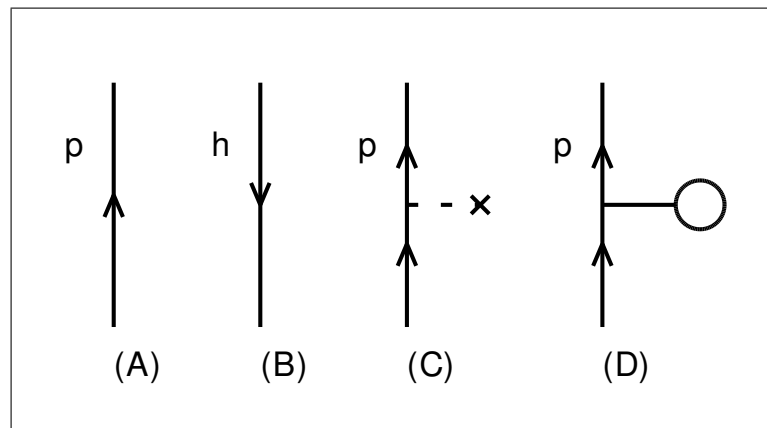


Figure 22.1: Schematic diagram for particle states (A), hole state (B), one-body interaction T for a particle state (C) and two-body interaction of a single-particle state with all particles in the closed core (D).

Bibliography

- [1] G. C. Wick, Phys. Rev. **80**, 268 (1950). link
- [2] J. Goldstone, Proc. Roy. Soc. **A239**, 267 (1957).

Chapter 23

Two-particle wavefunctions

23.1 Relative coordinates

23.1.1 Two neutrons or two protons

There are no bound states for two neutrons. However, there is a strong low-energy s-wave scattering resonance. First we will construct the antisymmetric wavefunction for two neutrons in the $\ell=0$ state. The wavefunctions are a product of the space, spin and isospin parts:

$$\psi = f(r) Y_m^\ell(\hat{r}) \phi(S) \chi(T). \quad (23.1)$$

Initially we will consider only the space and spin part. The parity associated with the change of phase of the spherical harmonics Y when \vec{r} is replaced by $-\vec{r}$ is $\pi=(-1)^\ell$. For a two-particle system the symmetry under the interchange of the two particles P_{12} is related to the parity since

$$P_{12}\vec{r} = P_{12}[\vec{r}_1 - \vec{r}_2] = [\vec{r}_2 - \vec{r}_1] = -\vec{r}, \quad (23.2)$$

and

$$P_{12}Y_m^\ell(\hat{r}) = (-1)^\ell Y_m^\ell(\hat{r}). \quad (23.3)$$

For $l = 0$, $\pi=+1$, and the spatial wave function is symmetric under the interchange of the two neutrons. In order to make the entire wavefunction antisymmetric the spin wave function must be antisymmetric. The spin wave functions are

$$|\alpha\rangle = |s = 1/2, s_z = 1/2\rangle, \quad (23.4)$$

$$|\beta\rangle = |s = 1/2, s_z = -1/2\rangle. \quad (23.5)$$

The neutron spins can be coupled to make wavefunctions $\phi(S, S_z)$ with total angular momentum S by using the Clebsch-Gordan coefficients $\langle 1/2, s_z, 1/2, s'_z | S, S_z \rangle$

$$\phi(1, 1) = |\alpha(1)\rangle |\alpha(2)\rangle, \quad (23.6)$$

$$\phi(1, 0) = \sqrt{\frac{1}{2}} [|\alpha(1)\rangle |\beta(2)\rangle + |\beta(1)\rangle |\alpha(2)\rangle], \quad (23.7)$$

$$\phi(1, -1) = |\beta(1)\rangle |\beta(2)\rangle, \quad (23.8)$$

$$\phi(0, 0) = \sqrt{\frac{1}{2}} [|\alpha(1)\rangle |\beta(2)\rangle - |\beta(1)\rangle |\alpha(2)\rangle], \quad (23.9)$$

where $\alpha(1)$ indicates that neutron “1” is in the state α . The $S = 1$ wavefunctions are symmetric under P_{12} , and $S = 0$ is antisymmetric. Thus the spin symmetry under P_{12} is $(-1)^{S+1}$. To make the entire $\ell=0$ wavefunction antisymmetric we must take the $S = 0$ solution. Thus the quantum numbers for the $\ell = 0$ state of the two neutrons are:

$$^1S_0 : \text{nn}, \ell = 0, S = 0, J^\pi = 0^+. \quad (23.10)$$

A similar analysis for the scattering in the $l = 1$ state would give:

$$^3P_J : \text{nn}, \ell = 1, S = 1, J^\pi = 0^-, 1^-, 2^-, \quad (23.11)$$

where the first symbol in Eqs. (23.10) and (23.11) indicates $^{2S+1}\ell_J$, with $(2S + 1) = 1$ for the “singlet” state and $(2S + 1) = 3$ for the “triplet” state. The values of J are restricted by the triangle condition for the coupling of ℓ and S .

In general the total symmetry under P_{12} must be negative:

$$(-1)^{\ell+S+1} = -1, \quad (23.12)$$

which means that $\ell + S$ must be even for the two neutrons. If we add isospin to the two-neutron system there is nothing new since the two neutrons must be in the state

$$\chi(T = 1, T_z = 1) = | t = 1/2, t_z = 1/2 (1) > | t = 1/2, t_z = 1/2 (2) >, \quad (23.13)$$

which is symmetric under P_{12} . The same results apply to the proton-proton system.

23.1.2 Proton-neutron

If we consider a proton and neutron in an $\ell=0$ state there is no antisymmetry requirement since these are not identical particle. Thus both S values are allowed. For $\ell=0$:

$$^1S_0 : \text{pn}, \ell = 0, S = 0, J^\pi = 0^+. \quad (23.14)$$

$$^3S_1 : \text{pn}, \ell = 0, S = 1, J^\Pi = 1^+. \quad (23.15)$$

The $J = 1$ wave function corresponds to the bound state of state of the deuteron that has $J^\pi = 1^+$. A similar set of states exist for higher ℓ values.

23.1.3 Two nucleons

When isospin is considered we also have to include the isospin coupling to $T = 0$ and 1 which, in analogy with the spin coupling, is:

$$\chi(1, 1) = |a(1)\rangle |a(2)\rangle, \quad (23.16)$$

$$\chi(1, 0) = \sqrt{\frac{1}{2}} [|a(1)\rangle |b(2)\rangle + |b(1)\rangle |a(2)\rangle], \quad (23.17)$$

$$\chi(1, -1) = |b(1)\rangle |b(2)\rangle, \quad (23.18)$$

$$\chi(0, 0) = \sqrt{\frac{1}{2}} [|a(1)\rangle |b(2)\rangle - |b(1)\rangle |a(2)\rangle], \quad (23.19)$$

where:

$$|a\rangle = |t = 1/2, t_z = 1/2\rangle, \quad (23.20)$$

$$|b\rangle = |t = 1/2, t_z = -1/2\rangle. \quad (23.21)$$

The symmetry under P_{12} is $(-1)^{T+1}$.

The total symmetry under P_{12} must be negative:

$$(-1)^{\ell+S+1+T+1} = (-1)^{\ell+S+T} = -1, \quad (23.22)$$

which means that $\ell + S + T$ must be odd. Thus with isospin the proton-neutron state with $\ell=0$ and $S = 0$ must have $T = 1$ and it is the $T_z = 0$ member of the $T = 1$ triplet, the other two being the neutron-neutron and proton-proton states

$$^1S_0 : T = 1, \ell = 0, S = 0, J^\pi = 0^+. \quad (23.23)$$

The state with $\ell=0$ and $S = 1$ must have $T = 0$

$$^3S_1 : T = 0, \ell = 0, S = 1, J^\pi = 1^+. \quad (23.24)$$

For $\ell=1$ and $\ell=2$ we have

$$^3P_J : T = 1, \ell = 1, S = 1, J^\pi = 0^-, 1^-, 2^-. \quad (23.25)$$

$$^1P_1 : T = 0, \ell = 1, S = 0, J^\pi = 1^-. \quad (23.26)$$

$$^1D_2 : T = 1, \ell = 2, S = 0, Jp = 2^+. \quad (23.27)$$

$$^3D_J : T = 0, \ell = 2, S = 1, J^\pi = 1^+, 2^+, 3^+. \quad (23.28)$$

In general only the total angular momentum J is a good quantum number. For $S = 0$, $J = \ell$ is unique. For $S = 1$, the wavefunction for a given J value can have $\ell = J - 1$ or $\ell = J + 1$. Thus bound state of the deuteron with $J^\pi = 1^+$ is in general a mixture of the 3S_1 and 3D_1 states. $\ell=0$ is the dominant part of the wavefunction but there is some $\ell=2$ (d -state) admixture.

23.2 Single-particle coordinates

The two-particle wavefunction in which particles in the states k_1 and k_2 with angular momentum \vec{j}_1 and \vec{j}_2 , respectively, are coupled to a total angular momentum \vec{J} is given in terms of the product wavefunctions by

$$| k_1 k_2 JM \rangle_p = \sum_{m_1 m_2} \langle j_1 m_1 j_2 m_2 | JM \rangle | k_1 m_1 k_2 m_2 \rangle_p, \quad (23.29)$$

where $M = m_1 + m_2$, and the subscript p indicates the product wavefunctions. As usual, the allowed values of J are from $J_{min} = | j_1 - j_2 |$ to $J_{max} = j_1 + j_2$ in integer steps. The result for the Slater determinant is not as simple, but takes the form

$$| k_1 k_2 JM \rangle = N_{12} \sum_{m_1 m_2} \langle j_1 m_1 j_2 m_2 | JM \rangle | k_1 m_1 k_2 m_2 \rangle, \quad (23.30)$$

where N_{12} can be evaluated by taking the norm of both sides

$$\langle k_1 k_2 JM | k_1 k_2 JM \rangle = 1$$

$$\begin{aligned}
&= N_{12}^2 \sum_{m_1 m_2 m_3 m_4} < j_1 m_1 j_2 m_2 | JM > < j_1 m_3 j_2 m_4 | JM > \\
&\times \frac{1}{2} \left\{ < k_1 m_1 k_2 m_2 | k_1 m_3 k_2 m_4 >_p - < k_1 m_1 k_2 m_2 | k_2 m_4 k_1 m_3 >_p \right. \\
&\left. - < k_2 m_2 k_1 m_1 | k_1 m_3 k_2 m_4 >_p + < k_2 m_2 k_1 m_1 | k_2 m_4 k_1 m_3 >_p \right\} \\
&= N_{12}^2 \sum_{m_1 m_2 m_3 m_4} < j_1 m_1 j_2 m_2 | JM > < j_1 m_3 j_2 m_4 | JM > \\
&\quad \times \{ \delta_{m_1 m_3} \delta_{m_2 m_4} - \delta_{m_1 m_4} \delta_{m_2 m_3} \delta_{k_1 k_2} \} \\
&= N_{12}^2 \left\{ \sum_{m_1 m_2} | < j_1 m_1 j_2 m_2 | JM > |^2 - \delta_{k_1 k_2} \sum_{m_1 m_2} < j_1 m_1 j_1 m_2 | JM > < j_1 m_2 j_1 m_1 | JM > \right\} \\
&= N_{12}^2 \{ 1 - \delta_{k_1 k_2} (-1)^{J-2j_1} \} = N_{12}^2 \{ 1 + \delta_{k_1 k_2} (-1)^J \}, \tag{23.31}
\end{aligned}$$

where the symmetry property of the Clebsch-Gordan coefficient has been used. Thus, the two-particle wavefunction vanishes if J is odd and $k_1 = k_2$. When the two-particle wavefunction does not vanish

$$N_{12} = \frac{1}{\sqrt{(1 + \delta_{k_1 k_2})}}. \tag{23.32}$$

The inverse of Eq. (23.30) is

$$| k_1 m_1 k_2 m_2 \rangle = \frac{1}{N_{12}} \sum_{JM} \langle JM | j_1 m_1 j_2 m_2 | k_1 k_2 JM \rangle. \quad (23.33)$$

Also note that

$$| k_2 k_1 JM \rangle = -(-1)^{j_1 + j_2 - J} | k_1 k_2 JM \rangle, \quad (23.34)$$

where a phase factor of (-1) arises from the antisymmetry of the two-particle wavefunction.

In terms of the a^+ operators, the angular momentum coupled two-particle wavefunction is

$$\begin{aligned} | k_1 k_2 JM \rangle &= N_{12} \sum_{m_1 m_2} \langle j_1 m_1 j_2 m_2 | JM \rangle a_{k_2 m_2}^+ a_{k_1 m_1}^+ | \rangle \\ &= -N_{12} \sum_{m_1 m_2} \langle j_1 m_1 j_2 m_2 | JM \rangle a_{k_1 m_1}^+ a_{k_2 m_2}^+ | \rangle \\ &= -N_{12} [a_{k_1}^+ \otimes a_{k_2}^+]_M^J | \rangle. \end{aligned} \quad (23.35)$$

The results for wavefunctions that have good J and good isospin T follow by doubling the terms that contain J . For example, the overlap is

$$\langle k_1 k_2 JMTT_z | k_1 k_2 JMTT_z \rangle = N_{12}^2 \{1 - \delta_{k_1 k_2} (-1)^{J-2j_1} (-1)^{T-2t}\} = N_{12}^2 \{1 - \delta_{k_1 k_2} (-1)^{J+T}\}, \quad (23.36)$$

where $t = 1/2$. Thus, $| k_1 k_2 JMTT_z \rangle$ vanishes if $J + T$ is even and $k_1 = k_2$. The symmetry of the two-particle wavefunctions under the exchange of k_1 and k_2 is

$$| k_2 k_1 JMTT_z \rangle = -(-1)^{j_1+j_2-J} (-1)^{2t-T} | k_1 k_2 JMTT_z \rangle = (-1)^{j_1+j_2-J-T} | k_1 k_2 JMTT_z \rangle. \quad (23.37)$$

Chapter 24

Many-body wavefunctions

24.1 Wavefunctions in the m -scheme

For a spherical potential the single-particle wavefunctions are labeled by their radial, orbital angular momentum, and total angular momentum quantum numbers, n_r, ℓ and j , respectively. This set of quantum numbers will be denoted by $k \equiv (n_r, \ell, j)$. Each j value has $(2j + 1)$ m -states, and the associated single-particle wavefunctions will be labeled by $\alpha \equiv (km)$.

In the M -scheme one starts with a set of basis states Φ for a given M value

$$M = \sum_{\alpha} m_{\alpha}, \quad (24.1)$$

where the sum is over the m values for the occupied states. In general there are an infinite number of basis states Φ , but a for a given situation one truncates the number of states based upon those that are lowest in unperturbed energy. Since the Hamiltonian is diagonal in M one need only consider the subset of basis states Φ with a single value of M in the construction of the many-particle wavefunctions Ψ . The many-body matrix elements of the

relevant one- and two-body operators can then be calculated with the techniques of second quantization. Many computer codes have been written to do this.

A basis state with a given value of M does not in general have a definite (good) value of the total angular momentum J . However, since the Hamiltonian is spherically symmetric, the Hamiltonian is also diagonal in J . Thus, the eigenvalues of H , that are linear combinations of the Φ basis, will automatically have good a J value with $J \geq M$, as long as the basis contains the complete set of states that are connected by the \hat{J}^2 operator. The J value can be determined by calculating the expectation value $\langle \Psi | \hat{J}^2 | \Psi \rangle$.

We can calculate the total number of states for a given J , the J -dimension $D(J)$, from the M-scheme dimensions $d(M)$. This is based upon the fact that for each J state there must be $(2J + 1)$ M -states. Thus we find:

$$D(J) = d(M = J) - d(M = J + 1). \quad (24.2)$$

The meaning of Eq. (24.2) is that the number of extra $M = J$ states compared to the number of $M = J + 1$ states must be the number of states with angular momentum J . Since $d(-M) = d(M)$ one only has to consider $M \geq 0$. Eq. (24.2) will be illustrated with

with some examples. The results for these examples only depend upon the (j, m) quantum numbers, and thus the (n_r, ℓ) values are not given explicitly.

Table (24.1) gives all possible M -states for the $[5/2]^2$ configuration for identical nucleons. Due to the Pauli principle we cannot have $M = 5$, and thus $J = 5$ is not allowed. The M -scheme dimensions for this case are given in Table (24.2). From the number of states for each M , one can make up Table (24.2). $M_{max} = 4$ means that the highest J value is $J = 4$ and this will account for nine of the M states, $M = 4, 3, 2, 1, 0, -1, -2, -3$ and -4 . $J = 3$ is not allowed since there is only one $M = 3$ state that must go with $J = 4$. The extra $M = 2$ state means that there is a state with $J = 2$ that accounts for five more M states $M = 2, 1, 0, -1$, and -2 . $J = 1$ is not allowed since all of the $M = 1$ states are now used, and the extra $M = 0$ states means that there is one state with $J = 0$. Thus, the allowed J values are 0, 2 and 4.

A second example is given for the $[5/2]^3$ configuration given in Table (24.3). From the multiplicity of the M values one can deduce that only $J = 3/2, 5/2$ and $9/2$ are allowed.

In general, the maximum J -value allowed for a $[k]^n$ configuration is given by the sum

Table 24.1: M values for the $[5/2]^2$ configuration for identical nucleons. The x's under columns headed by $2m$ indicate that the state is occupied, and the total M value is given on the right-hand side.

$2m$	5	3	1	-1	-3	-5	
							M
	x	x					4
	x		x				3
	x			x			2
	x				x		1
	x					x	0
	x	x					2
	x		x				1
	x			x			0
	x				x		-1
	x	x					0
	x		x				-1
	x			x			-2
		x	x				-2
		x		x			-3
		x	x				-4

Table 24.2: Table of dimensions for $[(5/2)^2]$.

M	$d(M)$	J	$D(J)$
4	1	4	1
3	1	3	0
2	2	2	1
1	2	1	0
0	3	0	1
-1	2		
-2	2		
-3	1		
-4	1		

Table 24.3: M values ($M \geq 0$) for the $[5/2]^3$ configuration for identical nucleons. The x's under columns headed by $2m$ indicate that the state is occupied, and the total M value is given on the right-hand side.

$2m$	5	3	1	-1	-3	-5	
							$2M$
	x	x	x				9
	x	x		x			7
	x	x			x		5
	x	x				x	3
	x		x	x			5
	x		x		x		3
	x		x			x	1
	x			x	x		1
	x	x	x				3
	x	x		x			1

of the n largest possible m values,

$$J_{max} = \sum_{i=1}^n m_i^{max}. \quad (24.3)$$

In the $[5/2]^3$ example, $J_{max} = 5/2 + 3/2 + 1/2 = 9/2$. The $[k]^n$ state with $J = J_{max} - 1$ is not allowed by the Pauli principle.

For combinations of more than one orbital, all possible J values are allowed that satisfy the triangle condition for the total J or each orbital. For example, for the $[5/2]^2[1/2]$ configuration, all possible J values allowed by the triangle condition of coupling $j = 1/2$ to the $J = 0, 2$ and 4 states allowed for two particles in the $j = 5/2$ state are allowed: $J = 9/2, 7/2, 5/2, 3/2$ and $1/2$.

If there is only one M value allowed, the wavefunctions of the J state is given by that of the single M state. If there is more than one M value allowed, then one must diagonalize the Hamiltonian in a space that has the dimension $d(M)$. The states of good J will be linear combinations of the M states. For a given J value of interest, one usually chooses $M = J$,

since the number of M states is minimized in this case. However, one could also choose any $M \leq |J|$ value.

Alternatively, the linear combination of M -states with good J can be calculated using angular-momentum projection methods. This is the method used by the code OXBASH to construct a matrix with dimension $D(J)$ corresponding to the states of good J in terms of the M -scheme basis.

A partition is defined as a specific distribution of the nucleons into the allowed (active) set of k states. The examples discussed above include the three partitions allowed for three neutrons (or three protons) the states with $j = 5/2$ and $j = 1/2$. Written in the form $[5/2]^a[1/2]^b$, we have $(a, b) = (3,0), (2,1)$ and $(1,2)$ (the $j = 1/2$ state cannot have more than two neutrons).

The first step in a shell model calculation is to specify the number of particles, the number of active orbits, and then to make a list of the complete set of partitions. Then for each partition we calculate the number of states for each J value. The total dimension is obtained by summing this over all partitions. The calculation may proceed with the full set

of partitions within a given model space (a full-space calculation) or it may be restricted to some subset of the partitions (a truncated calculation).

Compilations of $D(J)$ for j^n configurations for some values of j are available in the literature [1], and computer codes are available for the general case [2], [3], [4].

A similar procedure can be used to count the number of allowed isospin configurations for a given partition. For example, for $[5/2]^3$ and allowing for both protons and neutrons, we can start with the highest allowed $T = T_z = 3/2$ value for three neutrons where the allowed J values are $J = 3/2, 5/2$ and $9/2$. For $T_z = 1/2$ we couple one $j = 5/2$ proton to $[5/2]^2$ (two neutrons) with $J_n = 0, 2, 4$. to obtain $J = (5/2), (1/2, 3/2, 5/2, 7/2, 9/2), (3/2, 5/2, 7/2, 9/2, 11/2, 13/2)$. Then, as an example, for the three states with $J = 5/2$, one linear combination must have $(T, T_z) = (3/2, 1/2)$ [the isobaric analogue of the $J = 5/2$, $(T, T_z) = (3/2, 3/2)$ state], and the other two must have $T = 1/2$. This method can be extended to more complicated partitions and higher values of T .

24.2 Angular momentum projection

The angular-momentum projection operator can be used to construct explicit linear combinations of the M -scheme Slater determinants that have good total angular momentum. These linear combinations can thus be used to construct a Hamiltonian matrix that is block diagonal in J . Before discussing the angular-momentum projection operator, the results for the simpler types of angular-momentum operators will be reviewed.

The single-particle states $|k, m\rangle$ are eigenfunctions of the j^2 and j_z operators

$$j^2 |km\rangle = j(j+1) |km\rangle \quad (24.4)$$

and

$$j_z |km\rangle = m |km\rangle . \quad (24.5)$$

The j^2 operator can be written in terms of the raising and lowering operators j_{\pm}

$$j^2 = j_- j_+ + j_z^2 + j_z = j^2 = j_+ j_- + j_z^2 - j_z, \quad (24.6)$$

where

$$j_{\pm} | km \rangle = \sqrt{j(j+1) - m(m \pm 1)} | k, m \pm 1 \rangle. \quad (24.7)$$

The total angular momentum is a one-body operator given by a sum over the angular momenta of the particles

$$\vec{J} = \sum_{k=1}^n \vec{j}_k. \quad (24.8)$$

J^2 is a two-body operator given in terms of the vector components of Eq. (24.8) by

$$J^2 = J_- J_+ + J_z^2 + J_z. \quad (24.9)$$

The second-quantized form for the one-body vector operators are

$$\begin{aligned} \hat{J}_z &= \sum_{\alpha\beta} < \alpha | J_z | \beta > a_{\alpha}^{+} a_{\beta} = \sum_{\alpha\beta} m_{\alpha} \delta_{\alpha\beta} a_{\alpha}^{+} a_{\beta} \\ &= \sum_{km} m a_{km}^{+} a_{km}, \end{aligned} \quad (24.10)$$

and

$$\hat{J}_\pm = \sum_{km} \sqrt{j(j+1) - m(m \pm 1)} a_{k,m\pm 1}^+ a_{km}. \quad (24.11)$$

One can operate with \hat{J}^2 on any M -state Slater determinant to determine whether or not it has good angular momentum. For example, for the closed-shell configuration of a given single-particle state defined by

$$| C_k \rangle = a_{kj}^+ a_{k,j-1}^+ \dots a_{k,-j}^+ | \rangle \quad (24.12)$$

one obtains

$$\begin{aligned} \hat{J}_z | C_k \rangle &= M | C_k \rangle = \sum_{km} m a_{km}^+ a_{km} | C_k \rangle \\ &= \sum_{m=-j}^j m | C_k \rangle = 0 | C_k \rangle, \end{aligned} \quad (24.13)$$

and

$$\hat{J}_\pm | C_k \rangle = \sum_{km} \sqrt{j(j+1) - m(m \pm 1)} a_{k,m\pm 1}^+ a_{km} | C_k \rangle = 0, \quad (24.14)$$

since the state with quantum numbers $(k, m \pm 1)$ is already occupied in $|C_k\rangle$. Hence $M = 0$ and by Eq. (24.9) $J = 0$. That is, the closed-shell configuration is spherically symmetric. The general closed-shell configuration

$$|C\rangle = \prod_a |C_{k_a}\rangle \quad (24.15)$$

also has $J = M = 0$, and thus only partially filled shells contribute to non-zero angular momenta.

The closed-shell plus one-particle configuration (the single-particle configuration) can be represented by

$$|Ck_a\rangle \equiv a_{k_a m_a}^+ |C\rangle. \quad (24.16)$$

This state is also an eigenstate of \hat{J}^2 and \hat{J}_z with eigenvalues $j_a(j_a + 1)$ and m_a , respectively.

The closed-shell minus one-particle configuration (the single-hole configuration) with one particle absent in the state $(k_\alpha m_\alpha)$ is given by

$$|C(k_\alpha m_\alpha)^{-1}\rangle = (-1)^{j_\alpha - m_\alpha} a_{k_\alpha m_\alpha} |C\rangle \quad (24.17)$$

Operation of \hat{J}_z and \hat{J}^2 on this state gives

$$\begin{aligned}\hat{J}_z | C(k_\alpha m_\alpha)^{-1} \rangle &= \sum_{m=-j, m \neq m_\alpha}^{m=j} m | C(k_\alpha, m_\alpha)^{-1} \rangle \\ &= -m_\alpha | C(k_\alpha, m_\alpha)^{-1} \rangle.\end{aligned}\quad (24.18)$$

and

$$\hat{J}^2 | C(k_\alpha, m_\alpha)^{-1} \rangle = j_\alpha(j_\alpha + 1) | C(k_\alpha, m_\alpha)^{-1} \rangle. \quad (24.19)$$

Hence, the single-hole configuration as defined by Eq. (24.17) has $J = j_\alpha$ and $M = -m_\alpha$. The single-hole configuration with $J = j_\alpha$ and $M = m_\alpha$ is given by the closed-shell configuration with one particle absent in the state $(k_\alpha, -m_\alpha)$

$$| C k_\alpha^{-1} \rangle \equiv (-1)^{j_\alpha + m_\alpha} a_{k_\alpha, -m_\alpha} | C \rangle \equiv \tilde{a}_{k_\alpha m_\alpha} | C \rangle, \quad (24.20)$$

where \tilde{a} is the tensor operator of rank j_α .

In general, multi-particle M -states $|\Phi_\alpha(M)\rangle$ are not eigenstates of \hat{J}^2 (they do not have a good J value). However, states with good J are linear combinations of the M -states:

$$|\Psi(\omega JM)\rangle = \sum_{\alpha=1}^{d(M)} c_\alpha |\Phi_\alpha(M)\rangle. \quad (24.21)$$

Conversely, the M -states are linear combinations of the J -states:

$$|\Phi_a(M)\rangle = \sum_{J \geq M} \sum_{\omega=1}^{D(J)} d_{\omega J} |\Psi(\omega JM)\rangle. \quad (24.22)$$

The $d(M)$ and $D(J)$ are the M -scheme and J -scheme dimensions, respectively. Any configuration that has $d(M) = 1$ must have good angular momentum $J = M_{max}$, since there is only one term in Eqs. (24.21). In particular, the state $|\Phi(M_{max})\rangle$ with $M = M_{max}$ has $J = M_{max}$. This can also be seen from the fact that

$$\hat{J}_+ |\Phi(M_{max})\rangle = 0, \quad (24.23)$$

and hence

$$\hat{J}^2 |\Phi(M_{max})\rangle = (J_z^2 + J_z) |\Phi(M_{max})\rangle$$

$$= (M_{max} + 1)M_{max} | \Phi(M_{max}) > . \quad (24.24)$$

An operator that projects out the component with $J = J_o$ leaving the component with $J = J_i$ unchanged is

$$\bar{P}_{J_i J_o} \equiv \frac{\hat{J}^2 - J_o(J_o + 1)}{J_i(J_i + 1) - J_o(J_o + 1)}. \quad (24.25)$$

This can be seen by operating with \bar{P} on the wave function of Eq. (24.22)

$$\bar{P}_{J_i J_o} | \Phi_a(M) > = \sum_{J \geq M, J \neq J_o}^{J_{max}} \sum_{\omega=1}^{D(J)} d'_{\omega J} | \Psi(\omega JM) >, \quad (24.26)$$

where

$$d'_{\omega J} = \frac{J(J+1) - J_o(J_o+1)}{J_i(J_i+1) - J_o(J_o+1)} d_{\omega J}. \quad (24.27)$$

That is, the component with $J = J_o$ is missing and the component with $J = J_i$ has $d' = d$.

The operator, which projects out all of the unwanted components with $J = J_o$ leaving only one component with $J = J_i$, is thus

$$P_{J_i} \equiv \prod_{J_o=M, J_o \neq J_i}^{J_{max}} \bar{P}_{J_i J_o} = \prod_{J_o=M, J_o \neq J_i}^{J_{max}} \frac{\hat{J}^2 - J_o(J_o + 1)}{J_i(J_i + 1) - J_o(J_o + 1)}. \quad (24.28)$$

P_{J_i} acting on the wave function of Eq. (24.22) gives

$$P_{J_i} | \Phi_a(M) \rangle = \sum_{\omega=1}^{D(J)} d_{\omega J_i} | \Psi(\omega J_i M) \rangle. \quad (24.29)$$

Since each of the states $\Psi(\omega JM)$ is a linear combination of M -states, the sum in the above equation is also linear combination of M -states

$$\sum_{\omega=1}^{D(J)} d_{\omega J_i} | \Psi(\omega J_i M) \rangle = \sum_{b=1}^{d(M)} e_b | \Phi_b(M) \rangle. \quad (24.30)$$

Evaluation of the real coefficients e_b will be illustrated below by some examples.

When $d(M) > D(J)$, the set of J -states obtained from operating P_{J_i} on all of the M -states is overcomplete. Also it may happen the projection from different M -states produces states that are not linearly independent (as in the above examples). Thus, one must carefully choose $D(J)$ out of the total set of $d(M)$ projected states that will form a complete basis. In addition, when $D(J) > 1$, the projected states will not necessarily be orthogonal, and they must be orthogonalized by the Gram-Schmidt orthogonalization procedure.

In general, the angular-momentum projection operator can be applied to configurations with particles distributed over several single-orbital states. The projection operator cannot change the partition (the number of particles in each single-orbital state). Thus the overlaps between the good J states in different partitions is automatically zero. Only one partition need be considered at a time for constructing the good J states.

The projection operator is idempotent,

$$P_{J_i} P_{J_i} = P_{J_i}, \quad (24.31)$$

and it commutes with the spherically symmetric Hamiltonian operator,

$$[H, P_{J_i}] = 0. \quad (24.32)$$

Thus, matrix elements of the Hamiltonian operator with the states of good J can be obtained by projecting on only one side

$$\langle \Phi_a | P_{J_i} H P_{J_i} | \Phi_b \rangle = \langle \Phi_a | H P_{J_i} P_{J_i} | \Phi_b \rangle = \langle \Phi_a | H P_{J_i} | \Phi_b \rangle. \quad (24.33)$$

24.2.1 Examples for $[5/2]^n$ configurations

Example (i): For the $[5/2]^2$ configuration there are two M -states with $M = 2$

$$| a \rangle = a_{-1/2}^+ a_{5/2}^+ | \rangle \quad (24.34)$$

and

$$| b \rangle = a_{1/2}^+ a_{3/2}^+ | \rangle. \quad (24.35)$$

$(a_{-1/2}^+ \equiv a_{j=5/2, m=-1/2}^+$, etc.) These must be associated with the J -states that have $J = 2$ or 4. From Eq. (24.3), $J = 4$ is the maximum J -value allowed, and due to the Pauli principle $J = 3$ is not allowed. Operation with \hat{J}^2 gives

$$\hat{J}^2 |a\rangle = 15 |a\rangle + \sqrt{45} |b\rangle \quad (24.36)$$

and

$$\hat{J}^2 |b\rangle = \sqrt{45} |a\rangle + 11 |b\rangle. \quad (24.37)$$

The linear combination of $|a\rangle$ and $|b\rangle$ that has $J = 2$ can be obtained by projecting out the states with $J_o = 3$ and 4 by operating on $|a\rangle$ or $|b\rangle$ with $P_{J=2}$ and projecting out the states with $J_o = 3$ and 4; in particular $|a\rangle$ gives

$$\begin{aligned} P_{J=2} |a\rangle &= \bar{P}_{J=2, J_o=3} \bar{P}_{J=2, J_o=4} |a\rangle = \left\{ \frac{\hat{J}^2 - 12}{6 - 12} \right\} \left\{ \frac{\hat{J}^2 - 20}{6 - 20} \right\} |a\rangle \\ &= \left\{ \frac{\hat{J}^2 - 12}{6 - 12} \right\} \sqrt{\frac{5}{14}} \left\{ \sqrt{\frac{5}{14}} |a\rangle - \sqrt{\frac{9}{14}} |b\rangle \right\} \end{aligned}$$

$$= \frac{5}{14} |a\rangle - \frac{\sqrt{45}}{14} |b\rangle = \sqrt{\frac{5}{14}} \left\{ \sqrt{\frac{5}{14}} |a\rangle - \sqrt{\frac{9}{14}} |b\rangle \right\}. \quad (24.38)$$

(Note that the operation of projecting out $J_o = 3$ had no effect because $J_o = 3$ is forbidden by the Pauli principle.) The normalization factor taken out in front in the last line shows that the probability of finding the component $J = 2$ component in state $|a\rangle$ is $5/14$ (and thus the probability to find the $J = 4$ component must be $9/14$). The normalized wave function is

$$\frac{P_{J=2} |a\rangle}{N_a} = \sqrt{\frac{5}{14}} |a\rangle - \sqrt{\frac{9}{14}} |b\rangle \quad (24.39)$$

The same result (up to a phase factor) would be obtained from $P_{J=2}$ acting on the state $|b\rangle$.

In this two-particle example the result must be same within a phase factor of the Clebsch-Gordan coupling of two states, With $N_{12} = \frac{1}{\sqrt{2}}$:

$$\frac{1}{\sqrt{2}} (2) \langle 5/2, -1/2, 5/2, 5/2 | 2, 2 \rangle = -\sqrt{\frac{5}{14}} \quad (24.40)$$

and

$$\frac{1}{\sqrt{2}} (2) \langle 5/2, 1/2, 5/2, 3/2 | 2, 2 \rangle = \sqrt{\frac{9}{14}}, \quad (24.41)$$

where the factor of (2) comes from the fact that there are two terms that contribute to a given antisymmetric M -scheme basis state.

However, the projection operator can also be applied in the general case of the n -particle configuration to obtain wave functions with good J , as in the next example.

Example (ii): There are two M -states for the $(j = 5/2)^3$ configuration with $M = 5/2$

$$|c\rangle = a_{-3/2}^+ a_{3/2}^+ a_{5/2}^+ | \rangle \quad (24.42)$$

and

$$|d\rangle = a_{-1/2}^+ a_{1/2}^+ a_{5/2}^+ | \rangle \quad (24.43)$$

The operation of \hat{J}^2 on these states gives

$$\hat{J}^2 |c\rangle = \frac{67}{4} |c\rangle + \frac{32}{4} |d\rangle$$

and

$$\hat{J}^2 |d\rangle = \frac{67}{4} |c\rangle + \frac{32}{4} |d\rangle \quad (24.44)$$

Since there is no $J_o = 7/2$ component, the state with $J = 5/2$ can be obtained by projecting out the $J_o = 9/2$ component from state $|c\rangle$

$$P_{J=5/2}|c\rangle = \frac{(\hat{J}^2 - \frac{99}{4})}{(\frac{35}{4} - \frac{99}{4})} |c\rangle = \frac{1}{\sqrt{2}} \left\{ -\frac{1}{\sqrt{2}} |c\rangle + \frac{1}{\sqrt{2}} |d\rangle \right\}. \quad (24.45)$$

The normalized projected wave functions is given by

$$\frac{P_{J=5/2}|c\rangle}{N_c} = \left\{ -\frac{1}{\sqrt{2}} |c\rangle + \frac{1}{\sqrt{2}} |d\rangle \right\}. \quad (24.46)$$

24.3 Wavefunctions in the J -scheme

In order to reduce the size of the calculation it is useful to form a basis that has a definite J value. It is also useful to express the many-particle matrix elements in a way in which the trivial M -state dependence is taken into account. This section discusses the structure of the angular momentum-coupled wave functions. The structure of the operators and matrix elements, is considered in the next section.

In general, when more than two particles are coupled to good angular momentum, one finds that $N = 1$ as long as each particle is in a different k state. When more than two particles go into a single k state, the normalization factor becomes increasingly complicated. However, as discussed in the previous section, the number of allowed states for a given J value are easily deduced from the number of M values.

The wave functions associated with these allowed J values can be obtained with the projection operators discussed in Sec. 24.12. The n -particle wavefunction will be denoted

by

$$| k^n \omega JM \rangle \equiv Z^+(k^n \omega JM) | \rangle, \quad (24.47)$$

where ω is the additional quantum number that must be introduced when there is more than one state for a given value of J , and where Z^+ are the linear combinations of a^+ operators that create the antisymmetric n -particle state. In some cases ω may be a label associated with the seniority quantum number [5] or some group theoretical classification. It will be assumed that these states are constructed to be orthonormal. Computer programs are available for calculating the number of allowed J values in a k^n configuration. [6], [2]

When the n particles are distributed over two k -states, the wavefunctions take the form

$$\begin{aligned} | n\omega JM \rangle &= | (k_1^{n_1} \omega_1 J_1)(k_2^{n_2} \omega_2 J_2) JM \rangle \\ &= \sum_{M_1 M_2} \langle J_1 M_1 J_2 M_2 | JM \rangle Z^+(k_2^{n_2} \omega_2 J_2 M_2) Z^+(k_1^{n_1} \omega_1 J_1 M_1) | \rangle \\ &= (-1)^{n_1 n_2} [Z^+(k_1^{n_1} \omega_1 J_1) \otimes Z^+(k_2^{n_2} \omega_2 J_2)]_M^J | \rangle, \end{aligned} \quad (24.48)$$

where $n = n_1 + n_2$, and where the operators Z^+ are defined in Eq. (24.47) above. The phase factor of $(-1)^{n_1 n_2}$ arises from commuting n_1 particles in state k_1 with n_2 particles in state

k_2 . The values and multiplicities of J in Eq. (24.48) are those allowed by the vector coupling of all possible \vec{J}_1 and \vec{J}_2 .

When the n particles are distributed over many k states, the wavefunctions take one of the possible forms allowed by the successive vector coupling of the angular momenta. As an example, for three states

$$|n\omega JM\rangle = |[(k_1^{n_1}\omega_1 J_1)(k_2^{n_2}\omega_2 J_2)J_{12}][k_3^{n_3}\omega_3 J_3]JM\rangle, \quad (24.49)$$

where $n = n_1 + n_2 + n_3$. For a given total number of particles n , the distribution $n_1, n_2 \dots$ among the k states will be referred to as the partition.

24.4 Matrix elements in the J scheme

In this section, a few general results for the matrix elements for creation operator in the J -scheme are given. These will be used in subsequent sections when the matrix elments of

the J -coupled forms are derived.

In addition to the angular momentum recoupling, attention must be paid to the phase factors that occur due to the reordering of particles between groups. Examples of these phase factors for the wave functions themselves appear above in Eqs. (24.999) and (24.48). As an example for the particle-number-dependent phase factors in matrix elements of the creation and destruction operators, consider a matrix element involving the wave functions of Eqs. (24.48) and (24.999) with operators $O(k_i n''_i)$ that involve n''_i creation and/or destruction operators for the state k_i

$$\begin{aligned}
 & <(k_1^{n_1}\omega_1 J_1)(k_2^{n_2}\omega_2 J_2)JM \mid O(k_1 n''_1)O(k_2 n''_2) \mid (k_1^{n'_1}\omega'_1 J'_1)(k_2^{n'_2}\omega'_2 J'_2)J'M'> \\
 &= \sum_{M_i M'_i} < J_1 M_1 J_2 M_2 \mid JM > < J'_1 M'_1 J'_2 M'_2 \mid J'M' > \\
 &\quad \times <| Z(k_1^{n_1}\omega_1 J_1 M_1)Z(k_2^{n_2}\omega_2 J_2 M_2)O(k_1 n''_1)O(k_2 n''_2) \\
 &\quad \quad \quad \times Z^+(k_2^{n'_2}\omega'_2 J'_2 M'_2)Z^+(k_1^{n'_1}\omega'_1 J'_1 M'_1) | > \\
 &= (-1)^{n_2 n''_1 + n'_1(n_2 + n'_2 + n''_2)} \sum_{M_i M'_i} < J_1 M_1 J_2 M_2 \mid JM > < J'_1 M'_1 J'_2 M'_2 \mid J'M' >
 \end{aligned}$$

$$\begin{aligned} & \times \langle | Z(k_1^{n_1} \omega_1 J_1 M_1) O(k_1 n''_1) Z^+(k_1^{n'_1} \omega'_1 J'_1 M'_1) \\ & \times Z(k_2^{n_2} \omega_2 J_2 M_2) O(k_2 n''_2) Z^+(k_2^{n'_2} \omega'_2 J'_2 M'_2) | \rangle . \end{aligned} \quad (24.50)$$

The phase factor arises from first commuting the state operator Z for n_2 with the operator O for n''_1 , and next commuting the state operator Z^+ for n'_1 with the operators for n'_2 , n''_2 and n_2 . The phase factor can be simplified by noting that $n_i + n'_i + n''_i$ is always even. This can be seen by considering n''_i as a sum of the number of creation, c''_i , and destruction, d''_i , operators. It is clear that the total number of destruction operators, $n_i + d''_i$, must equal the total number of creation operators, $n'_i + c''_i$. Since $n_i + d''_i = n'_i + c''_i$, and both are integers, the sum $n_i + d''_i + n'_i + c''_i = n_i + n'_i + n''_i$ must be even. This also means that $(-1)^{n''_i} = (-1)^{n_i + n'_i}$. Thus the phase factor becomes

$$(-1)^{n_2 n''_1 + n'_1 (n_2 + n'_2 + n''_2)} = (-1)^{n_2 n''_1} = (-1)^{n_2 (n_1 + n'_1)}. \quad (24.51)$$

A general angular momentum recoupling result that is often needed is the matrix element for an operator that acts only on particles in a set of active states ($n_a J_a$) and not on those in a set of inactive states ($n_i J_i$)

$$\langle (n_i \omega_i J_i) (n_a \omega_a J_a) J | |O^\lambda(n''_a)| |(n'_i \omega'_i J'_i) (n'_a \omega'_a J'_a) J' \rangle$$

$$\begin{aligned}
&= (-1)^{J'_i + J'_a + J + \lambda} \sqrt{(2J+1)(2J'+1)} \left\{ \begin{array}{ccc} J_a & J'_a & \lambda \\ J' & J & J_i \end{array} \right\} \\
&\quad \times \langle n_a \omega_a J_a | | O^\lambda(n''_a) | | n'_a \omega'_a J'_a \rangle \delta_{n_i n'_i} \delta_{J_i J'_i} \delta_{\omega_i \omega'_i}. \tag{24.52}
\end{aligned}$$

where the number-dependent phase factor from Eq. (24.51) is $(-1)^{n_\alpha(2n_i)} = 1$. The matrix element with the active and inactive states interchanged is the same except for the phase factor

$$\begin{aligned}
&\langle (n_a \omega_a J_a) (n_i \omega_i J_i) J | | O^\lambda(n''_a) | | (n'_a \omega'_a J'_a) (n'_i \omega'_i J'_i) J' \rangle \\
&= (-1)^{J_a + J_i + J' + \lambda} \sqrt{(2J+1)(2J'+1)} \left\{ \begin{array}{ccc} J_a & J'_a & \lambda \\ J' & J & J_i \end{array} \right\} \\
&\quad \times \langle n_a \omega_a J_a | | O^\lambda(n''_a) | | n'_a \omega'_a J'_a \rangle \delta_{n_i n'_i} \delta_{J_i J'_i} \delta_{\omega_i \omega'_i}. \tag{24.53}
\end{aligned}$$

Bibliography

- [1] T. Sebe and M. Harvey, “Enumeration of Many-Body States of the Nuclear Shell Model with Definite Angular Momentum and Isobaric Spin with Mixed Single Particle Orbits”, ARCL, Chalk River preprint 3007 (1968).
- [2] W. D. M. Rae, A. Etchegoyen and B. A. Brown, *OXBASH, the Oxford-Buenos Aires-MSU Shell-Model Code*, Michigan State University Laboratory Report no. 524.

- [3] D. K. Sunko, Phys. Rev. C **33**, 1811 (1986). link
- [4] J. P. Draayer and H. T. Valdes, Comput. Phys. Comm. **36**, 313 (1985).
- [5] A. de Shalit and I. Talmi, *Nuclear Shell Theory*, (Academic Press, 1963).
- [6] L. B. Hubbard, Comput. Phys. Commun. **1**, 453 (1970).

Chapter 25

Two-body hamiltonian matrix elements

584

25.1 Introduction

The chapters on the nuclear Hamiltonian are broken into three parts. In this part we discuss the basic methods with applications to some simple type of two-body interactions. The results in this section can be obtained with the fortran program tbme.for. Then we qualitatively outline the procedures used to obtain realistic interactions starting from two-nucleon scattering data. In the second part we discuss core-polarization corrections for one- and two-body operators. In the final part we discuss the empirical Hamiltonians that have been developed for specific model spaces.

25.2 Form of the two-body matrix elements

Antisymmetric J -coupled two-body matrix elements are the primary ingredients for the setting up the Hamiltonian matrix. They can be evaluated by expanding them into direct

and exchange terms involving the product wavefunctions:

$$\begin{aligned}
 & \langle k_1 k_2 J | V | k_3 k_4 J \rangle \\
 &= N_{12} N_{34} \sum_{m_i} \langle j_1 m_1 j_2 m_2 | JM \rangle \langle j_3 m_3 j_4 m_4 | JM \rangle \\
 &\quad \times \langle k_1 m_1 k_2 m_2 | V | k_3 m_3 k_4 m_4 \rangle \\
 &= N_{12} N_{34} \sum_{m_i} \langle j_1 m_1 j_2 m_2 | JM \rangle \langle j_3 m_3 j_4 m_4 | JM \rangle \\
 &\quad \times \{ \langle k_1 m_1 k_2 m_2 | V | k_3 m_3 k_4 m_4 \rangle_p - \langle k_1 m_1 k_2 m_2 | V | k_4 m_4 k_3 m_3 \rangle_p \}, \tag{25.1}
 \end{aligned}$$

where the subscript p indicates that this is the “product” wavefunction. With the symmetry properties of the Clebsch-Gordan coefficients the sums of m_i can be carried to obtain:

$$\begin{aligned}
 & \langle k_1 k_2 J | V | k_3 k_4 J \rangle = \frac{1}{\sqrt{[(1 + \delta_{k_1 k_2})(1 + \delta_{k_3 k_4})]}} \\
 & \quad \times \left\{ \langle k_1 k_2 J | V | k_3 k_4 J \rangle_p - (-1)^{j_3 + j_4 - J} \langle k_1 k_2 J | V | k_4 k_3 J \rangle_p \right\}. \tag{25.2}
 \end{aligned}$$

Since the interaction V is Hermitian and the matrix elements are real, one has

$$\langle k_3 k_4 J | V | k_1 k_2 J \rangle = \langle k_1 k_2 J | V | k_3 k_4 J \rangle . \quad (25.3)$$

In addition, one has from the wavefunction anti-symmetry:

$$\langle k_1 k_2 J | V | k_4 k_3 J \rangle = -(-1)^{j_3+j_4-J} \langle k_1 k_2 J | V | k_3 k_4 J \rangle , \quad (25.4)$$

and

$$\langle k_2 k_1 J | V | k_3 k_4 J \rangle = -(-1)^{j_1+j_2-J} \langle k_1 k_2 J | V | k_3 k_4 J \rangle . \quad (25.5)$$

Thus it is sufficient to calculate the two-body matrix element for only one-ordering of k_1, k_2, k_3 and k_4 .

When isospin is introduced the factors associated with j and J are doubled with those involving $t = \frac{1}{2}$ and T and the last four equations become:

$$\langle k_1 k_2 J T | V | k_3 k_4 J T \rangle = \frac{1}{\sqrt{[(1 + \delta_{k_1 k_2})(1 + \delta_{k_3 k_4})]}}$$

$$\begin{aligned} & \times \left\{ \langle k_1 k_2 J T | V | k_3 k_4 J T \rangle_p \right. \\ & \left. - (-1)^{j_3 + j_4 - J + 1 - T} \langle k_1 k_2 J T | V | k_4 k_3 J T \rangle_p \right\}, \end{aligned} \quad (25.6)$$

$$\langle k_3 k_4 J T | V | k_1 k_2 J T \rangle = \langle k_1 k_2 J T | V | k_3 k_4 J T \rangle, \quad (25.7)$$

$$\langle k_1 k_2 J T | V | k_4 k_3 J T \rangle = -(-1)^{j_3 + j_4 - J + 1 - T} \langle k_1 k_2 J T | V | k_3 k_4 J T \rangle, \quad (25.8)$$

and

$$\langle k_2 k_1 J T | V | k_3 k_4 J T \rangle = -(-1)^{j_1 + j_2 - J + 1 - T} \langle k_1 k_2 J T | V | k_3 k_4 J T \rangle. \quad (25.9)$$

The M -scheme two-body matrix elements can be expressed in terms of these J -coupled two-body matrix elements

$$\begin{aligned} & \langle k_1 m_1 k_2 m_2 | V | k_3 m_3 k_4 m_4 \rangle = \sqrt{(1 + \delta_{k_1 k_2})(1 + \delta_{k_3 k_4})} \\ & \times \sum_{JM} \langle JM | j_1 m_1 j_2 m_2 \rangle \langle JM | j_3 m_3 j_4 m_4 \rangle \langle k_1 k_2 J | V | k_3 k_4 J \rangle. \end{aligned} \quad (25.10)$$

When isospin is introduced this becomes

$$\begin{aligned}
 & \langle (k_1 m_1 t_z) (k_2 m_2 t'_z) | V | (k_3 m_3 t_z) (k_4 m_4 t'_z) \rangle = \sqrt{(1 + \delta_{k_1 k_2})(1 + \delta_{k_3 k_4})} \\
 & \quad \times \sum_{JMTT_z} \langle JM | j_1 m_1 j_2 m_2 \rangle \langle JM | j_3 m_3 j_4 m_4 \rangle \\
 & \quad \times \langle TT_z | \frac{1}{2} t_z \frac{1}{2} t'_z \rangle \langle TT_z | \frac{1}{2} t_z \frac{1}{2} t'_z \rangle \langle k_1 k_2 JT | V | k_3 k_4 JT \rangle . \tag{25.11}
 \end{aligned}$$

There are two basic types of interactions. Those with $(t_z, t'_z) = (p, p)$ or $(t_z, t'_z) = (n, n)$ which must have $T = 1$, and those with $(t_z, t'_z) = (p, n)$ which are a linear combination of $T = 0$ and $T = 1$.

25.3 Conversion from isospin to proton-neutron form

The most general way to express the two-body matrix elements is in the proton-neutron form $\langle qq'J | V | qq'J \rangle$, where q stands for proton or neutron. Due to charge conservation there

are three unique types, $(qq') = (nn)$, $(qq') = (pp)$, $(qq') = (pn)$. The fourth combination (np) is the same as (pn) and codes are usually written to use only one form for the input. The Oxbash and NuShellX codes use (pn) .

If we leave out Coulomb and have isospin symmetry we can use the isospin basis where T is also good quantum number as in the form of Eq. (25.6). Starting from the matrix elements with good isospin we can obtain the proton-proton, neutron-neutron, and proton-neutron matrix elements from:

$$\begin{aligned} < k_1 k_2 J | V | k_3 k_4 J >_{pp} &= < k_1 k_2 J | V | k_3 k_4 J >_{nn} = < k_1 k_2 JT = 1 | V | k_3 k_4 JT = 1 >, \\ &\quad (25.12) \\ &< k_1 k_2 J | V | k_3 k_4 J >_{pn} = \frac{\sqrt{(1 + \delta_{k_1, k_2})(1 + \delta_{k_3, k_4})}}{2} \end{aligned}$$

$$\times [< k_1 k_2 JT = 1 | V | k_3 k_4 JT = 1 > + < k_1 k_2 JT = 0 | V | k_3 k_4 JT = 0 >]. \quad (25.13)$$

Many codes use this form for the input. However, Oxbash and NuShellX use the unnormalized form

$$< k_1 k_2 J | V | k_3 k_4 J >_{upn} =$$

$$[< k_1 k_2 J T = 1 | V | k_3 k_4 J T = 1 > + < k_1 k_2 J T = 0 | V | k_3 k_4 J T = 0 >]. \quad (25.14)$$

In Oxbash and NuShellX the T label in the proton-neutron form for the input does not affect the calculations. It is used only as a reminder of how the proton-neutron matrix element was obtained from the isospin matrix elements if they were used as the starting input. Most programs for calculations of the TBME in the proton-neutron basis produce output in the normalized form of Eq. (25.13). If one uses these in Oxbash or NuShellX then one must multiply them by the factor $2/\sqrt{(1 + \delta_{k_1, k_2})(1 + \delta_{k_3, k_4})}$.

If one starts with matrix elements with good isospin, then the most important aspect for isospin non-conservation is the addition of the Coulomb two-body matrix elements to Eq. (25.12) with $(qq) = (pp)$. In addition, the nucleon-nucleon interaction has small terms that violate isospin conservation at the level of a few percent and it is most straight-forward to include these by doing all aspects of the calculations in a proton-neutron basis.

25.4 General types of interactions

The general form of the two-body potential consists of central (c), spin-orbit (s) and spin-tensor (t) components:

$$V_c = f_c(r), \quad (25.15)$$

$$V_s = f_s(r) \vec{\lambda} \cdot \vec{S}, \quad (25.16)$$

and

$$V_t = f_t(r) S_{12}. \quad (25.17)$$

In these equations,

$$\vec{S} = (\vec{\sigma}_1 + \vec{\sigma}_2)/2, \quad (25.18)$$

$\vec{\lambda}$ is relative angular momentum operator, and S_{12} is the spin-tensor operator

$$S_{12} = 3(\vec{\sigma}_1 \cdot \hat{r})(\vec{\sigma}_2 \cdot \hat{r}) - (\vec{\sigma}_1 \cdot \vec{\sigma}_2), \quad (25.19)$$

where \vec{r} is the relative coordinate

$$\vec{r} = \vec{r}_1 - \vec{r}_2,$$

with magnitude $r = |\vec{r}|$. (25.20)

In order to carry out the tensor algebra it is useful to rewrite the potential in terms of tensor operators $U^{(q)}$ that act on the spatial coordinates and $X^{(q)}$ that act on the spin coordinates:

$$V = \sum_q V_q = \sum_q U^{(q)} \cdot X^{(q)}, \quad (25.21)$$

The interaction components are specified by $q = 0$ for central, $q = 1$ for spin-orbit and $q = 2$ for spin-tensor.

In order to carry out the tensor algebra one can rewrite the interaction of Eqs. (25.15)-(25.17) in the form of Eq. (25.21) with the spatial parts U given by:

$$U^{(0)}(\vec{r}) = f_{c,S=0}(r) + f_{c,S=1}(r), \quad (25.22)$$

$$U^{(1)}(\vec{r}) = f_s(r) \vec{\lambda}, \quad (25.23)$$

and

$$U^{(2)}(\vec{r}) = f_t(r) \sqrt{\frac{4\pi}{5}} Y^{(2)}(\hat{r}), \quad (25.24)$$

and the spin parts X given by

$$X^{(0)} = 1, \quad (25.25)$$

$$X^{(1)} = \vec{S}, \quad (25.26)$$

and

$$X^{(2)} = \sqrt{6}[\vec{\sigma}_1 \otimes \vec{\sigma}_2]^{(2)}. \quad (25.27)$$

Eq. (25.22) takes into account that the radial form and strength depends on the total spin S .

To evaluate the space and spin components of the matrix elements of Eq. (25.21) we need to transform from jj to LS coupling:

$$\begin{aligned} < k_a k_b JT | V | k_c k_d JT >_p = & \sum_{L S L' S'} \left[\begin{array}{ccc} \ell_a & 1/2 & j_a \\ \ell_b & 1/2 & j_b \\ L & S & J \end{array} \right] \left[\begin{array}{ccc} \ell_c & 1/2 & j_c \\ \ell_d & 1/2 & j_d \\ L' & S' & J \end{array} \right] \\ & \times < k_A k_B LSJT | V | k_C k_D L' S' JT >_p. \end{aligned} \quad (25.28)$$

k_A is shorthand for the set of quantum numbers $(n_a \ell_a)$ and k_a is shorthand for the set $(n_a \ell_a j_a)$, etc. The large square bracket is the LS to jj transformation coefficient given by Eq. 14.25. With Eq. (25.21), these LS coupled matrix elements are then expressed in terms of reduced matrix elements:

$$\begin{aligned} & \langle k_A k_B LSJT | V | k_C k_D L' S' JT \rangle_p \\ &= \sum_q \langle k_A k_B LSJT | V_q | k_C k_D L' S' JT \rangle_p = \sum_q (-1)^{S+L'+J} \left\{ \begin{array}{ccc} L & S & J \\ S' & L' & q \end{array} \right\} \\ & \quad \times \langle k_A k_B L || U^{(q)} || k_C k_D L' \rangle \langle ST || X^{(q)} || S' T \rangle. \end{aligned} \quad (25.29)$$

For the matrix element of Eq. (25.29) the spatial wavefunctions $| k_A k_B \rangle$ and $| k_C k_D \rangle$ are expressed in terms of the relative ($n\lambda$) and center-of-mass ($N\Lambda$) coordinates using the Talmi-Moshinsky transformation:

$$\langle k_A k_B L || U^{(q)} || k_C k_D L' \rangle = \sum_{n\lambda n' \lambda' N\Lambda N' \Lambda'} \langle n\lambda N\Lambda | k_A k_B L \rangle$$

$$\times \langle n' \lambda' N' \Lambda' | k_C k_D L' \rangle \langle n \lambda N \Lambda L | U^{(q)}(\vec{r}) | n' \lambda' N' \Lambda' L' \rangle . \quad (25.30)$$

This last integral reduces to:

$$\begin{aligned} \langle n \lambda N \Lambda L | U^{(q)}(\vec{r}) | n' \lambda' N' \Lambda' L' \rangle &= (-1)^{\lambda + \Lambda + L' + q} \sqrt{(2L+1)(2L'+1)} \\ &\times \left\{ \begin{array}{ccc} \lambda & \lambda' & q \\ L' & L & \Lambda \end{array} \right\} \langle n \lambda | U^{(q)}(\vec{r}) | n' \lambda' \rangle \delta_{NN'} \delta_{\Lambda\Lambda'} . \end{aligned} \quad (25.31)$$

With the $U(\vec{r})$ given by Eqs. (25.22)-(25.24) the relative integrals reduce to:

$$\langle n \lambda | U^{(0)}(\vec{r}) | n' \lambda' \rangle = \langle n \lambda | f_c(r) | n' \lambda' \rangle \sqrt{2\lambda+1} \delta_{\lambda\lambda'}, \quad (25.32)$$

$$\langle n \lambda | U^{(1)}(\vec{r}) | n' \lambda' \rangle = \langle n \lambda | f_s(r) | n' \lambda' \rangle \sqrt{\lambda(\lambda+1)(2\lambda+1)} \delta_{\lambda\lambda'}, \quad (25.33)$$

and

$$\begin{aligned} \langle n \lambda | U^{(2)}(\vec{r}) | n' \lambda' \rangle &= (-1)^\lambda \langle n \lambda | f_t(r) | n' \lambda' \rangle \sqrt{(2\lambda+1)(2\lambda'+1)} \left(\begin{array}{ccc} \lambda & 2 & \lambda' \\ 0 & 0 & 0 \end{array} \right) . \end{aligned} \quad (25.34)$$

The central matrix element ($q = 0$) of Eq. (25.29) simplifies to

$$\begin{aligned}
 & \langle k_A k_B L S J T | V_0 | k_C k_D L' S' J T \rangle_p = \\
 & = \sum_{n\lambda n'\lambda' N\Lambda N'\Lambda'} \langle n\lambda N\Lambda | k_A k_B L \rangle \langle n' \lambda' N' \Lambda' | k_C k_D L' \rangle \\
 & \quad \times \langle n\lambda | f_c(r) | n' \lambda' \rangle \delta_{N N'} \delta_{\Lambda \Lambda'} \delta_{L L'} \delta_{S, S'}.
 \end{aligned} \tag{25.35}$$

25.5 Simple potentials

The two-body Coulomb is given by the central interaction:

$$V_{coul} = e^2/r. \tag{25.36}$$

It is independent of spin and acts only between protons ($T = 1$).

The simplest short-ranged interaction might be approximated by a delta function:

$$V_{\text{delta}} = W\delta(r), \quad (25.37)$$

Only $\lambda=\lambda'=0$ contributes to the integral. The spatial symmetry of two nucleons in an $\lambda=0$ state is symmetric, and thus $S+T$ must be odd to make the total two-nucleon wavefunction antisymmetric. Thus the delta function only acts in the $(S, T) = (0, 1)$ and $(1, 0)$ states. Thus there are only two contributions that can be written:

$$V_{\text{delta,T}=0} = W_0\delta(r),$$

and

$$V_{\text{delta,T}=1} = W_1\delta(r). \quad (25.38)$$

Typical effective values for the strengths are $W_0 = -560$ MeV fm³ and $W_1 = -320$ MeV fm³.

25.6 One boson exchange potentials

The one-pion exchange potential (OPEP) is the longest ranged part of the NN interaction due to the small mass of 140 MeV for the pion. The form of the OPEP interaction is:

$$V_{OPEP}(r) = g^2 (\tau_1 \cdot \tau_2) [(\vec{\sigma}_1 \cdot \vec{\nabla})(\vec{\sigma}_2 \cdot \vec{\nabla})] f(r), \quad (25.39)$$

where g is the pion-nucleon coupling constant, and $f(r)$ is the Yukawa form:

$$Y(x) = \frac{e^{-x}}{x}, \quad (25.40)$$

where

$$x = r/\rho_\pi, \quad (25.41)$$

and the pion range ρ_π is

$$\rho_\pi = \hbar/(m_\pi c) = 1.414 \text{ fm}. \quad (25.42)$$

Eq. (25.39) can be expanded and written in terms of the central and spin-tensor operators (link to derivation from Martin Savage): (link to original webpage):

$$V_{\text{OPEP}}(r) = \frac{g^2}{3}(\tau_1 \cdot \tau_2) \left\{ S_{12} \left[\frac{3}{r^2} + \frac{3}{\rho_\pi r} + \frac{1}{\rho_\pi^2} \right] Y(x) + \frac{(\vec{\sigma}_1 \cdot \vec{\sigma}_2)}{\rho_\pi^2} Y(x) - 4\pi(\vec{\sigma}_1 \cdot \vec{\sigma}_2)\delta(r) \right\}. \quad (25.43)$$

In the G matrix one takes only the low-k components and the $\delta(r)$ term is dropped. For the spin operator we have $\vec{\sigma}_1 \cdot \vec{\sigma}_2 |S\rangle = [2S(S+1)-3] |S\rangle$, and likewise for the isospin operator $\tau_1 \cdot \tau_2 |T\rangle = [2T(T+1)-3] |T\rangle$. Thus, the central OPEP potential that contains the the term $(\tau_1 \cdot \tau_2)(\vec{\sigma}_1 \cdot \vec{\sigma}_2)$ gives a relative weighting of 9, -3, -3, and 1 to the (S, T) channels $(0,0)$, $(0,1)$, $(1,0)$ and $(1,1)$, respectively. The overall strength of the OPEP interaction as determined from pion-nucleon scattering data is $(g^2 \rho_\pi^2) = 42 \text{ MeV fm}^3$.

Another way to write the OPEP strength is in terms of the projection operators $P_{S,T} = P_S P_T$. These operators project out the part with specific S and T values. In terms of the spin operators:

$$P_{S=0} = \frac{1 - (\vec{\sigma}_1 \cdot \vec{\sigma}_2)}{4},$$

$$P_{S=1} = \frac{3 + (\vec{\sigma}_1 \cdot \vec{\sigma}_2)}{4}, \quad (25.44)$$

with an analogous results for the isospin projection. Thus we could write in terms of $P_{S,T}$:

$$(\tau_1 \cdot \tau_2)(\vec{\sigma}_1 \cdot \vec{\sigma}_2) = P_{11} - 3P_{01} - 3P_{10} + 9P_{00}.$$

25.7 Realistic potentials

The starting point for a microscopic approach to the nuclear Hamiltonian is based on NN potentials fit to the deuteron binding energy and NN scattering data. The resulting NN potentials are not unique and many versions of been developed, in historical order, Hamanda-Johnston (1962) [1], Reid (1968) [2], Paris (1979) [3], Bonn (1987) [4], [5], Nijmegen (1994) [6], Argonne V18 (AV18) (1995) [7], Argonne V8' (AV8') (1997) [8], CD-Bonn (2001) [9], and N³LO (2002) [10], [11].

The AV18 potential has been used to calculate the energies and wavefunctions for

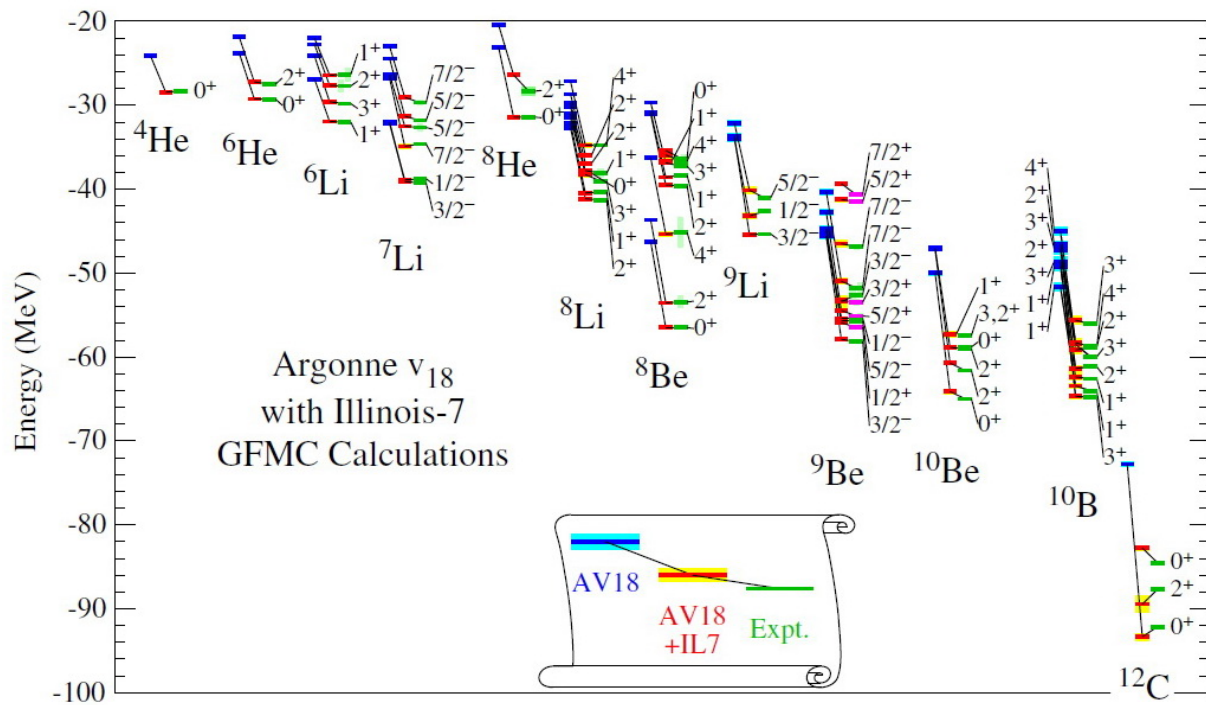


Figure 25.1: GFMC energies of light nuclear ground and excited states for the AV18 and AV18 + IL7 Hamiltonians compared to experiment [12].

light nuclei using the Green's Function Monte Carlo method (GFMC) [12]; the results for energies up to ^{12}C are shown in Fig. (25.1). The energies are systematically under-bound (blue) compared to experiment (green) by about 15 percent. This is improved by the addition of a three-body potential (IL7) as shown in yellow. The computational size of the GFMC calculations increases exponentially with mass, and ^{12}C is the largest mass for which results have been obtained.

For heavier nuclei we must truncate the calculation to a model space that contains a finite number of basis states, up to dimensions of about one billion. These are referred to as configuration-interaction (CI) or shell-model calculations. To apply the NN potentials to these model spaces, they must be renormalized to take into account the implicit effect of the infinite number of configurations that lie outside of the model space. This is not easy, and many approximate methods have been developed. One problem is that all of the NN potentials have a strongly repulsive short range behavior. Examples are shown in Fig. (25.2) for the $S = 0, T = 1$ channel. If we calculate the TBME in the model space with this bare potential they would be strongly positive resulting in nuclei that are unbound. Thus we must allow for a type of renormalization that modifies the relative wavefunction

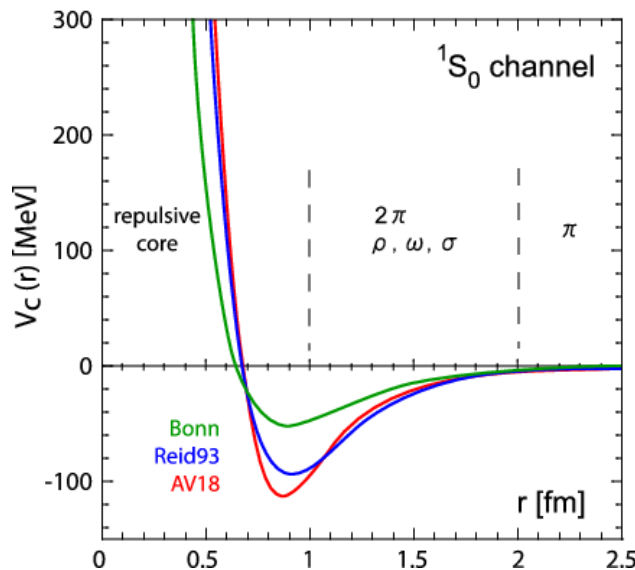


Figure 25.2: Some NN potentials that accurately describe proton-neutron scattering up to 300 MeV [13]. I, II and III correspond to the long, medium and short ranged parts of the Hamiltonian, respectively.

at short distances. An extreme example is that for an infinitely hard-core potential out to some radius r_c followed by an attractive OBEP beyond that. A bound state solution for this problem can be obtained by allowing the relative radial wavefunction to start at r_c . The correlated relative wavefunction must contain components that involve oscillator excitations to high values of $\hbar\omega$ that lie outside of the model space.

The matrix elements calculated with these correlated wavefunctions are sometimes called G matrix elements. The solution of this problem goes back to Brueckner [14] for the effective interaction for pairs of particles embedded in the Fermi sea of the remaining $N - 2$ particles of an N particle system. The Bethe-Goldstone (BG) equation [15] is time independent solutions for this problem. A method for the solution of the BG equations in the harmonic-oscillator basis was developed by Barrett, Hewitt and McCarthy [16]. Their solution depends upon the treatment of the intermediate state spectrum and the starting energy.

More recently others ways of treating the short-range problem have been developed; the V_{low-k} and the similarity renormalization group (SRG) methods [17].

25.8 Density-dependent interactions

Phenomenological density-dependent interactions have long played an important role in Hartree-Fock calculations [18], [19], [20] as well as in shell-model calculations [21], [22], [23]. From a more fundamental point of view, density dependence enters into the calculations of the G-matrix in finite nuclei [24]. There also has been a renewed interest in density dependence because of recent developments with relativistic models [25]. For a density-dependent interaction there is an additional dependence on the center-of-mass coordinate:

$$\vec{R} = (\vec{r}_1 + \vec{r}_2)/2. \quad (25.45)$$

The spatial functions $U^{(q)}$ are extended to include a dependence on R :

$$\tilde{U}^{(q)}(R, \vec{r}) = U^{(q)}(\vec{r}) F_q(R), \quad (25.46)$$

and Eq. (25.31) will become:

$$\langle n\lambda N\Lambda L | \tilde{U}^{(q)} | n'\lambda'N'\Lambda'L' \rangle = (-1)^{\lambda+\Lambda+L+q} \sqrt{(2L+1)(2L'+1)}$$

$$\times \left\{ \begin{array}{ccc} \lambda & \lambda' & q \\ L' & L & \Lambda \end{array} \right\} < n\lambda ||U^{(q)}(\vec{r})||n'\lambda' >< N\Lambda | F_q(R) | N'\Lambda' > \delta_{\Lambda\Lambda'}.$$
 (25.47)

A typical form for the density dependence is:

$$D(R) = 1 + A_d F(R)^{B_d},$$
 (25.48)

where and

$$F(R) = 1 + \exp[(R - R_o)/a]^{-1},$$
 (25.49)

where A_d and B_d are constants to be chosen. Initially we take $R_o = 1.1A^{1/3}$ fm (with $A=16$ for the sd shell) and $a = 0.6$ fm. In the original Skyrme Hartree-Fock calculations [26] and work by Migdal [23], linear density dependence ($B_d = 1$) was assumed. Note that $F(R)$ is the Fermi function that approaches unity as R goes to zero.

It is interesting to compare this density dependence with the commonly used surface-delta interaction (SDI) for the central component [21], [22]. For a zero-range interaction the radial dependence of the two-body matrix element reduces to the integral [21]

$$I = \int D(R)\psi_A(R)\psi_B(R)\psi_C(R)\psi_D(R)R^2dR.$$
 (25.50)

For a surface-delta interaction, one could evaluate this integral with $D(R) = \delta(R - R_o)$ for some value of R_o near the surface. However, in practice one usually replaces the integral by unity times a phase factor that takes into account the fact that the radial wavefunctions $\psi(R)$ conventionally are defined to be positive near the origin):

$$I = (-1)^{n_a + n_b + n_c + n_d}. \quad (25.51)$$

A more realistic form of the density dependence is given by $D(R)$ in Eq. (25.48) with $A_d = -1$ (i.e., an interaction that goes smoothly to zero in the nuclear interior). In Table (25.1) the radial matrix elements for the sd shell calculated with a density-independent zero-range interaction and with various versions of the density-dependent, zero-range interactions are compared. Very large differences among the various models is noted. Also, it is noted that the linear density dependence gives results that are closest to the commonly used constant approximation of Eq. (25.51). Many of the successful phenomenological global interactions, such the D1 interaction of Decharge and Gogny [19], have a density-dependence that makes the interaction smaller in the nuclear interior than on the surface.

25.9 The M3Y potential

Interactions obtained from the G-matrix approach have been parametrized in terms of one-boson-exchange potentials (OBEP) [27], [28], [29]. A widely used example is called the M3Y (Michigan sum of three Yukawas) potential [30] that is based on a particular choice of results given in [27] (those in Table I with the labels, 1, 4, 7, 8, 11, 14, 16 and 18). The functional forms of the M3Y potential for the central (c), spin-orbit (s) and tensor (t) parts are

$$f_{c,S,T}(r) = P_{S,T} \sum_i W_{c,i,S,T} Y(x_i), \quad (25.52)$$

$$f_{s,S,T}(r) = P_{S,T} \sum_i W_{s,i,S,T} Y(x_i), \quad (25.53)$$

and

$$f_{t,S,T}(r) = P_{S,T} \sum_i W_{t,i,S,T} r_i^2 Y(x_i). \quad (25.54)$$

x_i is r divided by the range parameter ρ_i :

$$x_i = r/\rho_i. \quad (25.55)$$

The M3Y uses the central part of the OPEP fixed at the form of Eq (25.39), and then adds potentials with shorter ranges and strengths, W , to fit the G-matrix results.

Contributions to the integral

$$\langle n\lambda | f_c(r) | n\lambda \rangle = \int \psi_{n,\lambda}(r) f_c(r) \psi_{n,\lambda} r^2 dr$$

for the central part of the M3Y interaction are shown in Figs. (25.3) - (25.6). The bottom panels show the contribution $W = \psi_{n,\lambda}^2$ in the integrand from the relative radial wavefunctions y , the middle panels show the radial part of the potential multiplied by r^2 and the top panels show the integral evaluated out to radius r . Note that the orbital angular momentum of the relative wavefunction is restricted by the symmetry condition that $\ell + S + T$ is odd for a two-particle wavefunction. Thus, for a short range potential, the most important contributions are for $\ell=0$ in the $(S, T) = (0,1)$ and $(1,0)$ channels.

The longest ranged part of the M3Y interaction corresponds to the one-pion-exchange (OPEP) potential. The OPEP contribution to the bare G-matrix provides about 1/3 of the attractive interaction needed for the $(S, T) = (0,1)$ and $(1,0)$ channels of the central

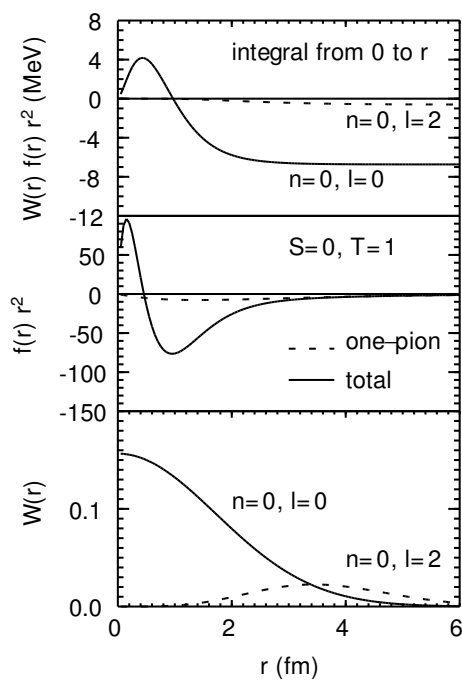


Figure 25.3: The central $S = 0, T = 1$ channel for the the M3Y interaction.

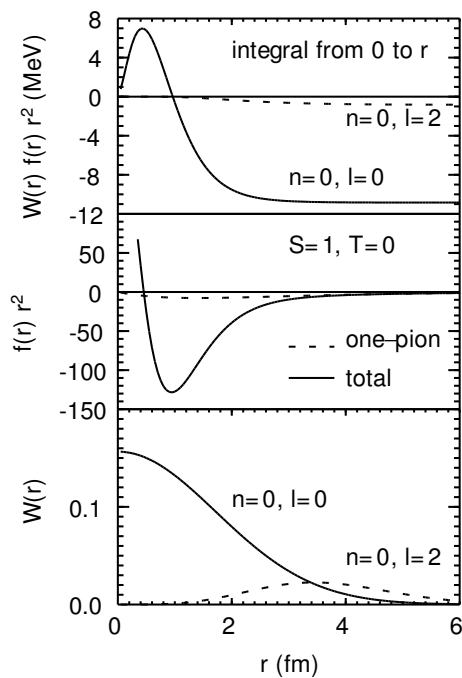


Figure 25.4: The central $S = 1, T = 0$ channel for the the M3Y interaction.

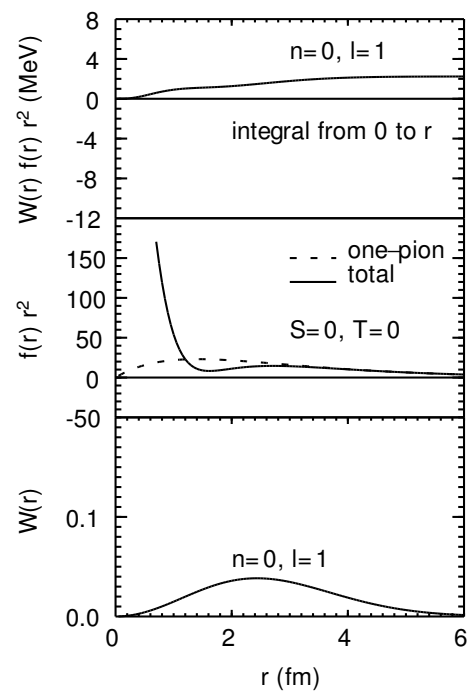


Figure 25.5: The central $S = 0$, $T = 0$ channel for the the M3Y interaction.

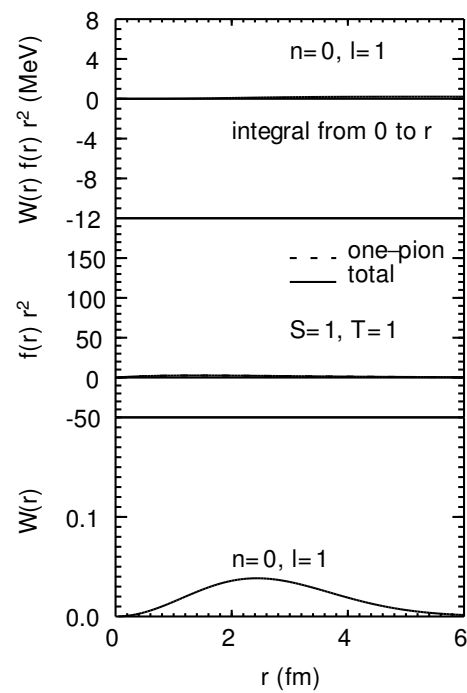


Figure 25.6: The central $S = 1$, $T = 1$ channel for the the M3Y interaction.

component. A common feature of this as well as other OBEP parametrizations is a strong attractive medium-range part that is partly canceled out by a repulsive short-range part.

The OPEP potential has a $q = 2$ tensor term. In the M3Y potential there is also some $q = 2$ tensor from the short-ranged part that is attributed to the ρ meson exchange that cancels part of the OPEP tensor.

25.10 Numerical examples

Table 1 compares some typical values of the two-body matrix elements obtained with the potentials discussed in the proceeding section.

$V_{con} = 1$,

V_{coul} is the Coulomb potential of Eq. (25.36),

V_{del} is the delta-function potential of Eq. (25.38),

V_{OPEP} is the one-pion exchange from Eq. (25.43),

V_G is the M3Y G-matrix potential from Eq. (25.52).

25.11 The N^3LO potential

Starting in 1990, Weinberg introduced a systematic method to derive an effective Lagrangian for the interaction involving nucleons and pions [31]. This involved the separation of the mesons into two groups; the low-mass pion with energy scale q and all of the heavier mesons with an energy scale Λ . The leading-order potential is approximated by the OPEP potential for the pions and a delta-function potential for all of the heavier mesons. The Lagrangian expanded in powers of $(q/\Lambda)^k$ in chiral effective field theory (EFT) is called (Next) k to Leading Order (N^kLO). The Chiral symmetry refers to the symmetry between the right-

Table 25.1: Values of some central potential matrix elements $\langle k_1 k_2 JT | V | k_3 k_4 JT \rangle$ (in MeV) with $\hbar\omega=13.9$ MeV. They are labeled by $k = 4$ for $0d_{5/2}$ and $k = 6$ for $1s_{1/2}$.

k_1	k_2	k_3	k_4	J	T	V_{con}	V_{coul}	V_{del}	V_{OPEP}	V_G
4	4	4	4	0	1	1	0.493	-3.11	-0.87	-2.32
4	4	4	4	2	1	1	0.416	-0.71	-0.24	-0.82
4	4	4	4	4	1	1	0.387	-0.30	-0.06	-0.43
4	4	4	6	2	1	0	0.029	-0.50	-0.18	-0.66
4	4	6	6	0	1	0	0.046	-1.07	-0.29	-0.72
4	6	4	6	2	1	1	0.420	-0.74	-0.42	-1.46
4	6	4	6	3	1	1	0.388	0.00	0.16	0.16
6	6	6	6	0	1	1	0.452	-2.53	-0.95	-2.31
4	4	4	4	1	0	1		-2.95	0.53	-0.85
4	4	4	4	3	0	1		-1.66	-0.04	-1.50
4	4	4	4	5	0	1		-2.59	-0.83	-4.26
4	4	4	6	3	0	0		-1.27	-0.27	-1.58
4	4	6	6	1	0	0		-1.28	-0.20	-0.81
4	6	4	6	2	0	1		-0.86	0.52	-0.55
4	6	4	6	3	0	1		-2.16	-0.80	-3.00
6	6	6	6	1	0	1		-4.43	-0.95	-3.68

and left-handed components of Dirac fermions in the underlying QCD Lagrangian with massless quarks. The total effective Lagrangian for N^k LO are all of the orders summed up to k . These are represented by graphs [32] shown in Fig. (25.7). The dashed lines between two nucleons with small circles represents the OPEP interaction. The various interactions with the heavy mesons (the symbols are explained in [32]) are given in terms of delta-functions with strengths that are fit to NN scattering data. For N^3 LO there are 26 parameters related to the four-nucleon low-energy interactions [11]. Starting at order $k = 3$ there are diagrams involving three nucleons. These involve parameters that cannot be determined from NN scattering data. They are usually fit to properties of the nuclei with $A = 3$ and 4.

25.12 Three-body interactions

As discussed above, the GFMC calculations for light nuclei up to ^{12}C under binding relative to experiment by about 15 percent. A specific three-body NNN interaction called IL7 was added with some parameters that were fitted to energies of these light nuclei. The N^3 LO

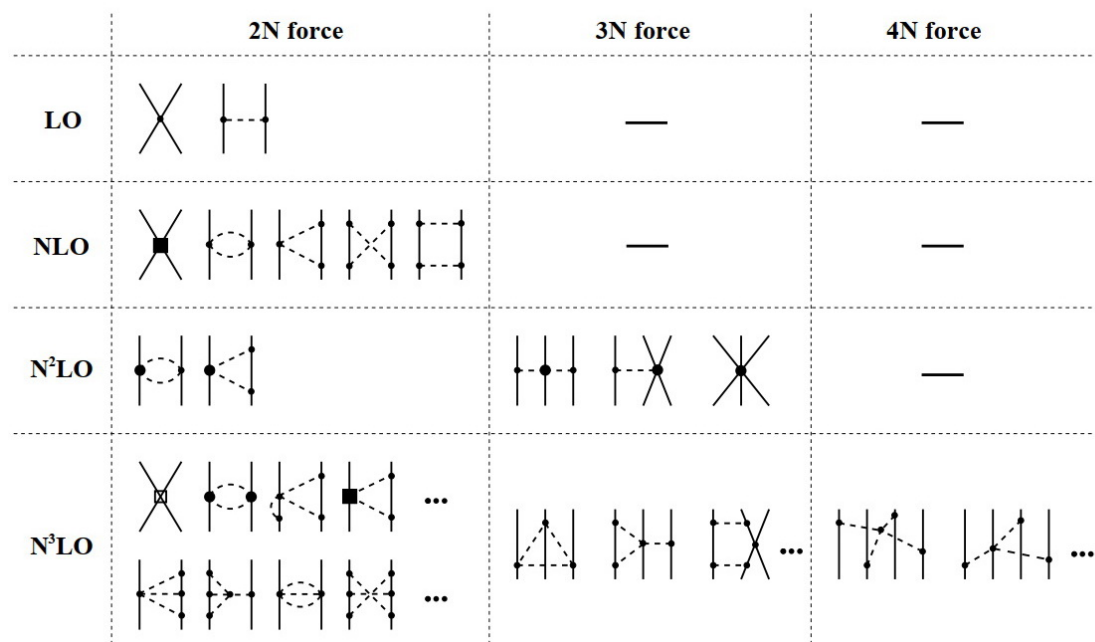


Figure 25.7: Diagrams that give rise to nuclear forces in the $N^k\text{LO}$ expansion.

interaction also requires a the addition of a three-body interaction with parameters that fitted to reproduce the properties of $A = 3$ and $A = 4$. It is difficult to carry out CI calculations with three-body interactions. But a large part of the three-body interaction contributes to the effective single-particle energy and two-body valence interaction as shown in Fig. (25.8). The remaining valence three-body interaction is small; on the order of $1/A$ compared to the three-body contribution to the valence two-body part. But if there are many valence particles in the CI calculations, we should try to include part of the valence-space configurations in the core summation part of the forth term of the bottom row.

It may not be possible to reproduce the properties of heavy nuclei with NN and NNN interactions obtained from $A=2-4$. This may be due to the effect of the many-body approximations used or it may be due to four nucleon (and higher) interactions which at present cannot be included. For example, it is found that the rms radii obtained for the oxygen isotopes is about 10% smaller than experiment for all of the oxygen isotopes [33]. This has lead to the development of a new Hamiltonian called $NNLO_{sat}$ that is simpler than N^3LO , but where the determination of the low-energy coupling constants includes data on the binding energies and charge radii of ^{14}C and $^{16,22,24,25}\text{O}$ as well as the charge radii of ^{14}C and ^{16}O [34],

[35]. The matter radii for the neutron-rich oxygen isotopes with NNLO_{sat} is much improved compared to experiment relative to those based on the N³LO input [33].

25.13 Multipole and spin-tensor decompositions

Sometimes it is useful to decompose the two-body matrix elements (TBME) in terms of an effective multipole operator:

$$\begin{aligned}
 < k_1 k_2 J | V | k_3 k_4 J > &= \sum_L v(k_1, k_2, k_3, k_4, L) < k_1 k_2 J | Q^{(L)} \cdot Q^{(Y)} | k_3 k_4 J > \\
 &= \sum_L v(k_1, k_2, k_3, k_4, L) (-1)^{j_2+j_3+J} (2J+1) \left\{ \begin{array}{ccc} j_1 & j_2 & J \\ j_4 & j_3 & L \end{array} \right\} \\
 &\quad \times < k_1 ||Q^{(L)}||k_3 > < k_2 ||Q^{(L)}||k_4 >, \tag{25.56}
 \end{aligned}$$

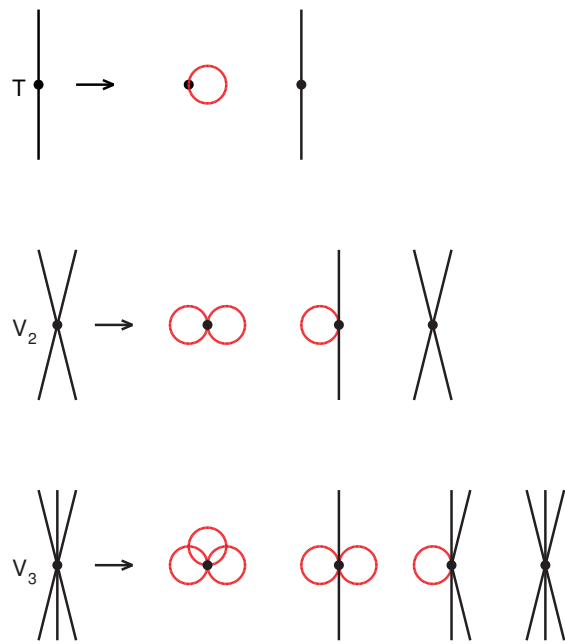


Figure 25.8: Schematic diagram for the kinetic energy, the two-body potential and the three-body potential (first column). The next columns show the results for a closed shell core for the closed-shell energy, the single-particle energy, the valence two-particle interaction and the valence three-body interaction. The red lines represent summations over the filled states.

where $Q^{(L)} = \sqrt{\frac{4\pi}{(2L+1)}} Y^{(L)}$, and $Y^{(L)}$ is the spherical harmonic of tensor rank L . To the extent that $v(k_1, k_2, k_3, k_4, L)$ only depends on L , this decomposition provides a simplified approximation to the TBME.

The interaction energy for a closed shell configuration only depends on the $(2J + 1)$ weighted sums of the diagonal TBME over the filled orbitals

$$\sum_J (2J + 1) \langle k_1 k_2 J | V | k_1 k_2 J \rangle = (2j_1 + 1)(2j_2 + 1) v(k_1, k_2, k_1, k_2, L = 0), \quad (25.57)$$

where we have used

$$\sum_J (-1)^{j_1+j_2+J} (2J + 1) \left\{ \begin{array}{ccc} j_1 & j_2 & J \\ j_2 & j_1 & L \end{array} \right\} = \sqrt{(2j_1 + 1)(2j_2 + 1)} \delta_{L,0}. \quad (25.58)$$

This $(2J + 1)$ weighted sum is called the momopole energy since it only depends on the $L = 0$ term of the multipole decomposition.

From Eq. (25.21) the two-body interaction is a sum over spin-tensor ranks $q = 0, 1, 2$. If one has a complete set of jj coupled TBME, one can decompose them into a sum over

terms with $q = 0, 1, 2$. This is called the spin-tensor decomposition [36], [37], [38]. First one makes an transformation of the TBME from jj to LS coupling

$$\begin{aligned} < k_A k_B J T | V | k_C k_D J T > &= [(1 + \delta_{AB})(1 + d_{CD})]^{-1/2} \sum_{L S L' S'} \left[\begin{array}{ccc} \ell_a & 1/2 & j_a \\ \ell_b & 1/2 & j_b \\ L & S & J \end{array} \right] \left[\begin{array}{ccc} \ell_c & 1/2 & j_c \\ \ell_d & 1/2 & j_d \\ L' & S' & J \end{array} \right] \\ &\times [(1 + \delta_{ab})(1 + d_{cd})]^{1/2} < k_a k_b L S J T | V | k_c k_d L' S' J T >, \end{aligned} \quad (25.59)$$

where k_A is shorthand for the set of quantum numbers $(n_a \ell_a)$ and k_a is shorthand for the set $(n_a \ell_a j_a)$, etc. Then these LS coupled TBME can be decomposed into a sum over q terms

$$\begin{aligned} < k_A k_B J' T | V_q | k_C k_D J' T > &= (-1)^{J'} (2q+1) \left\{ \begin{array}{ccc} L & S & J' \\ S' & L' & p \end{array} \right\} \\ &\sum_J (-1)^J \left\{ \begin{array}{ccc} L & S & J \\ S' & L' & p \end{array} \right\} < k_A k_B J T | V_q | k_C k_D J T >. \end{aligned} \quad (25.60)$$

This type of analysis has been used in [39], [40], [41], [42], [43], [44].

Bibliography

- [1] T. Hamada and I. D. Johnston, Nucl. Phys. **34**, 382 (1962).
- [2] R. Reid, Ann. of Phys. **50**, 411 (1968).
- [3] R. Vinh Mau, Mesons in Nuclei, vol. 1, ed. M. Rho and D. H. Wilkinson (North-Holland, Amsterdam, 1979) p. 151.
- [4] R. Machleidt, K. Holinde, and Ch. Elster, Phys. Rep. **149**, 1 (1987).

- [5] R. Machleidt, Adv. Nucl. Phys. **19**, 189 (1989).
- [6] V. G. J. Stoks, R. A. M. Klomp, C. P. F. Terheggen, and J. J. de Swart, Phys. Rev. C **49**, 2950 [1994].
- [7] R. B. Wiringa, V. G. J. Stoks, and R. Schiavilla, Phys. Rev. C **51**, 3851 (1995). link
- [8] B. S. Pudliner, V. R. Pandharipande, J. Carlson, S. C. Pieper and R. B. Wiringa, Phys. Rev. C **56**, 1720 (1997). link
- [9] R. Machiedt, Phys. Rev. C **63** 024001 (2001). link
- [10] D. R. Entem, R. Machleidt, Phys. Lett. B **524**, 93 (2002); Phys. Rev. C **68**, 041001(R) (2003). link
- [11] E. Epelbaum, W. Gleockle, and U.-G. Meissner, Nucl. Phys. A **747**, 362 (2005).
- [12] J. Carlson, S. Gandolfi, F. Pederiva, S. C. Pieper, R. Schiavilla, K. E. Schmidt and R. B. Wiringa, Rev. Mod. Phys. **87**, 1067 (2015).

- [13] S. Aoki, T. Hatsuda and N. Ishi, Computational Science and Discovery, **1**, 015009 (2008)
- [14] K. A. Brueckner, Phys. Rev. **96**, 508 (1954); **97**, 1353 (1955).
- [15] H. A. Bethe and J. Goldstone, Prof. Roy. Soc. (London) **A238**, 551 (1957).
- [16] B., R. Barrett, R. G. L. Hewitt and R. J. McCarthy, Phys. Rev. C **3**, 1137 (1971); B. R. Barrett and R. J. McCarthy, Z. Physik A **279**, 297 (1976).
- [17] H. Hergert, S. K. Bognera, T. D. Morrisb, A. Schwenk, and K. Tsukiyama, Physics Reports **621**, 165 (2016).
- [18] Nguyen van Giai and H. Sagawa, Phys. Lett. **106B**, 379 (1981).
- [19] J. Decharge and D. Gogny, Phys. Rev. C**21**, 1568 (1980). link
- [20] J. Friedrich and P. G. Reinhard, Phys. Rev. C**33**, 335 (1986). link
- [21] P. J. Brussaard and P. W. M. Glaudemans, *Shell Model Applications in Nuclear Spectroscopy* (North-Holland, 1977).

- [22] P. W. M. Glaudemans, P. J. Brussaard and B. H. Wildenthal, Nucl. Phys. A102, 593 (1967).
- [23] A. B. Migdal, *Nuclear Theory; The Quasiparticle Method* (Benjamin, New York, 1968); *Theory of Finite Fermi Systems and Applications to Atomic Nuclei* (Wiley, New York, 1967).
- [24] J. W. Negele, Phys. Rev. C1, 1260 (1970). link
- [25] M. R. Anastasio, L. S. Celenza, W. S. Pong and C. M. Shakin, Physics Reports 100, 328 (1983); L. S. Celenza, W. S. Pong and C. M. Shakin, Phys. Rev. Lett. 47, 3 (1981).
- [26] D. Vautherin and D. M. Brink, Phys. Rev. C5, 626 (1972). link
- [27] G. F. Bertsch, J. Borysowicz, H. McManus, and W. G. Love, Nucl. Phys. A284, 399 (1977).
- [28] N. Anantaraman, H. Toki, G. F. Bertsch, Nucl. Phys. A398, 269 (1983).

- [29] A. Hosaka, K. I. Kubo, H. Toki, Nucl. Phys. A444, 76 (1985). Note the following corrections: in Eq. (2) the $\vec{\sigma}$ in Eq. (2) should be replaced by \vec{s} , in Eq. (3) the $Y_{LS}(x)$ term should have the factor e^{-x}/x^2 rather than e^{-x}/x , and in Table 3 the range should be 0.40 rather than 0.50.
- [30] W. G. Love, The (p,n) reaction and the nucleon-nucleon force, ed. C. D. Goodman et al., (Plenum, New York, 1980) p. 23.
- [31] S. Weinberg, Phys. Lett. B **251**, 288 (1990); Nucl. Phys. B **363**, 3 (1991); Phys. Lett. B **295**, 114 (1992).
- [32] <https://arxiv.org/abs/1001.3229>
- [33] V. Lapoux, V. Soma, C. Barbieri, H. Hergert, J. D. Holt and S. R. Stroberg, Phys. Rev. Lett. **117**, 052501 (2016). link
- [34] A. Ekstrom, G. R. Jansen, K. A. Wendt, G. Hagen, T. Papenbrock, B. D. Carlsson, C. Forssen, M. Hjorth-Jensen, P. Navratil and W. Nazarewicz, Phys. Rev. C **91**, 051301 (2015). link

- [35] B. D. Carlsson, A. Ekstrom, C. Forssen, D. F. Stromberg, G. R. Jansen, O. Lilja, M. Lindby, B. A. Mattsson and K. A. Wendt, Phys. Rev. X **6**, 011019 (2016).
- [36] J. P. Elliott, A. D. Jackson, H. A. Mavromantis, E. A. Sanderson and B. Singh, Nucl. Phys. A121, 241 (1968).
- [37] M. W. Kirson, Phys. Lett. **47B**, 110 (1973).
- [38] K. Klingenbeck, W. Knupfer, M. G. Huber, and P. W. M. Glaudemans, Phys. Rev. C **15**, 1483 (1977). link
- [39] K. Yoro, Nucl. Phys. A333 ,67 (1980).
- [40] B. A. Brown, W. A. Richter and B. H. Wildenthal, Jour. Phys. G **11**, 1191 (1985).
- [41] B. A. Brown, W. A. Richter, R. E. Julies and B. H. Wildenthal, Ann. Phys. **182**, 191 (1988).
- [42] E. Osnes and D. Strottman, Phys. Rev. **45**, 662 (1992). link

- [43] M. Honma, T. Otsuka, B. A. Brown, and T. Mizusaki, Phys. Rev. C **69**, 034335 (2004).
[link](#)
- [44] N. A. Smirnova, B. R. Barrett, Y. Kim, I. J. Shin, A. M. Shirkov, E. Dikmen, P. Maris and J. P. Vary, Phys. Rev. C **100**, 054329 (2019). [link](#)

Chapter 26

Model spaces

632

26.1 Commonly used model spaces for light and heavy nuclei

Shell-model configuration mixing is carried out within a model space. The model space is a truncation of the infinite set of orbitals into a finite set. All operators in this model space must be renormalized to account for the orbitals left out.

For light nuclei up to about $A = 12$ we can consider a no-core basis where we start with the $0s_{1/2}$ orbital ($N = 0$) and go up to some maximum value N_{max} in the oscillator basis [1], [2]. Typically up to about $N_{max}=8$, but can go higher for few nucleon systems or lower above $A = 12$. The Hamiltonian in the no-core space is obtained from V_{lowk} [3] or similarity renormalization group (SRG) [4] methods. Some calculations also include a three-body interaction.

For heavier nuclei calculations can only be carried out exactly in a much smaller model space based upon a closed-shell, some valence orbitals in the model space, and followed by an

infinite set of empty orbitals. All operators in this model space must be corrected to account for this truncation. This is usually done in two steps, first a G matrix type interaction is obtained that takes into account the short-ranged repulsion, and then this is normalized with perturbation theory to account for the mixing of configurations beyond the model space. The choice of model space is determined by the computational limitations together with guidance from experiment as to which orbitals contribute to the observables for a given mass region. The model space is also guided by the observed shell gaps as indicated for example by the energies of the 2^+ states in even-even nuclei shown in Fig. (26.1). Some model spaces for $A = 4 - 100$ are shown in Fig. (26.2) and model spaces for A up to 300 are shown in Fig. (26.3).

In the NuShellX Hamiltonian library [15], the names of some model spaces for heavy nuclei are labeled by the number of orbitals that are between the standard magic numbers;

$$K = 4 \ (0f_{5/2}, 1p_{3/2}, 1p_{1/2}, 0g_{9/2}) \text{ for } 28 - 50;$$

$$K = 5 \ (0g_{5/2}, 1d_{5/2}, 1d_{3/2}, 2s_{1/2}, 0h_{11/2}) \text{ for } 50 - 82;$$

$$K = 6 \ (0h_{9/2}, 1f_{5/2}, 1f_{5/2}, 2p_{3/2}, 2p_{1/2}, 0i_{13/2}) \text{ for } 82 - 126;$$

etc. The model space names in proton-neutron formalism where isospin is not necessarily conserved are labeled jjK_pK_n . For example, the model space called $jj45$ is for protons in the group of four above and neutrons in the group of five above. When $K_p = K_n$, Hamiltonians in isospin or proton-neutron formalism can be used.

26.2 Intruder states and islands of inversion

A shell-model calculation with some choice of model space can be considered successful if it can describe some subset of the observed low-lying energy levels for the nuclei covered by the model space, with Hamiltonians and operators that are close to those expected from the renormalized properties of free nucleons. Intruder states are those whose configurations are dominated by nucleons excited across the shell gap into or out of the model space. If the single-particle energy gap is E_{gap} , then the single-particle energy contribution to the excitation energy of a configuration with n particles excited across the gap is just $n E_{gap}$. However, there is also a correlation energy contribution that lowers the energy of the intruder states

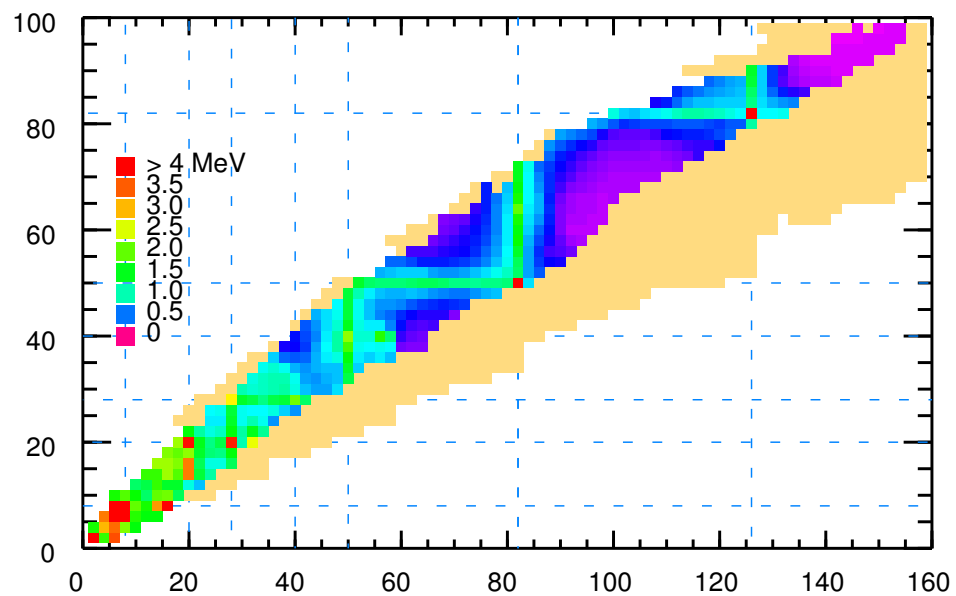


Figure 26.1: Energies of the first 2^+ states in even-even nuclei. The nuclei shaded in light-brown are those predicted to exist out to the drip lines but not yet observed.

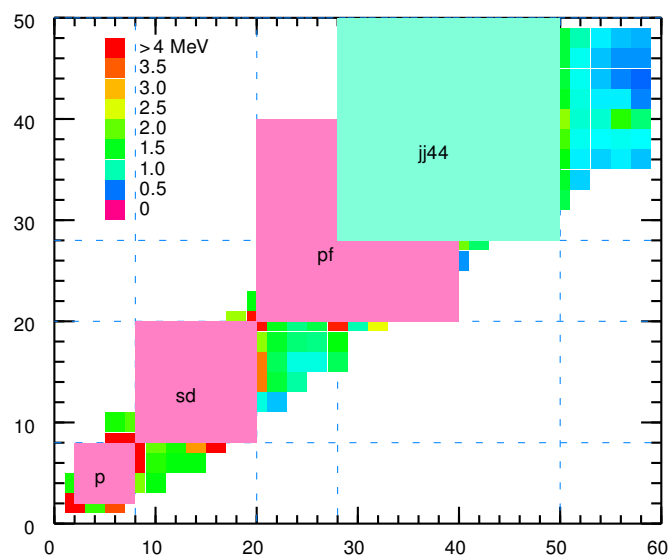


Figure 26.2: Model spaces for light nuclei.

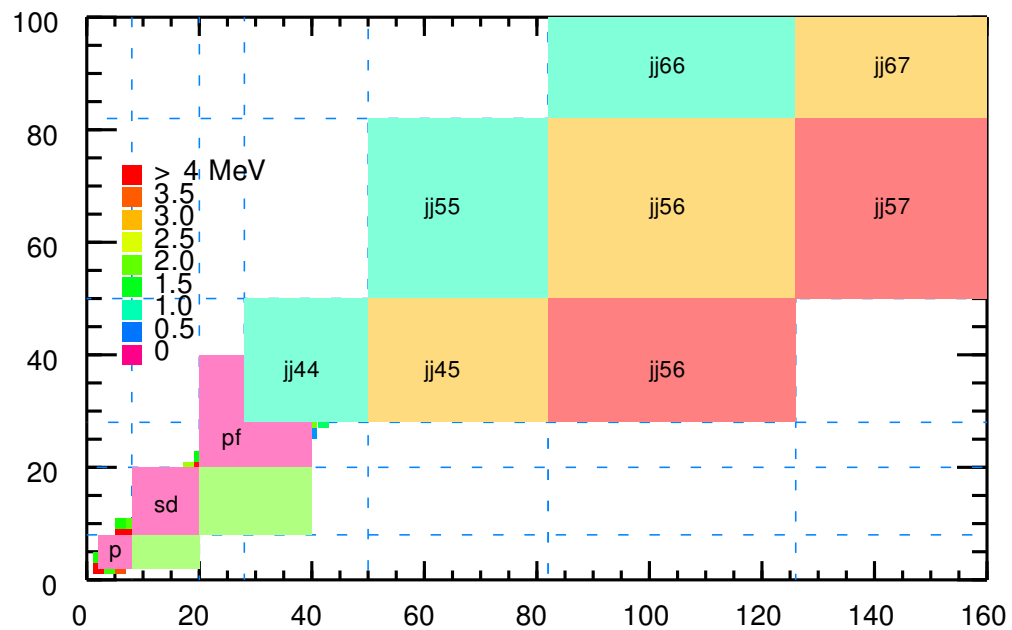


Figure 26.3: Model spaces for heavy nuclei.

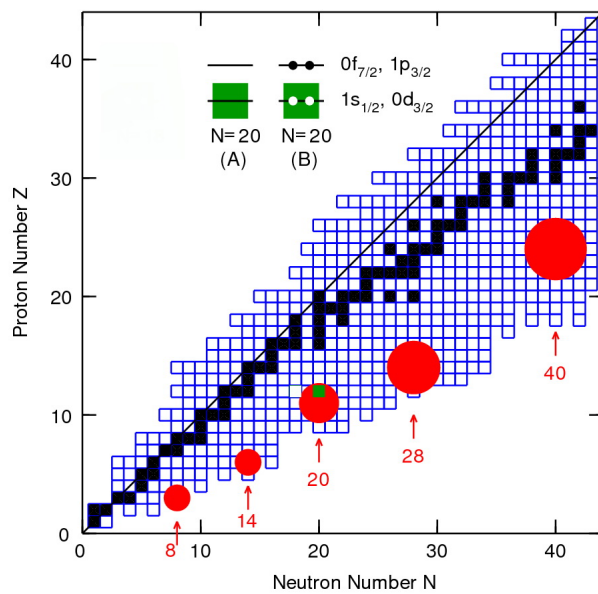


Figure 26.4: Islands of inversion.

relative to nE_{gap} . For example, the $N = 8$ gap energy near ^{16}O is about 11.5 MeV. But the experimental excitation energy of the intruder $1/2^+$ state in ^{19}F that involves one nucleon excited across the $N = 8$ gap is only 100 keV. In the sd model space the $1/2^+$ ground state of ^{19}F has the configuration $(sd)^3$, while the $1/2^-$ intruder state has the configuration $(p)^{-1}(sd)^4$. The extra correlation energy associated with the $(sd)^4$ “alpha-particle-like” configuration lowers the energy of the $1/2^-$ state relative to E_{gap} . Another example in ^{11}Be where the $1/2^+$ intruder state (with one neutron in the sd shell) comes 320 keV below the p shell $1/2^-$ state.

Two-particle two-hole ($2p - 2h$) intruder states have the same parity as those in the model space and can mix with them. For example, the structure of low-lying states in ^{18}O involves a complex mixture of $(sd)^2$ and $(p)^{-2}(sd)^4$ configurations [5]. Part of the correlation energy associated with $2p - 2h$ intruder states is the gain in pairing energy in the $2p$ and $2h$ configurations. These $2p - 2h$ intruder states are seen in all nuclei near the closed shells.

In light nuclei the intruder states are associated with excitations across the LS shell gaps. For heavier nuclei, the intruder states are associated with excitations across the JJ

shell gaps. In heavy nuclei the intruder states can also come very low in excitation energy, as in the case of nuclei around ^{186}Pb [6] related to the $Z = 82$ shell gap.

The history of the shell model has been to consider progressively larger and larger model spaces, so that states that would be called intruders in a small model space become fully incorporated into a larger model space. For example, early shell-model work on the region of ^{56}Ni used a truncated pf model space with only a limited number of excitations from the $0f_{7/2}$ orbital to the $(0f_{5/2}, 1p_{3/2}, 1p_{1/2})$ orbitals. Modern calculations in this region can take into account the full pf model space that has J -scheme basis dimensions of up to 10^8 .

A decrease in the shell gap can lead to situations where whole regions of nuclei have intruder states that come lower in energy than the normal state. The phrase “island of inversion” was used in [7] to describe a region of nuclei centered around ^{31}Na where the configuration of the ground states consists of intruder $np - nh$ excitations across the $N = 20$ shell gap. This region is illustrated in Fig. 7 by the red circle just above the arrow for $N = 20$. As an example, the normal (A) and $2p - 2h$ (B) neutron configurations for ^{32}Mg

are shown in upper part of Fig. 7. The energy of the $2p - 2h$ state is lowered by the additional pairing correlation and by a change in the proton-neutron interaction that gives a larger quadrupole deformation energy [7].

The island-of-inversion near ^{31}Na is part of an archipelago of islands related to the breaking of LS magic numbers, starting with an islet near ^{11}Li ($N=8$) and extending to a larger island centered around ^{64}Cr ($N=40$); the red circles in the Fig. 7. It has been predicted that there is an island-of-inversion related to excitations of neutrons across (JJ) $N = 50$ gap in the region of ^{76}Fe [8].

The main reason why these islands-of-inversion are found in neutron-rich nuclei is that E_{gap} tends to decrease as one approaches the neutron drip line. This is a generic feature of loosely bound levels in a finite potential well. More specifically, the single-particle energies with low ℓ values decrease in energy relative to those with higher ℓ values [9]. For example, in the region of $N = 8$, the $1s_{1/2}$ orbital from the sd shell is lowered in energy relative to $0p_{1/2}$ orbital as one goes from ^{16}O to ^{10}He with an associated decrease in the $N = 8$ shell gap [10]. In the region of ^{32}Mg , the lowering of the $1p_{3/2}$ energy relative to that of $0d_{3/2}$ is important

[11]. The proton-neutron tensor interaction [12], [13] also plays a role in reducing the shell gap in neutron-rich nuclei [11]. For example, for $N = 20$, as $0d_{5/2}$ protons are removed starting at $Z = 14$ the single-particle energy of the $0d_{3/2}$ orbital moves up the energy of the $0f_{7/2}$ orbital moves down, reducing the $N = 20$ energy gap [11] near $Z = 8$.

Bibliography

- [1] P. Navratil, J. P. Vary and B. R. Barrett, Phys. Rev. Lett. **84**, 5728 (2000), and references therin.
- [2] W. C. Haxton and C. L. Song, Phys. Rev. Lett. **84**, 5484 (2000). link
- [3] S. K. Bogner, T. T. S. Kuo and A. Schwenk, Phys. Rept. **386**, 1 (2003).
- [4] S. K. Bogner, R. J. Furnstahl and A. Schwenk, Prog. Part. Nucl. Phys. **65**, 94 (2010).

- [5] R. L. Lawson, F. J. D. Serduke and H. T. Fortune, Phys. Rev. C **14**, 1245 (1976). link
- [6] C. De Coster, B. Decroix and K. Heyde, Phys. Rev. C **61**, 067306 (2000). link
- [7] E. K. Warburton, J. A. Becker and B. A. Brown, Phys. Rev. C41, 1147 (1990). link
- [8] F. Nowacki, A. Poves, E. Caurier, and B. Bounthong, Phys. Rev. Lett. **117**, 272501 (2016). link
- [9] I. Hamamoto, Phys. Rev. C 76, 054319 (2007). link
- [10] H. Sagawa, B. A. Brown and H. Esbensen, Phys. Lett. **B309** 1, (1993).
- [11] A. Lepailleur, et al., Phys. Rev. C **92**, 054309 (2015). link
- [12] T. Otsuka et al., Phys. Rev. Lett. **95**, 232502 (2005). link
- [13] T. Otsuka et al., Phys. Rev. Lett. **104**, 012501 (2010). link

Chapter 27

Particle-hole States

646

27.1 Wavefunctions and energies

Excited states of a closed-shell configuration consist of n holes (h) coupled to n particles (p), e.g. $1p - 1h$, $2p - 2h$, $3p - 3h$, etc. All of these states for a given total J value will mix. A one-body operator only connects the $1p - 1h$ components to the ground state. So if we make an excitation from the $J^\pi = 0^+$ ground state, for example by Coulomb excitation, we will reach only the $1p - 1h$ components of these configurations. The wavefunctions for these $1p - 1h$ states will be written as $| k_a, k_b^{-1} \rangle$ or $| ph \rangle$, where p labels the unoccupied orbitals and h labels the occupied orbitals. For closed-shell nuclei with $N = Z$ the ground state isospin is $T_g = 0$ and the $1p - 1h$ states can have $T = 0, 1$. To make states with good isospin we must couple the proton (π) and neutron (ν) excitations with an isospin clebsch to have the form

$$| ph, T = 0, T_z = 0 \rangle = \frac{1}{\sqrt{2}}(| \pi_a, \pi_b^{-1} \rangle + | \nu_a, \nu_b^{-1} \rangle), \quad (27.1)$$

and

$$| ph, T = 1, T_z = 0 \rangle = \frac{1}{\sqrt{2}}(| \pi_a, \pi_b^{-1} \rangle - | \nu_a, \nu_b^{-1} \rangle). \quad (27.2)$$

The $T = 1$ states are a member of an isobaric triplet with

$$| ph, T = 1, T_z = 1 \rangle = | \nu_a, \pi_b^{-1} \rangle, \quad (27.3)$$

and

$$| ph, T = 1, T_z = -1 \rangle = | \pi_a, \nu_b^{-1} \rangle, \quad (27.4)$$

For closed-shells that have ground states $N \neq Z$ and isospin $T_g = | T_{gz} | > 0$, the particle-hole excited states $| \pi_a, \pi_b^{-1} \rangle$ and $| \nu_a, \nu_b^{-1} \rangle$ do not have to be mixed. But the residual ph interaction sometimes results in rather pure isoscalar combinations with $\Delta T = 0$ of the form

$$| ph, \Delta T = 0 \rangle = \frac{1}{\sqrt{2}}(| \pi_a, \pi_b^{-1} \rangle + | \nu_c, \nu_d^{-1} \rangle), \quad (27.5)$$

and pure isovector combinations with $\Delta T = 1$ of the form

$$| ph, \Delta T = 1 \rangle = \frac{1}{\sqrt{2}}(| \pi_a, \pi_b^{-1} \rangle - | \nu_c, \nu_d^{-1} \rangle). \quad (27.6)$$

The final state isospin for $\Delta T = 0$ is $T_f = T_i$, and the final state isospin for $\Delta T = 1$ is $T_f = T_i$ or $T_f = T_i + 1$.

The wavefunctions for $1p - 1h$ states will be a linear combinations of the various orbital combinations

$$|\psi_f\rangle = \sum_{p,h} \alpha_{f,ph} |ph\rangle. \quad (27.7)$$

The wavefunctions are obtained by diagonalizing the ph Hamiltonian matrix

$$\langle Ck_b k_a^{-1} J | H | Ck_d k_c^{-1} J \rangle = [E_C + e(k_b) - e(k_a)] \delta_{k_b, k_d} \delta_{k_a, k_c} + \langle V \rangle_{ph}, \quad (27.8)$$

where E_C is the energy of the closed shell, e are single-particle energies and $\langle V \rangle_{ph}$ is the residual ph interaction. The J coupled form of the residual interaction is

$$\langle V \rangle_{ph} = - \sum_{J'} (2J' + 1) \left\{ \begin{array}{ccc} j_b & j_c & J' \\ j_d & j_a & J \end{array} \right\} \langle (k_b k_c) J' | V | (k_d k_a) J' \rangle. \quad (27.9)$$

The minus sign accounts for the over counting of two-body interactions in the first three terms of Eq. (27.8). This result was first derived by Pandya [1] using coefficients of fractional parentage. It is derived by de-Shalit and Talmi [2] by making a multipole decomposition of the two-body interaction.

Extension to isospin formalism for the Eq. (27.8) gives

$$\begin{aligned} < Ck_b k_a^{-1} JT | H | Ck_d k_c^{-1} JT > &= [E_C + e(k_b) - e(k_a)] \delta_{k_b, k_d} \delta_{k_a, k_c} \\ &- \sum_{J' T'} (2J' + 1)(2T' + 1) \left\{ \begin{array}{ccc} j_b & j_c & J' \\ j_d & j_a & J \end{array} \right\} \left\{ \begin{array}{ccc} 1/2 & 1/2 & T' \\ 1/2 & 1/2 & T \end{array} \right\} \\ &\times < (k_b k_c) J' T' | V | (k_d k_a) J' T' >. \end{aligned} \quad (27.10)$$

Explicit evaluation of the isospin part for the last term gives:

$$< V >_{ph} (T = 0) = - \sum_{J'} (2J' + 1) \left\{ \begin{array}{ccc} j_b & j_c & J' \\ j_d & j_a & J \end{array} \right\} \left[\frac{3}{2} V_{J',1} - \frac{1}{2} V_{J',0} \right], \quad (27.11)$$

and

$$< V >_{ph} (T = 1) = - \sum_{J'} (2J' + 1) \left\{ \begin{array}{ccc} j_b & j_c & J' \\ j_d & j_a & J \end{array} \right\} \left[\frac{1}{2} V_{J',1} + \frac{1}{2} V_{J',0} \right], \quad (27.12)$$

where

$$V_{J',0} = < (k_b k_c) J' T' = 0 | V | (k_d k_a) J' T' = 0 >, \quad (27.13)$$

and

$$V_{J',1} = \langle (k_b k_c) J' T' = 1 | V | (k_d k_a) J' T' = 1 \rangle . \quad (27.14)$$

Given that the particle-particle matrix elements are typically attractive (negative) for both $T' = 0$ and $T' = 1$ this shows that the residual particle-hole matrix elements for $T = 1$ are repulsive (positive), but for $T = 0$ can be attractive if the particle-particle $T' = 0$ matrix element is strong enough relative to $T' = 1$.

27.2 One-body matrix elements

The reduced matrix elements for one-body operators

$$\hat{F}^\lambda = \sum_{\alpha\beta} \langle \alpha | F^\lambda | \beta \rangle a_\alpha^+ a_\beta \quad (27.15)$$

from the ground state $|>$ to the $1p - 1h$ states are given by

$$\langle \hat{F}^\lambda | ph \rangle = \langle h | F^\lambda | p \rangle . \quad (27.16)$$

The strength to a specific mixed final state ψ_f is

$$\langle \hat{F}^\lambda | \psi_f \rangle = \sum_{ph} \alpha_{f,ph} \langle p | F^\lambda | h \rangle , \quad (27.17)$$

and the total strength summed over all final states is

$$S_c = \sum_f |\langle \hat{F}^\lambda | \psi_f \rangle|^2 = \sum_{ph} |\langle \hat{F}^\lambda | ph \rangle|^2 = \sum_{ph} |\langle p | F^\lambda | h \rangle|^2 . \quad (27.18)$$

Since $J_g = 0$, we have must have $J_f = \lambda$.

In general the total strength S_c for a given operator is spread over all of the ψ_f states. But the residual interaction between the $1p - 1h$ states often results in mixing such that one particular ψ_f state contains a large fraction of the total strength given by Eq. (27.18). In

the most extreme case all of the strength is contained in one state called the coherent state ψ_c . The wave function for this state is

$$|\psi_c\rangle = \sum_{p,h} \alpha_{c,ph} |ph\rangle, \quad (27.19)$$

where

$$\alpha_{c,ph} = \langle p | F^\lambda | h \rangle / \sqrt{S_c}. \quad (27.20)$$

States which exhaust a large fraction of S_c are called collective particle-hole excitations or giant resonances with quantum numbers associated with the ($J = \lambda, T$) value of the ph states excited by the O^λ operator.

The ph approximation discussed above is sometimes called the Tamm-Danoff approximation (TDA) [3]. The next step would be include $2p - 2h$ admixtures in the ground state. This can be important because the $2p - 2h$ part can directly connect to $1p - 1h$ excited states. A approximation for including $2p - 2h$ is called the random-phase approximation (RPA) [4]. Away from closed shell the RPA can be extended to include the quasiparticle occupations generate from the pairing interaction, the QRPA approximation [5].

For a given λ , the one body operator summed over protons and neutrons can be rewritten in terms of a sum over nucleons with isoscalar ($\tau=0$) and isovector ($\tau=1$) operators by using

$$\begin{aligned} O &= \sum_{kq} F_{kq} = O_p + O_n = \sum_{kp} F_{kp} + \sum_{kn} F_{kn} \\ &= \sum_k F_{kp} \frac{1 - \tau_{kz}}{2} + \sum_k F_{kn} \frac{1 + \tau_{kz}}{2} = O^{\tau=0} + O^{\tau=1}, \end{aligned} \quad (27.21)$$

where

$$O^{\tau=0} = \sum_k \frac{F_{kp} + F_{kn}}{2}, \quad (27.22)$$

and

$$O^{\tau=1} = \sum_k \frac{F_{kp} - F_{kn}}{2} \tau_{kz}. \quad (27.23)$$

The operators written in this form are called isoscalar and isovector operators, respectively. The matrix elements of O^τ have the isospin selection rule $\Delta(T_i, \tau, T_f)$. For nuclei with $N = Z$, $T_i = T_g = 0$ and $T_f = \tau$. For $N \neq Z$, the ground state isospin is $T_i = |T_z|$. The

isoscalar operator can only go to final states with $T_f = T_i$, and the isovector operator can go to final states with $T_f = T_i$ and $T_i + 1$. For $N \gg Z$ most of the isovector strength goes to states with $T_f = T_i$.

The giant resonances are classified into their operator type λ and τ . For example, $\lambda=1$ with $\tau=1$ is the isovector giant dipole, and $\lambda=2$ with $\tau=0$ is the isoscalar giant quadrupole. The excitation energy of the giant resonances is determined by the energy difference between the $1p - 1h$ states. In the oscillator model the possible ph states are restricted by the $|N - N'| \leq \lambda$ selection rule for the radial matrix elements $\langle N | r^\lambda | N' \rangle$. For example, dipole excitations go to $J_f^\pi = 1^-$ states at an energy of $1\hbar\omega$. The quadrupole excitations go to $J_f^\pi = 2^+$ states at an energy of $2\hbar\omega$. The octupole excitation go to $J_f^\pi = 3^-$ states at energies of $1\hbar\omega$ and $3\hbar\omega$. In the oscillator model the highest energy for a $E\lambda$ excitation is $\lambda\hbar\omega$. An example for the E2 ph excitations in ^{40}Ca is shown in Fig. (27.1).

Monopole excited states have $J_f^\pi = 0^+$. The electromagnetic matrix element is zero. In electron scattering there is a momentum transfer q resulting in a one-body operator of the form $j_o(qr)$ where j_o is the spherical Bessel function. In the expansion $1 + (qr)^2/6$ the second

term connects to the monopole states at energy $2\hbar\omega$. The giant monopole resonances have been studied with the scattering of electrons and other hadronic probes such as protons and alphas.

The nuclear interaction between ph states is usually attractive for isoscalar and repulsive for isovector states. So the energy of the isoscalar resonances is lower than $\lambda\hbar\omega$, and the energy of isovector resonances is higher than $\lambda\hbar\omega$.

The excitation of collective ph states can also be classified by the change of the total spin from the ground state to the excited state, $\Delta S = 0$ or 1 . All of these modes can be viewed as collective motion of the radial ($\Delta L = \lambda$), proton-neutron ($\Delta T=\tau$) and isospin degrees of freedom (ΔS) as shown in Fig. (27.2).

With more realistic Woods-Saxon type single-particle basis, the strength distributions will be more spread out compared to the oscillator. The $1p - 1h$ states mix with $2p - 2h$ and $3p - 3h$ resulting in $1p - 1h$ strength that is spread over the large number of these states. This is called the spreading width. Also these highly excited states can usually decay by gammas, protons and neutrons giving rise to a decay width.

27.3 The giant dipole excitation

For Coulomb excitation the lowest allowed multipole of $\lambda = 1$ is associated with the giant dipole state.

The operator for electric dipole transitions is given by

$$O(E1) = \sum_{qk} r_{qk} Y_\mu^1(\hat{r}_{qk}) e_{qk} e = \sum_{qk} \sqrt{\frac{3}{4\pi}} \vec{r}_{qk} e_{qk} e, \quad (27.24)$$

where $e_p = 1$ for protons and $e_n = 0$ for neutrons. To make the center-of-mass correction we replace \vec{r}_{qk} by $\vec{r}_{qk} - \vec{R}$ where

$$\vec{R} = \frac{1}{A} \sum_{qk} \vec{r}_{qk}. \quad (27.25)$$

With this replacement we have

$$\sum_{qk} e_{qk} (\vec{r}_{qk} - \vec{R}) = \sum_{qk} e_{qk} \vec{r}_{qk} - Z \vec{R} = \sum_{qk} [e_{qk} - \frac{Z}{A}] \vec{r}_{qk} = \sum_{qk} \tilde{e}_{qk} \vec{r}_{qk}, \quad (27.26)$$

where \tilde{e} are effective charges for the proton and neutron are

$$\begin{aligned}\tilde{e}_p &= 1 - \frac{Z}{A} = \frac{N}{A} \\ \tilde{e}_n &= 0 - \frac{Z}{A} = -\frac{Z}{A}.\end{aligned}\tag{27.27}$$

In terms of the isospin operators we have

$$\begin{aligned}O^{\tau=0} + O^{\tau=1} &= \sum_{qk} \tilde{e}_{qk} \vec{r}_{qk} = \sum_k \frac{\tilde{e}_p + \tilde{e}_n}{2} \vec{r}_k + \sum_k \frac{\tilde{e}_p - \tilde{e}_n}{2} \tau_z \vec{r}_k \\ &= \sum_k \frac{N - Z}{2A} \vec{r}_k + \sum_k \frac{N + Z}{2A} \tau_{kz} \vec{r}_k.\end{aligned}\tag{27.28}$$

For $N = Z$ the isoscalar ($\tau=0$) matrix elements to final states with $T_f = 0$ vanish. These are called isospin forbidden $E1$ transitions. The giant dipole states in nuclei with $N = Z$ only go to final states with $T = 1$. Isospin mixing results in some small $E1$ strength to states that are predominantly $T = 0$.

For the $M1$ operator there is no dependence on \vec{r} and the center-of-mass is correction zero. For the $E\lambda$ operators with $\lambda > 1$ the center-of-mass correction in the harmonic-oscillator model is zero if the center of mass remains in the $0s$ state, for example by using the Lawson method of adding the center-of-mass Hamiltonian.

The giant dipole resonance was widely studied in the 1960s and 70s [6]. The peak of the resonance energy as shown in Fig. 45 of [6], drops rather linearly from about 18 MeV for $A = 50$ to 13 MeV for $A = 250$. In the oscillator model the unperturbed energy would be $1\hbar\omega$, and with $\hbar\omega = 45 A^{-1/3} - 25 A^{-2/3}$ we obtain 10.4 and 6.4 MeV, respectively. Thus the residual ph interaction pushes the GDR energy up to about $2\hbar\omega$. The ratio of the experimental energy-weighted cross sections for photo absorption (up to some maximum energy) to the Thomas-Reiche-Kuhn sum rule is close to one for heavy nuclei, see Table III of [6].

27.4 Energy Weighted Sum Rules

For eclectic $E\lambda$ transition operators, the summed strength to final states multiplied by the transition energy is often quoted in terms of the TRK sum rule after Thomas, Reiche and Kuhn who derived this result for atomic physics [7], [8], [9].

We consider the energy weighted sum over all final states

$$S = \sum_f (E_f - E_i) B(E\lambda, i \rightarrow f) = \sum_{f,\mu} (E_f - E_i) |< f | O_\mu | i >|^2, \quad (27.29)$$

where the sum over f on the right hand side includes the sum over M_f . The operator O (the dependence on λ is implicit) is given by

$$O_\mu = \sum_k F_{k,\mu}, \quad (27.30)$$

where

$$F_{k,\mu} = r^\lambda Y_\mu^\lambda(\hat{r}_k) e_k e. \quad (27.31)$$

The sum in Eq. (27.29) can be turned into a expectation value of a double commutator

$$\begin{aligned}
 S &= \sum_{f,\mu} (E_f - E_i) |< f | O_\mu | i >|^2 \\
 &= \sum_{f,\mu} (E_f - E_i) < f | O_\mu | i >^* < f | O_\mu | i > = \sum_{f,\mu} (E_f - E_i) < i | O_\mu^+ | f > < f | O_\mu | i > \\
 &= \frac{1}{2} \sum_{f,\mu} [< i | O_\mu^+ | f > < f | HO_\mu - O_\mu H | i > - < i | HO_\mu^+ - O_\mu^+ H | f > < f | O_\mu | i >] \\
 &= \frac{1}{2} \sum_\mu < i | O_\mu^+ [H, O_\mu] - [H, O_\mu^+] O_\mu | i > = \frac{1}{2} \sum_\mu < i | [O_\mu^+, [H, O_\mu]] | i >. \quad (27.32)
 \end{aligned}$$

We have used the property of the Y^λ that

$$\sum_\mu [H, O_\mu^+] O_\mu = \sum_\mu (-1)^\mu [H, O_{-\mu}] O_\mu = \sum_\mu (-1)^\mu [H, O_\mu] O_{-\mu} = \sum_\mu [H, O_\mu] O_\mu^+. \quad (27.33)$$

To evaluate the double commutator we take

$$H = T + V.$$

The main part of the potential V which depends on the particle coordinates (and not on their derivatives) commutes with the $F_{k,\mu}$ operator and gives $[V, O_\mu] = 0$. The momentum dependent part of V does not commute. It will be ignored for now and considered latter as a correction to the sum rule.

We need to evaluate the commutator for the kinetic energy part of H

$$T = \frac{-\hbar^2}{2m} \sum_k \nabla_k^2$$

The sum in Eq. (27.32) is

$$S = \frac{-\hbar^2}{4m} \sum_{k,k',k'',\mu} \langle i [F_{k,\mu}^+, [\nabla_{k'}^2, F_{k'',\mu}]] | i \rangle . \quad (27.34)$$

The operators commute unless $k = k' = k''$, and we have

$$\sum_\mu \langle i | [F_\mu^+, [\nabla^2, F_\mu]] | i \rangle = \sum_\mu \langle i | [F_\mu (\nabla^2 F_\mu^+) - F_\mu^+ (\nabla^2 F_\mu) - 2(\vec{\nabla} F_\mu) \cdot (\vec{\nabla} F_\mu^+)] | i \rangle$$

$$= - \sum_{\mu} \langle i | 2(\vec{\nabla} F_{\mu}) \cdot (\vec{\nabla} F_{\mu}^+) | i \rangle = - \sum_{\mu} \langle i | (\nabla^2 F_{\mu} F_{\mu}^+) | i \rangle, \quad (27.35)$$

$\sum_{\mu} [F_{\mu}(\nabla^2 F_{\mu}^+) - F_{\mu}^+(\nabla^2 F_{\mu})] = 0$ (see Eq. (27.33)). The sum over μ can now be carried out

$$\sum_{\mu} F_{k,\mu} F_{k,\mu}^+ = \sum_{\mu} r_k^{2\lambda} Y_{\mu}^{\lambda}(\hat{r}_k) [Y_{\mu}^{\lambda}(\hat{r}_k)]^* e_k^2 = r_k^{2\lambda} \frac{(2\lambda + 1)}{4\pi} e_k^2. \quad (27.36)$$

Thus with

$$\nabla^2 r^{2\lambda} = \frac{1}{r^2} \frac{\partial}{\partial r} r^2 \frac{\partial}{\partial r} r^{2\lambda} = 2\lambda(2\lambda + 1)r^{2\lambda-2}, \quad (27.37)$$

we have

$$\langle i | (\nabla^2 F F^+) | i \rangle = \frac{2\lambda(2\lambda + 1)^2}{4\pi} \langle i | r_k^{2\lambda-2} | i \rangle, \quad (27.38)$$

and

$$S = \frac{\lambda(2\lambda + 1)^2}{4\pi} \frac{\hbar^2}{2m} \sum_k e_k^2 \langle i | r_k^{2\lambda-2} | i \rangle. \quad (27.39)$$

For electric dipole transitions, $\lambda=1$, and

$$S = \frac{9}{4\pi} \frac{\hbar^2 e^2}{2m} \sum_k e_k^2. \quad (27.40)$$

With the center-of-mass correction for the $E1$ operator, e_k is replaced by \tilde{e}_k and we have

$$\sum_k \tilde{e}_k^2 = Z\left(\frac{N}{Z}\right)^2 + N\left(\frac{-Z}{A}\right)^2 = \frac{NZ}{A}, \quad (27.41)$$

and

$$S(E1) = \frac{9}{4\pi} \frac{\hbar^2 e^2}{2m} \frac{NZ}{A} = 14.8 \frac{NZ}{A} \text{ MeV fm}^2 e^2. \quad (27.42)$$

The momentum-dependent and tensor parts of the potential are not included in (27.42). Also the exchange term is not included. These usually increases its value, and their effect on the $E1$ sum rule is usually written in terms of an enhancement factor κ [10]

$$S(E1)(\text{total}) = S(E1)(1 + \kappa). \quad (27.43)$$

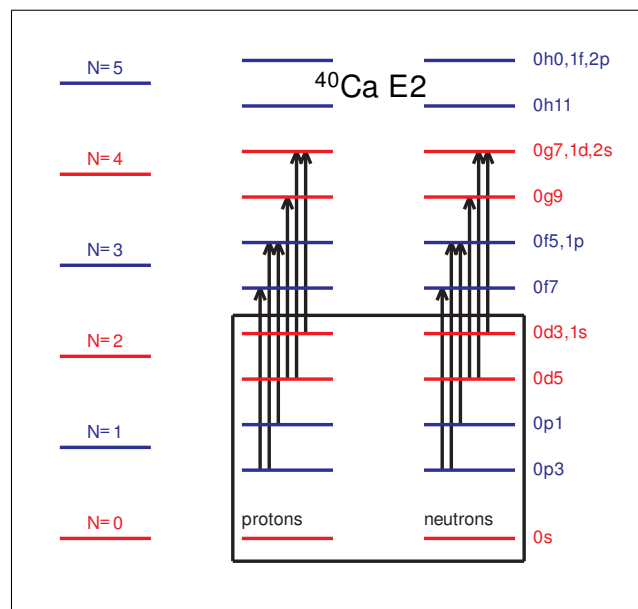


Figure 27.1: Schematic diagram showing the $E2$ ph excitations for ^{40}Ca . The box indicates those orbitals that are filled. The arrows show the particle-hole excitations allowed in the harmonic-oscillator model.

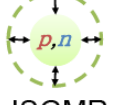
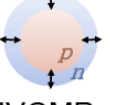
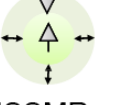
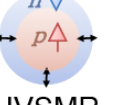
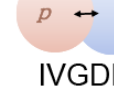
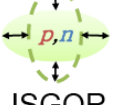
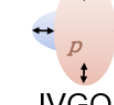
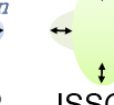
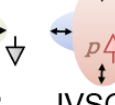
$\Delta L=0$				
$\Delta L=1$				
$\Delta L=2$				
	$\Delta S=0$ $\Delta T=0$	$\Delta S=0$ $\Delta T=1$	$\Delta S=1$ $\Delta T=0$	$\Delta S=1$ $\Delta T=1$

Figure 27.2: Collective excitations of nuclei. (From H. Sakai). The notation is $\Delta T = \tau = 0$ isoscalar (IS), $\Delta T = \tau = 1$ isovector (IV), $\Delta S = 0$ (G), $\Delta S = 1$ (S), $\Delta J = 0$ for the monopole resonance (MR), $\Delta J = 1$ for the dipole resonance (DR) and $\Delta J = 2$ for the quadrupole resonance (QR).

Bibliography

- [1] S. P. Pandya, Phys. Rev. **103**, 956 (1956). link
- [2] A. de Shalit and I. Talmi, *Nuclear Shell Theory*, (Academic Press, 1963).
- [3] I. Tamm, J. Phys. (U.S.S.R.) 9, 449 (1945); S. M. Dancoff, Phys Rev. **78**, 382 (1950).
- [4] D. Bohm and D. Pines, Phys. Rev. **82**, 625 (1951); Phys. Rev. **85**, 338 (1952); and Phys. Rev. **92**, 609 (1953). link

- [5] M. Baranger, Phys. Rev. **120**, 957 (1960). link
- [6] B. L. Berman and S. C. Fultz, Rev. Mod. Phys. **47**, 713 (1975).
- [7] L. H. Thomas, Naturwiss. **13**, 627 (1925).
- [8] R. Ladenburg and F. Reiche, Naturwiss. **11**, 873 (1923).
- [9] W. Kuhn, Z. Phys. **33**, 408 (1923).
- [10] G. Orlandindi an M. Trainai, Rep. Prog. Phys. **54**, 257 (1991).

Chapter 28

Corrections to Operators in a Model Space

669

Most configuration interaction calculations involve truncations to a subset of orbitals called the model space. This involves a division of the orbitals into three sets of increasing single-particle energy; those that make up the assumed closed shell (C), some active orbitals (A), and then an infinite number of empty orbitals (E). All one- and two-body operators calculated within this model space must be renormalized to take into account the mixing with configurations outside of this model space. This involves the coupling of the valence nucleons to particle-hole excitations from $C \rightarrow A$, $C \rightarrow E$ and $A \rightarrow E$. The procedure involves using perturbation theory with the operators written in second quantized form and using the rules of angular momentum coupling. Some details go beyond the scope of these lecture notes. They can be found, for example, in [1], [2], [3]. We will discuss results for the one-body electromagnetic the two-body Hamiltonian matrix elements.

28.1 One-body operators and effective charge

In the single-particle model of the nucleus we used a wavefunctions that represents a single particle or a single hole relative to a closed-shell configuration. In this section we look at the effect of the admixtures to the single-particle wavefunction to the matrix elements of one-body operators. The percentage of admixture is small (on the order to 10%) and the admixture will be treated with first-order perturbation methods. But the affect on the one-body matrix elements can be large since they enter linearly in the admixed amplitude.

The admixtures differ from the single-particle wavefunctions by the excitation of a particle-hole configuration relative to the closed-shell. The admixed wavefunctions have the form

$$| i \rangle = | a \rangle + \sum_{p,h} \alpha_{i,p,h} | \{[p \otimes h^{-1}]^\lambda \otimes c\}^{j_a} \rangle \quad (28.1)$$

and

$$| f \rangle = | b \rangle + \sum_{p,h} \alpha_{f,p,h} | \{[p \otimes h^{-1}]^\lambda \otimes d\}^{j_b} \rangle, \quad (28.2)$$

where

$$\alpha_{i,p,h} = \frac{\langle [p \otimes h^{-1}]^\lambda \otimes c \rangle^{j_a} | G | a \rangle}{\epsilon_a + \epsilon_h - \epsilon_p - \epsilon_c}, \quad (28.3)$$

and

$$\alpha_{f,p,h} = \frac{\langle p \otimes h^{-1}]^\lambda \otimes d \rangle^{j_b} | G | b \rangle}{\epsilon_b + \epsilon_h - \epsilon_p - \epsilon_d}. \quad (28.4)$$

In these equations, a is shorthand for single-particle wavefunction k_a with angular momentum, j_a , etc. Also it is implicit that wavefunctions are relative to a closed-shell C with angular moment $J_C = 0$. These are shown schematically in Fig. (28.1)

The consequence of this mixing is sometimes called core-polarization. The schematic picture for this is shown in Fig. (28.2). In (a-left) the total charge quadupole moment is zero since there is a deformed valence neutron and the core is spherical. In (b-left) the core is deformed due to the $1p - 1h$ admixtures. This gives rise to an effectice charge for the valence neutron coming from the deformation of the core protons. The right-hand side shows the core-polarizaiton for a valence proton. In (b) the core protons are deformed more for a valence neutron (compared to the proton), since the average neutron-proton interaction is

$$|i\rangle = \left| \begin{array}{c} * \\ \boxed{} \\ a \end{array} \right\rangle + \sum_{ph} \alpha_{iph} \left| \begin{array}{c} * \\ \boxed{} \\ c \\ \circ \\ h \end{array} \right\rangle$$

$$|f\rangle = \left| \begin{array}{c} * \\ \boxed{} \\ b \end{array} \right\rangle + \sum_{ph} \alpha_{fph} \left| \begin{array}{c} * \\ \boxed{} \\ d \\ \circ \\ h \end{array} \right\rangle$$

Figure 28.1: Schematic diagram for particle-hole admixtures into the single-particle wavefunctions.

stronger than that for the proton-proton interaction.

The reduced matrix element of a one-body operator O^L of tensor rank L is given by

$$\langle f || O^L || i \rangle = \langle b || O^L || a \rangle$$

$$\begin{aligned}
& + \sum_{p,h} \frac{\langle b || O^L || \{[p \otimes h^{-1}]^\lambda \otimes c\}^{j_a} \rangle \langle \{[p \otimes h^{-1}]^\lambda \otimes c\}^{j_a} | G | a \rangle}{\epsilon_a + \epsilon_h - \epsilon_p - \epsilon_c} \\
& + \sum_{p,h} \frac{\langle b | G | \{p \otimes h^{-1}\}^\lambda \otimes d \rangle \langle \{[p \otimes h^{-1}]^\lambda \otimes d\}^{j_b} || O^L || a \rangle}{e_b + \epsilon_h - \epsilon_p - \epsilon_d} \\
& = \langle b || O^L || a \rangle + B + C,
\end{aligned} \tag{28.5}$$

plus terms of order α^2 which are much smaller than the linear terms in α and will be ignored (in the spirit of first-order perturbation). This equation is shown diagrammatically in Fig. (28.3).

For the term $\langle \{[p \otimes h^{-1}]^\lambda \otimes d\}^{j_b} || O^L || a \rangle$, the one-body operator acts on the closed state on the right with $J = 0^+$ to make the particle-hole state on the left with $J = \lambda$. Thus $k_a = k_d$ and $L = \lambda$ (this is also obvious from Fig. (28.3)). Likewise for $\langle b || O^L || \{[p \otimes h^{-1}]^\lambda \otimes c\}^{j_a} \rangle$ we have $k_b = k_c$ and $L = \lambda$.

Altogether the first term in Eq. (28.5) gives

$$\begin{aligned} B = \sum_{p,h,J} (-1)^{j_a+j_h+J} (2J+1) & \langle h||O^L||p \rangle \left\{ \begin{array}{ccc} j_b & j_a & \lambda \\ j_h & j_p & J \end{array} \right\} \\ & \times \sqrt{(1+\delta_{a,h})(1+\delta_{b,p})} \frac{\langle bpJ \mid G \mid ahJ \rangle}{\epsilon_a + \epsilon_h - \epsilon_p - \epsilon_b} \end{aligned} \quad (28.6)$$

and the second term is

$$\begin{aligned} C = \sum_{p,h,J} (-1)^{j_b+j_p+J} (2J+1) & \langle h||O^L||p \rangle \left\{ \begin{array}{ccc} j_b & j_a & \lambda \\ j_p & j_h & J \end{array} \right\} \\ & \times \sqrt{(1+\delta_{a,p})(1+\delta_{b,h})} \frac{\langle bhJ \mid G \mid apJ \rangle}{\epsilon_b + \epsilon_h - \epsilon_p - \epsilon_a} \end{aligned} \quad (28.7)$$

If $a = b$ then $B = C$.

The number of terms that enter into the particle-hole sums in Eqs. (28.6) and (28.7) depends upon the selection rules for the $\langle h||O^L||p \rangle$ matrix elements. For light nuclei one

often considers a core where the spin-orbit partners are either filled or empty like that for ^{40}Ca shown in the last chapter for ^{40}Ca . The first-order correction for M1 is zero since all of the $\langle p||M1||h \rangle$ are zero. For the first-order for E2 many particle-hole excitations are allowed. In the harmonic-oscillator model the $1p - 1h$ states what contribute must have $N_p - N_h = 2$ since the radial matrix element is zero when $N_p - N_h > 2$.

For heavy nuclei the situation is usually like that shown in Figs. (28.4) and (28.5) for ^{208}Pb . In this case the closed core includes one of the spin-orbit partners. There are now two excitations that enter into first-order corrections for M1 matrix elements as shown in Fig. (28.4). For E2 there are also “low-lying” $\Delta N = 0$ terms to be included in the first-order correction as shown by the green arrows in Fig. (28.5). Due to these $\Delta = 0$ contributions, the E2 effective charges for heavy nuclei are often larger than those in light nuclei.

For the electric multipoles starting with the bare-nucleon charges of one for protons and zero for neutrons, one can define effective charges for protons and neutrons by $e_p = 1 + \delta_p$ and $e_n = \delta_n$, by

$$\langle b||O^L||a \rangle_p + A + B = \langle b||O^L||a \rangle_p (1 + \delta_p)$$

Table 28.1: Articles on first-order corrections to $M1$ and $E2$.

Year	Authors	Interaction	Comments
1954	Arima and Horoi [4]	δ	M1 single-particle
1955	Arima and Horoi [5]	δ	E2 single-particle
1958	Noya, Arima and Horoi [6]	δ	M1 and E2
1959	Fallieros and Ferrell [7]	collective	E2 ^{16}O
1969	Federman and Zamick [8]		E2 state dependence
1970	Siegel and Zamick [9]		E2 RPA
1972	Hamamoto [10]	collective	E4 ^{208}Pb region
1972	Astner et al. [11]	experiment	E2 ^{208}Pb region
1977	Brown et al. [12]	δ , experiment	E2 ^{16}O and ^{40}Ca
1979	Sagawa [13]	Skyrme	E4 E6 $f_{7/2}$
1980	Mano and Suekane [14]	δ , Woods-Saxon	E2 ^{40}Ca
1980	Castel et al. [15]	δ	E2 ^{40}Ca
1984	Sagawa and Brown [16]	Skyrme	E2 sd shell
1985	Sagawa and Brown [17]	Skyrme	E4 sd shell
1987	Sagawa et al. [18]	Skyrme	E2 ^{132}Sn region
1998	Johnstone and Towner [19]	OBEP	E2 ^{90}Zr region
1998	Johnstone and Towner [20]	OBEP	M1 ^{90}Zr region

and

$$\langle b || O^L || a \rangle_n + A + B = \langle b || O^L || a \rangle_n (0 + \delta_n).$$

Only the polarization of the core protons contributes to the effective charge. Valence protons can interact with the core protons only by the $T = 1$ part of the interaction, whereas valence neutrons can also interact with $T = 0$ part. Thus in microscopic calculations (for $N \geq Z$) the addition neutron effective charge δ_n is usually larger than the additional proton effective charge δ_p .

The core-polarization matrix elements $\langle b || O^L || \{[p \otimes h^{-1}]^\lambda \otimes c\}^{j_a} \rangle$ can be generalized for the isospin type operator $O^{L,\Delta T}$. The isoscalar/isovector effective operator comes from the isoscalar/isovector polarization of the core. Generally, the collective isoscalar/isovector L -multipole excitations are lowered/raised in energy from their unperturbed energies of $\epsilon_p - \epsilon_h$ due to the residual particle-hole interactions. For the electric multipole operator one usually finds that $\delta_0 > \delta_1 > 0$ so that that $\delta_n > \delta_p$.

The above results can be apply to one valence particle or one valence hole. The calculations become more complicated for many-valence nucleons. But empirically it is

sometimes found that the effective charge is independent of the number of valence nucleons. An example of this for the sd model space is shown in Figs. 5 and 6 of [21] where the average effective charges for the entire set of data for nuclei in the sd shell is $\delta_p = 0.36(5)$ and $\delta_n = 0.45(5)$, or $e_p = 1.36(5)$ and $e_n = 0.45(5)$.

28.2 Corrections to two-body Hamiltonian matrix elements

The two-body matrix elements in a given model space must also be corrected the core admixtures. The first and second-order diagrams are shown in Fig. (28.6). The first order diagram is just the two-body G-matrix element in the valence space, G_1 .

The second diagram for G_{3p-1h} involves the same $1p - 1h$ excitations discussed above for the effective charge. This is sometimes called the core-polarization correction to the valence two-body matrix interaction. The third diagram for G_{2p} involves the excitation

of two nucleons from the valence orbitals into higher orbitals at higher energy. The fourth diagram for G_{4p-2h} involves the excitation of two-nucleons from the filled core into the valence space where the intermediate state has the form $4p - 2h$. The explicit equations that result from these diagrams are given in [3]. A computer program for their evaluation is provided by Morten Hjorth-Jensen. The results for some two-body matrix elements in the sd shell are shown in Table 2. They are compared to the USDB empirical values [22] that are need to describe the energies of sd shell nuclei. The agreement of the calculation (total) with USDB is reasonable, but some matrix elements differ by as much as one MeV. As many nucleons are added to the sd this difference accumulates and the calculated binding energies and spectra do not agree with experiment. There are many reasons why the microscopic theory may not accurate. In Ref. [3] the third-order diagrams shown in Fig. 77 of that paper were evaluated. They are on the order of a few hundred keV. The agreement with USDB is not improved. One may need to go higher order. Also one may need to include three-body interaction.

More recently the coupled-cluster [23], [24] and similarity renormalization group (SRG) [25] methods have been developed as a better ways of summing higher-order diagrams.

Table 28.2: Values of some *sd* shell matrix elements $\langle k_1 k_2 JT | G | k_3 k_4 JT \rangle$ in MeV. They are labeled by $k = 4$ for $0d_{5/2}$ and $k = 6$ for $1s_{1/2}$.

k_1	k_2	k_3	k_4	J	T	G_1	G_{3p-1h}	G_{4p-2h}	G_{2p}	sum	USDB
4	4	4	4	0	1	-1.06	-0.68	-0.32	-0.32	-2.38	-2.56
4	4	4	4	2	1	-0.67	0.09	-0.05	-0.12	-0.51	-1.07
4	4	4	4	4	1	-0.09	0.40	0.00	-0.06	0.25	-0.21
4	4	4	6	2	1	-0.57	-0.18	-0.02	-0.07	-0.84	-0.93
4	4	6	6	0	1	-0.75	-0.21	-0.05	-0.08	-1.09	-1.56
4	6	4	6	2	1	-0.78	-0.02	-0.01	-0.14	-0.95	-0.94
4	6	4	6	3	1	0.05	0.47	0.00	-0.02	0.50	0.68
6	6	6	6	0	1	-1.94	0.03	-0.01	-0.15	-2.07	-1.69
4	4	4	4	1	0	0.06	-0.35	-0.12	-0.71	-1.12	-1.38
4	4	4	4	3	0	-0.47	0.12	-0.02	-0.25	-0.62	-1.67
4	4	4	4	5	0	-2.64	0.15	0.00	-0.41	-2.90	-4.32
4	4	4	6	3	0	-0.72	-0.15	-0.02	-0.19	-1.08	-1.21
4	4	6	6	1	0	-0.21	-0.21	-0.04	-0.24	-0.70	-0.53
4	6	4	6	2	0	-0.67	0.04	-0.01	-0.28	-0.92	-0.31
4	6	4	6	3	0	-1.41	0.08	-0.02	-0.27	-1.62	-4.18
6	6	6	6	1	0	-2.91	0.15	-0.13	-0.57	-3.46	-3.70

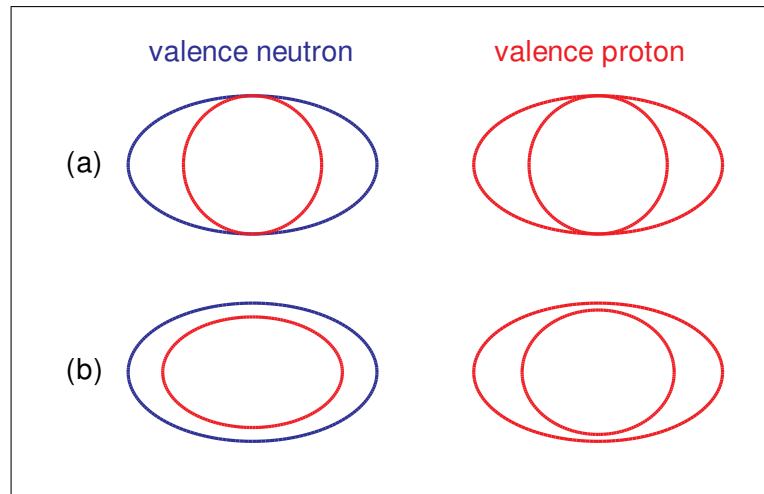


Figure 28.2: Qualitative picture of core-polarization. The red circles and ovals in the middle represent the distribution of the core protons. The outside ovals represent the distribution of the valence neutrons (left) and protons (right). In (a) the core remains spherical. In (b) the core is deformed due to the $1p - 1h$ admixtures.

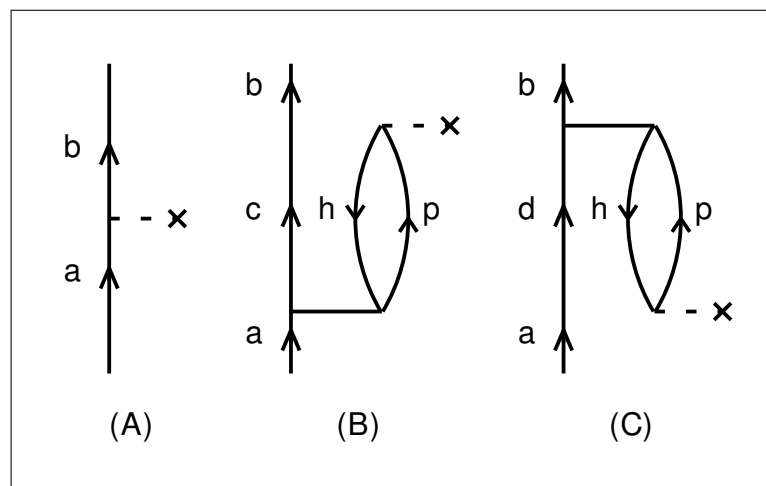


Figure 28.3: Diagrams for the single-particle matrix element (A) together with the first-order core-polarization corrections for admixtures into the final (B) and initial (C) states.

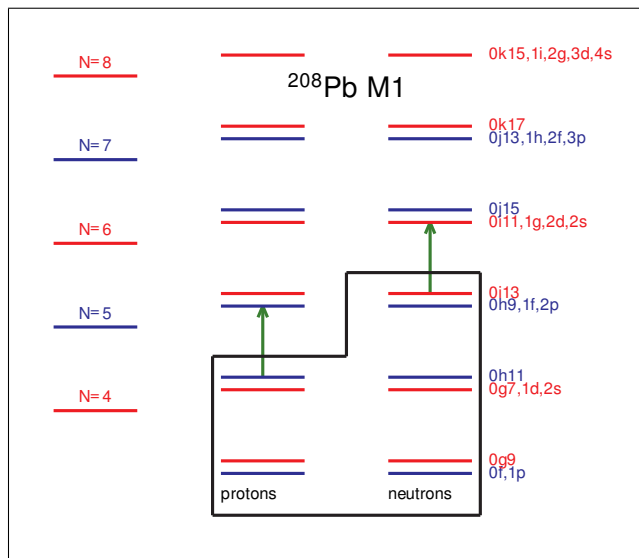


Figure 28.4: Schematic diagram for ^{208}Pb showing the excitations that enter into the first-order diagrams. The box indicates those orbitals that are filled. The arrows show the particle-hole excitations allowed in the harmonic-oscillator model.

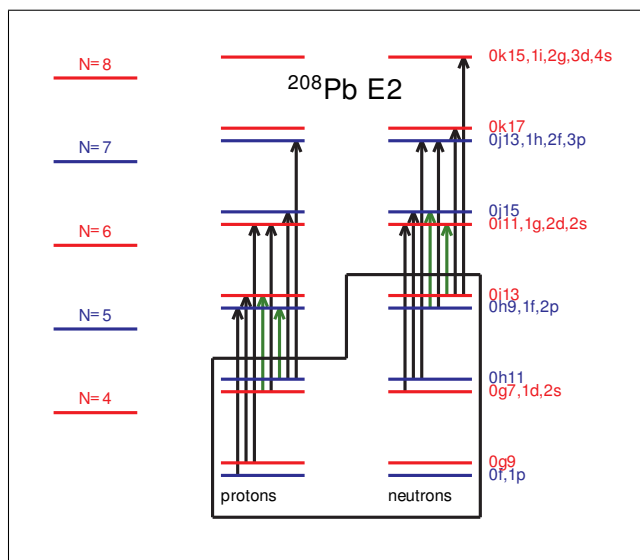


Figure 28.5: Schematic diagram for ^{208}Pb showing the excitations that enter into the first-order diagrams for E2 matrix elements. The box indicates those orbitals that are filled. The arrows show the particle-hole excitations allowed in the harmonic-oscillator model.

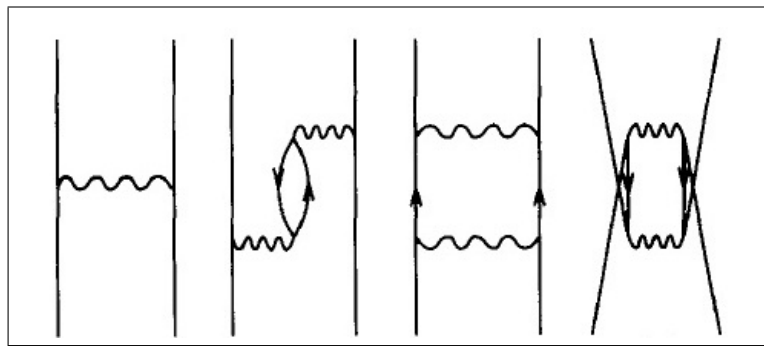


Figure 28.6: The first-order diagram G_1 for the valence two-body matrix element is shown in the left-hand side. The next three diagrams represent the second-order corrections. These will be denoted by G_{3p-1h} , G_{2p} and G_{4p-2h} .

Bibliography

- [1] T. T. S. Kuo, J. Shurpin, K. C. Tam, E. Osnes and P. J. Ellis, Ann. of Phys. **132**, 237 (1981).
- [2] J. Shurpin, T. T. S. Kuo and D. Strottman, Nucl. Phys. **A408**, 310 (1983).
- [3] M. Hjorth-Jensen, T. T. S. Kuo and E. Osnes, Phys. Rep. **261**, 125 (1995).
- [4] A. Arima and H. Horie, Prog. Theo. Phys. 12, 623 (1954).

- [5] H. Horie and A. Arima, Phys. Rev. 99, 778 (1955).
- [6] H. Noya, A. Arima and H. Horie, Supplement of Prog. Theor. Phys. No. 8, 33-112 (1958).
- [7] S. Fallieros and R. A. Ferrell, Phys. Rev. **116**, 660 (1959). link
- [8] P. Federman and L. Zamick, Phys. Rev. 177, 1534 (1969).
- [9] S. Siegel and L. Zamick, Nucl. Phys. A145, 89 (1970).
- [10] I. Hamamoto, Nucl. Phys. A196, 101 (1972).
- [11] G. Astner, I. Bergstrom, J. Blomqvist, B. Fant and K. Wikstrom, Nucl. Phys. A182, 219 (1972).
- [12] B. A. Brown, A. Arima and J. B. McGrory, Nucl. Phys. **A277**, 77 (1977).
- [13] H. Sagawa, Phys. Rev. C 19, 506 (1979). link
- [14] J. Mano and S. Suekane, Prof. Theor. Phys. **63**, 459 (1980).

- [15] B. Castel, G. R. Satschler and K. Goeke, Phys. Lett. **91B**, 185 (1980).
- [16] H. Sagawa and B. A. Brown, Nucl. Phys. **A430**, 84 (1984).
- [17] H. Sagawa and B. A. Brown, Phys. Lett. **150B**, 247 (1985).
- [18] H. Sagawa, O. Scholten, B. A. Brown and B. H. Wildenthal, Nucl. Phys. **A462**, 1 (1987).
- [19] I. P. Johnstone and I. S. Towner, Eur. Phys. Jour. A **2**, 263 (1998).
- [20] I. P. Johnstone and I. S. Towner, Eur. Phys. Jour. A **3**, 237 (1998).
- [21] W. A. Richter, S. Mkhize, and B. A. Brown, Phys. Rev. C 78, 064302 (2008). link
- [22] B. A. Brown and W. A. Richter, Phys. Rev. C 74, 034315 (2006). link
- [23] G. Hagen, T. Papenbrock, M. Hjorth-Jensen, and D. J. Dean, Reports on Progress in Physics **77**, 096302 (2014).

- [24] S. Binder, P. Piecuch, A. Calci, J. Langhammer, P. Navratil, and R. Roth, Phys. Rev. C **88**, 054319 (2013). link
- [25] H. Hergert, S. K. Bognera, T. D. Morrisb, A. Schwenk, and K. Tsukiyama, Physics Reports **621**, 165 (2016).

Chapter 29

Effective Hamiltonians

The Hamiltonian has the form

$$H = H_0 + H_1 + H_2. \quad (29.1)$$

The first term is the binding energy of the closed shell. The second term is a one-body operator whose matrix elements are given by the single-particle energies (SPE) multiplied by the orbital occupancy. It implicitly contains both the kinetic energy and the monopole interaction of the valence nucleon with those in the closed core. One often uses experimental information for the single-particle energies, or when this is not known, some approximate calculations such as results from a Woods-Saxon potential. The two-body part represented, H_2 , could be obtained in a variety of ways. For a qualitative understanding one could use schematic forms such as the delta-function interaction. More microscopic forms start with the potentials that reproduce nucleon-nucleon scattering data and then are renormalized for the chosen model space. Empirical Hamiltonians are based on fitting the two-body matrix elements (TBME) to a selection of experimental data. These empirical Hamiltonians implicitly contain the corrections due the addition of three-body interactions and to the limitations of the many-body approaches.

It is conventional to determine a Hamiltonian for one mass value and then to use the

same Hamiltonian over a wide mass region. Sometimes a smooth scaling of H_2 is used to account for an implicit mass scaling. For example, the USD interaction in the sd -shell model space assumes the form $\text{TBME}^A = \text{TBME}^{A=18}(A/18)^{-0.3}$, where the power was determined empirically [1]. The scaling is a result of the change of the (implicit) radial wave function as a function of mass (A). If one takes the simplest oscillator dependence of $\hbar\omega = 41A^{-1/3}$, then the TBME calculated with a delta function vary as $A^{-1/2}$ and the TBME for the long-range Coulomb interaction varies as $A^{-1/6}$. Nuclear interactions of intermediate range would vary somewhere between these two extremes. The smooth scaling is an approximation. As we approach the drip line one might expect to observe deviations from experiment due to the larger radial extent of the valence wave functions.

Usually the core, H_0 and one-body, H_1 (the SPE) terms are not changed as a function of mass. But there is no reason they should not change. The effective values for H_2 implicitly compensate for possible changes in H_0 and H_1 .

A common element of most configuration-mixing calculations in light nuclei is that the interactions used conserve isospin and are specified in terms of TBME which have good J

and T . The effects of the Coulomb interaction are usually treated by adding a Z -dependent constant. It can be deduced from the energy shift between analogue states. In practice, this means that a shell-model result for a given isotopic chain (fixed Z) gives the relative binding energy and excitation energy as a function of neutron number. To obtain the absolute binding energy, a constant must be added to connect it to a given experimental value which can be taken as that of the $T = 0$ ground state for even Z and that of the $T = 1/2$ ground state for odd Z . The levels in mirror nuclei are identical in this approximation. The experimental excitation energies in mirror nuclei are typically shifted by 100 keV or less relative to the ground state energy. This is small compared to the accuracy of most configuration-mixing calculations (200 keV or more). There are larger shifts in light nuclei associated with the Thomas-Ehrman shift of low ℓ orbitals, and these should be treated more carefully in terms of the structure change between mirror nuclei. Configuration mixing in light nuclei can be carried out in a proton-neutron basis [2], but the main interest is in the special problem of overlaps in Fermi beta decay [3] and in isospin forbidden processes [4].

29.1 Types of Hamiltonians

One usually begins with a set of TBME obtained from realistic Hamiltonian based on the renormalized G matrix. But quality of the predictions and applications for a given model space and mass region can be greatly improved if the values of the TBME are constrained to reproduce some selection of energy data. There are several approaches to doing this that are outlined below.

ETBME: For very small model spaces the wavefunctions for a large number of states arise from a relatively few TBME. One of the best examples is the $0f_{7/2}$ shell [5] where this one orbital is rather isolated. For the $0f_{7/2}$ shell there are only eight TBME and one SPE which can be used to obtain the energies and wave functions of several hundred levels in the $A = 40 - 56$ mass region [6] (a more complete model space for these nuclei is possible now).

ETBME+G: In larger model spaces the number of TBME is large and they cannot all be well determined by existing data. The data are sensitive to particular linear combinations of SPE and TBME. The well determined linear combinations can be obtained from the single-values

decomposition (SVD) discussed in the next section. The other linear combinations are left at their G matrix values. Early examples of this are [7], [8]. The SVD method was used in the sd model space to obtain the USD Hamiltonians [1] [9], and in the pf shell to obtain the GXPF pf-shell Hamiltonians [10].

G + MON: In larger model spaces the most important part of the Hamiltonian are the monopole combinations of TBME, because these determine the evolution of the SPE a function of mass. Effective interactions where some or all of the monopole are used to fit some selected set of energy data will be called G+MON. Examples of G + MON Hamiltonians are the KB3 [11] and KB3G [12] in the pf shell.

POT: Empirical Hamiltonians can also be based upon two-body potential models in which the strengths of the various channels (central, spin-orbit and tensor) are obtained from a fit to energy data. These will be called potential “POT” models for the shell-model Hamiltonian. The simplest form of the potential models are the delta functions and MSDI mentioned above. A more elaborate form is the modified-surface-one-boson-exchange-potential (MSOBEP) [13]. Other types of fits related to the potential models can be based upon the

relative matrix elements [14] and Talmi integrals [15], [13].

For heavy nuclei one usually finds Hamiltonians specifically designed for use only for a relatively small region of nuclei, such as those around ^{132}Sn or ^{208}Pb .

These empirical Hamiltonians provide a way to generate realistic wave functions (from which one calculates observables) and to extrapolate the known properties of nuclei to the unknown. When one observes something which does not agree with these extrapolations, it is usually an indication of “new physics” involving degrees of freedom which are not in the assumed model space. The observation of such “new physics” in neutron-rich nuclei is the essential aspect of the current and proposed radioactive-beam experimentations.

29.2 Hamiltonians for specific model spaces

The names of some commonly used effective Hamiltonians and the model-space they are associated with are given in Table (29.1). These Hamiltonians have been determined by a least-squares fit to binding energy and excitation energy data. This was accomplished by varying the full set of two-body matrix elements (ETBME), by varying well determined linear combinations of two-body matrix elements and keeping the rest fixed at some G matrix values (ETBME+G), by adding monopole corrections to the G matrix (G+MON), and by varying potential parameters (POT).

29.3 Hamiltonians in the $jj44$ model space

Historically, the first $jj44x$ type of Hamiltonian for the $jj44$ model space was called $jj44pna$ in the NuShellX library for the $jj44pn$ model space [30]. This Hamiltonian contains one set

Table 29.1: Table of model spaces and interactions names. The types of potentials for the s-p-sd-pf and sd-pf models space are discussed in the text.

Model space	A	Interaction	Type	Reference
0p (p)	A=5-16	(6-16)TBME	ETBME	[16]
		PJT	ETBME	[17] Table 1
		PJP	POT	[17] Table 1
	A=8-16	(8-16)POT (8-16)TBME	POT ETBME	[16] [16]
	A=10-16	PWBT	ETBME	[18]
1s0d (sd)	A=16-40	USD	ETBME+G	[1]
		SDPOTA	POT	[13]
		USDA	ETBME+G	[9]
		USDB	ETBME+G	[9]
1p0f (pf)	A=40-50	FPMG	G+MON	[19]
		FPD6	POT	[20]
		KB3	G+MON	[11]
	A=40-60	KB3G	G+MON	[12]
		GXPF1	ETBME+G	[10]
		GXPF1A	ETBME+G	[21]
s-p-sd-pf	A=10-20	MK		[22]
		WBP		[18]
		WBT		[18]
sd-pf	near N=20	WBMB		[23], [24]
		RCNP		[25]
		Utsuno et al.		[26]
		Dean et al.		[27]
	near N=28 Z > 14 near N=28 Z ≤ 14	SDPFU	G+MON	[28]
		SDPFUSI	G+MON	[sdpfu]
jj44	A=70-100	SDPFU	G+MON	[28]
		SDPFUSI	G+MON	[28]
		jun45	ETBME+G	[29]
		jj44pna	ETBME+G	[30]
		jj44b	ETBME+G	(see text)

of two-body matrix elements (TBME) with $T = 1$ for neutrons that are constrained to reproduce the binding energies and excitation energies for the nickel isotopes ($Z = 28$) with $N = 33 - 44$, and another set of TBME with $T = 1$ for protons that are constrained to reproduce the binding energies and excitation energies for isotones with $N = 50$ and $Z = 32 - 50$. The $jj44pna$ Hamiltonian does not contain proton-neutron TBME and cannot be used away from $Z = 28$ or $N = 50$. For $jj44pna$ the neutron and proton TBME are different. A consequence of this, the 8^+ seniority isomers obtained in ^{94}Ru and ^{96}Pd are not present in the analogous nuclei $^{72,74}\text{Ni}$ due to a crossing of some states dominated by seniority two and four [30].

The $jj44b$ and JUN45 Hamiltonians are for the $jj44$ model space. Both of these contain an assumed mass dependence of $(A/58)^{-0.3}$. The TBME for $jj44b$ are based on those obtained with the renormalized Bonn-C potential. The singular-value decomposition (SVD) method was used to constrain 30 linear combinations of the 133 TBME to 77 binding energies and 470 excitation energies in nuclei with $Z = 28 - 30$ ($N = 28 = 50$), and $N = 48 - 50$ ($Z = 28 - 50$). For a given Z , the binding energies are corrected by an overall shift obtained from the Coulomb part of a Skyrme energy-density functional calculation. The

rms deviation between the theoretical and experimental energies was about 240 keV. When the $jj44b$ Hamiltonian is used in the proton-neutron model space $jj44pn$ it is called $jj44bpn$; the results with $jj44b$ and $jj44bpn$ are the same. Starting in 2007, the $jj44b$ Hamiltonian has been used for comparison to data in many publications [where it is sometimes called $jj4b$ and sometimes cited as B. A. Brown and A. F. Lisetskiy (private communication)] [31], [32], [33], [34], [35], [36], [37], [38], [39], [40], [41].

The $T = 1$ TBME for $jj44b$ are approximately an average of those for protons and neutrons in the the $jj44pna$ Hamiltonian. When the $jj44b$ Hamiltonian is applied to $Z = 28$ or $N = 50$ it does work as well as the $jj44pna$ Hamiltonian. Starting with $jj44b$ another Hamiltonian called $jj44c$ was obtained by leaving out energy data above $Z = 38$. This is a better Hamiltonian to use for $Z = 28 - 30$.

A method similar to that used to obtain the $jj44b$ Hamiltonian was used by Honma et al. to obtain the JUN45 Hamiltonian [29]. For the JUN45 Hamiltonian, 45 SVD linear combinations were determined by a fit to about 69 binding energies and 330 excitation energies for nuclei in the range $N = 30 - 32$ and $Z = 46 - 50$, as shown in Fig. 1 of Ref.

[29]. The rms deviation was 185 keV. These data included the ground state and first three excited states in ^{76}Ge .

29.4 The singular-value decomposition fit

29.4.1 The SVD method

The shell-model effective Hamiltonian can be written as a sum of one- and two-body operators (the notation is similar to that used by Honma et al. [42] for the pf shell which is based on the work of Chung and Wildenthal [8], [1] for the sd shell).

$$H = \sum_a \epsilon_a \hat{n}_n + \sum_{a \leq b, c \leq d} \sum_{JT} V_{JT}(ab; cd) \hat{T}_{JT}(ab; cd), \quad (29.2)$$

where \hat{n}_a is the number operator for the spherical orbit a with quantum numbers (n_a, l_a, j_a) , and

$$\hat{T}_{JT}(ab; cd) = \sum_{MT_z} A_{JMTT_z}^\dagger(ab) A_{JMTT_z}(cd) \quad (29.3)$$

is the scalar two-body density operator for nucleon-pairs in orbits a, b and c, d coupled to spin quantum numbers JM and isospin quantum numbers TT_z . We use a simplified notation

$$H = \sum_{i=1}^p x_i O_i, \quad (29.4)$$

where the x_i stand for single-particle energies ϵ_a or the two-body matrix elements $V_{JT}(ab; cd)$, and the operators O_i stand for \hat{n} or \hat{T} , respectively. The vector $\vec{x} = (x_1, x_2, \dots, x_p)$ defines the Hamiltonian. This Hamiltonian will have eigenvectors ϕ_k and eigenvalues λ_k that can be expressed in terms of a linear combination of the Hamiltonian \vec{x}

$$\lambda_k = \langle \phi_k | H | \phi_k \rangle = \sum_{i=1}^p x_i \langle \phi_k | O_i | \phi_k \rangle = \sum_{i=1}^p x_i \beta_i^k, \quad (29.5)$$

where $\beta_i^k = \langle \phi_k | O_i | \phi_k \rangle$.

For a given starting Hamiltonian \vec{x}^s , we calculate β_i^k and then minimize the quantity

$$\chi^2 = \sum_{k=1}^N \left(\frac{E_{\text{exp}}^k - \lambda_k}{\sigma_{\text{exp}}^k} \right)^2, \quad (29.6)$$

where N is the number of data included in the fit, E_{exp}^k are the experimental energies, and σ_{exp}^k are the associated errors. This gives

$$\frac{\partial \chi^2}{\partial x_j} = \sum_{k=1}^N 2 \frac{(E_{\text{exp}}^k - \lambda_k)}{(\sigma_{\text{exp}}^k)^2} \frac{\partial}{\partial x_j} \left(- \sum_{i=1}^p x_i \beta_i^k \right) = 0. \quad (29.7)$$

Without taking into account the implicit dependence of β_i^k on x_j through ϕ_i we obtain p linear equations for an improved Hamiltonian \vec{x} .

$$\sum_{k=1}^N (E_{\text{exp}}^k - \sum_{i=1}^p x_i \beta_i^k) \frac{\beta_j^k}{(\sigma_{\text{exp}}^k)^2} = e_j - \sum_{i=1}^p \gamma_{ij} x_i = 0, \quad (29.8)$$

where $j = 1, 2, \dots, p$. This can be written in terms of a $p \times p$ matrix

$$G = (\gamma_{ij}) = \sum_{k=1}^N \frac{\beta_i^k \beta_j^k}{(\sigma_{\text{exp}}^k)^2} \quad (29.9)$$

and a p -dimensional vector

$$\vec{e} = (e_i) = \sum_{k=1}^N \frac{E_{\text{exp}}^k \beta_i^k}{(\sigma_{\text{exp}}^k)^2}, \quad (29.10)$$

as,

$$G\vec{x} = \vec{e}, \quad (29.11)$$

Since G can be inverted to obtain the new Hamiltonian \vec{x}

$$\vec{x} = G^{-1}\vec{e}. \quad (29.12)$$

To take into account the implicit dependence of β_i^k on x_j this procedure is repeated (iterated) until convergence.

The matrix G^{-1} is referred to as the error matrix [43] since the diagonal elements are the square of the parameter errors and the off-diagonal matrix elements are related to the correlations between the parameters. As in most multi-parameter fits, the resulting parameters x_i are highly correlated. In addition, the low-lying nuclear states are much more sensitive to some linear combinations of Hamiltonian parameters than others. These issues

can be quantified by diagonalizing the matrix G

$$D = AGA^T, \quad (29.13)$$

or in terms of the error matrix

$$D^{-1} = AG^{-1}A^T, \quad (29.14)$$

where D is a p -dimensional diagonal matrix with positive elements D_i . The eigenvalues of the error matrix D^{-1} are $d_i = \frac{1}{D_i}$. With this definition for A , Eq. (29.11) is equivalent to $D\vec{y} = \vec{c}$, where $\vec{y} = A\vec{x}$ and $\vec{c} = A\vec{e}$, that has the simple solution

$$y_i = c_i d_i. \quad (29.15)$$

The least-squares fit is thus reformulated in terms of uncorrelated linear combinations. The orthogonal parameters y_i are linear combinations of the Hamiltonian parameters x_i , with associated errors d_i . It is clear from Eq. (29.15) that, for large d_i , the values of y_i are strongly affected by a small change in the data c_i . Therefore, such linear combinations are only poorly determined by a given set of data. We can separate poorly determined linear combinations from well-determined ones by setting a certain criterion on the magnitude of the corresponding eigenvalues d_i .

The fitting procedure can be modified as follows. We start with the best available Hamiltonian \vec{x}^s . From the fit, mutually-independent linear combinations y_i are determined according to Eq. (29.15). At the same time linear combinations of the starting Hamiltonian \vec{x}^s are also obtained by $\vec{y}^s = A\vec{x}^s$. Then new linear combinations \vec{y}^a are defined by adopting only well-determined values of y_i and using the starting values for the rest,

$$y_i^a = y_i(d_i \leq \delta) + y_i^s(d_i > \delta), \quad (29.16)$$

where δ is taken to be a suitable value for the criterion. The number of well-determined linear combinations is denoted by N_d . A new Hamiltonian is obtained by $\vec{x}^a = A^{-1}\vec{y}^a$, which is used for the next iteration to obtain $\vec{x}^b = A^{-1}\vec{y}^b$ from

$$y_i^b = y_i(d_i \leq \delta) + y_i^s(d_i > \delta), \quad (29.17)$$

This procedure is iterated until convergence.

29.4.2 Results for the *sd* shell

For the data set we consider all ground-state binding energies and all positive-parity energy levels for sd-shell nuclei. The first criterion for inclusion of the n th J^π level in the fit is whether or not the J^π for all lower states are known. Generally this means that we cannot consider states above the energy where one level has an unknown J^π . This usually occurs starting at $E_x = 5\text{--}7$ MeV. The second criterion is the energy at which the experimental level density for a given J^π becomes suddenly higher than the theoretical level density. This is a signature of intruder states. There is a well-defined region of nuclei with $N = 19 - 20$ and $Z = 10 - 12$ where the difference between the experimental and theoretical ground-state binding energies is much larger than the rms average. These nuclei are in the island-of-inversion that requires the explicit extension of the *pf* shell orbits to the model space [24]. Ground and excited states for these six nuclei are not included in the fit. In the end we will show the comparison of all experimental levels to all theoretical levels.

With this selection we are able to consider 608 states in 77 nuclei with errors of less than 0.2 MeV (most experimental errors are 10 keV or less) [9]. The uncertainty used in Eq.

(29.6) is the experimental uncertainty σ_{exp} folded quadratically with a theoretical error that is close to the rms value obtained in the best fit for which we take $\sigma_{\text{th}} = 0.1$ MeV

$$(\sigma^k)^2 = (\sigma_{\text{exp}}^k)^2 + (\sigma_{\text{th}}^k)^2. \quad (29.18)$$

We include ground-state binding energies in the fit directly in terms of their calculated E and β values. Excited states are included in the fit by taking the differences $E - E_{gs}$ and $\beta - \beta_{gs}$. This allows for states in exotic nuclei to be included where the $E - E_{gs}$ is known more accurately (for example, from gamma-ray transitions) than E_{gs} .

As was done for USD, the single-particle energies (SPE) are taken to be constant (mass independent). One could add some mass-dependence to the SPE, but it has little effect on the rms since it can be compensated by a change in the TBME (in particular in the monopole TBME combinations).

As was done for USD, we employ a mass dependence of the two-body matrix elements of the form

$$V_{JT}(ab; cd)(A) = \left(\frac{18}{A}\right)^p V_{JT}(ab; cd)(A = 18), \quad (29.19)$$

with $p = 0.3$. This accounts qualitatively for the mass dependence expected from the evaluation of a medium-range interaction with harmonic-oscillator radial wavefunctions. With $\hbar\omega = 41A^{-1/3}$, the matrix elements for a delta-function interaction scale analytically as $A^{1/2}$ and the matrix elements of the Coulomb interaction scale analytically as $A^{1/6}$. The rms of the fit has a shallow minimum near $p = 0.3$. The minimum is shallow because the mass dependence can be partly compensated by a change in the fitted values of the TBME.

The poorly determined linear combinations of Hamiltonian parameters were always constrained to the values obtained from the renormalized G matrix applied to the sd shell (RGSD). The calculations were based on the Bonn-A NN potential and include diagrams up to third-order as well as folded diagrams. The TBME are given in Table 20 of [44].

For the present work the original USD Hamiltonian was used for the first iteration. Then the equations were iterated with $N_d = 30$ well-determined (varied) linear combinations with the remaining 36 poorly-determined linear combinations set to the RGSD values. This was continued until the energies and \vec{x} values converged to the level of about 10 keV. This rather highly constrained Hamiltonian is called USDA. In Fig. (29.1) we show the eigenvalues

D_i of the fit matrix for USDA. A physically interesting quantity from the fit is the rms deviation between experimental and theoretical energies

$$rms = \sqrt{\frac{1}{N} \sum_{k=1}^N (E_{\text{exp}}^k - E_{\text{th}}^k)^2}. \quad (29.20)$$

In Fig. (29.2) we show this rms deviation (solid line) as a function of the number of varied linear combinations N_d obtained for the final iteration of USDA (the actual USDA corresponds to the results obtained at $N_d = 30$). The individual contributions to Eq. (29.20) are shown in Fig. (29.3). The rms deviation of the fitted and RGSD two-body matrix elements as a function of N_d are shown by the points connected by a dashed line in Fig. (29.2).

The motivation for 30 linear combinations can be seen in Fig. (29.2). One observes a plateau in the rms energy deviation of about 170 keV between 30 and 45 linear combinations. Beyond this there is a gradual drop until about 56 linear combinations with an rms deviation of 130 keV that does not significantly decrease going out to the full set of 66 combinations.

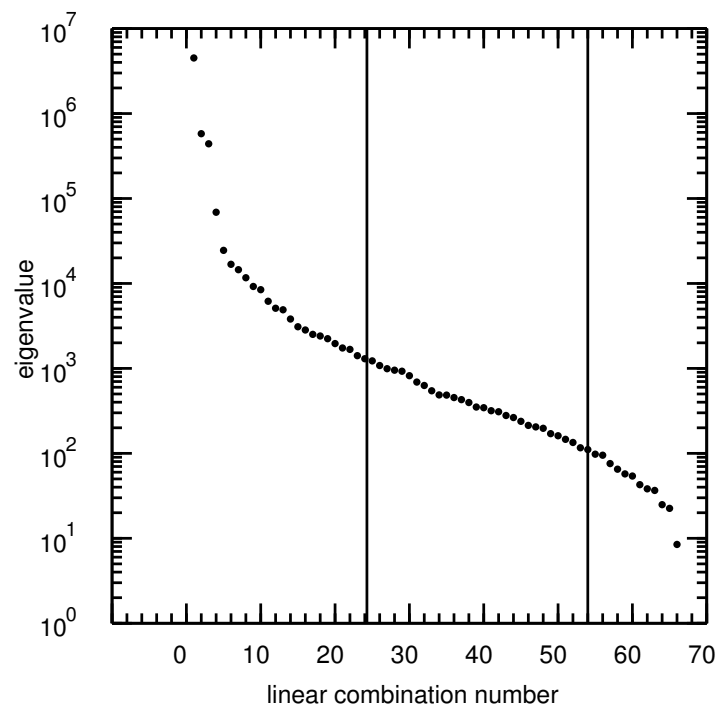


Figure 29.1: Eigenvalues D_i of the fit matrix.

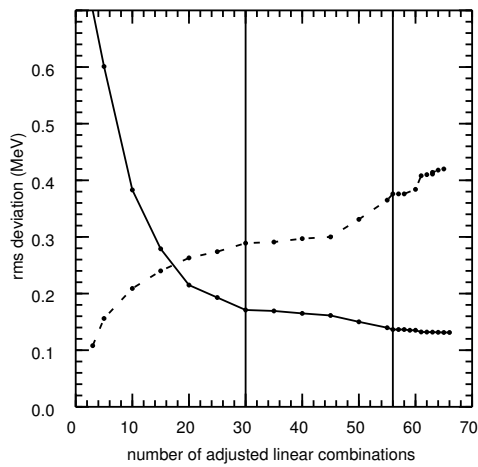


Figure 29.2: Rms deviations as a function of the number of fitted linear combinations for the final USDA iteration. The points connected by a line shows the deviation between experimental and theoretical sd-shell energies. The points connected by a dashed line shows the rms deviation between the two-body matrix elements for the USD and RGSD Hamiltonians.

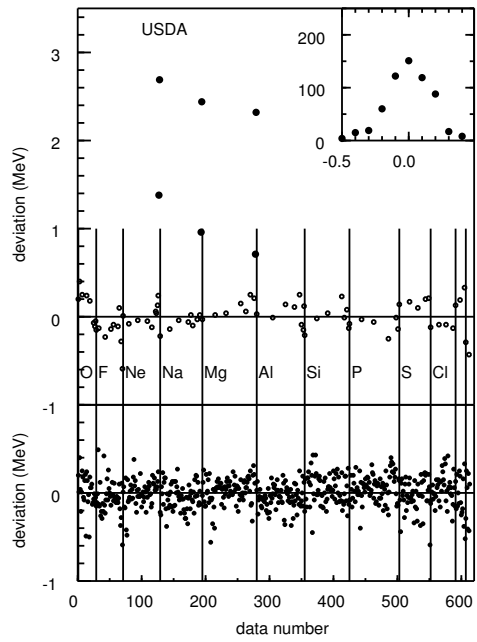


Figure 29.3: Deviations between experimental and theoretical energies for USDA. The ground-state binding energies are plotted in the top and the excitation energies in the bottom. The inset shows a histogram of the deviations binned over 100 keV intervals.

Thus we also derive another Hamiltonian called USDB by varying 56 linear combinations of parameters. Three more iterations were required for convergence. As seen in the histogram in the upper right-hand corners of Fig. (29.3) the scatter between experiment and theory for USDB is systematically reduced compared to that for USDA. We include in Fig. (29.3) six data points not included in the fit, those for the ground states of $^{29,30}\text{Ne}$, $^{30,31}\text{Na}$ and $^{31,32}\text{Mg}$ to show the large deviation for these nuclei in the island of inversion. The TBME for $A = 18$ are given in Tables I and II for $T = 1$ and $T = 0$, respectively. The TBME for other A values is given by Eq. (29.19).

The theoretical relative binding energies and spectra for all sd shell nuclei are compared to experiment in [45] (USDA) and [46] (USDB).

Bibliography

- [1] B. H. Wildenthal, Prog. Part. Nucl. Phys. **11**, 5 (1984).
- [2] W. E. Ormand and B. A. Brown, Nucl. Phys. **A491**, 1 (1989).
- [3] W. E. Ormand and B. A. Brown, Nucl. Phys. **A440**, 274 (1985).
- [4] W. E. Ormand and B. A. Brown, Phys. Lett. B **174**, 128 (1986).

- [5] A. de Shalit and I. Talmi, *Nuclear Shell Theory*, (Academic Press, 1963).
- [6] W. Kutschera, B. A. Brown and K. Ogawa, La Rivista del Nuovo Cimento **11**, 1 (1978).
- [7] A. Arima, S. Cohen, R. D. Lawson and M. H. MacFarlane, Nucl. Phys. **A108**, 94 (1968).
- [8] W. Chung, Pd. D. thesis, Michigan State University (1976).
- [9] B. A. Brown and W. A. Richter, Phys. Rev. C **74**, 034315 (2006). link
- [10] M. Honma, T. Otsuka, B.A. Brown and T. Mizusaki, Phys. Rev. C **65**, 061301(R) (2002). link
- [11] A. Poves and A. P. Zuker, Phys. Rep. **70**, 235 (1981).
- [12] A. Poves, J. Sanchez-Solano, E. Caurier and F. Nowacki, Phys. Rev. C, to be published.
- [13] B. A. Brown, W. A. Richter, R. E. Julies and B. H. Wildenthal, Ann. Phys. **182**, 191 (1988).

- [14] A. G. M. van Hees and P. W. M. Glaudemans, Z. Phys. **A315**, 223 (1984).
- [15] I. Talmi, Helv. Phys. Acta **25**, 185 (1952).
- [16] S. Cohen and D. Kurath, Nucl. Phys. **73**, 1 (1965), Nucl. Phys. **A101**, 1 (1967).
- [17] R. E. Julies, W. A. Richter and B. A. Brown, South African Jour. Phys. **15**, 35 (1992).
- [18] E. K. Warburton and B. A. Brown, Phys. Rev. C **46**, 923 (1992). link
- [19] J. B. McGrory, Phys. Rev. C **8**, 693 (1973). link
- [20] W. A. Richter, M. G. Van der Merwe, R. E. Julies and B. A. Brown, Nucl. Phys. **A523**, 325 (1991).
- [21] M. Honma, T. Otsuka, B.A. Brown and T. Mizusaki, Euro. Phys. Jour. A **25** Suppl. 1, 499 (2005).
- [22] D. J. Millener and D. Kurath, Nucl. Phys. **A255**, 315 (1975).

- [23] E. K. Warburton, J. A. Becker, D. J. Millener and B. A. Brown, BNL report 40890 (1987).
- [24] E. K. Warburton, J. A. Becker, and B. A. Brown, Phys. Rev. C **41**, 1147 (1990). link
- [25] J. Retamosa, E. Caurier, F. Nowacki and A. Poves, Phys. Rev. C **55**, 1266 (1997). link
- [26] Y. Utsuno, T. Otsuka, T. Mizusaki and M. Honma, Phys. Rev. C **60**, 054315 (1999). link
- [27] D. J. Dean, M. T. Ressell, M. Hjorth-Jensen, S. E. Koonin, and A. P. Zuker, Phys. Rev. C **59**, 2474 (1999). link
- [28] F. Nowacki and A. Poves, Phys. Rev. C **79**, 014310 (2009). link
- [29] M. Honma, T. Otsuka, T. Mizusaki and M. Hjorth-Jensen, Phys. Rev. C **80**, 064323 (2009). link
- [30] A. F. Lisetskiy, B. A. Brown, M. Horoi and H. Grawe, Phys. Rev. C **70**, 044314 (2004). link

- [31] D. Verney et al., Phys. Rev. C **76**, 054312 (2007). link
- [32] K. T. Flanagan et al., Phys. Rev. C **82**, 041302(R) (2010). link
- [33] A. Gade et al., Phys. Rev. C **81**, 064326 (2010). link
- [34] B. Cheal, Phys. Rev. Lett. **104**, 252502 (2010). link
- [35] P. Vingerhoets et al., Phys. Rev. C **82**, 064311 (2010). link
- [36] A. D. Becerril et al., Phys. Rev. C **84**, 041303(R) (2011). link
- [37] S. J. Q. Robinson, L. Zamick and Y. Y. Sharon, Phys. Rev. C **83**, 027302 (2011). link
- [38] D. Verney et al., Phys. Rev. C **87**, 054307 (2013). link
- [39] B. A. Brown, D. L. Fang and M. Horoi, Phys. Rev. C **92**, 041301(R) (2015). link
- [40] A. C. Dombos et al., Phys. Rev. C **93**, 064317 (2016). link
- [41] F. Recchia et al., Phys. Rev. C **94**, 054324 (2016). link

- [42] M. Honma, private communication.
- [43] P. R. Bevington and D. K. Robinson, “Data Reduction and Error Analysis”, Third Edition, (McGraw Hill, 2003).
- [44] M. Hjorth-Jensen, T. T. S. Kuo and E. Osnes, Phys. Rep. **261**, 125 (1995).
- [45] <https://people.nscl.msu.edu/brown/resources/usd-05ajpg/SDE.HTM>
- [46] <https://people.nscl.msu.edu/brown/resources/usd-05bjpg/SDE.HTM>

Chapter 30

Energies for simple configurations (monopole energies)

30.1 Interaction energies for closed shell, one-particle and one-hole configurations

The total energy for a single Slater determinant in the M -scheme is the sum of kinetic energy and interaction energy contributions.

$$E = E_K + E_I, \quad (30.1)$$

where the kinetic energy is

$$E_K = \sum_{\alpha} \langle \alpha | T | \alpha \rangle, \quad (30.2)$$

and the interaction energy is

$$E_I = \frac{1}{2} \sum_{\alpha, \beta} \langle \alpha\beta | V | \alpha\beta \rangle. \quad (30.3)$$

In this section we will derive the interaction energies for the closed-shell and closed-shell plus-or-minus one-particle configurations in terms of the J -coupled two-body matrix

elements. For a closed shell the sum runs over all of the filled states labeled by (k, m) , where k stands for (n_r, ℓ, j) . In terms of explicit sums over the k orbits the kinetic energy is

$$E_K(C) = \sum_{k_a, m_a} \langle k_a m_a | T | k_a m_a \rangle = \sum_{k_a} N_a \langle k_a | T | k_a \rangle, \quad (30.4)$$

where the factor of

$$N_a = (2j_a + 1) \quad (30.5)$$

comes from the number of degenerate m_a states that have the same kinetic energy. The interaction energy is

$$E_I(C) = \frac{1}{2} \sum_{k_a, k_b, m_a, m_b} \langle k_a m_a k_b m_b | V | k_a m_a k_b m_b \rangle. \quad (30.6)$$

We can replace the M -scheme two-body matrix element with the with a sum over J couple matrix elements:

$$E_I(C) = \frac{1}{2} \sum_{k_a, k_b, m_a, m_b} [1 + \delta_{k_a, k_b}] \sum_{JM J' M'} \langle JM | j_a m_a j_b m_b \rangle \langle J' M' | j_a m_a j_b m_b \rangle$$

$$\times \langle k_a k_b J | V | k_a k_b J \rangle . \quad (30.7)$$

With $\sum_{m_a, m_b} \langle JM | j_a m_a j_b m_b \rangle \langle J' M' | j_a m_a j_b m_b \rangle = \delta_{J,J'} \delta_{M,M'}$ this becomes:

$$E_I(C) = \frac{1}{2} \sum_{k_a, k_b} [1 + \delta_{k_a, k_b}] \sum_{JM} \langle k_a k_b J | V | k_a k_b J \rangle . \quad (30.8)$$

Note that $\frac{1}{2} \sum_{k_a, k_b} [1 + \delta_{k_a, k_b}]$ is equivalent to $\sum_{k_a \leq k_b}$. Also $\langle V \rangle$ does not depend on M and there are $(2J+1)$ values of M . Thus we have

$$E_I(C) = \sum_{k_a \leq k_b} \sum_J (2J+1) \langle k_a k_b J | V | k_a k_b J \rangle . \quad (30.9)$$

The average (monopole) interaction energy between two k orbits is defined as:

$$\bar{V}_{k_a k_b} = \frac{\sum_J (2J+1) \langle k_a k_b J | V | k_a k_b J \rangle}{\sum_J (2J+1)} . \quad (30.10)$$

When $k_a \neq k_b$ we have

$$\Sigma_J(2J+1) = N_a N_b, \quad (30.11)$$

where $N = (2j + 1)$ is the filled shell orbit occupancy. When both particles are in the same orbit k_a , then $\Sigma_J(2J+1) = N_a(N_a - 1)/2$, that represents the number of two-body interactions for the particles within orbit k_a . In terms of these average interactions the total closed-shell interaction energy is:

$$E_I(C) = \sum_{k_a} \frac{N_a(N_a - 1)}{2} \bar{V}_{k_a k_a} + \sum_{k_a < k_b} N_a N_b \bar{V}_{k_a k_b}, \quad (30.12)$$

where $N = (2j + 1)$.

We can use these average interactions to calculate the energy associated with one-hole and one-particle configurations. Thus for one-particle in orbit k_i outside the closed-shell we sum over the average interactions with the filled orbits k_a multiplied by the total number of particles $N_a = (2j_a + 1)$ in that orbit:

$$\epsilon_{k_i} = E(C | k_i) - E(C) = \langle k_i | T | k_i \rangle + \sum_{k_a} N_a \bar{V}_{k_a, k_i}. \quad (30.13)$$

For one hole in orbit k_i the result is:

$$\epsilon_{k_i} = E(C) - E(C k_i^{-1}) = \langle k_i | T | k_i \rangle + (N_i - 1) \bar{V}_{k_i, k_i} + \sum_{k_a \neq k_i} N_a \bar{V}_{k_a, k_i}, \quad (30.14)$$

where the factor in front of the \bar{V}_{k_i, k_i} term is the difference between the total number of interactions for the filled shell, $N_a(N_a - 1)/2$, and the total number of interactions for a filled shell minus one particle, $(N_a - 1)(N_a - 2)/2$.

When isospin is included the number of nucleons in the filled shell becomes:

$$N'_a = (2t + 1)(2j_a + 1) = 2(2j_a + 1), \quad (30.15)$$

where $t = 1/2$. The closed-shell kinetic energy is:

$$E_K(C) = \sum_{k_a, m_a} \langle k_a m_a | T | k_a m_a \rangle = \sum_{k_a} N'_a \langle k_a | T | k_a \rangle, \quad (30.16)$$

the closed-shell interaction energy is:

$$E_I(C) = \sum_{k_a \leq k_b} \sum_{J, T} (2T + 1)(2J + 1) \langle k_a k_b J T | V | k_a k_b J T \rangle, \quad (30.17)$$

the average interaction is:

$$\bar{V}_{k_a k_b} = \frac{\sum_{JT} (2J+1)(2T+1) \langle k_a k_b JT | V | k_a k_b JT \rangle}{\sum_{JT} (2J+1)(2T+1)}, \quad (30.18)$$

the total interaction energy is:

$$E_I(C) = \sum_{k_a} \frac{N'_a(N'_a - 1)}{2} \bar{V}_{k_a k_a} + \sum_{k_a < k_b} N'_a N'_b \bar{V}_{k_a k_b}, \quad (30.19)$$

the single-particle energy is:

$$\epsilon_{k_i} = \langle k_i | T | k_i \rangle + \sum_{k_a} N'_a \bar{V}_{k_a, k_i}, \quad (30.20)$$

and the single-hole energy is:

$$\epsilon_{k_i} = \langle k_i | T | k_i \rangle + (N'_i - 1) \bar{V}_{k_i, k_i} + \sum_{k_a \neq k_i} N'_a \bar{V}_{k_a, k_i}. \quad (30.21)$$

Table 30.1: Values of the some V_{lowk} and Coulomb two-body matrix elements used in this section. The orbits are labeled by $k = 1$ for $0s_{1/2}$, $k = 2$ for $0p_{3/2}$, $k = 3$ for $0p_{1/2}$, and $k = 4$ for $0d_{5/2}$. The average values is the $(2J + 1)(2T + 1)$ monopole weighted value.

k_1	k_2	k_3	k_4	$J\ T$	V_{lowk}	V_{coul}
1	1	1	1	1 0	-7.86	
	1	1	1	0 1	-6.72	0.67
				average	-7.29	0.67
1	2	1	2	1 0	-1.07	
	1	2	1	2 0	-7.86	
	1	2	1	1 1	-3.80	0.59
	1	2	1	2 1	-1.00	0.44
				average	-2.87	0.50
1	3	1	3	0 0	-7.86	
	1	3	1	1 0	-4.47	
	1	3	1	0 1	-1.88	0.44
	1	3	1	1 1	-0.88	0.52
				average	-2.18	0.50
2	2	2	2	1 0	-1.39	
	2	2	2	3 0	-3.95	
	2	2	2	0 1	-3.30	0.56
	2	2	2	2 1	-1.37	0.47
				average	-2.22	0.48
2	3	2	3	1 0	-5.54	
	2	3	2	2 0	-5.05	
	2	3	2	1 1	-0.53	0.44
	2	3	2	2 1	-2.50	0.49
				average	-2.63	0.47
3	3	3	3	1 0	-2.26	
	3	3	3	0 1	-0.63	0.50
				average	-1.44	0.50
4	4	4	4	1 0	-0.28	
	4	4	4	3 0	-0.72	
	4	4	4	5 0	-2.94	
	4	4	4	0 1	-1.79	
	4	4	4	2 1	-1.15	
	4	4	4	4 1	-0.51	

As an example, we can calculate the interaction energy for ^{16}O with the matrix elements of the low- k NN interaction derived by Bogner et al. [1] (the sum of the central, spin-orbit and spin-tensor terms). We take oscillator potential with $\hbar\omega=14$ MeV provides an approximation to the Hartree-Fock potential. The required two-body matrix elements are given in Table 1. The total sum from Eq. (30.17) is $E_I = -325.3$ MeV. The total kinetic energy is $E_K = 18\hbar\omega = 252$ MeV. We should also subtract the center-of-mass kinetic energy $E_K(cm) = \frac{3}{2}\hbar\omega = 21$ MeV. Finally we can add the total Coulomb energy by using Eq. (30.9) to sum the proton-proton two-body matrix elements of the Coulomb interaction to get $E(\text{coul}) = 13.8$ MeV. (The proton-proton matrix elements are given by the $T = 1$ Coulomb matrix elements in Table 1.) Thus the total energy is:

$$\begin{aligned} E &= E_I + E_K - E_K(cm) + E(\text{coul}) = \\ &= -325.3 + 252 - 21 + 13.8 \text{ MeV} = -80.5 \text{ MeV}. \end{aligned} \quad (30.22)$$

This should be compared with the experimental value of $E = -BE = -127.6$ MeV. That is, an difference of 58 MeV (corresponding to 18% in $E_I(\text{low } k)$). To do better we need to include configurations beyond the closed-shell such as two-particle two-hole admixtures. Also three-body interactions should be added.

One can also use the two-body matrix elements from Table 1 to obtain the single-hole energies for $0s_{1/2}$, $0p_{3/2}$ and $0p_{1/2}$. For example, for the $0p_{1/2}$ we would use Eq. (30.21) with $\bar{V}_{33} = -1.44$ MeV, $\bar{V}_{23} = -2.63$ MeV, and $\bar{V}_{13} = -2.18$ MeV to get $3\bar{V}_{33} + 8\bar{V}_{23} + 4\bar{V}_{13} = -34.1$ MeV for the interaction energy. The kinetic energy is $\frac{5}{4}\hbar\omega = 17.5$ MeV and the single-hole energy from the sum is -16.58 MeV. This is not too far from the experimental value of $\epsilon_n = -[\text{BE}(^{16}O) - \text{BE}(^{15}O)] = -15.66$ MeV for the neutron.

To get the $0p_{1/2}$ proton single-hole energy we would also include the contribution from the Coulomb interaction between protons. From Eq. (30.14) and Table 1 this is $(0.50) + 4(0.47) + 2(0.50) = 3.38$ MeV (for the sum over $0p_{1/2}$, $0p_{3/2}$ and $0s_{1/2}$, respectively). The proton $0p_{1/2}$ hole energy is thus $-16.58 + 3.38 = -13.20$ MeV compared to the experimental value of $\epsilon_p = -[\text{BE}(^{16}O) - \text{BE}(^{15}N)] = -12.13$ MeV. Finally we could also compare the calculated value for $\epsilon_p - \epsilon_n = 3.38$ MeV (just the Coulomb energy term) with the experimental value of 3.54 MeV.

30.2 Interaction energies for diagonal two-particle configurations

The diagonal matrix element of the Hamiltonian for two-particles outside of a closed shell is:

$$E(C+2) = \langle C\alpha\beta | H | C\alpha\beta \rangle = E(C) + \epsilon_\alpha + \epsilon_\beta + \langle \alpha\beta | V | \alpha\beta \rangle, \quad (30.23)$$

where C represents all of the orbitals in the closed shell, and where ϵ are interpreted in Hartree-Fock theory as the single-particle energies for a single-particle outside the closed shell. In the M -scheme the α and β could be in two different m values in the same $k = (n_r, \ell, j)$ orbital or in two different orbitals k_a and k_b . It is useful to define an energy relative to that of the closed shell:

$$\Delta E = E(C+2) - E(C) = \epsilon_\alpha + \epsilon_\beta + \langle \alpha\beta | V | \alpha\beta \rangle, \quad (30.24)$$

In the J -scheme with both particles in the same k orbit we would have:

$$\Delta E = E(C+2) - E(C) = 2\epsilon_k + \langle k^2 J | V | k^2 J \rangle. \quad (30.25)$$

For example, as a model for ^{18}O we could use Eq. (30.25) with the observed single-particle energy of the lowest $5/2^+$ state in ^{17}O .

$$\epsilon_{0d_{5/2}} = -[\text{BE}(^{17}\text{O}) - \text{BE}(^{16}\text{O})] = -4.14 \text{ MeV} \quad (30.26)$$

For two neutrons in $j = 5/2$ we can have $J = 0, 2$ and 4 . If we take the lowest states with these spins in ^{18}O (the 2^+ and 1.98 MeV and the 4^+ at 3.55 MeV) has having these configurations we have from the experimental binding energies:

$$\Delta E_{exp}(0^+) = -[\text{BE}(^{18}\text{O}), 0^+] - \text{BE}(^{16}\text{O})] = -12.19 \text{ MeV},$$

$$\Delta E_{exp}(2^+) = -[\text{BE}(^{18}\text{O}), 2^+] - \text{BE}(^{16}\text{O})] = -10.21 \text{ MeV},$$

and

$$\Delta E_{exp}(4^+) = -[\text{BE}(^{18}\text{O}), 4^+] - \text{BE}(^{16}\text{O})] = -8.64 \text{ MeV}. \quad (30.27)$$

These can be compared to those calculated with the experimental single-particle energy of -4.14 MeV and the theoretical two-body matrix elements from Table 1:

$$\Delta E_{th}(0^+) = 2(-4.14) - 1.79 = -10.07 \text{ MeV},$$

$$\Delta E_{th}(2^+) = 2(-4.14) - 1.15 = -9.43 \text{ MeV},$$

and

$$\Delta E_{th}(4^+) = 2(-4.14) - 0.51 = -8.79 \text{ MeV}. \quad (30.28)$$

The deviation between experiment and theory is largest for $J = 0$. This difference is mainly due to mixing with other configurations as will be discussed in the next section.

This simple model for two-particles in one orbit outside of a closed shell works best when that one orbit is isolated in energy from the others. The best examples of these $T = 1$ two-particle spectra are found in ^{50}Ti for two $0f_{7/2}$ protons outside of ^{48}Ca , ^{92}Mo for two $0g_{9/2}$ protons outside of ^{90}Zr and ^{210}Po for two $0h_{9/2}$ protons outside of ^{208}Pb .

In this one-orbit approximation, we can use the equations to deduce “experimental” values for the ($T = 1$) two-body matrix elements:

$$\begin{aligned} < k^2 J | V | k^2 J >_{exp} &= [E(C+2) - E(C)] - 2\epsilon \\ &= [E(C+2) - E(C)] - 2[E(C+1) - E(C)] \end{aligned}$$

$$= -[\text{BE}(C+2) - \text{BE}(C)] + 2[\text{BE}(C+1) - \text{BE}(C)]. \quad (30.29)$$

In the example for ^{18}O

$$\begin{aligned} <(0d_{5/2})^2J=0 | V | (0d_{5/2})^2J=0>_{exp} &= -3.91 \text{ MeV}, \\ <(0d_{5/2})^2J=2 | V | (0d_{5/2})^2J=2>_{exp} &= -1.93 \text{ MeV}, \end{aligned}$$

and

$$<(0d_{5/2})^2J=4 | V | (0d_{5/2})^2J=4>_{exp} = -0.36 \text{ MeV}. \quad (30.30)$$

These can be compared to the theoretical values of -1.79, -1.15 and -0.51 MeV, respectively.

30.3 Interaction energies for diagonal two-hole configurations

The diagonal matrix element of the Hamiltonian for two-holes relative to a closed shell is:

$$E(C-2) = < C\alpha^{-1}\beta^{-1} | H | C\alpha^{-1}\beta^{-1} > = E(C) - \epsilon_\alpha - \epsilon_\beta + < \alpha\beta | V | \alpha\beta >, \quad (30.31)$$

where C represents all of the orbitals in the closed shell, and where ϵ are interpreted in Hartree-Fock theory as the single-particle energies for the one-hole configuration. The energy relative to that of the closed shell is:

$$\Delta E = E(C - 2) - E(C) = -\epsilon_\alpha - \epsilon_\beta + \langle \alpha\beta | V | \alpha\beta \rangle, \quad (30.32)$$

The formalism for two-holes is identical to that of two-particles except for the sign in front of ϵ . This result can be generalized to many holes; the formalism for n holes is the same as that for n particles except for the sign in front of ϵ .

In the J -scheme for two holes in the same orbit:

$$\Delta E = E(C - 2) - E(C) = -2\epsilon_k + \langle k^2 J | V | k^2 J \rangle. \quad (30.33)$$

A comparison of Eqs. (30.25) and (30.33) shows that the energy spectra for the hole configuration is the same as that of the particle configuration, as long as the two-body matrix elements are the same. Experimental values for the two-body matrix elements can be derived for the properties of the hole nuclei by:

$$\langle k^2 J | V | k^2 J \rangle_{exp} = [E(C - 2) - E(C)] + 2\epsilon$$

$$\begin{aligned} &= [E(C-2) - E(C)] + 2[E(C) - E(C-1)] \\ &= [\text{BE}(C) - \text{BE}(C-2)] - 2[\text{BE}(C) - \text{BE}(C-1)]. \end{aligned} \quad (30.34)$$

One of best examples can be found in the nucleus ^{54}Fe with two holes in the $0f_{7/2}$ orbit relative to a closed shell for ^{56}Ni .

Bibliography

- [1] S. Bogner, T. T. S. Kuo, L. Coraggio, A. Covello and N. Itaco, Phys. Rev. C 65, 051130(R) (2002). link

Chapter 31

Configuration mixing

31.1 General two-state mixing

739

Consider the mixing of two states. The Hamiltonian is represented by a symmetric matrix with the diagonal terms, H_{11} and H_{22} , and an off diagonal term H_{12}

$$\begin{bmatrix} H_{11} & H_{12} \\ H_{21} & H_{22} \end{bmatrix}. \quad (31.1)$$

We will assume that the matrix is arranged such that:

$$H_{11} < H_{22} \dots,$$

e.g. H_{11} is the lowest diagonal energy. The eigenvalues E for this two-by-two matrix are given by the two solutions of the quadratic equation obtained from determinant $|H - E|$:

$$E_{1/2} = \frac{1}{2} \left[H_{22} + H_{11} \pm \sqrt{(H_{22} - H_{11})^2 + 4H_{12}^2} \right]. \quad (31.2)$$

The subscripts 1(2) indicate the eigenstates that are associated with $\Phi_{1(2)}$ when $H_{12} = 0$. We can write the energies as:

$$E_1 = H_{11} - \delta,$$

and

$$E_2 = H_{22} + \delta, \quad (31.3)$$

where

$$\delta = \frac{1}{2} \left[\sqrt{(H_{22} - H_{11})^2 + 4H_{12}^2} - (H_{22} - H_{11}) \right], \quad (31.4)$$

where $\delta > 0$. In terms of δ the eigenfunctions are given by:

$$|\Psi_1\rangle = \frac{1}{N} [|\Phi_1\rangle - (\delta/H_{12}) |\Phi_2\rangle],$$

and

$$|\Psi_2\rangle = \frac{1}{N} [|\Phi_2\rangle + (\delta/H_{12}) |\Phi_1\rangle], \quad (31.5)$$

with normalization:

$$N^2 = 1 + (\delta/H_{12})^2$$

Note that $-|\Psi_i\rangle$ are also eigenstates. Thus there are “random” phase factors in the wave functions that must be kept consistent throughout the calculations of physical observables (which always involve a given wavefunction twice).

It is useful to look at various limits of these results. When the states start out degenerate $H_{11} = H_{22}$, then $\delta = H_{12}$, and the states are repelled to have a total separation energy of $E_2 - E_1 = 2\delta$, and the eigenstates are equal mixtures of the basis states $|\Phi_1\rangle$ and $|\Phi_2\rangle$.

When the diagonal separation energy is large compared to off-diagonal matrix element; $H_{22} - H_{11} \gg |H_{12}|$, then

$$\begin{aligned} E_1 &= H_{11} - \delta \approx H_{11} - \frac{H_{12}^2}{H_{22} - H_{11}}, \\ E_2 &= H_{22} + \delta \approx H_{22} + \frac{H_{12}^2}{H_{22} - H_{11}}, \end{aligned} \quad (31.6)$$

$$\begin{aligned} |\Psi_1\rangle &\approx |\Phi_1\rangle - \frac{H_{12}}{H_{22} - H_{11}} |\Phi_2\rangle, \\ |\Psi_2\rangle &\approx |\Phi_2\rangle + \frac{H_{12}}{H_{22} - H_{11}} |\Phi_1\rangle, \end{aligned} \quad (31.7)$$

where the normalization in the wavefunction is ignored since the last term is small. These are equivalent to the perturbation theory results given in Eq. 9.13 and 9.15, respectively.

When $H_{12} = 0$ the eigenstates start out at energies of H_{11} and H_{22} and as H_{12} is turned on the states repel each other by an additional amount 2δ .

31.2 Two-state mixing for ^{18}O

In ^{17}O one observes that the $1s_{1/2}$ orbit lies only 0.87 MeV above the $0d_{5/2}$ ground state. Thus both of these orbits should be considered for the two-particle configuration in ^{18}O . For $J^\pi = 0^+$ we take the two J -coupled basis states:

$$|\Phi_1\rangle = |C, aa J\rangle = |C, (0d_{5/2})^2 J\rangle,$$

and

$$|\Phi_2\rangle = |C, bb J\rangle = |C, (1s_{1/2})^2 J\rangle, \quad (31.8)$$

where C indicates all orbits in the ^{16}O closed shell. The ground state will be a linear combination of these two basis states that are determined by diagonalizing the Hamiltonian

Table 31.1: Values of the some $V(lowk)$ two-body matrix elements used in this section. The orbits are labeled $j = 5$ for $0d_{5/2}$, $j = 3$ for $0d_{3/2}$ and $j = 1$ for $1s_{1/2}$.

j_1	j_2	j_3	j_4	$J\ T$	V_{lowk}
5	5	5	5	0 1	-1.79
5	5	3	3	0 1	-3.47
5	5	1	1	0 1	-0.83
3	3	3	3	0 1	-0.37
3	3	1	1	0 1	-0.68
1	1	1	1	0 1	-2.53
5	5	5	5	2 1	-1.15
5	5	5	3	2 1	-0.44
5	5	5	1	2 1	-0.63
5	5	3	3	2 1	-0.69
5	5	3	1	2 1	-0.60
5	3	5	3	2 1	-0.42
5	3	5	1	2 1	-0.23
5	3	3	3	2 1	-0.87
5	3	3	1	2 1	0.69
5	1	5	1	2 1	-1.27
5	1	3	3	2 1	-0.80
5	1	3	1	2 1	1.51
3	3	3	3	2 1	-0.28
3	3	3	1	2 1	0.07
3	1	3	1	2 1	-0.66
5	5	5	5	4 1	-0.51
5	5	5	3	4 1	-1.09
5	3	5	3	4 1	-2.15

matrix:

$$\begin{bmatrix} \tilde{H}_{11} & \tilde{H}_{12} \\ \tilde{H}_{21} & \tilde{H}_{22} \end{bmatrix}, \quad (31.9)$$

where

$$\tilde{H}_{11} = \langle C, aa J | H | C, aa J \rangle = E(C) + 2\epsilon_a + \langle aa J | V | aa J \rangle,$$

$$\tilde{H}_{22} = \langle C, bb J | H | C, bb J \rangle = E(C) + 2\epsilon_b + \langle bb J | V | bb J \rangle,$$

and

$$\tilde{H}_{12} = \tilde{H}_{21} = \langle C, aa J | H | C, bb J \rangle = \langle aa J | V | bb J \rangle. \quad (31.10)$$

For the off-diagonal matrix element, $\tilde{H}_{21} = \tilde{H}_{12}$, since the matrix is real and hermitian. Since the two basis states differ by the change of two particles between orbits a and b , the only contribution to H_{12} comes from the operator $\sum_{\alpha\beta\gamma\delta} a_\alpha^+ a_\beta^+ a_\gamma a_\delta$ acting to move the two particles between orbits a and b (if H operates on a state other than those in a and b the remaining overlaps of the form $\langle a | b \rangle$ will give zero).

The core energy $E(C)$ appears as a constant in the diagonal of the matrix. Thus we can consider the energies E relative to the closed-shell energy given by the eigenvalues Eq.

(31.1) with

$$H = \tilde{H} - E(C)$$

We can apply these results to the ^{18}O $J^\pi = 0^+$ state by using the experimental single-particle energies:

$$\epsilon_5 = \epsilon_{0d_{5/2}} = -[\text{BE}(^{17}\text{O}, 5/2^+, gs) - \text{BE}(^{16}\text{O}] = -4.14 \text{ MeV},$$

and

$$\epsilon_1 = \epsilon_{1s_{1/2}} = -[\text{BE}(^{17}\text{O}, 1/2^+, 0.87 \text{ MeV}) - \text{BE}(^{16}\text{O}] = -3.27 \text{ MeV}.$$

The basis states for $J = 0$ are:

$$|\Phi_1\rangle = |55J\rangle = |(0d_{5/2})^2 J=0\rangle,$$

and

$$|\Phi_2\rangle = |11J\rangle = |(1s_{1/2})^2 J=0\rangle, \quad (31.11)$$

The single-particle energies together with the low-k two-body matrix elements from Table 1 give the Hamiltonian matrix elements:

$$H_{11} = 2\epsilon_5 + \langle 55J | V | 55J \rangle = 2(-4.14) - 1.79 = -10.07 \text{ MeV}$$

$$H_{22} = 2\epsilon_1 + \langle 11J | V | 11J \rangle = 2(-3.27) - 2.53 = -9.07 \text{ MeV}$$

and

$$H_{12} = \langle 55J | V | 11J \rangle = -0.83 \text{ MeV}, \quad (31.12)$$

The lowest eigenenergy is -10.54 MeV, which is an improvement over the single-orbit ($0d_{5/2}$) result of -10.07 MeV, but still not as low as the experimental value of -12.19 MeV.

31.3 Three-state mixing for ^{18}O

For the 0^+ state the next configuration to consider would be

$$| \Phi_3 \rangle = | 33J \rangle . \quad (31.13)$$

for the $0d_{3/2}$ orbit. If we take the $3/2^+$ state at 5.08 MeV as the single-particle state in ^{17}O , its single-particle energy is:

$$\epsilon_3 = \epsilon_{0d_{3/2}} = -[\text{BE}({}^{17}\text{O}, 3/2^+, 5.08 \text{ MeV}) - \text{BE}({}^{16}\text{O})] = 0.94 \text{ MeV},$$

The Hamiltonian matrix is then a 3x3 matrix of the form:

$$\begin{bmatrix} H_{11} & H_{12} & H_{13} \\ H_{21} & H_{22} & H_{23} \\ H_{31} & H_{32} & H_{33} \end{bmatrix}, \quad (31.14)$$

where in addition to the terms given in Eq. (31.12) we need:

$$H_{33} = 2\epsilon_3 + \langle 33J | V | 33J \rangle = 2(0.94) - 0.37 = 1.51 \text{ MeV},$$

$$H_{13} = \langle 55J | V | 33J \rangle = -3.47 \text{ MeV},$$

and

$$H_{23} = \langle 11J | V | 33J \rangle = -0.68 \text{ MeV}. \quad (31.15)$$

The lowest eigenvalue of the 3x3 matrix is -11.44 MeV, which is close to the experimental value of -12.19 MeV. To get better results we will need to include configurations that will break the closed shell of ^{16}O .

From the matrix elements given in Table 1 we can also consider configuration mixing for $J = 2$. There are five ways to make $J = 2$:

$$|\Phi_1\rangle = |55J\rangle,$$

$$|\Phi_2\rangle = |53J\rangle,$$

$$|\Phi_3\rangle = |51J\rangle,$$

$$|\Phi_4\rangle = |33J\rangle,$$

and

$$|\Phi_5\rangle = |31J\rangle. \quad (31.16)$$

There will be off-diagonal matrix elements in which one-particle is moved from one orbit to another. For example:

$$H_{12} = \langle 55J | V | 53J \rangle. \quad (31.17)$$

Single-particle matrix elements of the kinetic energy (or the Hartree-Fock potential U_{HF}) are non-zero only for the diagonal M -scheme matrix elements of the type $\langle \alpha | T | \alpha \rangle$, and thus can only enter into the diagonal part of the Hamiltonian matrix. Matrix elements of the type, $\langle \alpha | T | \beta \rangle$ with $\alpha \neq \beta$ are zero since the one-body scalar operators cannot change m or j .

31.4 Many-particle configurations

The basic ideas explored in the previous section for the configuration mixing of two particles in the sd model space can be extended to many-particles. We start with a J -coupled basis of the form:

$$\begin{aligned} | n\omega J \rangle &= | [(k_1^{n_1}\omega_1 J_1)(k_2^{n_2}\omega_2 J_2)J_{12}][k_3^{n_3}\omega_3 J_3]J \rangle, \\ | n\omega' J \rangle &= | [(k_1^{n'_1}\omega'_1 J'_1)(k_2^{n'_2}\omega'_2 J'_2)J'_{12}][k_3^{n'_3}\omega'_3 J'_3]J \rangle, \end{aligned} \quad (31.18)$$

where $n = n_1 + n_2 + n_3 = n'_1 + n'_2 + n'_3$. For a given total number of particles n , the distribution n_1, n_2, \dots among the k states is called the partition. The maximum number of particles in one orbit is $n = (2j + 1)$. The ω indices distinguish the various basis states with the same J value.

The diagonal Hamiltonian matrix elements have the form:

$$\langle n\omega J | H | n\omega J \rangle = n_1\epsilon_{k_1} + n_2\epsilon_{k_2} + n_3\epsilon_{k_3} + \sum_i D_i(\omega, \omega, J) \langle V \rangle_i, \quad (31.19)$$

and the off-diagonal matrix elements have the form:

$$\langle n\omega J | H | n\omega' J \rangle = \sum_i D_i(\omega, \omega', J) \langle V \rangle_i. \quad (31.20)$$

The $\langle V \rangle_i$ represent all possible two-body matrix elements in the model space, and the D_i are numerical coefficients obtained from the matrix elements of $\Sigma_{\alpha\beta\gamma\delta} a_\alpha^+ a_\beta^+ a_\gamma a_\delta$. For example if we take the closed-shell configuration:

$$| n\omega J \rangle = | [k_1^{2j_1+1} J = 0] \rangle,$$

then $D_i = (2J' + 1)$ and $V_i = \langle k_1^2 J' | V | k_1^2 J' \rangle$ for the allowed J' values. If we take the two-particle configuration:

$$| n\omega J \rangle = | [k_1^2 J] \rangle,$$

then there is only one non-zero value of D with $D_i = 1$ for $V_1 = \langle k_1^2 J | V | k_1^2 J \rangle$. In general, one must write an M -scheme or a J -scheme shell-model computer code to calculate D_i . If isospin is introduced, then all of the J in the equations are replaced by (J, T) and the maximum number of particles in one orbit is $n = 2(2j + 1)$.

Note that the off-diagonal matrix element does not contain the single-particle energies for the same reasons as discussed in the two-particle example. The off-diagonal matrix element is zero if the set of numbers (n_1, n_2, n_3) differs from (n'_1, n'_2, n'_3) by the change of more than two particles. Thus if the basis states are ordered by their diagonal energy, the matrix will be “banded” with regions off-diagonal regions in which are zero. An example of this banded matrix is shown in Fig. (31.1) for the 0^+ , $T = 0$ levels for 12 particles in the sd-shell ($0d_{5/2}, 0d_{3/2}, 1s_{1/2}$) model space for the nucleus ^{28}Si , where the matrix dimension is 839.

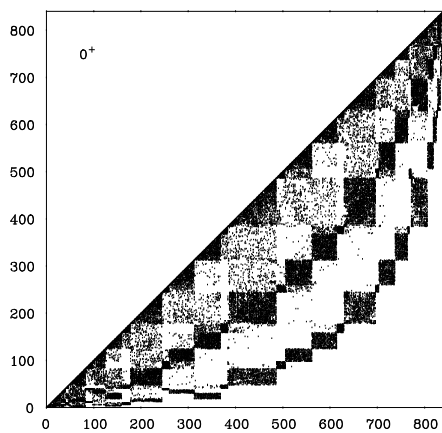


Figure 31.1: The Hamiltonian matrix for the 0^+ , $T = 0$ sd-shell basis in ^{28}Si . The points represent the non-zero matrix elements. The matrix is symmetric and only the bottom half is shown.

For the energy level spectrum I will use the example of the $0^+, T = 0$ states obtained for the nucleus ^{24}Mg with 8 nucleons in the $(0d_{5/2}, 0d_{3/2}, 1s_{1/2})$ model space. For this calculation there are 35 partitions and $\omega_{max} = 325$ basis states. In the sd-shell there are 63 independent (J, T) two-body matrix elements, so the sums over i in Eqs. (31.19) and (31.20) is over 63 terms. The Hamiltonian matrix is shown in Fig. 1 where one observes the bands of zeros corresponding to the regions where the partitions differ by the change of more than two particles.

Fig. (31.2) shows the eigenvalues has a function of the strength of the off-diagonal part of the matrix. 100 percent corresponds to the standard strength. One observes an overall level repulsion with the lowest state decreasing monotonically in energy. The levels never cross but always show a repulsion typical of the two-level mixing model.

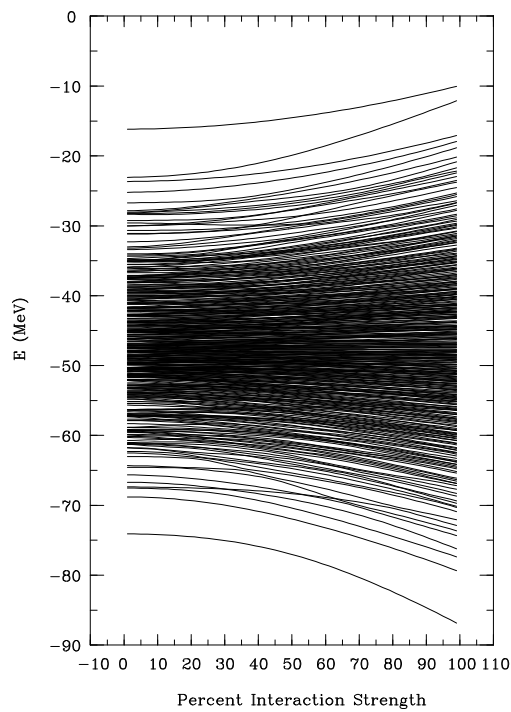


Figure 31.2: The spectrum of 0^+ states in ^{24}Mg as a function of the strength (in percent) of the off-diagonal part of the Hamiltonian matrix.

Chapter 32

Configuration-Interaction Codes

32.1 Types of basis states

For configuration-interaction model calculations we need to;

- (i) select a complete basis,
- (ii) calculate the matrix elements of the Hamiltonian in this basis,
- (iii) find the eigenvalues and eigenvectors of this matrix.

The matrix is symmetric and Hermitian.

There are several ways to specify the basis:

- 1) The $M - pn$ scheme makes a basis that has fixed total M and T_z values. Diagonalization will give all states with $J \geq M$ and $T \geq T_z$. The J values are obtained by comparing $\langle \psi_f | \hat{J}^2 | \psi_i \rangle$ to expected results of $J(J+1)\delta_{fi}$. Isospin is obtained by $\langle \psi_f | \hat{T}^2 | \psi_i \rangle$. If the Hamiltonian conserves isospin, then this will be $T(T+1)\delta_{fi}$. If the Hamiltonian does not conserve isospin then the results will deviate from this and there will be non-zero off-diagonal terms.

- 2) The $J - pn$ scheme makes a basis that has fixed J and T_Z value. The J basis states are linear combinations of M states obtained by applying the J -projection operator to a selected set of M basis states. Diagonalization will give all states $T \geq T_z$.
- 3) The $J - T$ scheme makes a basis that has fixed J and T . The $J - T$ basis states are obtained by applying the $J - T$ projection operator to a selected set of the M, T_z basis states.

The matrix dimension depends on the type of basis. For example, for ^{20}Ne in the sd shell model space there are;

$M - pn$: 640 states with $M = 0$ and $T_z = 0$,

$J - pn$: 46 states with $J = 0$ and $T_z = 0$,

$J - T$: 21 states with $J = 0$ and $T = 0$.

If we only want states with $J = 0$ and $T = 0$, the matrix will be smallest for the $J - T$ basis. But the construction of the matrix is easiest in the $M - pn$ basis. If the Hamiltonian does not conserve isospin then we must use pn basis. Various CI codes have been written to be most efficient for a given type of basis.

The original $M - pn$ code was written by Whitehead et al., [1]. Other codes that use this basis are ANTOINE [2], MFDn [3] and BIGSTICK [4].

The code Oxbash [5] uses the $J - T$ or the $J - pn$ basis. Since the entire matrix is stored, the maximum basis dimension is on the order of 100,000.

The code NuShellX [6] only uses the $J - pn$ basis. For states with both protons and neutrons, dimensions up to about 10^8 can be considered. Details of this code are given in the next section.

32.2 The Lanczos method

We are usually interested in only the lowest n states, where typically $n = 10$. But the dimension d of the matrix H is much larger. All CI codes use a version of what is called the Lanczos method. The Lanczos method is based on the power-iteration method for finding

the eigenfunction for the eigenvalue λ that has the largest absolute value. For nuclear Hamiltonians this is the most negative λ corresponding to the ground state for a given matrix, λ_g with wavefunction $|v_g\rangle$. We start with any vector $|v_0\rangle$ that contains some of $|v_g\rangle$, for example a vector generated by random numbers. (One might also start with the unit vector $(1, 1, 1, \dots)$). But in some cases there might be some eigenfunctions that are orthogonal to this unit vector.) Then multiply this by the matrix and normalize

$$|v_1\rangle = H|v_0\rangle, \quad |v_1\rangle / |\langle v_1 | v_1 \rangle| \rightarrow |v_1\rangle. \quad (32.1)$$

Continue this for k times

$$|v_k\rangle = H|v_{k-1}\rangle \quad (32.2)$$

The $|v_k\rangle$ will converge to $|v_g\rangle$ for $k \ll d$. The reason for this is that $|v_0\rangle$ contains a random linear combination of all of the eigenfunctions, $|u_i\rangle$

$$|v_0\rangle = \sum_{i=1,d} \alpha_i |u_i\rangle, \quad (32.3)$$

with

$$H|u_i\rangle = \lambda_i |u_i\rangle. \quad (32.4)$$

Operating with $(H^k/\lambda_g)^k$ gives

$$(H/\lambda_g)^k | u_0 \rangle = \sum_{i=1,d} \alpha_i (\lambda_i/\lambda_g)^k | u_i \rangle . \quad (32.5)$$

All of the terms with become small except for the one with $i = g$ leaving the (unnormalized) wavefunction $\alpha_g | v_g \rangle$.

The Lanczos method starts with power method and then also generates orthogonal excited states that converge into series of excited state wavefunctions [7]. The procedure is as follows:

1. Start with some initial vector $| v_i \rangle$, for example, one obtained with random numbers in the range of -1 to 1 and normalized.
2. Multiply by the Hamiltonian matrix to get $| w_i \rangle = H | v_i \rangle$.
3. Take the overlap, $\alpha_i = \langle v_i | w_i \rangle$.

4. Orthogonalize against the initial vector, $| w_i \rangle - \alpha_i | v_i \rangle \rightarrow | w_i \rangle$.
5. If $i > 1$ orthogonalize against the prior vector, $| w_i \rangle - \beta_{i-1} | v_{i-1} \rangle \rightarrow | w_i \rangle$.
6. Find the norm to get $\beta_i = \sqrt{\langle w_i | w_i \rangle}$.
7. Normalize to get the next Lanczos vector $| v_{i+1} \rangle = | w_i \rangle / \beta_i$.
8. Repeat this process this process n times until convergence.

Due to round-off errors it is better to replace (4) with an orthogonalization against all previous vectors. This procedure results in an n dimensional symmetric tridiagonal matrix with the α_i as the diagonal and β_i as the off diagonal, e.g.

$$\begin{aligned} H | v_1 \rangle &= \alpha_1 | v_1 \rangle + \beta_1 | v_2 \rangle \\ H | v_2 \rangle &= \beta_1 | v_1 \rangle + \alpha_2 | v_2 \rangle + \beta_2 | v_3 \rangle \\ H | v_3 \rangle &= \beta_2 | v_2 \rangle + \alpha_3 | v_3 \rangle + \beta_3 | v_4 \rangle \end{aligned}$$

continued up to

$$H | v_n \rangle = \beta_{n-1} | v_{n-1} \rangle + \alpha_n | v_n \rangle .$$

The eigenvalues and eigenvectors of this tridiagonal matrix converge to the exact results. Typically 10 states converged to 1 keV accuracy requires about $n = 100$ Lanczos iterations. An example of the convergence in energy for the first 30 states in ^{48}Cr is shown in Fig. (32.1).

32.3 The NuShellX code

NuShellX is a set of computer codes written by Bill Rae. NuShellX@MSU is a set of wrapper codes written by Alex Brown [6]. that use data files for model spaces and Hamiltonians to generate input for NuShell32. The wrapper codes also convert the NuShellX output into figures and tables for energy levels, gamma decay and beta decay.

The NuShellX code uses a proton-neutron basis and a technique similar to that used

for the code NATHAN [8]. The first step is to make a list of partitions with a given set of orbital occupation restrictions for protons (neutrons). Then for each partition the $d(M)$ M states are constructed and stored in terms a string of binary numbers (0 or 1) that give the state occupancy. Then the $D(J)$ J basis states are obtained as linear combinations of these M states using an angular momentum projection operator.

The two-body part of the Hamiltonian is written as a sum of three terms:

$$H = H_{nn} + H_{pp} + H_{pn} \quad (32.6)$$

for the sum of the neutron-neutron (nn), proton-proton (pp) and proton-neutron (pn) interactions. The pp (nn) Hamiltonian matrix elements are calculated for each partition and its connection to all other partitions that differ in not more than two protons (neutrons) being moved between different orbitals.

The second quantized form for H_{pn} is

$$H_{pn} = \sum_{pnp'n', J_o} \langle pnJ_o | V | p'n'J_o \rangle \{ [a_p^+ a_n^+]^{J_o} \otimes [\tilde{a}_{p'} \tilde{a}_{n'}]^{J_o} \}^{(0)}. \quad (32.7)$$

We can recouple the operators to:

$$\begin{aligned} \{[a_p^+ a_n^+]^{J_o} \otimes [\tilde{a}_{p'} \tilde{a}_{n'}]^{J_o}\}^{(0)} &= - \sum_{\lambda} \sqrt{(2\lambda + 1)(2J_o + 1)} (-1)^{j_n + j_{p'} - \lambda - J_o} \\ &\times \left\{ \begin{array}{ccc} j_p & j_n & J_o \\ j_{n'} & j_{p'} & \lambda \end{array} \right\} \times \{[a_p^+ \tilde{a}_{p'}]^{\lambda} \otimes [a_n^+ \tilde{a}_{n'}]^{\lambda}\}^{(0)}, \end{aligned} \quad (32.8)$$

where, for example, p stands for the single-particle wavefunction (n_p, ℓ_p, j_p) . H_{pn} can thus be written in the particle-hole form:

$$H_{pn} = \sum_{pp'nn'\lambda} F_{\lambda}(pp'nn') \{[a_p^+ \tilde{a}_{p'}]^{\lambda} \otimes [a_n^+ \tilde{a}_{n'}]^{\lambda}\}^{(0)}, \quad (32.9)$$

where

$$\begin{aligned} F_{\lambda}(pp'nn') &= - \sum_{J_o} \sqrt{(2\lambda + 1)(2J_o + 1)} (-1)^{n+p'-\lambda-J_o} \\ &\times \left\{ \begin{array}{ccc} p & n & J_o \\ n' & p' & \lambda \end{array} \right\} <pnJ_o | V | p'n'J_o>. \end{aligned} \quad (32.10)$$

The NuShellX basis states have the form:

$$|B_i, J\rangle = |[(J_{p_i}, \alpha_{p_i}) \otimes (J_{n_i}, \alpha_{n_i})]J\rangle \equiv |[P_i \otimes N_i]J\rangle, \quad (32.11)$$

where, P_i stands for labels (J_{p_i}, α_{p_i}) , where J_{p_i} is the proton angular momentum and α_{p_i} are all of the other quantum numbers needed to specify the complete basis. These proton (neutron) basis states can be subdivided into partitions of the protons (neutrons) among the orbitals p . For the Lanczos multiplications we need the matrix elements of H_{pp}

$$\langle B_f, J | H_{pp} | B_i, J \rangle = \delta_{N_f, N_i} \delta_{J_{p_f}, J_{p_i}} \langle P_f | H_{pp} | P_i \rangle, \quad (32.12)$$

H_{nn}

$$\langle B_f, J | H_{nn} | B_i, J \rangle = \delta_{P_f, P_i} \delta_{J_{n_f}, J_{n_i}} \langle N_f | H_{nn} | N_i \rangle, \quad (32.12)$$

and H_{pn}

$$\begin{aligned} \langle B_f, J | H_{pn} | B_i, J \rangle &= \sum_{pp'nn', \lambda} F_\lambda(pp'nn') \langle B_f, J | \{[a_p^+ \tilde{a}_{p'}]^\lambda \otimes [a_p^+ \tilde{a}_{n'}]^\lambda\}^{(0)} | B_i, J \rangle . \\ &= \sum_{pp'nn'\lambda} F_\lambda(pp'nn') \Gamma_\lambda(J_{p_f}, J_{p_i}, J_{n_f}, J_{n_i}, J) \end{aligned}$$

$$\times \text{RDM}(P_f, P_i, p, p', \lambda) \text{ RDM}(N_f, N_i, n, n', \lambda), \quad (32.13)$$

where

$$\Gamma_\lambda(J_{p_f}, J_{p_i}, J_{n_f}, J_{n_i}, J) = \begin{Bmatrix} J_{p_f} & J_{p_i} & \lambda \\ J_{n_f} & J_{n_i} & \lambda \\ J & J & 0 \end{Bmatrix} \quad (32.14)$$

and RDM are the reduced density matrices:

$$\text{RDM}(P_f, P_i, p, p', \lambda) = \langle P_f | [a_p^+ \tilde{a}_{p'}]^\lambda | P_i \rangle, \quad (32.15)$$

and

$$\text{RDM}(N_f, N_i, n, n', \lambda) = \langle N_f | [a_n^+ \tilde{a}_{n'}]^\lambda | N_i \rangle.$$

These RDM are precalculated and stored.

Starting with an initial vector

$$| \omega_i, J \rangle = \sum_{P_i, N_i} A(P_i, N_i, J) \mid [P_i \otimes N_i] J \rangle. \quad (32.16)$$

Multiplying H_{pn} on $|\omega_i, J\rangle$ gives:

$$H_{pn} |\omega_i, J\rangle = |\omega_f, J\rangle = \sum_{P_f, N_f} A'(P_f, N_f, J) |[P_f \otimes N_f]J\rangle, \quad (32.17)$$

with

$$\begin{aligned} A'(P_f, N_f, J) &= \delta_{N_f, N_i} \delta_{J_{p_f}, J_{p_i}} \langle P_f | H_{pp} | P_i \rangle + \delta_{P_f, P_i} \delta_{J_{n_f}, J_{n_i}} \langle N_f | H_{nn} | N_i \rangle, \\ &+ \sum_{\lambda pp' nn'} F_\lambda(pp' nn') \sum_{P_i} \text{RDM}(P_f, P_i, p, p', \lambda) \\ &\times \sum_{N_i} \text{RDM}(N_f, N_i, n, n', \lambda) \Gamma_\lambda(J_{p_f}, J_{p_i}, J_{n_f}, J_{n_i}, J) A(P_i, N_i, J). \end{aligned} \quad (32.18)$$

The Hamiltonian matrix elements are calculated “on-the-fly”. The amount of storage associated with the separate proton and neutron basis and the combined proton-neutron vectors is modest. NuShellX makes use of OpenMP to use many cores with nearly 100% efficiency for the Lanczos iterations. The power of this method is illustrated in Fig. (32.2)

where the J-scheme and M-scheme dimensions for 8 protons and 8 neutrons in the pf model space. The eigenvectors associated with the very large J-scheme combined dimensions are generated from the pre-calculated information on the separate proton and neutron basis states that each have relative small dimensions. The proton and neutron basis states are obtained by J -projection on M -states with the code NuShell. NuShell is a modern Fortran replacement for the original JT projection code Oxbash.

The layout of NuShellX@MSU is shown in Fig. (32.3). NuShellX is surrounded by a wrapper codes that bring in information from a library of previously derived Hamiltonians (bottom left). Or the Hamiltonians may obtained from ab-initio approaches such as those available from the from [9] (top left). At the end the wrapper combines the theoretical energies with the information from the ENSDF files to produce a figure for the comparison between experiment and theory. An example is shown in the figure (32.4) for the levels of ^{57}Fe obtained in the pf model space with the GPFX1A Hamiltonian [10].

As a second step NuShellX takes the overlaps for the operators a^+ , a^+a^+ and a^+a . The wrapper converts these into spectroscopic factors, two-nucleon transfer amplitudes and

one-body transition densities, respectively. The one-body transition densities are then used together with the program DENS to calculate the matrix elements for $M\lambda$, $E\lambda$ and Gamow-Teller (GT) operators. The $M1$ and $E2$ results are used to obtain a gamma-ray decay scheme together with the magnetic and quadrupole moments for all states in the calculation. The GT matrix elements are used to obtain an allowed beta-decay scheme. The program DENS allows one to use radial wavefunctions from harmonic-oscillator, Woods-Saxon or Skyrme energy-density functions methods for the matrix elements.

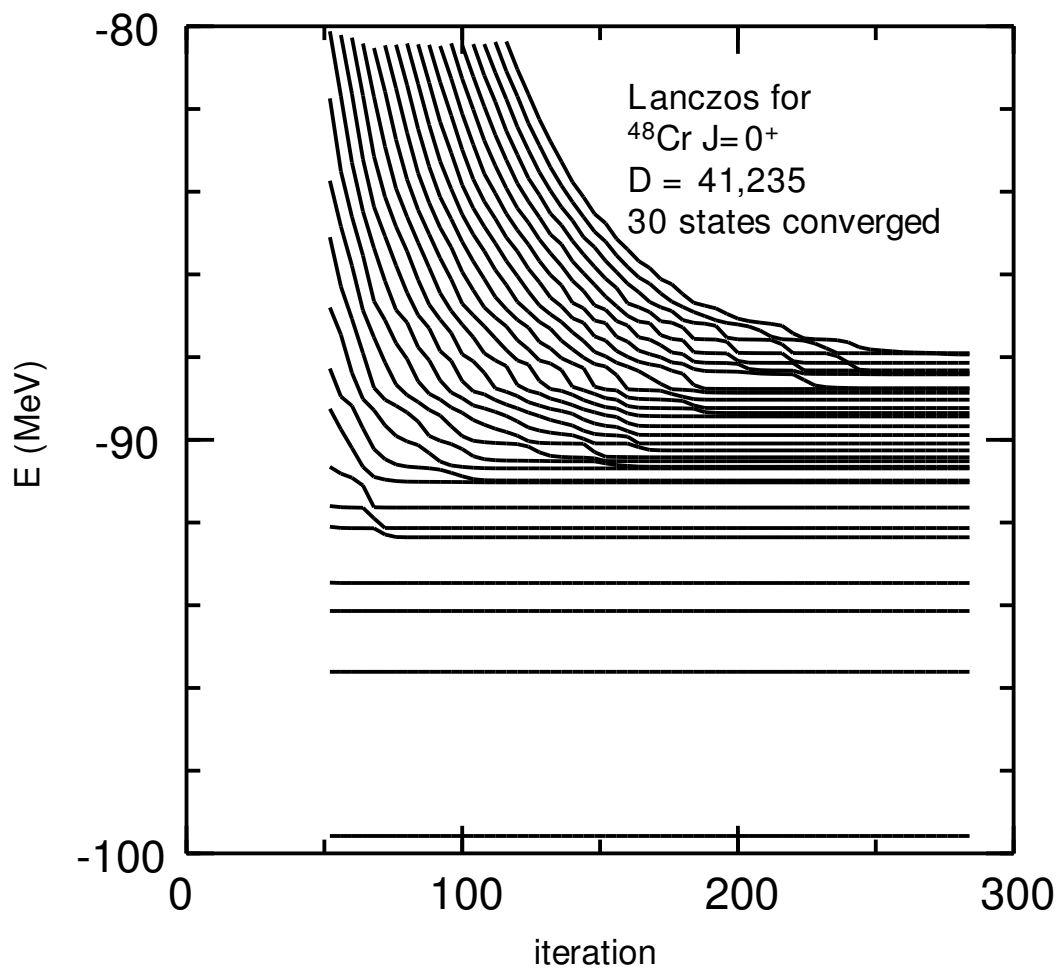


Figure 32.1: Energies for first 30 states with $J = 0$ in ^{48}Cr as a function of the number of Lanczos iterations.

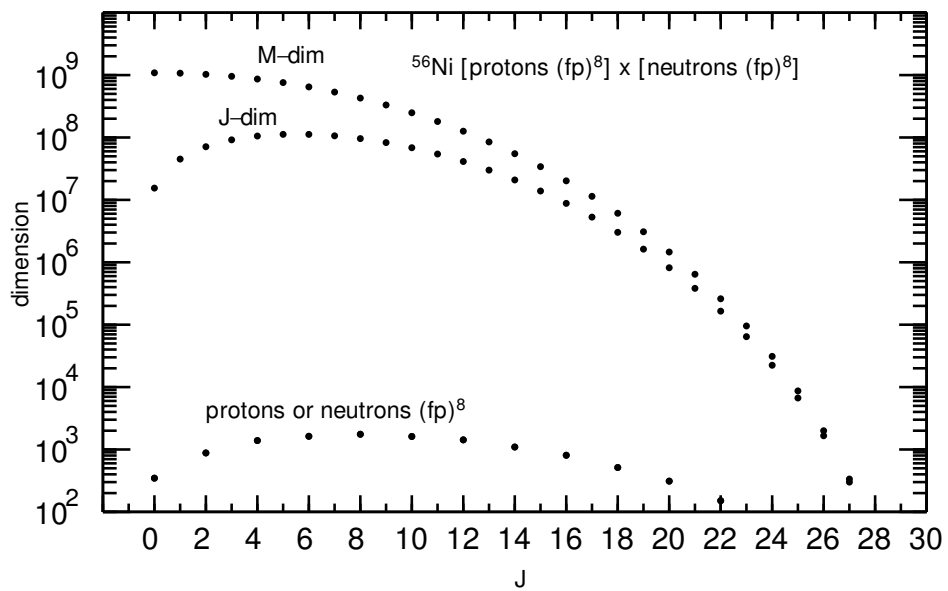


Figure 32.2: Basis dimensions for the 8 protons or 8 neutrons in the pf model space (bottom). The combined proton-neutron J -scheme and M -scheme dimensions are shown at the top.

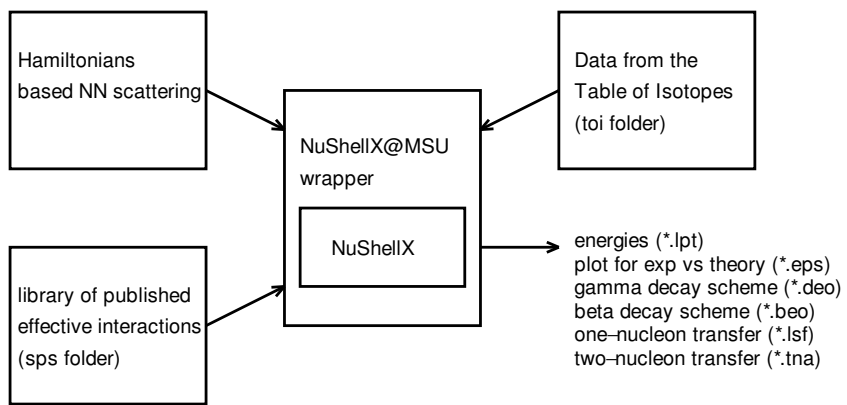


Figure 32.3: Schematic layout of the NuShellX@MSU codes.

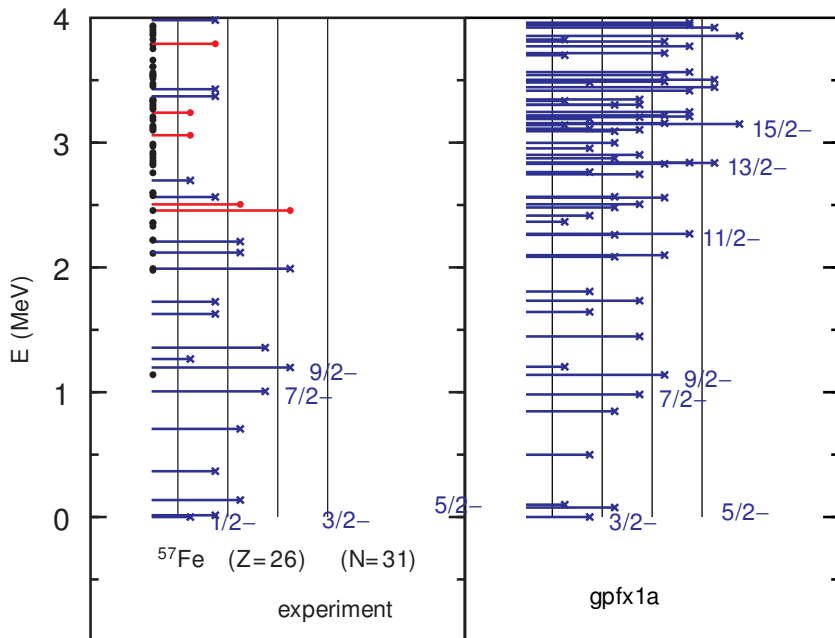


Figure 32.4: Levels up to 3 MeV in excitation obtained with the GPFX1A Hamiltonian in the full pf model space are shown in the right-hand side. The length of each line indicates the J value. These are compared with the experimental energies from NNDC on the left-hand side. The blue lines are states with negative parity, and the red line are states with positive parity. If the spin-parity is uncertain it is shown as a black circle on the y axis.

Bibliography

- [1] R. R. Whitehead, A. Watt, B. J. Cole, and I. Morrison, Adv. Nucl. Phys. 9, 123 (1977).
- [2] E. Caurier and F. Nowacki, Acta Phys. Pol. B 30, 705 (1999).
- [3] J. P. Vary, The Many-Fermion Dynamics Shell-Model Code, Iowa State University (1992) (unpublished); J.P. Vary and D.C. Zheng, *ibid.*, (1994) (unpublished); P. Sternberg, E. Ng, C. Yang, P. Maris, J.P. Vary, M. Sosonkina, H. Viet Le, Accelerat-

ing configuration interaction calculations for nuclear strucure, in the Proceedings of the 2008 ACM/IEEE Conference on Supercomputing, IEEE Press, Piscataway, NJ, doi.acm.org/10.1145/1413370.1413386.

- [4] C. W. Johnsona, W. E. Ormandb, P. G. Krastev, <https://arxiv.org/pdf/1303.0905.pdf>
- [5] B. A. Brown, A. Etchegoyen, and W. D. M. Rae, computer code OXBASH, the Oxford University-Buenos Aires-MSU shell model code, Michigan State University Cyclotron Laboratory Report No. 524, 1985.
- [6] B. A. Brown and W. D. M. Rae, Nuclear Data Sheets 120, 115 (2014).
- [7] https://en.wikipedia.org/wiki/Lanczos_algorithm
- [8] E. Caurier, G. Martinez-Pinedo, F. Nowacki, A. Poves, J. Retamosa and A. P. Zuker, PHYS. REV. C **59**, 2033 (1999). link
- [9] CENS, Computational Environment for Nuclear Structure, T. Engeland, M. Hjorth-Jensen, and G.R. Jansen, unpublished; M. Hjorth-Jensen, T. T. S. Kuo, and E. Osnes, PHYS. REP. **261**, 125 (1995).

- [10] M. Honma, T. Otsuka, B.A. Brown and T. Mizusaki, Euro. Phys. Jour. A **25** Suppl. 1, 499 (2005).

Chapter 33

The pairing part of the Hamiltonian

33.1 Experimental evidence for pairing

Fig. (33.1) shows the spectra of nuclei that can be approximately described by a closed shell plus or minus two nucleons in a single orbital. One observes that the two-particle energy (bottom panel) is largest for the 0^+ states, sometimes significant for 2^+ states, and relatively small for higher J states.

These patterns are those expected for a short-ranged nuclear interaction in the $T = 1$ channel. In general one must use the jj to LS and center-of-mass to relative coordinate transforms to calculate the two-body matrix elements. But in the extreme case of a delta-function interaction the two-body matrix elements for orbital $k_a = (n_a, \ell_a, j_a)$ can be simplified to an expression involving a Clebsch-Gordan coefficient squared for the angular part times a radial integral [1], [2]:

$$\langle k_a^2 J | \delta(r) | k_a^2 J \rangle = \frac{(2j_a + 1)^2}{4\pi(2J + 1)} [\langle j_a 1/2 j_a - 1/2 | J 0 \rangle]^2 \int [R_a(r)]^4 r^2 dr. \quad (33.1)$$

As an example, the interaction energies for an assumed $(1f_{7/2})^2$ configuration for ^{134}Sn are

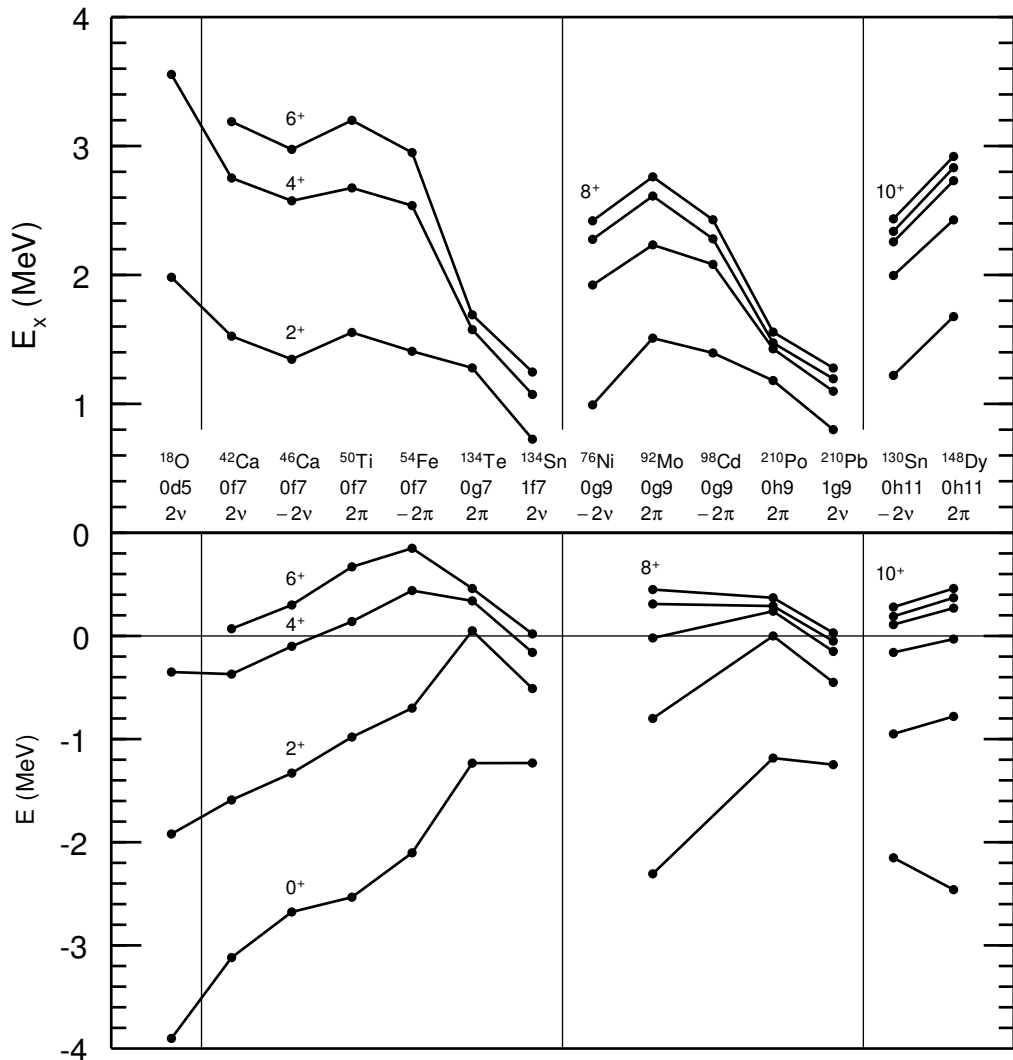


Figure 33.1: The top panel shows the energy spectra of some nuclei that are two nucleons removed from a closed shell. The J values are those states that can be approximately interpreted in terms of two nucleons in a single orbital with the given $(n, \ell, 2j)$ value. The bottom panel show the energy of these states relative to the closed-shell energy and with two times the appropriate single-particle energy subtracted.

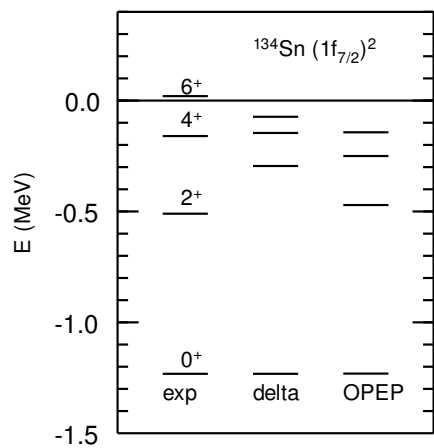


Figure 33.2: Interaction energy for states in ^{134}Sn assuming a $(1f_{7/2})^2$ configuration. The experimental values are compared to those from a delta function interaction and from a central Yukawa with a one-pion exchange range of 1.414 fm.

compared to those from the delta function and those from a Yukawa function with the range for a one-pion exchange.

A semi-classical picture can be used to understand the strong attraction for $J = 0$. To form a $J = 0$ state the angular momenta for the two orbitals must be oriented opposite to each other. If one of them is pointing up on the z axis it has an angular density distribution associated with $|Y_m^\ell(\hat{r})|^2$ that is concentrated in the $x - y$ plane. The one pointing down has the same density distribution and the two densities have a maximum overlap. This is also the case for the maximal J coupling, but this configuration is forbidden by the Pauli principle for two neutrons (or two protons). (The interaction energy for a proton and neutron in the maximal J state is large.)

The spectra shown in Fig. (33.1) are determined by configuration mixing with other orbitals. In the example of ^{18}O discussed previously, the interaction of $0d_{5/2}$ with $1s_{1/2}$ and $0d_{3/2}$ is important within the sd model space. The diagonal and off-diagonal interactions for $J = 0$ are all large because of the large spatial overlap. In addition, orbits beyond the sd model space must be taken into account, for example with second-order perturbation

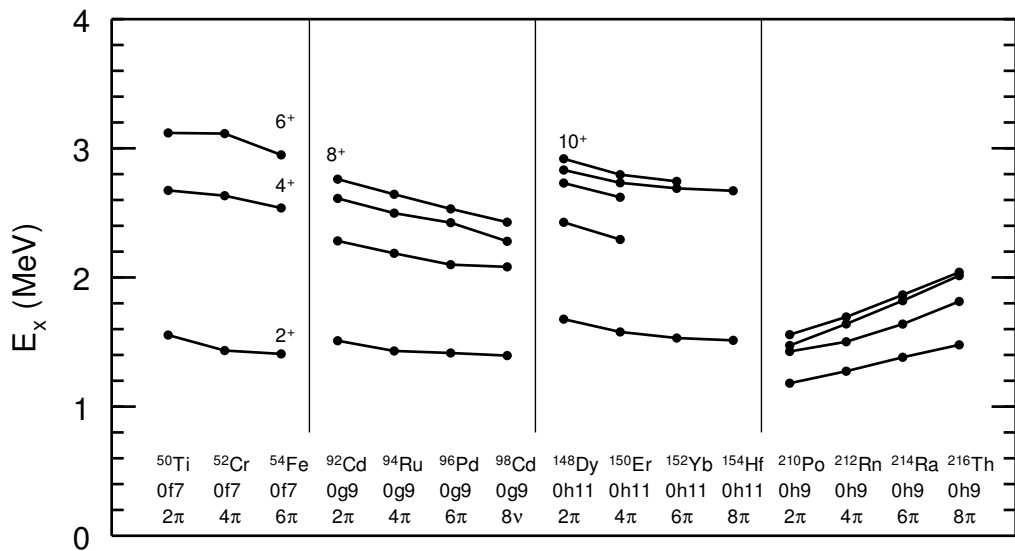


Figure 33.3: Energy spectra of some nuclei that can be described by $(n, \ell, 2j)^n$ protons beyond a closed shell. The energy of the 4^+ state in ^{52}Cr takes into account the seniority mixing between the first and second 4^+ states [3].

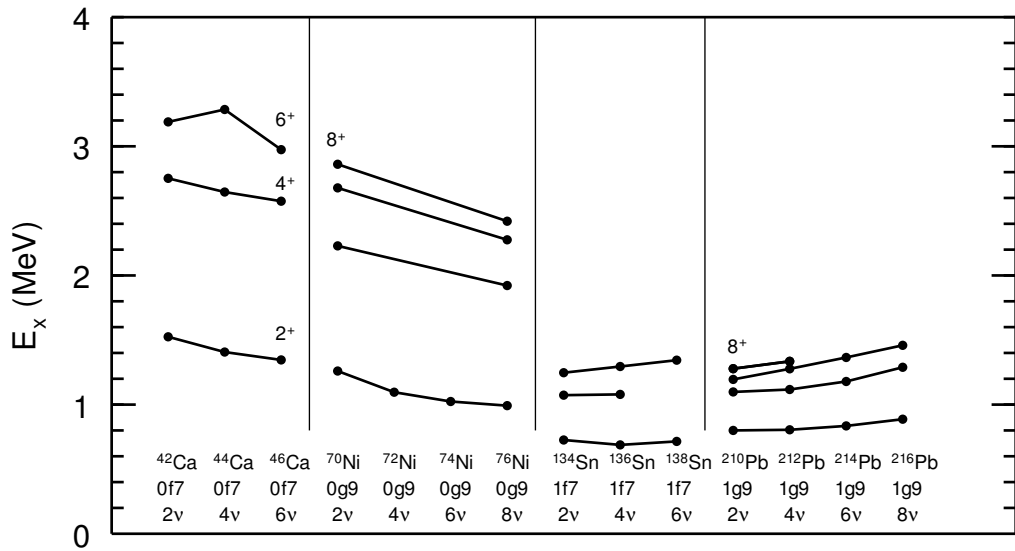


Figure 33.4: Energy spectra of some nuclei that can be described by $(n, \ell, 2j)^n$ neutrons beyond a closed shell. The energy of the 2^+ and 4^+ states in ^{54}Ca takes into account the mixing between the first and second states of each as observed in the $^{42}\text{Ca}(t,p)$ reaction [4].

corrections.

33.2 Many-body approximations for pairing

In the area of atomic physics, Racah introduced the idea of seniority [5]. The $L = 0$ coupled electronic pair was called a seniority-zero state. The addition of another unpaired electron formed a seniority-one state. The addition of two electrons with $L > 0$ formed a seniority two state. For a schematic “paring” interaction of the form $\langle \ell^2 LM | V | \ell^2 LM \rangle = -g(2l+1)\delta_{L,0}$, where g is a constant, Racah derived formulas for the interaction energy among many electrons that could be classified according to seniority. He later found simplifications through the use of group theory [6]. For the Coulomb interaction between electrons the pairing interation approximation is not very good since higher L value are also important.

Racah’s idea is even better for nuclear physics where the interaction is more short-

ranged, and a schematic interation of the form $\langle k^2 JM | V | k^2 JM \rangle = -g(2j+1)\delta_{J,0}$ is a better approximation. For more than one orbital, Talmi introduced the idea of generalized seniority [7]. Van Isaker has given a recent review of the use of seniority for nuclear wavefunctions [8]. One of the consequences of the seniority is that one can form seniority zero and two states for n valence neutrons (or protons) in orbital k . The seniority zero and two energy spectrum is independent of n . There are many cases where one can qualitatively observe this. Those for valence protons are shown in Fig. (33.3) and those for valence neutrons are shown in Fig. (33.4).

The pairing problem was also the basis of the first calculations were carried out for macroscopic superconductivity based on the theory of Bardeen, Cooper and Schrieffer (BSC) [9], [10]. The BSC model was then used to describe pairing phenomena in nuclei [11], [12], [13]. The BSC model only considers the $J = 0$ ($T = 1$) part of the two-body interaction. The BSC wavefunction does not conserve particle number. Also there is only a BSC-type solution if the single-particle spacing is small compared to the strength of the interaction. The formalism for the BSC model in nuclear physics is given in [14].

An exact solutions for just the $J = 0$ ($T = 1$) part of the full Hamiltonian can be obtained with numerical methods. Richardson reduced the problem to set of coupled equations [15], [16], [17]. Volya et al. [18] solved the problem based on SU(2) quasispin algebra [18].

In the following I discuss results related to the pairing interaction based upon configuration-interaction (CI) calculations within a given model space. Seniority is not a good quantum number, but it still a good approximation to discuss the seniority of a state. When CI calculations can be carried out they are more exact than the BCS method or those based on just the $J = 0$ part of the Hamiltonian. But when the CI basis dimensions are too large one must use one of the approximate methods.

33.3 Pairing contributions to the nuclear binding energy

One of the most robust signatures of pairing in nuclei is the odd-even oscillation in binding energies (BE) as a function of neutron or proton number. This is illustrated in Fig. (33.5) that shows the energies, E , and one-neutron separation energies, S_n , for the calcium isotopes ($\text{BE} = -E$). The figure shows the results of a shell-model calculation in the $(0f_{7/2}, 0f_{5/2}, 1p_{3/2}, 1p_{1/2})(fp)$ model space with the GX1A Hamiltonian (also referred to as GXPF1A in the literature [19]) compared with experiment. We will discuss the oscillation in the one-neutron separation energies as a function of neutron number in terms of the energy differences

$$\begin{aligned} D_n(N) &= (-1)^N [S_n(Z, N) - S_n(Z, N + 1)] = \\ &= (-1)^N [2\text{BE}(Z, N) - \text{BE}(Z, N - 1) - \text{BE}(Z, N + 1)] \end{aligned} \quad (33.2)$$

where

$$S_n(N) = \text{BE}(Z, N) - \text{BE}(Z, N - 1) \quad (33.3)$$

is the one-neutron separation energy. N is the number of neutrons and Z is the number of protons. This quantity turns out to be always positive and reflects the fact that the even nuclei are always more bound on the average than the neighboring odd nuclei. We will distinguish the results for even and odd N value by, D_{ne} and D_{no} , respectively. In the literature one commonly finds the related quantity

$$\Delta_n(N) = \frac{D_n(N)}{2}. \quad (33.4)$$

We use D rather than Δ because its values are more directly connected to simple underlying quantities associated with pairing and shell gaps. Equivalent equations for oscillations as a function of proton number are obtained by fixing N and varying Z .

Fig. (33.6) shows values of D_n for the calcium isotopes ($N > 20$) obtained from experiment and from two commonly used Hamiltonians in the fp model space, KB3G [20] and GX1A [19]. We also show the excitation energies for the lowest 2^+ states of the even nuclei. The trends observed in Fig. (33.6) will be understood on the basis of both simple and realistic models. This will lead to an understanding of the results for all nuclei.

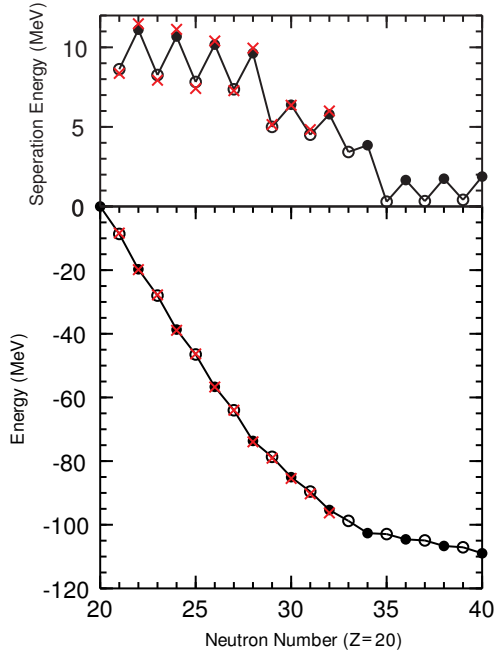


Figure 33.5: The bottom panel shows the ground-state energies for the calcium isotopes obtained from the pf shell-model calculation with the GX1A Hamiltonian relative to ^{40}Ca with filled circles even N and open circles for odd N , all connected by a line. The crosses (in red) are the experimental data. The top panel shows the one-neutron separation energies for GX1A and experiment.

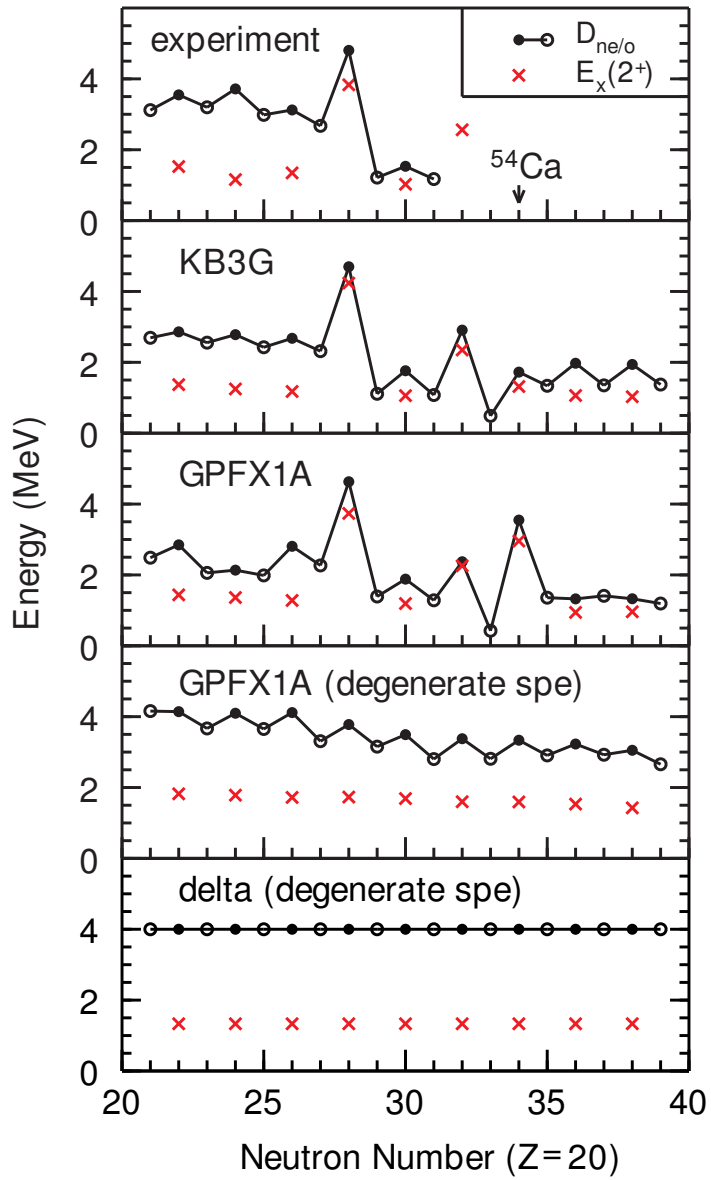


Figure 33.6: D and $E_x(2^+)$ for the calcium isotopes as a function of neutron number. D values are shown by the filled circles for even N and open circles for off N , all connected by a line. The $E_x(2^+)$ values are shown by the crosses (in red). Experiment is shown in the top panel followed by the results obtained with the KB3G, GX1A and GX1A* Hamiltonians. The second panel from the bottom are the results obtained with the GX1A Hamiltonian when all of the single-particle energies are set equal to each other at $A = 41$. The bottom panel shows the results obtained with the SDI interaction discussed in the text.

All of the Hamiltonians we use have the form

$$H = E_C + \sum_{\alpha} e_{\alpha} a_{\alpha}^+ a_{\alpha} + \frac{1}{4} \sum_{\alpha, \beta, \gamma, \delta} \langle \alpha, \beta | V | \gamma, \delta \rangle a_{\alpha}^+ a_{\beta}^+ a_{\delta} a_{\gamma}, \quad (33.5)$$

where α, β, γ and δ label the single-particle states with quantum numbers (n, ℓ, j, m), E_C is the energy of the core nucleus (^{40}Ca in the case of the calcium isotopes), e_{α} are the single-particle energies, and $\langle | V | \rangle$ are M -scheme two-body matrix elements.

One observes in Fig. (33.6) a rather complicated experimental trend that is rather well reproduced by the calculations. The results for the two Hamiltonians are similar up to $N = 33$ where the experimental data are known. Beyond $N = 33$ there are differences, in particular for $N = 34$ (^{54}Ca), where the GX1A result for the D and $E_x(2^+)$ values are nearly two times larger than for those for KB3G.

Fig. (33.6) also shows the results obtained for GX1A when all of the single-particle energies are set equal to each other. The result does not depend on the value of the single-particle energy since in this degenerate case the one-body part of the Hamiltonian does not contribute differences of Eq. 1. The result is a very regular oscillating pattern. What we

learn from this is that the larger irregularities observed in the upper panels of Fig. (33.6) are due to the finite spacing of the single-particle energies related to the shell gaps.

In this contribution we show how the results for D in Fig. (33.6) and other nuclei arise from schematic and realistic interactions between nucleons. An essential ingredient will be the pairing part of the interaction, but the consequences of pairing will be influenced by shell gaps and other components of the interactions. We start with the schematic surface-delta interaction in the next few sections, and then come to more realistic interactions. In the last few sections we examine the results for D in light nuclei out to the neutron-drop line, and finally the systematics for all nuclei. The experimental masses were taken from the intermediate evaluation of Audi and Meng [21] supplemented by more recent data on $^{51,52}\text{Ca}$ [22] and ^{26}O . [23]

33.4 The surface-delta interaction model

To get some insight into the reasons for the patterns observed in Fig. (33.6), we start with the simple “surface-delta-function” (SDI) model for V . [24] The two-body matrix elements for a delta function $V(|\vec{r}_1 - \vec{r}_2|) = A\delta(|\vec{r}_1 - \vec{r}_2|)$ can be obtained analytically as a product of angular and radial matrix elements,

$\langle V \rangle = \langle V \rangle_{\text{ang}} \langle V \rangle_{\text{rad}}$ where

$$\langle V \rangle_{\text{rad}} = \int R_a(r) R_b(r) R_c(r) R_d(r) r^2 dr. \quad (33.6)$$

where a, b, c and d label the single-particle states with quantum numbers (n, ℓ, j) , and $R(r)$ are the radial wavefunctions. For the SDI one evaluates this integral at the surface, $r = r_o$, and assumes that

$|R_a(r_o)| = |R_b(r_o)| = |R_c(r_o)| = |R_d(r_o)| = R$. Then

$$\langle V \rangle_{\text{rad}} = (-1)^{n_a+n_b+n_c+n_d} R^4 r_o^2 = (-1)^{n_a+n_b+n_c+n_d} C,$$

where the phase factor is used for the radial wavefunction convention of being positive near the origin. The SDI two-body matrix elements for $J = 0$ are

$$\langle aaJ = 0 | \text{SDI} | bbJ = 0 \rangle = -(A'/2)\sqrt{(2j_a + 1)(2j_b + 1)}. \quad (33.7)$$

The results obtained with SDI for the fp model space with degenerate single-particle energies is shown in Fig. (33.7). We have chosen the constant $A' = 4\pi A(-1)^{n_a+n_b+n_c+n_d}C = 0.4$ MeV in order to make the value $D = 4$ MeV similar to that obtained for the GX1A Hamiltonian when the single-particle energies are degenerate.

For the SDI the D and $E_x(2^+)$ are constant and there is no oscillation in the D values. The SDI with degenerate single-particle energies has some very simple and interesting properties. [25] The $J = 0$ pairing properties are determined only by strength of the interaction and by the total number of possible pairs, $m/2 = 10$ in our example, where $m = 20$ is the maximum number of valence neutrons. Exactly the same results are obtained if there were a single orbital with $j = 19/2$ or ten states with $j = 1/2$. Use of a delta function with the radial integral evaluated with oscillator or Woods-Saxon radial wavefunctions gives results that are close to SDI (within about 5%), but the properties are more complicated

but analytic (oscillator) or non analytic (Woods-Saxon).

In addition to D and $E_x(2^+)$ we show in Fig. (33.8) the energies obtained when the degenerate single-particle energies are zero (if the energies were not zero there would be an additional linear dependence to the total energies). The total energy for SDI [line (a) in Fig. (33.7)] as a function of the number of valence neutrons, n , is very simple

$$E(n) = \frac{nV_o}{2} \text{ (even } n\text{),}$$

and

$$E(n) = \frac{(n-1)V_o}{2} \text{ (odd } n\text{),} \quad (33.8)$$

where V_o is the interaction energy for two-nucleons in the $J = 0$ paired state. We also have $D = -V_o$. All of the odd N nuclei have four degenerate states with $J^\pi = 1/2^-, 3/2^-, 5/2^-$ and $7/2^-$.

One can also make a “mean-field” approximation for the total energy [line (b) in Fig.

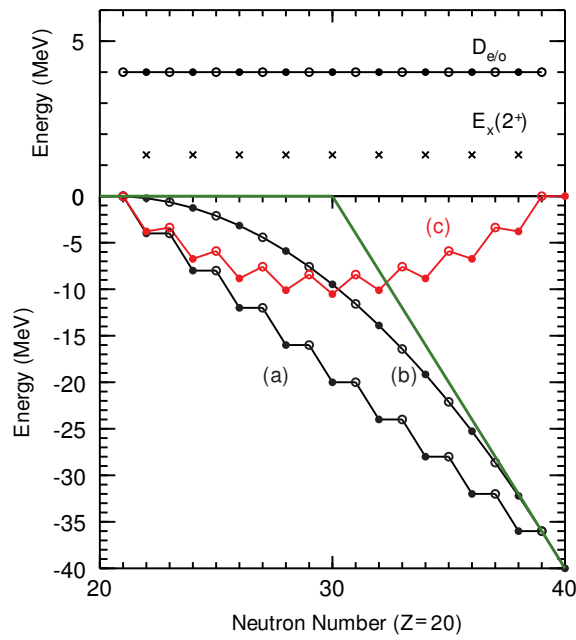


Figure 33.7: Results obtained with the SDI interaction. The bottom panel shows the total energy (a), the monopole energy (b) and the correlation energy (c). The top panel shows the values of D and $E_x(2^+)$.

(33.7)]:

$$\bar{E}(n) = \frac{n(n-1)\bar{V}}{2}, \quad (33.9)$$

where the average (monopole) energy, \bar{V} is the total closed shell energy divided by the total number of m state two-particle combinations ($m = 20$ in this case)

$$\bar{V} = \frac{\sum_a [n_a(n_a - 1))/2] \bar{V}_{aa} + \sum_{a < b} (n_a + 1)(n_b + 1) \bar{V}_{ab}}{m(m-1)/2}, \quad (33.10)$$

where $n_a = 2j_a + 1$ is the maximum number of neutrons in orbital a , and

$$\bar{V}_{ab} = \frac{\sum_J (2J+1) \langle a, b, J | V | a, b, J \rangle}{\sum_J (2J+1)}. \quad (33.11)$$

are the average (monopole) interactions between the orbitals a and b .

For the filled shell $n = m$ there is only one state and we have:

$$E_m = \bar{E}_m = \frac{mV_o}{2} = \frac{m(m-1)\bar{V}}{2} \text{ (for SDI).} \quad (33.12)$$

This equation that relates the two-body matrix elements with $J = 0$ to a sum over the two-body matrix elements for all J is a special property of the SDI interaction. We can define the pairing correlation energy as the difference between Eqs. (33.8) and (33.9), and this is given by curve (c) in Fig. (33.7):

$$E^{\text{corr}}(n) = E(n) - \bar{E}(n). \quad (33.13)$$

For even n SDI this is

$$E^{\text{corr}}(n) = \frac{nV_o}{2} - \frac{n(n-1)V_o}{2(m-1)} \text{ (for even } n \text{ SDI).} \quad (33.14)$$

This is maximized in the middle of the shell when $n = m/2$. When $m/2$ is even the maximum is

$$E^{\text{max-corr}} = \frac{m^2 V_o}{8(m-1)}. \quad (33.15)$$

For our example this is $(50/19)V_o = -10.53$ MeV (see Fig. (33.8)). For the SDI the two-body interaction contribution to the ground-state energies is given by two parallel lines, Eq. (33.8), whereas the centroid energies have the quadratic dependence of Eq. (33.9).

The results given in Fig. (33.7) were obtained by a full diagonalization of the fp shell matrix where the largest M-scheme dimension is 17,276 for ^{50}Ca . They can also be obtained analytically with equations above. However, the diagonalization provides a way of going beyond the analytic models and we can examine the effects of shell gaps as discussed below. It also provides information on the level density of states. We find that the energies of all states lie below the green line in Fig. (33.7). Many of the energies are degenerate at values on the green line or in spacings of $| V_o |$ between the ground state and the green line. But there are also many states at other energies. One could understand this in terms of a seniority or broken-pair model. The distribution of states depends upon how the total of 20 m-states is divided among the j values. For example, in the case of $(0f_{7/2}, 0f_{5/2}, 1p_{3/2}, 1p_{1/2})$ the two particle spectrum has four non-zero energy states with $J = 0, 2, 4, 6$ and 18 states at zero energy. The extreme limits in our example are ten $j = 1/2$ states or one $j = 19/2$. For ten $j = 1/2$ all states must have $J = 0$ and the two-particle system has one non-zero

state at V_o and nine states at zero energy. For one $j = 19/2$ the two-particle system has ten nonzero energy states with $J = 0, 2, 4, 6, 8, 10, 12, 14, 16, 18$. The energy of the 2^+ state depends upon the j -state distribution (it does not exist for ten $j = 1/2$). Also the spectrum of the odd nuclei depends on the j distribution with just one $J = 19/2$ for $j = 19/2$ and four, $J = 1/2, 3/2, 5/2$ and $7/2$, for the fp model space (for ten $j = 1/2$ there can be several degenerate states with $J=1/2$). For the SDI one has spikes in the density of the levels spaced at energies of $| V_o |$ above the ground state. In a model with finite single-particle level spacing and more realistic interactions, these spikes will be smoothed out. In addition, in comparison to experiment there will be contributions to the level density from excitations of proton and neutrons outside of the model space starting around the energy of the shell gaps.

33.5 The modified surface-delta interaction model

One observes two differences between the results in the two lower panels of Fig. (33.6). One is that the GX1A result tends to fall off as a function of the number of neutrons whereas the

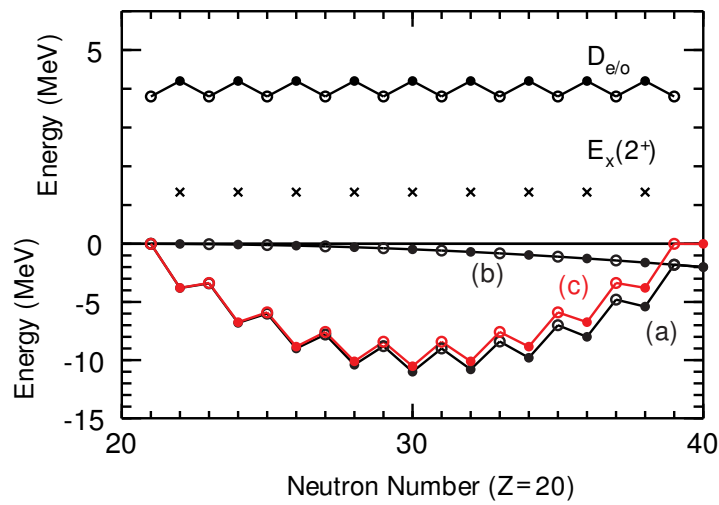


Figure 33.8: Results obtained with the MSDI interaction. The bottom panel shows the total energy (a), the monopole energy (b) and the correlation energy (c). The top panel shows the values of D and $E_x(2^+)$.

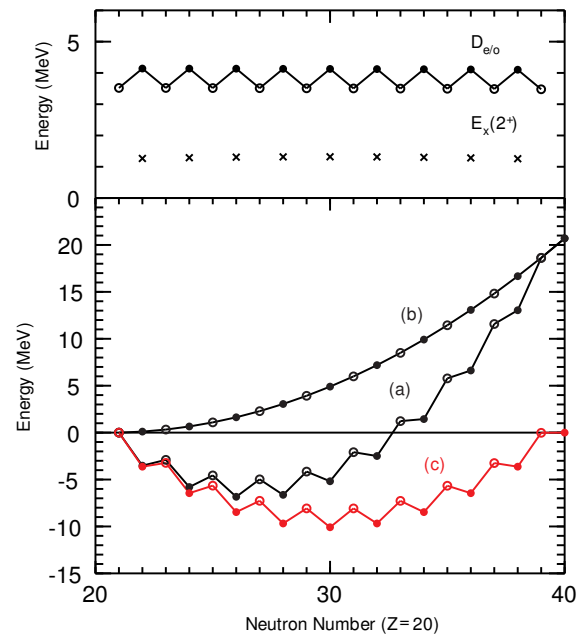


Figure 33.9: Results obtained with the SDI plus Coulomb interactions. The bottom panel shows the total energy (a), the monopole energy (b) and the correlation energy (c). The top panel shows the values of D and $E_x(2^+)$.

SDI result is flat. A part of this is due to the fact that GX1A contains an assumed smooth mass dependence of the form $(A/42)^{0.3}$ that is meant to take into account a smooth increase the harmonic oscillator parameters $\hbar\omega$ as a function of A . This was not included in the SDI. The main reason for the fall off is that the average interactions, \bar{V}_{ab} , differ from SDI and lead to a splitting in the single-hole energies for ^{60}Ca that reduces the effective pairing for larger N values.

The other feature is that the GX1A result for D oscillates whereas the SDI result does not. In the 1960's this was recognized as a basic failure of the delta and SDI Hamiltonians. It was empirically fixed by adding a constant to the interaction to make the so-called modified-delta interaction [1] of the form

$$V(|\vec{r}_1 - \vec{r}_2|) = A\delta(|\vec{r}_1 - \vec{r}_2|) + B, \quad (33.16)$$

where B is the added constant. In terms of two-body interaction it is infinitely long range. With the SDI form of the radial integral this becomes the so-called modified-surface-delta interaction (MSDI). The modern interpretation of this constant is that it comes from core-polarization corrections and/or three-body interactions. The energy and D values obtained

with $B = 0.2$ MeV are shown in Fig. (33.8). This constant simply adds a term

$$\frac{n(n-1)B}{2}$$

to the all energies, and does not change the correlation energy. It gives an oscillation in D

$$D_o = -V_o - B \quad (\text{odd } n)$$

and

$$D_e = -V_o + B \quad (\text{even } n) \quad (33.17)$$

Half the sum of neighboring even and odd D gives the pairing contribution:

$$\begin{aligned} D_a(N-\text{even}) &= -V_o = \frac{1}{2}[D_e(N) + D_o(N-1)] \\ &= \frac{1}{2}[3\text{BE}(Z, N) - 3\text{BE}(Z, N-1) + \text{BE}(Z, N-2) - \text{BE}(N+1)]. \end{aligned} \quad (33.18)$$

Half of the difference of neighboring even and odd D eliminates the pairing and gives the purely quadratic dependence of the BE:

$$\begin{aligned} D_b(N\text{-even}) &= B = \frac{1}{2}[D_e(N) - D_o(N - 1)] \\ &= \frac{1}{2}[\text{BE}(Z, N) + \text{BE}(Z, N - 1) - \text{BE}(Z, N - 2) - \text{BE}(N + 1)]. \end{aligned} \quad (33.19)$$

A microscopic calculation of these quadratic monopole corrections requires an explicit consideration of core-polarization the real and induced three-body interactions (those between two-valence nucleons and one in the core). It has been proposed that the density-dependent interactions empirically included in the Skyrme parameters can be used to obtain B values for the valence shell-model interactions. [26] This method improves the relative binding energies obtained for shell model calculations in heavy nuclei.

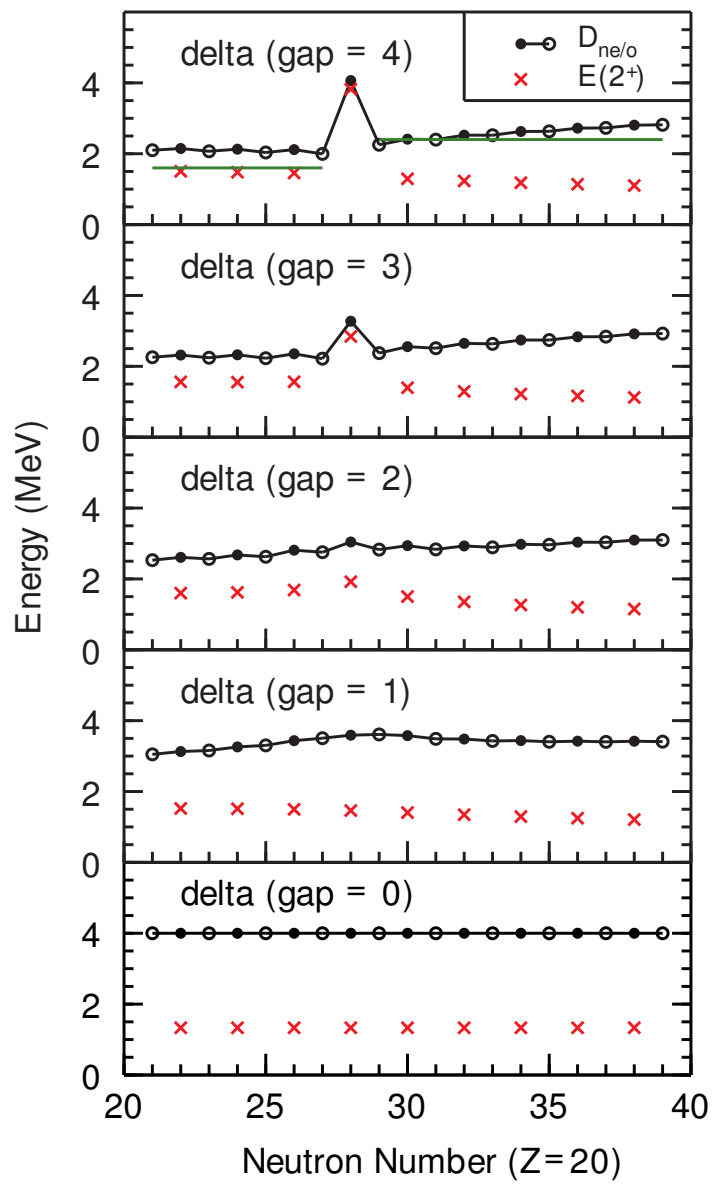


Figure 33.10: Results obtained with the SDI interaction as a function of the shell gap between the $0f_{7/2}$ and $(0f_{5/2}, 1p_{3/2}, 1p_{1/2})$ set of orbitals. The top panel also show the results for D (green lines) obtained with the shell gap is infinite.

33.6 The surface-delta interaction plus Coulomb model

We can also consider what happens for protons when one adds a Coulomb interaction to the SDI. The results obtained with a Coulomb interaction evaluated with oscillator radial wavefunctions appropriate for ^{40}Ca are shown in Fig. (33.9). The addition of the Coulomb behaves like the addition of a long-range monopole term with $D_b = B \approx 0.31$ MeV. There is also a small repulsive addition to D_a of about +0.17 MeV. This will be important later when we look at the global trends for protons.

33.7 The surface-delta interaction model with a shell gap

Next we show how D changes when the single-particle energies are not degenerate. This requires a computational experiment with the SDI applied to the fp orbits divided into two

groups, $f = (0f_{7/2})$, and $r = (0f_{5/2}, 1p_{3/2}, 1p_{1/2})$ with a variable gap in between them, so that the second group is raised in energy relative to the the $0f_{7/2}$. The result is shown in Fig. (33.9) where the gap starts at zero and is increased up to four MeV. Four MeV is approximately equal to the experimental shell gap found for ^{48}Ca ($N = 28$). When the gap is small (one MeV), the energies of the 2^+ states remain flat, and the pairing correlation starts to fall off away from the break at $N = 28$. When the gap is two MeV there is a small rise in the 2^+ energy and a small increase in D at $N = 28$. When the gap is above two MeV there is an obvious increase in the 2^+ energy and D and $D \approx E_x(2^+)$ at the gap. Thus, the relative values of D and $E_x(2^+)$ provide a confirming measure of shell gaps. For the calcium isotopes the calculations are carried out with only neutrons in the fp model space and the 2^+ energies are those for neutrons. The experimental values used for comparison are also dominated by the neutron configuration. In other cases when the gap is between orbitals with difference parity, the excitation energy of the relevant negative parity state (like 3^-) should be used. When experimental values of $E_x(2^+)$ are used one should confirm that the 2^+ state in question has the appropriate neutron or proton configuration. Away from semi-magic nuclei the 2^+ states usually have strongly mixed proton and neutron configurations.

In the limit of an infinite gap, the results are those shown by the green line in the top panel of Fig. (33.9). In this case the total pairing energy that starts out at $V_o = -4$ MeV in the degenerate cases gets divided into two parts, $V_o^f = -1.6$ for the $0f_{7/2}$ below $N = 28$ and $V_o^r = -2.4$ for the other three orbitals above $N = 28$. Unlike the D_e , which shows a large increase at the shell gap at some even N , the D_o for odd N does not show any direct evidence of the shell gap. As in this example, the D_o values often change across a gap because the orbitals that are involved in the pairing change.

A related aspect of the shell gap is the percentage of $(0f_{7/2})^8$ component in the ground state of the eight particle system. As the gap increases from zero to four MeV this percentage changes as 0.48%, 4.75%, 31.6%, 58.9% to 84.2%. These values are important for the applications of the coupled-cluster theory [27] where the assumed starting configuration (the reference state), must be large enough for the coupled-cluster expansion to converge. [28] This quantity cannot be measured experimentally. One can measure one-nucleon removal spectroscopic factors. For example, in the degenerate case, the $a = (0f_{7/2})$ removal spectroscopic factor is nn_a/m for all n ($n_a = 8$ and $m = 20$). For $N = 28$ ($n = 8$) this is 3.2. When the gap is four MeV the spectroscopic factor for $N = 28$ ($n = 8$) increases to 7.5. A

systematic study of spectroscopic factors provides information on pairing and shell gaps.

When there is a shell gap one also finds pairing vibrations. These are $J = 0^+$ excited states corresponding to moving two nucleons from the orbitals just below the gap to those just above the gap. In the limit of infinite gap these are purely two-particle two-hole ($2p - 2h$) states relative to the closed-shell configuration. For finite gaps they are sometimes loosely referred to as $2p - 2h$ excitations because this is the dominate configuration relative to the ground state. The ground state also contains some smaller amount of $2p - 2h$ and there are smaller mixing of $4p - 4h$ and higher in all states. In our SDI example with a four MeV single-particle energy gap this $2p - 2h$ state occurs in ^{48}Ca at 4.78 MeV. The energy of this state is smaller than two times the single-particle energy gap of eight MeV due to pairing correlations. The experimental situation for ^{48}Ca will be discussed below. The neutron pairing vibration in ^{208}Pb is observed at 4.87 MeV [29]. The proton pairing vibration in ^{208}Pb and its mixing with the double-octupole vibration is dicussed in [30]. In deformed nuclei one can consider the coupling of shape and pairing vibrations [31].

Pairing is also important for two-proton decay. The two-proton decay “phase-space”

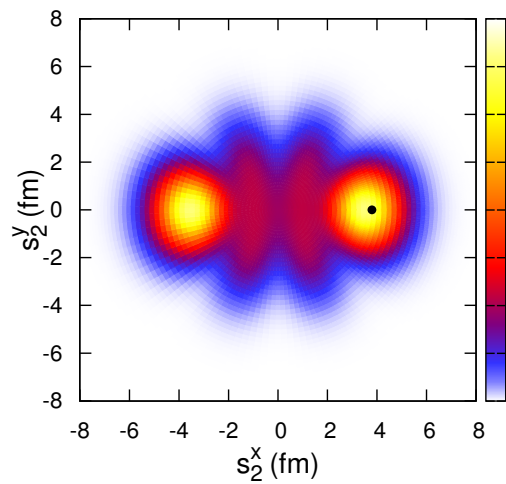


Figure 33.11: ^{48}Ca ground-state to ^{46}Ca ground-state overlap obtained with the SDI model with degenerate single-particle energies. This shows the probability of finding the second nucleon in the $x - y$ plane if the first nucleon is at the position of the black spot on the x -axis, integrated along the z axis.

is very dependent on the ℓ_a value with $\ell=1$ being about two orders of magnitude faster than $\ell=3$. [32] Thus, in a model with pairing there will always be some admixtures of ℓ values that will be important for the two-proton decay lifetime. [33]

33.8 Features for the calcium and chromium isotopes

We can now understand the features of the calcium isotopes shown in Fig. (33.6). With the GX1A Hamiltonian there are two large shell gaps at $N = 28$ and $N = 34$, and a smaller shell gap at $N = 32$, related to preferential filling of the orbitals in the order $0f_{7/2}$, $1p_{3/2}$, $1p_{1/2}$ and $0f_{5/2}$. The results for KB3G are similar except that above $N = 32$ the $1p_{1/2}$ and $f_{5/2}$ orbitals are closer together and there is no shell gap at $N = 34$. The smallest D_{no} value occurs for ^{53}Ca ($N = 35$) (0.43 MeV for GX1A). If confirmed experimentally this would be smallest D_{no} value in all nuclei. It is related to the filling the $1p_{1/2}$ orbital that has the smallest possible pairing matrix element [see Eq. (33.7)]. The $J = 0$ matrix element for this orbital is 0.053 MeV with GX1A and 0.161 MeV with KB3G compared to the SDI value of

-0.4 MeV. The value of D_{no} at $N = 35$ is mainly determined from the mixing of the $1p_{1/2}$ and $0f_{5/2}$ configurations.

^{48}Ca experimentally exhibits a neutron pairing vibration at 5.46 MeV that is determined from its observation in $^{46}\text{Ca}(\text{t},\text{p})^{48}\text{Ca}$. [34] The theoretical values are 5.28 MeV with GX1A and 5.18 MeV with KB3G. Experimentally this excited state has a two-neutron transfer cross section that is about 1.6 times larger than that of the ^{48}Ca ground state. This is in qualitative agreement with calculations obtained with Fresco that include both direct and sequential mechanisms. [35]

GX1A and KB3G are derived from G-matrix interactions obtained from nucleon-nucleon scattering data and then renormalized to the pf shell model space. Also, some of the two-body matrix elements have been modified to better reproduce the experimental data for binding energies and excitation energies. These modifications might arise from interactions of two-valence nucleons with one core nucleon due to three-body forces. For pairing the relevant $J = 0$ two-body matrix elements for $(2j_a 2j_b)$ (SDI, GX1A, KB3G) in MeV are: (77)(-1.60,-2.24,-1.92); (73)(-1.13,-0.72,-0.78);

(75)(-1.38,-1.38,-2.79); (71)(-0.80,-0.38,-0.71); (33)(-0.80,-1.12,-0.81);
 (35)(-0.98,-1.25,-0.78); (31)(-0.56,-1.49,-1.47); (55)(-1.20,-1.21,-0.86);
 (51)(-0.69,-0.31,-0.39) and (11)(-0.40,+0.05,+0.15). Given the variation between the two effective interactions the matrix elements are not too different from SDI. But the origin of the effective interaction is complex. One starts by renormalizing the short-range part of the nucleon-nucleon interaction for a model space of about 10 oscillator shells with the G-matrix or V_{lowk} method. [36] This can be represented as a set of bare two-body matrix elements. Then one uses the techniques of core-polarization and many-body perturbation theory to renormalize down into the fp model space. [37] Typical results are obtained with the N3LO nucleon-nucleon interaction [38] with a V_{lowk} short-range renormalisation, and with second-order core-polarization up to $6\hbar\omega$ with a ^{40}Ca core. [39] For example, contributions to the pairing matrix element for $(0f_{7/2})^2 J = 0, T = 1$ are (in MeV), -0.94 (first order), -0.64 (bubble diagrams), -0.37 ($4p - 2h$ diagrams), -0.41 (2p-ladder diagrams), giving a total of -2.36 MeV that gets reduced to -1.96 MeV when folded-diagrams are included (see [37] for the notation). The main contribution to $2p$ and $4p - 2h$ diagrams is the pairing ($J = 0$) interactions from orbits outside the fp model space treated in second order. The tensor interaction of the valence neutrons with core-protons gives the main contribution to the bubble diagram

core-polarization corrections. Any microscopic consideration of pairing matrix elements in nuclei must take into account the model space and associated core-polarization corrections.

The results for D and $E_x(2^+)$ obtained with the single-particle energies from GX1A but with the two-body part replaced by these renormalized N3LO matrix elements are shown in Fig. (33.11). There is a large difference between first and second order. Pairing is increased by almost a factor of two, and the odd-even oscillation changes sign. The second-order results are rather similar to experiment and those obtained with the two effective Hamiltonians. In particular the pairing strength and the quadratic background (the oscillation in D) comes out about right. The main difference is that the sizes of the shell gaps are not the same. The differences between SDI, N3LO, GX1A and KB3G that leads to the different shell gaps are in the values of the average (monopole) interactions given by Eq. (33.11). With the effective Hamiltonians GX1A and KB3G some of the two-body matrix elements have been modified to achieve a better fit to the data. For KB3G this was done mainly by modifying these monopole interactions. Recently, three-body interactions have been added to the N3LO-type results to obtain improved shell-gap sizes for oxygen [40] and calcium. [41] [42]

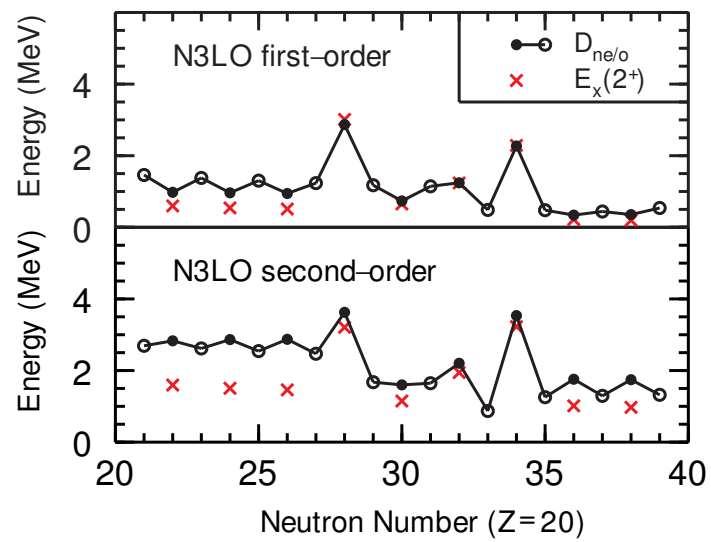


Figure 33.12: Values for D and $E_x(2^+)$ obtained from the renormalized N3LO Hamiltonian.

For calculations of the calcium isotopes in the fp model space, only valence neutrons are considered explicitly. The protons enter implicitly in the values of the effective two-body matrix elements as determined from many-body perturbation theory or as determined by adjustments to experimental data. The deviations between experiment and theory observed in the D values near $N = 20$ may reflect the need for the treatment of explicit proton excitations from the sd to the fp shell. Indeed, there are many low-lying states in nuclei just above ^{40}Ca that are dominated by proton excitations, such as the low-lying 0^+ state at 1.837 MeV in ^{42}Ca .

In order to examine the role of explicit proton-neutron interaction, we take the example of the chromium isotopes where there are explicitly four valence protons in the fp model space. The interactions between protons and neutrons give deformed-type correlations. The D_n values for experiment and theory are shown in Fig. (33.13). One observes overall good agreement between experiment and theory. The energies for the 2^+ states are shown, but in this case, unlike for calcium, they all have strongly mixing proton and neutrons configurations.

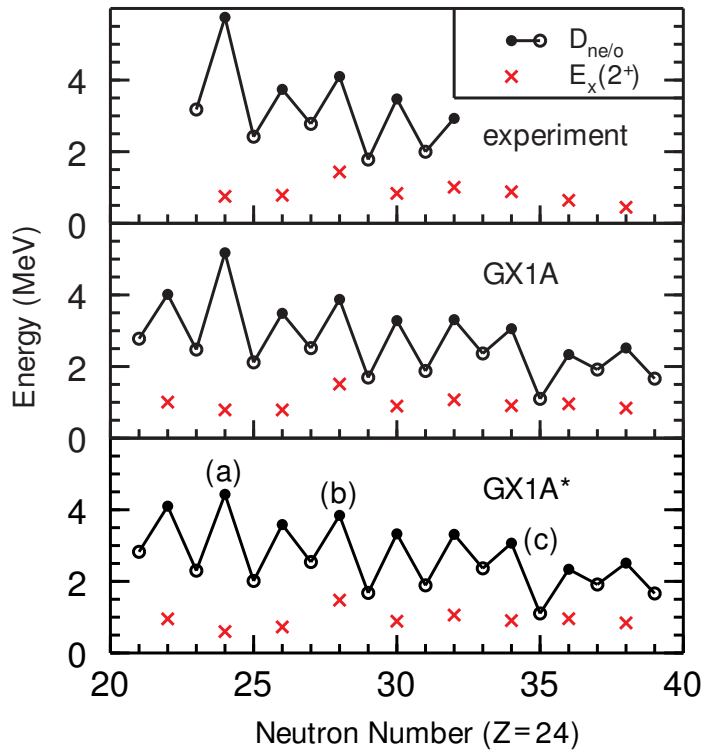


Figure 33.13: D and $E_x(2^+)$ for the chromium isotopes as a function of neutron number. D values are shown by the filled circles for even N and open circles for off N , all connected by a line. The $E_x(2^+)$ values are shown by the crosses (in red). Experiment is shown in the top panel followed by the results obtained with the KB3G and GX1A Hamiltonians.

Compared to the calcium isotopes there is a larger difference between D_{ne} and D_{no} due to a larger positive quadratic dependence in the energies. The origin of this will be discussed in the last section.

The shell gap at $N = 28$ drops from $D_{ne} = 4.8$ MeV in calcium to 4.1 MeV in chromium [(b) in Fig. (33.13)]. This is typical of the change observed going from a doubly-magic (proton and neutron) nucleus (^{48}Ca) to a singly-magic (only neutron) nucleus (^{52}Cr). This is due to the effect of the extra proton-neutron interactions on the pairing correlations.

Another difference is the peak in D_{ne} at $N = 24$ [(a) in Fig. (33.13)]. This is not a shell gap, but a consequence of an enhanced binding energy for open-shell nuclei with $N = Z$ coming mainly from the pairing interaction between protons and neutrons in the $T = 1, J = 0$ state. The results labeled GX1A* were obtained by setting these matrix elements equal to zero. The results change little from GX1A except for the reduction of the peak at $N = 24$. This proton-neutron interaction is always included in shell-model calculations and is needed to conserve isospin. But in most Hartree-Fock models it is not included with the result that one has to add a correction due to what is called the “Wigner-cusp” at $N = Z$. Models for

including the full and exact pairing corrections to Hartree-Fock have been considered. [43]

For chromium we observe a dip in D_{no} at $N = 35$ [(c) in Fig. (33.13)]. The nucleus at this point, ^{59}Cr , has a $J^\pi = 1/2^-$ ground state and the dip may be related to the preferential filling of the $1p_{1/2}$ orbital and small- j pairing discussed above for ^{53}Ca . But the states with $J^\pi = 1/2^-, 3/2^-, 5/2^-$ and $9/2^+$ are all within 500 keV of each other. This indicates the importance of the $g_{9/2}$ orbital in the neutron-rich chromium that is not included in the pf model space calculations. Inclusion of $0g_{9/2}$ (and possible $1d_{5/2}$ and $2s_{1/2}$) is necessary for understanding the neutron-rich chromium isotopes. [44] The occupancy of $g_{9/2}$ should show up in values of D that are larger than those obtained in the fp model space. More experimental data on the masses are needed.

33.9 Light nuclei toward the neutron drip line

How do the D values change as we approach the neutron drip line? The heaviest isotope for which the neutron drip line has been reached is oxygen where it is located at $N = 16$ (^{24}O). Recent experiments on neutron decay have established the energies of the lowest neutron-unbound state in ^{25}O [45] and ^{26}O . [23] These results together with other mass data have been used for Fig. (33.14) that shows the D_n values for carbon, oxygen and neon. Large shell gaps are observed for $N = 6$ (a) and 8 (b) with two smaller ones at 14 (c) and 16 (d). ^{20}Ne with $N = 10$ shows the Wigner-cusp (e) enhancement due to proton-neutron pairing. ^{12}C at $N = 6$ (a) should also have a Wigner-cusp, but it is on top of the shell gap at $Z = 6$. The 2^+ energies for neutron-rich carbon and oxygen are dominated by the the neutron configuration and can be compared to the D values. Other excited states shown have mixed proton-neutron configurations.

The small D_{no} values at $N = 15$ (f) is related to the filling of the $1s_{1/2}$ orbital at this point (^{25}O and ^{27}Ne have $1/2^+$ ground states). Shell-model calculations such as those in the $p - sd$ model space with the WBP Hamiltonian [46] and in the sd model space

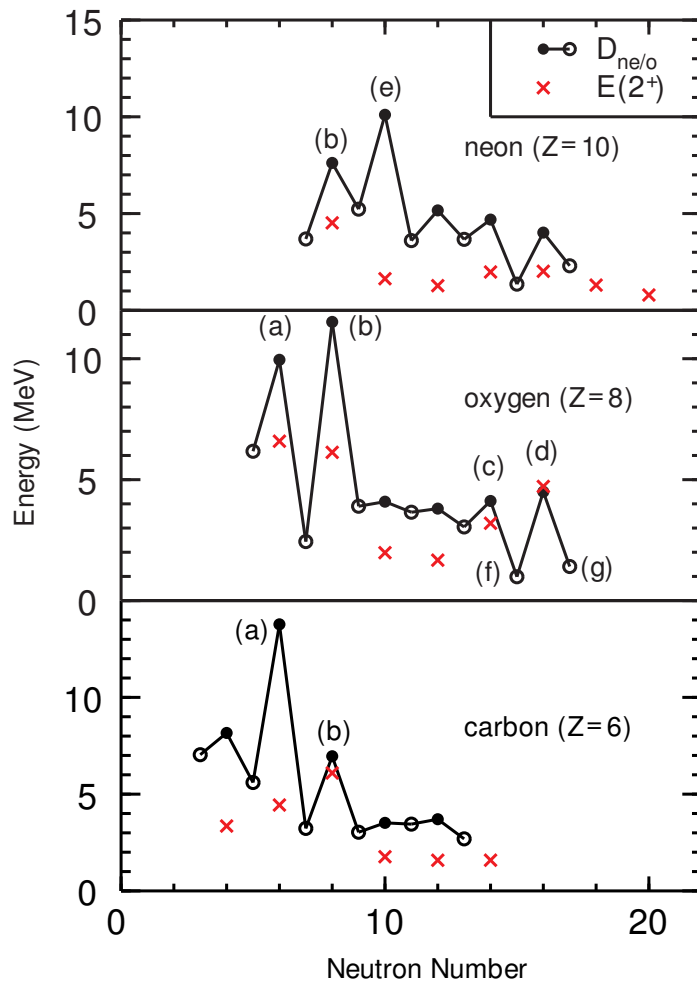


Figure 33.14: Experimental values for D and $E_x(J^\pi)$ for the carbon, oxygen and neon isotopes. J^π is 2^+ except for ^{14}C , ^{16}O and ^{18}Ne where it is the lowest observed negative parity state.

with the USDA/B Hamiltonian are in general good agreement with these data. The main exception is that WBP strength needs to be reduced by about 25% in order to reproduce the experimental energies for the neutron-rich carbon. [47] For WBP one assumed that the interaction (including pairing) is the same for oxygen and carbon. A similar situation exists for a reduction of the interaction strength in the silicon isotopes ($Z = 14$) compared to calcium. [48] Two possible reasons for this reduction are: (1) The radial matrix for the bare interaction elements become smaller for more loosely bound neutrons. This can be qualitatively modeled by evaluating Eq. (33.6) with Woods-Saxon or Hartree-Fock radial wavefunctions. (2) The core-polarization corrections to the matrix elements change.

Both of these effects have been considered in Ref [49], where it was found that (1) is most important for silicon. Thus we may expect pairing to be reduced as one approaches the drip line simply due to the fact that the neutrons are on the average further apart. This is confirmed by the small value of D_{no} for ^{25}O ($N = 17$) (g) where the $0d_{3/2}$ and possibly the $1p_{3/2}$ orbitals start to fill. Understanding the situation near and beyond the neutron drip line will require an explicit consideration of the continuum part of the wavefunctions.

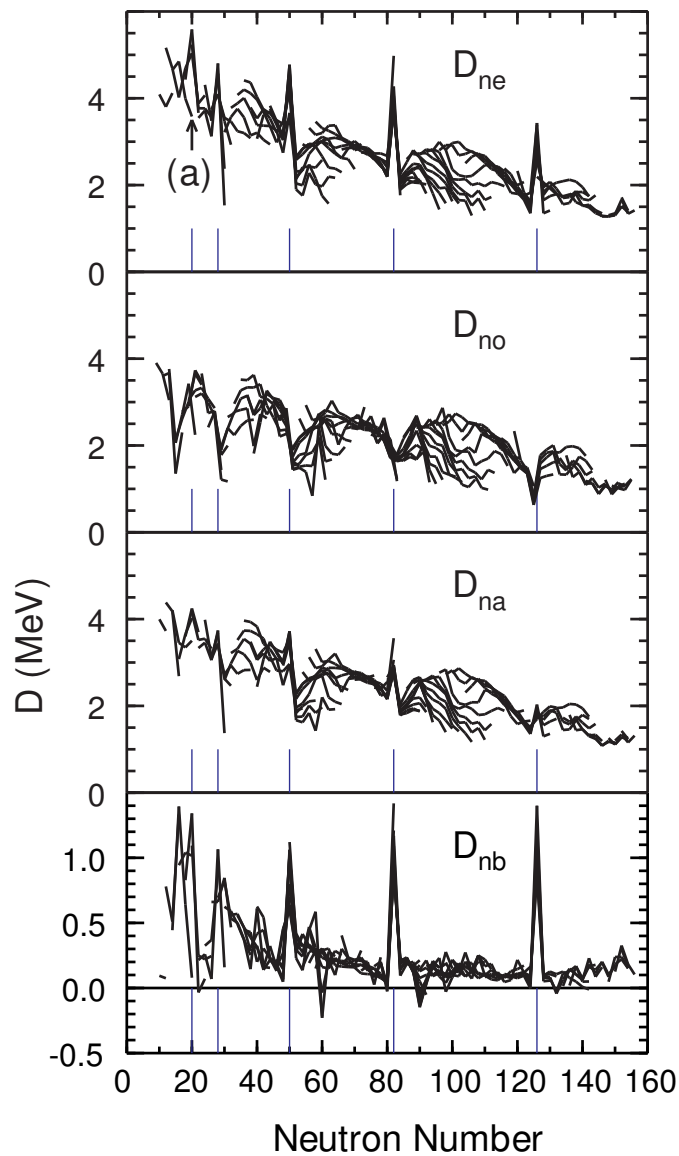


Figure 33.15: D values for neutrons for all nuclei. Values for even Z are given as a function of the number of neutrons ($N > Z$) connected by lines. D_{ne} are for even N , D_{no} are for odd N values, D_{na} are the averages given by Eq. (33.18) and D_{nb} are the differences given by Eq. (33.19). The blue lines show the location of the magic numbers 20, 28, 50, 82 126.

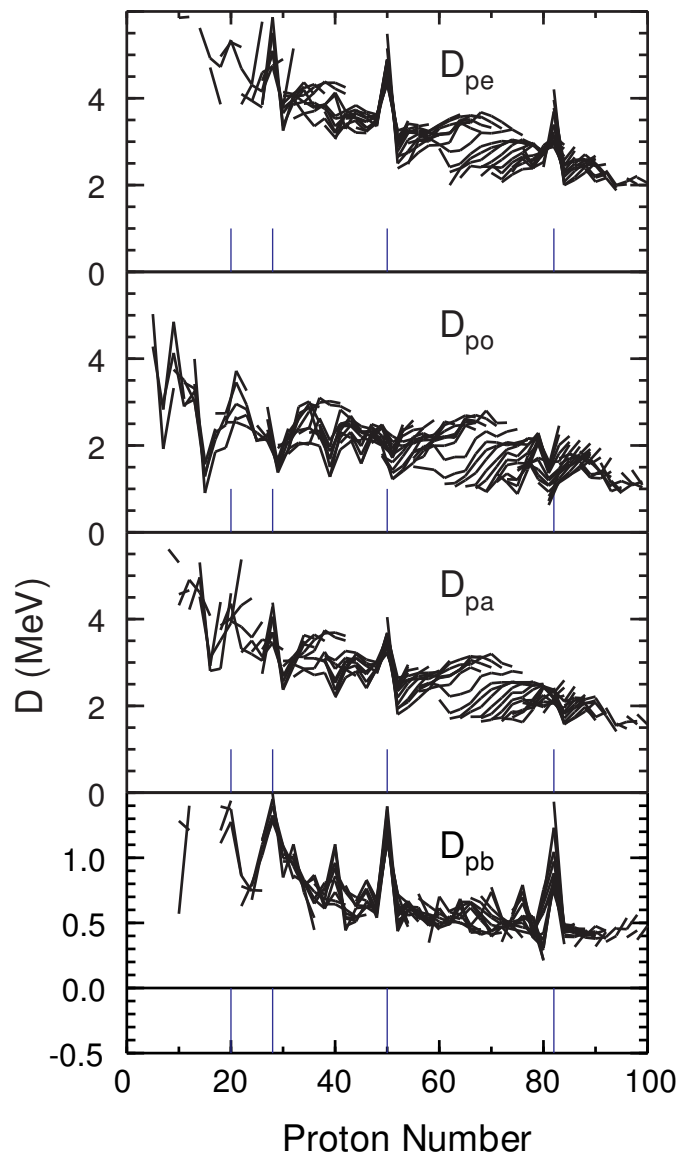


Figure 33.16: D values for protons for all nuclei. Values for even N are given as a function of the number of protons ($N > Z$) connected by lines. D_{pe} are for even N , D_{po} are for odd N values, D_{pa} are the averages given by Eq. (33.18) and D_{pb} are the differences given by Eq. (33.19). The blue lines show the location of the magic numbers 20, 28, 50 and 82.

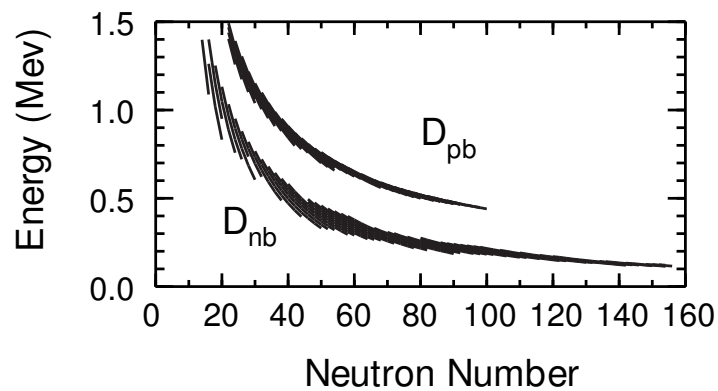


Figure 33.17: D_b values for protons and neutrons obtained with the liquid-drop model for all nuclei considered in Figs. (33.15) and (33.16).

33.10 Global results for neutrons and protons

The results for D_n and D_p for all nuclei are shown in Chapter 2. It is informative to examine D_n values for isotopes and D_p values for isotones individually to understand pairing in nuclei and its dependence on orbital occupancies and shell gaps. Here we consider the global trends for all nuclei, with the D_n for neutrons in Fig. (33.15) and the D_p for protons in Fig. (33.16). These plots include all data for $N > Z$.

The D_b determines the size of the quadratic dependence in the energies. As expected, it is larger for protons than for neutrons due to the Coulomb interaction. The overall positive values for D_b indicates that the background curvature in the energy is overall positive. To help to understand this we show in Fig. (33.15) the values for the D_{nb} and D_{pb} obtained for the same set of nuclei shown in Figs. (33.13) and (33.14), but calculated with the liquid-drop model without pairing (for the liquid-drop $D_a \approx 0$, and hence $D_e \approx D_b \approx -D_o$). The liquid-drop model gives a positive curvature that is overall a little larger than experiment. The difference between experiment and liquid drop is due the effects of deformation that generally give a negative curvature. The $D_{nb} \approx 0.6$ for chromium are close to liquid-drop

value (≈ 0.7). In contrast, the $D_{nb} \approx 0.3$ for calcium are smaller than the liquid-drop model. The two places where D_{nb} significantly drops below zero, $N = 60$ ($Z = 38 - 42$) and $N = 90$ ($Z = 62 - 68$), correspond to gains in energy from the relatively sudden changes from spherical to deformed shapes in these regions.

The D_a isolates the size of the two-particle pairing interaction $|V_o|$ (except for some residual peaks at the magic numbers). The D_o with average values for D_b added give similar information on $|V_o|$. For heavy nuclei the $|V_o|$ for both protons and neutrons average about two MeV. But there are fluctuations due to the effective number of orbitals involved in the pairing. There are several minima in D_a associated with the filling of relatively isolated low- ℓ orbitals at $N = 15$ ($1s_{1/2}$), $N = 29$ ($1p_{3/2}$), $N = 39$ ($1p_{1/2}$), $N = 57$ ($2s_{1/2}$), $N = 127$ ($2p_{1/2}$), $Z = 15$ ($1s_{1/2}$) and $Z = 39$ ($1p_{1/2}$).

For both protons and neutrons one observes in D_{ne} and D_{nb} strong shell gaps at $N=20$, 28, 50, 82 and 126. The $N = 20$ gap is broken at ^{32}Mg ($Z = 12$) [(a) with an arrow in Fig. (33.15)]. This is in the “island of inversion” [50] where the $N = 20$ shell gap becomes reduced compared to calcium ($Z = 20$) due to the dependence of the shell gap on the

tensor interaction [51] and on the smaller separation energy of the fp orbitals. [52] This gap reduction together with the enhanced interaction of protons with the $2p-2h$ neutron “pairing vibration” configuration brings the total energy of this configuration below the energy of the $0p - 0h$ configuration. [50] This island of inversion near ^{32}Mg is one of an archipelago of islands in neutron-rich nuclei related to the changing of magic numbers.[50]

In the next decade we expect a tremendous growth in the data for masses of neutron-rich nuclei from radioactive beam facilities. These are essential for understanding how the pairing and shell gap properties evolve as one approaches the neutron drip line.

Bibliography

- [1] P. W. M. Glaudemans, P. J. Brussaard and B. H. Wildenthal, Nucl. Phys. **A102**, 593 (1967).
- [2] J. Hadermann and K. Alder, Helvetica Physica Acta, **42**, 497 (1969).
- [3] B. A. Brown, D. B. Fossan, J. M. McDonald and K. A. Snover, Phys. Rev. C **9**, 1033 (1974). link

- [4] J. H. Bjerregaard, O. Hansen, O. Nathan, C. Chapman, S. Hinds and R. Middleton, Nucl. Phys. **A103**, 33 (1967).
- [5] G. Racah, Phys. Rev. **63**, 367 (1943). link
- [6] G. Racah, Phys. Rev. **76**, 1352 (1949). link
- [7] I. Talmi, Nucl. Phys. A **172**, 1 (1971).
- [8] P. Van Isacker, AIP Conference Proceedings, **1323**, 141 (2010).
- [9] J. Bardeen, L. N. Cooper and J. R. Schrieffer, Phys. Rev. **106**, 162; **108**, 1175 (1957).
- [10] *BSC 50 years*, Eds. Cooper and Feldman, World Scientific Publishing Co. (Singapore, 2011).
- [11] A. Bohr, B. R. Mottelson and D. Pines, Phys. Rev. **110**, 936 (1958). link
- [12] V. G. Soloviev, Nucl. Phys. **9**, 655 (1958).

- [13] *Fifty Years of Nuclear BSC, Pairing in Finite Systems*, Eds. R. A. Broglie and V. Zelevinsky, World Scientific Publishing Co. (Singapore, 2013).
- [14] *Physics of Atomic Nuclei*, V. Zelevinsky and A. Volya, Wiley 2017.
- [15] R. W. Richardson, Phys. Lett. **3**, 277 (1963).
- [16] R.W. Richardson, Phys. Lett. **5**, 82 (1963).
- [17] R.W. Richardson, Phys. Lett. **14**, 325 (1965).
- [18] A. Volya, B. A. Brown and V. Zelevinsky, Phys. Lett. **B509**, 37 (2001).
- [19] M. Honma, T. Otsuka, B.A. Brown and T. Mizusaki, Phys. Rev. C **65**, 061301(R) (2002); Phys. Rev. C **69**, 034335 (2004); Euro. Phys. Jour. A **25** Suppl. 1, 499 (2005).
- [20] A. Poves, J. Sanchez-Solano, E. Caurier and F. Nowacki, Nucl. Phys. A **694**, 157 (2001).
- [21] Georges Audi and Wang Meng, private communication, (2011).

- [22] A. T. Gallant et al., arxiv, 1204.1987 (2012).
- [23] E. Lunderberg et al., Phys. Rev. Lett. **108**, 142503 (2012). link
- [24] A. Plastino, R. Arvieu and S. A. Moszkowski, Phys. Rev. **145**, 837 (1966). link
- [25] I. Talmi, *Simple Models of Complex Nuclei*, Contemporary Concepts in Physics, Volume 7, (Harwood Academic Publishers, 1993).
- [26] B. A. Brown, A. Signoracci and M. Hjorth-Jensen, Phys. Lett. B 695, 507 (2011).
- [27] G. Hagen, T. Papenbrock, D. J. Dean, and M. Hjorth-Jensen, Phys. Rev. C **82**, 034330 (2010). link
- [28] M. Horoi et al., Phys. Rev. Lett. **98**, 112501 (2007). link
- [29] G. Igo, P. Barnes, and E. Flynn, Ann. Phys. (NY) **66**, 60 (1971).
- [30] B. A. Brown, Phys. Rev. Lett. **85**, 5300 (2000). link

- [31] J. Xiang, Z. P. Li, T. Niksic, D. Vretenar, and W. H. Long, Phys. Rev. **101**, 064301 (2020). link
- [32] L. V. Grigorenko, R. C. Johnson, I. G. Mukha, I. J. Thompson and M. V. Zhukov, Phys. Rev. C **64**, 054002 (2001); L.V. Grigorenko and M.V. Zhukov, Phys. Rev. C **68**, 054005 (2003). link
- [33] P. Ascher et al., Phys. Rev. Lett. **107**, 102502 (2011). link
- [34] B. F. Bayman and N. M. Hintz, Phys. Rev. **172**, 1113 (1968). link
- [35] B. A. Brown and I. J. Thompson, unpublished.
- [36] S. K. Bogner, R. J. Furnstahl and A. Schwenk, Prog. Part. Nucl. Phys. **65**, 94 (2010).
- [37] M. Hjorth-Jensen, T. T. S. Kuo, E. Osnas, Phys. Rep. **261**, (1995) 125.
- [38] D.R. Entem, R. Machleidt, Phys. Rev. C **68**, 041001 (2003). link

- [39] T. Engeland, M.Hjorth-Jensen and G.R. Jansen, CENS, a Computational Environment for Nuclear Structure, University of Oslo, unpublished.
- [40] T. Otsuka et al., Phys. Rev. Lett. **105**, 032501 (2010). link
- [41] G. Hagen, M. Hjorth-Jensen, G. R. Jansen, R. Machleidt and T. Papenbrock, arXiv, 1202.2839 (2012).
- [42] J. D. Holt, T. Otsuka, A. Schwenk and T. Suzuki, arXiv, 1009.5984v2 (2011).
- [43] R. Senkov, G. F. Bertsch, B. A. Brown, Y. L. Luo and V. Zelevinsky, Phys. Rev. C **78**, 044304 (2008). link
- [44] S. M. Lenzi et al., Phys. Rev. C **82**, 054301 (2010). link
- [45] C. R. Hoffman et al., Phys. Rev. Lett. **100**, 152502 (2008). link
- [46] E. K. Warburton and B. A. Brown, Phys. Rev. C **46**, 923 (1992). link
- [47] M. Stanoiu et al., Phys. Rev. C **78**, 034315 (2008). link

- [48] F. Nowacki and A. Poves, Phys. Rev. C **79**, 014310 (2009). link
- [49] A. Signoracci, B. A. Brown and M. Hjorth-Jensen, Phys. Rev. C **83**, 024315 (2011). link
- [50] E. K. Warburton and B. A. Brown, Phys. Rev. C46, 923 (1992). link
- [51] T. Otsuka, R. Fujimoto, Y. Utsuno, B. A. Brown, M. Honma and T. Mizusaki, Phys. Rev. Lett. **87**, 082502 (2001). link
- [52] I. Hamamoto, Phys. Rev. C **76**, 054319 (2007). link
- [53] B. A. Brown, Physics **3**, 104 (2010).

Chapter 34

Spectroscopic factors

There are many observables in nuclear physics that relate to the removal or addition of one nucleon. One of the simplest is proton or neutron decay.

Many types of reactions involve the removal of a nucleon. Reactions such as $(d, {}^3\text{He})$ or (p,d) are called “pickup” reactions since a nucleon is picked up by the light projectile and removed from the target nucleus. Reactions such as $(e,e'p)$ are called “knockout” reactions since the electron hits a proton and knocks it out of the nucleus. The collision of radioactive beams with light and heavy targets can also knockout protons or neutrons from the radioactive beam.

Also many type of reactions involve the addition of a nucleon. Reactions such as $({}^3\text{He},d)$ or (d,p) are often called “stripping” reactions since since a nucleon is stripped from the light projectile and added to the target nucleus.

The calculation of these decay rates or cross sections involve a combination of reaction theory and structure theory. In this simplest approximation these can be factorized in terms of a reaction calculation involving one nucleon in a single-particle (sp) state (n, ℓ, j) times a structure factor, S , that gives the “probability” that the overlap of the initial and final

state looks like the single-particle assumed in the reaction calculation [1]. For example the decay width given by

$$\Gamma = \Gamma_{sp}S, \quad (34.1)$$

or the reaction cross section given by

$$\sigma = \sigma_{sp}S. \quad (34.2)$$

The Γ_{sp} can be calculated scattering phase shift of a nucleon in a potential, for example, as done with the WSPOT program discussed in a previous Chapter. The calculation of σ_{sp} is carried out with a reaction code.

The sum-rules for the spectroscopic factors are related to orbital occupation numbers discussed in Sec. 1. In Sec. 2 we define the spectroscopic factors in proton-neutron formalism and give results for the sum-rules and for their values in simple configurations. In Sec. 3 we define the spectroscopic factors in isospin formalism and their relationship with those in proton-neutron formalism. In Sec. 4 we give the center-of-mass corrections for spectroscopic factors. In Sec. 5 we discuss the radial wavefunctions to be used in the

calculations of decay widths and single-particle transfer cross sections. Finally in Sec. 6 we discuss the special case of one-orbital and the related coefficient of fractional parentage.

34.1 Occupation numbers

The number operator for orbital $k = (n, \ell, j)$ is

$$\hat{N}_k = \sum_m a_{k,m}^+ a_{k,m}, \quad (34.3)$$

where the sum runs over all of the m states of orbital k . Its matrix element is

$$\langle n_k \rangle_i = \langle \Psi_i^A J_i | \hat{N}_k | \Psi_i^A J_i \rangle, \quad (34.4)$$

where $\langle n_k \rangle_i$ is the average number of protons (or neutrons) in orbit k in state Ψ_i . $\langle n_k \rangle_i$ is the average number of particle in orbit k in state Ψ_i . If one has a pure configuration the

number is an integer. For example, if one has a basis states from a single partition, e.g.

$$| n\omega J \rangle_i = | [(k_1^{n_1}\omega_1 J_1)(k_2^{n_2}\omega_2 J_2)J_{12}][k_3^{n_3}\omega_3 J_3]J \rangle_i,$$

then

$$\langle n_{k_a} \rangle_i = n_a,$$

for $a = 1, 2$ and 3 .

In general the wavefunction is a mixture of different partitions, and the occupation number is a non-integer value that comes from an average. For example for a mixture of two partitions with a wavefunction

$$| \Psi \rangle_i = \alpha | \Phi \rangle + \beta | \Phi' \rangle,$$

where $\alpha^2 + \beta^2 = 1$ and

$$| \Phi \rangle = | [(k_1^{n_1}\omega_1 J_1)(k_2^{n_2}\omega_2 J_2)J_{12}][k_3^{n_3}\omega_3 J_3]J \rangle,$$

and

$$| \Phi' \rangle = | [(k_1^{n'_1}\omega'_1 J'_1)(k_2^{n'_2}\omega'_2 J'_2)J'_{12}][k_3^{n'_3}\omega'_3 J'_3]J \rangle,$$

then

$$\langle n_{k_a} \rangle_i = \alpha^2 n_a + \beta^2 n'_a, \quad (34.5)$$

for $a = 1, 2$ and 3 .

34.2 Spectroscopic factors in proton-neutron formalism

The matrix elements of the creation, a^+ , and annihilation, \tilde{a} , operators connect configurations that differ by one proton ($q = p$) or one neutron ($q = n$)

$$\langle \Psi_b^A J_b M_b | a_{k,q,m}^+ | \Psi_a^{A-1} J_a M_a \rangle = \langle \Psi_a^{A-1} J_a M_a | a_{k,q,m}^- | \Psi_b^A J_b M_b \rangle. \quad (34.6)$$

We will use a to label the light nucleus and b to label the heavy nucleus. The spectroscopic factor for a particle (proton or neutron) in orbital k being removed from state Ψ_b^A going to

the final state Ψ_a^{A-1} is defined as

$$S_{k,q} \equiv \frac{|\langle \Psi_b^A J_b | |a_{k,q}^+| \Psi_a^{A-1} J_a \rangle|^2}{(2J_b + 1)} = \frac{|\langle \Psi_a^{A-1} J_a | |\tilde{a}_{k,q}| \Psi_b^A J_b \rangle|^2}{(2J_b + 1)} \quad (34.7)$$

where the $(2J_b + 1)$ factor is by convention associated with the heavier mass A . S implicitly depends upon the quantum numbers of the initial and final wavefunctions. S is the square of the spectroscopic amplitude

$$A_{k,q} \equiv \frac{\langle \Psi_b^A J_b | |a_{k,q}^+| \Psi_a^{A-1} J_a \rangle}{\sqrt{(2J_b + 1)}} \quad (34.8)$$

The sign of $A_{k,q}$ is important in cases like multi-nucleon transfer where several different paths enter into a calculation. But for a transition from one initial to one final state one only needs $S_{k,q}$. (In the case where several k values enter into the transition between one initial and one final state one can show that they do no interfere, i.e., $S_q = \sum_k S_{k,q}$.)

The cross section for reactions involving the removal of a particle from nucleus A_b going to nucleus $(A - 1)_a$ is proportional to the matrix element of the destruction operator

a summed over m and the final M -states M_a :

$$\begin{aligned}\sigma^- &\sim \sum_{M_a, m} |<\Psi_a^{A-1} J_a M_a | a_{k,q,m} | \Psi_b^A J_b M_b >|^2 \\ &= \sum_{M_a, m} \begin{pmatrix} J_a & j_k & J_b \\ -M_a & m & M_b \end{pmatrix}^2 |<\Psi_a^{A-1} J_a ||\tilde{a}_{k,q}|| \Psi_b^A J_b >|^2 \\ &= \frac{|<\Psi_a^{A-1} J_a ||\tilde{a}_{k,q}|| \Psi_b^A J_b >|^2}{(2J_b + 1)} = S_{k,q}.\end{aligned}\quad (34.9)$$

From the reaction theory one usually calculates a “single-particle” cross section σ_{sp} (i.e. assuming that $S = 1$) for the removal of one particle (proton or neutron) in orbit k and thus:

$$\sigma^- = S_{k,q} \sigma_{sp}. \quad (34.10)$$

Similarly, the cross section for the addition of a particle to nucleus A_b going to nucleus $(A+1)_c$ is obtained from the matrix element of a^+ summed over m and M_c :

$$\sigma^+ \sim \sum_{M_c, m} |<\Psi_c^{A+1} J_c M_f | a_{k,q,m}^+ | \Psi_b^A J_b M_b >|^2$$

$$\begin{aligned}
&= \sum_{M_c, m} \begin{pmatrix} J_c & j_k & J_b \\ -M_c & m & M_b \end{pmatrix}^2 |<\Psi_c^{A+1} J_c || a_{k,q}^+ || \Psi_b^A J_b >|^2 \\
&= \frac{|<\Psi_c^{A+1} J_c || a_{k,q}^+ || \Psi_b^A J_b >|^2}{(2J_b + 1)} \equiv S_{k,q}^+ = \frac{(2J_c + 1)}{(2J_b + 1)} S_{k,q}, \tag{34.11}
\end{aligned}$$

where $S_{k,q}$ is the spectroscopic factor for the removal of a particle from $(A+1)_c$ to A_b . Thus the cross section for the addition of a particle is given by:

$$\sigma^+ = S_{k,q}^+ \sigma_{sp} = \frac{(2J_c + 1)}{(2J_b + 1)} S_{k,q} \sigma_{sp}, \tag{34.12}$$

Thus one can infer a value of S only if the initial and final J values are known. When they are not known, one often just gives a value for S^+ (although in many cases it is still called S).

A sum rule for the spectroscopic factors can be obtained starting with the equation for the number operator, and then inserting a complete set of intermediate states:

$$< n_{k,q} >_b = \sum_m < \Psi_b^A J_b M_b | a_{k,q,m}^+ a_{k,q,m} | \Psi_b^A J_b M_b >$$

$$\begin{aligned}
&= \sum_{m,a,M_a} <\Psi_b^A J_b M_b | a_{k,q,m}^+ | \Psi_a^{A-1} J_a M_a> <\Psi_a^{A-1} J_b M_a | a_{k,q,m} | \Psi_b^A J_b M_b> \\
&= \sum_{m,a,M_a} |<\Psi_b^A J_b M_b | a_{k,q,m}^+ | \Psi_a^{A-1} J_a M_a>|^2 \\
&= \sum_{m,a,M_a} \left(\begin{array}{ccc} J_b & j_k & J_a \\ -M_b & m & M_a \end{array} \right)^2 |<\Psi_b^A J_b | a_{k,q}^+ | \Psi_a^{A-1} J_a>|^2 = \sum_a S_{k,q}.
\end{aligned}$$

This particle removal sum-rule will be written as:

$$\sum_a S_{b,a,k,q} = < n_{k,q} >_b \quad [A_b \rightarrow (A-1)_a], \quad (34.13)$$

The particle addition sum-rule for spectroscopic factors can be obtained starting with the matrix element of the number operator in the form:

$$\hat{N}_{k,q} = \sum_m a_{k,q,m}^+ a_{k,q,m} = \sum_m [1 - a_{k,q,m} a_{k,q,m}^+] = (2j_k + 1) - \sum_m a_{k,q,m} a_{k,q,m}^+, \quad (34.14)$$

in the state Ψ_b^A and inserting a complete set of states Ψ_c^{A+1} to obtain:

$$\sum_c \frac{(2J_c + 1)}{(2J_b + 1)} S_{b,c,k,q} = (2j_k + 1) - \langle n_{k,q} \rangle_b \quad [A_b \rightarrow (A+1)_c], \quad (34.15)$$

The total sum-rule is:

$$\sum_a S_{b,a,k,q} + \sum_c \frac{(2J_c + 1)}{(2J_b + 1)} S_{b,c,k,q} = (2j_k + 1). \quad (34.16)$$

If we sum Eq. (34.13) over all orbits we have a sum-rule for the total number of particles (protons or neutrons) in the nucleus:

$$\sum_{a,k,q} S_{b,a,k,q} = Z \text{ or } N \quad [A \rightarrow (A-1)]. \quad (34.17)$$

For the situations where there is only one term in the summation in Eqs. (34.13) or (34.15) one obtains the analytic results given in Fig. (34.1). If we have a k^n configuration with $n=\text{even}$ and spin $J_b = 0$ then the final state for $(n+1)$ particles must have $J_c = j_k$ and the sum rules give $S_{k,q} = (2J_c + 1 - n)/(2J_c + 1)$.

34.3 Isospin dependence

The spectroscopic factors $S_{k,q}$ as defined in the previous section apply to protons or neutrons without regard to isospin. One can generalize the results to nucleons in the state (J, T) by adding the isospin labels to Eq. (34.7) and making a matrix element that is reduced in both J and T what is designated by the triple bars:

$$S_k = \frac{|\langle \Psi_b^A J_b T_b | |a_k^+| | \Psi_a^{A-1} J_a T_a \rangle|^2}{(2J_b + 1)(2T_b + 1)} = \frac{|\langle \Psi_a^{A-1} J_a T_a | | \tilde{a}_k | | \Psi_b^A J_b \rangle|^2}{(2J_b + 1)(2T_b + 1)}, \quad (34.8)$$

The sum-rules can be applied to the nucleon occupancies, e.g.

$$\sum_a S_{b,a,k} = \langle n_k \rangle_b \quad [A_b \rightarrow (A-1)_a], \quad (34.18)$$

where $\langle n_k \rangle_b$ is the average occupation of nucleons in orbit k in the initial state b , with a maximum possible value of $2(2j + 1)$, and

$$\sum_{a,k} S_{a,b,k} = A \quad [A_b \rightarrow (A-1)_a], \quad (34.19)$$

When isospin is introduced we can also make explicit relationships between proton and neutron spectroscopic factors, $S_{k,q}$, and nucleon spectroscopic factors, S_k . Starting with Eq. (34.7) and adding the explicit T_z dependence we obtain:

$$S_{k,q} = \frac{|\langle \Psi_b^A J_b T_b T_{zb} | |a_{k,q}^+| | \Psi_z^{A-1} J_a T_a T_{za} \rangle|^2}{(2J+1)}, \quad (34.20)$$

where our convention is $(t, q) = (\frac{1}{2}, \frac{1}{2})$ for a neutron and $(t, q) = (\frac{1}{2}, -\frac{1}{2})$ for a proton. We use the Wigner-Eckhart theorem in isospin space to obtain for the removal of a nucleon:

$$\begin{aligned} S_{k,q} &= \left(\begin{array}{ccc} T_b & \frac{1}{2} & T_a \\ -T_{zb} & q & T_{za} \end{array} \right)^2 \frac{|\langle \Psi_b^A J_b T_b | |a_k^+| | \Psi_a^{A-1} J_a T_a \rangle|^2}{(2J+1)} \\ &= |\langle T_a T_{za} t q | T_b T_{zb} \rangle|^2 \frac{|\langle \Psi_b^A J_b T_b | |a_k^+| | \Psi_a^{A-1} J_a T_a \rangle|^2}{(2J_b+1)(2T_b+1)}. \end{aligned} \quad (34.21)$$

For the addition of a nucleon we have:

$$S_{k,q} = |\langle T_b T_{zb} t q | T_c T_{zc} \rangle|^2 \frac{|\langle \Psi_c^{A+1} J_c T_c | |a_k^+| | \Psi_b^A J_b T_b \rangle|^2}{(2J_c+1)(2T_c+1)}, \quad (34.22)$$

for the addition of a nucleon. Thus in shorthand notation:

$$S_{k,q} \equiv C^2 S_k, \quad (34.23)$$

where C^2 is the square the isospin Clebsch and S_k is the nucleon spectroscopic factor given by Eq. (34.8).

Although the $S_{k,q}$ are always the basic quantities measured, for nuclei near $N = Z$ it is convenient to convert to S_k in isospin formalism to understand the relationships between isobaric analogue states. Some compilations are made in terms of S_k [2]. With good isospin there is an isospin selection rule related to the triangle condition $\Delta(T_b, \frac{1}{2}, T_a)$.

When isospin is conserved, for an initial nucleus with $N = Z$, $S_p = S_n$ by mirror symmetry. If we add a nucleon to $(T_b = 0, T_{zb} = 0)$ then we must go to $T_f = 1/2$ with $C^2 = 1$. If we remove a nucleon from $(T_b = 0, T_{zb} = 0)$ then we go to $T_f = 1/2$ with $C^2 = \frac{1}{2}$.

When isospin is conserved, in a neutron-rich nucleus with isospin (T, T_z) , nucleon removal can go to states with $T_f = T + 1/2 = T_>$ ("T-upper" final states) and $T_f = T - 1/2 = T_<$ ("T-lower" final states). Proton removal to final states with $T_{zf} = T_z + 1/2$

can only go the $T_>$ states:

$$(T, T_z) \text{ proton} \rightarrow (T + \frac{1}{2}, T_z + \frac{1}{2}) = (T_>, T_z + \frac{1}{2}). \quad (34.24)$$

Transitions to final states with higher isospin are forbidden. Neutron removal to final states with $T_{zf} = T_z - 1/2$ can go to both isospin values:

$$(T, T_z) \text{ neutron} \rightarrow (T + \frac{1}{2}, T_z - \frac{1}{2}) = (T_>, T_z - \frac{1}{2}), \quad (34.25)$$

that are the isobaric analogues of the $(T + \frac{1}{2}, T_z + \frac{1}{2})$ states, and

$$(T, T_z) \text{ neutron} \rightarrow (T - \frac{1}{2}, T_z - \frac{1}{2}) = (T_<, T_z - \frac{1}{2}). \quad (34.26)$$

The C^2 values for these three types of transitions are:

$$| < T, T_z | T + \frac{1}{2}, T_z + \frac{1}{2}, t, -\frac{1}{2} > |^2 = \left(\frac{2T+1}{2T+2} \right), \quad (34.27)$$

$$|\langle T, T_z | T + \frac{1}{2}, T_z - \frac{1}{2}, t, +\frac{1}{2} \rangle|^2 = \left(\frac{1}{2T+2} \right), \quad (34.28)$$

and

$$|\langle T, T_z | T - \frac{1}{2}, T_z - \frac{1}{2}, t, +\frac{1}{2} \rangle|^2 = 1. \quad (34.29)$$

The explicit relations between $S_{k,q}$ and S_k are:

$$S(\text{proton}, k) = \left(\frac{2T+1}{2T+2} \right) S(T_>, k), \quad (34.30)$$

$$S(>, \text{neutron}, k) = \left(\frac{1}{2T+2} \right) S(T_>, k) = \left(\frac{1}{2T+1} \right) S(\text{proton}, k), \quad (34.31)$$

and

$$S(<, \text{neutron}, k) = S(T_<, k). \quad (34.32)$$

Thus, in neutron-rich nucleus one can measure “proton” spectroscopic factors, by neutron removal to the $T_>$ states. Although these $T_>$ states lie at a high excitation energy their neutron decay is often isospin forbidden [$\Delta(T_>, t, T_f = T_> - 3/2) = 0$]. Isospin mixing with

$T_<$ states leads to a small neutron spectroscopic factor. These $T_>$ states have only been observed in nuclei not too far from $N = Z$ since where the $(2T + 1)$ factor is not too large.

French-Macfarlane sum-rules [3] are obtained from these results. For proton removal to $T_> = T_i + \frac{1}{2}$ ($T_z = T_i + \frac{1}{2}$) states:

$$\sum_f S(\text{proton}) = \langle n_{k,\text{proton}} \rangle_i, \quad (34.33)$$

for neutron removal to the isobaric analogues of $T_>$ ($T_z = T_i - \frac{1}{2}$) states:

$$\sum_f S(>, \text{neutron}) = \frac{\langle n_{k,\text{proton}} \rangle_i}{2T + 1}. \quad (34.34)$$

For the total neutron removal:

$$\sum_f S(\text{neutron}) = S(<, \text{neutron}) + S(>, \text{neutron}) = \langle n_{k,\text{neutron}} \rangle_i, \quad (34.35)$$

and thus for neutron removal to the $T_<$ ($T_z = T_i - \frac{1}{2}$) states:

$$\sum_f S(<, \text{neutron}) = < n_{k,\text{neutron}} >_i - \frac{< n_{k,\text{proton}} >_i}{2T + 1}. \quad (34.36)$$

If we make a simple model for the initial and final states the values for the spectroscopic factors are sometimes easy to calculate. For example, ^{16}O might be assumed to be the closed-shell configuration $(0s_{1/2})^4 (0p_{3/2})^8 (0p_{1/2})^4$. One nucleon removal to $A = 15$ would then go to only three states each of which has a definite sum: $1/2^-$ with $S(0p_{1/2}) = 4$, $3/2^-$ with $S(0p_{3/2}) = 8$ and $1/2^+$ with $S(0s_{1/2}) = 4$. One proton or neutron removal for $T_i = 0$ going to $T_f = 1/2$ has $C^2 = 1/2$ and the sum rules are 2, 4 and 2, respectively, the same result one would obtain from the proton and neutron occupancies. (Center-of-mass corrections for these quantities will be discussed below.)

The spectroscopic factor for adding a $0d_{5/2}$ neutron to the closed-shell configuration for ^{16}O to make ^{17}O is $S_{0d_{5/2}} = 1$ and the stripping sum rule of Eq. (34.15) ($J_f = 5/2$ and $J_i = 0$) gives 6, which is the number of $0d_{5/2}$ neutron holes outside of ^{16}O .

34.4 Center-of-mass corrections

The center-of-mass (CM) correction to spectroscopic factors is closely associated with the problem of spurious states. Let's consider again the ^{16}O to $A = 15$ transition with a closed-shell configuration $(0s_{1/2})^4(0p_{3/2})^8(0p_{1/2})^4$ for ^{16}O . We take a single-particle basis that corresponds to the motion of the nucleons around a fixed center. In actuality, we should take them with respect to the CM of the $A - 1$ nucleons. However, with harmonic-oscillator wave functions, the CM of the nucleus is in a $0s$ state as long as the nucleons fill the lowest possible oscillator states. There are effects due to CM motion, but they are the simple ones associated with the CM being on its $0s$ state. We will refer to these as "non-spurious" states. All oscillator states of the form $(0s_{1/2})^4(0p_{3/2})^n(0p_{1/2})^m$ are non-spurious and in particular the $A = 15$ the $1/2^-$ and $3/2^-$ states formed in this way are non-spurious.

Starting from a non-spurious state we can make $1\hbar\omega$ excited states either by an intrinsic $1\hbar\omega$ excitation leaving the CM in the $0s$ state, or by the $1\hbar\omega$ excitation of the CM state from $0s$ to $1p$. These latter are spurious states in the nuclear shell model. A method for generating spurious states is to construct a two-body Hamiltonian corresponding to the oscillator CM

motion and then diagonalize this in the shell-model basis. When the coefficient in front of the CM Hamiltonian is large enough, the spurious states will be pushed to a high excitation energy and are prevented from mixing into the low-lying (non-spurious) states.

The lowest $1\hbar\omega$ excitation for $A = 15$, $1/2^+$ corresponds to a mixture of $(0s)^3(0p)^8$ and $(0s)^4(0p)^7(1s0d)^1$ configurations (i.e., the notation $0p$ stands for all possible arrangements involving the $0p_{1/2}$ and $0p_{3/2}$). There are a total of 18 basis states and diagonalization of the CM Hamiltonian results in two spurious states that are linear combinations of these basis states.

We can calculate the summed spectroscopic strength from the closed-shell configuration of ^{16}O to the non-spurious $A = 15$ states. The result is $S(T) = 12$ for the $0p$ shell and $S(T) = 3.2$ for the $0s$ shell - the remaining $S = 0.8$ for the $0s$ shell is in the two spurious states. However, the sum rule of $S(T) = 16$ still applies to the wave-functions the intrinsic frame, and in order to recover this result we must make the following correction to the $0p$ spectroscopic factors [4], [5]:

$$S_{0p} \rightarrow \frac{A}{(A-1)} S_{0p}. \quad (34.37)$$

where $A = 16$ in this example. This correction is the largest at the lower end of the 0p shell, e.g. $(7/6)$ for the 0p-shell $A=7$ to $A=6$ spectroscopic factors. The general derivation and result is given in [4], [5]:

$$S_k \rightarrow \left[\frac{A}{(A-1)} \right]^{2n_r+\ell} S_k. \quad (34.38)$$

For example, for the removal of the $0d_{5/2}$ in ^{17}O to ^{16}O , the CM correction factor is $(17/16)^2 = 1.129$, and for the removal of the $0f_{7/2}$ in ^{48}Ca to ^{47}Ca the CM correction factor is $(48/47)^3 = 1.065$. [The first Variational Monte Carlo (VMC) calculations [6] for the $^{16}\text{O}(\text{e},\text{e}'\text{p})$ reaction indicated that the CM correction had the effect of reducing the 0p spectroscopic factor by about 12 percent, however subsequently an error was found [7] and the new VMC result is consistent with the 7 percent enhancement expected from the CM correction.]

34.5 Overlap functions

34.5.1 Definition and properties

Spectroscopic factors are used together with models for single particle decay to calculate decay widths, $\Gamma = \Gamma_{sp}S_{k,q}$, and with model for single-particle transfer to calculate cross section, $\sigma = \sigma_{sp}S_{k,q}$. The single-particle calculations require some assumptions about the single-particle radial wavefunctions. The most common starting point are those obtained from Woods-Saxon or energy-density-functional models in the form

$$\phi_k(\vec{r}) = \frac{R_k(r)}{r} [Y^{(\ell)}(\hat{r}) \otimes \chi^s]^j, \quad (34.39)$$

With this assumption the overlap function θ is given by

$$\theta_{i,f,\ell,j}(\vec{r}) = A_{i,f,k} \phi_k(\vec{r}), \quad (34.40)$$

where A is the spectroscopic amplitude between the initial and final state, and k represents a specific orbital in the assumed model space. More generally the overlap function should

be expressed in terms a sum over a complete set of radial wavefunctions:

$$\theta_{i,f,\ell,j}(\vec{r}) = \sum_{n_r} a_{i,f,k} \phi_k(\vec{r}) \quad (34.41)$$

In practice, one uses Eq. (34.40) with the ϕ_k generated to reflect properties of the decay or transition. Most commonly, one starts with specific k in a reasonable potential geometry and then adjusts the well depth in order to give the observed Q value for the decay or reaction. For nuclear reactions the next step is to adjust the radius and/or diffuseness of the potential to reproduced the shape of the angular distribution [8].

34.5.2 Asymptotic properties

We can consider the overlap in Eq. (34.40) as a function of r . At large r where the nuclear interactions are negligible this overlap must be governed by the kinematical asymptotic appropriate for the energy difference $\Delta E = E_f - E_i$ ($E = -\text{BE}$ where BE is the binding energy). For example for $^{17}\text{O}(5/2^+)$ to $^{16}\text{O}(0^+)$, $\Delta E = -4.14$ MeV and there is an exponential

decay appropriate for a d wave bound by 4.14 MeV.

In some reactions such as (${}^3\text{He}, d$) and ($d, {}^3\text{He}$), the optical potentials are such that only the part of the overlap function near the nuclear surface is important. When the incident energy far below the Coulomb barrier, the projectile wavefunction is nonzero only for large radii, and it is only the asymptotic part of the overlap function that is important. The assumptions about the potential only influence the overall normalization, $N_{\ell,j}$, of the asymptotic wave function:

$$\theta_{i,f,\ell,j}(\vec{r}) \rightarrow N_{\ell,j} f_{\ell}(r), \quad (34.42)$$

where $f_{\ell}(r)$ is an asymptotic form independent of the strong potential that depends upon ℓ due to the the centrifugal barrier. It is usually taken as the Whittaker function [9]. In the single-particle model the asymptotic behavior is that of the single-particle radial wavefunction

$$\frac{R_k(r)}{r} \rightarrow N_k f_{\ell}(r), \quad (34.43)$$

34.5.3 The well-depth prescription

In some cases the nuclear model may explicitly contain the correct asymptotic behavior, such as a Hartree-Fock model for ^{17}O in which the last neutron is bound by 4.14 MeV. But usually many-body nuclear models are developed that do not explicitly contain the correct asymptotic form. For example, a typical shell-model calculation for ^{18}O consists of calculating the sd-shell configuration mixing and total energy by evaluating the G matrix elements of a two-body residual interaction in an harmonic-oscillator basis. The implicit radial wave functions used are the same for both ^{17}O and ^{18}O and have the incorrect (oscillator) asymptotic for both the ^{17}O to ^{16}O and the ^{18}O to ^{17}O overlaps.

The general method for generating an overlap function with the correct asymptotic form is to start with a realistic mean-field potential for the single-particle wave functions and then to modify this potential such that the single-particle (ϵ) energy is equal to the actual energy difference (ΔE). One way to do this is to multiply the mean-field potential by a constant such that the $\epsilon = \Delta E$. This is the “well-depth” prescription. Historically, the well-depth prescription was easy to apply numerically and has become the default method in

many codes and analyzes. For example, for the $^{18}\text{O}(\text{gs})$ to $^{17}\text{O}(5/2^+ \text{ gs})$ reaction one would increase the potential depth in order to bind the $0d_{5/2}$ orbital by the experimental energy difference $\Delta E = -12.19$ MeV. Likewise for the $^{18}\text{O}(\text{gs})$ to $^{17}\text{O}(1/2^+ 0.87 \text{ MeV}$ excited state) reaction one would increase the potential for the $1s_{1/2}$ orbital in order to give the experimental energy difference of $\Delta E = -13.06$ MeV.

In cases where the single-particle wave function generated by the well-depth prescription is close to that of a realistic mean-field (e.g. the multiplying factor is not too different from unity) this method is a reasonable procedure. This usually applies to cases where the spectroscopic factor is near the sum-rule limit. But when the spectroscopic factor is small, this prescription may be questioned. For example, in the $(0d_{5/2})^3$ configuration there are states with $J = 3/2, 5/2$ and $9/2$. The overlap function between $(0d_{5/2})^2, J = 0$ and $(0d_{5/2})^3, J = 3/2$ must vanish ($S = 0$) since the $J = 3/2$ does not match the $j = 5/2$ of the transferred particle. A non-vanishing spectroscopic factor would result from a small $(0d_{5/2})^2(0d_{3/2})$ admixture into the $(0d_{5/2})^3$ wave functions. The single-particle potential needed to give the correct asymptotic for this small component is quite different from the mean-field potential. Thus rather than multiply the mean-field potential it may be more appropriate to add a

surface peaked term to the mean-field potential as discussed in the next section.

A common way to implement the well-depth prescription is to generate an overlap function from the single-particle wave functions obtained from a Woods-Saxon potential. For the well-depth prescription, one would adjust the strength of the central potential to obtain a single-particle wave function ϕ_j that has a single-particle energy equal to the energy difference between the initial and final states under consideration. This wave function goes into the reaction theory to calculate a cross section, and then from comparison to experiment one deduces the spectroscopic factor S . However, one should keep in mind that the value for S depends upon the assumptions made about the reaction models and about the overlap function.

34.5.4 Beyond the well-depth prescription

One would like to carry out an experiment that is sensitive to the shape as well as the magnitude of the overlap function. But the nuclear reactions are generally only sensitive to

the surface or asymptotic part, and thus the assumption about the fixed Woods-Saxon shape cannot be easily tested. As mentioned above the prescription based on the adjustment of the depth of a central potential is appropriate only when the transition under consideration is actually close to single-particle in nature. When the single-particle strength is fragmented due to residual interactions (beyond the mean-field) one should consider additions to the central potential that are related to the residual interaction.

Pinkston and Satchler [10] discussed the situation for the (p,d) reactions in the $0f_{7/2}$ shell region, for example $^{48}\text{Ti}(p,d)$ leading to the lowest $T_< = 3/2$ and $T_> = 5/2$ states in ^{47}Ti that differ in separation energy by 7.3 MeV. This isospin splitting of the $0f_{7/2}$ orbit can be related to an isovector residual interaction that peaks near the nuclear surface and might be modeled on the derivative of the central Woods-Saxon potential. Thus the shape as well as the strength of the central potential must be considered. In terms of the original Woods-Saxon shape, the surface potential has the effect of effectively increasing the radius r_o for the $T_>$ state (in contrast to the well-depth prescription where the well-depth V_o is increased). This results in a relatively larger radius for the overlap function, a larger DWBA cross section, and hence a smaller spectroscopic factor. Similar considerations regarding the

shape of the potential are related to the collective model [10]. More detailed models of these residual-interaction effects have discussed some of which involve solving a set of coupled equations for the bound state [11], [12], [13], [14], [15], [16], [17].

In these examples, the energy difference ΔE for the transition is usually larger than the single-particle energy. The well-depth prescription thus gives an rms radius for the overlap function that is smaller than the rms radius of the single-particle state. The surface effect of the residual interaction correction leads to an overlap function that has a relatively larger rms radius (back in the direction the single-particle rms radius). In the $0f_{7/2}$ shell it was found that a practical prescription is to fix the Woods-Saxon well depth and radius to give the correct energy difference and a *state-independent* rms radius for the overlap function [18]. The spectroscopic factors obtained with the residual interaction corrections are typically up to a factor of two smaller than those obtained with the well-depth prescription.

The other extreme is stripping to a nearly filled orbit. For example $^{40}\text{Ca}(\text{d},\text{p})^{41}\text{Ca}$ leading to the $3/2^+$ state (at 2.04 MeV). The spectroscopic factor would be zero in the limit where the $0d_{3/2}$ orbit is filled in ^{40}Ca . The energy difference is $\Delta E = -10.4$ MeV

as compared to the single-particle energy of about $\epsilon = -15.6$ MeV (e.g. the ^{40}Ca - ^{39}Ca binding energy difference). The well-depth prescription thus leads to an rms radius for the overlap function ($\Delta E = -10.4$ MeV) that is larger than that of the single-particle state ($\Delta E = -15.6$ MeV). The surface property of the residual interaction leads to an overlap function that has a relatively smaller rms radius [19] (again back in the direction of the single-particle rms radius).

34.6 Fractional parentage coefficients

Historically, spectroscopic factors for many-body configurations were expanded and tabulated in terms of the simplest case of one orbital. With the advance of computational methods these tables are not often used. But the methods and notation provide insight into the analytical properties of spectroscopic factors, and are discussed here for completeness.

We will consider wavefunctions for n particles in one orbital: $| k^n \omega J \rangle$ where ω is

a label that is used if there are more than one state for a given J value. The removal spectroscopic amplitude is given by

$$A_k \equiv \frac{\langle k^n \omega J | |a_k^+| |k^{n-1} \omega' J' \rangle}{\sqrt{2J+1}}. \quad (34.44)$$

The sum of $S = A^2$ over all final states is n . Coefficients of fractional parentage [20] (CFP) are the spectroscopic amplitudes divided by \sqrt{n} , so that the sum over final states is unity

$$\langle j^n \omega J | \{ j^{n-1} \omega' J' \rangle \equiv \frac{\langle k^n \omega J | |a_k^+| |k^{n-1} \omega' J' \rangle}{\sqrt{n(2J+1)}} = \frac{A_k}{\sqrt{n}}. \quad (34.45)$$

The notation $\{ \}$ signifies the removal of one-particle from the state on the left-hand side leading to the state on the right-hand side. The j is used in the CFP rather than k , in order to emphasize the fact that these coefficients depend only on j and not on n and ℓ . In terms of CFP the sum-rule becomes:

$$\sum_{\omega' J'} |\langle j^n \omega J | \{ j^{n-1} \omega' J' \rangle|^2 = 1. \quad (34.46)$$

Thus, the square of the one-particle CFP is the probability of taking one particle in the state k from the configuration $| k^n \omega J \rangle$ leaving it in the antisymmetric configuration $| k^{n-1} \omega' J' \rangle$. One can use the CFP to express the wavefunction $| k^n \omega J \rangle$ as a sum over $| k^{n-1} \omega' J' \rangle$ states coupled to a single-particle state:

$$| k^n \omega J \rangle = \sum_{\omega' J'} | < j^n \omega J | j^{n-1} \omega' J' > | [| k^{n-1} \omega' J' \rangle \otimes | k \rangle]^J. \quad (34.47)$$

When there is only one initial and final state, the CFP are unity. The basic examples are:

$$| < j^1, J = j | j^0, J' = 0 > | = 1, \quad (34.48)$$

$$| < j^2 J | j^1, J' = j > | = 1, \quad (34.49)$$

where J is even, and

$$| < j^{2j+1}, J = 0 | j^{2j}, J' = j > | = 1. \quad (34.50)$$

The CFP for a closed shell minus $(n - 1)$ particles can be expressed in terms of those

for n particles:

$$\begin{aligned} & \langle j^{2j+1-(n-1)} \omega J | \} j^{2j+1-n} \omega' J' \rangle \\ &= (-1)^{j+J'-J} \sqrt{\frac{n(2J'+1)}{(2j+2-n)(2J+1)}} \langle j^n \omega' J' | \} j^{n-1} \omega J \rangle. \end{aligned} \quad (34.51)$$

We can convert the special results of Eqs. (34.48) and (34.49) for particles to those for holes. When $n = 1$, $J' = j$, and $J = 0$ one obtain the same result as in Eq. (34.50). For the case when $n = 2$ and $J = j$ one obtains

$$|\langle j^{2j}, J = j | \} j^{2j-1} J' \rangle| = \sqrt{\frac{(2J'+1)}{j(2j+1)}} |\langle j^2 J' | \} j^1, J = j \rangle| = \sqrt{\frac{(2J'+1)}{j(2j+1)}}, \quad (34.52)$$

where J' is even. For example when we take one particle from the $[(j = 5/2)^5, J = 5/2]$ configuration the probability to leave the system in the states $[(j = 5/2)^4, J']$ is $\frac{1}{15}$, $\frac{5}{15}$ and $\frac{9}{15}$, for $J' = 0, 2$ and 4 , respectively.

There are a variety of methods and computer programs for calculating the one-particle CFP [21], [22], [23], [24], [25], [26], and they are tabulated in the literature [20], [27], [28], [29], [30], [31] for small values of n and j . Also the projection operator method discussed in the next section can be used to calculate these CFP. All matrix elements in the J -scheme can be reduced to equations involving these one-particle CFP, and thus they are a primary input to any calculation or computer code that utilizes a J -coupled basis. As an example, the one-particle CFP for the $(j = 5/2)^3$ and $(j = 7/2)^3$ configuration [20] are given in Tables (34.1) and (34.2).

The results for specific CFP given in the text and tables implicitly have associated a choice for the phase factors of the initial and final wavefunctions. It is important to keep these phase factors consistent throughout the intermediate stages of a calculation, especially when the CFP are combined with the outputs of other programs.

Table (34.1). One-particle CFP for the $(j = 5/2)^3$ configuration.

$J \setminus J'$	0	2	4
3/2	0	$-\sqrt{\frac{5}{7}}$	$\sqrt{\frac{2}{7}}$
5/2	$-\sqrt{\frac{2}{9}}$	$\sqrt{\frac{5}{18}}$	$\sqrt{\frac{1}{2}}$
9/2	0	$\sqrt{\frac{3}{14}}$	$-\sqrt{\frac{11}{14}}$

Table (34.2). One-particle CFP for the $(j = 7/2)^3$ configuration.

$J \setminus J'$	0	2	4	6
3/2	0	$\sqrt{\frac{3}{14}}$	$-\sqrt{\frac{11}{14}}$	0
5/2	0	$\sqrt{\frac{11}{18}}$	$\sqrt{\frac{2}{33}}$	$-\sqrt{\frac{65}{198}}$
7/2	$-\sqrt{\frac{1}{4}}$	$\sqrt{\frac{5}{36}}$	$\sqrt{\frac{1}{4}}$	$\sqrt{\frac{13}{36}}$
9/2	0	$\sqrt{\frac{13}{126}}$	$-\sqrt{\frac{50}{77}}$	$\sqrt{\frac{49}{198}}$
11/2	0	$-\sqrt{\frac{5}{18}}$	$\sqrt{\frac{13}{66}}$	$-\sqrt{\frac{52}{99}}$
15/2	0	0	$\sqrt{\frac{5}{22}}$	$-\sqrt{\frac{17}{22}}$

34.7 Experimental results for specific nuclei

There have been many experimental papers related to the extraction of spectroscopic factors. The details obtained have been and continue to be tremendously important in guiding the our understanding of nuclear structure. The first large-scale review of theory and experiment for spectroscopic factors is given in [1]. In this section we will give a few examples of the wide range of data available.

We will mainly look at examples where nucleons are removed from the nucleus. Reactions such as $(d, {}^3He)$ or (p,d) are called “pickup” reactions since a nucleon is picked up by the light projectile and removed from the target nucleus. Reactions such as $(e,e'p)$ are called “knockout” reactions since the electron hits the proton and knocks it out of the nucleus. The collision of radioactive beams with light and heavy targets can also knockout protons or neutrons from the radioactive beam. In addition, the spontaneous decay of a proton or neutron from an unbound state removes a nucleon from the nucleus.

We will also look at examples for spectroscopic factors when nucleons are added to

the nucleus. Reactions such as (${}^3\text{He}, \text{d}$) or (d, p) are often called “stripping” reactions since a nucleon is stripped from the light projectile and added to the target nucleus. Sometimes the spectroscopic factors for the a given pair of states can be studied in both stripping and pickup reactions. For consistency the same spectroscopic factor should be obtained from both reactions.

34.7.1 ${}^{51}\text{V} \rightarrow {}^{50}\text{Ti}$

One of the best examples for proton removal spectroscopic factors in a one-orbit model is given by the reaction ${}^{51}\text{V} \rightarrow {}^{50}\text{Ti}$. In this mass region the $0f_{7/2}$ orbit is rather well isolated. In this model the structure of ${}^{51}\text{V}$ is a closed shell, $(0f_{7/2})^8$, for neutrons and $(0f_{7/2})^3$ for protons. For this configuration there is only one $J = 7/2$ state, and the spectroscopic factors can be obtained immediately from the Table of CFP together with the relationship:

$$S = n |< j^n \omega_i J_i | \} j^{n-1} \omega_f J_f >|^2 . \quad (34.53)$$

This gives the values in the first column of Table (34.3) whose sum is three - the total number of protons in the $0f_{7/2}$. This particular structure leads to nontrivial values for the spectroscopic factors that are in excellent agreement with the original $^{51}\text{V}(\text{d},^3\text{He})$ (52 MeV) experiment (Table 22.1.a) [32]. An analysis of $^{51}\text{V}(\text{d},^3\text{He})$ data at several energies [33] shows that absolute spectroscopic factors are sensitive to the reaction model, but the relative spectroscopic factors for the various J_f values are rather insensitive. A more recent finite-range DWBA analysis of 80 MeV data results in spectroscopic factors that are about 0.6 of those expected from the $0f_{7/2}$ shell model (Table 22.1.b). This reduction from unity is consistent with the more recent ($e,e'\text{p}$) results (Table 22.1c) that will be discussed in more detail below.

34.7.2 $(^3\text{He},\text{d})$ in the sd shell

The sd-shell provides one of the best examples of how shell-model configuration mixing can be applied consistently over a wide mass range. One can find an effective two-body interaction [35] which is able to reproduce the energies of about 1000 levels for nuclei over the mass range

Table (34.3). Proton spectroscopic factors for $^{51}\text{V} \rightarrow ^{50}\text{Ti}$

J_f	$(f_{7/2})^3$ model	$(d, {}^3\text{He})$ (a)	$(d, {}^3\text{He})$ (b)	$(e, e'p)$ (c)	$(d, {}^3\text{He})$ (c)
0	0.75	0.73	0.40(1)	0.37(3)	0.30
2	0.42	0.39	0.21(1)	0.16(2)	0.15
4	0.75	0.64	0.42(1)	0.33(3)	0.26
6	1.08	1.05	0.66(1)	0.49(4)	0.39
sum	3.00	2.81	1.69	1.35(7)	1.10

a) 1967 analysis of Hinterberger et al. [32] for 52 MeV data.

b) 1976 analysis of Craig et al. [33] for 80 MeV data.

c) 2001 analysis of Kramer et al. [34].

$A=17-39$ to within an rms deviation of a few hundred keV [36]. The electromagnetic and beta decay properties of these levels are also rather well understood in this sd-shell model [37].

Endt has made a compilation of spectroscopic factors for the sd-shell [2]. Vernotte et al. [38] has made an analysis of spectroscopic factors in the sd-shell with a unified analysis of $(^3\text{He},d)$ (nucleon removal) data obtained with a ^3He energy of 25 MeV. The data themselves are rather precise and the statistical error is relatively small. Most of the uncertainty associated with the extracted spectroscopic factors is related to the reaction-model interpretation. The data provides information for 39 transitions between specific initial and final states over the mass region $A=17-40$. The analysis depends upon a zero-range DWBA analysis for which one must provide optical potentials for the ^3He and d. The overlap function is based upon the well-depth method.

The initial analysis was carried out with Woods-Saxon shape parameters $r_o = 1.25$ fm and $a = 0.65$ fm. Initially the same shape parameters were used for the spin-orbit potential. The experimental and theoretical spectroscopic factors are shown on the left-hand side of

Fig. (34.3) (In [38] the results for the nucleonic spectroscopic factors are given, but here I have converted these to proton spectroscopic factors by dividing by the C^2 factor.) In the top one observes good agreement in terms of the variation from large to small values. The largest value for $0d_{5/2}$ (filled circle) corresponds to the $^{27}\text{Al}(5/2^+ \text{ gs}) \rightarrow ^{28}\text{Si}(0^+ \text{ gs})$ transition. In the simplest $(0d_{5/2})^n$ model the theoretical value would be six, but this gets reduced to 3.61 due to configuration mixing in the full sd shell. The largest value for $0d_{3/2}$ (cross) is for the $^{39}\text{K}(3/2^+) \rightarrow ^{40}\text{Ca}(0^+)$ transition. In the simple $(0d_{3/2})^n$ model as well as in the full sd-shell model it has a theoretical value of 4.

In the bottom of Fig. (34.3) the ratios are plotted vs the theoretical value. The ratios for $0d_{3/2}$ (crosses) are systematically higher than those for $0d_{5/2}$ (filled circles). A way to correct this problem was noted by Vernotte et al., and I will discuss this in some detail to illustrate the problems that can arise in the model dependence in the analysis. Namely, the ratios can be improved if the value of r_{so} used in the Woods-Saxon potential is reduced from 1.25 to 1.00 fm. To better understand how this works, the central and spin-orbit Woods-Saxon potentials are plotted on the bottom left-hand of Fig. (34.4). The central potential is the one required to bind a 0d orbit by 3 MeV (no spin-orbit). The spin-orbit potential plotted

represents the total change in potential between the $0d_{5/2}$ and $0d_{3/2}$ orbits that is required to reproduce the spin-orbit energy difference of about 6 MeV. The well-depth prescription is now used to generate a wave function for the $0d_{5/2}$ and $0d_{3/2}$ orbits with a fixed binding energy of 3 MeV (an arbitrary but typical value) by adjusting the strength V_o of the central potential. The “effective” total potential (the sum of the adjusted central and spin-orbit terms and excluding Coulomb) for the $0d_{5/2}$ and $0d_{3/2}$ are shown in the middle part of Fig. (34.4). The square of the radial wave functions are shown at the top. The effective potential for $0d_{5/2}$ has an effectively larger radius than that for $0d_{3/2}$ and the resulting $0d_{5/2}$ radial density is larger than that $0d_{3/2}$.

The $(^3\text{He},\text{d})$ cross section is mainly sensitive to the overlap function near the surface, and essentially only the asymptotic normalization is important. On the left-hand side of Fig. (34.4) this asymptotic normalization is 25% larger for $0d_{5/2}$ compared to $0d_{3/2}$ that arises from the spin-orbit potential. Thus for a given separation energy, the spin-orbit potential causes the extracted spectroscopic factor for $0d_{5/2}$ to be 25% less than that for $0d_{3/2}$ (in the direction of the deviation noted in Fig. (34.3)).

Vernotte et al. were able to improve this situation by reducing the range of the spin-orbit potential to from 1.25 fm to 1.00 fm (the ratio of the diffuseness to the range of the spin-orbit potential was fixed at 0.52). This results in effective potentials for $0d_{5/2}$ and $0d_{3/2}$ that are nearly the same at the nuclear surface. The resulting spectroscopic factors shown in Fig. (34.3) have a more consistent average ratio for $0d_{5/2}$ and $0d_{3/2}$.

This analysis brings into focus the model dependence of extracting spectroscopic factors. One could use other models for the bound states. I show, as an example, the potentials that one obtains from the SKX Skyrme Hartree-Fock model [39] at the bottom of Fig. (34.4), together with the effective potentials obtained by adjusting the central part of the HF potential to obtain binding energies of 3 MeV for $0d_{5/2}$ and $0d_{3/2}$. It turns out that the spin-orbit potential from the Skyrme interaction is peaked at a smaller radius compared to the conventional Woods-Saxon model and that this leads to very similar effective potentials near the surface. In this sense the Skyrme HF justifies the empirical result obtained by Vernotte et al. The reason why the Skyrme spin-orbit potential peaks at a smaller radius is that it is obtained from the derivative of the matter density that has a smaller effective radius than the potential.

The possible uncertainty in the spin-orbit potential is part of a larger question as to how accurately the central potential and the resulting asymptotic normalizations can be calculated. In terms of the $(^3\text{He},\text{d})$ reaction Vernotte et al. pointed out the strong dependence of the extracted spectroscopic factors on the range of the central potential. They noted that an increase of 0.01 fm in r_o decreased the extracted spectroscopic factors by 3-4% (see Fig. 8 in [38]). Since the reaction takes place at the nuclear surface and depends mainly on the asymptotic normalization, there is very little dependence of the shape of the angular distributions on r_o .

There are also issues related to the reaction model. Vernotte et al. used the convenient zero-range form of DWBA, but they noted that non-locality corrections and finite-range correction would decrease the overall spectroscopic factors by about 25%. Thus to attempt to summarize the sd-shell data in terms of absolute spectroscopic factors I show in Fig. (34.5) the values obtained with the new reduced-radius spin-orbit interaction and multiplied by 0.75 are plotted as the ratio of experiment over theory vs the mass value.

34.7.3 (e,e'p)

The (e,e'p) reaction is perhaps the most direct way to measure the proton spectroscopic factor. It is largely determined by the well understood electromagnetic interaction and the only hadronic reaction theory involved is for the final-state interactions of the protons as they leave the nucleus. [40], [34] Unlike the reactions such as the (${}^3\text{He},\text{d}$) and ($\text{d},{}^3\text{He}$) discussed above that depend mainly on the surface part of the overlap function, the (e,e'p) reaction is sensitive to the overlap function at all radii. The shape of the momentum proton distributions is sensitive to the radial shape of the overlap function. Thus, one can adjust the well depth and the radius of the potential to give the separation energy and the shape of the momentum distribution. The analysis of many data have recently been carried out Kramer et al. [34] and I give the some of the resulting proton spectroscopic factors in Table (34.4).

Table (34.4) also gives the spectroscopic factors obtained from the conventional analysis of ($\text{d},{}^3\text{He}$) data based upon zero-range DWBA and a Woods-Saxon potential with a radius of $r_o = 1.25$ fm. The spectroscopic factors deduced from (e,e'p) are systematically smaller than

Table (34.4). Proton spectroscopic factors for a range of nuclei

Nuclei	E_x (MeV)	J_f	(e,e'p)(a) NR(b)	(e,e'p) R(c)	(d, $^3\text{He}^{\text{(a)}}$) (old)	(d, $^3\text{He}^{\text{(a)}}$) (new)
$^{12}\text{C} \rightarrow ^{11}\text{B}$	0.00	$3/2^-$	1.72(11)		2.98	1.72
	2.12	$1/2^-$	0.26(2)		0.69	0.27
	5.02	$3/2^-$	0.20(2)		0.31	0.11
$^{16}\text{O} \rightarrow ^{15}\text{N}$	0.00	$1/2^-$	1.27(13)	1.46(e)	2.30	1.02
	6.32	$3/2^-$	2.25(22)	2.8(e)	3.64	1.94
	9.93	$3/2^-$	0.133(15)(d)			
	10.70	$3/2^-$	0.222(4)(d)			
$^{30}\text{Si} \rightarrow ^{29}\text{Al}$	0.00	$5/2^+$	2.21(20)(g)		3.96(g)	
$^{31}\text{P} \rightarrow ^{30}\text{Si}$	0.00	0^+	0.40(3)		0.62	0.36
$^{40}\text{Ca} \rightarrow ^{39}\text{K}$	0.00	$3/2^+$	2.58(19)	3.32(f)	3.70	2.30
	2.52	$1/2^+$	1.03(7)		1.65	1.03
$^{48}\text{Ca} \rightarrow ^{47}\text{K}$	0.00	$1/2^+$	1.07(7)		1.55	0.96
	0.36	$3/2^+$	2.26(16)		4.16	2.39
$^{51}\text{V} \rightarrow ^{50}\text{Ti}$	0.00	$(0,2,4,6)^+$	1.35(7)		2.81	1.10
$^{208}\text{Pb} \rightarrow ^{207}\text{Tl}$	0.00	$1/2^+$	0.98(9)	1.40(8)(h)	1.8	1.5
	0.35	$3/2^+$	2.31(22)	2.92(16)(h)	3.8	2.2
	1.35	$11/2^-$	6.85(68)		7.7	5.4
	1.67	$5/2^+$	2.93(28)		3.5	3.1
	3.47	$7/2^+$	2.06(20)		3.5	2.9

a) From Kramer et al. [34] except where noted.

b) Non-relativistic analysis from Kramer et al. [34] except where noted.

c) Relativistic analysis.

d) From Leuschner et al. [41].

e) From Gao et al. [42].

d) From Wessling et al. [43].

g) From Jin et al. [44].

h) From Udias et al. [45].

those from the old ($d, {}^3He$) analysis by a factor of 0.6-0.7. They are also about this much smaller than that expected from a shell-model or sum-rule estimate. The ($d, {}^3He$) analysis based upon a zero-range reaction theory and a simple shape for the form factor appears to “accidentally” give spectroscopic factors that are close to the single-particle (sum-rule) model. Kramer et al., also carry out a new analysis of the ($d, {}^3He$) data based on a finite-range DWBA and with Woods-Saxon wave functions for the overlap function with r_o adjusted to give the correct shape of the ($e, e'p$) momentum distributions. A non-locality correction [34] was also applied to the Woods-Saxon wave functions. This adjustment of bound state wave functions has the effect of increasing the rms radius of the orbitals, increasing the asymptotic normalization, and hence reducing the spectroscopic factors. The total effect of changing the reaction model and overlap function is to bring the spectroscopic factors deduced from the new ($d, {}^3He$) analysis into much better agreement with those from ($e, e'p$) (see Table (34.4)).

The values of r_o that are needed to fit the ($e, e'p$) momentum distributions [34] are typically in the range 1.20 to 1.30 fm - close to the average accepted value of 1.25 fm. But there are exceptional cases, such as the value of $r_o = 1.65$ required for the relatively weak ${}^{12}C$ to ${}^{11}B(1/2^-, 2.1 \text{ MeV})$ transition.

For consistency we can compare the spectroscopic factors obtained from the nucleon removal reactions in Table (34.4) to those from the (${}^3\text{He},\text{d}$) nucleon addition reaction of Vernotte [38]. The results based on the discussion in the previous section with the reduced-radius spin-orbit potential and then multiplied by 0.75 are $C^2S = 0.49$ for ${}^{30}\text{Si} \rightarrow {}^{31}\text{P}$ and $C^2S = 2.69$ for ${}^{39}\text{K} \rightarrow {}^{40}\text{Ca}$. These are close to those obtained in ($e,e'\text{p}$) but somewhat larger than those from the new ($\text{d},{}^3\text{He}$) analysis given in Table (34.4).

Most of the ($e,e'\text{p}$) data in Table (34.4) is for the pickup of states below the Fermi surface. One of the few ($e,e'\text{p}$) data available for states above the Fermi surface is from the ${}^{209}\text{Bi}$ data of Branford et al. [46]. The data for ${}^{209}\text{Bi}(e,e'\text{p}){}^{208}\text{Pb(gs)}$ are not very good, but from the most accurate data points in Fig. 2 of [46] one would interpret this experiment as giving $C^2S = 1$ for $0\text{h}_{11/2}$ knockout. as expected in the extreme single-particle shell model. Branford et al. also study the excited states in ${}^{208}\text{Pb}$ corresponding to knocking out the hole states given in Table (34.4) and leaving ${}^{208}\text{Pb}$ in multiplet of states corresponding to the one-particle one-hole configurations. From a comparison to the ${}^{208}\text{Pb}(e,e'\text{p}){}^{207}\text{Tl}$ data, they conclude that the model of ${}^{209}\text{Bi}$ based on a $0\text{h}_{9/2}$ proton coupled to an inert ${}^{208}\text{Pb}$ core has a high degree of validity.

It is important that the spectroscopic factor extracted from the (e,e'p) data does not depend on the electron energy and/or the reaction model that is used to understand the data. For the (e,e'p) data typical of those for Table (34.4), the electron energy is about 500 MeV and the outgoing proton kinetic energy is about 100 MeV. The relevant variable is the four-momentum squared, Q^2 , transferred by the virtual photon to the knocked-out nucleon that is about 0.2 (GeV/c)² in this case. For these low Q^2 a proton optical potential was used for the final-state interactions. The $^{12}\text{C}(\text{e},\text{e}'\text{p})$ data has been taken and analyzed over a wide range of Q^2 . At high Q^2 values (0.8 and higher) one usually uses a Glauber model for the final-state interactions of the protons. At an intermediate Q^2 of about 0.6 both the optical model and the Glauber model can be used. Lapikas et al. [47] found that the two methods of analysis gave different spectroscopic factors. For sum of the three 0p shell states in Table (34.4), the proton spectroscopic factors deduced from the optical-model analysis is about 2.2 (consistent with Table (34.4)) but the Glauber model analysis gave 3.56 (much closer to the simple shell model result of 4). However, more recently Radici et al. [48] have analyzed a similarly wide range of data for $^{16}\text{O}(\text{e},\text{e}'\text{p})$ and find a consistently small spectroscopic factor over the whole range of Q^2 values.

Table (34.5). Observed and calculated [49] proton decay widths for $A = 11 - 16$.

Nucleus	J^π	Γ^{th} (keV)	Γ^{exp} (keV)	Dominant Component
^{11}N	$\frac{1}{2}^+$	1467	1440	81% $s_{1/2}(\text{gs})$
^{12}N	2^-	87	118(14)	70% $s_{1/2}(\text{gs})$
	1^-	894	750(250)	76% $s_{1/2}(\text{gs})$
	1^-	311	260(30)	77% $s_{1/2}(\frac{1}{2}^-)$
^{13}N	$\frac{1}{2}^+$	32	31.7(8)	89% $s_{1/2}(\text{gs})$
	$\frac{3}{2}^+$	84	115(5)	87% $s_{1/2}(2^+)$
	$\frac{5}{2}^+$	7	11	74% $s_{1/2}(2^+)$
^{14}O	$\frac{1}{2}^-$	28.8	30(1)	76% $s_{1/2}(\text{gs})$
^{15}F	$\frac{1}{2}^+$	934	1000(200)	98% $s_{1/2}(\text{gs})$
^{16}F	0^-	21	40(20)	100% $s_{1/2}(\text{gs})$
	1^-	78	< 40	97% $s_{1/2}(\text{gs})$
^{11}N	$\frac{5}{2}^+$	535	600(50)	67% $d_{5/2}(\text{gs})$
^{12}N	3^-	220	220(25)	88% $d_{5/2}(\text{gs})$
	4^-	610	744(25)	82% $d_{5/2}(\text{gs})$
	3^-	280	180(23)	70% $d_{5/2}(\frac{1}{2}^-)$
^{13}N	$\frac{9}{2}^+$	258	280(30)	91% $d_{5/2}(2^+)$
	$\frac{7}{2}^+$	3	9.0(5)	92% $d_{5/2}(2^+)$
	$\frac{5}{2}^+$	45	47(7)	80% $d_{5/2}(\text{gs})$
^{14}O	3^-	13.4	16(2)	84% $d_{5/2}(\text{gs})$
	2^-	38.2	41(2)	66% $d_{5/2}(\text{gs})$
^{15}F	$\frac{5}{2}^+$	222	240(30)	93% $d_{5/2}(\text{gs})$
^{16}N	2^-	3.5	40(30)	96% $d_{5/2}(\text{gs})$
	3^-	12	< 15	96% $d_{5/2}(\text{gs})$

34.7.4 Proton decay

The widths for proton or neutron decay are related the spectroscopic factors. The usual method for calculating these decay widths is to multiply the single-particle width for the decay of a nucleon in orbital j with the spectroscopic factor, $\Gamma = (C^2 S) \Gamma_{sp}$, where Γ_{sp} is the single-particle width calculated from the scattering of a nucleon from a central potential. Usually a Woods-Saxon potential is used and the well depth V_o is adjusted to reproduce the experimental centroid of the state.

Millener [49] has compared the the experimental proton decay widths for $A = 11 - 16$ to those obtained in a $1\hbar\omega$ model space where one proton is allowed to be excited from the $0p$ shell to the $0d1s$ shell. The results are given in Table (34.5). (The center-of-mass corrections of Eq. (34.38) are not included in the theory.) He used a Woods-Saxon potential with $r_o = 1.25$ fm and $a_o = 0.60$ fm. The calculated widths are based upon spectroscopic factors obtained with the Millener-Kurath interaction [50] (which are similar to those obtained with WBP [51]). There is good overall agreement between experiment and theory.

An increase of 0.01 fm in r_o increases the calculated single-particle width by about 1%, and an increase of 0.01 fm in a_o increases the calculated single-particle width by about 2% [49]. Thus for example a change of a_o from 0.60 to 0.65 would increase the calculated width by about 10%.

34.7.5 Radioactive beams

It has recently become possible to carry out one-nucleon transfer reactions with radioactive beams. One way is to do the traditional reactions such as $A(p, d)A'$ in inverse kinematics where the nucleus A is the beam rather than the target, e.g., $p(A, A')d$. A new way that has been developed is to knock out a nucleon in a reaction on a light target such as ^9Be . The spectroscopic factor for a specific final state is obtained by analyzing the momentum distribution of the $(A - 1)$ fragment in coincidence with gamma rays. Recent results are summarized in [52]. The ratios of the experimental cross section to the theoretical cross section are found to depend on the separation energies.

For neutron knock-out the ratio, R_s , depends on the difference between the neutron, S_n , and proton, S_p , separation energies, $\Delta S = S_n - S_p$. These ratios are shown by the red points in Fig. (34.6). On the neutron-rich side the neutron separation energy is small (loosely bound) and the proton separation energy is large (deeply bound). For example for ^{19}C they are $S_n = 0.6$ and $S_p = 26.7$ MeV, giving $\Delta S = -26.1$ MeV. On the proton-rich side this is in the opposite, for example for ^{32}Ar they are, $S_n = 21.9$ and $S_p = 2.4$ MeV, giving $\Delta S = 19.5$ MeV. When the neutron is deeply bound, the ratio is greatly reduced from unity.

For proton knock-out the ratio depends on the difference $\Delta S = S_p - S_n$. These ratios are shown by the blue points in Fig. (34.6). On the proton-rich side the proton separation energy is small (loosely bound) and the neutron separation energy is large (deeply bound). For example for ^{28}S they are $S_p = 2.4$ and $S_n = 21.4$ MeV, giving $\Delta S = -19.0$ MeV. On the neutron-rich side this is in the opposite, for example for ^{40}Si they are, $S_p = 23.0$ and $S_n = 5.0$ MeV, giving $\Delta S = 18.0$ MeV. When the proton is deeply bound, the ratio is greatly reduced from unity.

The points in the middle of Fig. (34.6) are for the stable nuclei discussed in the previous

sections. They give an average reduction factor of about 0.6. When ΔS is negative (e.g. a loosely bound removed nucleon) the ratio rises to toward unity, and when ΔS is positive (e.g. a deeply bound removed nucleon) the ratio is reduced to about 0.3 to 0.4. This has not been fully explained. But it is thought to arise from the short-range correlation of proton-neutron pairs into high-momentum states that become removed from the shell-model (single-particle) type basis (see Fig. 2 in [53]).

34.8 Structure models for specific nuclei

The mean-field model for nuclear structure corresponds to the extreme single-particle value for the spectroscopic factor. The residual interaction results in correlations in the nuclear wave function beyond the mean field that will change the spectroscopic factors. We can attempt to distinguish between long- and short-range correlation. By long range correlation I mean the mixing of the configurations near the Fermi surface. This results in a spread of the orbital occupations and fractionation of the spectroscopic strength into many states

up to about 10 MeV in the spectrum. Short-range interactions can scatter the nucleons into very high single-particle states and spread the spectroscopic strength up to as high as 100 MeV in excitation. In this section I will discuss the results in terms of these long- and short-range correlations.

Shell-model configuration mixing takes into account the residual interaction for single-particle states near the Fermi surface (the valence states). This type of configuration mixing is mainly related to the long-range correlations. The short-range correlation enters implicitly in terms of a renormalization of the two-body interaction (the G matrix). I will first concentrate on the spectroscopic factors obtained from shell-model calculations. The ratio of the experimental spectroscopic factors to the extreme single-particle model will be denoted by R and the ratio to the configuration mixed shell-model spectroscopic factors will be denoted by R_s . The subscript s means that its deviation from unity will be attributed to the effect of short-range correlations. The notation R'_s will be used when the $(e,e'p)$ experimental data are interpreted with a relativistic model for the reaction theory. A summary of R values from the results discussed below is given in Table (34.6).

Table (34.6). Ratio between experimental and shell-model spectroscopic factors

Nucleus	J_f	R(a)	R _s (b)	R' _s (c)
⁷ Li	3/2 ⁻	0.52	0.52	
¹² C	1/2 ⁻ ,3/2 ⁻	0.50	0.51	0.84
¹⁶ O	1/2 ⁻ ,3/2 ⁻	0.60	0.66	0.81
³⁰ Si	5/2 ⁺	0.37	0.58	
⁴⁰ Ca	3/2 ⁺	0.64	0.70	0.90
⁴⁸ Ca	3/2 ⁺	0.56	0.75	
⁵¹ V	(0,2,4,6) ⁺	0.45	0.50	
²⁰⁸ Pb	3/2 ⁺	0.58	0.65	0.82

a) Non-relativistic analysis of Kramer et al. [34] compared to the extreme single-particle model.

b) Non-relativistic analysis of Kramer et al. [34] compared to valence shell-model calculations.

c) Relativistic or Glauber model analysis compared to valence shell-model calculations.

34.8.1 ^7Li

The $^7\text{Li}(\text{e},\text{e}'\text{p})$ reaction has recently been studied by Lapikas et al. [54] The spectroscopic factors for non-relativistic analysis of the $^7\text{Li}(\text{e},\text{e}'\text{p})$ data summed over the 0^+ and 2^+ states in ^6He is 0.58(5). The 0p sum-rule value is 1.00 and typical 0p shell configuration mixing leads to about 0.95 in these lowest two states. Thus we would infer $R_s = (6/7) \times (0.58)/(0.95) = 0.52$, where (6/7) is the center-of-mass correction.

34.8.2 ^{12}C

^{12}C can easily be treated in the full 0p-shell. The WBP interaction [51] gives a ground state wave function with 48% $(0\text{p}_{3/2})^8$, 41% $(0\text{p}_{3/2})^6-(0\text{p}_{1/2})^4$, 4.7% $(0\text{p}_{3/2})^5-(0\text{p}_{1/2})^3$ and 5.5% $(0\text{p}_{3/2})^4-(0\text{p}_{1/2})^4$. The proton occupancies are 3.41 for $0\text{p}_{3/2}$ and 0.59 for $0\text{p}_{1/2}$. The spectroscopic strength gets split into $C^2S = 3.16$ to the $3/2^-$ ^{11}B ground state, 0.58 to a $1/2^-$ state at 1.85 MeV and 0.19 to a $3/2^-$ state at 4.31 MeV. The small remainder of

0.07 is fragmented over many states above 10 MeV in excitation. A common feature of all calculations within the 0p shell with a variety of effective interactions is that most (3.9 out of 4.0) of the p-shell sum-rule strength is contained in the lowest three states in ^{11}B . The sum of the spectroscopic strength obtained from the non-relativistic analysis of the $^{12}\text{C}(\text{e},\text{e}'\text{p})$ data for the lowest three states in ^{13}B is 2.18 (Table (34.4)) giving $R_s = (11/12) \times (2.18)/(3.9) = 0.51$. The Glauber model analysis gives $R'_s = (11/12) \times (3.56)/(3.9) = 0.84$.

34.8.3 ^{16}O

For ^{16}O it is possible to go up to $4\hbar\omega$ beyond the closed-shell configuration explicit configuration mixing [55]. Configuration mixing for ^{16}O with the WBP interaction [51] gives a ground state wave function with 49% closed-shell configuration and 39% $2\hbar\omega$ (mainly 2p-2h) and 12% $4\hbar\omega$ (mainly 4p-4h). The proton occupation numbers are 2.00 ($0\text{s}_{1/2}$), 3.70 ($0\text{p}_{3/2}$), 1.68 ($0\text{p}_{1/2}$), 0.36 ($0\text{d}_{5/2}$), 0.17 ($0\text{d}_{3/2}$) and 0.07 ($1\text{s}_{1/2}$) (with about 0.01 in the $1\text{p}_{0\text{f}}$ shell). For the $^{16}\text{O} \rightarrow ^{15}\text{N}$ transition, the transition to the $1/2^-$ ground state has $\text{C}^2\text{S}=1.65$ (most of the $0\text{p}_{1/2}$ strength) and the transition to the lowest $3/2^-$ state has $\text{C}^2\text{S}=3.29$ (89% of the $0\text{p}_{3/2}$ strength).

The ratio of the spectroscopic factors obtained from the non-relativistic analysis of the (e,e'p) data (Table (34.4)) to these calculated values is $R_s(1/2^-, gs) = (15/16) \times (1.27)/(1.65) = 0.72$ and $R_s(3/2^-, 6.32\text{MeV}) = (15/16) \times (2.25)/(3.29) = 0.64$, or $R_s = 0.66$ for the sum. The relativistic analysis gives a higher value of $R'_s = 0.81$.

34.8.4 The sd-shell

One of the most complete models available is for configuration mixing in the sd shell. In Fig. (34.7) I show the proton occupation numbers that result from the wave functions obtained with the USD interaction in the full sd-shell basis. They are compared to the extreme single-particle (ESP) model. For ^{28}Si in the middle of the sd-shell the ESP model corresponds to a closed-shell $(0d_{5/2})^{12}$ configuration with a proton occupation of number of 6 and a proton spectroscopic model of 6. In the full sd-shell model with 839 basis states, the ground-state wave function has only 22% of the $(0d_{5/2})^{12}$ state. However, the other basis states contain some nucleons in the $0d_{5/2}$ orbital and the proton occupancy is 4.62. Thus the sum-rule strength for $0d_{5/2}$ pickup in the full sd-shell model is 4.62. The transition to the ^{27}Al ground

state gets 3.61 of this sum and the rest gets fragmented over several excited states in ^{27}Al . The spectroscopic factor from the ($^3\text{He},\text{d}$) of Vernotte et al. (with the 0.75 DWBA reduction) of 2.75 is 25% smaller than the sd-shell value.

The $^{28}\text{Si}(\text{e},\text{e}'\text{p})$ reaction was studied at low resolution in one of the first experiments of this type [56], and an unexpectedly large spectroscopic factor of 5.5 for protons in 0d orbit inferred (it would be nice to have a new experiment on ^{28}Si). In place of ^{28}Si , we can consider the $^{30}\text{Si}(\text{e},\text{e}'\text{p})^{29}\text{Al}$ result from [43] that gives an experimental spectroscopic factor of 2.21(20) for the transition to the ground state that, when compared to the sd-shell calculation of 3.79 gives, $R_s = 0.58(6)$.

The ratio of experiment to theory for 39 transitions in the sd-shell is plotted vs mass in Fig. (34.5). For the 0d states one observes a mass-dependent ratio from about $R_s = 0.9$ at the lower end to $R_s = 0.6$ at the upper end. An interpretation of this will be discussed below.

34.8.5 ^{40}Ca and ^{48}Ca

One can treat configuration mixing in ^{40}Ca in terms of $(0d_{3/2}, 0f_{7/2})^n$ configuration outside of an assumed closed shell for ^{32}S . The ground state obtained with the HJMW interaction [57] has 76% $(0d_{3/2})^8$, 21% $(0d_{3/2})^6 - (0f_{7/2})^2$, 2.4% $(0d_{3/2})^4 - (0f_{7/2})^4$, and 0.13% $(0d_{3/2})^2 - (0f_{7/2})^6$. The $0d_{3/2}$ proton occupancy is 3.73 and most of this (3.70) goes to the spectroscopic factor for the ^{39}K $3/2^+$ ground state. Taking the $(e, e'p)$ experimental value from Table (34.4) gives $R_s = 0.70$ for the non-relativistic model and $R'_s = 0.90$ for the relativistic model. The $0f_{7/2}$ occupancy is 0.27 and 0.18 of this goes to the lowest ^{39}K $7/2^-$ state at 2.34 MeV.

For ^{48}Ca the HJMW ground state has 92% $(0d_{3/2})^8 - (0f_{7/2})^8$, 7% $(0d_{3/2})^6 - (0f_{7/2})^{10}$ and 0.17% $(0d_{3/2})^4 - (0f_{7/2})^{12}$. The $0d_{3/2}$ proton occupancy is 3.85 and 3.00 of this goes to the spectroscopic factor of the ^{47}K $3/2^+$ state. Taking the $(e, e'p)$ experimental value of 2.26 from Table (34.4) gives $R_s = 0.75$.

34.8.6 ^{51}V

Calculations can be carried out in the full pf shell [58]. The dimension for the ^{51}V ground state is large, 938,626 $J=7/2$, $T=t5/2$ states, but the wave function is still dominated by the $0f_{7/2}$ configurations and the average occupation proton number obtained with the FPD6 interaction [59] is about 2.68. Most of this into the spectroscopic factors in the lowest states of ^{50}Ti given in Table (34.4). The ratio of experiment (Table (34.4)) to the full pf shell value is $R_s = 0.50$.

34.8.7 ^{208}Pb

It has recently become possible to consider the nucleus ^{208}Pb in a 24 orbit model space with 2p-2h mixtures into the closed-shell ground state [60]. The resulting wave function is 32% closed shell plus 68% 2p-2h. The resulting proton occupation numbers for the orbits observed in Table (34.4) are 7.91 ($0g_{7/2}$), 5.88 ($1d_{5/2}$), 11.83 ($0h_{11/2}$), 3.85 ($0d_{3/2}$) and 1.91

($2s_{1/2}$). Although the ground state is only 32% closed shell the occupations are close to the $(2j + 1)$ ESP limit. Of this total occupation about 90% (with the exception of $0g_{7/2}$) goes into the lowest state of each spin. About 60% of the $0g_{7/2}$ strength goes into the lowest state with the rest fragmented over more highly excited states. The average ratio of experiment to theory is to shell-model theory is about $R_s = 0.65$ for the non-relativistic analysis and $R'_s = 0.82$ for the relativistic analysis.

34.9 Short-range correlations

Summarizing the results from previous sections, we find that there usually a reduction in the spectroscopic strength compared to valence shell-model calculations. The reduction appears to be largest for cases in which a nucleon is picked up from a closed-shell configuration leading to a single-particle state that is below the Fermi surface. The size of the reduction has some reaction model-dependence ranging from an average value of $R_s = 0.65$ for the non-relativistic analysis of $(e, e' p)$ data to $R'_s = 0.85$ for a relativistic analysis of the same

data. I will express this result in terms of a correction factor δ_s defined by:

$$R_s = (1 - \delta_s) \quad (34.54)$$

There is a trend for the 0d orbit within the sd-shell, Fig. (34.5) for a smaller correction factor ($\delta_s \approx 0.1$) at the beginning of the shell ($A=17$) where the single-particle state is above the Fermi surface to a larger correction factor ($\delta_s \approx 0.4$) at the upper end of the shell ($A=39$) where the state is below the Fermi surface. [However, the mass dependence observed in Fig. (34.5) may also be related to the incorrect use of a constant value of $r_o = 1.25$ fm for all sd-shell nuclei.] Other examples for spectroscopic factors of states above the Fermi surface where the correction factor is small are those obtained from the radioactive beam studies [61] and those obtained from the proton decay of unbound states discussed above.

One might expect that the correction factor due to short-range correlations to depend on the radial size of the overlap function relative to the size of the core density. When the overlap function is composed of orbitals below the Fermi surface, the nucleon being removed will be spatially close to the core nucleons and the interaction may result in a relatively large short-range correlation. On the other hand if the nucleon being removed is above the Fermi

surface, there is a smaller spatial overlap with the core and the short-range correlation will be smaller. A semi-quantitative model for a hard-core potential of radius a_h has been derived by Birse and Clement [62]. For valence protons, the correction is given in terms of an integral containing the valence proton density, $\rho_{vp}(r)$, and the core density, $\rho_m(r) = f\rho_p(r) + \rho_n(r)$:

$$\delta_s = \frac{4}{3}\pi a_h^3 \int \rho_{vp}(r)\rho_m(r)r^2 dr. \quad (34.55)$$

where $f = 1/2$. The factor of $(1/2)$ comes from the fact that for a short-ranged interaction, the spin-up valence proton can only interact with the core protons that have spin-down (the spin-up spin-up state is forbidden by the Pauli principle). For valance neutrons, the proton and neutron labels are interchanged. (If only the $T = 0$ interaction was considered then $f = 0$.)

In Fig. (34.8) I plot the components of this integral for a selection of neutron valance orbits in the closed-shell configurations of ^{16}O and ^{40}Ca obtained from SKX Skyrme Hartree-Fock calculations [39]. For ^{16}O the valence states below the Fermi surface are $0s_{1/2}$ bound by -30 MeV and $0p_{3/2}$ bound by -18 MeV. For ^{16}O the valence states above the Fermi surface are $0d_{5/2}$ bound by 5 MeV (a typical value at the beginning of the shell) and $1s_{1/2}$ bound

by 0.5 MeV (the value of its separation energy in ^{11}Be). For ^{40}Ca the valence state below the Fermi surface is the $0d_{3/2}$ bound by 14.8 MeV. The relative value of the integrals are 0.200, 0.144, 0.097, 0.048 and 0.160 for $0s_{1/2}$, $0p_{3/2}$, $0d_{5/2}$, $1s_{1/2}$ and $0d_{3/2}$, respectively. Thus we find that a significant binding energy dependence for the short-range corrections with the most loosely bound states having the smallest values.

Variational Monte-Carlo (VMC) calculations should contain both long and short ranged correlations. VMC calculations for the $^7\text{Li}(\text{e},\text{e}'\text{p})$ reaction give good agreement with the data. The small R_s value in this case may be influenced by the difference in structure between ^7Li and ^6He caused by the weak binding (and large neutron radius) of ^6He . That is, the overlap between the two valence neutrons that are tightly bound in ^7Li with those that are loosely bound in ^6He will be reduced. The alpha-triton clustering aspects of ^7Li may also enter. Both of these are relatively long-range effects that are special to these light nuclei and which should be taken into account within the VMC model.

The VMC calculation [6], [7] for $^{16}\text{O}(\text{e},\text{e}'\text{p})$ gives $R^{th} = 0.90$ for the ratio to the extreme single-particle model (without center-of-mass corrections) for the $0p_{3/2}$ orbit. The role of

the various types of short-range correlations has been studied in the correlated-basis-function theory [63] where it was found that tensor correlations are most important. Since the VMC calculations do not include the effect of fragmentation of the hole strength, but should contain the long-range correlations, we should compare this to the ratio obtained from the sum of the $3/2^-$ states in Table (34.4), e.g. $R = (15/16) \times (2.60)/(4.0) = 0.61$. Use of the relativistic ($e,e'p$) reaction model [42] would bring this up to about $R' = 0.76$. If we assume that the VMC calculation does not include the long-range correlation included in the shell-model calculation then we should compare $R^{th} = 0.90$ to the value of $R'_s = 0.81$ found in the previous section.

34.10 Conclusions

It appears possible to quantitatively understand spectroscopic factors in terms of a sum of short and long-long-range correlations for the overlap function and with the relativistic analysis of the ($e,e'p$) data. When the spectroscopic factors obtained from the relativistic

reaction theory are compared to valence shell-model calculations (which account for the long-range correlations) one obtains an average value of about $R'_s = 0.85$ for states below the Fermi surface. This 15% reduction could be attributed to short-range correlations. Calculations based upon the NN interaction [6], [7] can account for most of this, $R_s^{th} = 0.90$.

The long-range correlations have the effect of fragmenting the spectroscopic strength over many states in the $A + 1$ and $A - 1$ nuclei, and are strongly dependent on the spacing and occupancy of the single-particle states around the Fermi surface. Configuration mixing with empirical two-body matrix elements or renormalized G matrix interaction can account for the observed fragmentation, but the details are sensitive to the use of the correct single-particle energies. The details of the fragmentation and comparison to experiment is one of the most direct ways of testing nuclear structure models.

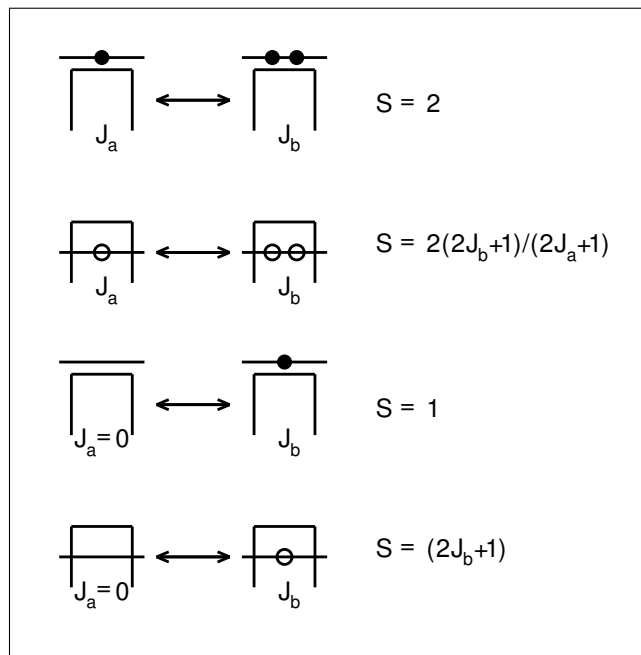


Figure 34.1: Schematic diagram for the spectroscopic factors for nucleon transfer for simple configurations where the sum-rules can be used to obtain the results. The box indicates a closed-shell configuration with holes (open circles) and particle (filled circles) added to one orbital.

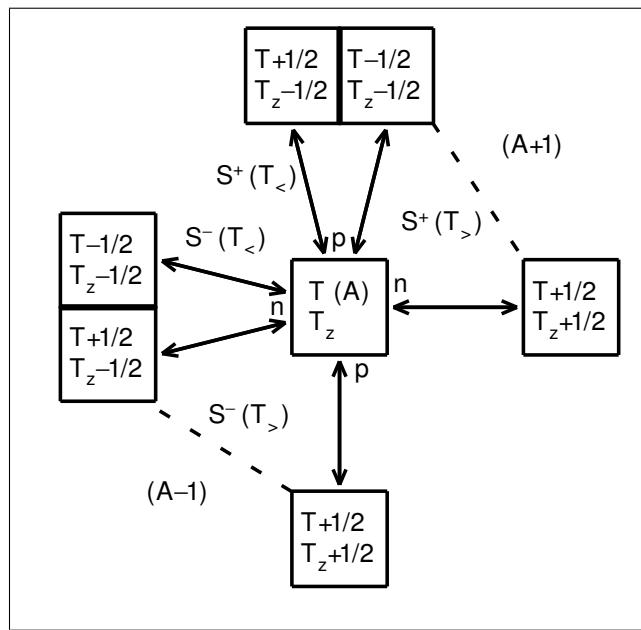


Figure 34.2: Schematic diagram for particle removal from a neutron-rich target nucleus nucleon number (A) to final nuclei with nucleon number ($A - 1$) ($S = S^-$), and particle addition to final nuclei with nucleon number ($A + 1$). The dashed line connects isobaric analogue states. Note that for the nuclei with $T_f = T_z - 1$, the lowest energy states are usually those with $T_f = T - 1/2$.

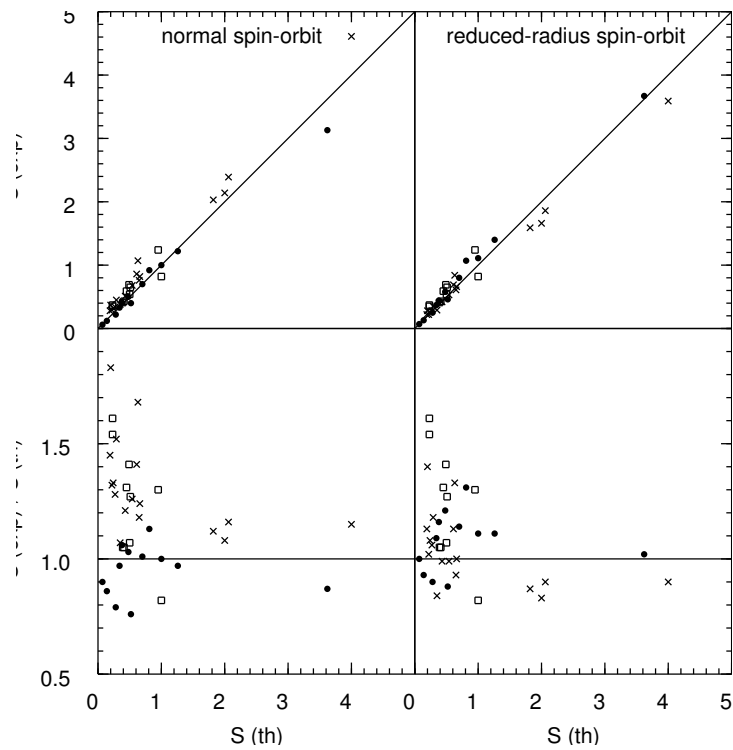


Figure 34.3: Theoretical vs experimental spectroscopic factors for 39 transitions in the sd shell. The parameters of the Woods-Saxon potential are $r_o = 1.25$ fm and $a = 0.65$ fm. The results on the left-hand side were obtained with the normal spin-orbit potential $r_{so} = r_o$ and $a_{so} = a_o$. The results on the right-hand side were obtained with the reduced-radius spin-orbit potential $r_{so} = 1.00$ fm and $a_{so} = 0.52$ fm. The points are for $0d_{5/2}$ (filled circles), $0d_{3/2}$ (crosses) and $1s_{1/2}$ (squares).

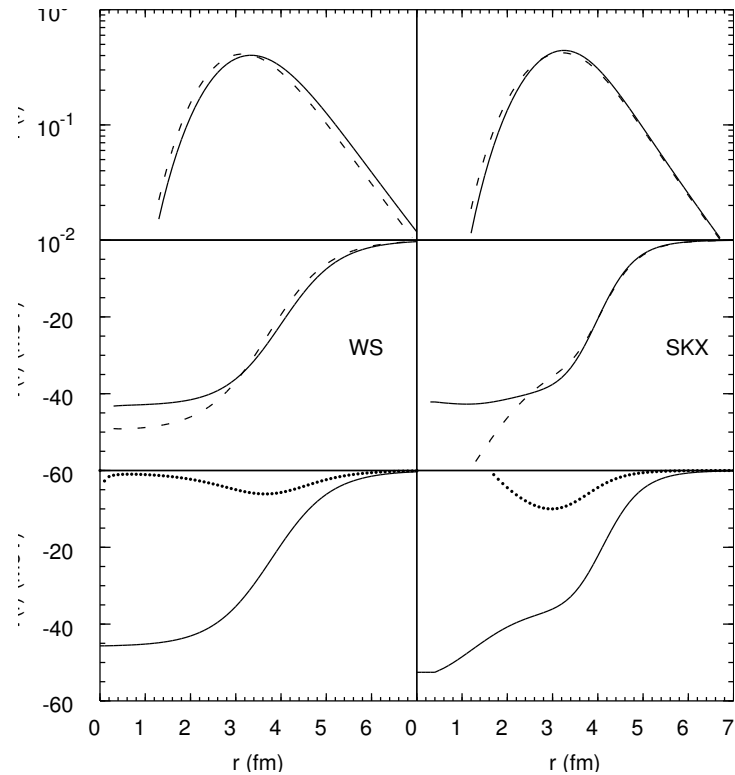


Figure 34.4: Bound state potentials and radial wave functions for the Woods-Saxon (left-hand side) and SKX Skyrme Hartree Fock (right-hand side). The bottom panel shows the central (line) and spin-orbit (dots) potentials for $A = 28$. The middle panel shows the effective total potentials for $0d_{5/2}$ (line) and $0d_{3/2}$ (dashes) required to bind the orbitals by 3 MeV. The top panel shows the radial density probability for $0d_{5/2}$ (line) and $0d_{3/2}$ (dashes) resulting from the effective potentials.

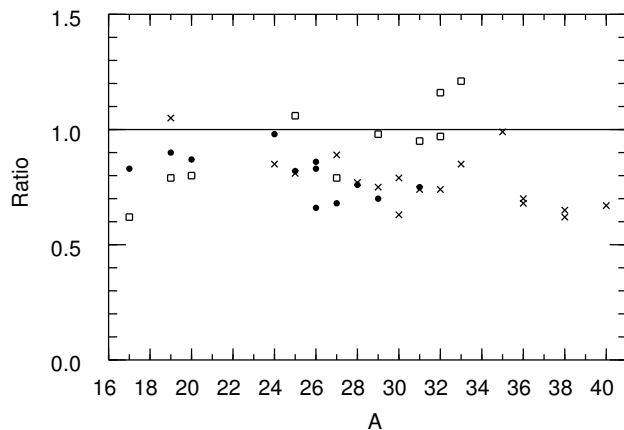


Figure 34.5: Ratio of the experimental to theoretical spectroscopic factors for $(A - 1)(^3\text{He},\text{d})A$ in the sd shell. The experimental values obtained from the reduced-radius spin-orbit potential model are multiplied by 0.75. (Center-of-mass corrections are not included in the theory.) Filled circles are for $0d_{5/2}$ crosses are for $0d_{3/2}$ and squares are for $1s_{1/2}$.

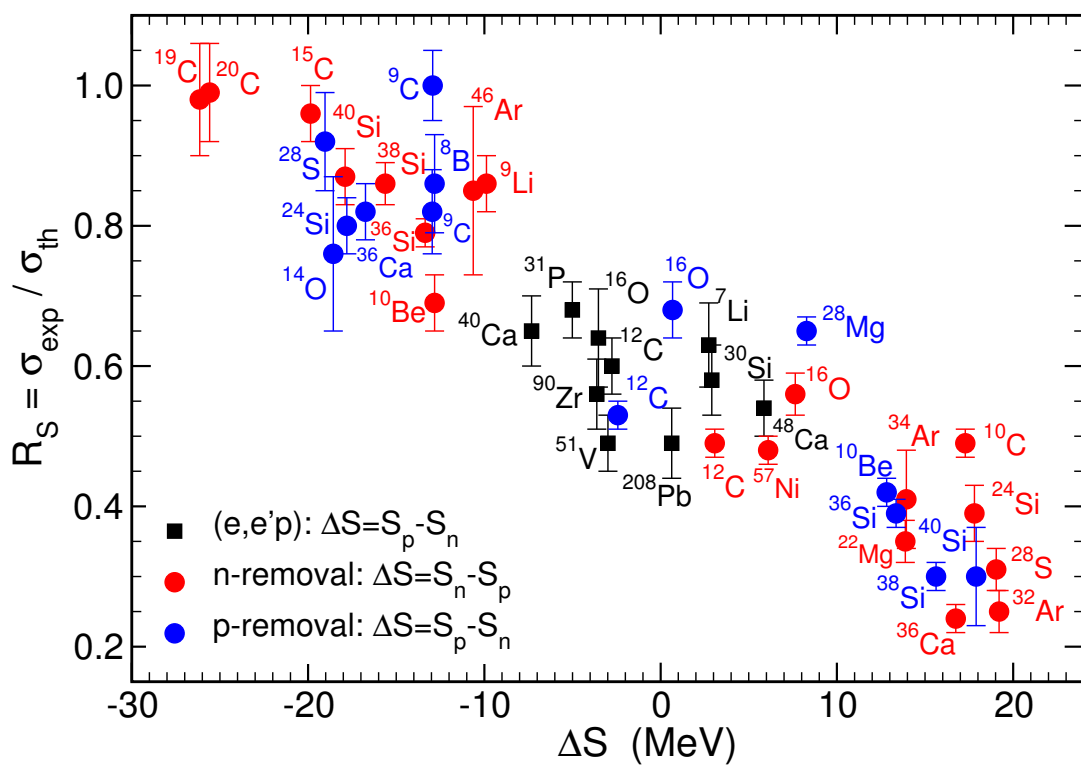


Figure 34.6: (See text)

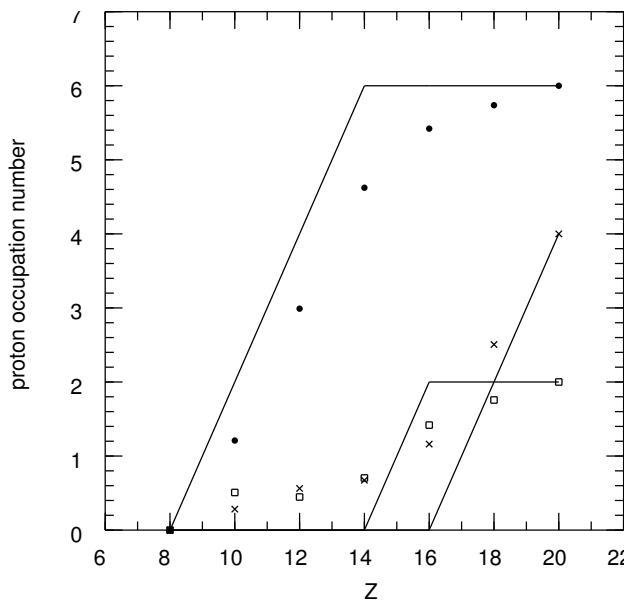


Figure 34.7: Proton occupation numbers for the even-even $N = Z$ sd shell nuclei as a function of mass. The lines are those expected in the extreme single-particle shell model and the symbols are those from the USD interaction: $0d_{5/2}$ (filled circles), $0d_{3/2}$ (crosses) and $1s_{1/2}$ (squares).

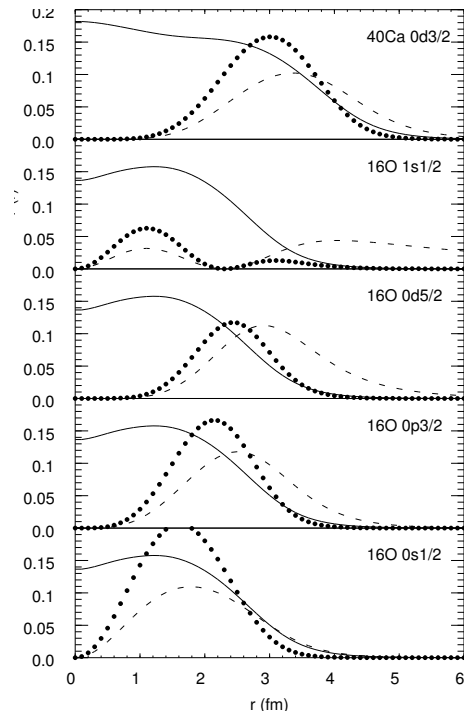


Figure 34.8: Components of the overlap function of Eq. (34.55). The solid line is the matter density, $\rho_m(r)$, (normalized by $4\pi \int \rho_m(r) r^2 dr = A$). The dashed line is $r^2 \rho_v(r)$ (in arbitrary units) and the dotted line is $r^2 \rho_m(r) \rho_v(r)$ (in arbitrary units).

Bibliography

- [1] M. H. Macfarlane and J. B. French, Rev. Mod. Phys. **32**, (1960).
- [2] “Spectroscopic Factors for Single Nucleon Transfer for $A = 21\text{-}44$ ”, P. M. Endt, Atomic and Nuclear Data Tables **19**, 23 (1977).
- [3] J. B. French and M. H. Macfarlane, Nucl. Phys. **26**, 168 (1961).
- [4] A. E. L. Dieperink and T. de Forest, Phys. Rev. C **10**, 543 (1974). link

- [5] M. Ichimura, A. Arima, E. C. Halbert and T. Terasawa, Nucl. Phys. **A204**, 225 (1973).
- [6] M. Radici, S. Boffi, S. C. Pieper and V. R. Pandharipande, Phys. Rev. C **50**, 3010 (1994). link
- [7] D. Van Neck, M. Waroquier, A. E. L. Dieperink, S. C. Pieper and V. R. Pandharipande, Phys. Rev. C **57**, 2308 (1998). link
- [8] J. M. Bang, F. G. Gareev, W. T. Pinkston and J. S. Vaagen, Phys. Rep. **125**, 253 (1985).
- [9] P. G. Hansen and J. A. Tostevin, Ann. Rev. Nucl. Part. Sci. **53**, 219 (2003).
- [10] W. T. Pinkston and G. R. Satchler, Nucl. Phys. **72**, 641 (1965).
- [11] E. Rost, Phys. Rev. **154**, 994 (1967). link
- [12] T. Tamura, Phys. Rev. **165**, 1123 (1968). link
- [13] T. Tamura, Phys. Rev. Lett. **19**, 321 (1967). link

- [14] A. Prakash, Phys. Rev. Lett. **20**, 864 (1968). link
- [15] A. Prakash and N. Austern, Ann. of Phys. **51**, 418 (1969).
- [16] J. L. Hutton, Nucl. Phys. **A210**, 567 (1968).
- [17] R. J. Philpott, W. T. Pinkston and G. R. Satchler, Nucl. Phys. **A119**, 241 (1968).
- [18] A. Moalem, J. F. A. van Heinen and E. Kashy, Nucl. Phys. **A307**, 277 (1978).
- [19] W. T. Pinkston, R. I. Philpott and G. R. Satchler, Nucl. Phys. **A125**, 176 (1969).
- [20] A. de Shalit and I. Talmi, *Nuclear Shell Theory*, (Academic Press, 1963).
- [21] L. B. Hubbard, Comput. Phys. Commun. **1**, 225 (1970); D. Zwart, Comput. Phys. Commun. **38**, 656 (1985); L. D. Skouras and S. Kossionides, Comput. Phys. Commun. **39**, 197 (1986).
- [22] L. B. Hubbard, Comput. Phys. Commun. **1**, 453 (1970).

- [23] L. D. Skouras and S. Kossionides, Comput. Phys. Commun. **39**, 197 (1986).
- [24] L. B. Hubbard, Comput. Phys. Commun. **1**, 453 (1970).
- [25] A. Novoselsky, J. Katriel and R. Gilmore, Jour. Math. Phys. **29**, 1368 (1988).
- [26] X. Ji and M. Vallieres, Phys. Rev. C **35**, 1583 (1987). link
- [27] R. D. Lawson, *Theory of the Nuclear Shell Model*, (Clarendon Press, 1980).
- [28] B. F. Bayman and A. Lande, Nucl. Phys. **77**, 1 (1966); I. S. Towner and J. C. Hardy, Nucl. Data Tables A6, 153 (1969); L. B. Hubbard, Nucl. Data Tables A9, 85 (1971); S. Shlomo, Nucl. Phys. **A184**, 545 (1972).
- [29] I. S. Towner and J. C. Hardy, Nucl. Data Tables A6, 153 (1969).
- [30] L. B. Hubbard, Nucl. Data Tables A9, 85 (1971).
- [31] S. Shlomo, Nucl. Phys. **A184**, 545 (1972).

- [32] F. Hinterberger et al., Z. Phys. **202**, 236 (1967).
- [33] J. N. Craig, N. S. Wall and R. H. Bassel, Phys. Rev. Lett. **36**, 656 (1976). link
- [34] G. J. Kramer, H. P. Blok and L. Lapikas, Nucl. Phys. **A679**, 267 (2001).
- [35] B. H. Wildenthal, Prog. in Part. and Nucl. Physcis **11**, 5 (1984).
- [36] <http://www.nscl.edu/~brown/sde.htm>
- [37] B. A. Brown and B. H. Wildenthal, Ann. Rev. Nucl. Part. Sci. **38**, 29 (1988).
- [38] J. Vernotte et al., Nucl. Phys. **A571**, 1 (1994).
- [39] B. A. Brown, Phys. Rev. C **58**, 220 (1998). link
- [40] J. W. A. den Herder et al., Phys. Rev. Lett. **57**, 1843 (1986). link
- [41] M. Leuschner et al., Phys. Rev. C **49**, 955 (1994). link
- [42] J. Gao et al., Phys. Rev. Lett. **84**, 3265 (2000). link

- [43] J. Wesseling et al., Nucl. Phys. **A547**, 519 (1992).
- [44] Y. Jin, J. K. Zhang, D. S. Onley and L. E. Wright, Phys. Rev. C **47**, 2024 (1993). link
- [45] J. M. Udias, P. Sarriguren, E. Moya de Guerra, E. Garrido and J. A. Caballero, Phys. Rev. C **48**, 2731 (1993). link
- [46] D. Branford et al., Phys. Rev. C **63**, 014310 (2000). link
- [47] L. Lapikas, G. van der Steenhoven, L. Frankfurt, M. Strikman and M. Zhalov, Phys. Rev. C **61**, 064325 (2000); L. Frankfurt, M. Strikman and M. Zhalov, Phys. Lett. B **503**, 73 (2001).
- [48] M. Radici, W. H. Dickhoff and E. Roth Stoddard, Phys. Rev. C **66**, 014613 (2002). link
- [49] D. J. Millener, private communication.
- [50] D. J. Millener and D. Kurath, Nucl. Phys. **A255**, 315 (1975).
- [51] W. K. Warburton and B. A. Brown, Phys. Rev. C **46**, 923 (1992). link

- [52] J. A. Tostevin and A. Gade, Phys. Rev. C **90**, 057602 (2014). link
- [53] W. H. Dickhoff, J. Phys. G **37**, 064007 (2010).
- [54] L. Lapikas, J. Wesseling and R. B. Wiringa, Phys. Rev. Lett. **82**, 4404 (1999). link
- [55] E. K. Warburton, B. A. Brown and D. J. Millener, Phys. Lett. **B293**, 7 (1992).
- [56] J. Mougy et al., Nucl. Phys. **A262**, 461 (1976).
- [57] S. T. Hsieh, X. Ji, R. Mooy and B. H. Wildenthal, AIP Conference Proceedings **142**, 357 (1986).
- [58] M. Honma, private communication.
- [59] W. A. Richter, M. G. van der Merwe, R. E. Julies and B. A. Brown, Nucl. Phys. **A523**, 325 (1991).
- [60] B. A. Brown, Phys. Rev. Lett. **85**, 5300 (2000). link

- [61] P. G. Hansen and B. M. Sherrill, "Reactions and Single-Particle Structure of Nuclei Near the Drip Lines", Nucl. Phys. A 693, 133 (2001).
- [62] M. C. Birse and C. F. Clement, Nucl. Phys. **A351**, 112 (1981).
- [63] D. Van Neck, L. Van Daele, Y. Dewulf and M. Waroquier, Phys. Rev. C **56**, 1398 (1997).
link

Chapter 35

One-body transition operators and the OBTD

The M -scheme one-body transition operator is:

$$\hat{O}_\mu^\lambda = \sum_{\alpha\beta} \langle \alpha | O_\mu^\lambda | \beta \rangle a_\alpha^+ a_\beta. \quad (35.1)$$

The tensor coupled form for this operator is:

$$\begin{aligned} \hat{O}_\mu^\lambda &= \sum_{k_\alpha k_\beta} \langle k_\alpha | | O^\lambda | | k_\beta \rangle \sum_{m_\alpha m_\beta} (-1)^{j_\alpha - m_\alpha} \begin{pmatrix} j_\alpha & \lambda & j_\beta \\ -m_\alpha & \mu & m_\beta \end{pmatrix} a_\alpha^+ a_\beta \\ &= \sum_{k_\alpha k_\beta} \langle k_\alpha | | O^\lambda | | k_\beta \rangle \frac{[a_{k_\alpha}^+ \otimes \tilde{a}_{k_\beta}]_\mu^\lambda}{\sqrt{(2\lambda + 1)}}. \end{aligned} \quad (35.2)$$

Where α stands for $(n_\alpha \ell_\alpha j_\alpha m_\alpha)$, and k_α stands for $(n_\alpha \ell_\alpha j_\alpha)$. It is convenient to express the reduced matrix element for the n -particle wave function in the form of a product over one-body transition densities (OBTD) times reduced single-particle matrix elements

$$\langle f | | \hat{O}^\lambda | | i \rangle = \langle n\omega_f J_f | | \hat{O}^\lambda | | n\omega_i J_i \rangle = \sum_{k_\alpha k_\beta} \text{OBTD}(f i k_\alpha k_\beta \lambda) \langle k_\alpha | | O^\lambda | | k_\beta \rangle, \quad (35.3)$$

where the OBTD is given by

$$\text{OBTD}(fik_\alpha k_\beta \lambda) = \frac{\langle n\omega_f J_f | [a_{k_\alpha}^+ \otimes \tilde{a}_{k_\beta}]^\lambda | n\omega_i J_i \rangle}{\sqrt{(2\lambda + 1)}}. \quad (35.4)$$

The labels i and f are a short-hand notation for the initial and final state quantum numbers ($n\omega_f J_f$) and ($n\omega_i J_i$), respectively. The OBTD represents in a compact form, the most general information needed to calculate the matrix elements of one-body operators between a given initial and final state. The OBTD can be calculated in an M -scheme basis by dividing a nonvanishing expectation value of the M -scheme matrix element by the $3j$ factor from the Wigner-Eckhart theorem

$$\langle J_f | [a_{k_\alpha}^+ \otimes \tilde{a}_{k_\beta}]^\lambda | J_i \rangle = \frac{\langle J_f M_f | [a_{k_\alpha}^+ \otimes \tilde{a}_{k_\beta}]_\mu^\lambda | J_i M_i \rangle}{(-1)^{J-M} \left(\begin{array}{ccc} J_f & \lambda & J_i \\ M_f & \mu & M_i \end{array} \right)} \quad (35.5)$$

The OBTD can be evaluated in a J -coupled basis by inserting a complete set of states

with $(n - 1)$ particles between the a^+ and \tilde{a} operators to obtain:

$$\begin{aligned}
 \text{OBTD}(fik_\alpha k_\beta \lambda) &= (-1)^{J_f + \lambda + J_i} \sum_{\omega_m J_m} \left\{ \begin{array}{ccc} J_i & J_f & \lambda \\ j_\alpha & j_\beta & J_m \end{array} \right\} \\
 &\times \langle n\omega_f J_f | |a_{k_\alpha}^+| |(n-1)\omega_m J_m \rangle \langle (n-1)\omega_m J_m | |\tilde{a}_{k_\beta}| |n\omega_i J_i \rangle \\
 &= \sum_{\omega_m J_m} (-1)^{J_f + \lambda + J_m + j_\beta} \left\{ \begin{array}{ccc} J_i & J_f & \lambda \\ j_\alpha & j_\beta & J_m \end{array} \right\} \\
 &\times \langle n\omega_f J_f | |a_{k_\alpha}^+| |(n-1)\omega_m J_m \rangle \langle n\omega_i J_i | |a_{k_\beta}^+| |(n-1)\omega_m J_m \rangle. \quad (35.6)
 \end{aligned}$$

These last two matrix elements can also be expressed as one-particle CFP. The explicit forms of the OBTD for the cases of a single- k configuration and for a two-orbital configuration are derived in the next two sections.

35.1 Isospin and proton-neutron formalism

The formulae in the previous section are immediately applicable to the proton-neutron formalism. In this case the labels for the orbits k implicitly include the proton or neutron label for the orbital. For transition within a given nucleus we can have $q = q' = 1/2$ for a neutron and $q = q' = -1/2$ for a proton. For β^- decay or (p,n) reactions we would destroy a neutron ($q = 1/2$) and create a proton ($q' = -1/2$):

$$\text{OBT}(f_{ik_{\alpha,q'}k_{\beta,q}\lambda}) = \frac{\langle n\omega_f J_f | [a_{k_{\alpha},q'}^+ \otimes \tilde{a}_{k_{\beta},q}]^\lambda | n\omega_i J_i \rangle}{\sqrt{(2\lambda + 1)}}, \quad (35.7)$$

and for β^+ decay or (n,p) reactions we would destroy a proton and create a neutron.

To obtain the equivalent expression in terms of a reduced matrix element in isospin formalism we would label the wavefunctions explicitly with their (T, T_z) values and the operator in terms of the isospin rank τ , and then use the Wigner-Eckhart theorem in isospin

space to obtain:

$$\begin{aligned}
\text{OBTD}(fik_{\alpha,q'}k_{\beta,q}\lambda) &= \frac{\langle n\omega_f J_f T_f T_z | [a_{k_\alpha,q'}^+ \otimes \tilde{a}_{k_\beta,q}]^{\lambda,\tau,\Delta T_z} | n\omega_i J_i T_i T_z \rangle}{\sqrt{(2\lambda+1)}} \\
&= (-1)^{T-T_z} \begin{pmatrix} T_f & \tau & T_i \\ -T_z & \Delta T_z & T_z \end{pmatrix} \frac{\langle n\omega_f J_f T_f | | [a_{k_\alpha,q'}^+ \otimes \tilde{a}_{k_\beta,q}]^{\lambda,\tau} | | n\omega_i J_i T_i \rangle}{\sqrt{(2\lambda+1)}} \\
&= \langle T_i T_z \tau \Delta T_z | T_f T_z \rangle \sqrt{\frac{(2\tau+1)}{(2T+1)}} \frac{\langle n\omega_f J_f T_f | | [a_{k_\alpha,q'}^+ \otimes \tilde{a}_{k_\beta,q}]^{\lambda,\tau} | | n\omega_i J_i T_i \rangle}{\sqrt{(2\lambda+1)(2\tau+1)}} \\
&= \langle T_i T_z \tau \Delta T_z | T_f T_z \rangle \sqrt{\frac{(2\tau+1)}{(2T+1)}} \text{OBTD}(fik_{\alpha}k_{\beta}\lambda\tau) \tag{35.8}
\end{aligned}$$

where the last line contains the one-body transition density in isospin formalism:

$$\text{OBTD}(fik_{\alpha}k_{\beta}\lambda\tau) = \frac{\langle n\omega_f J_f T_f | | [a_{k_\alpha}^+ \otimes \tilde{a}_{k_\beta}]^{\lambda,\tau} | | n\omega_i J_i T_i \rangle}{\sqrt{(2\lambda+1)(2\tau+1)}}. \tag{35.9}$$

The triple-bar matrix elements indicate that they are reduced in both space and isospin.

35.2 OBTD for a single-orbital configuration

The OBTD for a single-orbital configuration is given by

$$\text{OBTD}(f, i) = \sum_{\omega_m J_m} (-1)^{J_j + \lambda + J_m + j_\beta} \left\{ \begin{array}{ccc} J_i & J_f & \lambda \\ j_\alpha & j_\beta & J_m \end{array} \right\}$$

$$\times \langle k^n \omega_f J_f | |a_{k_\alpha}^+| |k^{n-1} \omega_m J_m \rangle \langle k^n \omega_i J_i | |a_{k_\beta}^+| |k^{n-1} \omega_m J_m \rangle \quad (35.10).$$

The only possibility for the set $(k_\alpha k_\beta)$ in the summation in Eq. (35.6) is (k, k) and one has in terms of the one-particle CFP:

$$\text{OBTD}(fi) = n \delta_{k_\alpha k} \delta_{k_\beta k} \sqrt{(2J_f + 1)(2J_i + 1)} \sum_{\omega_m J_m} (-1)^{J_f + \lambda + J_m + j}$$

$$\times \left\{ \begin{array}{ccc} J_i & J_f & \lambda \\ j & j & J_m \end{array} \right\} \langle j^n \omega_f J_f | \} j^{n-1} \omega_m J_m \rangle \langle j^n \omega_i J_i | \} j^{n-1} \omega_m J_m \rangle . \quad (35.11)$$

35.3 Scalar one-body matrix elements

For the Hamiltonian one is interested in matrix elements of scalar operators. For the special case of a scalar ($\lambda=0$) one-body operator

$$\langle n\omega_f J_f | \hat{O}^{\lambda=0} | n\omega_i J_i \rangle = \sum_{k_\alpha k_\beta} \text{OBTD}(fik_\alpha k_\beta) \langle k_\alpha | O^{\lambda=0} | k_\beta \rangle, \quad (35.12)$$

is useful to define a new quantity OBTDS related to the unreduced matrix elements by

$$\langle n\omega_f J_f | \hat{O}^{\lambda=0} | n\omega_i J_i \rangle = \sum_{k_\alpha k_\beta} \text{OBTDS}(fik_\alpha k_\beta) \langle k_\alpha | O^{\lambda=0} | k_\beta \rangle, \quad (35.13)$$

where OBTDS is given by

$$\begin{aligned}
\text{OBTDS}(fik_\alpha k_\beta) &= \delta_{j_\alpha j_\beta} \delta_{J_f J_i} \sqrt{\frac{(2j_a + 1)}{(2J_f + 1)}} \text{OBTD}(fik_\alpha k_\beta \lambda = 0) \\
&= \delta_{j_\alpha j_\beta} \delta_{J_f J_i} \sqrt{\frac{(2j_\alpha + 1)}{(2J_f + 1)}} \langle n\omega_f J_f | [a_{k_\alpha}^+ \otimes \tilde{a}_{k_\beta}]^{\lambda=0} | n\omega_i J_i \rangle \\
&= \delta_{j_\alpha j_\beta} \delta_{J_f J_i} \sqrt{2j_a + 1} \langle n\omega_f J_f | [a_{k_\alpha}^+ \otimes \tilde{a}_{k_\beta}]^{\lambda=0} | n\omega_i J_i \rangle \\
&= \delta_{j_\alpha j_\beta} \delta_{J_f J_i} \frac{1}{(2J_f + 1)} \sum_{\omega_m J_m} \langle n\omega_f J_f | a_{k_\alpha}^+ | (n-1)\omega_m J_m \rangle \\
&\quad \times \langle n\omega_i J_i | a_{k_\beta}^+ | (n-1)\omega_m J_m \rangle, \tag{35.14}
\end{aligned}$$

where the factor of $\sqrt{\frac{(2j_a+1)}{(2J_f+1)}}$ comes from going from the reduced matrix element of Eq. (35.3) to the unreduced matrix element of Eq. (35.14) for a scalar operator. For a single-orbital

configuration considered in Eq. (35.11), OBTDS reduces to

$$\begin{aligned} \text{OBTDS}(fi) &= n\delta_{k_\alpha k}\delta_{k_\beta k}\delta_{J_f J_i} \sum_{\omega_m J_m} \langle j^n \omega_f J_f | \} j^{n-1} \omega_m J_m \rangle \\ &\times \langle j^n \omega_i J_i | \} j^{n-1} \omega_m J_m \rangle = n\delta_{\omega_f \omega_i} \delta_{J_f J_i}. \end{aligned} \quad (35.15)$$

where the last line follows from the sum rule of Eq. [20.8].

A special case of Eq. (35.14) is obtained for $k_\alpha = k_\beta = k_o$ and $\omega_f = \omega_i = \omega$.

$$\begin{aligned} \text{OBTDS}(fi, k_\alpha = k_\beta = k_o) &\equiv \sqrt{2j_o + 1} \langle n\omega J | [a_{k_o}^+ \otimes \tilde{a}_{k_o}]^{\lambda=0} | n\omega J \rangle \\ &= \sqrt{2j_o + 1} \sum_m \langle j_o m j_o, -m | 0, 0 \rangle \langle n\omega J | a_{k_o m}^+ \tilde{a}_{k_o, -m} | n\omega J \rangle \\ &= \sum_m \langle n\omega J | a_{k_o m}^+ a_{k_o m} | n\omega J \rangle = \langle n\omega J | \hat{N}_{k_o} | n\omega J \rangle, \end{aligned} \quad (35.16)$$

where in the last line the single-state number operator is

$$\hat{N}_{k_o} = \sum_m a_{k_o m}^+ a_{k_o m}. \quad (35.17)$$

Chapter 36

Electromagnetic transitions

36.1 Electromagnetic Operators and Matrix Elements

The reduced transition probability B is defined in terms of reduced matrix elements of a one-body operator by:

$$B(i \rightarrow f) = \frac{|\langle J_f | \hat{O}^\lambda | J_i \rangle|^2}{(2J_i + 1)}. \quad (36.1)$$

With our definition of the reduced matrix element,

$$|\langle J_f | \hat{O}^\lambda | J_i \rangle|^2 = |\langle J_i | \hat{O}^\lambda | J_f \rangle|^2. \quad (36.2)$$

B depends upon the direction of the transition by the factor of $(2J_i + 1)$. For electromagnetic transitions J_i is that for the higher-energy initial state. But in Coulomb excitation the initial is usually taken as the ground state, and one can use the notation $B(\uparrow)$ for this situation.

The one-body operators \hat{O}^λ represent a sum over the operators for the individual nucleon degrees of freedom i

$$\hat{O}^\lambda = \sum_i O_i^\lambda, \quad (36.3)$$

The reduced matrix element for the n -particle wave function can be expressed in the form of a product over one-body transition densities (OBTD) times reduced single-particle matrix elements

$$\langle n\omega_f J_f || \hat{O}^\lambda || n\omega_i J_i \rangle = \sum_{k_\alpha k_\beta} \text{OBTD}(f i k_\alpha k_\beta \lambda) \langle k_\alpha || O^\lambda || k_\beta \rangle, \quad (36.4)$$

where the OBTD is given by

$$\text{OBTD}(f i k_\alpha k_\beta \lambda) = \frac{\langle n\omega_f J_f || [a_{k_\alpha}^+ \otimes \tilde{a}_{k_\beta}]^\lambda || n\omega_i J_i \rangle}{\sqrt{(2\lambda + 1)}}. \quad (36.5)$$

The labels i and f are a short-hand notation for the initial and final state quantum numbers ($n\omega_i J_i$) and ($n\omega_f J_f$), respectively. $\langle k_\alpha || O^\lambda || k_\beta \rangle$ are the single-particle reduced matrix elements (SPME) that will be given below for the most common types of operators. There are two type of OBTD one for protons $a_p^+ a_p$ and one for neutrons $a_n^+ a_n$

The electric transition operator given by:

$$O(E\lambda) = r^\lambda Y_\mu^\lambda(\hat{r}) e_q e, \quad (36.6)$$

were Y_μ^λ are the spherical harmonics and q stands for proton $q = p$ or neutron $q = n$. Gamma transitions with $\lambda=0$ are forbidden because the photon must carry off at least one unit of angular momentum. The e_q are the electric charges for the proton and neutron in units of e . For the free-nucleon charge we would take $e_p = 1$ and $e_n = 0$, for the proton and neutron, respectively. Although the bare operator acts upon the protons, we will keep the general expression in terms of e_q in order to incorporate the “effective charges” for the proton and neutron, which represent the center-of-mass corrections and the average effects of the renormalization from wavefunction admixtures outside the model space.

The magnetic transition operator is given by:

$$\begin{aligned} O(M\lambda) &= \left[\vec{\ell} \frac{2g_{\ell q}}{(\lambda+1)} + \vec{s} g_{sq} \right] \vec{\nabla} [r^\lambda Y_\mu^\lambda(\hat{r})] \mu_N \\ &= \sqrt{\lambda(2\lambda+1)} \left[[Y^{\lambda-1}(\hat{r}) \otimes \vec{\ell}]_\mu^\lambda \frac{2g_{\ell q}}{(\lambda+1)} + [Y^{\lambda-1}(\hat{r}) \otimes \vec{s}]_\mu^\lambda g_{sq} \right] r^{\lambda-1} \mu_N, \end{aligned} \quad (36.7)$$

where μ_N is the nuclear magneton,

$$\mu_N = \frac{e\hbar}{2m_p c} = 0.105 \text{ efm}, \quad (36.8)$$

and where m_p is the mass of the proton. The g-factors $g_{\ell q}$ and g_{sq} are the orbital and spin g-factors for the proton and neutron. free-nucleon values for the g-factors are $g_{\ell p} = 1$, $g_{\ell n} = 0$, $g_{sp} = 5.586$ and $g_{sn} = -3.826$. We may use effective values for these g-factors to take into account the truncation of the model space.

The most common types of transitions are $E1$, $E2$ and $M1$. The $E1$ transition operator is given by Eq. (36.6) with $\lambda=1$:

$$O(E1) = r Y_\mu^{(1)}(\hat{r}) e_q e = \sqrt{\frac{3}{4\pi}} \vec{r} e_q e. \quad (36.9)$$

The center-of-mass correction (see previous Section) the effective charges for $E1$ are

$$e_p = \frac{N}{A}$$

and

$$e_n = -\frac{Z}{A}. \quad (36.10)$$

For the $M1$ operator there is no dependence on \vec{r} and the center-of-mass is zero. For the $E\lambda$ operators with $\lambda > 1$ the center-of-mass correction in the harmonic-oscillator model is zero if the center of mass is in the $0s$ state (see page 342 of [1]).

The $E2$ transition operator is given by Eq. (36.6) with $\lambda=2$:

$$O(E2) = r^2 Y_{\mu}^{(2)}(\hat{r}) e_q e, \quad (36.11)$$

The $M1$ transition operator is given by Eq. (36.7) with $\lambda=1$ and $Y^0 = 1/\sqrt{4\pi}$:

$$O(M1) = \sqrt{\frac{3}{4\pi}} [\vec{\ell} g_{\ell q} + \vec{s} g_{sq}] \mu_N. \quad (36.12)$$

The selection rules are given by the triangle condition for the angular momenta in Eq. (36.2), $\Delta(J_i, J_f, \lambda)$. The electromagnetic interaction conserves parity, and the elements

of the operators for $E\lambda$ and $M\lambda$ can be classified according to their transformation under parity change:

$$POP^{-1} = \pi_O O. \quad (36.13)$$

$\pi_O = (-1)^\lambda$ for Y^λ , $\pi_O = -1$ for the vectors \vec{r} , $\vec{\nabla}$ and \vec{p} , and $\pi_O = +1$ for pseudo vectors $\vec{l} = \vec{r} \times \vec{p}$ and $\vec{\sigma} = 2\vec{s}$.

For a given matrix element we have:

$$\langle \Psi_f | \hat{O} | \Psi_i \rangle = \langle \Psi_f | P^{-1} P \hat{O} P^{-1} P | \Psi_i \rangle = \pi_i \pi_f \pi_O \langle \Psi_f | \hat{O} | \Psi_i \rangle. \quad (36.14)$$

The matrix element will vanish unless $\pi_i \pi_f \pi_O = +1$. Thus the transitions are divided into two classes, the ones which do not change parity change $\pi_i \pi_f = +1$ which go by the operators with $\pi_O = +1$:

$$\pi_i \pi_f = +1 \text{ for } M1, E2, M3, E4 \dots, \quad (36.15)$$

and the ones which do change parity change $\pi_i \pi_f = -1$ which go by the operators with $\pi_O = -1$:

$$\pi_i \pi_f = -1 \text{ for } E1, M2, E3, M4 \dots. \quad (36.16)$$

36.2 Moments in terms of electromagnetic operators

The electromagnetic moments can be expressed in terms of the matrix elements of the electromagnetic transition operators. By the parity selection rule of Eq. (36.15), the moments are nonzero only for $M1, E2, M3, E4, \dots$. The most common are:

$$\begin{aligned}\mu &= \sqrt{\frac{4\pi}{3}} \langle J, M = J | \hat{O}(M1) | J, M = J \rangle \\ &= \sqrt{\frac{4\pi}{3}} \left(\begin{array}{ccc} J & 1 & J \\ -J & 0 & J \end{array} \right) \langle J || \hat{O}(M1) || J \rangle,\end{aligned}\quad (36.17)$$

and

$$\begin{aligned}Q &= \sqrt{\frac{16\pi}{5}} \langle J, M = J | \hat{O}(E2) | J, M = J \rangle \\ &= \sqrt{\frac{16\pi}{5}} \left(\begin{array}{ccc} J & 2 & J \\ -J & 0 & J \end{array} \right) \langle J || \hat{O}(E2) || J \rangle.\end{aligned}\quad (36.18)$$

36.3 Single-particle matrix elements

The SPME for $E\lambda$ operator of (36.6) is given by:

$$\begin{aligned} < k_a || O(E\lambda) || k_b > &= (-1)^{j_a+1/2} \frac{[1 + (-1)^{\ell_a+\lambda+\ell_b}]}{2} \\ &\times \sqrt{\frac{(2j_a+1)(2\lambda+1)(2j_b+1)}{4\pi}} \left(\begin{array}{ccc} j_a & \lambda & j_b \\ 1/2 & 0 & -1/2 \end{array} \right) < k_a | r^\lambda | k_b > e_q e, \end{aligned} \quad (36.19)$$

where $k_a = (n_a, \ell_a, j_a)$ etc. The SPME for the spin part of the magnetic operator of Eq. (36.7) is:

$$\begin{aligned} < k_a || O(M\lambda, s) || k_b > &= \\ &= \sqrt{\lambda(2\lambda+1)} < j_a | | [Y^{\lambda-1}(\hat{r}) \otimes \vec{s}]^\lambda | | j_b > < k_a | r^{\lambda-1} | k_b > g_{sq} \mu_N \\ &= \sqrt{\lambda(2\lambda+1)} \sqrt{(2j_a+1)(2j_b+1)(2\lambda+1)} \left\{ \begin{array}{ccc} \ell_a & 1/2 & j_a \\ \ell_b & 1/2 & j_b \\ \lambda-1 & 1 & \lambda \end{array} \right\} \end{aligned}$$

$$\times \langle \ell_a | |Y^{\lambda-1}(\hat{r})| | \ell_b \rangle \langle s | |\vec{s}| |s \rangle \langle k_a | r^{\lambda-1} | k_b \rangle g_{sq} \mu_N, \quad (36.20)$$

where

$$\langle s | |\vec{s}| |s \rangle = \sqrt{3/2}. \quad (36.21)$$

The SPME for the orbital part of the magnetic operator of (36.7) is:

$$\begin{aligned} & \langle k_a | |O(M\lambda, \ell)| | k_b \rangle = \\ &= \frac{\sqrt{\lambda(2\lambda+1)}}{\lambda+1} \langle j_a | |[Y^{\lambda-1}(\hat{r}) \otimes \vec{\ell}]^\lambda| | j_b \rangle \langle k_a | r^{\lambda-1} | k_b \rangle g_{\ell q} \mu_N \\ &= \frac{\sqrt{\lambda(2\lambda+1)}}{\lambda+1} (-1)^{\ell_a+1/2+j_b+\lambda} \sqrt{(2j_a+1)(2j_b+1)} \\ &\times \left\{ \begin{array}{ccc} \ell_a & \ell_b & \lambda \\ j_b & j_a & 1/2 \end{array} \right\} \langle \ell_a | |[Y^{\lambda-1}(\hat{r}) \otimes \vec{\ell}]^\lambda| | \ell_b \rangle \langle k_a | r^{\lambda-1} | k_b \rangle g_{\ell q} \mu_N, \end{aligned} \quad (36.22)$$

where

$$\langle \ell_a | |[Y^{\lambda-1}(\hat{r}) \otimes \vec{\ell}]^\lambda| | \ell_b \rangle = (-1)^{\lambda+\ell_a+\ell_b} \sqrt{(2\lambda+1)\ell_b(\ell_b+1)(2\ell_b+1)}$$

$$\times \left\{ \begin{array}{ccc} \lambda - 1 & 1 & \lambda \\ \ell_b & \ell_a & \ell_b \end{array} \right\} \langle \ell_a || Y^{\lambda-1}(\hat{r}) || \ell_b \rangle, \quad (36.23)$$

with

$$\langle \ell_a || Y^{\lambda-1}(\hat{r}) || \ell_b \rangle = (-1)^{\ell_a} \sqrt{\frac{(2\ell_a + 1)(2\ell_b + 1)(2\lambda - 1)}{4\pi}} \left(\begin{array}{ccc} \ell_a & \lambda - 1 & \ell_b \\ 0 & 0 & 0 \end{array} \right). \quad (36.24)$$

For the $M1$ operator of (36.12) the radial matrix element is:

$$\langle k_a | r^0 | k_b \rangle = \delta_{n_a, n_b}, \quad (36.25)$$

and the SPME simplify to:

$$\begin{aligned} \langle k_a || O(M1, s) || k_b \rangle &= \sqrt{\frac{3}{4\pi}} \langle j_a || \vec{s} || j_b \rangle \delta_{n_a, n_b} g_{sq} \mu_N \\ &= \sqrt{\frac{3}{4\pi}} (-1)^{\ell_a + j_a + 3/2} \sqrt{(2j_a + 1)(2j_b + 1)} \left\{ \begin{array}{ccc} 1/2 & 1/2 & 1 \\ j_b & j_a & \ell_a \end{array} \right\} \end{aligned}$$

$$\times \langle s || \vec{s} || s \rangle \delta_{\ell_a, \ell_b} \delta_{n_a, n_b} g_{sq} \mu_N, \quad (36.26)$$

where

$$\langle s || \vec{s} || s \rangle = \sqrt{3/2},$$

and

$$\begin{aligned} \langle k_a || O(M1, \ell) || k_b \rangle &= \sqrt{\frac{3}{4\pi}} \langle j_a || \vec{\ell} || j_b \rangle \delta_{n_a, n_b} g_{\ell q} \mu_N \\ &= \sqrt{\frac{3}{4\pi}} (-1)^{\ell_a + j_b + 3/2} \sqrt{(2j_a + 1)(2j_b + 1)} \left\{ \begin{array}{ccc} \ell_a & \ell_b & 1 \\ j_b & j_a & 1/2 \end{array} \right\} \\ &\quad \times \langle \ell_a || \vec{\ell} || \ell_b \rangle \delta_{n_a, n_b} g_{\ell q} \mu_N, \end{aligned} \quad (36.27)$$

where

$$\langle \ell_a || \vec{\ell} || \ell_b \rangle = \delta_{\ell_a, \ell_b} \sqrt{\ell_a(\ell_a + 1)(2\ell_a + 1)}.$$

Thus the $M1$ operator connects only those orbitals which have the same n and ℓ values.

36.4 Applications to simple situations

36.4.1 Closed shell plus one particle

For a closed shell plus one particle one finds that OBTD=1 and the only term contributing to the sum (for $\lambda > 0$) comes from the transition between two specific particle states with $J = j$ (since $J_c = 0$)

$$\langle J_f = j_f | \hat{O}(\lambda) | J_i = j_i \rangle = \langle k_f | O(\lambda) | k_i \rangle, \quad (36.28)$$

and the reduced transition probability for this cases is:

$$B(\lambda) = \frac{|\langle k_f | O(\lambda) | k_i \rangle|^2}{(2j_i + 1)}. \quad (36.29)$$

36.4.2 Single-orbit configurations

For a closed shell plus n particles in a single state k these expressions (for $\lambda > 0$) reduce to:

$$\langle k^n, \omega_f, J_f | \hat{O}(\lambda) | k^n, \omega_i, J_i \rangle = \text{OBTD}(fik\lambda) \langle k | O(\lambda) | k \rangle, \quad (36.30)$$

$$\begin{aligned} \text{OBTD}(fik\lambda) &= n\sqrt{(2J_f + 1)(2J_i + 1)} \sum_{\omega J} (-1)^{J_f + \lambda + J + j} \\ &\times \left\{ \begin{array}{ccc} J_i & J_f & \lambda \\ j & j & J \end{array} \right\} \langle j^n \omega_f J_f | \} j^{n-1} \omega J \rangle \langle j^n \omega_i J_i | \} j^{n-1} \omega J \rangle. \end{aligned} \quad (36.31)$$

For $n = 1$ this simplifies to the equivalent to Eq. (36.28)

$$\langle J_f = j | \hat{O}(\lambda) | J_i = j \rangle = \langle k | O(\lambda) | k \rangle, \quad (36.32)$$

which is the reduced matrix element which can be used in Eqs. (36.17) and (36.18) for the single-particle moments of the state k .

Table 36.1: Coefficients C for k^2 E2 transitions.

transition	$(3/2)^2$	$(5/2)^2$	$(7/2)^2$	$(9/2)^2$	$(11/2)^2$	$(13/2)^2$
$2 \rightarrow 0$	0.800	0.914	0.952	0.970	0.979	0.985
$4 \rightarrow 2$		0.630	0.950	1.114	1.207	1.265
$6 \rightarrow 4$			0.433	0.771	0.990	1.132
$8 \rightarrow 6$				0.308	0.612	0.841
$10 \rightarrow 8$					0.229	0.491
$12 \rightarrow 10$						0.177

For $n = 2$, the CFP are unity and the sum only contains $J = j$ in which case Eq. (36.31) simplifies to

$$\text{OBTD}(fik\lambda) = (-1)^{J_f+\lambda+1} n \sqrt{(2J_f + 1)(2J_i + 1)} \left\{ \begin{array}{ccc} J_i & J_f & \lambda \\ j & j & j \end{array} \right\}. \quad (36.33)$$

The reduced transition rate becomes:

$$B(\lambda) = n^2(2J_f + 1) \left\{ \begin{array}{ccc} J_i & J_f & \lambda \\ j & j & j \end{array} \right\}^2 |< k ||O(\lambda)||k >|^2. \quad (36.34)$$

$$\begin{aligned} &= n^2(2J_f + 1)(2j + 1) \left\{ \begin{array}{ccc} J_i & J_f & \lambda \\ j & j & j \end{array} \right\}^2 \frac{|< k ||O(\lambda)||k >|^2}{(2j + 1)} \\ &= C(J_i, J_f, j) \frac{|< k ||O(\lambda)||k >|^2}{(2j + 1)}, \end{aligned} \quad (36.35)$$

where the last line is written in terms of a coefficient which depends upon J_i and J_f times a reduced “single-particle” transition rate. These coefficients for some j value are given in Table (36.1).

36.5 Results for the *sd* shell nuclei

In this section we show comparison between calculated and experimental M1 and E2 observables for the *sd* shell nuclei. The active orbitals are $0d_{5/2}$, $0d_{3/2}$ and $1s_{1/2}$ for protons and neutrons. Also we show comparisons between matrix elements obtained with different Hamiltonians in order to illustrate some of the interaction sensitivity of these data.

We use three Hamiltonians. USDA and USDB, [2] have been obtained from fits of 63 two-body matrix (TBME) elements and three single-particle energies to the experimental values for 608 energies (for the ground states and low-lying excited states) of the sd-shell nuclei from $A = 16$ to $A = 40$ as described in a previous chapter.

The experimental data for M1 and E2 transition matrix elements [3] and for the Gamow-Teller matrix elements [4] is the same set used to test the original USD Hamiltonian. For M1 and E2 moments we use the recent compilation by Stone [5]. For ^{35}K a new value from [6] has been used. The data for spectroscopic factors between ground states is taken from Tsang et al [7].

The electromagnetic and beta decay operators involve one-body operators that must be renormalized [3]. Thus for all of these we carry out least-square fits to data to determine the values of the parameters. The experimental error bars on some of the data are much smaller than can be accounted for by the theoretical models. The χ^2 value in a fit based on just the experimental error bars would be very large and parameters obtained would not be reflective of the data set as a whole. For this reason we add a “theoretical error” to each datum in the form

$$\sigma^2 = \sigma_{exp}^2 + \sigma_{th}^2, \quad (36.36)$$

where σ_{exp} is the experimental error for each datum, and σ_{th} is a theoretical error for each type of observable. The theoretical error is chosen so that the χ^2 value is near unity and its value reflects the overall theoretical uncertainty.

36.5.1 Magnetic moments and M1 transitions

The $M1$ operator is defined by

$$O(M1) = \sqrt{\frac{3}{4\pi}} \{ g_{sq} \vec{s}_q + g_{\ell q} \vec{\ell}_q + g_{tq} \sqrt{8\pi} [Y^2(\hat{r}_q) \otimes \vec{s}_q]^{(1)} \} \mu_N \quad (36.37)$$

The last term in (36.37) is the so-called tensor $M1$ operator [8] that is added to account for the higher-order corrections to the wavefunctions beyond those contained within the sd . shell. It is zero for the free-nucleon operator. It allows for transitions with $\delta\ell = 2$ that are forbidden by the free-nucleon form of the $M1$ operator.

We consider results with the free-nucleon g-factors $g_{\ell p} = 1, g_{sp} = 5.586, g_{tp} = 0, g_{\ell n} = 0, g_{sn} = -3.826, g_{tn} = 0$, as well as with effective values for the these six terms obtained from a least-square fit to the $M1$ data (moments as well as transitions). The two observables are magnetic moments, and $M1$ transition matrix elements given by

$$M(M1) = | \langle \Psi_f | \hat{O}(M1) | \Psi_i \rangle |, \quad (36.38)$$

related to the $M1$ transition probabilities by, $B(M1) = [M(M1)]^2/(2J_i + 1)$.

Comparison of theory with experiment is shown in Fig. (36.1) (for 48 magnetic moments) and 4 (for 111 $M1$ transitions). The sign for the magnetic moments of ^{19}O , ^{23}Mg , ^{31}S , not determined by experiment, are taken from theory. Magnetic moments for neutron-rich Ne [9], Na [10] and Mg [11] sd-shell nuclei are not included. These will be compared and discussed in comparison with theory at the end of this section. The agreement with experiment with the free-nucleon g-factors is already fairly good. Use of the effective g-factors leads to a visible improvement for both moments and transitions. Even though there are differences between the results for the different Hamiltonians, one cannot say any one of them is better.

The rms deviations and resulting values for the effective g-factors are given in Table (36.2) (we used $\sigma_{th}=0.2$). The rms values for the deviation between experiment and theory for the $M1$ data is reduced from the free-nucleon values ($N = 0$) with the effective-operator fit, and all of the Hamiltonians give similar results for the rms deviations and effective g-factors. There is a small but significant improvement in the rms deviations if the tensor- $M1$ terms are included in the fit ($N = 6$). There is a small dependence of the values of the

effective g-factors on the Hamiltonian, but they are within the uncertainties obtained for each fit. Thus, the previous work on the interpretation of the values of the effective $M1$ operator based upon the USD Hamiltonian [3] is still valid. Given (as discussed above) that there is some dependence of the calculated matrix elements on the Hamiltonian, we might expect a further reduction in the rms deviation (and reduction of the errors of the effective g-factors) if the $M1$ data could be included in a fit of the Hamiltonian parameters to energy data.

36.5.2 Electric quadrupole moments and transitions

The $E2$ operator is

$$O(E2) = e_q r_q^2 Y^2(\hat{r}_q) e \quad (36.39)$$

We consider results with the free-nucleon effective charges $e_p = 1$ and $e_n = 0$, as well as with effective values for these two terms obtained from a least-square fit to the $E2$ data. The two

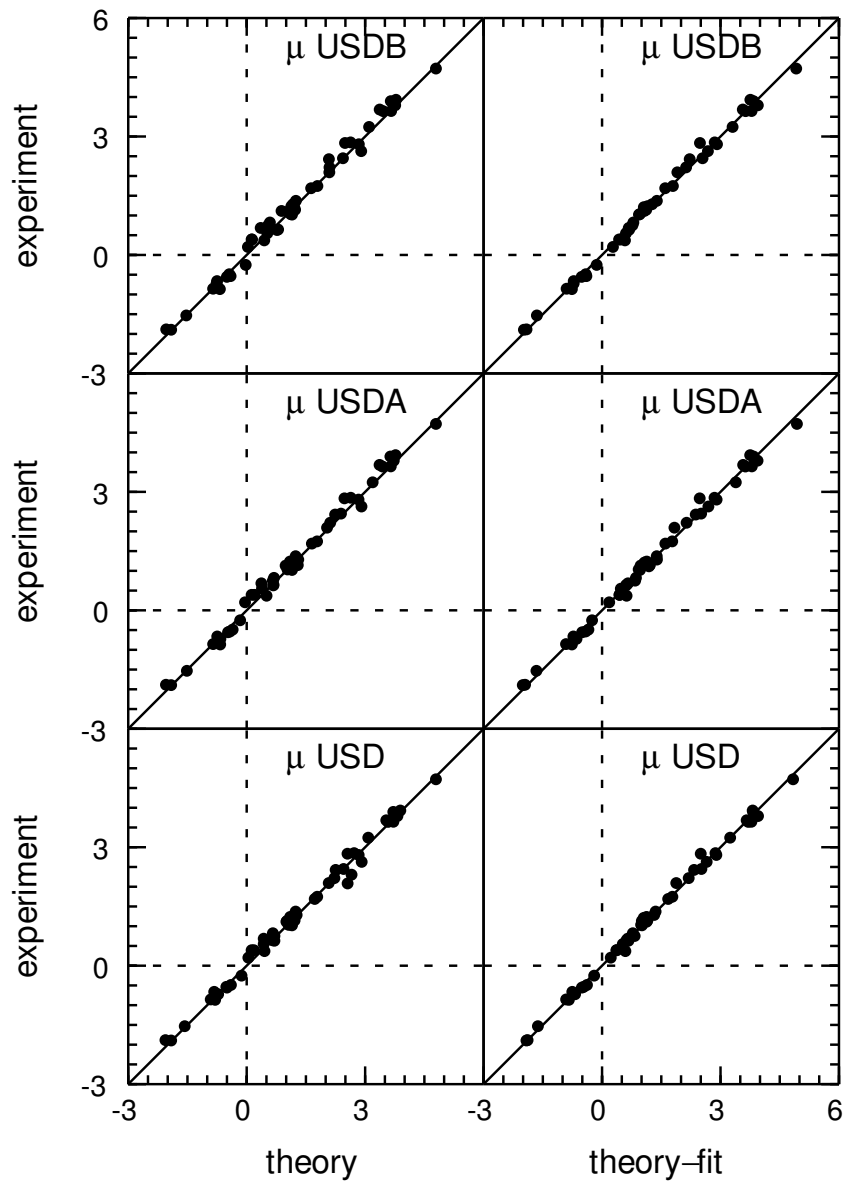


Figure 36.1: Comparison of experiment and theory for magnetic moments. The left-hand side shows the theoretical results obtained with the free-nucleon operator, and the right-hand side shows the results obtained with the fitted effective operator for $N = 6$ from Table 2.

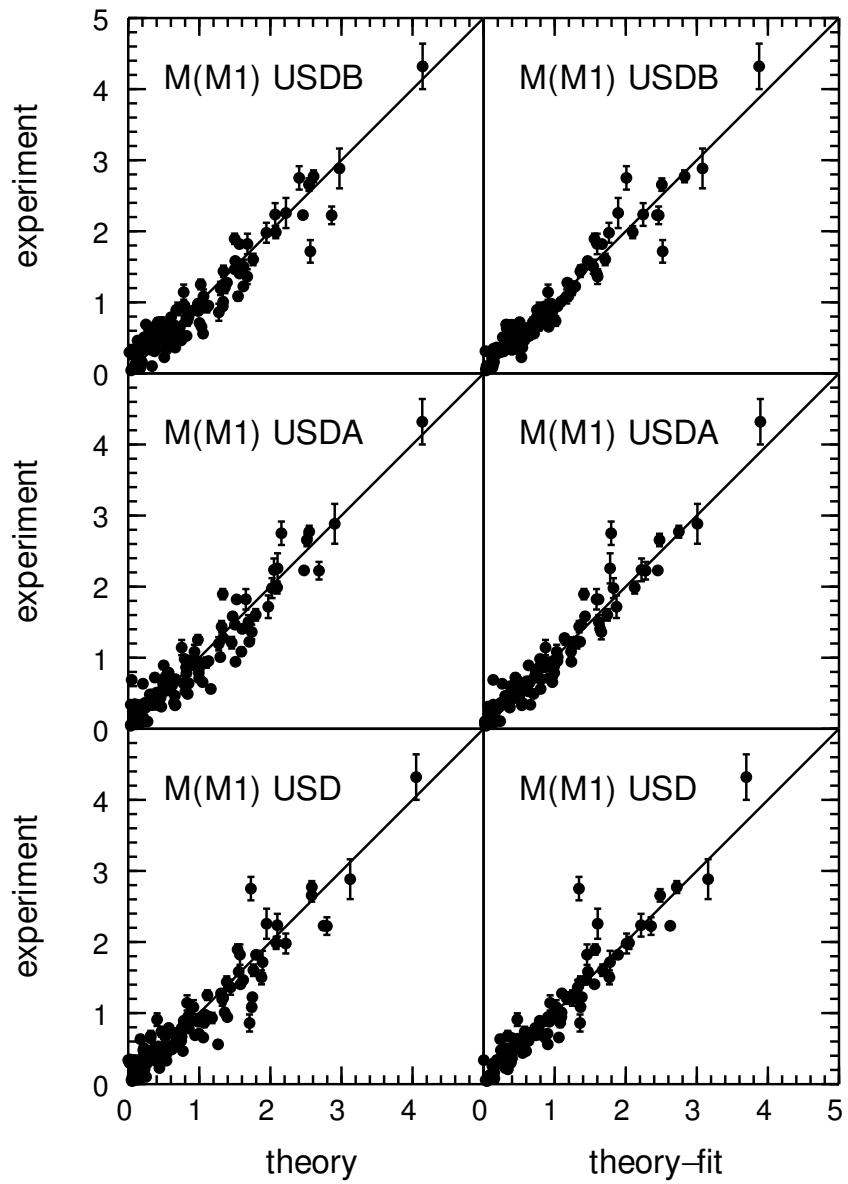


Figure 36.2: Comparison of experiment and theory for $M1$ transition matrix elements. The left-hand side shows the theoretical results obtained with the free-nucleon operator, and the right-hand side shows the results obtained with the fitted effective operator for $N = 6$ from Table 2.

Table 36.2: Results for the rms deviation and effective g-factors with the fits to M1 data with four ($N = 4$) and six parameters ($N = 6$) compared to the free-nucleon values ($N = 0$).

Ham(N)	$g_{\ell p}$	g_{sp}	g_{tp}	$g_{\ell n}$	g_{sn}	g_{tn}	rms μ	rms $M(M1)$
USD(0)	1	5.586	0	0	-3.826	0	0.125	0.264
USD(4)	1.114(23)	5.12(9)	0	-0.054(26)	-3.52(10)	0	0.104	0.241
USD(6)	1.137(24)	4.94(11)	0.34(9)	-0.079(28)	-3.38(13)	-0.22(11)	0.094	0.229
USDA(0)	1	5.586	0	0	-3.826	0	0.153	0.271
USDA(4)	1.155(23)	5.19(9)	0	-0.084(26)	-3.63(10)	0	0.124	0.236
USDA(6)	1.175(24)	5.00(11)	0.26(9)	-0.106(28)	-3.50(13)	-0.17(11)	0.118	0.223
USDB(0)	1	5.586	0	0	-3.826	0	0.165	0.252
USDB(4)	1.159(23)	5.15(9)	0	-0.09(26)	-3.55(10)	0	0.117	0.212
USDB(6)	1.174(24)	5.00(11)	0.24(9)	-0.11(28)	-3.44(13)	-0.16(13)	0.110	0.202

observables are quadrupole moments, and $E2$ transition matrix elements,

$$M_p = \langle \Psi_f | \hat{O}(E2) | \Psi_i \rangle, \quad (36.40)$$

related to the $E2$ transition probabilities by $B(E2) = M_p^2 / (2J_i + 1)$. We also write these in terms of the explicit proton and neutron components:

$$Q = e_p Q_p + e_n Q_n, \quad (36.41)$$

and

$$M_p = e_p A_p + e_n A_n, \quad (36.42)$$

where A_p are the matrix elements for protons ($e_p = 1$ and $e_n = 0$), and A_n are the matrix elements for neutrons ($e_p = 0$ and $e_n = 1$). The radial matrix elements were calculated with harmonic-oscillator radial wavefunctions with oscillator lengths fitted to the rms charge radius of the stable isotopes [12].

The result for the three Hamiltonians are compared in Figs. (36.3) and (36.4) for both the proton components (Q_p and A_p) and neutron components (Q_n and A_n) of the matrix

elements. Except for a few points, the results are remarkably the same. The largest difference shows up in USDB vs USD for A_p and A_n , by the point near the coordinates (0, 3) in the lower panels of Fig. (36.4). It corresponds to the ^{32}P $4_1^+ \rightarrow 2_1^+$ transition. The experimental matrix element for this transition is (in units of e fm 2) $M_p = 1.91(12)$ compared to the calculated results (with effective charges) of 5.30, 2.24 and 0.10 for USD, USDA and USDB, respectively. So this singular point favors the USDA Hamiltonian. In the future we will make a complete comparison for odd-odd nuclei such as ^{30}P (and ^{34}Cl mentioned in Sec. II) as a more complete test of the Hamiltonians. For the other cases considered all of the Hamiltonians give essentially the same comparison to data which we show in the top panel of Figs. (36.3) (for 26 quadrupole moments) and (36.4) (for 144 $E2$ transitions) for experiment compared to the USDB results.

The least-square fit for the effective charges (with $\sigma_{th} = 2.0$ e fm 2) gave essentially the same results for all three Hamiltonians:

$$e_p = 1.36(5)$$

and

$$e_n = 0.45(5). \quad (36.43)$$

The effective charge is essential for these $E2$ observables. There is a very large deviation with bare charges (left-hand side of the top panels in Figs. (36.3) and (36.4)) giving systematically much too small theoretical values. The effective charges reproduce the data with rms deviations of 2.1 e fm^2 for $E2$ transitions and 1.9 e fm^2 for quadrupole moments. Since all three Hamiltonians give essentially the same result for this set of observables, all of the previous analysis obtained with the USD Hamiltonian about the dependence of the effective charges on the assumptions about the radial wavefunctions is still valid [3].

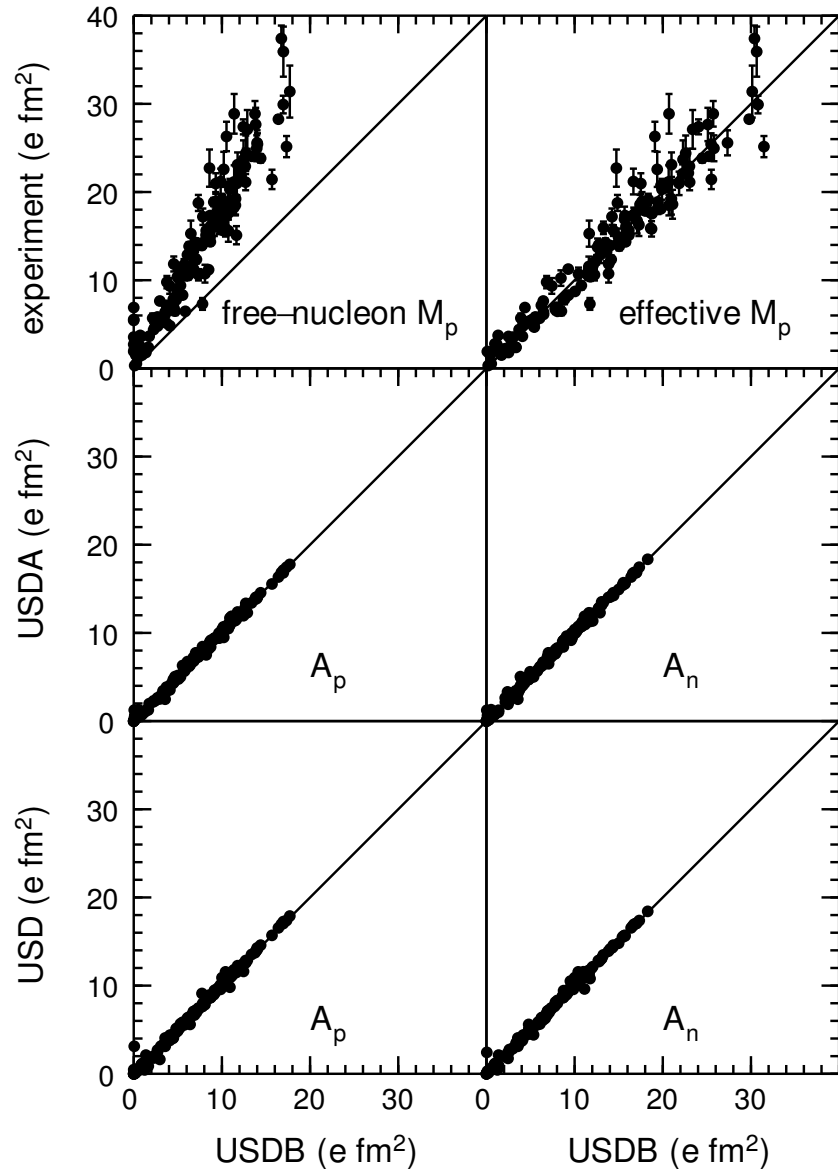


Figure 36.3: E2 transition matrix elements. The lower panels show the comparison with the different Hamiltonians. The top panel shows the comparison of experiment with the USDB calculations. The left-hand side shows the theoretical results obtained with the free-nucleon operator, and the right-hand side shows the results obtained with the fitted effective operator from Eq. (36.43).

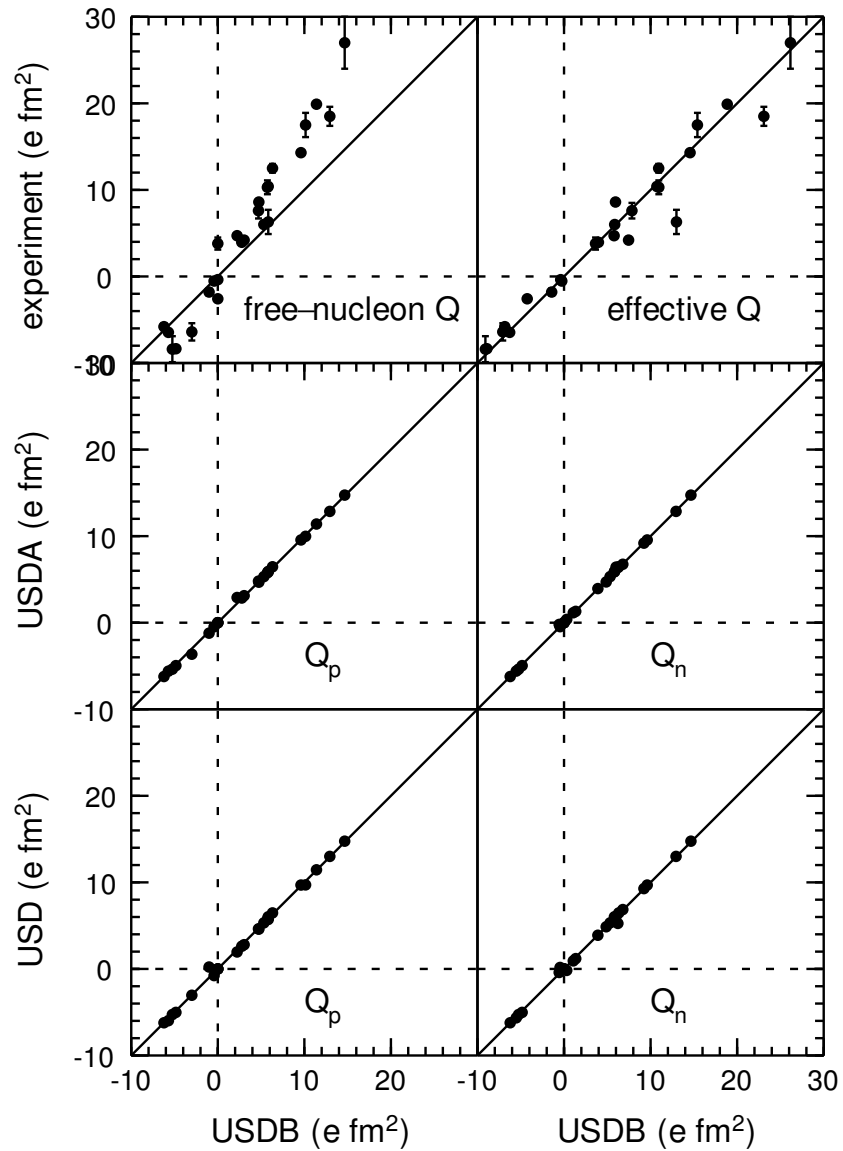


Figure 36.4: Quadrupole moments. The lower panels show the comparison with the different Hamiltonians. The top panel shows the comparison of experiment with the USDB calculations. The left-hand side shows the theoretical results obtained with the free-nucleon operator, and the right-hand side shows the results obtained with the fitted effective operator from Eq. (36.43).

Bibliography

- [1] A. Bohr and B. R. Mottelson, Nuclear Structure, Volume I, (W. A. Benjamin Inc., 1969).
- [2] B. A. Brown and W. A. Richter, Phys. Rev. C **74**, 034315 (2006) link
- [3] B. A. Brown and B. H. Wildenthal, Ann. Rev. of Nucl. Part. Sci. **38**, 29 (1988).
- [4] B. A. Brown and B. H. Wildenthal, Atomic Data and Nuclear Data Tables. **33**, 347 (1985).

- [5] N.J. Stone, Atomic and Nuclear Data Tables **90**, 75 (2005).
- [6] T. J. Mertzimekis, P. F. Mantica, A. D. Davies, S. N. Liddick and B. E. Tomlin, Phys. Rev. C **73**, 024318 (2006) link
- [7] M. B. Tsang, Jenny Lee and W. G. Lynch, Phys. Rev. Lett. **95**, 222501 (2005). link
- [8] B. A. Brown, and B. H. Wildenthal, Phys. Rev. C **28**, 2397 (1983). link
- [9] W. Geithner et al., Phys. Rev. C **71**, 064319 (2005). link
- [10] G. Huber et al., Pgts. Rev. C **18**, 2342 (1978).
- [11] M. Kowalska et al., Phys. Rev. C **77**, 034307 (2008). link
- [12] B. A. Brown, W. Chung and B. H. Wildenthal, Phys. Rev. C **22**, 774 (1980). link

Chapter 37

Allowed beta decay

964

The study of nuclear beta decay provides information both about the nature of the weak interaction and about the structure of nuclear wave functions. The types of beta decay can be classified by the angular momenta carried away by the electron and neutrino. The most important are those for $\Delta\ell=0$ which are referred to as “allowed” beta decay. There are two type of allowed beta decay - Fermi (F) and Gamow-Teller (GT). The operator associated with Fermi decay is proportional to the isospin raising and lowering operator. When isospin is conserved it can only connect isobaric analogue states and it provides an exacting test of isospin conservation in the nucleus. The operator associated with Gamow-Teller decay also contains the nucleon spin operator. Since the total spin S is not a good quantum number, Gamow-Teller beta decay goes in general to many final states and provides a sensitive test of shell-model configuration mixing in the nucleus.

37.1 Fermi decay

37.1.1 Operators and matrix elements for Fermi transitions

The operator for Fermi beta decay in terms of sums over the nucleons is

$$\hat{O}(F_{\pm}) = T_{\pm} = \sum_k t_{k\pm}. \quad (37.1)$$

where T_{\pm} is the total isospin raising and lowering operator for isospin constructed out of the basic nucleon isospin raising and lowering operators

$$t_- |n\rangle = |p\rangle, \quad t_- |p\rangle = 0,$$

and

$$t_+ |p\rangle = |n\rangle, \quad t_+ |n\rangle = 0. \quad (37.2)$$

The reduced matrix element is

$$B(F) = | \langle f | T_{\pm} | i \rangle |^2 = \frac{M(F)^2}{2J_i + 1}, \quad (37.3)$$

where

$$M(F) = \langle f || T_{\pm} || i \rangle,$$

The matrix elements obey the triangle conditions $J_f = J_i$ ($\lambda = 0$). The Fermi operator has $\pi_O = +1$, and thus the initial and final nuclear states must have $\pi_i \pi_f = +1$ for the matrix element to be nonzero under the parity transform.

The matrix element can be expanded in terms of one-body transition densities

$$M(F_{\pm}) = \delta_{j_a j_b} \sum_{k_a k_b} \langle k_a, q | | t_{\pm} | | k_b, q' \rangle \text{OBTD}(k_a, k_b, f, i), \quad (37.4)$$

where $(q, q') = (p, n)$ for β_- and $(q, q') = (n, p)$ for β_+ and

$$\text{OBTD}(k_a, k_b, f, i) = \langle f || [a_{k_a, q}^+ \otimes \tilde{a}_{k_b, q'}]_{\lambda=0} || i \rangle \quad (37.5)$$

The single-particle matrix element is

$$\langle k_a, q | t_{\pm} | k_b, q' \rangle = \sqrt{2j_a + 1} \int R_{k_a, q} R_{k_b, q'} dr \delta_{j_a, j_b}. \quad (37.6)$$

37.1.2 Results for Fermi transitions when isospin is conserved

When isospin is conserved the Fermi operator can only connect isobaric analogue states. For β_{\pm} decay

$$\begin{aligned} T_{\pm} &| \omega_i, J_i, M_i, T_i, T_{zi} \rangle \\ &= \sqrt{T_i(T_i + 1) - T_{zi}(T_{zi} \pm 1)} | \omega_i, J_i, M_i, T_i, T_{zi} \pm 1 \rangle, \end{aligned} \quad (37.7)$$

and

$$\begin{aligned} B(F_{\pm}) &= |\langle \omega_f, J_f, M_f, T_f, T_{zi} \pm 1 | T_{-} | \omega_i, J_i, M_i, T_i, T_{zi} \rangle|^2 \\ &= [T_i(T_i + 1) - T_{zi}(T_{zi} \pm 1)] \delta_{\omega_f, \omega_i} \delta_{J_f, J_i} \delta_{M_f, M_i} \delta_{T_f, T_i}. \end{aligned} \quad (37.8)$$

For neutron-rich nuclei ($N_i > Z_i$) we have $T_i = T_{zi}$ and thus

$$B(F_-)(N_i > Z_i) = 2T_{zi} = (N_i - Z_i) \delta_{\omega_f, \omega_i} \delta_{J_i, J_f} \delta_{M_i, M_f} \delta_{T_i, T_f}, \quad (37.9)$$

and

$$B(F_+)(N_i > Z_i) = 0. \quad (37.10)$$

For proton-rich nuclei ($Z_i > N_i$) we have $T_{zi} = -T_i$ and thus

$$B(F_+)(Z_i > N_i) = -2T_{zi} = (Z_i - N_i) \delta_{\omega_f, \omega_i} \delta_{J_i, J_f} \delta_{M_i, M_f} \delta_{T_i, T_f}, \quad (37.11)$$

and

$$B(F_-)(Z_i > N_i) = 0. \quad (37.12)$$

For $N_i = Z_i$, and $T = T_z = 0$, we get $B(F_-) = B(F_+) = 0$. For $N_i = Z_i$, and $T = 1$ and $T_z = 0$, we get $B(F_+) = B(F_-) = 2$.

37.1.3 Sum rule for Fermi

For the Fermi transition in nuclei $N > Z$, the sum rule is obtained from

$$\sum_f [B_{i,f}(F_-) - B_{i,f}(F_+)] = \sum_f [| \langle f | T_- | i \rangle |^2 - | \langle f | T_+ | i \rangle |^2] \quad (37.13)$$

The final states f in the T_- matrix element go with the $Z_f = Z_i + 1$ nucleus and those in the T_+ matrix element to with the $Z_f = Z_i - 1$ nucleus. One can explicitly sum over the final states to obtain

$$\begin{aligned} & \sum_f [\langle i | T_+ | f \rangle \langle f | T_- | i \rangle - \langle i | T_- | f \rangle \langle f | T_+ | i \rangle] \\ &= \langle i | T_+ T_- - T_- T_+ | i \rangle = \langle i | 2T_z | i \rangle = (N_i - Z_i). \end{aligned} \quad (37.14)$$

Thus,

$$\sum_f [B_{i,f}(F_-) - B_{i,f}(F_+)] = (N_i - Z_i) \quad (37.15)$$

For nuclei with $Z > N$

$$\sum_f [B_{i,f}(F_+) - B_{i,f}(F_-)] = (Z_i - N_i). \quad (37.16)$$

The sum-rule for the Fermi matrix elements applies even when isospin is not conserved.

When isospin is conserved we recover the results given by Eqs. (37.8) and (37.999). In particular for transitions to isobaric analogue states, for $N > Z$, $B(F_+) = 0$ and $B(F_-) = (N_i - Z_i)$, and for $Z > N$, $B(F_-) = 0$ and $B(F_+) = (Z_i - N_i)$. For $N = Z(T_{zi} = 0)$ and $T_i = 0$ we have from Eqs. (37.8) and (37.999) $B(F_+) = B(F_-) = 0$, and for $T_i = 1$ we have $B(F_+) = B(F_-) = 2$. Fermi transitions which would be zero if isospin is conserved are called isospin-forbidden Fermi transitions.

37.1.4 Data on pure Fermi decays and the KCM matrix

A compilation of results for 0^+ to 0^+ Fermi decay is made in Table IX of a recent review by Hardy and Towner [1]. The range of nuclei considered is shown in Fig. (37.1) from [2]. Many of these half-lives and branching ratios for these decays are measured with extremely high precision, down to about one part in a thousand. Towner and Hardy use phase space factors and radiative corrections that are expected to be accurate to this level. The $B(F)$ values extracted from this analysis are smaller than the expected value of 2 by 0.5 to 1.0 percent. This reduction is attributed mainly to two contributions, and nucleus dependence radiative correction called δ_{NS} , and state dependence isospin mixing factor called $\delta_C = \delta_{C1} + \delta_{C2}$. With the Coulomb interaction, the radial wavefunctions of the proton and neutron in Eq. (37.6) are slightly different resulting in slight reduction from unity. This is the δ_{C2} correction in Table X of [1] that ranges from 0.16 percent for $A = 10$ to 1.5 percent for $A = 74$. There is also a reduction from isospin mixing in the valence space that changes the OBTD values in Eq. (37.4) so that they do not add up to $\sqrt{2}$ (assuming the radial integral is unity). This is the δ_{C1} correction in Table X of [1] that ranges from 0.01 percent for $A = 10$ to 0.44 percent for $A = 70$.

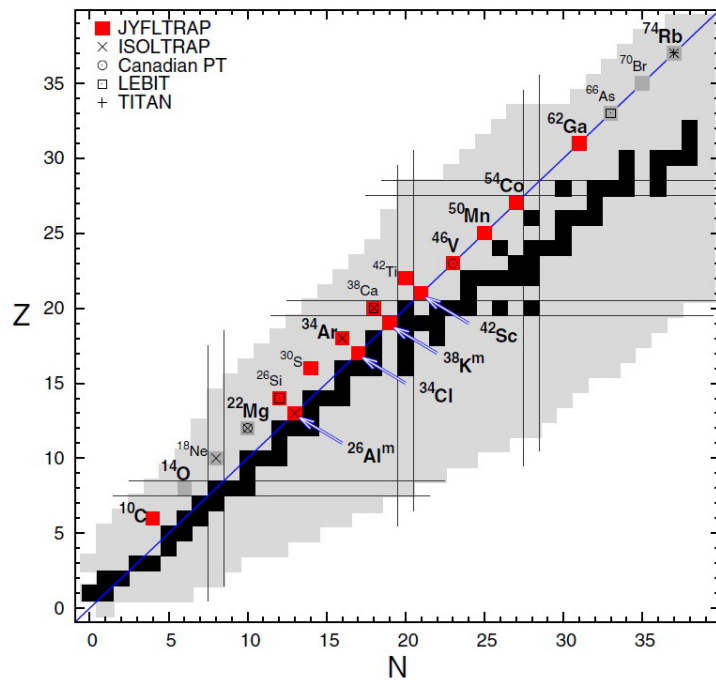


Figure 37.1: All superallowed-beta decaying nuclides that have so-far been studied in Penning-trap mass spectroscopy. The nuclei in bold are those with the highest accuracy data that contribute to the CVC hypothesis and the average Ft value.

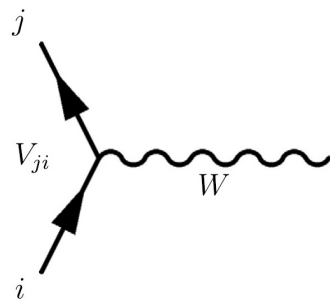


Figure 37.2: Basic Feynman diagram for the weak interaction with quarks.

When these corrections are applied to the data, the corrected ft values, called Ft , are consistent for 14 difference decays from $A = 10$ to $A = 74$ with an average value of $3072.27(72)$ s. The consistency of these data is a test of the conserved vector current (CVC) hypothesis which says that the vector part of the weak interaction is not influenced by the strong interaction [3]. However, a test of CVC requires making radiative corrections for the electromagnetic interaction.

$$V = \begin{pmatrix} V_{ud} & V_{us} & V_{ub} \\ V_{cd} & V_{cs} & V_{cb} \\ V_{td} & V_{ts} & V_{tb} \end{pmatrix}$$

Figure 37.3: The KCM matrix.

$$|V_{ud}|^2 + |V_{us}|^2 + |V_{ub}|^2 = 1$$

$$|V_{cd}|^2 + |V_{cs}|^2 + |V_{cb}|^2 = 1$$

$$|V_{td}|^2 + |V_{ts}|^2 + |V_{tb}|^2 = 1.$$

Figure 37.4: Unitarity condition for the KCM matrix.

The results provides one of the key elements, V_{ud} , for the weak interaction between quarks shown in Fig. (37.2). In the standard model the rotation between the mass eigenstates and the weak interaction eigenstates of the six quarks is described by a unitary transformation called the Cabibbo-Kobayashi-Maskawa (KCM) matrix [4] shown in Fig. (37.3). The unitarity property implies that norm of each row adds up to exactly one as shown in Fig. (37.4). V_{ud} is obtained by correcting the Ft value for the radiative decay of the neutron [5], Δ_R^V , and by dividing my the ft value for the leptonic decay of a muon into an electron. The results is

$$V_{ud} = 0.94900(42). \quad (37.17)$$

The largest source of uncertainty is in the theoretical calculations of Δ_R^V [1]. The other terms needed for the unitarity check of the top row if the KCM matrix come from particle decays, $K_{\ell 3}$ decays, $| V_{us} | = 0.2253(8)$ and $| V_{ub} | = 0.0041(5)$. In total we have

$$| V_{ud} |^2 + | V_{us} |^2 + | V_{ub} |^2 = 0.99978(55). \quad (37.18)$$

that gives a remarkably accurate test of the KCM sector of the standard model for which many precision nuclear experiments have contributed. Uncertainties related to QED corrections to V_{us} are discussed in Ref. [1].

37.2 Gamow-Teller

37.2.1 Operators and matrix elements for Gamow-Teller transitions

The operator for Gamow-Teller beta decay in terms of sums over the nucleons is

$$\hat{O}(GT_{\pm}) = \sum_k \sigma_k t_{k\pm}. \quad (37.19)$$

The reduced matrix elements is

$$B_{i,f}(GT_{\pm}) = \frac{| \langle f | \hat{O}(GT_{\pm}) | i \rangle |^2}{(2J_i + 1)} = \frac{[M_{i,f}(GT_{\pm})]^2}{(2J_i + 1)}, \quad (37.20)$$

where

$$M_{i,f}(GT_{\pm}) = \langle f | \hat{O}(GT_{\pm}) | i \rangle \quad (37.21)$$

The matrix elements are reduced in orbital space and the $(2J_i+1)$ factor comes from the sum over final M_f states. The magnitude of reduced matrix element $M(GT)$ does not depend on the direction of the transition, i.e.,

$$| M(GT, a \rightarrow b) | = | M(GT, b \rightarrow a) | \quad (37.22)$$

whereas

$$B(GT, a \rightarrow b) = \frac{(2J_b + 1)}{(2J_a + 1)} B(GT, b \rightarrow a). \quad (37.23)$$

The matrix elements obey the triangle $\Delta(J_f, J_i, \lambda = 1)$. The Gamow-Teller operator has $\pi_O = +1$, and thus the initial and final nuclear states must have $\pi_i \pi_f = +1$ for the matrix element to be nonzero under the parity transform. When isospin is conserved the Gamow-Teller matrix elements obey the isospin triangle condition $\Delta(T_f, T_i, \tau = 1)$.

In second-quantized form the GT_{\pm} operator has the form

$$O(GT_{\pm}) = \sum_{\alpha\beta} < \alpha q | \sigma t_{\pm} | \beta q' > a_{\alpha,q}^+ a_{\beta,q'}^- . \quad (37.24)$$

For GT_- we have $q = p$ and $q = n$ and for GT_+ we have $q = n$ and $q = p$. $a_{\beta,q'}$ destroys a neutron/proton in state β and $a_{\alpha,q}^+$ creates a proton/neutron in state α . The J -coupled form is

$$O(GT_{\pm}) = \sum_{k_a k_b} \langle k_a, q | |\sigma t_{\pm}| |k_b, q' \rangle \frac{[a_{k_a, q}^+ \otimes \tilde{a}_{k_b, q'}]^{J=1}}{\sqrt{(2\lambda + 1)}}. \quad (37.25)$$

The reduced matrix element for the transition from an initial state i to a final state f is given by

$$M(GT_{\pm}) = \sum_{k_a k_b} \langle k_a, q | |\sigma t_{\pm}| |k_b, q' \rangle \text{OBTD}(k_a, k_b, f, i), \quad (37.26)$$

where

$$\text{OBTD}(k_a, k_b, f, i) = \frac{\langle f | [a_{k_a, q}^+ \otimes \tilde{a}_{k_b, q'}]^{J=1} | i \rangle}{\sqrt{(2\lambda + 1)}} \quad (37.27)$$

The reduced single-particle matrix elements are given by

$$\langle k_a, q | |\sigma t_{\pm}| |k_b, q' \rangle = 2 \langle k_a | \vec{s} | k_b \rangle \int R_{k_a, q} R_{k_b, q'} dr. \quad (37.28)$$

In the harmonic oscillator model the proton and neutron radial wavefunctions are the same and the radial integral is unity. When a realistic potential with the Coulomb interaction is used the radial integral will be reduced from unity by a few percent. This can result in some mirror asymmetry in the $B(GT)$ values. But in most cases (unless explicitly stated) the radial integral is replaced by unity.

The matrix elements of \vec{s} are given by

$$\begin{aligned} & \langle k_a || \vec{s} || k_b \rangle = \langle j_a || \vec{s} || j_b \rangle \delta_{n_a, n_b} \\ & = (-1)^{\ell_a + j_a + 3/2} \sqrt{(2j_a + 1)(2j_b + 1)} \left\{ \begin{array}{ccc} 1/2 & 1/2 & 1 \\ j_b & j_a & \ell_a \end{array} \right\} \langle s || \vec{s} || s \rangle \delta_{\ell_a, \ell_b} \delta_{n_a, n_b}, \end{aligned} \quad (37.29)$$

with

$$\langle s || \vec{s} || s \rangle = \sqrt{3/2},$$

The matrix elements of \vec{s} has the selection rules δ_{ℓ_a, ℓ_b} and δ_{n_a, n_b} . Thus the orbits which are connect by the GT operator are very selective; they are those in the same major oscillator shell with the same ℓ value. The matrix elements such as $1s_{1/2} - 0d_{3/2}$ which have the

allowed $\lambda = 1$ coupling but are zero since the beta decay operator cannot change ℓ are called “ ℓ -forbidden” matrix elements.

37.2.2 Sum rule for Gamow Teller

Sum rules for Fermi and Gamow-Teller matrix elements can be obtained.

The sum rule for Gamow-Teller for nuclei with $N > Z$ is obtained as follows.

$$\begin{aligned} & \sum_{f,\mu} | \langle f | \sum_k \sigma_{k,\mu} t_{k-} | i \rangle |^2 - \sum_{f,\mu} | \langle f | \sum_k \sigma_{k,\mu} t_{k+} | i \rangle |^2 \\ &= \sum_{f,\mu} \langle i | \sum_k \sigma_{k,\mu} t_{k+} | f \rangle \langle f | \sum_{k'} \sigma_{k',\mu} t_{k'-} | i \rangle \\ & - \sum_{f,\mu} \langle i | \sum_k \sigma_{k,\mu} t_{k-} | f \rangle \langle f | \sum_{k'} \sigma_{k',\mu} t_{k'+} | i \rangle \end{aligned}$$

$$\begin{aligned}
&= \sum_{\mu} \left[\langle i | \left(\sum_k \sigma_{k,\mu} t_{k+} \right) \left(\sum_{k'} \sigma_{k',\mu} t_{k'-} \right) - \left(\sum_k \sigma_{k,\mu} t_{k-} \right) \left(\sum_{k'} \sigma_{k',\mu} t_{k'+} \right) \right] | i \rangle \\
&= \sum_{\mu} \langle i | \sum_k \sigma_{k,\mu}^2 [t_{k+} t_{k-} - t_{k-} t_{k+}] | i \rangle = 3 \langle i | \sum_k [t_{k+} t_{k-} - t_{k-} t_{k+}] | i \rangle \\
&= 3 \langle i | T_+ T_- - T_- T_+ | i \rangle = 3 \langle i | 2T_z | i \rangle = 3(N_i - Z_i). \tag{37.30}
\end{aligned}$$

We have used the fact that $\sigma_x^2 = \sigma_y^2 = \sigma_z^2 = 1$. When $k \neq k'$ the operators commute and cancel. Thus

$$\sum_f [B_{i,f}(GT_-) - B_{i,f}(GT_+)] = 3(N_i - Z_i). \tag{37.31}$$

For nuclei with $Z > N$ we have

$$\sum_f [B_{i,f}(GT_+) - B_{i,f}(GT_-)] = 3(Z_i - N_i). \tag{37.32}$$

When $N > Z$ there are some situations where one has $B(GT_+) = 0$, and then from (37.31) we have $B(GT_-) = 3(N_i - Z_i)$. In particular for the β_- decay of the neutron we have $B(F_-) = 1$ and $B(GT_-) = 3$.

37.2.3 Effective operators for Gamow-Teller matrix elements

There are several reasons why the “free-nucleon” calculations may differ from experiment. In reality the nuclear wave functions are more complicated than the theoretical model we use in that they incorporate nucleon degrees of freedom beyond the sd-shell space. In addition, non-nucleonic degrees of freedom involving the delta isobars and mesons in the nucleus may be important in the observed rates. The calculation of the corrections corresponding to these processes have been the subject of many theoretical investigations. Most recently these were carried out by Towner and Khanna [6], [7]. For references and comparisons to the earlier works, see [7] and [8].

Equivalently one can express the renormalization in terms of corrections to the GT operator. It is convenient to express the effective GT operator as:

$$O(GT_{\pm})^{eff} = 2 [(1 + \delta_s) \vec{s} + \delta_{\ell} \vec{\ell} + \delta_p \vec{p}] t_{\pm}, \quad (37.33)$$

where

$$\vec{p} = (8\pi)^{1/2} [Y^{(2)}(\vec{r}) \otimes \vec{s}]^{(1)}. \quad (37.34)$$

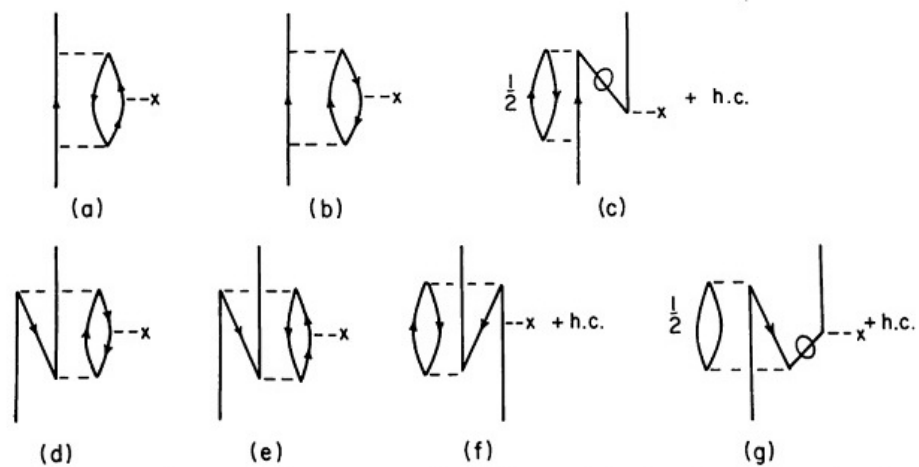


Figure 37.5: Second-order correction configuration mixing (CM) diagrams for one-body operators. This figure is taken from Fig. 10 of [7]

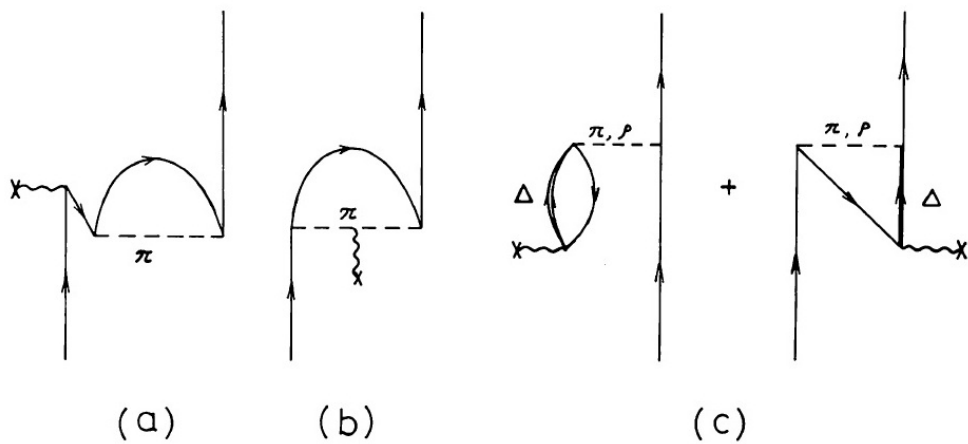


Figure 37.6: Mesonic-exchange correction diagrams for one-body operators. The corrections are divided between those involving the Δ isobar (c) and those involving the mesonic-exchange currents (MEC) (a and b). This figure is taken from Fig. 1 of [9].

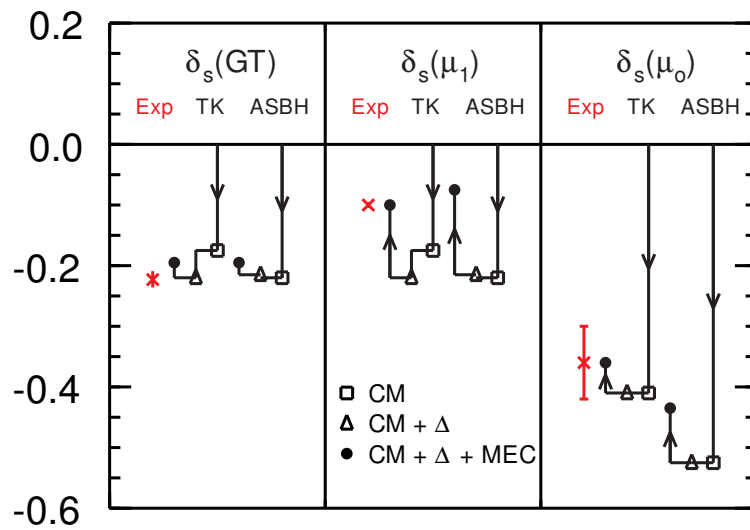


Figure 37.7: Corrections to the spin operator for Gamow-Teller (GT), isovector part of M1 (ν_1) and the isoscalar part of the M1 (ν_0). The arrows show the cumulative contributions of second-order configuration mixing (CM), the Δ isobar contribution, and the mesonic-exchange currents from Fig. (37.6).

The δ coefficients characterize the renormalizations which are needed when working within the sd-shell model space. The reduced single-particle matrix elements for the individual operator components \vec{s} , $\vec{\ell}$ and \vec{p} are given in [8]. δ_ℓ and δ_p turn out to be relatively small compared to δ_s . Thus to a good approximation we may take the effective operator as just:

$$O(GT_{\pm})^{eff} \approx 2(1 + \delta_s) \vec{s} t_{\pm} = 2 q_{GT} \vec{s} t_{\pm}, \quad (37.35)$$

q_{GT} is the Gamow-Teller quenching factor. Since the factor g_A^2 appears in front of $B(GT)$ one sometimes uses an effective g_A value. However, one must remember that this effective g_A is associated with the Gamow-Teller operator. The use of the same effective g_A for other type of operators associated with the axial-vector current must be justified.

A small δ_p value means that the ℓ -forbidden $0d_{3/2} \rightarrow 1s_{1/2}$ single-particle matrix element is not zero but is relatively small. The small branching for the beta decay of the ^{39}Ca $3/2^+$ state to the $1/2^+$ state in ^{39}K has been measured [10]. In the sd shell model these levels are just the $0d_{3/2}$ and $1s_{1/2}$ single-particle states and the ft value for this transition thus directly provides a value for the ℓ -forbidden matrix element or for the parameter $\delta_p(s-d)$. From the $A = 39$ datum a value of $|\delta_p(s-d)| = 0.017 \pm 0.003$ is obtained. The δ_p value extracted

from a fit to many sd-shell GT decays [11] is $\delta_p = +0.021(8)$. The value of δ_p is positive as expected theoretically [7].

37.2.4 Gamow-Teller transitions in the *sd* shell

The comparison of theory with experiment in the sd-shell [12] is shown in Fig. (37.8). A one parameter fit of the theory to the data with an overall quenching-factor q_{GT} gives 0.776(13), 0.791(13) and 0.764(13) for USD, USDA and USDB, respectively. It was shown in [12] that some of the scatter observed in (37.8) comes from uncertainties in the Hamiltonian.

37.2.5 Charge-exchange reactions

Charge exchange reactions can be carried out to obtain information that is complementary to that obtained in allowed beta decay. β^- , (p,n), (${}^3\text{He},\text{t}$) all have $\Delta T_z = -1$, and β^+ , (n,p),

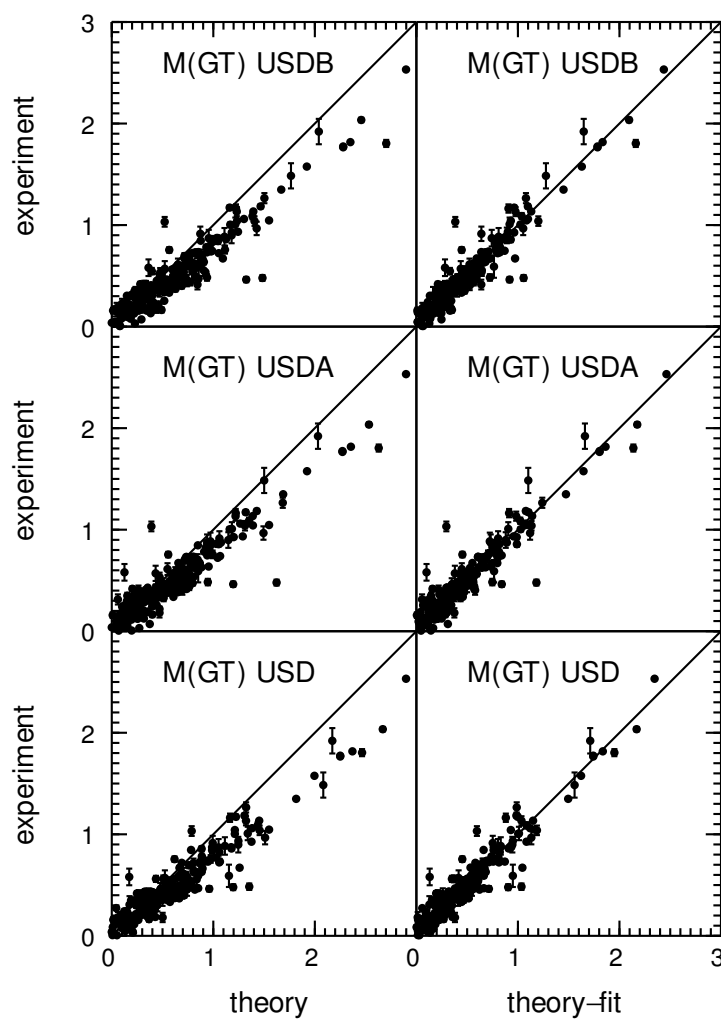


Figure 37.8: Comparison of experiment and theory for Gamow-Teller decay matrix elements.

$(t, {}^3\text{He})$ all have $\Delta T_z = -1$. It has been shown that cross sections at small angles for these types of reactions with energies of a few hundred MeV are closely proportional to the $B(F)$ and $B(GT)$ values obtained from beta decay. The information from beta decay is limited to those states that are below the beta decay Q value in the final nucleus. But reactions are not limited by this and the $B(GT)$ values can be obtained for a final states up to high excitation.

Because of the wider energy reach of charge exchange reactions is it useful to consider the isospin dependence of the strength of transition to analogue states as shown in Fig. (37.9) from [13].

The connections between isobaric analogues states can be obtained by writing the matrix element for the isovector operator in terms the square of the isospin reduced matrix element

$$\begin{aligned} & |< T_f, T_{zf} || \hat{O}^{\tau, \Delta T_z} || T_o, T_z >|^2 \\ &= \left(\begin{array}{ccc} T_f & \tau & T_o \\ -T_{zf} & \Delta T_z & T_z \end{array} \right)^2 |< T_f || \hat{O}^{\tau=1} || T_o >|^2, \end{aligned} \quad (37.36)$$

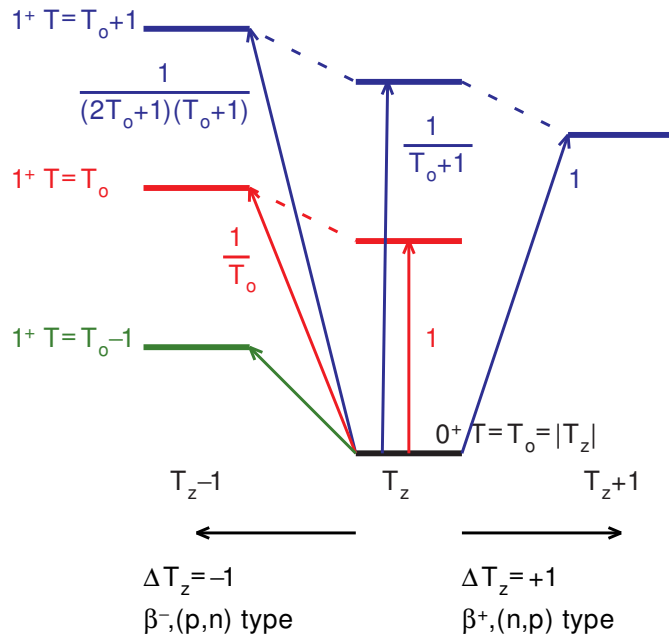


Figure 37.9: Basic isospin structure associated with charge-exchange reaction. The dotted lines indicate analog states. The states with the same color all have the same J and T as shown on the left. The arrows indicate the possible transitions and the isospin factor next to each arrow indicates the isospin factor in the isospin-reduced transition strengths. In (\bar{p}, n) -type charge-exchange reactions, the $T_0 - 1$ and T_0 states are sometimes referred to as the $T_<$ and $T_>$ states. Note that in charge-exchange reactions from nuclei with $N = Z$ ($T = T_z = 0$), only final states with $T = 1$ can be populated in both $\Delta T_z = \pm 1$ directions.

where $\tau=1$. The three- j factor gives the results for the relative strengths of transitions shown in Fig. (37.9). These results applied to ^{26}Mg are shown in Fig. (37.10), where in addition we show the Fermi β^- decay of the mirror nucleus ^{26}Si that was among those used for the extraction of V_{ud} discussed in a previous section.

By definition, charge-exchange reactions involve the t_{\pm} operators which have isospin rank ($\tau=1$). The projection of the isospin quantum number (T_z) can be raised ($\Delta T_z = +1$) in a reaction like (n,p) and or lowered ($\Delta T_z = -1$) by selecting either (n,p) or (p,n)-type charge-exchange reactions. Selectivity to other quantum numbers can be gained by selecting specific types of charge-exchange reactions, or by varying the momentum and energy transfer between the projectile and the target nucleus. A variety of charge-exchange probes have been utilized in experiments, ranging from the above-mentioned nucleonic probes to light-ion probes, such as $(^3\text{He},t)$, $(^7\text{Li},^7\text{Be})$ and heavier probes. In all of these experiments, selectivity to the angular-momentum transferred (ΔL) can be obtained by observing the response as a function of linear momentum transfer (q), which can be accomplished by studying the reaction cross sections as a function of scattering angle. Hence, it is possible qualify and quantify the response observed in charge-exchange experiments in terms of spin, isospin, and

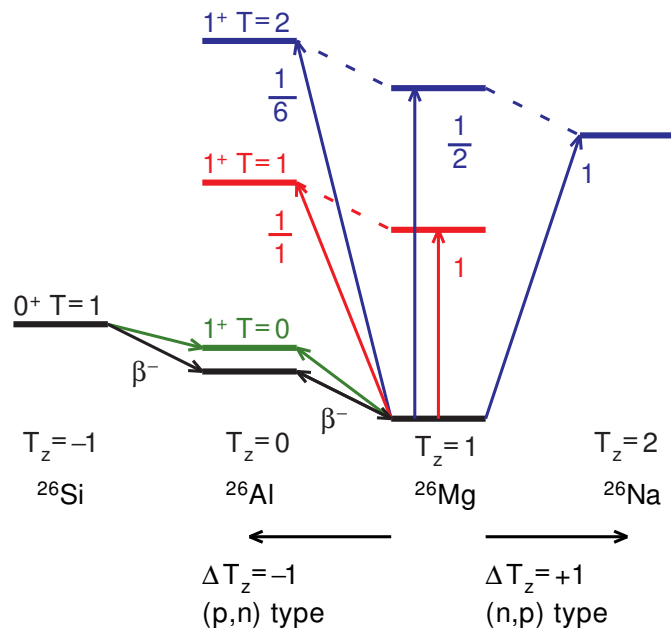


Figure 37.10: Isospin structure associated with $A = 26$ Fermi and Gamow-Teller beta decay and charge-exchange reactions. The states with the same color all have the same J and T as shown on the left.

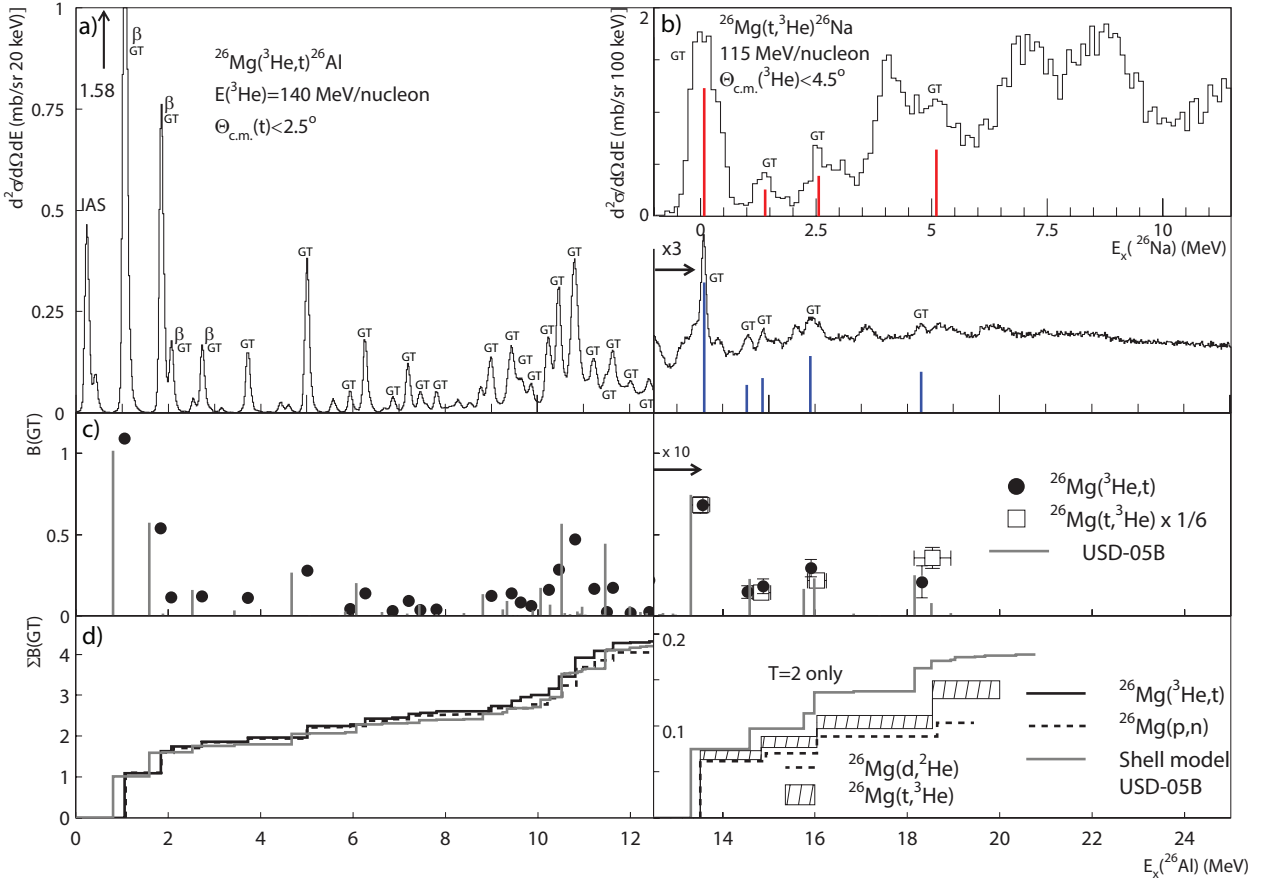


Figure 37.11: Excitation-energy spectra measured for the $^{26M}\text{g}(^3\text{He},\text{t})$ reaction at 140 A-MeV (a) and $^{26}\text{Mg}(\text{t},^3\text{He})$ reaction at 115 A-MeV (b) [14]. The latter spectrum is placed above the former such that analog 1^+ states with $T = 2$ in ^{26}Al and ^{26}Na overlap, as indicated by the dashed lines. All transitions that were identified as Gamow-Teller transitions are indicated with “GT”. For the states indicated with the symbol “ β ”, the Gamow-Teller strength is known from the ground-state decay of ^{26}Al . Panel (c) displays the extracted GT strength distribution from the above reactions, with the strength distribution from the $^{26}\text{Mg}(\text{t},^3\text{He})$ reaction shifted such that the first $T = 2$ states in both spectra align. Also shown is the GT strength distribution calculated in the sd shell-model space using the USDB interaction. The calculations have been multiplied by a factor 0.6, representing the quenching. In panel (d), the running sums of the GT strengths as a function excitation energy are shown for the $^{26}\text{Mg}(^3\text{He},\text{t})$ and $^{26}\text{Mg}(\text{p},\text{n})$ [15], [16] reactions (below 12.5 MeV), and $^{26}\text{Mg}(\text{t},^3\text{He})$ and $^{26}\text{Mg}(\text{d},^2\text{He})$ [17] reactions (above 12.5 MeV). The shell-model results are also included. The good correspondence between the results obtained with different probes shows that the extraction of the GT strengths from the charge-exchange data is probe-independent and accurate up to high excitation energies.

angular momentum transfer.

Bibliography

- [1] J. C. Hardy and I. S. Towner, Phys. Rev. C **91**, 025501 (2015). link
- [2] K. Blaum, J. Dilling, and W. Nortershauaser, Phys. Scr. **T152**, 014017 (2013).
- [3] R. P. Feynman and M. Gell-Mann, Phys. Rev. **109**, 193 (1958). link
- [4] F. C. Porter, Prog. in Part. Nucl. Phys. **91**, 101 (2016).

- [5] W. J. Marciano and A. Sirlin, Phys. Rev. Lett. **96**, 032002 (2006). link
- [6] I. S. Towner and F. C. Khanna, Nucl. Phys. A399, 334 (1983).
- [7] I. S. Towner, Phys. Rep. **155**, 263 (1987).
- [8] B. A. Brown and B. H. Wildenthal, Phys. Rev. C28, 2397 (1983). link
- [9] T. Suzuki and H. Hyuga, Nucl. Phys. **A402**, 491 (1983).
- [10] E. C. Adelberger, J. L. Osborne, H. E. Swanson and B. A. Brown, Nucl. Phys. A **417**, 269 (1984).
- [11] B. A. Brown and B. H. Wildenthal, Atomic Data Nucl. Data Tables **33**, 347 (1985).
The $B(GT)$ as defined in the present work is related to the $M(GT)$ of this references by
$$B(GT) = [M(GT)/1.251]^2/(2J_i + 1).$$
- [12] W. A. Richter, S. Mkhize, and B. A. Brown, Phys. Rev. C **78**, 064302 (2008). link

- [13] R. G. T. Zegers, B. A. Brown, G. Colo, H. Sakai and M. Sassano, Rev. of Mod. Phys. (in preparation). An example of this for the sd shell is shown in Fig. (37.12).
- [14] R. G. T. Zegers, et al., Phys. Rev. C **74**, 024309 (2006). link
- [15] R. B. S. Madey, et al., Phys. Rev. C **36**, 1647 (1987). link
- [16] R. B. S. Madey, et al., Phys. Rev. C **35**, 2011 (1987). link
- [17] T. H. Niizeki, et al., Nucl. Phys. A **577**, 37 (1994).

Chapter 38

Two-nucleon spectroscopic factors

The operator that creates an antisymmetric state of two particles coupled to angular momentum J is defined by

$$A^+(k_\alpha k_\beta J_o M_o) |> = | k_\alpha k_\beta J_o M_o >, \quad (38.1)$$

and hence from Sec. 16.2:

$$\begin{aligned} A^+(k_\alpha k_\beta J_o M_o) &= N_{12} \sum_{m_\alpha m_\beta} < j_\alpha m_\alpha j_\beta m_\beta | J_o M_o > a_{k_\beta m_\beta}^+ a_{k_\alpha m_\alpha}^+ \\ &= -N_{12} \sum_{m_\alpha m_\beta} < j_\alpha m_\alpha j_\beta m_\beta | J_o M_o > a_{k_\alpha m_\alpha}^+ a_{k_\beta m_\beta}^+ = -N_{12} [a_{k_\alpha}^+ \otimes a_{k_\beta}^+]_{M_o}^{J_o}, \end{aligned} \quad (38.2)$$

where $N_{12} = \frac{1}{\sqrt{(1+\delta_{k_\alpha k_\beta})}}$. The two-particle destruction operator is

$$\begin{aligned} A(k_\alpha k_\beta J_o M_o) &= \{A^+(k_\alpha k_\beta J_o M_o)\}^+ = \\ &= N_{12} \sum_{m_\alpha m_\beta} < j_\alpha m_\alpha j_\beta m_\beta | J_o M_o > a_{k_\alpha m_\alpha} a_{k_\beta m_\beta}. \end{aligned} \quad (38.3)$$

The tensor form of the two-particle destruction operator is

$$\begin{aligned} \tilde{A}(k_\alpha k_\beta J_o M_o) &= (-1)^{J_o - M_o} \{ A^+(k_\alpha k_\beta J_o, -M_o) \}^+ \\ &= N_{12} (-1)^{J_o - M_o} \sum_{m_\alpha m_\beta} \langle j_\alpha m_\alpha j_\beta m_\beta | J_o, -M_o \rangle a_{k_\alpha m_\alpha} a_{k_\beta m_\beta} = N_{12} [\tilde{a}_{k_\alpha} \otimes \tilde{a}_{k_\beta}]_{M_o}^{J_o}. \end{aligned} \quad (38.4)$$

Matrix elements involving \tilde{A} can be converted into those involving A^+ :

$$\begin{aligned} &\langle (n-2)\omega J | \tilde{A}(k_\alpha k_\beta J_o) | n\omega' J' \rangle \\ &= (-1)^{J_o + J - J'} \langle n\omega' J' | A^+(k_\alpha k_\beta J_o) | (n-2)\omega J \rangle. \end{aligned} \quad (38.5)$$

The two-nucleon spectroscopic amplitude (TNA) for the removal of two nucleons is defined by

$$\text{TNA}(\omega, J, \omega', J', k_\alpha, k_\beta, J_o) = \frac{\langle (n-2)\omega J | \tilde{A}(k_\alpha k_\beta J_o) | n\omega' J' \rangle}{\sqrt{(2J+1)}}. \quad (38.6)$$

The TNA be reduced to a sum over one-particle spectroscopic amplitudes by inserting a complete set of intermediate states with $(n - 1)$ particles between the a^+ of Eq. (38.2)

$$\begin{aligned} < k^n \omega J || A^+(k_\alpha k_\beta J_o) || k^{n-2} \omega' J' > &= -\frac{1}{(1 + \delta_{k_\alpha k_\beta})} (-1)^{J+J_o+J'} \sqrt{2J_o + 1} \\ &\times \sum_{\omega'', J''} \left\{ \begin{array}{ccc} J' & J & J_o \\ j_\alpha & j_\beta & J'' \end{array} \right\} < A \omega J || a_{k_\alpha}^+ || (A - 1) \omega'' J'' > < (A - 1) \omega'' J'' || a_{k_\beta}^+ || (A - 2) \omega' J' >. \end{aligned} \quad (38.7)$$

Two-particle tranfer will involve a sum over many combinations of these orbits k_α and k_β with phases that are sensitive to the correlations in the wavefunctions. Thus, what we learn from two-particle transfer experiments goes beyond what we can learn from the individual one-particle transfer.

38.1 Connection to CFP for one orbital

The matrix element for $\alpha = \beta$ is related to the two-particle CFP, denoted by

$$\langle j^n \omega J | A^+(kkJ_o) | j^{n-2} \omega' J' \rangle \equiv \sqrt{\frac{n(n-1)(2J+1)}{2}} \langle j^n \omega J | j^2(J_o); j^{n-2} \omega' J' \rangle. \quad (38.8)$$

There are a variety of notations in the literature for the two-particle CFP and the particular choice made in Eq. (38.8) is made to reflect the structure of the A^+ matrix element. Note that j is used in the two-particle CFP rather than k in order to emphasize the fact that it does not depend on the $(n\ell)$ quantum number. Wave function expansion relations and sum rules for the two-particle CFP can be derived by applying the two-particle number operator

$$\begin{aligned} & \sum_{J_o M_o} A^+(kkJ_o M_o) A(kk J_o M_o) \\ &= \frac{1}{2} \sum_{J_o M_o m_i} \langle jm_1 jm_2 | J_o M_o \rangle \langle jm_3 jm_4 | J_o M_o \rangle a_{km_2}^+ a_{km_1}^+ a_{km_3} a_{km_4} \end{aligned}$$

$$= \frac{1}{2} \sum_{m_1 m_2} a_{km_2}^+ a_{km_1}^+ a_{km_1} a_{km_2} = \frac{1}{2} (\hat{N}_k^2 - \hat{N}_k) \quad (38.9)$$

to the k^n configuration and inserting a complete set of states with $(n-2)$ particles to obtain

$$\begin{aligned} & \frac{1}{2} (\hat{N}_k^2 - \hat{N}_k) | k^n \omega JM \rangle = \frac{1}{2} n(n-1) | k^n \omega JM \rangle \\ &= \sum_{\omega'' J'' J_o} \frac{\langle k^n \omega J || A^+(kkJ_o) || k^{n-2} \omega'' J'' \rangle}{\sqrt{(2J+1)}} [Z^+(k^{n-2} \omega'' J'') \otimes A(kkJ_o)]_M^J | \rangle, \end{aligned} \quad (38.10)$$

and

$$\sum_{\omega'' J'' J_o} \langle j^n \omega' J' | \} j^2(J_o); j^{n-2} \omega'' J'' \rangle \langle j^n \omega J | \} j^2(J_0); j^{n-2} \omega'' J'' \rangle = \delta_{\omega \omega'} \delta_{JJ'}. \quad (38.11)$$

The square of the two-particle CFP is the probability that the removal of two particles in state k coupled to angular momentum J_o from the state $| k^n(\omega J) \rangle$ will leave the system in the state $| k^{n-2}(\omega'' J'') \rangle$. Since the CFP are normalized to unity, the square of the CFP for a given initial state leading only one possible final state is unity, and thus

$$|\langle j^2 J | \} j^2(J_o); j^0, J' = 0 \rangle| = \delta_{JJ_o}. \quad (38.12)$$

One finds for the two-particle CFP

$$\begin{aligned} & \langle j^{-(n-2)}\omega J | \}j^2(J_o); j^{-n}\omega' J' \rangle \equiv \langle j^{2j+1-(n-2)}\omega J | \}j^2(J_o); j^{2j+1-n}\omega' J' \rangle \\ & = (-1)^{J_o+J'-J} \sqrt{\frac{n(n-1)(2J'+1)}{[(2j+3-n)(2j+2-n)(2J+1)]}} \langle j^n\omega' J' | \}j^2(J_o); j^{n-2}\omega J \rangle. \end{aligned} \quad (38.13)$$

The case when $n = 2$ and $J = 0$ gives

$$\begin{aligned} & |\langle j^{-0}, J = 0 | \}j^2(J_o); j^{-2}J' \rangle| \\ & = \sqrt{\frac{2J'+1}{j(2j+1)}} |\langle j^2J' | \}j^2(J_o); j^0, J = 0 \rangle| = \sqrt{\frac{2J'+1}{j(2j+1)}} \delta_{J'J_o}. \end{aligned} \quad (38.14)$$

For the k^3 configuration the matrix element of A^+ can be related to the matrix element of a^+ :

$$\langle k^3J || a_k^+ || k^2J' \rangle = (-1)^{J-J'-j} \langle k^3J || A^+(kkJ') || kj \rangle, \quad (38.15)$$

which in terms of CFP is

$$\langle j^3J | \}j^2J' \rangle = (-1)^{J-J'-j} \langle j^3J | \}j^2(J'); j^1j \rangle. \quad (38.16)$$

The two-particle CFP can also be reduced to a sum over one-particle CFP by inserting a complete set of intermediate states with $(n - 1)$ particles between the a^+ of Eq. (38.2) (with $\delta_{jj} = 1$):

$$\begin{aligned}
 < k^n \omega J || A^+(kkJ_o) || k^{n-2} \omega' J' > &= -\frac{1}{\sqrt{2}} (-1)^{J+J_o+J'} \sqrt{2J_o + 1} \sum_{\omega'' J''} \left\{ \begin{array}{ccc} J' & J & J_o \\ j & j & J'' \end{array} \right\} \\
 &\times < k^n \omega J || a_k^+ || k^{n-1} \omega'' J'' > < k^{n-1} \omega'' J'' || a_k^+ || k^{n-2} \omega' J' > \\
 &= \frac{1}{\sqrt{2}} (-1)^{J+J_o+J'+1} \sqrt{(2J_o + 1)(2J + 1)n(n - 1)} \\
 &\times \sum_{\omega'' J''} \sqrt{2J'' + 1} \left\{ \begin{array}{ccc} J' & J & J_o \\ j & j & J'' \end{array} \right\} < j^n \omega J | \} j^{n-1} \omega'' J'' > < j^{n-1} \omega'' J'' | \} j^{n-2} \omega' J' >. \quad (38.17)
 \end{aligned}$$

In terms of CFP this becomes

$$\begin{aligned}
 < j^n \omega J | \} j^2(J_o); j^{n-2} \omega' J' > &= (-1)^{J+J_o+J'+1} \sqrt{2J_o + 1} \\
 &\times \sum_{\omega'' J''} \sqrt{2J'' + 1} \left\{ \begin{array}{ccc} J' & J & J_o \\ j & j & J'' \end{array} \right\} < j^n \omega J | \} j^{n-1} \omega'' J'' > < j^{n-1} \omega'' J'' | \} j^{n-2} \omega' J' >. \quad (38.18)
 \end{aligned}$$

Chapter 39

Two-body transition operators and the TBTD

1007

The M -scheme form for the two-body transition operator is:

$$\hat{T}_\mu^\lambda = \frac{1}{4} \sum_{\alpha\beta\gamma\delta} \langle \alpha\beta | T_\mu^\lambda | \gamma\delta \rangle a_\alpha^+ a_\beta^+ a_\delta a_\gamma \quad (39.1)$$

The tensor coupled form for this two-body operator is:

$$\hat{T}_\mu^\lambda = \frac{1}{4} \sum_{\substack{k_\alpha k_\beta k_\gamma k_\delta \\ m_\alpha m_\beta m_\gamma m_\delta}} \langle k_\alpha m_\alpha k_\beta m_\beta | T_\mu^\lambda | k_\gamma m_\gamma k_\delta m_\delta \rangle a_{k_\alpha m_\alpha}^+ a_{k_\beta m_\beta}^+ a_{k_\delta m_\delta} a_{k_\gamma m_\gamma} \quad (39.2)$$

$$\begin{aligned} &= \frac{1}{4} \sum_{\substack{k_\alpha k_\beta k_\gamma k_\delta \\ J_o M_o J'_o M'_o}} \sqrt{(1 + \delta_{k_\alpha k_\beta})} \sqrt{(1 + \delta_{k_\gamma k_\delta})} \langle k_\alpha k_\beta J_o M_o | T_\mu^\lambda | k_\gamma k_\delta J'_o M'_o \rangle \\ &\times \sum_{\substack{m_\alpha m_\beta \\ m_\gamma m_\delta}} \langle J_o M_o | j_\alpha m_\alpha j_\beta m_\beta \rangle \langle J'_o M'_o | j_\gamma m_\gamma j_\delta m_\delta \rangle a_{k_\alpha m_\alpha}^+ a_{k_\beta m_\beta}^+ a_{k_\delta m_\delta} a_{k_\gamma m_\gamma} \quad (39.3) \\ &= \frac{1}{4} \sum_{\substack{k_\alpha k_\beta k_\gamma k_\delta \\ J_o M_o J'_o M'_o}} \langle k_\alpha k_\beta J_o M_o | T_\mu^\lambda | k_\gamma k_\delta J'_o M'_o \rangle \end{aligned}$$

$$\times (1 + \delta_{k_\alpha k_\beta})(1 + \delta_{k_\gamma k_\delta}) A^+(k_\alpha k_\beta J_o M_o) A(k_\gamma k_\delta J'_o M'_o) \quad (39.4)$$

$$= \frac{1}{4} \sum_{\substack{k_\alpha k_\beta k_\gamma k_\delta \\ J_o J'_o}} \langle k_\alpha k_\beta J_o | |T^\lambda| |k_\gamma k_\delta J'_o \rangle$$

$$\times (1 + \delta_{k_\alpha k_\beta})(1 + \delta_{k_\gamma k_\delta}) \frac{[A^+(k_\alpha k_\beta J_o) \otimes \tilde{A}(k_\gamma k_\delta J'_o)]_\mu^\lambda}{\sqrt{2\lambda + 1}} \quad (39.5)$$

$$= \sum_{\substack{k_\alpha \leq k_\beta k_\gamma \leq k_\delta \\ J_o J'_o}} \langle k_\alpha k_\beta J_o | |T^\lambda| |k_\gamma k_\delta J'_o \rangle \frac{[A^+(k_\alpha k_\beta J_o) \otimes \tilde{A}(k_\gamma k_\delta J'_o)]_\mu^\lambda}{\sqrt{2\lambda + 1}}. \quad (39.6)$$

Eq. (39.3) is obtained by the M -scheme expansion of the J -coupled two-body matrix elements, Eq. [16.9], Eq. (39.4) comes from the definition of the two-particle operators in Eqs. [23.2] and [23.3], and Eq. (39.5) comes from the tensor coupling of the A^+ and A operators. Also note in Eq. (39.5) that the (-1) obtained from commuting $a_{k_\delta m_\delta}$ with $a_{k_\gamma m_\gamma}$ is cancelled by the (-1) from Eq. [23.2]. It is convenient to express the reduced matrix element for the n -particle wave function in the form of a product over two-body transition densities (TBTD)

times reduced two-particle matrix elements

$$\langle n\omega J || \hat{T}^\lambda || n\omega' J' \rangle = \sum_{\substack{k_\alpha \leq k_\beta, k_\gamma \leq k_\delta \\ J_o J'_o}} \text{TBTD}(fikJ_o J'_o \lambda) \langle k_\alpha k_\beta J_o || T^\lambda || k_\gamma k_\delta J'_o \rangle, \quad (39.7)$$

where the TBTD is given by

$$\text{TBTD}(fikJ_o J'_o \lambda) = \frac{\langle n\omega J || [A^+(k_\alpha k_\beta J_o) \otimes \tilde{A}(k_\gamma k_\delta J'_o)]^\lambda || n\omega' J' \rangle}{\sqrt{2\lambda + 1}}. \quad (39.8)$$

We can evaluate these in terms of matrix elements of the two-particle transfer operators by inserting a complete set of states for the $(n - 2)$ particle system

$$\begin{aligned} \text{TBTD}(fikJ_o J'_o \lambda) &= (-1)^{J+\lambda+J'} \sum_{\omega'' J''} \left\{ \begin{array}{ccc} J' & J & \lambda \\ J_o & J'_o & J'' \end{array} \right\} \\ &\times \langle n\omega J || A^+(k_\alpha k_\beta J_o) || (n-2)\omega'' J'' \rangle \langle (n-2)\omega'' J'' || \tilde{A}(k_\gamma k_\delta J'_o) || n\omega' J' \rangle \\ &= \sum_{\omega'' J''} (-1)^{J+\lambda+J''+J'_o} \left\{ \begin{array}{ccc} J' & J & \lambda \\ J_o & J'_o & J'' \end{array} \right\} \end{aligned}$$

$$\times < n\omega J || A^+(k_\alpha k_\beta J_o) || (n-2)\omega'' J'' > < n\omega' J' || A^+(k_\gamma k_\delta J'_o) || (n-2)\omega'' J'' >. \quad (39.9)$$

The dependence of the TBTD on $k_\alpha, k_\beta, k_\gamma$ and k_δ is abbreviated by k , and the dependence of the TBTD on the initial and final states is abbreviated by i and f , respectively. The TBTD represents in a compact form, the most general information needed to calculate the matrix elements of two-body operators between a given initial and final state. The results given in Sec. 23 can be used to reduce the matrix elements of A^+ to one-particle and two-particle CFP. The TBTD can be evaluated for specific configurations following the procedures given in Sec. 22 for the OBTD. The analogous results for a scalar two-body operator will be given in the next section.

39.1 Scalar two-body operators

For the special case of a scalar ($\lambda=0$) two-body operator, it is useful to define a new quantity TBTDS related to the unreduced matrix elements by

$$\begin{aligned} & \langle n\omega J | \hat{T}^{\lambda=0} | n\omega' J' \rangle \\ &= \sum_{\substack{k_\alpha \leq k_\beta \\ k_\gamma \leq k_\delta J_o}} \text{TBTDS}(fikJ_o) \langle k_\alpha k_\beta J_o | T^{\lambda=0} | k_\gamma k_\delta J_o \rangle, \end{aligned} \quad (39.10)$$

where TBTDS is given by

$$\begin{aligned} \text{TBTDS}(fikJ_o) &= \delta_{J_o J'_o} \delta_{JJ'} \sqrt{\frac{(2J_o + 1)}{(2J + 1)}} \text{TBTD}(fikJ_o J_o \lambda = 0) \\ &= (2J + 1)^{-1} \sum_{\omega'' J''} \langle n\omega J || A^+(k_\alpha k_\beta J_o) || (n - 2)\omega'' J'' \rangle \\ &\quad \times \langle n\omega' J || A^+(k_\gamma k_\delta J_o) || (n - 2)\omega'' J'' \rangle. \end{aligned} \quad (39.11)$$

This result is most often used with respect to the scalar two-body interaction V

$$\langle n\omega J | V | n\omega' J \rangle = \sum_{\substack{k_\alpha \leq k_\beta \\ k_\gamma \leq k_\delta, J_o}} \text{TBTDS}(fikJ_o) \langle k_\alpha k_\beta J_o | V | k_\gamma k_\delta J_o \rangle, \quad (39.12)$$

In the next few subsections, the TBTDS for some simple configurations will be evaluated.

39.2 Scalar TBTD for a single-orbital configuration

First consider the evaluation of the TBTDS for a single-orbital configuration

$$\begin{aligned} \text{TBTDS}(fikJ_o) &= (2J+1)^{-1} \sum_{\omega'', J''} \langle k^n \omega J || A^+(k_\alpha k_\beta J_o) || k^{n-2} \omega'' J'' \rangle \\ &\times \langle k^n \omega' J || A^+(k_\gamma k_\delta J_o) || k^{n-2} \omega'' J'' \rangle. \end{aligned} \quad (39.13)$$

The only possibility for the set $(k_\alpha k_\beta k_\gamma k_\delta)$ in the summation in Eq. (39.12) is $(kkkk)$ and, in terms of the two-particle CFP:

$$\begin{aligned} \text{TBTDS}(fikJ_o) &= \delta_{(k_\alpha k_\beta k_\gamma k_\delta), (kkkk)} \frac{n(n-1)}{2} \\ &\times \sum_{\omega'' J''} \langle j^n \omega J | \} j^2(J_o); j^{n-2} \omega'' J'' \rangle \langle j^n \omega' J | \} j^2(J_o); j^{n-2} \omega'' J'' \rangle . \end{aligned} \quad (39.14)$$

39.3 Scalar TBTD for a two-orbital configuration

For the second example, consider the interaction energy coefficient for the two-orbital configuration in which the initial and final states have the form

$$\langle i | \equiv \langle n \omega' J | = \langle (k_1^{n_1} J'_1)(k_2^{n_2} J'_2) J | ,$$

and

$$\langle f | \equiv \langle n \omega J | = \langle (k_1^{n_1} J_1)(k_2^{n_2} J_2) J | .$$

Consideration of Eq. (39.11) shows that there are three possible intermediate states

$$\begin{aligned} |a\rangle &\equiv |(n-2)\omega''J''\rangle = |(k_1^{n_1-2}J_1'')(k_2^{n_2}J_2'')J''\rangle, \\ |b\rangle &\equiv |(n-2)\omega''J''\rangle = |(k_1^{n_1-1}J_1'')(k_2^{n_2-1}J_2'')J''\rangle, \end{aligned}$$

and

$$|c\rangle \equiv |(n-2)\omega''J''\rangle = |(k_1^{n_1}J_1'')(k_2^{n_2-2}J_2'')J''\rangle.$$

The TBTDS is given by Eq. (39.12) with a sum of three terms corresponding to these three types intermediate states

$$\text{TBTDS} = \text{TBTDS}^a + \text{TBTDS}^b + \text{TBTDS}^c.$$

In case (a), the set $(\alpha\beta\gamma\delta)$ must be $(1, 1, 1, 1)$, in case (b), the set $(\alpha\beta\gamma\delta)$ must be $(1, 2, 1, 2)$, and in case (c), the set $(\alpha\beta\gamma\delta)$ must be $(2, 2, 2, 2)$. For case (a), the TBTDS can be obtained after application of Eq. [13.49] and the sum rule of Eq. [13.27] for the $6j$ coefficients

$$\text{TBTDS}^a = \delta_{(\alpha\beta\gamma\delta),(1,1,1,1)}(2J+1)^{-1}$$

$$\begin{aligned}
& \times \sum_{\omega''_1 J''_1 \omega''_2 J''_2 J''} (-1)^{2J''_2 + J'_1 + J_1 + 2J + 2J_o} \delta_{\omega_2, \omega''_2} \delta_{J_2, J''_2} \delta_{\omega'_2, \omega''_2} \delta_{J'_2, J''_2} \\
& \times < k_1^{n_1} J_1 | | A^+(k_1 k_1 J_o) | | k_1^{n_1-2} J''_1 > < k_1^{n_1} J'_1 | | A^+(k_1 k_1 J_o) | | k_1^{n_1-2} J''_1 > \\
& \times (2J+1)(2J''+1) \left\{ \begin{array}{ccc} J_1 & J''_1 & J_o \\ J'' & J & J_2 \end{array} \right\} \left\{ \begin{array}{ccc} J'_1 & J''_1 & J_o \\ J'' & J & J_2 \end{array} \right\} \\
& = \delta_{(\alpha\beta\gamma\delta), (1,1,1,1)} \frac{n_1(n_1-1)}{2} \delta_{\omega_2 \omega'_2} \delta_{J_2 J'_2} \delta_{J_1 J'_1} \\
& \times \sum_{\omega''_1 J''_1} < j_1^{n_1} \omega_1 J_1 | \} j_1^2(J_o); j_1^{n_1-2} \omega''_1 J''_1 > < j_1^{n_1} \omega'_1 J_1 | \} j_1^2(J_o); j_1^{n_1-2} \omega''_1 J''_1 > . \quad (39.15)
\end{aligned}$$

Similarly the contribution from intermediate state (c) is

$$\begin{aligned}
\text{TBTDS}^c &= \delta_{(\alpha\beta\gamma\delta), (2,2,2,2)} \frac{n_2(n_2-1)}{2} \delta_{\omega_1 \omega'_1} \delta_{J_1 J'_1} \delta_{J_2 J'_2} \\
& \times \sum_{\omega''_2 J''_2} < j_2^{n_2} \omega_2 J_2 | \} j_2^2(J_o); j_2^{n_2-2} \omega''_2 J''_2 > < j_2^{n_2} \omega'_2 J_2 | \} j_2^2(J_o); j_2^{n_2-2} \omega''_2 J''_2 > . \quad (39.16)
\end{aligned}$$

The contribution from the intermediate state $| b \rangle$ is obtained by application of Eq. [13.46]

$$\begin{aligned}
\text{TBTD}^b &= \delta_{(\alpha\beta\gamma\delta), (1,2,1,2)} (2J_o + 1) n_1 n_2 \sqrt{(2J_1 + 1)(2J_2 + 1)(2J'_1 + 1)(2J'_2 + 1)} \\
&\times \sum_{\omega''_1 J'_1 \omega''_2 J'_2} \langle j_1^{n_1} \omega_1 J_1 | \} j_1^{n_1-1} \omega''_1 J''_1 \rangle \langle j_2^{n_2} \omega_2 J_2 | \} j_2^{n_2-1} \omega''_2 J''_2 \rangle \\
&\times \langle j_1^{n_1} \omega'_1 J'_1 | \} j_1^{n_1-1} \omega''_1 J''_1 \rangle \langle j_2^{n_2} \omega'_2 J'_2 | \} j_2^{n_2-1} \omega''_2 J''_2 \rangle \\
&\times \sum_{J''} (2J'' + 1) \left\{ \begin{array}{ccc} J_1 & J_2 & J \\ J''_1 & J''_2 & J'' \\ j_1 & j_2 & J_o \end{array} \right\} \left\{ \begin{array}{ccc} J'_1 & J'_2 & J \\ J''_1 & J''_2 & J'' \\ j_1 & j_2 & J_o \end{array} \right\}. \tag{39.17}
\end{aligned}$$

There are two types of off-diagonal two-orbital terms. One in which the final states have partitions that differ from the initial state by the change of one particle

$$\langle f' | = \langle (k_1^{n_1-1} \omega_1 J_1)(k_2^{n_2+1} \omega_2 J_2) J |,$$

and another in which the final states have partitions which differ from the initial state by the change of two particles

$$\langle f'' | = \langle (k_1^{n_1-2} \omega_1 J_1) (k_2^{n_2+2} \omega_2 J_2) J | .$$

In analogy with the derivation given above for the diagonal case, explicit formulae for the TBTDS can be derived. The result for the case $|f''\rangle$ is given in [1]. Although the general analytical results for the many-orbital case become quite complicated, [2], [3] they are easily obtained numerically by using an M -scheme shell-model code or a J -projection shell-model code such as OXBASH [4].

39.4 Sample calculations for interaction energies

As a sample application, the interaction energy for the $(j = 5/2)^3$ configuration will be calculated. This is obtained from Eqs. (39.12) and (39.14) by making use of the relationship between one- and two-particle CFP as given by Eq. [23.14] together with the one-particle

CFP in Table [20.1]. For $J = 9/2$ one obtains

$$\text{TBTDS}(J = 9/2, J_o = 2) = \frac{9}{14},$$

and

$$\text{TBTDS}(J = 9/2, J_o = 4) = \frac{33}{14},$$

and thus

$$\begin{aligned} < j^3, J = 9/2 | V | j^3, J = 9/2 > &= \frac{9}{14} < j^2, J_o = 2 | V | j^2, J_o = 2 > \\ &+ \frac{33}{14} < j^2, J_o = 4 | V | j^2, J_o = 4 >. \end{aligned}$$

As a check, note that for a constant two-body interaction, $V = C$

$$< j^2, J_o = 2 | C | j^2, J_o = 2 > = < j^2, J_o = 4 | C | j^4, J_o = 4 > = C,$$

giving

$$< j^3, J = 9/2 | C | j^3, J = 9/2 > = 3C = \frac{n(n-1)C}{2},$$

where $n = 3$.

As an example of the application for the two-orbital configuration, the interaction energy for the configuration

$$| [(5/2)^2, J_1 = 4], [(1/2)^1, j_2 = 1/2], J = 9/2 >$$

is obtained with $\text{TBTDS}^a = 1$ ($J''_1 = 0$), $\text{TBTDS}^c = 0$, and

$$\text{TBTDS}^b = 18(2J_o + 1) \left\{ \begin{array}{ccc} 5/2 & 4 & 5/2 \\ 1/2 & J_o & 9/2 \end{array} \right\},$$

giving

$$\begin{aligned} < J = 9/2 | V | J = 9/2 > &= < (5/2)^2, 4 | V | (5/2)^2, 4 > \\ &+ 0.17 \times < 5/2, 1/2, 2 | V | 5/2, 1/2, 2 > \\ &+ 1.83 \times < 5/2, 1/2, 3 | V | 5/2, 1/2, 3 >. \end{aligned}$$

Bibliography

- [1] I. Talmi, *Simple Models of Complex Nuclei*, (Harwood Academic Publishers, 1993).
- [2] J. B. French, E. C. Halbert, J. B. McGrory and S. S. M. Wong, Advances in Nuclear Physics **3**, 193 (1969).
- [3] J. Q. Chen, A. Novoselsky, M. Valliers and R. Gilmore, Phys. Rev. C **39**, 1088 (1989).
[link](#)

1021

- [4] B. A. Brown, et al., the computer code OXBASH.

Chapter 40

Electron Scattering

1023

The differential cross section in the one-photon exchange approximation for the scattering of an electron with initial total energy E_i and final total energy E_f from a nucleus of mass M and charge Z through an angle θ is given in terms of the Coulomb, F_C , and transverse, F_T , form factors by [1], [2], [3], [4])

$$\frac{d\sigma(\theta, q, f, i)}{d\Omega} = \sigma_{\text{Mott}} \eta [\epsilon^2 F_C^2(q, f, i) + f(\theta) F_T^2(q, f, i)] \quad (40.1)$$

where

$$\sigma_{\text{Mott}} = \left[\frac{Z\alpha \cos(\theta/2)}{2E_i \sin^2(\theta/2)} \right]^2, \quad (40.2)$$

$$f(\theta) = \left[\frac{\epsilon}{2} + \tan^2(\theta/2) \right], \quad (40.3)$$

$$\eta = \frac{1}{\left[1 + \frac{2E_i}{M} \sin^2(\theta/2) \right]}, \quad (40.4)$$

and

$$\epsilon = 1 - \left[\frac{\omega}{(q\hbar c)} \right]^2. \quad (40.5)$$

The q and $\omega = (E_i - E_f)$ are the three-momentum transfer and energy loss, respectively, which are related by

$$(\hbar c q)^2 = 4E_i E_f \sin^2(\theta/2) + \omega^2. \quad (40.6)$$

The quantity $\alpha = e^2/\hbar c$ is the fine structure constant. The quantities η and ϵ are related to the nuclear recoil correction and are usually close to unity. The indices i and f stand for all quantum numbers that are needed to specify uniquely the initial and final nuclear states.

The nuclear form factors for inelastic scattering between an initial (i) and final (f) state or for elastic scattering ($i = f$) for a given multipolarity L are denoted by the longitudinal electric, or Coulomb, form factor $F(CL, q, f, i)$, the transverse magnetic form factor $F(ML, q, f, i)$ and the transverse electric form factor $F(EL, q, f, i)$. The total form factors are related to these by

$$F_C^2(q, f, i) = \sum_L F^2(CL, q, f, i), \quad (40.7)$$

and

$$F_T^2(q, f, i) = \sum_L [F^2(ML, q, f, i) + F^2(EL, q, f, i)]. \quad (40.8)$$

The transverse form factors can be further divided into the components Lc and Lm arising from the convection currents (due to the orbital motion of the nucleons) and the magnetization currents (due to the intrinsic magnetic moments of the nucleons), respectively:

$$F(EL, q, f, i) = F(ELc, q, f, i) + F(ELm, q, f, i), \quad (40.9)$$

$$F(ML, q, f, i) = F(MLc, q, f, i) + F(MLm, q, f, i). \quad (40.10)$$

With our normalization, $F(C0, q = 0, i = f) = 1$, for the elastic cross section. The F are sometimes normalized differently in the literature. For example, the form factor defined by Donnelly and Wakecka [4], F_{DW} , is related to our form factor, F , by $F^2 = (4\pi/Z^2)F_{DW}^2$.

The coordinate space operators associated with the proton ($t_z = 1/2$) and neutron ($t_z = -1/2$) contributions to these five kinds of form factors are

$$O(CL, q, t_z) = Y^{(L)}(\hat{r})j_L(qr)\rho_{t_z}(\vec{r}), \quad (40.11)$$

$$O(MLc, q, t_z) = \vec{M}(L, L, q, \vec{r}) \cdot \vec{J}_{t_z}(c, \vec{r}), \quad (40.12)$$

$$O(MLm, q, t_z) = \vec{M}(L, L, q, \vec{r}) \cdot \vec{J}_{t_z}(m, \vec{r}), \quad (40.13)$$

$$O(ELc, q, t_z) = (1/q)[\vec{\nabla} \otimes \vec{M}(L, L, q, \vec{r})] \cdot \vec{J}_{t_z}(c, \vec{r}), \quad (40.14)$$

and

$$O(ELm, q, t_z) = (1/q)[\vec{\nabla} \otimes \vec{M}(L, L, q, \vec{r})] \cdot \vec{J}_{t_z}(m, \vec{r}). \quad (40.15)$$

In these equations $\rho(\vec{r})$ is the charge density operator,

$$\rho_{t_z}(\vec{r}) = g_\ell(t_z)e \sum_k \delta(\vec{r} - \vec{r}_{k,t_z}), \quad (40.16)$$

$\vec{J}(c, \vec{r})$ is the convection current operator,

$$\vec{J}_{t_z}(c, \vec{r}) = -ig_\ell(t_z)u_N \sum_k [\vec{\nabla}_k \delta(\vec{r} - \vec{r}_{k,t_z}) + \delta(\vec{r} - \vec{r}_{k,t_z}) \vec{\nabla}_k], \quad (40.17)$$

and $\vec{J}(m, \vec{r})$ is the magnetic current operator

$$\vec{J}_{t_z}(m, \vec{r}) = g_s(t_z)u_N \sum_k [\vec{\nabla} \otimes (\vec{\sigma}_k/2)] \delta(\vec{r} - \vec{r}_{k,t_z}). \quad (40.18)$$

The quantities g_ℓ and g_s are the free-nucleon g factors;

$$g_\ell(p) = 1, \quad g_\ell(n) = 0, \quad (40.19)$$

and

$$g_s(p) = 5.586, \quad g_s(n) = -3.826. \quad (40.20)$$

The nuclear magniton is denoted by $u_N = e\hbar/2m_p c = 0.1051e$ fm. When the matrix elements of Eq. (40.17) are evaluated, the left and right $\vec{\nabla}$ operators operate on the wave functions to the left and right, respectively. The $\vec{\nabla}$ operator inside the brackets [] of Eqs. (40.14) and (40.15) acts only on $\vec{M}(L, L', q, \vec{r})$. The \vec{M} are the products of spherical Bessel functions and vector spherical harmonics [5], [6] $\vec{Y}^{(L,L')}(r)$:

$$\vec{M}(L, L', q, \vec{r}) = j_{L'}(qr) \vec{Y}^{(L,L')}(r), \quad (40.21)$$

where

$$\vec{Y}^{(L,L')}(r) = [Y^{(L)} \otimes r]^{(L')}. \quad (40.22)$$

In this expression the spherical components of \hat{r} are $\hat{r}_o = \hat{r}_z$ and $\hat{r}_{+1} = -(1/\sqrt{2})(\hat{r}_x + i\hat{r}_y)$ and $\hat{r}_{-1} = +(1/\sqrt{2})(\hat{r}_x - i\hat{r}_y)$. In particular, for the case $L' = L$

$$\vec{Y}^{(L,L)}(\hat{r}) = \frac{\vec{LY}^{(L)}(\hat{r})}{\sqrt{L(L+1)}}. \quad (40.23)$$

The final expression for the form factors is given by

$$F^2(XL, q, f, i) = N_p G_{\text{cm}}^2(q) \left[\sum_{t_z, x} W_{fs}(XLx, q, f, i, t_z) \right]^2, \quad (40.24)$$

where

$$N_p = \left[\frac{4\pi}{Z^2(2J_i + 1)} \right]. \quad (40.25)$$

The argument x indicates the convection (c) and magnetic current (m) contributions for the electric ($X = E$) and magnetic ($X = M$) form factors, and where x stands for the single term of Eq. (40.7) in the case of the Coulomb ($X = C$) form factor. $W_{fs}(XLx, q, f, i, t_z)$

are reduced matrix elements calculated taking into account the finite-size of the nucleons. The $(2J_i + 1)$ arises on going from the matrix element summed over final M -substates to the reduced matrix element. The normalization $4\pi/Z^2$ is chosen to make $F^2(C0, q = 0, i = f) = 1$.

The term G_{cm} is the center-of-mass correction. It divides out the form factor due to the spurious motion of the center of mass which is inherent in the fixed-center shell-model formulation. The conventional harmonic-oscillator approximation for this correction is usually used. In this approximation the center of mass is assumed to be in a $0s$ state [7],[3]. This gives

$$G_{cm}(q) = \exp(b^2 q^2 / 4A), \quad (40.26)$$

where b is the oscillator length parameter chosen to reproduce the rms radius of the nucleus.

To take into account the finite size of the nucleons one should replace the free-nucleon g factors in Eqs. (40.16), (40.17) and (40.18)

$$g(Mc, t_z) = g(Ec, t_z) = g(C, t_z) = g_\ell(t_z) \quad (40.27)$$

and

$$g(Mm, t_z) = g(Em, t_z) = g_s(t_z). \quad (40.28)$$

by the equivalent q -dependent form factors for free nucleons [3]:

$$g_{fs}(Mc, q, t_z) = g_{fs}(Ec, q, t_z) = g_{fs}(C, q, t_z) = g(c, q, t_z) \quad (40.29)$$

and

$$g_{fs}(Mm, q, t_z) = g_{fs}(Em, q, t_z) = g(m, q, t_z). \quad (40.30)$$

These are normalized so that

$$g_{fs}(X, q = 0, t_z) = g(X, t_z). \quad (40.31)$$

Three quantities $g_{fs}(c, q, p)$, $g_{fs}(c, q, n)$, and $g_{fs}(m, q, p)$ are relatively well determined experimentally [8], and for the fourth one usually assumes

$$\frac{g_{fs}(m, q, n)}{g_s(n)} = \frac{g_{fs}(m, q, p)}{g_s(p)} \quad (40.32)$$

The matrix that include the finite-size effects obtained from the point-nucleon reduced matrix $W(XLx, q, f, i, t_z)$ elements by

$$W_{fs}(XLx, q, f, i, t_z) = W(XLx, q, f, i, t_z) \frac{g_{fs}(Xx, q, t_z)}{g(Xx, t_z)}. \quad (40.33)$$

For most purposes the longitudinal form factor can be approximated in terms of the point-proton form factor, by

$$F^2(CL, q, f, i) = N_p G_{\text{cm}}^2(q) \left[g_{fs}(c, q, p) + \frac{N}{Z} g_{fs}(c, q, n) \right]^2 W^2(CL, q, f, i, p). \quad (40.34)$$

40.1 Form Factors and Transition Densities

The reduced matrix element of a one-body tensor operator $O^{(L)}$ between multi-particle states can be expressed as a sum of the products of the elements of one-body transition densities

(OBTD) times single-particle matrix elements, where the sum runs over all pairs of single-particle states in the model space:

$$\langle f || O^{(L)}(t_z) || i \rangle = \sum_{k,k'} \text{OBTD}(L, k, k', f, i, t_z) \langle k, t_z || O^{(L)} || k', t_z \rangle. \quad (40.35)$$

The OBTD are given by

$$\text{OBTD}(L, k, k', f, i, t_z) = \frac{\langle f || [a_{k,t_z}^+ \otimes \tilde{a}_{k',t_z}]^{(L)} || i \rangle}{\sqrt{2L+1}} \quad (40.36)$$

where a^+ and \tilde{a} are the nucleon creation and destruction operators.

In this context, the total transition densities (H) and total form factors (W) take the form

$$H(XL, r, f, i, t_z) = \sum_{k,k'} \text{OBTD}(L, k, k', f, i, t_z) h(XL, r, k, k', t_z), \quad (40.37)$$

$$W(XL, q, f, i, t_z) = \sum_{k,k'} \text{OBTD}(L, k, k', f, i, t_z) w(XL, q, k, k', t_z), \quad (40.38)$$

where X stands for C , Mc , Mm , Ec or Em .

With wave functions which have good isospin, it is often convenient to calculate the OBTD in isospin formalism

$$\text{OBTD}^{\Delta T}(L, k, k', f, i) = \frac{< f | | [a_k^+ \otimes \tilde{a}_{k'}]^{(L, \Delta T)} | | i >}{\sqrt{(2L + 1)(2\Delta T + 1)}}. \quad (40.39)$$

For a given T_Z , the transformation to the pn formalism is given by

$$\begin{aligned} \text{OBTD}[L, k, k', f, i, t_z = \pm 1/2] &= \\ &= \frac{1}{2} (-1)^{T_f - T_Z} \left[\sqrt{2} \begin{pmatrix} T_f & 0 & T_i \\ -T_Z & 0 & T_Z \end{pmatrix} \text{OBTD}^{\Delta T=0}(L, k, k', f, i) \right. \\ &\quad \left. \pm \sqrt{6} \begin{pmatrix} T_f & 1 & T_i \\ -T_Z & 0 & T_Z \end{pmatrix} \text{OBTD}^{\Delta T=1}(L, k, k', f, i) \right]. \end{aligned} \quad (40.40)$$

40.2 Single-Particle Form Factors and Transition Densities

The single-particle wave functions in proton-neutron (p/n) formalism by are specified by

$$| k, m, t_z \rangle = u_{k,t_z}(r) [Y^{(\ell)}(\hat{r}) \otimes \chi^s]_m^j, \quad (40.41)$$

where χ^s is the spin wave function, $k = (n, \lambda, j)$ and $t_z = p/n$. The normalization of the radial wave function is given by

$$\int | u_{k,t_z}(r) |^2 r^2 dr = 1. \quad (40.42)$$

The reduced single-particle form factors $w(q, k, k', t_z)$ are given by integrals of the appropriate multipole operators [1], [2], [3], [4]

$$w(CL, q, k, k', t_z) = \int < k, t_z | | Y^{(L)}(\hat{r}) j_L(qr) \rho_{t_z}(\vec{r}) | | k', t_z > d^3 r, \quad (40.43)$$

$$w(MLc, q, k, k', t_z) = \int \langle k, t_z | \vec{M}(L, L, q, \vec{r}) \cdot \vec{J}_{t_z}(c, \vec{r}) | k', t_z \rangle d^3r, \quad (40.44)$$

$$w(MLm, q, k, k', t_z) = \int \langle k, t_z | \vec{M}(L, L, q, \vec{r}) \cdot \vec{J}_{t_z}(m, \vec{r}) | k', t_z \rangle d^3r, \quad (40.45)$$

$$\begin{aligned} w(ELc, q, k, k', t_z) &= \\ &= (1/q) \int \langle k, t_z | [\vec{\nabla} \otimes \vec{M}(L, L, q, \vec{r})] \cdot \vec{J}_{t_z}(c, \vec{r}) | k', t_z \rangle d^3r, \end{aligned} \quad (40.46)$$

$$\begin{aligned} w(ELm, q, k, k', t_z) &= \\ &= (1/q) \int \langle k, t_z | [\vec{\nabla} \otimes \vec{M}(L, L, q, \vec{r})] \cdot \vec{J}_{t_z}(m, \vec{r}) | k', t_z \rangle d^3r. \end{aligned} \quad (40.47)$$

The integrals implicit in $\langle \rangle$ are over the nucleon coordinates \vec{r}_k .

The angular matrix elements of Eqs. (40.44)-(40.47) can be evaluated in terms of $9j$ symbols [1],[2],[4], [3], [9]). They can be expressed still more compactly by making use of the properties of the spherical Bessel functions and the $9j$ symbols [10], [11]. More details of the derivations of the expressions for the transverse magnetic form factor are given in Sec.

40.2.b. The relationships between our notations and those of Donnelly and Haxton [9] are given in Sec. 40.2.a.

All five of single-particle form factors of Eqs. (40.43)-(40.47) can be reformulated in a concise notation consisting of integrals over the radial coordinate of spherical Bessel functions $j_L(qr)$ multiplied by single-particle transition densities $h(r, k, k')$:

$$w(CL, q, k, k', t_z) = g_\ell(t_z) e \int h(CL, r, k, k', t_z) j_L(qr) r^2 dr, \quad (40.48)$$

$$w(MLc, q, k, k', t_z) = g_\ell(t_z) u_N i \int h(MLc, r, k, k', t_z) j_L(qr) r^2 dr, \quad (40.49)$$

$$w(MLm, q, k, k', t_z) = g_s(t_z) u_N i \int h(MLm, r, k, k', t_z) j_L(qr) r^2 dr, \quad (40.50)$$

$$w(ELc, q, k, k', t_z) = g_\ell(t_z) u_N (1/q) \int h(ELc, r, k, k', t_z) j_L(qr) r^2 dr, \quad (40.51)$$

and

$$w(ELm, q, k, k', t_z) = g_s(t_z) u_N q \int h(ELm, r, k, k', t_z) j_L(qr) r^2 dr. \quad (40.52)$$

The single-particle transition densities $h(r, k, k')$ are given by

$$h(CL, r, k, k', t_z) = C(EL, k, k')D(r, k, k', t_z), \quad (40.53)$$

$$h(MLc, r, k, k', t_z) = \sqrt{L(L+1)} C(ML, k, k') \left[1 + \frac{B(k, k')}{L} \right] \left[1 - \frac{B(k, k')}{L+1} \right] \frac{D(r, k, k', t_z)}{r}, \quad (40.54)$$

$$\begin{aligned} h(MLm, r, k, k', t_z) &= \frac{1}{2} \frac{1}{\sqrt{L(L+1)}} C(ML, k, k') \\ &\times \left\{ B(k, k') D'(r, k, k', t_z) + \frac{[B(k, k') - L(L+1)]}{r} D(r, k, k', t_z) \right\}, \end{aligned} \quad (40.55)$$

$$\begin{aligned} h(ELc, r, k, k', t_z) &= \frac{1}{\sqrt{L(L+1)}} C(EL, k, k') \\ &\times (1/r) \left\{ L(L+1) D^-(r, k, k', t_z) + [\ell(\ell+1) - \ell'(\ell'+1)] D'(r, k, k', t_z) \right\}, \end{aligned} \quad (40.56)$$

and

$$\begin{aligned} h(ELm, r, k, k', t_z) &= \frac{1}{2} \frac{1}{\sqrt{L(L+1)}} C(EL, k, k') \\ &\times [j(j+1) - j'(j'+1) - \ell(\ell+1) + \ell'(\ell'+1)] D(r, k, k', t_z). \end{aligned} \quad (40.57)$$

The quantities B , C and D are given by

$$B(k, k') = j(j+1) + j'(j'+1) - \ell(\ell+1) - \ell'(\ell'+1) + 1/2, \quad (40.58)$$

$$C(EL, k, k') = \langle k | Y^{(L)} | k' \rangle = P(EL, \ell, \ell') C(L, k, k'), \quad (40.59)$$

$$C(L, k, k') = (-1)^{j+1/2} \sqrt{\frac{(2j+1)(2L+1)(2j'+1)}{4\pi}} \begin{pmatrix} j & L & j' \\ 1/2 & 0 & -1/2 \end{pmatrix}, \quad (40.60)$$

$$C(ML, k, k') = P(ML, \ell, \ell') C(L, k, k'), \quad (40.61)$$

and

$$D(r, k, k', t_z) = u_{k,t_z}(r) u_{k',t_z}(r), \quad (40.62)$$

$$D'(r, k, k', t_z) = u_{k,t_z}(r) u'_{k',t_z}(r) + u'_{k,t_z}(r) u_{k',t_z}(r), \quad (40.63)$$

$$D^-(r, k, k', t_z) = u_{k,t_z}(r)u'_{k',t_z}(r) - u'_{k,t_z}(r)u_{k',t_z}(r), \quad (40.64)$$

where u' is the derivative of the radial wave function u . The $P(XL)$ in Eqs. (40.59) and (40.61) contain the parity selection rules

$$P(EL, \ell, \ell') = [1 + (-1)^{\ell+\ell'+L}]/2 \quad (40.65)$$

$$P(ML, \ell, \ell') = [1 + (-1)^{\ell+\ell'+L+1}]/2. \quad (40.66)$$

Under interchange of k and k' , $C(XL, k, k')$ has the property that

$$C(XL, k', k) = (-1)^{j'-j}C(XL, k, k'). \quad (40.67)$$

Hence the functions $h(r)$ have the properties

$$h(CL, r, k', k, t_z) = (-1)^{j'-j}h(CL, r, k, k', t_z), \quad (40.68)$$

$$h(ML, r, k', k, t_z) = (-1)^{j'-j}h(ML, r, k, k', t_z), \quad (40.69)$$

$$h(EL, r, k', k, t_z) = (-1)^{j'-j+1}h(EL, r, k, k', t_z). \quad (40.70)$$

40.3 Relationship With Other Notations

From the expressions for the transition densities given above, the coefficients given in tabular form by Donnelly and Haxton [11] can be reduced to simple expressions involving only a $3j$ symbol. The mapping between our coefficients $C(XL, k, k')$, Eq. (40.59), and $B(k, k')$, Eq. (40.58), and the coefficients A_L, B_L, C_L, D_L and E_L of Donnelly and Haxton:

$$A_L(k, k') = \sqrt{4\pi} C(EL, k, k'), \quad (40.71)$$

$$B_L(k, k') = -\sqrt{\pi L(L+1)(2L+1)} C(EL, k, k') \left[1 + \frac{B(k, k')}{L} \right] \left[1 - \frac{B(k, k')}{L+1} \right], \quad (40.72)$$

$$C_L(k, k') = \sqrt{\frac{\pi}{L(L+1)}} C(EL, k, k'), \quad (40.73)$$

$$D_L(k, k') = \sqrt{\frac{4\pi}{L(L+1)}} C(EL, k, k') \left[j(j+1) - j'(j'+1) - \ell(\ell+1) + \ell'(\ell'+1) \right], \quad (40.74)$$

$$D_L^+(k, k') = \frac{\sqrt{4\pi(L+1)}}{2L+1} C(ML, k, k') \left[1 - \frac{B(k, k')}{L+1} \right], \quad (40.75)$$

$$D_L^-(k, k') = -\frac{\sqrt{4\pi L}}{2L+1} C(ML, k, k') \left[1 + \frac{B(k, k')}{L} \right], \quad (40.76)$$

$$E_L(k, k') = -\sqrt{4\pi} C(ML, k, k'). \quad (40.77)$$

40.4 Derivation of the Transverse Magnetic Matrix Elements

After some algebra the TM single-particle matrix elements can be written in the form [1], [4]

$$w(MLc, q, k, k', t_z) = 2i\sqrt{\frac{1}{L(L+1)}} \int < k, t_z | \left\{ \sqrt{\frac{L}{(2L+1)}} \right. \\ \times \vec{M}(L, L-1, q, \vec{r}) + \sqrt{\frac{(L+1)}{(2L+1)}} \vec{M}(L, L+1, q, \vec{r}) \left. \right\} \cdot \vec{\ell}_{t_z}(\vec{r}) || k', t_z > d^3 r, \quad (40.78)$$

and

$$w(MLm, q, k, k', t_z) = (iq/2) \int < k, t_z | \left\{ \sqrt{\frac{(L+1)}{(2L+1)}} \vec{M}(L, L-1, q, \vec{r}) \right. \\ \left. - \sqrt{\frac{L}{(2L+1)}} \vec{M}(L, L+1, q, \vec{r}) \right\} \cdot \vec{\sigma}_{t_z}(\vec{r}) || k', t_z > d^3 r, \quad (40.79)$$

where $\vec{\ell}$ and $\vec{\sigma}$ are the orbital and spin operators

$$\vec{\ell}_{t_z}(\vec{r}) = g_\ell(t_z) u_N(-i/2) \sum_k \{ \vec{r} \otimes [\vec{\nabla}_k \delta(\vec{r} - \vec{r}_{k,t_z}) + \delta(\vec{r} - \vec{r}_{k,t_z}) \vec{\nabla}_k] \}, \quad (40.80)$$

and

$$\vec{\sigma}_{t_z}(\vec{r}) = g_s(t_z)u_N \sum_k (\vec{\sigma}_k/2)\delta(\vec{r} - \vec{r}_{k,t_z}). \quad (40.81)$$

These matrix elements can be reduced to [10]

$$\begin{aligned} w(MLc, q, k, k', t_z) &= iqg_\ell(t_z)u_N [\int h(MLc+, r, k, k', t_z)j_{L+1}(qr)r^2 dr \\ &\quad + \int h(MLc-, r, k, k', t_z)j_{L-1}(qr)r^2 dr] \end{aligned} \quad (40.82)$$

and

$$\begin{aligned} w(MLm, q, k, k', t_z) &= iqg_s(t_z)u_N [\int h(MLm+, r, k, k', t_z)j_{L+1}(qr)r^2 dr \\ &\quad + \int h(MLm-, r, k, k', t_z)j_{L-1}(qr)r^2 dr], \end{aligned} \quad (40.83)$$

where

$$h(MLc+, r, k, k', t_z) = h(MLc-, r, k, k', t_z) = \left[\sqrt{\frac{L(L+1)}{(2L+1)}} \right]$$

$$\times C(ML, k, k') \left[1 + \frac{B(k, k')}{L} \right] \left[1 - \frac{B(k, k')}{(L+1)} \right] D(r, k, k', t_z), \quad (40.84)$$

$$h(MLm+, r, k, k', t_z) = \left[-\frac{1}{2} \sqrt{\frac{L(L+1)}{(2L+1)}} \right] C(ML, k, k') \left[1 - \frac{B(k, k')}{(L+1)} \right] D(r, k, k', t_z) \quad (40.85)$$

and

$$h(MLm-, r, k, k', t_z) = \left[-\frac{1}{2} \sqrt{\frac{L(L+1)}{(2L+1)}} \right] C(ML, k, k') \left[1 + \frac{B(k, k')}{L} \right] D(r, k, k', t_z), \quad (40.86)$$

and where B and C are given by equations (40.58) and (40.59), respectively. By integrating equations (40.82) and (40.83) by parts and using the properties of the spherical Bessel functions, one obtains the results in the form of equations (40.49) and (40.50) where

$$h(MLc, r, k, k', t_z) = h'(MLc+, r, k, k', t_z) + \frac{(L+2)}{r} h(MLc+, r, k, k', t_z)$$

$$-h'(MLc-, r, k, k', t_z) + \frac{(L-1)}{r}h(MLc-, r, k, k', t_z), \quad (40.87)$$

and

$$\begin{aligned} h(MLm, r, k, k', t_z) &= h'(MLm+, r, k, k', t_z) + \frac{(L+2)}{r}h(MLm+, r, k, k', t_z) \\ &\quad -h'(MLm-, r, k, k', t_z) + \frac{(L-1)}{r}h(MLm-, r, k, k', t_z), \end{aligned} \quad (40.88)$$

where h' is the derivative of h . Substituting equations (40.84), (40.85) and (40.86) into equations (40.87) and (40.88) one obtains the results given in equations (40.54) and (40.55).

40.5 Relationships Provided by the Continuity Equation

The density and convection current operators for the nucleons are related by the continuity equation

$$(d/dt)\rho_{tz}(\vec{r}) = -\vec{\nabla} \cdot \vec{J}_{tz}(c, \vec{r}). \quad (40.89)$$

If one assumes the Hamiltonian to be a sum of two independent (single-particle) terms $H = H_p + H_n$ then

$$(d/dt)\rho_{tz}(\vec{r}) = (i/\hbar)[H, \rho_{tz}(\vec{r})], \quad (40.90)$$

and the matrix element of $\vec{\nabla} \cdot \vec{J}$ can then be related to that of the density operator by

$$\begin{aligned} & \langle f | \vec{\nabla} \cdot \vec{J}_{tz}(c, \vec{r}) | i \rangle = - \langle f | (d/dt)\rho_{tz}(\vec{r}) | i \rangle = \\ & = -(i/\hbar) \langle f | [H, \rho_{tz}(\vec{r})] | i \rangle = (i/\hbar)(E_{bi} - E_{bf}) \langle f | \rho_{tz}(\vec{r}) | i \rangle, \end{aligned} \quad (40.91)$$

where E_b are the binding energies. The right-hand side of this equation is sometimes easier to evaluate than the left-hand side. For example, for a single-particle Hamiltonian of the

form $H = T + U(r) + f_{so}(r)\ell \cdot \vec{s}$, the single-particle matrix element in Eq.(40.91) between spin-orbit pairs $j = l \pm \frac{1}{2}$ is zero on both sides when $f_{so} = 0$. It is clearly zero on the right-hand side because $\epsilon_i = \epsilon_f$ and will turn out to be zero on the left-hand side due to an exact cancellation between two terms. With a realistic value for $f_{so}(r)$ the matrix element $\langle f | \rho_{t_z}(\vec{r}) | i \rangle$ is not very sensitive to the spin-orbit term and all of the sensitivity comes in the single-particle energy term, $\epsilon_i - \epsilon_f$, which can easily be calculated or estimated. The matrix element on the right-hand side can be obtained to a good approximation by using, for example, harmonic-oscillator wave functions for the matrix element together with a calculation of the energy splitting. A nonzero result on the left-hand side can only be obtained by using the exact wave functions in $\langle f | \vec{\nabla} \cdot \vec{J}_{t_z}(c, \vec{r}) | i \rangle$, and again will result from the cancellation between two terms.

In general, the total Hamiltonian also contains proton-neutron interaction terms H_{pn} and the above relations can be generalized to the total isoscalar Hamiltonian, H_o , and to the total isoscalar density, $\rho_o(\vec{r}) = \rho_p(\vec{r}) + \rho_n(\vec{r})$, and current to obtain

$$\begin{aligned} & \langle f | \vec{\nabla} \cdot \vec{J}_o(\vec{r}) | i \rangle = - \langle f | (d/dt)\rho_o(\vec{r}) | i \rangle = \\ & = -(i/\hbar) \langle f | [H, \rho_o(\vec{r})] | i \rangle = (i/\hbar)(E_{bi} - E_{bf}) \langle f | \rho_o(\vec{r}) | i \rangle . \end{aligned} \quad (40.92)$$

The application of this equation can then be extended to the case where the current on the left-hand side contains not only the nucleon convection current but also mesonic-exchange currents. The exchange currents are relatively important because of the large difference in the masses of the nucleons and mesons. However, the matrix element of the density operator on the right-hand side is not very sensitive to the exchange currents because the nuclear density is dominated by the nucleon contribution. The complication due to exchange currents on the right-hand side is implicit in the binding energy terms which can be calculated independently or taken from experiment. The replacement of the current matrix element with the density matrix element is known as Seigert's theorem [12].

Even though the Seigert's theorem applies only to the isoscalar current, one usually applies it also to the isovector terms as well, with the understanding that the isovector mesonic-exchange current corrections must be considered explicitly. There is not a unique method for introducing Siegert's theory into the transverse matrix element [13]. But, the most common method [14], [15] is to integrate Eq. (40.46) by parts to obtain the single-particle form factor in the form

$$w(ELc, q, k, k', t_z) = w(ELc_1, q, k, k', t_z) + w(ELc_2, q, k, k', t_z), \quad (40.93)$$

where

$$\begin{aligned} w(ELc_1, q, k, k', t_z) &= (i/q) \frac{1}{\sqrt{L(L+1)}} \\ &\times \int < k, t_z | | j_L(qr) Y^{(L)} [(\vec{r} \cdot \vec{\nabla} + 2) \vec{\nabla} \cdot \vec{J}_{t_z}(c, \vec{r})] | | k', t_z > d^3 r, \end{aligned} \quad (40.94)$$

and

$$\begin{aligned} w(ELc_2, q, k, k', t_z) &= -(i/q) \frac{1}{\sqrt{L(L+1)}} \\ &\times \int < k, t_z | | j_L(qr) Y^{(L)} \{ \vec{\nabla}^2 [\vec{r} \cdot \vec{J}_{t_z}(c, \vec{r})] \} | | k', t_z > d^3 r. \end{aligned} \quad (40.95)$$

Using the continuity equation, the term $\vec{\nabla} \cdot \vec{J}$ in Eq. (40.94) can be replaced by $-(d/dt)\rho$, and the single-particle form factor of Eq. (40.94) can then be expressed in the form

$$\begin{aligned} w(ELc_1, q, k, k', t_z) &= \\ &= g_\ell(t_z)(e/\hbar c)(\epsilon_k - \epsilon_{k'})(1/q) \int h(ELc_1, r, k, k', t_z) j_L(qr) r^2 dr \end{aligned} \quad (40.96)$$

with

$$h(ELc_1, r, k, k', t_z) = \frac{1}{\sqrt{L(L+1)}} [2h(CL, r, k, k', t_z) + rh'(CL, r, k, k', t_z)], \quad (40.97)$$

where ϵ_k are the single-particle energies. Evaluation of Eq. (40.95) gives

$$w(ELc_2, q, k, k', t_z) = g_\ell(t_z) u_N q \int h(ELc_2, r, k, k', t_z) j_L(qr) r^2 dr, \quad (40.98)$$

with

$$h(ELc_2, r, k, k', t_z) = \frac{1}{\sqrt{L(L+1)}} C(EL, k, k') r D^-(r, k, k', t_z). \quad (40.99)$$

Since the continuity equation cannot be employed for the term ELc_2 , the exchange-current corrections should be added explicitly for this term.

In the case of multi-particle states, the relation between the longitudinal and transverse form factors provided by the continuity equation should apply to the total Hamiltonian, and

Eq. (40.96) becomes

$$W(ELc_1, q, f, i, t_z) = g_\ell(t_z)(e/\hbar c)(E_{bf} - E_{bi})(1/q) \int H(ELc_1, r, f, i, t_z) j_L(qr) r^2 dr \quad (40.100)$$

with

$$H(ELc_1, r, f, i, t_z) = \frac{1}{\sqrt{L(L+1)}} [2H(CL, r, f, i, t_z) + rH'(CL, r, f, i, t_z)], \quad (40.101)$$

where E_{bi} and E_{bf} are the total binding energies of the initial and final states, respectively.

40.6 Gamma-decay Transition Probabilities and Electron Scattering

The gamma-decay transition matrix elements $M(EL)$ and $M(ML)$, are related to the form factors $F(EL)$ and $F(ML)$, respectively, in the limit at which $\hbar c$ times the momentum

transfer is equal to the transition energy $E_\gamma = E_{bf} - E_{bi}$, or $q \rightarrow q_0 = E_\gamma/\hbar c$

$$\begin{aligned} |M(EL, f, i)| &= \lim_{q \rightarrow q_0} \sqrt{\frac{L}{(L+1)}} \frac{(2L+1)!!}{q^L N_p} F(EL, f, i, q) = \\ &= \lim_{q \rightarrow q_0} \frac{(2L+1)!!}{q^L} \sqrt{\frac{L}{(L+1)}} \sum_{t_z} W(EL, q, f, i, t_z), \end{aligned} \quad (40.102)$$

and

$$\begin{aligned} |M(ML, f, i)| &= \lim_{q \rightarrow q_0} \frac{(2L+1)!!}{q^L N_p} \sqrt{\frac{L}{(L+1)}} F(ML, f, i, q) = \\ &= \lim_{q \rightarrow q_0} \frac{(2L+1)!!}{q^L} \sqrt{\frac{L}{(L+1)}} \sum_{t_z} W(ML, q, f, i, t_z). \end{aligned} \quad (40.103)$$

[N_p is given by Eq. (40.25)]. These results are obtained by using evaluating the form factors with

$$j_L(qr) \rightarrow (qr)^L / (2L+1)!! , \quad (40.104)$$

$G_{\text{cm}}(q) \rightarrow 1$, $g_{fs}(q, t_z)/g_{t_z} \rightarrow 1$ and $g_{fs}(c, q, n) \rightarrow 0$.

When $q \rightarrow E_\gamma/\hbar c$ there is a unique relationship between $W(EL)$ and $W(CL)$ provided by the continuity equation. The term $W(ELc_2)$ can be neglected relative to $W(ELc_1)$ in Eq. (40.93), and integrating the derivative term in (40.101) by parts, one obtains

$$\begin{aligned} \lim_{q \rightarrow q_0} W(EL, q, f, i, t_z) &= \lim_{q \rightarrow q_0} W(ELc, q, f, i, t_z) = \lim_{q \rightarrow q_0} W(ELc_1, q, f, i, t_z) = \\ &= \frac{g_\ell(t_z) eq^L}{(2L+1)!!} \int H(ELc_1, r, f, i, t_z) r^L r^2 dr = \\ &= -g_\ell(t_z) e \frac{q^L}{(2L+1)!!} \sqrt{\frac{(L+1)}{L}} \int H(CL, r, f, i, t_z) r^L r^2 dr = \\ &= -\lim_{q \rightarrow q_0} \sqrt{\frac{(L+1)}{L}} W(CL, q, f, i, t_z). \end{aligned} \quad (40.105)$$

Thus the EL matrix element can be expressed in terms of the longitudinal form factor

$$| M(EL, f, i) | = \lim_{q \rightarrow q_0} \frac{(2L+1)!!}{q^L N_p} F(CL, f, i, q). \quad (40.106)$$

We can use these results to obtain explicit expressions for the electromagnetic matrix elements in the notations we have used for electron scattering

$$\begin{aligned}
|M(EL, f, i, t_z)| &= \lim_{q \rightarrow q_0} \frac{(2L+1)!!}{q^L} W(CL, q, f, i, t_z) = \\
&= e g_\ell(t_z) \int H(CL, r, f, i, t_z) r^L r^2 dr = \\
&= e \sum_{k, k'} g_\ell(t_z) \text{OBTD}(L, k, k', f, i, t_z) C(EL, k, k') \int D(r, k, k', t_z) r^L r^2 dr = \\
&= e g_\ell(t_z) \langle f | \sum_k r_{k, t_z}^L Y^{(2)}(\hat{r}_{k, t_z}) | i \rangle. \tag{40.107}
\end{aligned}$$

From Eq. (40.103) and those given in Sec. 40.2, the $M(ML)$ matrix element can be obtained explicitly as

$$|M(ML, f, i, t_z)| = u_N \sqrt{\frac{L}{(L+1)}} \left[g_\ell(t_z) \int H(MLc, r, f, i, t_z) r^L r^2 dr \right]$$

$$\begin{aligned}
& + g_s(t_z) \int H(MLm, r, f, i, t_z) r^L r^2 dr \Big] = \\
& = u_N (2L+1) \sqrt{\frac{L}{(L+1)}} \left[g_\ell(t_z) \int H(MLc-, r, f, i, t_z) r^{L-1} r^2 dr \right. \\
& \quad \left. + g_s(t_z) \int H(MLm-, r, f, i, t_z) r^{L-1} r^2 dr \right] = \\
& = u_N \sum_{k,k'} \text{OBTD}(L, k, k', f, i, t_z) C(ML, k, k') \\
& \times \left\{ g_\ell(t_z) L \left[1 + \frac{B(k, k')}{L} \right] \left[1 - \frac{B(k, k')}{(L+1)} \right] \int D(r, k, k', t_z) r^{L-1} r^2 dr \right. \\
& \quad \left. - g_s(t_z) \frac{L}{2} \left[1 + \frac{B(k, k')}{L} \right] \int D(r, k, k', t_z) r^{L-1} r^2 dr \right\}. \tag{40.108}
\end{aligned}$$

The reason for the particular choice of constants in Eqs. (40.102) and (40.103) is to make Eq. (40.107) and (40.33) take the conventional forms associated with the notations for

electromagnetic decay. The gamma-decay transition probabilities for $X = E$ or $X = M$ are given by

$$B(XL) = \frac{M(XL)^2}{(2J_i + 1)}. \quad (40.109)$$

40.7 Model-Space Truncation Effects for the Longitudinal Transition Densities

It is well established that the $B(EL)$ values which are obtained in the valence model-space calculations, and the associated CL form factors through the first maximum, are too small by about factors of three ($C2$) and four ($C4$) [16]. The primary reason for this is that the giant resonance excitations for the $C2$ and $C4$ operators couple coherently with the low lying states. Since these excitations involve, for example for the $0d1s$ shell $(0s) \rightarrow (0d1s)$ and $(0p) \rightarrow (0f2p)$ transitions, they lie outside the valence model space and must be put in by a separate calculation. This could be done microscopically using perturbation theory

[17]. A more empirical method is to use effective charges which are globally adjusted to reproduce the strengths. These effective charge can then be compared to those obtained with microscopic models.

The effective-charge model is usually applied just to the $B(EL)$ in terms of the model-space gamma-decay matrix elements $M_{\text{valence}}(EL, t_z)$ defined in analogy with (40.107) by

$$\begin{aligned} M_{\text{valence}}(EL, f, i, t_z) &= \int H_{\text{valence}}(EL, r, f, i, t_z) r^{L+2} dr = \\ &= \sum_{k,k'} \text{OBTD}(L, k, k', f, i, t_z) C(EL, k, k') \int D(r, k, k', t_z) r^{L+2} dr, \end{aligned} \quad (40.110)$$

The total matrix element is then given in terms of these $M_{\text{valence}}(EL)$ and the effective charges $\delta e(EL, t_z)$

$$M(EL, p) = M_{\text{valence}}(EL, p)e + \delta M(EL, p), \quad (40.111)$$

where

$$\delta M(EL, p) = \delta e(EL, p) M_{\text{valence}}(EL, p) + \delta e(EL, n) M_{\text{valence}}(EL, n). \quad (40.112)$$

(Here and below the explicit dependence of the quantities on f, i , is dropped.)

In order to extend this formulation to the CL form factor, it is most natural to add onto the valence transition density $H_{valence}$ a collective transition density H_T which is normalized so that its gamma-decay matrix element M_T is equal to $\delta M(EL, p)$ in Eq. (40.112). The simplest assumption we can make is that the radial shape of the of δM is the same as that obtained in the valence space. We will call this the “valence model” for the core-polarization density. Since the core-polarization arises from the coupling to the giant EL resonance it may be better to use the a transition density associated with this excitation. This shape of this collective density can be approximated by the the Tassie model [18] for the collective transition density, and thus

$$H(CL, r) = H_{valence}(CL, r) + H_T(CL, r), \quad (40.113)$$

where $H_{valence}(CL, r)$ is the point-proton transition density calculated with the SD model space OBTD and $H_T(CL, r)$ is the Tassie collective model transition density for the point protons

$$H_T(CL, r) = N_T r^{L-1} H'[C0(\text{elastic}), r, p]. \quad (40.114)$$

N_T is chosen so that the gamma-decay matrix element for $H_T(CL, r)$ is equal to $\delta M(CL, p)$.

From a systematic study of $C2$ and $C4$ form factors for even-even nuclei in the sd shell [16], it has been established that the optimum empirical values for the effective charges are

$$\delta e(E2, p) = \delta e(E2, n) = 0.35e \quad (40.115)$$

and

$$\delta e(E4, p) = \delta e(E4, n) = 0.50e. \quad (40.116)$$

For the PSD calculation, the $3\hbar\omega$ excitations give rise to a similar renormalization for the $C3$ operator. Our PSD comparisons have been made with

$$\delta e(E3, p) = \delta e(E3, n) = 0.50e. \quad (40.117)$$

In addition, one expects similar model-space truncation effects for the other operators; $C0, M1, E2, M3, E4$ and $M5$ in the SD space and $C1, E1, M2, E3$ and $M4$ in the PSD space. Usually one uses the free-nucleon orbital and spin g factors for these. The comparison

with experiment will then indicate, among other things the importance of the extra-model-space configurations to these processes. (The effective charges are used in the calculation of $H(CL, r)$ which appears in Eq. (40.101) for the convection current part of the transverse electric operator.)

40.8 Center-of-Mass Correction for the Electric Dipole Transition Density

The usual prescription for the center-of-mass correction to the form factors (Eq. (40.26)) applies only for the $0\hbar\omega$ excitations, when the center of mass is in a $0s$ state. In this section the center of mass corrections for the electric dipole ($C1$) operator are discussed.

The gamma-decay $C1$ operator is particularly simple (it is just proportional to the vector radial operator), and the associated center-of-mass correction is important and straightforward to evaluate [19]. The result can be expressed in the form of Eqs. (40.111) and

(40.112) with the effective charges

$$\delta e(C1, p) = \delta e(C1, n) = -\frac{Ze}{A}. \quad (40.118)$$

The most naive correction which would incorporate this center-of-mass correction into the $C1$ transition density would be to subtract a term proportional to the center-of-mass radial vector. This, however, would diverge for large q . This divergence can be corrected by introducing the harmonic-oscillator exponential radial factor. Thus the center-of-mass corrected quantity $H_{cm}(C1, r)$ becomes

$$H_{cm}(C1, r) = H(C1, r) + N_{cm}r \exp(-r^2/b^2), \quad (40.119)$$

where the normalization N_{cm} is chosen so that the gamma-decay matrix element for the term $N_{cm}r \exp(-r^2/b^2)$ is equal to

$$-\frac{Z}{A}[M(E1, p) + M(E1, n)]e. \quad (40.120)$$

The integral of $r \exp(-r^2/b^2)$ can be evaluated analytically to obtain

$$N_{\text{cm}} = -\frac{Z}{A} \frac{[M(E1, p) + M(E1, n)]}{[\frac{3}{8} b^5 \sqrt{4\pi}]}. \quad (40.121)$$

40.9 Differences between PWBA and DWBA

In the plane-wave Born approximation (PWBA) we neglect the influence of the electron energy on the Coulomb interaction between the electron and the nucleus. To take this interaction into account we should use the distorted-wave Born approximation (DWBA). Some of the effects the distortion can be approximated by replacing the momentum transfer q with an effective value of [20]

$$q_{\text{eff}} = q \left[1 - \frac{V_C(r)}{E_i} \right] = q \left[1 + \frac{f_c Z e^2}{E_e R_{ch}} \right], \quad (40.122)$$

where the hard-sphere radius R_{ch} is related to the rms charge radius by r_{ch} , by $R_{ch} = \sqrt{(5/3)} r_{ch}$. The value of f_c is determined from the Coulomb potential for a sphere of radius R_{ch}

$$V_C(r) = \frac{-Ze^2}{2R_{ch}} [3R_{ch}^2 - r^2]. \quad (40.123)$$

where $f_c = 3/2$ if the scattering occurs at the center of the nucleus and $f_c = 1$ if the scattering occurs at the surface. In practice one uses this by comparing the calculated PWBA form factor $F_{\text{PWBA}}^2(q)$ with a “corrected” experimental form factor $F_{\text{exp}}^2(q_{eff})$ with the rms charge radius taken from experiment for each nucleus. This approximation is good when the experimental form factors exhibit sharp minima. When the minima are washed out (filled in) it indicates that the spread in the effective electron energy at the nucleus implied by equation (40.123) is important and one should use DWBA to make a quantitative comparison of theory with data. This can be done for example with the DUELS inelastic code [21]. But PWBA is much easier to carry out and is more practical to use when appropriate. In the case of ^{25}Al [22] an empirical value of $f_c = 1.2$ give an good overlap between the DWBA form factor obtained with DUELS $F_{\text{DUELS}}^2(q_{eff})$ and that obtained with PWBA $F_{\text{PWBA}}^2(q)$.

40.10 Conversion of form factors to q -dependent matrix elements $M(q)$

The conventional display of form factors, in which $F^2(q)$ is plotted against q does not allow a simultaneous display of the $B(EL)$ value obtained from measurements of gamma-ray transition strengths with the scattering data. In addition, the exponential-type dependencies of $F(q)$ upon q dictates a logarithmic display scales which tend to submerge details. Finally, the psychological perception of conventional form-factor plots tends to be dominated by their trivial Bessel-function aspects, which makes it difficult to detect the consequences of different choices for models of nuclear structure. One can display the form factors in a representation which removes much of these trivial q dependencies. The first of these involves the factors in Eq. (40.106) for the low- q behaviour that provides a method for graphical comparisons of the form factors at small q together with the matrix element measured by gamma decay. We can also remove much of the exponential dependence on q by dividing the form factors by the exponential dependence obtained with harmonic-oscillator wave functions, namely,

the $\exp(-b^2q^2/4)$. Thus we define a momentum-dependent matrix element by

$$M(q) = |F(q)| / D(q), \quad (40.124)$$

where $D(q)$ is given by

$$D(q) = \frac{N_p q^L}{(2L+1)!!} \exp(-b_0^2 q^2/4) \exp(b_0^2 q^2/(4A)) \exp(-0.43q^2/4). \quad (40.125)$$

The harmonic-oscillator length b_0 is defined in terms of

$$\hbar\omega_0 = \frac{41.46}{b_0^2} = 45A^{-1/3} - 25A^{-2/3}. \quad (40.126)$$

The first term in Eq. (40.125) takes into account the low- q limit. The first exponential term takes into account the exponential part of the form factor in the oscillator model, the second exponential term is the center-of-mass correction and the third exponential term is the proton finite size correction. Eq. (40.124) is applied to both calculated and measured form factors in order to obtain the corresponding calculated and measured $M(q)$.

In the oscillator model, $M(q)$, is a polynomial in $(bq)^2$. For example, in the sd shell

$$M_{L=4}(q) = M_{L=4}(q = 0), \quad (40.127)$$

and

$$M_{L=2}(q) = M_{L=2}(q = 0)[1 + (qb)^2/4] \left[1 - \frac{4R_{tr}^2}{(4L + 6)b^2} \right], \quad (40.128)$$

where R_{tr} is the transition radius defined by

$$R_{tr}^2 = \frac{\int r^{L+4} \rho_L(r) dr}{\int r^{L+2} \rho_L(r) dr}. \quad (40.129)$$

For the highest possible L value L_{max} in a given oscillator shell (for example, $L_{max}=4$ for the sd shell), the form factor is proportional to $(qb)^L \exp(-b^2 q^2/4)$. This function has a maximum at

$$q_{max}^2 = (2L)/b^2, \quad (40.130)$$

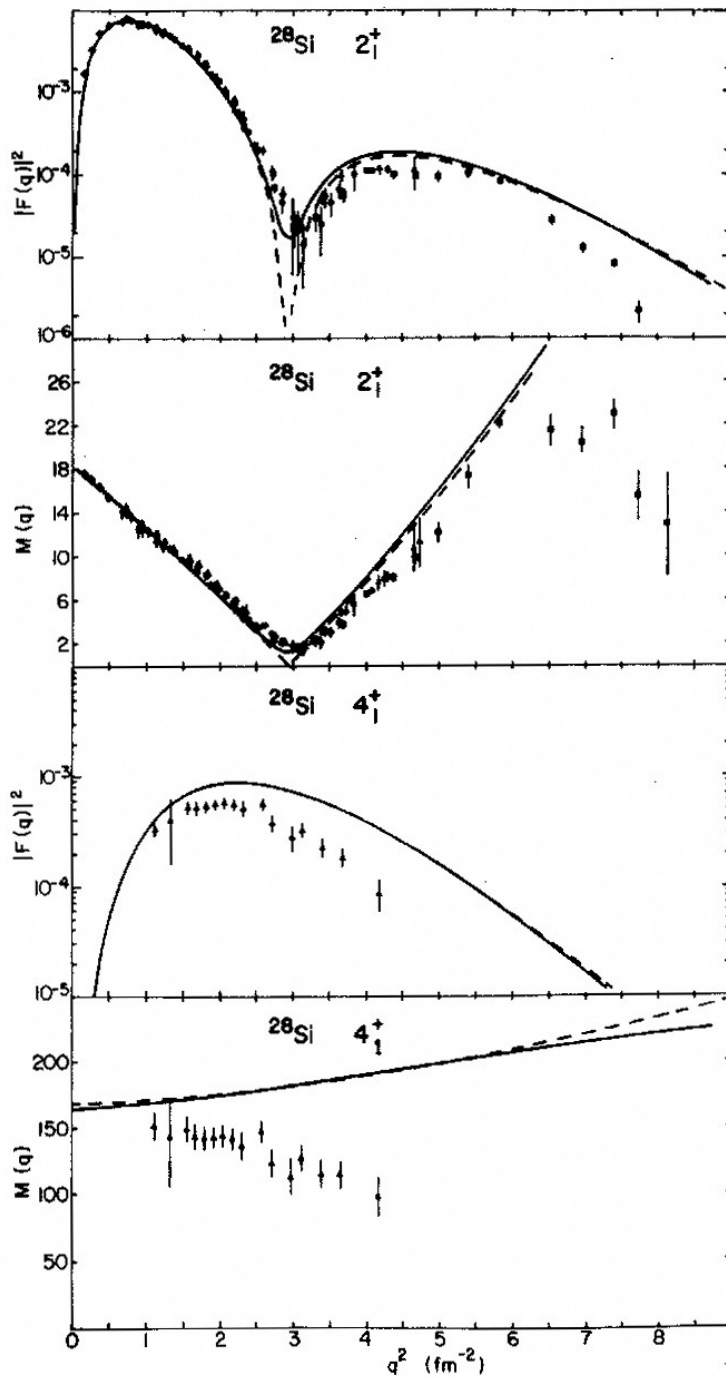


Figure 40.1: Form factors $0^+ \rightarrow 2^+$ and $0^+ \rightarrow 4^+$ inelastic scattering transitions of ^{28}Si from [16]. The DUELS DWBA results plotted vs q_{eff} (solid lines) are compared to PWBA form factors plotted vs q for the same transitions (dashed lines). The calculations incorporate the sd shell one-body transition density matrix elements obtained with the USD interaction and with harmonic-oscillator radial wavefunctions with $b = 1.827$ fm and for the valence model for the core-polarization transition density. Also shown at the $M(q)$ for theory and experiment.

and the value of the form factor at the maximum is independent of b .

A review of elastic magnetic scattering is given by Donnelly and Sick [23].

Bibliography

- [1] R. S. Willey, Nucl. Phys. 40, 529 (1963).
- [2] T. De Forest and J. D. Walecka, Adv. in Phys. 15, 1 (1966).
- [3] H. Uberall, *Electron Scattering from Complex Nuclei*, (Academic Press, Ney York and London, 1971).

- [4] T. W. Donnelly and J. D. Walecka, Nucl. Phys. A201, 81 (1973) and T. W. Donnelly and J. D. Walecka, Ann. Rev. Nucl. Sci. 1975.
- [5] M. Abramowitz and I. A. Stegun, *Handbook of Mathematical Functions* (Dover, New York, 1965).
- [6] A. R. Edmonds, *Angular Momentum in Quantum Mechanics*, (Princeton University Press, 1960).
- [7] L. J. Tassie and F. C. Barker, Phys. Rev. 111, 940 (1958).
- [8] H. Chandra and G. Sauer, Phys. Rev. C13, 245 (1976). link
- [9] T. W. Donnelly, and W. C. Haxton, Atomic and Nuclear Data Tables 23, 103 (1979).
- [10] K. Arita, Genshikaku Kenkyu 22, 119 (1977).
- [11] T. W. Donnelly, and W. C. Haxton, Atomic and Nuclear Data Tables 25, 1 (1980).
- [12] A. J. F. Siegert, Phys. Rev. 52, 787 (1937).

- [13] J. L Friar and S. Fallieros, Phys. Lett. 114B, 403 (1982).
- [14] D.Cha, Phys.Rev. C21, 1672 (1980)
- [15] J. D. Jackson, *Classical Electrodynamics*, (John Wiley and Sons, Inc.) 1962, p.556
- [16] B. A. Brown, R. Radhi and B. H. Wildenthal, Physics Reports 101, 314 (1983).
- [17] H. Sagawa and B. A. Brown, Nucl. Phys. A430, 84 (1984); and H. Sagawa and B. A. Brown, Phys. Lett. 150B, 247 (1985).
- [18] L. J. Tassie, Austr. Jour. Phys. 9, 407 (1956).
- [19] P. J. Brussaard and P. W. M. Glaudemans, *Shell-Model Applications in Nuclear Spectroscopy*, (North-Holland) 1977.
- [20] H. Uberall, Electron Scattering from Complex Nuclei (Academic Press, New York, 1971).
- [21] S. T. Tuan, L. E. Wright and D. S. Onley, Nucl. Instr. and Methods **60**, 70 (1968).

- [22] H. Euteneuer et al., Phys. Rev. **16**, 1703 (1977). link
- [23] T. W. Donnelly and I. Sick, Rev. Mod. Phys. 56, 461 (1984).